ESCAPE 34 - PSE 24

BoA

Book of Abstracts

Edited by

AIDIC

AIDIC Servizi Srl

ISBN: 979-12-81206-15-1

DOI :10.3303/BOA2401

BOOK of ABSTRACTS

34th European Symposium on Computer -Aided Process Engineering

15th International Symposium on Process Systems Engineering

ESCAPE 34 - PSE 24

AIDIC

EFCE Event #799

2-6 June 2024

Florence, Italy

Edited by AIDIC Servizi Srl

ISBN: 979-12-81206-15-1
DOI :10.3303/BOA2401

Venue

Florence, Italy
Palazzo dei Congressi- Villa Vittoria
Piazza Adua, 1, 50123 Firenze (Italy)

Administration

AIDIC SERVIZI SRL
Via Giuseppe Colombo 81A, 20133 Milano (Italy)
Website: www.aidic.it
Email: aidic_accounting@aidic.it

General Secretariat

Email: escape34-pse24@aidic.it
Phone: +39-02-70608276
Website: https://www.aidic.it/escape34-pse24/

Promoters

Computer Aided Process Engineering (CAPE)
EFCE's Working Party

The Italian Association of Chemical Engineering

European Federation of Chemical Engineering

Organizers

The Italian Association of Chemical Engineering

Governing Board

MANENTI Flavio, WP Chairman, Politecnico di Milano, Italy
REKLAITIS Gintaras V. (Rex), PSE Executive Board, Purdue University, USA
Giorgio VERONESI (AIDIC General Secretary, Techint, EFCE President)

ISC Members

ADAMS Thomas, Canada
AGRAWAL Rakesh, USA
ALMEIDA RIVERA Cristhian, The Netherlands
ARSENYEVA Olga, Ukraine
ASPRION Norbert, Germany
AVISO Kathleen, Philippines
BALDEA Michael, USA
BANDYOPADHYAY Santanu, India
BARATTI Roberto, Italy
BARBOSA POVOA Ana Paola, Portugal
BEZZO Fabrizio, Italy
BIEGLER Lorenz, USA
BOGLE David, UK
BOLLAS George, USA
BOUKOUVALA Fani, USA
BOZZANO Giulia, Italy
BROECKER Soenke, Germany
CAFARO Diego, Argentina
CAO Yankai, Canada
CHANG Chuei-Tin, Taiwan
CHEMMANGATTUVALAPPI Nishanth, Malaysia
CHENG-LIANG Chen, Taiwan
CHIEN I Lung, Taiwan
CHIU Min Sen, Singapore
CISTERNAS Luis, Chile
CREMASCHI Selen, USA
CRUZ Nicolas, Germany
DENG Chun, China
DIAZ Felipe, Chile
DOWLING Alex, USA
DURAND Helen, USA
EDEN Mario Richard, USA
EL-HALWAGI Mahmoud, USA
ENGELL Sebastian, Germany
ESPUNA Antonio, Spain
FAIRWEATHER Michael, UK
FIKAR Miroslav, Slovakia
FLORES TLACAUHUAC Antonio, Mexico
FOO Dominic C.Y., Malaysia
FORD-VERSYPT Ashlee, USA
FRIEDLER Ferenc, Hungary
FURLAN Felipe Fernando, Brazil
GANI Rafiqul, Denmark
GEORGIADIS Michail, Greece
GOMEZ Jorge Mario, Colombia
GOUNARIS Chrysanthos, USA
GROSSMANN Ignacio, USA
HANDOGO Renanto, Indonesia
HASAN Farouqe, USA
HE Yijun, China
HIRAO Masahiko, Japan
HOADLEY Andrew, Australia
HOFMANN Rene, Austria
HUSSAIN Mohd Azlan, Malaysia
IERAPETRITOU Marianthi, USA
JIMINEZ Arturo, Mexico
KANO Manabu, Japan
KAPUSTENKO Petro, Ukraine
KARIMI Iftekhar, Singapore
KAWAJIRI Yoshiaki, Japan
KELLER Andreas, Switzerland
KHEAWHOM Soorathep, Thailand
KIM Jin-Kuk, South Korea
KITTISUPAKORN Paisan, Thailand
KOKOSSIS Antonis, Greece
KONDILI Aimilia, Greece
KRASLAWSKI Andrzej, Finland
KRAVANJA Zdravko, Slovenia
KUBICEK Milan, Czech Republic
LAIRD Carl, USA
LATIFI Abderrazak, France
LE ROUX Galo Cariiillo, Brazil
LEE Jongmin, South Korea
LEE Jui-Yuan, Taiwan
LEONARD Gregoire, Belgium
LIAO Zuwei, China
LOGIST Filip, Belgium
MACIEL FILHO Rubens , Brazil
MAHALEC Vladimir, Canada
MAJOZI Thokozani, South Africa
MANCA Davide, Italy
MARECHAL Francois, Switzerland
MARTELLI Emanuele, Italy
MATOS Henrique, Portugal
MATSUMOTO Hideyuki, Japan
MCAULEY Kim, Canada
MENDEZ Carlos, Argentina
MENSHUTINA Natalia V., Russia
MHAMDI Adel, Germany
MIRCEA CRISTEA Vasile, Romania
MITSOS Alexander, Germany
MIZSEY Peter, Hungary
MOIOLI Stefania, Italy
MONTASTRUC Ludovic, France
MOON Il, South Korea
NAGY Zoltan, USA
NG Denny, Malaysia
NODA Masaru, Japan
PAPADOKONSTANTAKIS Stavros, Austria
PEREGO Patrizia, Italy
PETERS Bernhard, Luxembourg
PISTIKOPOULOS Stratos, USA
PLAZL Igor, Slovenia
PLESU Valentin, Romania
PONCE ORTEGA Jose Maria, Mexico
PREISIG Heinz, Norway
PUIGJANER Luis, Spain
REALFF Matthew, USA
RENGASWAMI Raghunathan, India
RICARDEZ-SANDOVAL Luis, Canada
RODRIGUEZ Analia, Argentina
SAMAVEDHAM Lakshminarayanan, Singapore
SECCHI Argimiro, Brazil
SEGOVIA Juan Gabriel, Mexico
SHAN-HILL WONG David, Taiwan
SIN Gurkan, Denmark
SKOGESTAD Sigurd, Norway
SMITH Robin, UK
SOHELL MANSOURI Seyed, Denmark
SOLEDAD DIAZ Maria, Argentina
SRINIVASAN Rajagopalan, India
STUBER Matt, USA
TADE Moses, Australia
TAN Raymond, Philippines
TASIC Marija, Serbia
TORRES Ana, USA
TRUSOVA Olga, Russia
TURKAY Metin, Turkey
VARBANOV Petar, Czech Republic
VECCHIETTI Aldo, Argentina
WALMSLEY Michael, New Zealand
YOO ChangKyoo, South Korea
YOSHIYUKI Yamashita, Japan
YUAN Xigang, China
YUAN Zhihong, China
ZHANG Lei, China
ZHANG Qi, USA
ZHAO Jinsong, China
ZONDERVAN Edwin, The Netherlands

CONTENT

PRINTED IN MILANO, ITALY, May 8th, 2024

PREFACE

The joint Symposium is combining the 34th European Symposium on Computer -Aided Process Engineering and the 15th International Symposium on Process Systems Engineering (PSE)

The **PSE series** of triennial conferences was initiated in 1982, rotates between venues in the Americas, Asia-Pacific and Europe and has proved to be an attractive global platform for PSE academics, researchers, and practitioners from all corners of the world to share advances in PSE education, research, and application.
The **ESCAPE series** is an annual series initiated in 1991 by the CAPE Working Party of the European Federation of Chemical Engineering which is convened at sites rotating through the member countries of the European Federation.
A joint symposium occurs in the years when the PSE rotation brings the event to Europe. The 2024 Symposium is only the fourth time that this joint event has been held (Copenhagen 2015, Garmisch-Partenkirchen 2006 and Trondheim 1997) and will combine the innovative PSE research conducted in Europe with exciting PSE developments occurring on a global scale.

The keynotes, presentations and discussions will extend over 4 stimulating days and will cover the progress made in the broad range of the methodologies of the PSE toolkit, including AI, data analytics and digitalization, as well as impactful applications in the energy, food, healthcare, materials and sustainability domains. The venue in Florence, one of the premier cultural centers of Europe, will also provide the opportunity for participants to further enrich their understanding, appreciation and enjoyment of the fine arts and cuisine of Italy.

Starting since 1966 with the former name "The use of Computers in Chemical Engineering", the Working Pary pioneered the approach to Process System Engineering with the limited tools offered at that time.
In 1991 the Working Party redefined its Terms of Reference and adopted a new Title, CAPE, Computer Aided Process Engineering.
Today computers are routinely applied throughout the entire spectrum of process and product engineering activities covering chemical, petrochemical, bio-chemical, and pharmaceutical industries and thereby, reflecting the success of the Working Parties activities. In its current form, the Working Party aims at: Acting as a focal point, within CAPE and related fields, for other EFCE Working Parties and National and International bodies, e.g. IChemE, IFAC, and AIChE. Promote good industrial practice by encouraging the development and use of CAPE methods and tools, by sharing experience in the application of existing CAPE methods and tools, by providing strategic reviews of the ongoing needs of the profession, and by identifying the potential opportunities for beneficial CAPE developments. Encourage and promote CAPE research by providing a European forum for the presentation and debate of new ideas and developments, by preparing state-of-the-art reviews of CAPE methods and tools, by stimulating new projects to meet identified needs and opportunities, both present and future The European Symposium on Computer-Aided Process Engineering (ESCAPE) is the reference event promoted every year by CAPE Working Party since 1992. It is expected that the continued participation of the past years will be maintained and enhanced also in this event.

The previous events attracted leading Industrialists and Academics worldwide and provided a state-of-the-art on Chemical and Process Engineering.

Previous events were:

ESCAPE 33, Athene, Greece, 2023
ESCAPE 32, Toulouse, France, 2022
ESCAPE 31, Istanbul, Turkey, 2021
ESCAPE 30, Milan, Italy, 2020
ESCAPE-29, Eindhoven, The Netherlands, 2019
ESCAPE-28, Graz, Austria, 2018
ESCAPE-27, Barcelona, Spain, 2017
ESCAPE-26, Portorose, Slovenia, 2016
ESCAPE-25, Copenhagen, Denmark, 2015 (Joint event with PSE 12)
ESCAPE-24, Budapest, Hungary, 2014
ESCAPE-23, Lappeenranta, Finland, 2013

ESCAPE-22, London, United Kingdom, 2012
ESCAPE-21, Porto Carras, Greece, 2011
ESCAPE-20, Ischia, Italy, 2010
ESCAPE-19, Krakow, Poland, 2019
ESCAPE-18, Lyon, France, 2008
ESCAPE-17, Bucharest, Romania, 2007
ESCAPE-16, Garmisch-Partenkirchen, Germany, 2006 (Joint event with PSE 9)
ESCAPE-15, Barcelona, Spain, 2005
ESCAPE-14, Lisbon, Portugal, 2004
ESCAPE-13, Lappeenranta, Finland, 2003
ESCAPE-12, The Hague, The Netherlands, 2002
ESCAPE-11, Kolding, Denmark, 2001
ESCAPE-10, Firenze, Italy, 2000
ESCAPE-9, Budapest, Hungary, 1999
ESCAPE-8, Brugge, Belgium, 1998
ESCAPE-7, Trondheim, Norway, 1997 (Joint event with PSE 6)
ESCAPE-6, Rhodos, Greece, 1996
ESCAPE-5, Bled, Slovenia, 1995
ESCAPE-4, Dublin, Ireland, 1994
ESCAPE-3, Graz, Austria, 1993
ESCAPE-2, Toulouse, France, 1992
ESCAPE-1, Helsingor, Denmark, 1992

PSE SERIES

The International Symposia on Process Systems Engineering (PSE) have been a triennial tradition since 1982.

The series was arranged by the International Organization for Process Systems Engineering with representation from the Asia Pacific Confederation of Chemical Engineering, the European Federation of Chemical Engineering, and the Inter-American Confederation of Chemical Engineering. It has proved to be an attractive global platform for the PSE academics, researchers, and practitioners from all corners of the world for sharing advances in PSE education, research, and application. PSE-24 is the 15th in the series.

Previous events were:

PSE 14 Kyoto, Japan, 2021
PSE 13 San Diego, USA, 2018
PSE 12 Copenhagen, Denmark, 2015 (Joint event with ESCAPE 25)
PSE 11 Singapore, Singapore, 2012
PSE 10 Salvador Bahia, Brazil, 2009
PSE 9 Garmisch Partenkirchen, Germany, 2006 (Joint event with ESCAPE 16)
PSE 8 Beijing, China, 2003
PSE 7 Keystone, USA, 2000
PSE 6 Trondheim, Norway, 1997 (Joint event with ESCAPE 7)
PSE 5 Kyongiu, Korea, 1994
PSE 4 Montebello, Canada, 1991
PSE 3 Sydney, Australia, 1988
PSE 2 Cambridge, England, 1985
PSE 1 Kyoto, Japan, 1982

The scientific programme of ESCAPE34-PSE24 features about 700 Lecture and Poster presentations, including 7 plenary lectures by outstanding Researchers.

This Book of Abstracts consists of a summary of the topics treated and listed during the Symposium.

prof. Flavio Manenti,
prof. Gintaras V. Reklaitis

ISC Chairboard

ABSTRACT Index

Modelling and Simulation

Synthesis and Design

Process Control and Operations

CAPE in Sustainable Energy Applications

Bioresources, Bioprocesses and Biomedical Systems

Digitalization and Machine Learning

Concepts, Methods and Tools

Education in CAPE and Knowledge Transfer

AUTHOR Index

ESCAPE-34 PSE-2024
European Symposium on Computer Aided Process Engineering
&
Process Systems Engineering

Flavio Manenti, Gintaras V. Reklaitis (Eds.), Book of Abstract of the 34th European Symposium on Computer Aided Process Engineering / 15th International Symposium on Process Systems Engineering (ESCAPE34/PSE24), June 2-6, 2024, Florence, Italy.

Hydrogen Trade Scenarios: Impact of Transportation Methods and Geopolitical Dynamics

Dawood Hjeij,[a*] Yusuf Bicer,[a] Muammer Koc[a]

[a] *Hamad Bin Khalifa University, Doha, Qatar*
dhjeij@hbku.edu.qa

Abstract

In the rapidly evolving hydrogen economy, the means of transportation and geopolitical factors can significantly influence the global hydrogen trade landscape. This research introduces a dynamic analysis of potential scenarios shaping hydrogen trade in medium to long-term horizons, assessing their feasibility based on technological advancements, economic implications, and external factors.

We incorporate various energy scenarios into our analysis using an agent-based model approach in the AnyLogic simulation software. These range from a full-scale transition to hydrogen as a primary renewable energy carrier, a partial transition, to a potential retreat from hydrogen consumption. Each scenario incorporates varying hydrogen production methodologies, storage solutions, and transportation channels. Specific emphasis is placed on contrasting transportation methods: pipelines, liquified hydrogen in ships, and ammonia conversion. Moreover, geopolitical considerations, such as the closure of marine chokepoints, are integrated to visualize their potential impact on hydrogen trade.

In this paper, we provide preliminary results that offer initial insights into the evolving scenarios of the hydrogen trade. These early findings, focusing on diverse aspects of hydrogen transportation and geopolitical influences, introduce more detailed analyses that will be conducted as our research progresses.

Keywords: Agent-based model, Hydrogen economy, Hydrogen market, Trade, Simulation

1. Introduction

The evolution of the global energy landscape is increasingly characterized by a shift towards more sustainable and low-carbon sources. In this context, hydrogen emerges as a pivotal element in the global energy transition, offering a versatile energy storage and transportation solution. The production of hydrogen is achievable through diverse methodologies, such as renewable energy-powered water electrolysis and natural gas-based methane reforming coupled with carbon capture. This versatility and the growing

need for cleaner alternatives have positioned hydrogen as a central player in the sustainable energy dialogue.

As the hydrogen sector witnesses exponential growth, significant advancements in production technology and distribution methods are becoming apparent. A substantial increase in investments and technological innovations underpins this growth trajectory. An estimated $ 8 trillion in hydrogen-related investments is needed by 2050 to develop international hydrogen trade (Hydrogen Council and McKinsey & Company, 2023). However, the hydrogen market faces several challenges, including the high costs associated with production, the emerging state of its delivery and storage infrastructure, and the need for more robust policy frameworks to encourage further investments and expansion. Despite these hurdles, the unique advantages offered by hydrogen, notably its clean energy credentials, have spurred considerable interest globally. Numerous countries, especially those rich in renewable resources or natural gas reserves, are actively exploring ways to enhance their hydrogen production and utilization capabilities (IEA, 2023a).

Recent years have seen a surge in interest in the hydrogen market from the research community. While studies on the hydrogen market are still evolving, parallels can be drawn from the extensively researched liquefied natural gas (LNG) market. In LNG market research, various models have been employed to understand the dynamics between market players, including producers and importers (Meza et al., 2021). These studies have yielded crucial insights into energy markets' workings and growth potential and can serve as a reference for hydrogen market research.

In addition to agent-based modeling, other methodologies have been employed to analyze the hydrogen market. These include market simulations to forecast future hydrogen supply and demand, economic models to examine the impact of policy measures, and life cycle analyses to assess the environmental implications of hydrogen production and usage. These varied methodologies provide a holistic view of the hydrogen market and its growth potential, offering insights ranging from market projections to environmental sustainability assessments.

This study endeavors to explore the hydrogen market, focusing on the role of leading energy exporters. This research projects hydrogen and ammonia supply and demand up to 2050, evaluating market costs and investment opportunities using an agent-based model. The model accounts for various factors, including hydrogen/ammonia producers, importers, delivery contracts, shipping methods, and infrastructure, treating each country as an independent entity. The findings of this study will be instrumental in understanding the growth potential of the hydrogen market and the pivotal role of major energy exporters.

Understanding the dynamics of the hydrogen market is crucial for achieving net-zero targets and transitioning to sustainable energy sources. This research will provide essential insights into the costs and investment opportunities within the hydrogen market, highlighting the significance of key energy exporters in its expansion. The insights gained from this study will aid in shaping policies that foster the development of the hydrogen sector and support the transition toward cleaner energy.

This research presents a novel approach to examining the hydrogen market, utilizing an agent-based model to analyze the interplay among various market participants. By conducting a comprehensive analysis of the hydrogen market and its growth prospects, this study addresses existing gaps in research, contributing significantly to the body of knowledge in this field.

2. Methodology

2.1. Agent-based model

This model simulates the dynamics of hydrogen production, consumption, and trade among 40 different countries from 2022 to 2050. It integrates various parameters and databases to analyze scenarios under three different conditions. The model's core components include agents, parameters, databases, variables, and functions.

2.2. Agents

Each country is an agent in the model with unique characteristics and behaviors. A total of 40 countries were selected based on different criteria to represent the hydrogen trade using manageable computational resources. Initially, countries were ranked using a hydrogen competitiveness index from a previous publication (Hjeij et al., 2023), assessing their potential in the hydrogen market. Additionally, the hydrogen investability index was used to gauge the attractiveness of countries for hydrogen sector investments (Cranmore Partners and Energy Estate, 2021). Insights from Deloitte's "Green Hydrogen" report, which identified countries actively involved or with significant potential in the green hydrogen sector, were also considered (Deloitte, 2023). This multi-source approach ensured a well-rounded and informed selection of countries.

2.3. Parameters

2.3.1. Hydrogen demand

To project hydrogen demand up to the year 2050, we employed data from the International Energy Agency's (IEA) World Energy Review (IEA, 2023b). Specifically, we based our projections on three distinct scenarios outlined in the review:

- STEPS (Stated Policies Scenario): Reflects the impact of current policy frameworks and announced policy intentions.
- APS (Announced Pledges Scenario): Takes into account the targets and pledges announced by different countries but not yet implemented as policies.
- NZE (Net Zero Emissions by 2050 Scenario): Envisions a pathway to achieve net-zero global emissions by 2050.

These scenarios provide a comprehensive range of possible futures, with assumptions and outcomes regarding energy consumption and hydrogen demand.

To distribute the projected global hydrogen demand among the 40 countries in our model, we utilized the primary energy consumption data from the Energy Institute's (EI) Statistical Review of World Energy (Energy Institute, 2023). This approach allowed us to align hydrogen demand with energy consumption and ensure proportional representation.

The projected hydrogen demand, split among the countries based on the methodology above, was then integrated into our agent-based model. This integration is crucial for accurately simulating future hydrogen trade dynamics, production needs, and the overall functioning of the hydrogen market under different global scenarios.

2.3.2. Natural gas production

To obtain accurate and current data on natural gas production by country for 2022, we utilized the GlobalData Oil & Gas Upstream Fields Database (GlobalData, 2023a). This comprehensive database provides detailed information on natural gas production across various countries, offering a reliable baseline for our analysis. The data extracted from this source were instrumental in establishing the current landscape of natural gas production globally, serving as a foundation for future projections.

For projecting natural gas production from 2022 to 2050, we referred to the International Energy Agency's (IEA) World Energy Review. The review's scenarios provided a structured framework for forecasting, encompassing STEPS, APS, and NZE. We then calculated the expected annual growth rates of natural gas production based on these scenarios. This enabled us to simulate future scenarios with natural gas production, assessing its impact on hydrogen production and the broader energy landscape.

2.3.3. Renewable energy

For our study's renewable energy generation component, we employed GlobalData's Power IC – Capacity and Generation Database, a resource that provides extensive data on capacity and generation for 171 countries spanning from 2000 to 2035 (GlobalData, 2023b). This detailed database categorizes information based on various power-generating sources and further segments it according to specific technologies or installations.

To extend our analysis up to 2050, we integrated the International Energy Agency's (IEA) Global Energy Review, which allowed us to incorporate three distinct scenarios (STEPS, APS, NZE) into our projections of renewable energy generation, providing a comprehensive and forward-looking view of the renewable energy sector.

3. Results and Discussion

This section introduces our preliminary findings, which lay the groundwork for a deeper exploration of the hydrogen trade's dynamics. The results discussed here highlight key aspects of hydrogen transportation and the influence of geopolitical factors. These early insights are a stepping stone towards a more comprehensive analysis in the subsequent phases of our research.

The global hydrogen demand is expected to evolve significantly by 2050 across three scenarios: STEPS, APS, and NZE. Under the current policy-committed STEPS scenario, demand is projected to rise from 86 million tonnes (Mt) in 2022 to 122 Mt by 2050, reflecting a steady, modest growth. The APS scenario, with more aggressive policy support, anticipates a near tripling in demand to 252 Mt, highlighting the impact of enhanced policies and investment in hydrogen technologies. The most ambitious, the NZE scenario, aiming for net-zero emissions by 2050, forecasts an exceptional increase to 366 Mt, underscoring hydrogen's potential role in achieving a low-carbon economy and meeting environmental objectives.

The analysis highlights key global demand centers for hydrogen, with China as the largest, followed by the United States and India, especially under the APS and NZE scenarios. This trend indicates a growing reliance on hydrogen as a sustainable energy

source, influenced by policy shifts. The evolving energy landscape sees hydrogen as a crucial element, with demand varying significantly based on policy and environmental commitments.

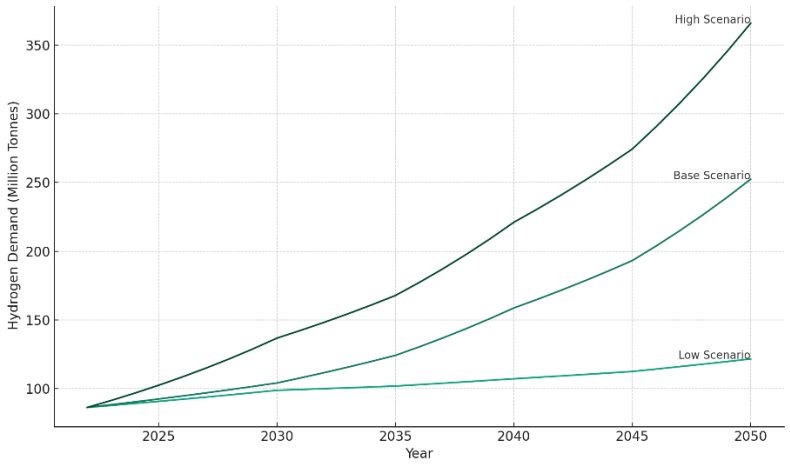

Figure 1: Global hydrogen demand until 2050 according to the different scenarios

By 2050, a notable misalignment is expected between the locations of major hydrogen demand centers and optimal production sites, presenting opportunities for international hydrogen trade. Regions like Japan, South Korea, and parts of Europe, constrained in hydrogen production by their decarbonization commitments, are likely to become importers. In contrast, areas like South America and the Middle East, with excess production capacity, could emerge as key exporters in the hydrogen market.

Local hydrogen production will often be more cost-effective than imports, especially involving long-distance transportation. This is due to the additional costs incurred in the conversion to intermediaries for transport and re-conversion at the point of use, alongside the costs associated with hydrogen losses and other necessary inputs such as electricity. Consequently, long-distance hydrogen transport is expected to be a less favored option, reserved for cases where local production is not viable.

However, the transportation costs for hydrogen derivatives like ammonia and synthetic kerosene are relatively low compared to the overall product costs due to their higher volumetric densities. This aspect could make long-distance trade in these derivatives from low-cost production centers economically competitive, even in high-cost markets.

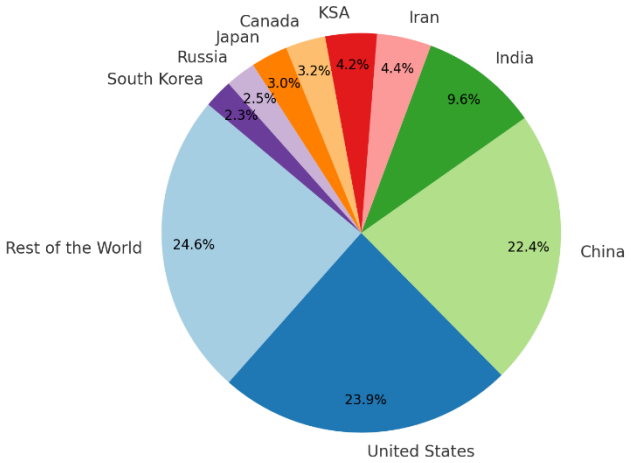

Figure 2: Hydrogen demand in the base scneario by country, 2050

4. Conclusions

The future hydrogen trade landscape will likely be shaped by production costs, the nature of the products being transported, and the availability of local resources. While local production will generally be preferable, long-distance trade in hydrogen and its derivatives will play a crucial role, especially connecting regions with excess production capacity to those with significant demand but limited production capabilities. This global trade in hydrogen and its derivatives could significantly reduce overall investment requirements in the energy sector, fostering a more interconnected and efficient global energy market. The international hydrogen trade will also influence global geopolitics, potentially redefining energy alliances and shifting power balances between nations based on their roles as producers or consumers.

References

Cranmore Partners and Energy Estate, 2021, Hydrogen Investability Index: Emerging Hydrogen Superpowers.
Deloitte, 2023, Green hydrogen: Energizing the path to net zero.
GlobalData, 2023a, Oil & Gas Upstream Fields Database.
GlobalData, 2023b, Power IC – Capacity and Generation Database.
Hjeij, D, Biçer, Y, Al-Sada, M., and Koç, M., 2023, Hydrogen export competitiveness index for a sustainable hydrogen economy, Energy Reports, 9, 5843-5856.
Hydrogen Council and McKinsey & Company, 2023, Global Hydrogen Flows - 2023 Update.
IEA, 2023a, Global Hydrogen Review.
IEA, 2023b, World Energy Review.
IEA, 2023c, Net Zero Roadmap: A Global Pathway to Keep the 1.5 °C Goal in Reach.
Meza, A., Ari, I., Al-Sada, M., and Koc, M., 2021, Future LNG competition and trade using an agent-based predictive model, Energy Strategy Reviews, 38, 100734.
The Energy Institute (EI), 2023, Statistical Review of World Energy.

ESCAPE-34 PSE-2024
European Symposium on Computer Aided Process Engineering
&
Process Systems Engineering

Flavio Manenti, Gintaras V. Reklaitis (Eds.), Book of Abstract of the 34th European Symposium on Computer Aided Process Engineering / 15th International Symposium on Process Systems Engineering (ESCAPE34/PSE24), June 2-6, 2024, Florence, Italy.

Multi-objective Optimization of Hybrid Fossil/Renewable Carbon Clusters for Methanol Production

Sachin Jog,[a] Juan D. Medrano-García,[a] Gonzalo Guillén-Gosálbez[a]*

[a]*Institute for Chemical and Bioengineering, Department of Chemistry and Applied Biosciences, ETH Zurich, Vladimir-Prelog-Weg 1, 8093 Zurich, Switzerland*
gonzalo.guillen.gosalbez@chem.ethz.ch

Abstract

Transitioning to more sustainable chemicals will require shifting to renewable carbon technologies (captured CO_2, waste, or biomass), which are often evaluated decoupled from each other. However, opportunities for energy and mass integration may arise that could improve their economic and environmental performance, thus making them more appealing than originally thought. In this work, we consider integrated chemical clusters based on fossil and renewable carbon for methanol production. We apply multi-objective optimization to the integrated cluster and unintegrated configuration, finding that the integrated solution can substantially improve the environmental performance *via* hybridization of technologies, with reductions in global warming potential (GWP) impact ranging from 19 % to 183 % for a given unitary cost target.

Keywords: integrated chemical clusters, multi-objective optimization, global warming potential

1. Introduction

The climate goals set by the Paris Agreement have spurred efforts in the chemical industry to move away from the current fossil-based synthesis. This requires shifting to renewable carbon feedstock, including captured CO_2 *via* carbon capture and utilization (CCU), waste, and biomass. Many current studies of such alternative synthesis routes, which may differ in the feedstock and the reaction pathway, focus on isolated processes and neglect the potential synergistic effects between them, thus failing to evaluate their full potential as an integrated industrial system minimizing material and energy usage, waste generation, etc. (Boix *et al.*, 2015). Notably, savings realized *via e.g.*, heat and mass integration, common waste disposal systems and wastewater treatment plants, could substantially improve such emerging technologies when deployed in integrated clusters. For example, Baliban *et al.* (2013) proposed an optimization framework for a biomass-to-liquid fuels (BTL) system, which simultaneously addressed heat, electricity, and water integration along with process synthesis decisions, finding that BTL refineries using existing technologies with capacities above 5,000 barrels per day could be economically feasible across the United States. Ioannou *et al.* (2023) conducted a techno-economic and

life-cycle assessment of an integrated CO_2 refinery co-producing methanol, olefins, and aromatics, with an Allam cycle (Allam *et al.*, 2017) for residual gas utilization. The Allam cycle operates at high pressures (*i.e.*, up to 330 bar), and utilizes oxy-combustion of the purge stream to generate power and pure CO_2. The authors reported savings of 135 % in the GWP impact in the integrated CO_2 refinery compared to the business-as-usual. Therefore, exploiting synergies between various synthesis routes can lead to substantial savings resulting from heat and mass integration. Moreover, integrating emerging technologies for residual gas utilization (*e.g.*, the Allam cycle) provides additional benefits in terms of environmental impact reduction. Thus, in order to optimize economic and environmental performance, we focus here on multi-objective optimization of a chemical cluster for methanol production that integrates fossil and renewable carbon technologies.

2. Process modeling and optimization

We explore the hybridization of fossil and renewable carbon technologies for methanol production through the multi-objective optimization (production cost and GWP impact) of the integrated and unintegrated configurations, as shown in Figure 1.

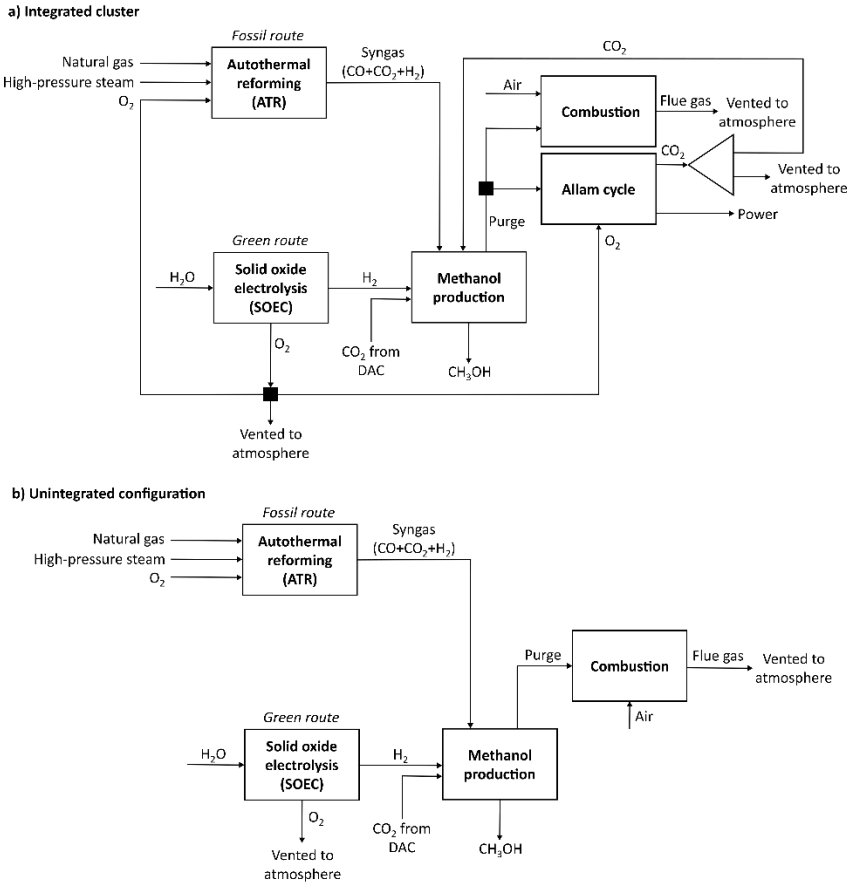

Figure 1: Process block diagrams of the integrated cluster and the unintegrated configuration.

The fossil-based route consists of the autothermal reforming (ATR) of natural gas with high-pressure steam and oxygen (O_2) for syngas production. The renewable route uses

direct air-captured carbon dioxide (CO_2) with hydrogen (H_2) obtained from wind-powered water electrolysis *via* solid oxide electrolysis (SOEC). In the integrated cluster, the purge from the methanol process, which comes from the flash units (vapor stream consisting mainly of CH_4, CO_2, CO, and H_2) and distillation column (vapor stream consisting mainly of CH_3OH and CO_2), can be utilized in an Allam cycle to generate electricity and pure CO_2, or can be combusted using air. Note that the specific composition of the purge depends on the route/s chosen (*i.e.*, green and/or fossil), and the values of the other degrees of freedom. Moreover, the O_2 generated in the SOEC can also be used in the Allam cycle and in the ATR. All processes are simulated in Aspen HYSYS® v11, where Aspen Custom Modeler® (ACM) v11 is used to model the SOEC. To calculate the climate change impact, we quantify the 100-year time horizon (hierarchist perspective) GWP following the ReCiPe 2016 v1.13 methodology. The multi-objective optimization is carried out using the algorithm *surrogateopt* in MatLab® vR2021b through the COM interface. For simplicity, we use the weighted sum of objectives method, which can only identify solutions lying in the convex envelope of the Pareto front. We consider nine degrees of freedom: ATR – natural gas molar flow rate, O_2/natural gas molar ratio, and steam/natural gas molar ratio; SOEC – H_2 molar flow rate; CH_3OH – Plug flow reactor (PFR) temperature, PFR pressure, PFR volume, and purge percentage; Allam cycle – feed temperature.

3. Results and Discussion

The Pareto frontier obtained from the multi-objective optimization is shown in Figure 2. The minimum cost solution implements the ATR process (*i.e.*, fossil route), while the minimum GWP impact solution deploys CO_2 hydrogenation (*i.e.*, renewable route). Note that the GWP can attain negative values due to the cradle-to-gate scope of the life cycle assessment (LCA) that omits the use phase of methanol. The integrated cluster shows substantial improvements over the unintegrated configuration. More specifically, the reduction in GWP impact in the integrated cluster with respect to the unintegrated configuration falls in the range 19-183 % for the Pareto points shown in the figure. These savings are due to mass and heat integration, and the incorporation of the Allam cycle, which enables recycling of pure CO_2 to the methanol process (instead of venting the flue gas resulting from the combustion process directly into the atmosphere). Additionally, the intermediate Pareto points show the different levels of hybridization between the fossil and renewable carbon technologies.

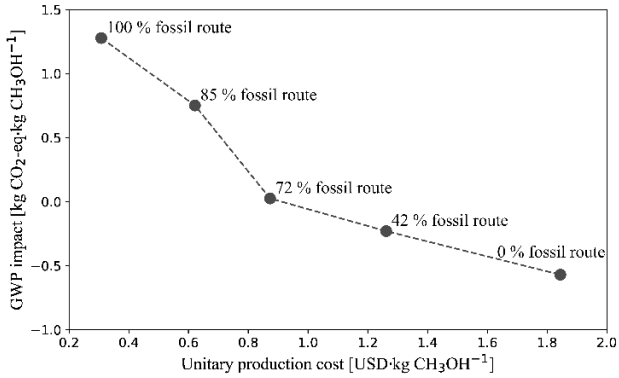

Figure 2: Pareto frontier from the multi-objective optimization (the percentages are calculated based on the mole fraction of natural gas used as feed in the ATR process, *i.e.*, the fossil route).

4. Conclusions

In this work, we studied the synergistic effects of integrating fossil and renewable processes based on heat, mass and power integration. Our results show that the integrated cluster can greatly reduce the environmental impact (*i.e.*, between 19 % and 183 %). In addition, the Pareto-optimal frontier demonstrates different combinations of the fossil and renewable routes, showing their hybridization potential that could enable a gradual transition to more sustainable chemicals.

References

Allam, R., Martin, S., Forrest, B., Fetvedt, J., Lu, X., Freed, D., Brown, G.W., Sasaki, T., Itoh, M., Manning, J., 2017. Demonstration of the Allam Cycle: An Update on the Development Status of a High Efficiency Supercritical Carbon Dioxide Power Process Employing Full Carbon Capture. Energy Procedia 114, 5948–5966.

Baliban, R.C., Elia, J.A., Floudas, C.A., 2013. Biomass to liquid transportation fuels (BTL) systems: process synthesis and global optimization framework. Energy Environ. Sci. 6, 267–287.

Boix, M., Montastruc, L., Azzaro-Pantel, C., Domenech, S., 2015. Optimization methods applied to the design of eco-industrial parks: a literature review. J. Clean. Prod. 87, 303–317.

Ioannou, I., Javaloyes-Antón, J., Caballero, J.A., Guillén-Gosálbez, G., 2023. Economic and Environmental Performance of an Integrated CO_2 Refinery. ACS Sustain. Chem. Eng. 11, 1949–1961.

ESCAPE-34 PSE-2024
European Symposium on Computer Aided Process Engineering
&
Process Systems Engineering

Flavio Manenti, Gintaras V. Reklaitis (Eds.), Book of Abstract of the 34th European Symposium on Computer Aided Process Engineering / 15th International Symposium on Process Systems Engineering (ESCAPE34/PSE24), June 2-6, 2024, Florence, Italy.

Mixed Convection Heat Transfer of Non-Catalytic CH_4 Pyrolysis for Hydrogen Production in a Vertical Tube Using Computational Fluid Dynamics

Mazhar Ali[a], Son Ich Ngo[a], Young-Il Lim[a,*], Sojeong An[b,c], Young Jae Lee[b], Uen-Do Lee[d]

[a]*Center of Sustainable Process Engineering (CoSPE), Department of Chemical Engineering, Hankyong National University, Gyeonggi-do, Anseong-si, Jungang-ro 327, 17579 Korea*
[b]*Carbon Neutral Technology R&D Department, Korea Institute of Industrial Technology (KITECH), 89, Yangdaegiro-gil, Ipjang-myeon, Seobuk-gu, Cheonan-si, Chungcheongnam-do, 31056 Korea*
[c]*Department of Chemical and Biomolecular Engineering, Yonsei University, 50 Yonsei-ro, Seodaemun-gu, Seoul, 03722, Korea*
[d]*Energy System R&D Group, Korea Institute of Industrial Technology (KITECH), Cheonan 331-825, Korea*
limyi@hknu.ac.kr

Abstract

Greenhouse gas (GHG) emissions are at the forefront of global concerns. The development of low-carbon hydrogen (H_2) production methods has gained prominence due to the ability to substitute fossil fuels in the transport and power generation sectors. Non-oxidative CH_4 pyrolysis for low-carbon H_2 production holds significant potential to produce H_2 and solid carbon without CO_2 emissions. A three-dimensional (3D) computational fluid dynamics (CFD) model coupled with chemical reactions and heat transfer was developed to investigate the hydrodynamics, reaction kinetics, and heat transfer of non-catalytic CH_4 pyrolysis in a vertical tube reactor. The vertical tube experienced buoyancy forces due to the density variations caused by the significant temperature differences. The mixed convection heat transfer phenomena were observed due to buoyancy forces leading to distortion in the velocity field. The distortion in velocity fields enhanced the heat transfer coefficient in the reactor. The overall convective heat transfer coefficient from wall to fluid was 30.0 $W/m^2/K$. The CFD model is a valuable tool for the identification of chemical reactions and heat transfer coupled with hydrodynamics of the reactor.

Keywords: H_2 production, non-catalytic CH_4 pyrolysis, reactor hydrodynamics, mixed convection heat transfer, computational fluid dynamics (CFD),

1. Introduction

Hydrogen (H_2), as a clean energy source, offers a promising alternative to fossil fuels and holds the potential to become a leading fuel for sustainable transportation, providing a

reliable and secure energy source (Qureshi et al., 2022). The non-oxidative CH_4 pyrolysis generates H_2 and solid carbons without CO_2 emissions, as long as the thermal source remains free from emissions (Catalan and Rezaei, 2020).

The phenomenon occurring inside the noncatalytic CH_4 pyrolysis reactor is difficult to investigate due to the high operating temperature (Paxman et al., 2017). Computational fluid dynamics (CFD) simulations are commonly used to study the hydrodynamics and heat transfer characteristics of the reactor following geometric and operational modifications (Ngo and Lim, 2020; Ngo et al., 2023). Ozalp studied the effect of temperature and gas flowrate on methane conversion (X_{CH_4}) for noncatalytic CH_4 decomposition (Ozalp and JayaKrishna, 2010). Previously published studies have neglected the effect of buoyancy forces on the heat transfer characteristics in the CH_4 pyrolysis reactor for CFD modelling. Mixed convection occurs due to the simultaneous effect of buoyancy forces and externally applied inertia forces and plays a vital role in the reactor heat transfer (Gorai and Das, 2020).

This study aims to develop a 3D CFD model coupled with chemical reactions, and heat transfer to investigate mixed convection heat transfer for noncatalytic CH_4 pyrolysis through a vertical tube. CFD model for CH_4 decomposition has the potential to be a useful tool for enhancing heat transfer, particularly in the context of mixed convection caused by buoyancy forces within the reactor.

2. Model description

A single-phase Eulerian 3D CFD model was developed for the noncatalytic CH_4 pyrolysis in a vertical tube at 1000 °C and 0.5 LPM. The Eulerian single-phase was modeled by a set of continuity equation, a Navier-Stokes (NS) momentum equation, and an energy equation. The CFD model uses the widely adopted shear-stress transport (SST) k-ω turbulence model for simulating laminar and turbulent mixed flows (Menter, 1994). Figure 1 presents the Eulerian CFD model description of the CH_4 pyrolysis reactor.

The 3D geometry and meshing of the computational domain for CH_4 pyrolysis are depicted in Figure 2. Poly-hexcore meshes were adopted and mesh independence test was performed to ensure numerical accuracy. The CFD simulation was performed using a commercial CFD code, ANSYS Fluent R2022b (ANSYS Inc., USA) with a 24-core workstation.

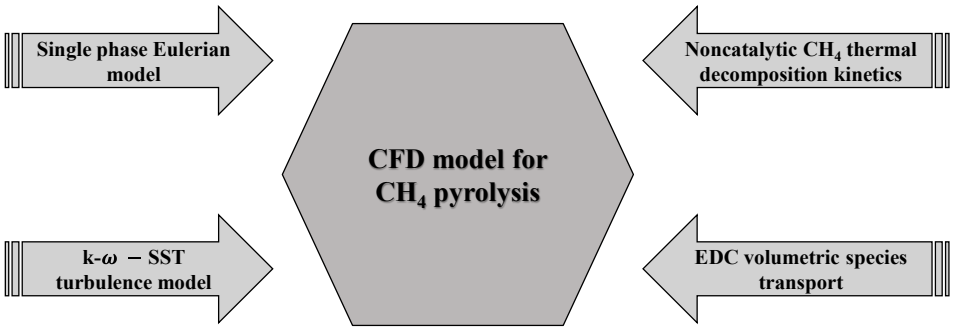

Figure 1. Single-phase Eulerian 3D CFD model description

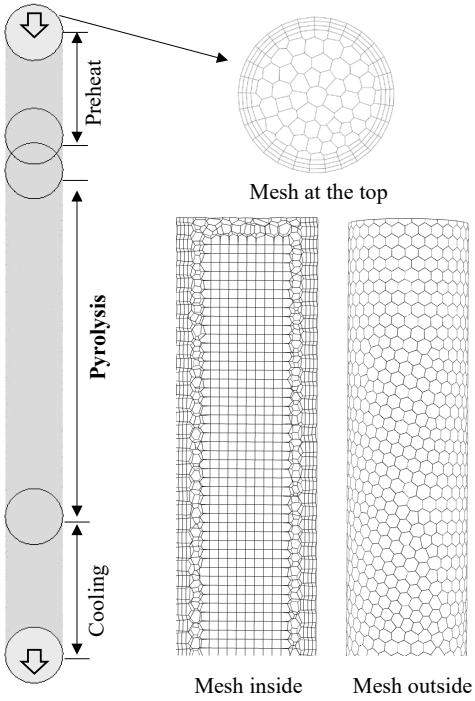

(a) Computation domain (b) Mesh structure

Figure 2. (a) Computational domain (b) meshing of the computational domain

3. Results and Discussions

The reliability and accuracy of the Eulerian CFD model were confirmed through a process of verification and validation. Fig 3 shows the verification and validation of the CFD model. In the verification step, coarse (50,000 cells), medium (200,000 cells), fine (600,00 cells) meshes were tested for velocity (u_g) and temperature (T) profiles as shown in Fig 3a. Medium mesh has been selected for the further investigation considering both computational accuracy and cost. Figure 3b shows a comparison of the axial temperature profile in the tube reactor between the CFD results and experimental data. Temperature readings were taken at different axial positions to assess the temperature profile along the tube height (h). It can be observed that the CFD simulation results align well with the experimental measurements.

Mixed convection is the combined form of natural and forced convection heat transfer and holds a crucial role in the reactor heat transfer (Gorai and Das, 2020). The impact of buoyancy on heat transfer coefficients can either enhance or impair the process, depending on the flow orientation (upward or downward) (Jackson et al., 1989). This investigation involves the process of downward heating and cooling of fluid in a vertical tube. In Fig 4(a), the velocity (u_g) contours are depicted at an operating temperature of 1000 °C and a gas flow rate of 0.5 LPM. The cooling zone of the tube reactor experiences a reversal flow attributed to the buoyancy effect owing to the sudden temperature change (see Fig 4b). Figure 4b shows the temperature contour on the slice normal to the transversal direction ($z=0$). As the gas flows under laminar flow conditions, the gas

attains thermal stability (T~ 950 °C) in the pyrolysis zone. Fig 4c shows the CH_4 mole fraction (Y_{CH_4}) along the tube reactor. The concentration of CH_4 (Y_{CH_4}) decreases as the endothermic reaction progresses, attributed to the high pyrolysis temperature (see Fig 4b). Figure 5a presents a dimensionless parameter, the Richardson number ($Ri = \frac{Gr}{(Re)^2}$) was calculated to investigate the presence of mixed convection phenomena in the CH_4 pyrolysis tube reactor. In mixed convection heat transfer, Ri plays a crucial role in assessing the impact of natural and forced convection. When $Ri \gg 1$, natural convection dominates the heat transfer process and $Ri \ll 1$. forced convection predominates in governing the heat transfer (Cengel, 2000). At the beginning of the preheat, Ri indicates the presence of natural convection, transitioning to forced convection as the gas moves towards the pyrolysis. In the absence of buoyancy forces in the pyrolysis region, the reactor shows a domination of forced convection. In the cooling region, strong buoyancy forces lead to the predominance of natural convection. Fig 5b illustrates the heat transfer coefficient (HTC), calculated along the column height (h) using Eq. (1). HTC stabilizes at a constant value (HTC ~ 34 W/m^2/K) as the temperature reaches thermal stability in pyrolysis region and fluctuates in the cooling zone due to flow recirculation. The area-averaged overall HTC is 30.03 W/m^2/K for the noncatalytic CH_4 pyrolysis tube reactor.

$$HTC = \frac{q_W}{T_W - T_c} \tag{1}$$

where q_W is wall heat flux (W/m^2), T_w is wall temperature (°C) and T_c is temperature (°C) at the center of the tube reactor.

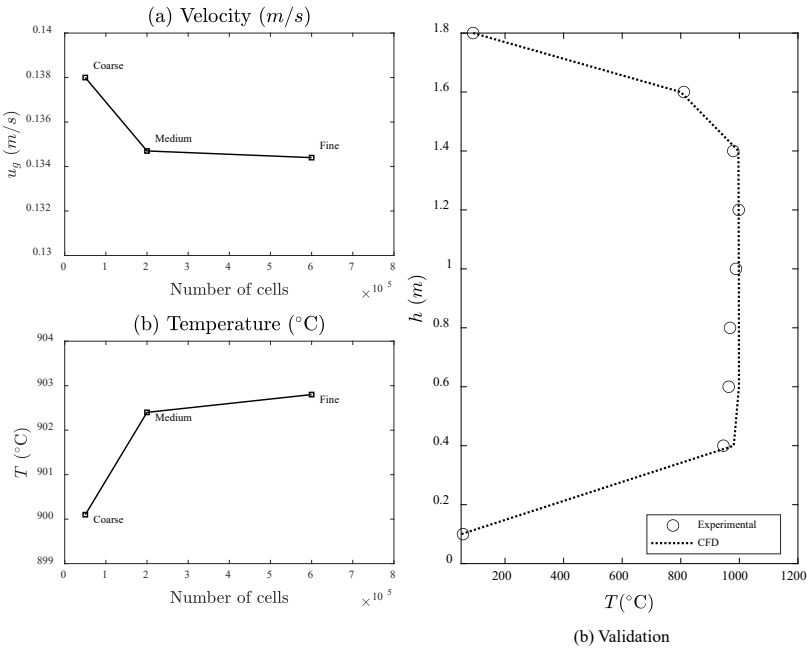

Figure 3. Verification of numerical accuracy and validation of the CFD model

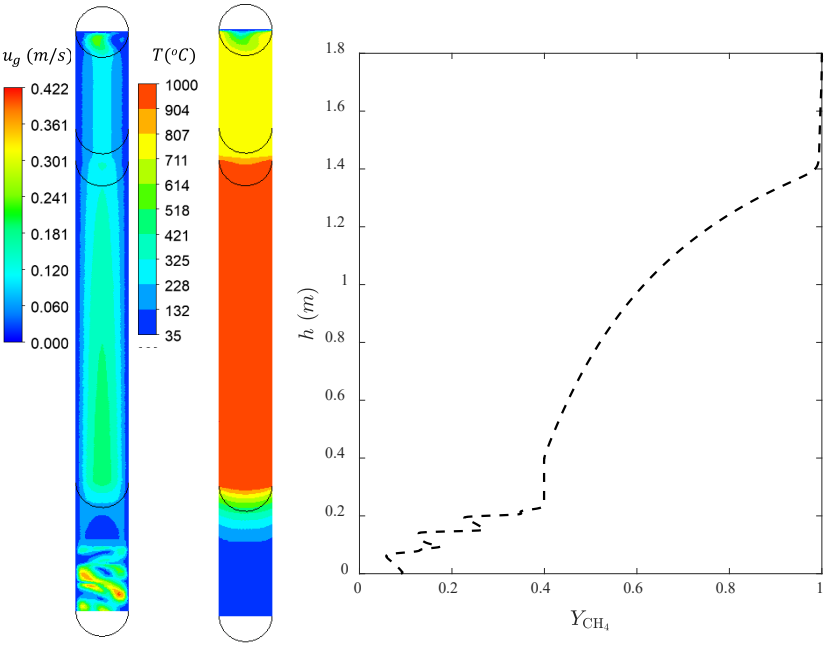

(a) (u_g) contour (b) (T) contour (c) CH_4 mole fraction (Y_{CH_4})

Figure 4. (a) Contour of velocity (u_g); (b) Contour of temperature (T) profile; (c) Axial profile of CH_4 mole fraction (Y_{CH_4})

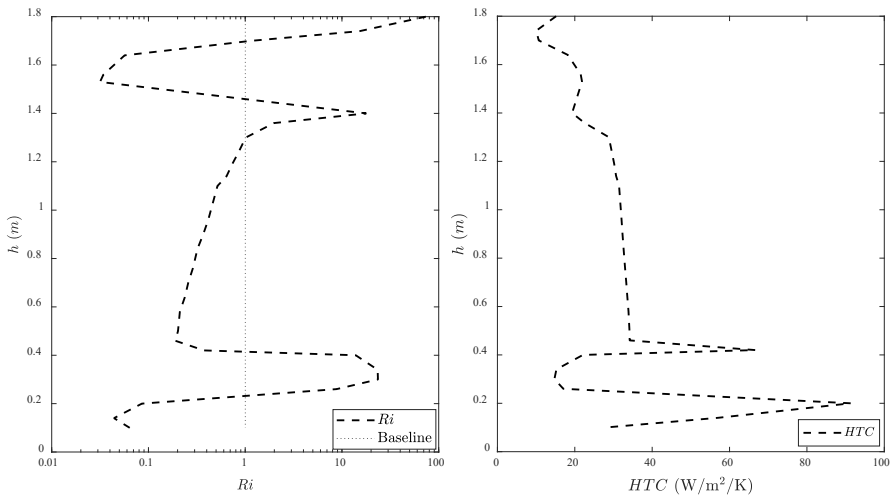

(a) Richardson number (Ri) (b) Heat transfer coefficient (HTC)

Figure 5 (a) Axial profile of Richardson number (Ri) (b) Axial profile heat transfer coefficient (HTC)

The influence of buoyancy flow becomes more pronounced when operating at lower temperatures, mainly due to the decreased gas velocity. Mixed convection heat transfer phenomena were observed because of buoyancy forces induced by density changes in the tube.

4. Conclusions

The noncatalytic CH_4 pyrolysis for low-carbon H_2 production in a vertical tube was analysed using computational fluid dynamics. A single-phase Eulerian 3D CFD model coupled with heat transfer, turbulence and reaction kinetics was developed to investigate the presence of mixed convection heat transfer phenomena in the CH_4 pyrolysis reactor tube. The findings emphasize that the 3D CFD model has the potential to recognize the buoyancy phenomenon that happens within the reactor during noncatalytic CH_4 pyrolysis. The buoyancy effect can be reduced by either reducing temperature differences or increasing the gas flow rate in the reactor.

Acknowledgments

This study was supported by a National Research Foundation of Korea (NRF) grant funded by the Korean government (MEST) (2022M3J5A1051728). This work was also supported by the National Research Council of Science and Technology (NST) grant funded by the Korean Government (MSIT) (No. CAP22021-101).

References

Catalan, L.J., Rezaei, E., 2020. Coupled hydrodynamic and kinetic model of liquid metal bubble reactor for hydrogen production by noncatalytic thermal decomposition of methane. international journal of hydrogen energy 45, 2486-2503.

Cengel, Y.A., 2000. Heat and mass transfer McGraw-Hill Education New York, NY 10121, United States of America

Gorai, S., Das, S.K., 2020. Studies on Mixed Convection and Its Transition to Turbulence—A Review. 50 Years of CFD in Engineering Sciences: A Commemorative Volume in Memory of D. Brian Spalding, 317-361.

Jackson, J., Cotton, M., Axcell, B., 1989. Studies of mixed convection in vertical tubes. International journal of heat and fluid flow 10, 2-15.

Menter, F.R., 1994. Two-equation eddy-viscosity turbulence models for engineering applications. AIAA journal 32, 1598-1605.

Ngo, S.I., Lim, Y.-I., 2020. Multiscale Eulerian CFD of Chemical Processes: A Review. ChemEngineering 4, 23.

Ngo, S.I., Lim, Y.-I., Kwon, H.M., Lee, U.-D., 2023. Hydrodynamics of molten-metal bubble columns in the near-bubbling field using volume of fluid computational fluid dynamics. Chemical Engineering Journal 454, 140073.

Ozalp, N., JayaKrishna, D., 2010. CFD analysis on the influence of helical carving in a vortex flow solar reactor. international journal of hydrogen energy 35, 6248-6260.

Paxman, D., Trottier, S., Flynn, M., Kostiuk, L., Secanell, M., 2017. Experimental and numerical analysis of a methane thermal decomposition reactor. international journal of hydrogen energy 42, 25166-25184.

Qureshi, F., Yusuf, M., Kamyab, H., Vo, D.-V.N., Chelliapan, S., Joo, S.-W., Vasseghian, Y., 2022. Latest eco-friendly avenues on hydrogen production towards a circular bioeconomy: Currents challenges, innovative insights, and future perspectives. Renewable and Sustainable Energy Reviews 168, 112916.

ESCAPE-34 PSE-2024
European Symposium on Computer Aided Process Engineering
&
Process Systems Engineering

Flavio Manenti, Gintaras V. Reklaitis (Eds.), Book of Abstract of the 34th European Symposium on Computer Aided Process Engineering / 15th International Symposium on Process Systems Engineering (ESCAPE34/PSE24), June 2-6, 2024, Florence, Italy.

The Benefits of a Multi-Software Approach for Implementing Complex Kinetic Models in Process Simulators

Viktória Flóra Csendes[a]*, Attila Egedy[b], Alex Kummer[b], Sébastien Leveneur[a]

[a] *INSA Rouen Normandie, Univ Rouen Normandie, Normandie Univ, LSPC UR 4704, F-76000 Rouen, France*
[b]*Department of Process Engineering, University of Pannonia, Egyetem st. 10, H-8200 Veszprém, Hungary*

viktoria_flora.csendes@insa-rouen.fr

Abstract

Limitations regarding process design, optimization, and control often occur when using particular process simulators. A single software tool could not provide models of such a large application range and perform properly without making compromises in some areas (Pistikopoulos et al. (2021)). With the implementation of connection methodologies, integrated tools could be made by coupling popular process simulation software with each other or with external programming environments. These hybrid systems can handle complex user-defined problems and can be used for decision support, performing custom unit operations, operator training, process optimization, building control systems, and developing digital twins (Khan et al. (2021)).

Sustainable practices are more and more desired in the industry, and the development of technologies based on recycled and/or nature-derived feedstocks is in demand. For example, biomass valorization requires a more complex reaction system with unique components and kinetic models, which is often a rather time-consuming and complex task to implement into current process simulators (Alshehri et al. (2020)).

This work presents an example of an application where the shortcomings of commercial process simulators with restricted reaction kinetic structures can be solved (Csendes et al. (2023)). We proposed using the process simulator Aspen HYSYS linked with a MATLAB optimization algorithm to solve a reaction kinetic parameter identification problem regarding the production of γ-valerolactone in a dynamic simulation setting. A co-simulation setup was chosen to solve this MIMO problem, as the integration of the two software gives us the ability to run several simulation models, perform parameter identification, and validate the data at the same time from a main program, and that way obtain results in 'one-go' and organize data in one place.

Keywords: software linking, co-simulation, kinetic parameter identification, multi-software engineering

1. Multi-Software Engineering

Modelling chemical equipment, processes and reactions is a complex task, engineers and researchers highly rely on powerful software to solve these problems. Commercial process simulators are a great tool to perform simulation, where the mathematical equation systems are behind easy-to-use graphical interfaces. However, the manipulation or customization of the deeper mathematical correlations are often come with limitations, or simply restricted by the programs (Csendes et al. (2023)).

Multi-software engineering is used to overcome this problem, by using different parts of one or two software to complement each other. Programming environments for example have the advantage of containing more complex numerical methods, and this means that optimization algorithms and response surface methodology can also be used to achieve a wider application range (Rangaiah et al. (2020)). Building user-defined equation systems and utilising algorithms created in numerical solvers can be used via built-in toolboxes or native integration with commercial process simulators (Furda et al. (2020)). Like this, integrated tools can complement each other providing a more robust and complex system for modelling, parameter estimation, data regression, sensitivity analysis, optimization and control.

Multi-software engineering is a novel tool for connecting a priori and a posteriori models to keep up with the evolution of information technology.

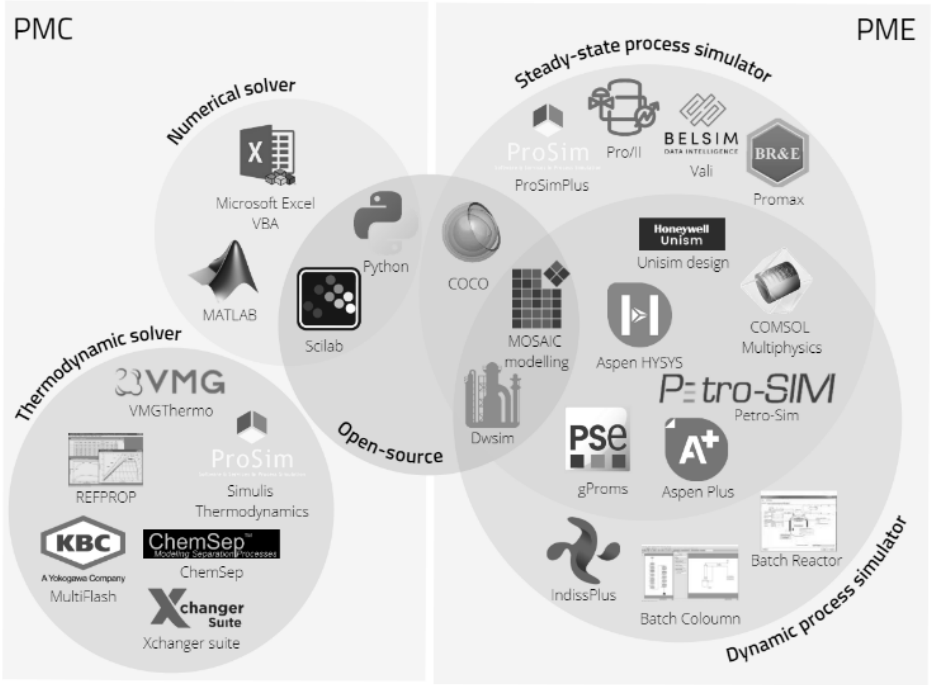

Figure 1. Categorization of popular process modelling components and environments.

2. Case study

Our case study showcases a kinetic parameter identification with software linking for the production of γ-valerolactone (GVL) from butyl-levulinate (BL) in a two-step hetero-catalytic reaction over Ru/C catalyst.

2.1. Simulator Development of the Case Study

A detailed description of the characteristics of the components as well as the setup used for the experiments is written in the works of Capecci and Wang (Capecci et al. (2021), Wang et al. (2020)). Four dynamic HYSYS simulation files were built according to the experimental setup. When generating the simulation in Aspen HYSYS, kinetics were simplified to Arrhenius type for the three reactions present in the system, where the pre-exponential factors and the activation energies could be reached via an internal HYSYS spreadsheet. The unit design contains a batch reactor equipped with a temperature controller to operate in an isotherm mode. Isobaric conditions were obtained with a high-pressure H2 inlet stream, similar to the experimental conditions.

2.2. Multi-Software Based Identification Framework for Kinetic Parameter Identification

The kinetic parameters were identified by linking the HYSYS simulator to the MATLAB environment, where the latter acted as the main program. The HYSYS models were run from MATLAB, where kinetic parameters were modified directly through the HYSYS spreadsheets. The identification framework within the MATLAB environment calculates the kinetic parameters of the HYSYS files, where their values were varied in each iteration step to achieve better fitting to the experimental data sets in each case based on the objective function, which is a minimum search with a quadratic error function.

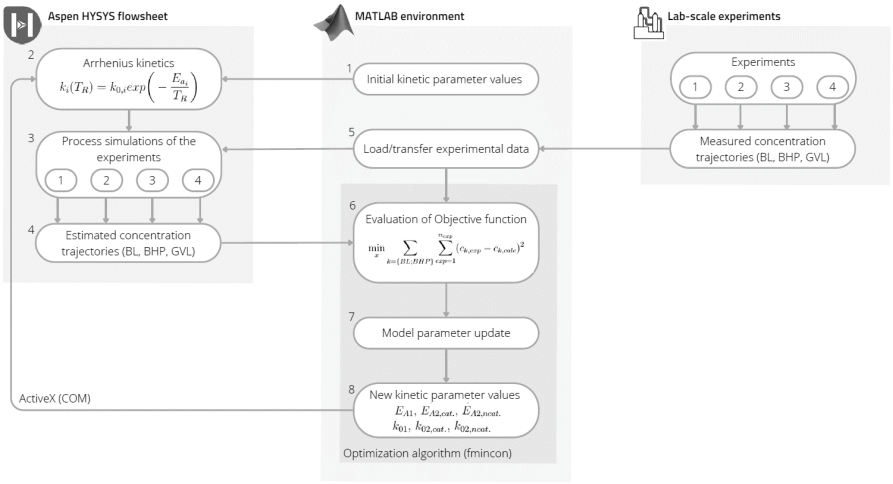

Figure 2. Outline of the identification framework connecting Aspen HYSYS and MATLAB.

3. Results

It can be seen in Figure 3. that the calculated concentration trajectories fit the experimental data well. The predictive ability of our simpler kinetic model is comparable with Capecci's model based on the R^2 indicator, their fitting to the concentration trajectories is 0.976 while ours is 0.952.

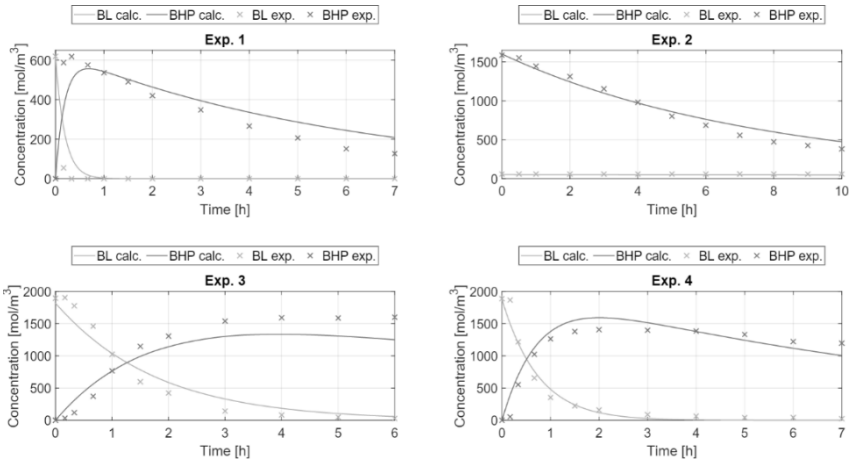

Figure 3. The concentration curve fittings resulting from the identification.

4. Conclusion

In a case study, parameter identification with multi-software engineering was performed to showcase one of the many application aspects of the technique. In our case, the lack of kinetics definition was crucial for model building inside the simulator. Therefore, a link between the dynamic process simulator Aspen HYSYS and the coding environment MATLAB was made utilizing an ActiveX connection. We found that the method provided good results and performed well in fitting the available experimental data.

References

A. S. Alshehri, R. Gani, F. You, 2020. Deep learning and knowledge-based methods for computer-aided molecular design—toward a unified approach: State-of-the-art and future directions. Computers & Chemical Engineering 141, 107005.

V. F. Csendes, A. Egedy, S. Leveneur, A. Kummer, 2023. Application of multi-software engineering: A review and a kinetic parameter identification case study. Processes 11 (5), 1503.

F. Khan, P. Amyotte, S. Adedigba, 2021. Process safety concerns in process system digitalization. Education for Chemical Engineers 34, 33–46.

E. N. Pistikopoulos, A. Barbosa-Povoa, J. H. Lee, R. Misener, A. Mitsos, G. V. Reklaitis, V. Venkatasubramanian, F. You, R. Gani, 2021. Process systems engineering–the generation next? Computers & Chemical Engineering 147, 107252.

P. Furda, M. Variny, Z. Labovská, T. Cibulka, 2020. Process drive sizing methodology and multi-level modeling linking MATLAB® and Aspen Plus® environment. Processes 8, 1495.

G.P. Rangaiah, Z. Feng, A.F. Hoadley, 2020. Multi-objective optimization applications in chemical process engineering: Tutorial and review. Processes 8, 508.

S. Capecci, Y. Wang, J. Delgado, V. Casson Moreno, M. Mignot, H. Grénman, D.Y. Murzin, S. Leveneur, 2021. Bayesian Statistics to Elucidate the Kinetics of g-Valerolactone from n-Butyl Levulinate Hydrogenation over Ru/C. Ind. Eng. Chem. Res. 60, 11725–11736.

Y. Wang, I. Plazl, L. Vernières-Hassimi, S. Leveneur, 2020. From calorimetry to thermal risk assessment: γ-Valerolactone production from the hydrogenation of alkyl levulinates. Process Saf. Environ. Prot. 144, 32–41.

ESCAPE-34 PSE-2024
European Symposium on Computer Aided Process Engineering
&
Process Systems Engineering

Flavio Manenti, Gintaras V. Reklaitis (Eds.), Book of Abstract of the 34th European Symposium on Computer Aided Process Engineering / 15th International Symposium on Process Systems Engineering (ESCAPE34/PSE24), June 2-6, 2024, Florence, Italy.

Hybrid Modelling Based on Model Order Reduction and Machine Learning, and its Application for Thermal Cracking Furnace

Jin Ma,[a] Meihong Wang,[b,*] Wenli Du,[a] Feng Qian[a]

[a]*Key Laboratory of Smart Manufacturing in Energy Chemical Process, Ministry of Education, East China University of Science and Technology, Shanghai 200237,China*
[b]*Department of Chemical and Biological Engineering, The University of Sheffield, Sheffield S1 3JD, UK*
Meihong.wang@sheffield.ac.uk

Abstract

High-fidelity modelling is fundamental in simulation, control and optimization of chemical processes. However, high-fidelity model is usually of strong nonlinearity, multivariable coupling and strong system constraints, which requires high computational demand. Developing a multi-dimensional model with lower computational demand poses a critical challenge. Our research will combine reduced order models (ROM) with machine learning to address the challenge. ROM is the projection of a multidimensional system into a low-dimensional subspaces, whereas machine learning is used to overcome the limitation of ROM applying to nonlinear and multi-physics models. A three-step framework is proposed. Firstly, adaptive sampling strategy is adopted to collect the "fewer but better" snapshots calculated by full order model with high computational demand. Then, proper orthogonal decomposition is adopted to generate reduced bases. Finally, relying on exposed polynomial structure, learning a physics-based ROM. The proposed method is demonstrated in thermal cracking furnace. Numerical case studies show that the proposed method can accurately predict temperature, velocity and species concentration profiles in cracking furnace. The optimisation of the oxygen content in the fuel gas of thermal cracking furnace is performed. The results show that the computation demand can be reduced significantly while ensuring the optimisation accuracy.

Keywords: hybrid modelling, thermal cracking furnace, reduced order models, machine learning, computational demand, optimisation

1. Introduction

1.1. Background

High-fidelity modelling is fundamental in simulation, control and optimization of chemical processes. In recent decades, beneficial from the development of computational fluid dynamic (CFD) technology, the detailed three-dimensional high-fidelity models coupled mass, heat transfer and reactions were established for solving various physical information of process such as temperature, pressure and species concentration field,

which is important for equipment design and parameter optimization. However, the dimensional of CFD models involving complicated physiochemical phenomena explodes to several million degrees as the models become more detailed. When high-fidelity model needs to be repeated calculations in optimization and design, three is a tradeoff between expensive computational resources and accuracy.

1.2. Literature review

In such situation, lots of various simplified methods is proposed to address this problem. Several works focus on the reduction of process mechanisms, which would lead to excellent performance with constraint conditions. For example, the Hottel zone method for simplifying the calculation of radiative heat transfer in thermal cracking furnace (Joo et al., 2000). Improvements based on first-principles models are not trivial, a long trial-and-error process is required to match the improved model to the detailed model under specific conditions. Another approach used to cut computational cost is model order reduction. The classical generation of reduced order model (ROM) is on the basis of proper orthogonal decomposition (POD) and Galërkin projection. Cutillo et al. (2023) developed a low computational cost ROM based on POD-Galërkin to predict the statement of methanation reactor. Since ROM is derived by projecting the full order model onto a low-dimensional subspace, it is precise for linear models. However, it still makes the numerical solution computationally expensive for nonlinear models. The upgraded model order reduction methods combined POD with discrete empirical interpolation method (DEIM) is usually selected to address this problem by evaluating the nonlinear problems at only fewer interpolation points.

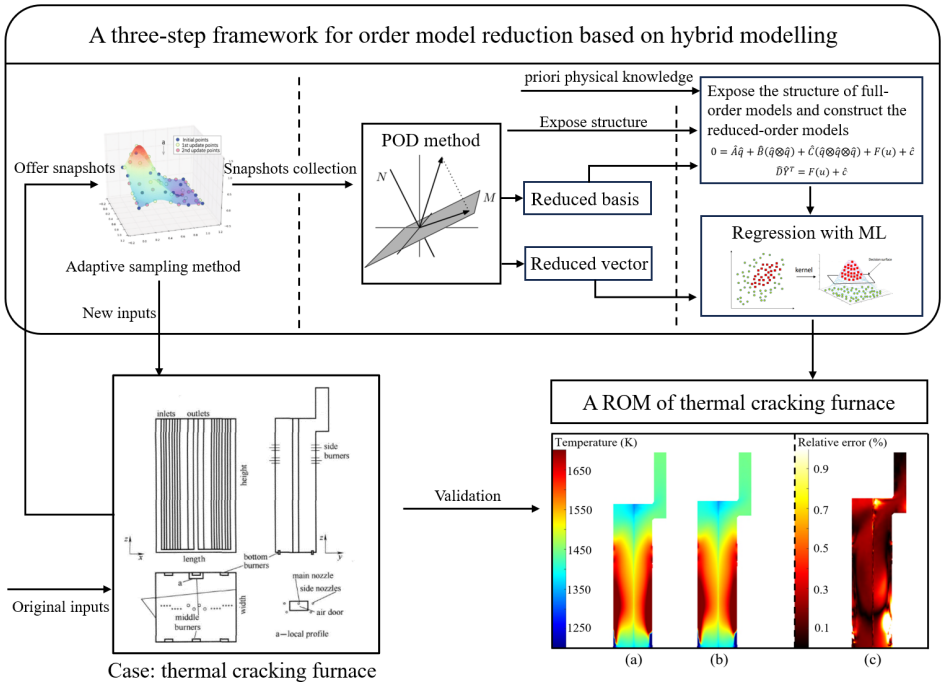

Figure 1 Framework of the proposed ROM approach for thermal cracking furnace

Bizon and Continillo (2020) applied the POD/DEIM method to optimize the design of a non-isothermal hybrid catalyst pellet and reduced the calculation cost. Bremer et al.

(2016) employed the POD/DEIM method for model order reduction of non-linear model of catalytic tubular reactors. One of the drawbacks of POD/DEIM is not a significant reduction in computational efficiency, because a more accurate ROM often involves more interpolation points. The challenge of model order reduction for nonlinear models can also be solved using existing machine learning methods. Lee et al., (2021) built ROM using POD integrated machine learning for 500 MWe tangentially fired pulverized coal boiler. However, ROM constructed with machine learning have poor extrapolation performance. Another effective method to address the mentioned challenge is hybrid modelling (Swischuk et al., 2020), which combines first principles knowledge and machine learning to improve model accuracy and reliability of the model.

1.3. Novelty of this study

In this work, a three-step framework for commercial-scale CFD model with combustion process is proposed based on model order reduction and hybrid modelling approaches, providing an accurate and effective solution for data-driven modelling of commercial-scale steady-state processes. The constructed nonintrusive ROM exploits hard-earned data to the maximum extent possible and show a good predictive performance in the face of complex nonlinear and multivariate coupled problems. We show the implementation of this framework. First, adaptive sampling strategy is adopted to collect the "fewer but better" snapshots calculated by full order model with high computational cost. Then, POD method is adopted to generate the reduced bases. Finally, relying on exposed polynomial structure, learning a physics-based ROM for high-fidelity model. The model developed by proposed framework can be applied for cracking furnace to design, performance prediction, operation control and process optimization. The novel contributions of this study are as follows:

(1) Reduced the reliance on the amount of data using two measures: improved adaptive sampling methods and hybrid modelling.
(2) Hybrid modelling is used as a substitute for a generic off-the-shelf machine learning approach, the prior knowledge is extracted to correlate the inputs and outputs, thus improving model extrapolation performance.
(3) Developing a ROM of ethylene cracking furnace to significantly increase computational efficiency and save time cost with minimal loss of model fidelity.

2. Methodology

2.1. Proper orthogonal decomposition (POD)

The POD approach used to develop projection-based ROM has been widely adopted in physical fields approximation in geomechanics, aerospace, and other fields. In this work, a collection of the snapshots of full order model is given using high-fidelity CFD model developed in Fluent®, and POD is used to produce the basis via these snapshots.

Consider the nonlinear equations $G(q,u) = \mathbf{0}$ with state vector $q \in \mathbb{R}^{dn_x}$ and input $u \in \mathbb{R}^m$. These equations can be solved under the specific input u, that is, the operating condition, and the solution (state vector q) are available. Information of the process can be obtained by processing state vector q. In order to acquire the ROM in a low-dimensional subspace, a reduced basis $V_r = [v_1, v_2, \ldots v_r]$need to be defined and satisfied:

$$\tilde{q} = \sum_{i=1}^{r} v_i \hat{q}^i \tag{1}$$

Where $\tilde{q}$ is the approximation of state vector q, and $\hat{q} = [\hat{q}^1, \hat{q}^2, \dots \hat{q}^r]^T$ is the vector projected from the state vector q to the r- dimensional subspace, typically called reduced vector, and in general, $r \ll dn_x$. A set of state vectors solved by corresponding inputs is called a snapshot. The n snapshots and their corresponding inputs are collected and used to generate the matrices $Q = [q_1, q_2, \dots q_n] \in \mathbb{R}^{dn_x \times n}$ and $U = [u_1, u_2, \dots u_n] \in \mathbb{R}^{m \times n}$. The tall and skinny matrix Q is called snapshot matrix and contain snapshots as its columns. POD approach is implemented by computing the SVD of the snapshot matrix and obtain the reduced basis.

2.2. Adaptive sampling method

Snapshots used for ROM have a significant impact on the accuracy of ROM, as POD methods can't describe details beyond the training data. In the reduced order model problem, considering the cost of high-fidelity model for more extensive snapshots may not be computationally affordable, adaptive sampling method is adopted, which is to reduce the time cost of data collection by analysing known snapshots to reduce unnecessary sampling. Considering the Eq. 1, prediction quality of the ROM is subject to the influence of the reduced basis and the reduced vector. The influence of reduced basis and reduced vector is quantified in different methods. The sample space is fitted to the influence using off-the-shelf machine learning methods to guide the next new snapshot. The next sample is selected as the largest quantified influence given as Eq. 2.

$$u_{new} = argmax_{u^{pre} \in P} f_{NN}(u^{pre}) \tag{2}$$

The new sample is added to the initial set, and the adaptive sampling process is repeated until $maxI^b < \epsilon^b$, where ϵ^b is tolerance criterion defined by user.

2.3. Learning physics-based reduced order model

For the nonlinear equations $G(q, u) = \mathbf{0}$ in CFD model, it can be decomposed into polynomial structure in mathematics. Qian et al. (2019) derivate the polynomial structures of Navier-stokes equation by convert terms and transformed dependent variables. Consider the governing equation discrete nonlinear equation rewritten in polynomial form:

$$0 = Aq + B(q \otimes q) + C(q \otimes q \otimes q) + f(u) + c \tag{3}$$

The governing equations in polynomial form is projected into the defined low-dimensional subspace by the established reduced basis V_r. The approximation of state vector q, $q \approx V_r \hat{q}$, is introduced. The equation is then left multiplied by the transpose of V_r, generating the ROM is written as

$$0 = \hat{A}\hat{q} + \hat{B}(\hat{q} \otimes \hat{q}) + \hat{C}(\hat{q} \otimes \hat{q} \otimes \hat{q}) + F(u) + \hat{c} \tag{4}$$

The unknown operators $\hat{A}$, $\hat{B}$, $\hat{C}$ are combined in the matrix $\widehat{D}$, and the term including reduced vector $\hat{q}$ are combined in the vector $\hat{Y}$. The governing equation in low-dimensional subspace is then written as Eq. 5.

$$\widehat{D}\hat{Y}^T = F(u) + \hat{c} \tag{5}$$

In order to eliminate the operator $\widehat{D}$ of output, POD approach is used twice to reduce the order of $\hat{Y}^T$ from $r + r^2 + r^3$ to r, and the training data that used to generate the reduced

basis V_r is used again to generate the reduced basis of $\hat{Y}^T$ shown in Eq. 6. The governing equation in low-dimensional subspace is transformed into the Eq. 7.

$$\hat{Y}^T \approx vr \times \widehat{Y_{hat}}^T \tag{6}$$

$$\widehat{Y_{hat}}^T = \widehat{D_{hat}}^{(-1)} F(u) + \hat{c}_{hat} \tag{7}$$

Where $\widehat{D_{hat}} = \hat{D} \times vr \in \mathbb{R}^{r \times r}$ is a square matrix that can be inverted in practical applications. This form is the same as multioutput support vector machine (MSVM), and this method is adopted to regression the relationship between $\widehat{Y_{hat}}^T$ and input u.

3. Application for thermal cracking furnace

3.1. Cracking furnace full order model and numerical method

A steady-state solver of the commercial CFD software ANSYS Fluent® is used to produce training data (snapshots) of published thermal cracking furnace (Hu et al., 2015). Standard k-ε method is applied as turbulence model, Discrete Ordinates model was used to calculate the radiation source term, and eddy dissipation concept is used to couple GRI 3.0 chemical reaction mechanisms. The semi-implicit method for pressure-linked equations (SIMPLE) algorithm for pressure-velocity coupling is selected to solve the nonlinear governing equations for the conservation of mass momentum, energy, radiation and species based on finite volume method.

The nonlinear governing equations discretized implicitly by a second-order upwind scheme, turn into a series of equations for the specific dependent variables in every computational cell. For a spatial discretization with n_x cells and d dependent variables, the partial differential equations composed of steady-state governing equations lie in a dnx-dimensional system of nonlinear equations.

3.2. Model validation and results

The high-fidelity thermal cracking furnace CFD model was run with 278,397 divided grids, and each set of steady state data was run for 20-30 hours in a computer with 64 cores CPU and 128G RAM, and a total of 40 sets of data were obtained for training and validation. The ROM of the thermal cracking furnace has been established using the proposed framework and its predicted longitudinal section temperature of the furnace is shown below. The results show a very good agreement between the temperature calculated by high-fidelity CFD model and predicted by the ROM.

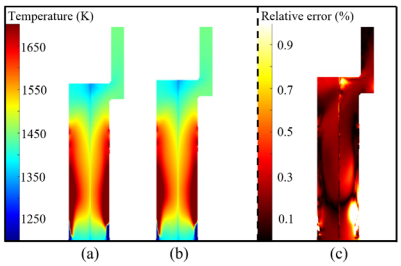

Figure2. (a) Temperature of High-fidelity model (b) temperature of ROM and (c) relative error.

3.3. Case study on optimisation of the oxygen content

Turbulence in the cracker results in irregular mixing of air and fuel. It is necessary to increase the air flow rate to avoid the generation of CO. In practice, the excess air factor for thermal cracking furnace is determined empirically and is generally set at 1.1 (i.e. 1.1 times the amount of oxygen required for complete combustion of the fuel). The ROM developed by the proposed framework allows for a fast prediction of the outlet CO content at different fuel flow rates to determine the optimal excess air coefficient.

The optimal excess air coefficient of 1.086 was determined using a high-fidelity full-order model with the condition of the fuel flow rate 11,000 kg/h. A total of 24 runs were performed, requiring more than 20 days to perform the calculation. In contrast, the optimal excess air coefficient of 1.088 can be quickly obtained in less than 15 minutes using the ROM.

4. Conclusion

In this paper, we propose a three-step framework for model order reduction based on POD and machine learning. Firstly, an adaptive sampling strategy is used to collect "fewer but better" snapshots computed from the high-fidelity CFD model. Then, POD is performed to generate the reduced basis. Finally, a polynomial structure of the model mechanism is derived to learn the physical-based ROM for the high-fidelity model. The proposed method is applied to the thermal cracking furnace. Very good agreement between the high-fidelity CFD model and ROM validates the proposed methodology. A case study of oxygen content optimization is carried out and this demonstrated that the proposed method can significantly reduce the computational demand.

References

EJ. Joo, KH. Lee, MY. Lee, SW. Park, 2000, CRACKER-A PC based simulator for industrial cracking furnaces, Computers & Chemical Engineering, 24(2e7), 1523e8.

EA. Cutillo, E. Mancusi, K. Bizon, P. Bareschino, G. Continillo, 2023, A Reduced Order Model for the Prediction of the Dynamics of a Methane Reactor, Computer Aided Chemical Engineering, Volume 52, Pages 1199-1204, ISSN 1570-7946, ISBN 9780443152740. https://doi.org/10.1016/B978-0-443-15274-0.50191-8.

K. Bizon, and G. Continillo, 2020, Optimal Design of a Non-isothermal Hybrid Catalyst Pellet based on POD-DEIM Reduced-order Methodology, Computer Aided Chemical Engineering, Volume 48, Pages 271-276, ISSN 1570-7946, ISBN 9780128233771. https://doi.org/10.1016/B978-0-12-823377-1.50046-X.

J. Bremer, P. Goyal, L. Feng, P. Benner, K. Sundmacher, 2016, Nonlinear Model Order Reduction for Catalytic Tubular Reactors, Computer Aided Chemical Engineering, Volume 38, Pages 2373-2378, ISSN 1570-7946, ISBN 9780444634283. https://doi.org/10.1016/B978-0-444-63428-3.50400-8.

W. Lee, K. Jang, W. Han, KY. Huh, 2021, Model order reduction by proper orthogonal decomposition for a 500 MWe tangentially fired pulverized coal boiler, Case Studies in Thermal Engineering, Volume 28, 101414, ISSN 2214-157X. https://doi.org/10.1016/j.csite.2021.101414.

R. Swischuk, B. Kramer, C. Huang, K. Willcox, 2020, Learning Physics-Based Reduced-Order Models for a Single-Injector Combustion Process, AIAA J, 58. https://doi.org/10.2514/1.J058943.

E. Qian, B. Kramer, A. Marques, K. Willcox, 2019, Transform & Learn: A Data-Driven Approach to Nonlinear Model Reduction, AIAA Aviation and Aeronautics Forum and Exposition, 2019-3707. https://doi.org/10.2514/6.2019-3707.

G. Hu, CM. Schietekat, Y. Zhang, F. Qian, 2015, Impact of Radiation Models in Coupled Simulations of Steam Cracking Furnaces and Reactors, Industrial & Engineering Chemistry Research, 54 (9), 2453-2465. https://doi.org/10.1021/ie5042337.

ESCAPE-34 PSE-2024
European Symposium on Computer Aided Process Engineering
&
Process Systems Engineering

Flavio Manenti, Gintaras V. Reklaitis (Eds.), Book of Abstract of the 34th European Symposium on Computer Aided Process Engineering / 15th International Symposium on Process Systems Engineering (ESCAPE34/PSE24), June 2-6, 2024, Florence, Italy.

Waste-to-Methanol-to-Ethylene for Future Circular Plastics

Cecilia Salah[a], Robert Istrate[b], Anders Bjørn[c], Gonzalo Guillén-Gosálbez[a*]

[a] *Institute for Chemical and Bioengineering, Department of Chemistry and Applied Biosciences, ETH Zürich, 8093 Zürich, Switzerland*

[b] *Institute of Environmental Sciences (CML), Department of Industrial Ecology, Leiden University, 2300 RA Leiden, The Netherlands*

[c] *Center for Absolute Sustainability, Department of Environmental and Resource Engineering, Technical University of Denmark, 2800 Kongens Lyngby, Denmark*
gonzalo.guillen.gosalbez@chem.ethz.ch

Abstract

The global demand for polymers is increasing at a fast pace, which creates a clear need for alternative pathways to produce them more sustainably. Specifically, the linear nature of the current plastics economy based on fossil carbon poses a threat to the environment, as it is highly resource and carbon intense. In this work, we assess the environmental performance of an alternative circular carbon strategy for plastics based on chemical recycling routes with high technology readiness level, whereby polymer waste is first converted into methanol via gasification, and the latter is subsequently transformed into building blocks for plastics production. Results showcase that the circular route based on chemical recycling enables a significant reduction of the life-cycle emissions of the plastics economy, more so in the future as power mixes get decarbonized.

Keywords: ethylene, chemical recycling, life cycle assessment, prospective life cycle assessment.

1. Introduction

The increasing demand for polymers, notably in the plastic packaging sector, is coupled with large amounts of waste generated globally, with only a small fraction being recycled (Geyer et al., 2017). Moreover, polymers production is carbon and resource intensive, following a mostly linear economy, with most polymers deriving from fossil feedstock. The need for a circular polymer economy has motivated the development and implementation of new recycling technologies aiming to extend the lifetime of materials and decrease the detrimental environmental effects caused by mismanaged plastic waste (Ellen MacArthur Foundation, 2016).

For instance, Meys et al. (2021) have explored pathways to enable net-zero plastics, heavily relying on renewable energies, carbon capture and utilization, and increasing recycling rates up to 70%. However, their study excludes high technology readiness level (TRL) technologies for chemical recycling, focusing instead on low TRL routes that have

not been deployed at scale yet and, thus, are affected by more pronounced uncertainties. Moreover, this study omitted how expected changes in the economy, e.g., due to decarbonization trends in power systems, will influence the performance of the investigated chemical recycling technologies.
We here study the emission-reduction potential of closing the ethylene loop by deploying high TRL technologies based on waste polymers-to-methanol and methanol-to-olefins routes. We find that this route enables polymers with a lower carbon footprint than the current plastics economy, notably in a future with low-carbon power mixes.

2. Methodology

The chemical recycling route consists of the gasification of plastic waste to produce syngas (Salah et al. 2023), which is then converted into methanol and further transformed into ethylene based on the work by Ioannou et al. (2023). We implemented detailed process simulations in Aspen v12 and computed the mass and energy balances of the waste-to-methanol-to-olefins process to build the life cycle inventory needed for the environmental assessment.
The life cycle assessment (LCA) was carried out in Brightway2, using Ecoinvent v3.8, following a cradle-to-grave approach. The aforementioned circular route was compared to the business-as-usual (BAU) fossil ethylene obtained from naphtha steam cracking. Both systems considered the production of ethylene, its transformation to polyethylene, collection, sorting and end-of-life treatment. The BAU end-of-life was defined considering the global average waste management of waste polymers in 2015 described by Geyer et al. (2017). In the circular route, it is necessary to account for losses of the waste-to-methanol-to-olefins process in order to close the mass balance. For that reason, this scenario also accounts for a make-up of BAU ethylene.
The climate change impact of both routes was calculated according to the IPCC 2021 GWP100 method. Additionally, we explored the evolution of environmental impacts with time, by performing the LCA in 2020 and 2050 using scenario information from an integrated assessment model (IAM) for the background system. Specifically, this prospective assessment was carried out for the climate policy scenario PkBudg500 of the socioeconomic pathway SSP2, following the REMIND framework.

3. Results and Discussion

Implementing the chemical recycling technology for circular polymers in 2020 would enable a 17.5% reduction of the global warming impact (GWI) relative to the BAU scenario. Analysing the process contributions to the overall GWI (Figure 1), we find that the emissions linked to the incineration of waste polymers are the main contributor to the GWI in the BAU scenario, followed by electricity and the direct emissions of the fossil route deployed for ethylene production. Analogously, more than half of the circular polymers' GWI comes from the electricity used in its life cycle.
Moreover, following the decarbonization pathway PkBudg500 of REMIND, we find that the emissions gap between the circular economy of polymers and the BAU will grow in the future substantially. This is because the former is much more sensitive to the carbon footprint of the power mix, which will be drastically reduced in the future.

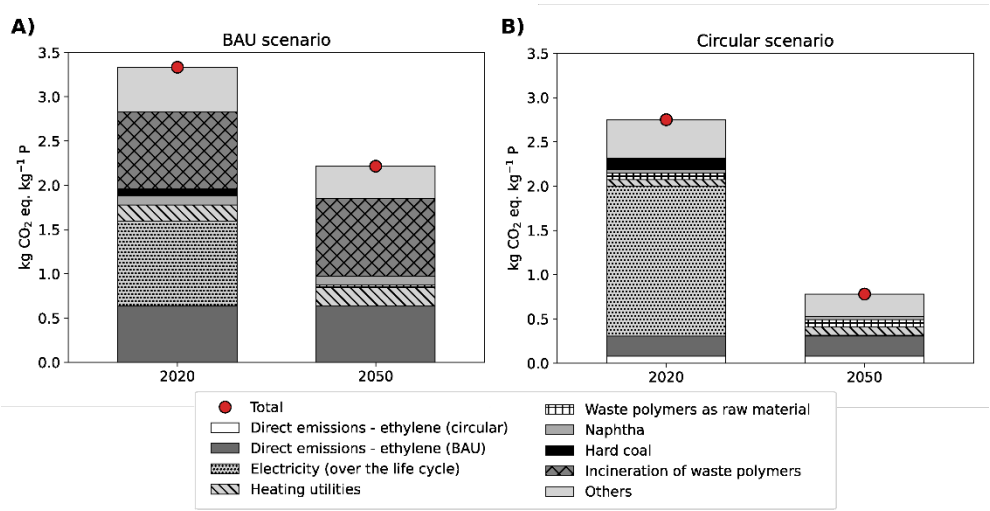

Figure 1. Global warming impact of the BAU (A) and circular (B) scenarios in 2020 and 2050 following the REMIND decarbonization pathway PkBudg500.

4. Conclusions

Our work studied the environmental potential of implementing a high-TRL chemical recycling route to decarbonize the plastics economy. We found that the waste-to-methanol-to-olefins route already outperforms the BAU technology at present (17.5% less carbon footprint). Moreover, the gap between both will most likely grow substantially in the future due to decarbonization trends across sectors. We therefore highlight the need to further investigate circular carbon models for plastics production. Moreover, our results underscore the importance of conducting prospective life cycle assessments to support decision- and policy-making more effectively in the quest for a circular plastics economy.

Acknowledgements

This publication was created as part of NCCR Catalysis (grant 180544), a National Centre of Competence in Research funded by the Swiss National Science Foundation.

References

Ellen MacArthur Foundation, 2016, The New Plastics Economy - Rethinking the Future of Plastics.

C. Salah, S. Cobo, J. Pérez-Ramírez, G. Guillén-Gosálbez, 2023, Environmental Sustainability Assessment of Hydrogen from Waste Polymers, 11, 3238-3247.

I. Ioannou, J. Javaloyes-Antón, J.A. Caballero, G. Guillén-Gosálbez, 2023, Economic and Environmental Performance of an Integrated CO_2 Refinery, ACS Sustainable Chemistry & Engineering, 11, 1949-1961.

R. Geyer, J. Jambeck, K. Law, 2017, Production, Use, and Fate of All Plastics Ever Made, Science Advances, 3, e1700782.

R. Meys, A. Kältelhorn, M. Bachmann, B. Winter, C. Zibunas, S. Suh, A. Bardow, 2021, Achieving net-zero greenhouse gas emission plastics by a circular carbon economy, Science, 374, 71-76.

ESCAPE-34 PSE-2024
European Symposium on Computer Aided Process Engineering
&
Process Systems Engineering

Flavio Manenti, Gintaras V. Reklaitis (Eds.), Book of Abstract of the 34th European Symposium on Computer Aided Process Engineering / 15th International Symposium on Process Systems Engineering (ESCAPE34/PSE24), June 2-6, 2024, Florence, Italy.

Modeling of Slurry Bubble Column Reactor for Hydrogenolysis of PET Waste

Jae Hwan Choi, Jong Min Lee*

School of Chemical and Biological Engineering, Seoul National University, 1 Gwanak-ro, Gwanak-gu, Seoul 08826, Korea
jongmin@snu.ac.kr

Abstract

The modeling of slurry bubble column reactor (SBCR) for hydrogenolysis of polyethylene terephthalate (PET) was conducted. The axial dispersion model is commonly employed for modelling SBCRs. However, its suitability for application to PET hydrogenolysis reactors may be limited due to extremely viscous molten PET and high operating pressure, distinguishing them from conventional reaction systems Therefore, a model incorporating both axial and radial dispersion was employed. The partial differential equations of the model were approximated using a finite difference scheme and solved by iterative method. Through this approach, we found that the radial velocity and radial gradients of concentration and axial velocity are negligible. And sensitivity analysis revealed that the axial dispersion coefficient has a greater impact on PET conversion compared to the radial dispersion coefficient.

Keywords: modelling, slurry bubble column reactor, hydrogenolysis, PET recycle

1. Introduction

Over 300 million tons of plastics are manufactured annually, with PET ranking as the fourth most produced. Currently, thermal degradation is the predominant method for recycling PET, but it compromises some thermal and mechanical properties of PET. Consequently, there is a need to investigate more efficient and economical PET recycling techniques. Hydrogenolysis of PET, known for its cost-efficiency, has gained significant attention (Wu, 2021). This process, characterized by relatively slow reaction rates, high pressure, and high viscosity, differs from conventional three-phase reaction systems. Thus, reactor design for PET hydrogenolysis requires consideration of numerous unique factors, yet research in this area remains sparse.

Among the diverse three-phase reactors, the stirring reactors are suitable for highly viscous system but are challenging to implement in industrial-scale reactors at high pressure. Similarly, the trickle bed reactor, commonly employed in industrial applications, is unsuitable for highly viscous system and therefore, not a suitable choice for PET hydrogenolysis reactors. Consequently, this research modeled a PET hydrogenation reactor based on the SBCR, capable of handling both high pressure and viscous system. Then, instead of the axial dispersion model commonly used for SBCR modeling, we employed a model that accounts for both axial and radial dispersion. Through this model,

we analyzed the velocity and concentration in the radial direction and the radial gradient of the axial velocity. Finally, a sensitivity analysis of the dispersion coefficient was performed.

2. Mathematical model

2.1. Governing equations

The process of PET hydrogenolysis is relatively slow which requires a low liquid flowrate to achieve sufficient conversion. Given that the catalyst particles are sufficiently small, it is deemed suitable to use a homogeneous model. Additionally, fluctuations in gas partial pressure and mass transfer limitations are negligible since the reactor is operated under high pressure (100 bar). Taking all these factors into account, an isothermal and steady-state reactor model was developed, incorporating mole, mass and momentum balance as shown below.

$$-\nabla \cdot (C_i \vec{u}) + \nabla \cdot \left(\vec{D} \cdot \nabla C_i\right) + r_i = 0 \tag{1}$$

$$\nabla \cdot (\rho \vec{u}) = 0 \tag{2}$$

$$-\nabla \cdot (\rho \vec{u}\vec{u}) + \rho \vec{g} - \nabla P + \nabla \cdot \tau = 0 \tag{3}$$

$$\tau = \nabla \cdot (\mu_{eff} (\nabla \vec{u} + \nabla \vec{u}^T)) \tag{4}$$

where r_i is generation rate of species i, τ is the stress tensor, C_i is the concentration, $\vec{u}$ is the velocity vector, $\vec{D}$ is the dispersion coefficient, ρ is the density of liquid, $\vec{g}$ is the gravity acceleration vector and μ_{eff} is the effective viscosity of liquid.

The radial and axial dispersion coefficient was represented as follows, based on the work of Kim (1928) and Kang (1986), respectively.

$$Pe_l = \frac{d_p U_l}{D_z} = 20.19 \left(\frac{d_p}{D_{column}}\right)^{1.66} \left(\frac{U_l}{U_l + U_g}\right)^{1.03} \tag{5}$$

$$Pe_r = \frac{d_p U_l}{D_r} = 28.3 \left(\frac{d_p}{D_{column}}\right) \left(\frac{U_l}{U_l + U_g}\right)^{1.16} \tag{6}$$

2.2. Reaction kinetics

The product of PET hydrogenolysis reaction depend on the catalyst. In this study, we assumed xylene as final product based on the study of Wu (2021). Also, the reaction was simplified with assuming direct conversion of PET into xylene by the 1st order reaction.

$$PET + H_2 \rightarrow Xylene + 2CO_2 \tag{7}$$

As mentioned above, mass transfer limitation was negligible. So, the concentration of H_2 and CO_2 was expressed by follows.

$$C_i = P_i * He_i \tag{8}$$

where He_i is the Henry constant of the component i. Then, the reaction rate can be expressed by

$$r_{PET} = -kC_{PET}C_{H_2}w_{cat} \quad (9)$$

where w_{cat} is the mass of the catalyst. The reaction rate constant (k) was assumed to be 0.000340 $m^3/mol \cdot s \cdot kgcat$, which is equivalent to 10 grams of PET being converted to 99.99 mol% within 12 hours in the batch reactor experiment.

2.3. Model solution

Boundary conditions of the system are below.

$$z = 0,\ v = \text{inlet condition} \quad (10)$$

$$z = L,\ u_r = 0,\ \frac{\partial u_z}{\partial z} = 0\ , \frac{\partial P}{\partial z} = 0,\ \ \frac{\partial C_i}{\partial z} = 0 \quad (11)$$

$$r = 0,\ u_r = 0,\ \frac{\partial u_z}{\partial r} = 0\ , \frac{\partial P}{\partial r} = 0,\ \ \frac{\partial C_i}{\partial r} = 0 \quad (12)$$

$$r = R,\ u_r = 0,\ u_z = 0\ , \frac{\partial P}{\partial r} = 0,\ \ \frac{\partial C_i}{\partial r} = 0 \quad (13)$$

where v stands for the all variables. Then, the partial derivatives in the radial and axial coordinates are approximated by finite difference method. In general, simulations of reactor systems employ 2nd order central difference or backward Euler for the computational simplification. However, in this study, a 4th order central difference scheme was employed to minimize errors, particularly when sparse grids were used. The approximated nonlinear equations were implemented in Python, utilizing Pyomo, and solved by interior point method with IPOPT (Hart et al., 2017).

3. Result and Discussion

3.1. Laboratory-scale simulation

For the laboratory-scale reactor simulation, the reactor diameter and height were assumed to be 0.5 m and 2 m, respectively. Then simulations were carried out with varying grid sizes, and the results are presented in Figure 1 and Figure 2.

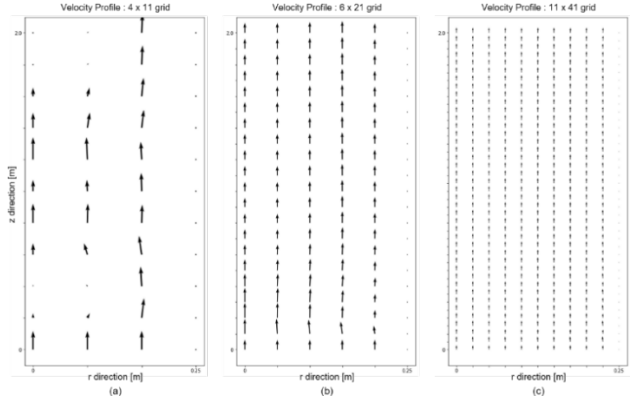

Figure 1. Velocity profile of the reactor. (a), (b), (c) correspond to grid sizes of 4 x 11, 6 x 21, and 11 x 41 in the radial (r) and axial (z) directions, respectively

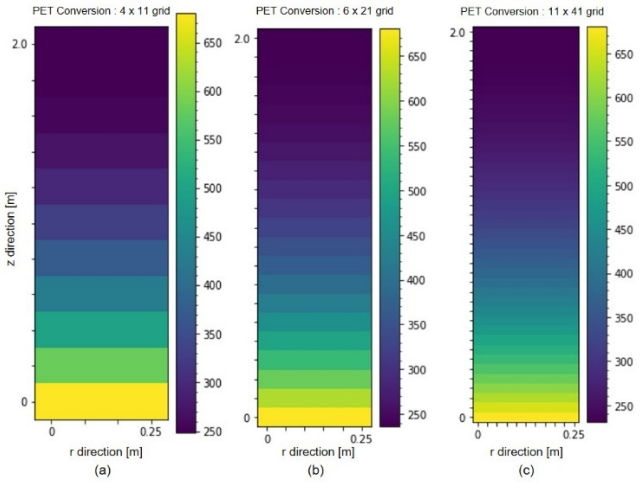

Figure 2. PET concentration profile of the reactor. (a), (b), (c) correspond to grid sizes of 4 x 11, 6 x 21, and 11 x 41 in the radial (r) and axial (z) directions, respectively.

In Figure 1.a, for small grid number, a distorted velocity field is observed, transitioning into a plug flow configuration as the grid number increases. This transition is attributed to the error of the 4th order central difference method, where the leading error is proportional to the fourth power of the grid size, resulting in a smaller error with a larger grid number. Notably, in Figure 1.c, radial velocity is nearly absent, underscoring the suitability of employing an axial dispersion model for the laboratory-scale reactor that disregards radial dispersion.

Figure 2 shows concentration profiles exhibiting a more regular pattern in contrast to the velocity field. However, the observed conversions stand at 63.4 mol%, 65.2 mol%, and 66.0 mol% in Figure 2.a, 2.b and 2.c, respectively. This discrepancy is likely due to grid size-related errors. Nevertheless, when the grid size is increased to 21 x 51, the conversion is recorded at 66.0 mol%, indicating that an 11 x 41 grid size yields a sufficiently low error for the laboratory-scale reactor simulation.

3.2. Effect of the dispersion coefficient

Diverse correlations for dispersion coefficients have been proposed, but none have specifically addressed systems characterized by high viscosity and high pressure, as in our present study. Furthermore, many dispersion coefficient correlations tend to lose accuracy under different system conditions (Pham, 2022). Due to the uncertainty associated with the dispersion coefficients derived from Eq. (5) and Eq. (6), a sensitivity analysis on the dispersion coefficient was conducted to analyze its impact on the system.

3.2.1. Radial dispersion coefficient

As shown in Figure 3, the impact of changes in the radial dispersion coefficient, D_r, on PET concentration was negligible. This trend is consistent with analogous observations in the velocity field. Therefore, applying an axial dispersion model to an SBCR reactor for PET hydrogenolysis is a suitable choice.

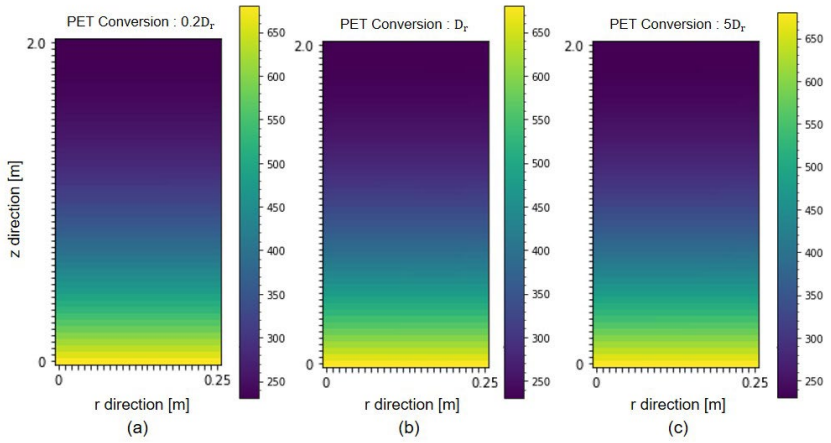

Figure 3. PET concentration profile in the reactor with changing the radial dispersion coefficient. (a), (b), (c) corresponds to radial dispersion coefficients scaled by 0.2, 1(unchanged) and 5, respectively.

3.2.2. Axial dispersion coefficient

The impact of the axial dispersion coefficient on the conversion of PET in the reactor is greater than that of the radial dispersion coefficient (Figure 4). With the dispersion coefficient calculated by Eq. (5), the conversion rate was found to be 0.6 in mol. However, when the dispersion coefficient was varied to 0.2 times and 5 times its calculated value, the conversion rates are measured at 0.65 and 0.55, respectively. While these variations have a minimal impact on the velocity field, their significant influence on the concentration within the reactor underscores the importance of selecting an appropriate axial dispersion coefficient.

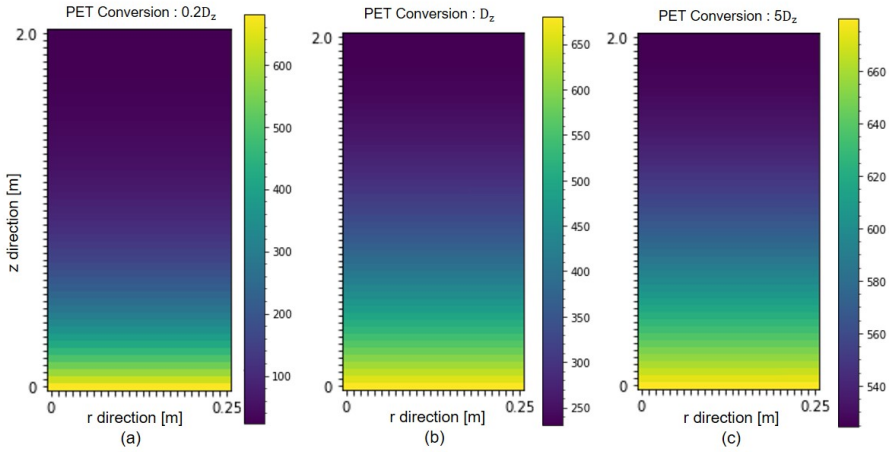

Figure 4. PET concentration profile in the reactor with changing the axial dispersion coefficient. (a), (b), (c) corresponds to radial dispersion coefficients scaled by 0.2, 1(unchanged) and 5, respectively.

In the majority of dispersion coefficient correlation studies, the coefficient is expressed in terms of the superficial velocities of gas and liquid which are constant along the reactor.

Even in cases where this is not explicitly stated, many studies assume a constant dispersion coefficient throughout the SBCR for computational simplification. Under such circumstances, the $\vec{D}$ in Eq. (1) is treated as a constant, eliminating the need for gradient calculation. However, as demonstrated in the above, the axial dispersion coefficient has a significant impact on the concentration profile in the reactor, which can make the model less accurate in the above case. Consequently, for a more precise and accurate model, it is essential to employ a correlation that consider changes in the axial dispersion coefficient.

4. Conclusion

In this study, we show that the impact of radial dispersion in the SBCR for PET hydrogenolysis can be neglected. Utilizing a sufficient number of grid points to simulate the SBCR, radial velocity approached nearly zero, and the radial gradient of concentration and axial velocity was negligible. Furthermore, with significant variations in the radial dispersion coefficient from the original calculated values, its influence was confirmed to be negligible. Therefore, the commonly employed axial dispersion model for SBCR modeling can be applied to this highly viscous system. However, the influence of the axial dispersion coefficient is relatively large on the concentration profile of the reactor, unlike the radial dispersion coefficient. Particularly, considering that correlations established in prior research may not align well with the characteristics of a given system, it is crucial to utilize an appropriate correlation tailored to the specific system for accurate modeling.

Acknowledgements

This research was supported by the program of Development of Eco-friendly Chemicals as Alternative Raw Materials to Oil through the National Research Foundation of Korea (NRF) funded by the Ministry of Science and ICT (2023M3J5A1092133).

Reference

Pengyu Wu, Guoping Lu, and Chun Cai. "Cobalt–molybdenum synergistic catalysis for the hydrogenolysis of terephthalate-based polyesters." Green Chemistry 23.21 (2021): 8666-8672Z.

S. D. Kim, and C. H. Kim. "Axial dispersion characteristics of three phase fluidized beds." Journal of chemical engineering of Japan 16.3 (1983): 172-178.

Y. Kang and S. D. Kim. "Radial dispersion characteristics of two-and three-phase fluidized beds." Industrial & Engineering Chemistry Process Design and Development 25.3 (1986): 717-722.

Hart, W. E., Laird, C. D., Watson, J. P., Woodruff, D. L., Hackebeil, G. A., Nicholson, B. L., and Siirola, J. D. Pyomo-optimization modeling in python. Vol. 67. Berlin: Springer, 2017.

Cristian Maretto and Rajamani Krishna. "Modelling of a bubble column slurry reactor for Fischer–Tropsch synthesis." Catalysis today 52.2-3 (1999): 279-289.

H. H. Pham, S. H. Lim, K. S. Go, N. S. Nho, E. H. Kwon, K. H. Kim, Y. I. Lim, H. J. Ryu and S. Y. Park. "Modeling and simulation of a bench-scale bubble column reactor for slurry phase hydrocracking of vacuum residue." Fuel 310 (2022): 122481.

ESCAPE-34 PSE-2024
European Symposium on Computer Aided Process Engineering
&
Process Systems Engineering

Flavio Manenti, Gintaras V. Reklaitis (Eds.), Book of Abstract of the 34th European Symposium on Computer Aided Process Engineering / 15th International Symposium on Process Systems Engineering (ESCAPE34/PSE24), June 2-6, 2024, Florence, Italy.

Enhanced Sustainable Natural Gas Production using Biomass Biodigestion and Gasification Integrated with Solid Oxide Electrolysis Cell

Meire Ribeiro Domingos[a], Daniel Flórez-Orrego[a,b], Dareen Dardor[a], François Maréchal[a]

[a]*Federal Polytechnic School of Lausanne, IPESE group, Sion, Switzerland.*
[b]*Faculty of Minas, National University of Colombia, Medellin, Colombia.*
meire.ribeirodomingos@epfl.ch

Abstract

In this work, a computational approach is used to identify the operating conditions and arrangements that minimize the consumption of energy resources for sustainable natural gas production. The gasification process of the digestate derived from the biodigestion unit as well as the high temperature electrolysis system are modelled using Aspen Plus® software, whereas the OSMOSE Lua platform handles the solution to the optimization problem of minimum energy consumption and the total cost of the chemical plant. Breakthrough technologies played an important role to reduce the intermittency of renewable energy sources. The effective CO_2 management and storage systems ensure a reliable supply of sustainable natural gas, even during times of high electricity demand and market volatility. This can increase plant revenues, but indirect emissions from the electricity mix remain a challenge to decarbonizing important commodities.

Keywords: process integration, sustainable natural gas, renewable energy, solid oxide electrolysis, gasification

1. Introduction

Biomethane is a renewable fuel produced from waste-derived biomass (biowaste), which offers significant reductions of greenhouse gas emissions and resource consumption. Biomethane is currently produced via anaerobic digestion of wet biowaste followed by upgrading processes in order to achieve grid specifications. An alternative production strategy is the gasification of the biowaste with downstream cleaning, conditioning, methanation, and final upgrading of obtained syngas (Domingos et al., 2023).

Hydrogen production from water electrolysis has recently drawn attention as a versatile solution for balancing intermittent renewable electricity generation, particularly from sources like wind and solar. In addition, integrating water electrolysis to biomass energy conversion processes may offers the potential for a complete transformation of biogenic carbon into biofuels. In fact, hydrogen could be added to biomass gasification syngas in order to balance the syngas composition before the biofuel production step. The biogenic

CO_2 may also come from biodigestion processes, thus further increasing the sustainable natural gas yield. Thus, in this work, a systematic approach that considers time-varying energy demands in view of the seasonal energy costs and the intermittency of renewable energy resources is addressed aiming the integration of anaerobic digestion, gasification and high temperature electrolysis in order to enhance the sustainable natural gas production. The optimal CO_2 management using storage systems is also assessed to demonstrate this operating strategy role in future energy systems.

2. Methods

2.1. Process modeling and simulation

Figure 1 illustrates the proposed integrated sustainable natural gas production using anaerobic digestion, digestate gasification and high temperature electrolysis. The biodigestion process is modelled considering a biomethane potential of 300 Nm^3 CH_4 per t of volatile solids using organic wastes (Wellinger et al 2013). The DMT Carborex MS technology is considered for the biogas upgrading, since it can obtain methane concentration of >99% CH_4, and has a high energy recovery (>98%) consuming only 0.18-0.22 kWh/Nm^3 and presenting <0.5% methane loss. The CO_2 is also recovered in the upgrading system with a purity above 99.5% (Lems et al., 2008). The upgraded biomethane is marketed and the CO_2 rich stream follows to the biomethane production.

In addition, the anaerobic digestion process produces the digestate, that can be further gasified to enhance the methane production. The ultimate mass-based digestate composition is set to 36.04%C, 5.14%H, 31.66%O, 2.28%N, 1.85%S and 23.03%ash, whereas the mass-based proximate analysis is considered as 5.96% moisture (after drying), 11.1% fixed carbon, 59.91% volatiles, 23.03% and ash in balance (Chen et al., 2017). The initial moisture of the digestate is assumed as 50%. The digestate gasification system shown in Fig. 1 operates at atmospheric pressure and uses steam as gasification medium (Kinchin and Bain, 2009). The combustion and gasification processes occur in separate columns, thus avoiding the dilution with nitrogen of the syngas produced. After leaving the gasifier, the syngas is treated to remove tars and impurities. A fraction of the char produced in the pyrolysis step is combusted to supply the heat required by the endothermic drying, pyrolysis and reduction reactions. The syngas subsequently follows to shift reactors and to a CO_2 capture unit in order to adjust the composition to be suitable for the methanation reaction (H_2/CO_2 4:1).

The CO_2 captured in the syngas purification unit could be liquefied and stored in a tank at -50 °C and 7 bar (1,155 kg/m^3). Liquefied CO_2 can be later regasified and fed to a methanation system, in which the hydrogen necessary is provided by a high temperature solid oxide electrolyzer. The solid oxide electrolyzer (SOEC) operates at 1 bar, 800 °C, steam conversion rate of 81%. The SOEC system is modelled considering the concentration, ohmic and activation overpotentials (Ni et al 2006).

The methanation system is based on the TREMP® process (Topsøe, 2009), in which a series of methanation beds are intercooled either by recycling or indirect inter-cooling in order to achieve higher reactants conversion.

The simulations are performed in the Aspen Plus® software (Aspentech, 2015), using the Peng-Robinson EoS with Boston-Mathias modifications as thermodynamic model. the Perturbed-Chain Statistical Associating Fluid Theory (PC-SAFT) is used to model the physical absorption of CO_2 with dimethyl ethers of polyethylene glycols (DEPG).

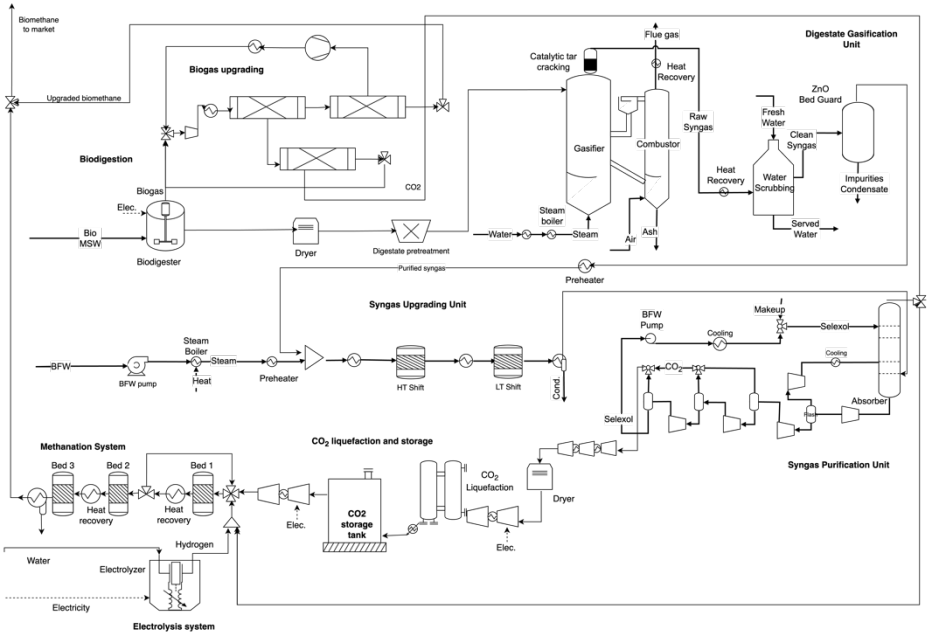

Figure 1. Integrated biomethane production considering anaerobic digestion, gasification and high temperature electrolysis.

2.2. Optimization problem definition

The new energy technologies in Fig. 1 require a redefinition of the energy balance for traditional biomethane plants. A systematic method and computational tool are needed for the complex energy integration and optimization problem. The OSMOSE Lua platform is used to determine the minimum energy requirements (MER) and solve the energy integration problem (Domingos *et* al., 2023). OSMOSE follows a two-step approach, in which the nonlinearities are limited to the Aspen Plus® models and it is considered that those representative values can be scaled linearly. The slave problem consists of a mass and energy integration framework and it is developed as a mixed-integer linear programming (MILP) problem described in Eqs. (1-5). The goal is to minimize the objective function, Eq. (1), and determine the binary variables y_w related to the selection of a given utility unit ω, and its corresponding continuous load factor, f_w, as well as the investment cost associated to the implementation of these technologies. In summary, the optimization problem accounts for the trade-off between buying the new technologies and affording the operating costs and revenues that are associated to a certain operating scenario.

$$\min_{\substack{f_\omega, y_\omega \\ R_r, W}} \left[f_{MSW} \times (B.c)_{MSW} + f_{\substack{power \\ grid}} \times (W.c)_{\substack{power \\ grid}} + f_{envEm} \times (m.tax)_{envEm} + f_{water} \times (B.c)_{water} - f_{CH4} \times (B.c)_{CH4} + \frac{z_{equip} * AF}{N_{hours\ per\ year}} \right] \quad (1)$$

Subject to:

Heat balance at the temperature interval *(r):*

$$\sum_{\omega=1}^{N_\omega} f_\omega q_{\omega,r} + \sum_{i=1}^{N} Q_{i,r} + R_{r+1} - R_r = 0 \quad \forall r = 1..N \tag{2}$$

Balance of produced/consumed power:

$$\sum_{\omega=1}^{N_\omega} f_\omega W_\omega + \sum_{\substack{chemical \\ units}} W_{net} + W_{imp} - W_{\exp} = 0 \tag{3}$$

Existence and size of the utility unit:

$$f_{\min,\omega} y_\omega \le f_\omega \le f_{\max,\omega} y_\omega \qquad \forall \omega = 1..N_\omega \tag{4}$$

Feasibility of the solution (MER):

$$R_1 = 0,\ R_{N+1} = 0,\ R_r \ge 0 \text{ and } W_{imp} \ge 0,\ W_{\exp} \ge 0 \tag{5}$$

where:

N_w is the number of units in the set of utility systems; B is the exergy flow rate (kW) of the resources entering or leaving the integrated energy system; c stands for the buying costs of the waste feedstock (0.001 EUR/kWh) and the electricity consumed (for March-October assumed as 0.001 EUR/kWh, and for November-February as 0.15 EUR/kWh), along with the CO_2 taxation set as 120 EUR/t_{CO2} (IEA, 2021), as well as for the selling price of the marketable CH_4 (0.07 EUR/kWh); q is the heating/cooling flow rates supplied by the selected utility systems (kW); W is the power domestically produced by either the utility systems (i.e. steam network) or the chemical processes (e.g. expanders); or imported from/exported to the grid (kW); AF is the annualization factor; $N_{hours\ per\ year}$ is the number of operative hours per year (8760 h); Z_{equip} is the investment cost (EUR).

The electricity price assumption allows us to model the seasonal energy costs of intermittent and renewable energy resources, as well as the factors that affect energy and CO_2 management in the integrated production system in this case study.

Equations (6) and (7) are the balance equations for the amount of liquefied gas stored in the tanks, being that the continuous variable f_{tank} accounts for the optimization variable of the tank capacity, and the mass or energy coming in or out the storage systems depend on the operating capacities of the energy systems (f), which are also optimized for each time step t.

$$Storage\_level_t = f_{\text{tank},t} \tag{6}$$

$$Storage\_level_{t+1} - Storage\_level_t = Mass\ or\ Energy_{IN,t} - Mass\ or\ Energy_{OUT,t} \tag{7}$$

3. Results and discussion

The results of the optimal processes parameters for the integrated case are summarized in Table 1. During the March-October period, the methane production via the SOEC route and using biogenic CO_2 coming from either the gasification and from the anerobic digestion, is activated, as an adaption to lower electricity prices and more affordable renewable energy. This can be also noticed in Fig. 3, where the stored CO_2 is preferably used in the months in which the electricity price is low, avoiding a large import of costly electricity from the grid. Carbon abatement units and liquid fuel storage are essential advanced energy conversion technologies that ensure the reliable operation of cogeneration systems, especially for electricity supply.

The integrated setup presented 6.2 MEUR/y of annualized investments costs and -16.4 MEUR/y of operating costs, which reinforces that the operating strategy can be attractive to increase the operating revenues leading to a lower total cost of the plant. In addition,

in the months where the electrolyzer is activated, the indirect emissions from the electricity grid can reach 0.54 kg_{CO2}/kg_{CH4}. Thus, the indirect emissions associated electricity supply chain still represent a challenge for the decarbonization of the extended production process.

Table 1. Optimal process parameters for the integrated case.

	Mar-Oct	Nov-Feb
Feedstock MSW consumption (MJ/kg_{CH4})	51.69	118.86
Utility electricity cosumption (MJ/kg_{CH4})	30.77	1.06
Water from market (m^3/kg_{CH4})	0.001	0.000
Indirect CO_2 emissions from electricity[1] (kg_{CO2}/kg_{CH4})	0.54	0.02
Rankine cycle power generation (MJ/kg_{CH4})	4.12	4.59
CH_4 production from biogas (MJ/kg_{CH4})	7.65	17.58
CH_4 production from SOEC + bioCO_2 (MJ/kg_{CH4})	28.25	0.00
CH_4 production from gasification (MJ/kg_{CH4})	14.10	32.42

1. The indirect CO_2 emissions associated with the fossil fuel consumption in the upstream supply chains is assumed as 62.63 gCO_2 per kWh of electricity (Flórez-Orrego et al., 2015).

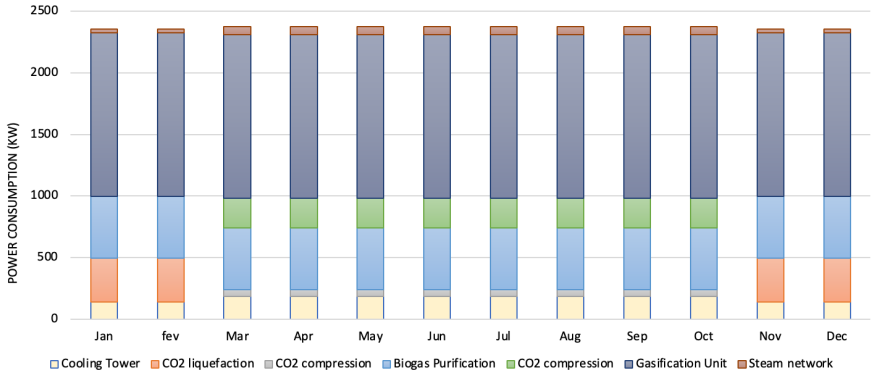

Figure 2. Monthly power consumption. During Mar-Oct the SOEC power consumption is 30.7 MW.

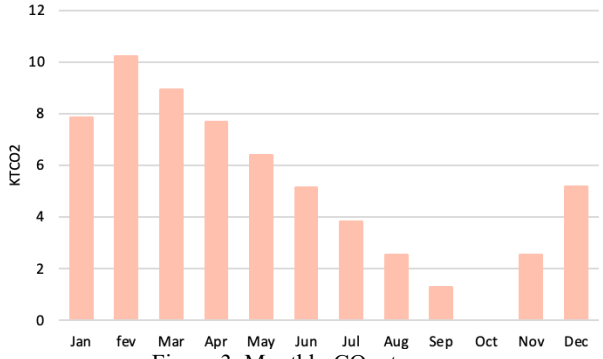

Figure 3. Monthly CO_2 storage.

4. Conclusions

In this work a systematic analysis of the integration of a gasification system and a solid oxide electrolyzer into an anaerobic digestion plant that processes the organic fraction of the municipal solid waste is assessed. To mitigate the seasonal electricity fluctuations of renewable electricity generation, a strategy involving the storage and utilization of CO_2 streams is also investigated. This process is employed for the production of methane exclusively during periods of low-cost electricity, utilizing a power-to-gas methodology that capitalizes on surplus electricity generated by prosumers throughout the non-peak months. The integration of power-to-gas systems with liquefied gas storage units has demonstrated its significance as a pivotal strategy, ensuring a synergistic supply for operational needs. Biogenic CO_2 sources and an electric input with a low carbon load can enhance the potential of power-to-gas plants to act as a CO_2 sink, however the indirect contributions of electricity grid emissions are still a challenge for the decarbonization strategies. For future works, an incremental financial analysis that incorporates the uncertainty related to the acquisition and selling costs of the feedstock and fuels produced will be performed through Monte Carlo method, by simulating the stochastic variation of the commodities price profiles.

Acknowledgments

MD thank European Union's Horizon Europe Research and Innovation programme under Grant Agreement No. 101084288.

References

M.E.G.R. Domingos et al., 2023. Process modeling and integration of hydrogen and synthetic natural gas production in a kraft pulp mill via black liquor gasification. Renewable Energy, 219, p.119396.
A. Wellinger et al., 2013. The biogas handbook: science, production and applications. Elsevier.
R. Lems et al, 2008. "Next generation biogas upgrading using highly selective gas separation membranes" Showcasing the Poundbury project. DMT Environmental Technology: Joure, The Netherlands.
G. Chen et al., 2017. Air gasification of biogas-derived digestate in a downdraft fixed bed gasifier. Waste management, 69, pp.162-169.
C. M. Kinchin, R. L. Bain. 2009. Hydrogen Production from Biomass via Indirect Gasification: The Impact of NREL Process Development Unit Gasifier Correlations, Technical Report NREL/TP-510-44868, May 2009. National Renewable Energy Laboratory.
H. Topsøe, 2009. From solid fuels to substitute natural gas (SNG) using TREMP Topsøe Recycle Energy-efficient Methanation Process.
M. Ni et al., 2006. A modeling study on concentration overpotentials of a reversible solid oxide fuel cell. Journal of Power Sources, 163(1), pp.460-466.
Aspentech, 2011. Aspen physical property system - physical property methods V7.3.
Statista, 2023. Natural gas prices for households in the European Union (28 countries) from 2014 to 2022, semi-annually. Available at: https://www.statista.com/statistics/460305/natural-gas-prices-for-households-in-eu-28/. Accessed 01 Nov 2023.
O.W. Awe et al., 2017. A review of biogas utilisation, purification and upgrading technologies. Waste and Biomass Valorization, 8, pp.267-283.

ESCAPE-34 PSE-2024
European Symposium on Computer Aided Process Engineering
&
Process Systems Engineering

Flavio Manenti, Gintaras V. Reklaitis (Eds.), Book of Abstract of the 34th European Symposium on Computer Aided Process Engineering / 15th International Symposium on Process Systems Engineering (ESCAPE34/PSE24), June 2-6, 2024, Florence, Italy.

Surrogate Modeling for CFD Simulation in Coating Process using Proper Orthogonal Decomposition and Deep Neural Networks

Sung Hyun Ju, Kyeongmin Min, Jong Min Lee*, Jaewook Nam *

Seoul National University, Department of Chemical and Biological Engineering, 1 Gwanak-ro, Gwanak-gu, Seoul, 08826, Korea
jongmin@snu.ac.kr; jaewooknam@snu.ac.kr

Abstract

Coating processes, integral in various industrial applications such as Li-ion battery electrode manufacturing, rely on accurate model of fluid dynamics for optimal outcomes. However, the dynamic nature of coating material conditions at the inlet of the coating apparatus poses challenges, leading to time and cost-intensive fluid dynamics calculations. To address this, there have been a growing demand for surrogate models capable of providing efficient and precise approximations of CFD results. Our approach leverages previously obtained CFD train data under diverse coating material conditions. Through a surrogate model integrating proper orthogonal decomposition and deep neural network, we efficiently derived CFD results for test conditions, reducing the need for resource-intensive CFD simulations. Our research applied this methodology to a practical coating apparatus, assuming the coating material properties align with those of Carreau fluid. This study holds promise for enhancing industrial efficiency in modeling and optimizing coating processes.

Keywords: Coating, Computational Fluid Dynamics, Surrogate model, Proper Orthogonal Decomposition

1. Introduction

Coating processes are employed in various industrial processes, including the manufacturing of lithium-ion battery electrodes (Li, et al. 2021). Typically positioned at the tail end of coating material production and transportation processes, coating processes involve the application of coating material slurry onto substrate as it passes through coating apparatus, such as slot die coater. For overall process modeling, the fluid dynamics inside the coating apparatus are important. This is because the pattern of coating material application on the substrate is determined by the slurry flow at the outlet of the coating apparatus.

It is worth noting that during transportation process or grade change, the rheological properties, such as viscosity, of the coating slurry can change due to factors such as deformations in the internal microstructure of the slurry (Sullivan, et al. 2022). When the rheological properties change, it affects the flow through the coating apparatus, resulting

in variations of the velocity and pressure profile at the outlet of the coating apparatus and influencing the coated product significantly.
Simulating the outlet flow of the coating apparatus for each change in rheological properties of the inlet poses practical challenges, as it requires substantial time and resources for each computational fluid dynamics (CFD) simulations. Numerous efforts have been directed towards minimizing the time and cost from repetitive CFD simulations. Since first proposed by Raissi, et al. (2017), physics-informed neural networks (PINNs) have garnered a lot of attention from the field of fluid mechanics. While PINNs substantially reduce time and cost for CFD simulation inference, PINNs suffer from inherent inaccuracies due to the soft constraint formulation of loss function during its optimization process. This limitation particularly affects predictions related to fluid flow aspects, such as conservation principles, boundary conditions, and initial conditions (Krishnapriyan, et al. 2021, Wang, et al. 2021).
There also have been trials with model order reduction techniques based on existing CFD simulation data. Proper orthogonal decomposition (POD) (Berkooz, et al. 1993) is among the prominent techniques. The fundamental concept underlying this technique involves decomposing CFD data into reduced bases encapsulating distinctive flow behaviors inherent in the data and their corresponding projection coefficients. Surrogate model can be constructed with the reduced bases, which satisfy the fluid flow aspects aforementioned because they are extracted from existing simulation data already satisfying the conditions. Zhang and Zhao (2021) suggested matching the projection coefficients for each reduced base with CFD simulation parameters using deep neural network (DNN). This approach not only ensured a sufficiently short inference time, but also offered satisfaction of boundary conditions. This is particularly crucial for our coating system, as the outlet of the coating apparatus corresponds to such boundary conditions. In this work, we propose a surrogate model for CFD simulation of an actual coating process using POD and DNN. The prediction performance of the surrogate model is compared with the CFD simulation result of the same process.

2. Process and Data Description

The target process is a typical slot die coater apparatus widely used in practical coating applications, as shown in Figure 1 (a). The geometry of the shape through which fluid flows in the apparatus, as shown in Figure 1 (b), was designed in a mesh configuration using Pointwise 18.2R1. Numerical solutions were computed using Ansys Fluent 2021R1. Carreau model was employed to describe the viscosity of the coating material slurry. This choice is based on a previous study by Lee, et al. (2022) where the Carreau model proved effective in simulating the viscosity properties of battery slurries. The Carreau model has the following mathematical form:

$$\eta(\dot{\gamma}) = \eta_\infty + (\eta_0 - \eta_\infty)[1 + (\lambda\dot{\gamma})^2]^{(n-1)/2} \quad (1)$$

where η and $\dot{\gamma}$ denote the shear viscosity and shear rate respectively. η_∞(Pa·s), η_0(Pa·s), λ(s), and n(unitless) are the parameters of Carreau model. The flow was assumed to be isothermal and incompressible with a density of 2,230 kg/m^3, following Lee, et al. (2022). Coating apparatus inlet, wall, outlet boundary conditions were considered. To consider the transient pump inlet boundary condition in the actual coating process, the following mass flow inlet boundary condition equation was applied:

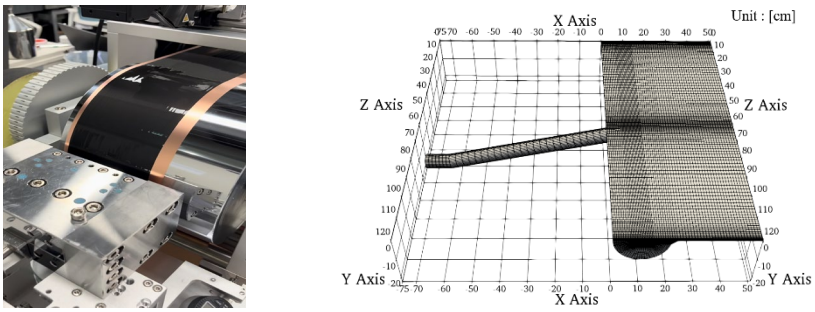

(a) (b)

Figure 1. (a) The slot die coater apparatus used in coating process, and (b) the mesh with 230k nodes designed for the region of fluid in the identical apparatus. The coating slurry is injected into the left pipe section, and exits through the right feed slot section.

$$q = q_{average}(1 + A \sin 2\pi t f) \tag{2}$$

where $q_{average}$ is the average inlet mass flow rate of the steady-state flow, A is the amplitude, and f is the pump frequency. Here, $q_{average}$, A, and f were fixed at 80 mL/min, 0.01, and 1 Hz respectively. Taking the mass flow rate into account, a laminar flow was assumed. A no-slip boundary condition was specified at the walls, and atmospheric pressure at the outlet was specified as the outlet boundary condition.
The parameters, η_0, λ and n, of the Carreau model were varied to generate a total of 64 time-series CFD simulation data. All possible combinations of (η_0, λ, n) for $\eta_0 \in$ [25, 50, 100, 200], $\lambda \in$ [0.1, 1, 10, 100], and $n \in$ [0.4, 0.5, 0.6, 0.7] were explored with η_∞ fixed to 0.01. The time step size was set to 0.01second. Simulation results of 100 time steps after residence time, equivalent to one pump cycle, were prepared for our surrogate model.

3. Proposed Surrogate Modeling Approach

This section outlines a surrogate modeling procedure for the CFD simulation of a slot die coater detailed in Section 2. First, the overall model structure is introduced. Then, the procedures for data decomposition through POD and projection coefficient regression with DNN are discussed.

3.1. Overall Model Structure

75% of the entire time-series CFD simulation data were randomly selected for training, with the remaining 25% reserved for testing. POD was applied to the train dataset, producing reduced bases and their corresponding projection coefficients. These reduced bases were assumed as the bases for the test dataset. The DNN regression model, trained on the coefficients of the train dataset, predicted the coefficients for the test dataset. Each predicted coefficient for the test dataset was then multiplied by the corresponding reduced base, and the resulting values were summed to obtain predictions for the CFD simulation data. The overall model structure is shown in Figure 2.

3.2. Data Decomposition through POD

Mathematically, POD minimizes the following error:

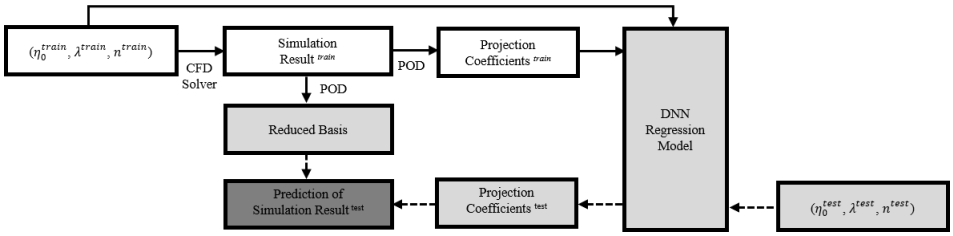

Figure 2. The Overall CFD Surrogate Model Structure

$$Error = \sum_{i=1}^{N^{train}} \|\mathrm{x}_i - \mathrm{P}_r \mathrm{x}_i\|^2 \tag{3}$$

where N^{train} is the number of train samples, x_i is the ith train sample on a vector space V, P_r is the projection of rank r, and the operation $\|\cdot\|$ is the induced norm from the inner product $\langle\cdot,\cdot\rangle$ on V. The projection of x_i, $\mathrm{P}_r \mathrm{x}_i$, is expressed as follows:

$$\mathrm{P}_r \mathrm{x}_i = \sum_{j=1}^{r} \langle \varphi_j, \mathrm{x}_i \rangle \, \varphi_j \tag{4}$$

where $\varphi_j \in V$ is the orthonormal basis of rank r. φ_j and $\langle \varphi_j, \mathrm{x}_i \rangle$ are the reduced base and projection coefficient previously mentioned. We set the inner product weighting matrix, W, to the identity matrix in the general inner product expression, $\langle \mathrm{x}_i, \mathrm{x}_j \rangle = \mathrm{x}_i^* W \mathrm{x}_j$. Minimizing the error in (3) leads to the following eigenvalue problem:

$$\mathrm{X}\mathrm{X}^* \Phi = \Phi \Sigma \tag{5}$$

where Σ is a diagonal matrix filled with eigenvalues, and X and Φ are as follows:

$$\mathrm{X} = \begin{bmatrix} \vdots & \vdots & & \vdots \\ \mathrm{x}_1 & \mathrm{x}_2 & \cdots & \mathrm{x}_{N^{train}} \\ \vdots & \vdots & & \vdots \end{bmatrix} \tag{6}$$

$$\Phi = \begin{bmatrix} \vdots & \vdots & & \vdots \\ \varphi_1 & \varphi_2 & \cdots & \varphi_r \\ \vdots & \vdots & & \vdots \end{bmatrix} \tag{7}$$

In this study, the columns of X are flattened vectors of time-series CFD simulation train data from the coating apparatus outlet. Matrix X was scaled before implementing POD.

3.3 Projection Coefficient Regression with DNN

The DNN regression model predicts projection coefficients for the Carreau model parameter combinations (η_0, λ, n). To prevent overfitting, batch normalization, dropout, L2 regularization, and early stopping were employed. The model used ReLU activation function, mean-squared error loss, and Adam optimizer. Grid search, based on 4-fold

cross validation errors, determined the optimal hyperparameter combination from the parameter space $\Omega_{h \times N_h \times Do \times Wd \times Lr \times SM_{POD} \times SM_{NN}} = \{4, 8, 16, 32, 64\} \times \{1, 2, 3, 4, 5\} \times \{0.1, 0.2, 0.3, 0.4\} \times \{10^{-8}, 10^{-7}, 10^{-6}, 10^{-5}, 10^{-4}, 10^{-3}\} \times \{10^{-4}, 10^{-3}, 10^{-2}\} \times \{\text{MinMax, Standard}\} \times \{\text{MinMax ,Standard}\}$, where $h, N_h, Do, Wd, Lr, SM_{POD}, SM_{NN}$ represents the hidden size, number of hidden layers, dropout rate, learning rate, scaling method before implementing POD, and scaling method of input and output of the neural network respectively. Using the optimal hyperparameter combination, the DNN model was trained with 25 % of the train dataset as a cross validation dataset.

4. Result and Discussions

The rank of Φ, r, and the optimal hyperparameter combination, $(h, N_h, Do, Wd, Lr, SM_{POD}, SM_{NN})$, were determined to be 48 and (8, 1, 0.3, 10^{-6}, 10^{-2}, MinMax, MinMax), respectively. The CFD simulation result and surrogate model prediction for a randomly selected test sample, corresponding to (η_0, λ, n) = (200, 0.1, 0.5), at a randomly selected simulation time, t = 0.83 second, are illustrated in Figure 3. When comparing the velocities in the x, y, and z directions predicted by the surrogate model with those predicted by the CFD simulation, a close alignment was observed, capturing key features such as the no-slip wall boundary condition, symmetry of x-velocity, y-velocity, and z-velocity profiles, and the parabolic flow profile in the x-velocity. To quantitatively evaluate the performance of the surrogate model, Figure 4 illustrates the mean absolute percentage errors in the surrogate model predictions at the coating apparatus outlet over time. This analysis specifically focuses on the x-velocity for the same test sample because, in the actual coating process, the x-velocity profile is the most influential factor affecting the application of the coating slurry onto the substrate. The remaining y and z velocity profiles have considerably lower orders of magnitudes,

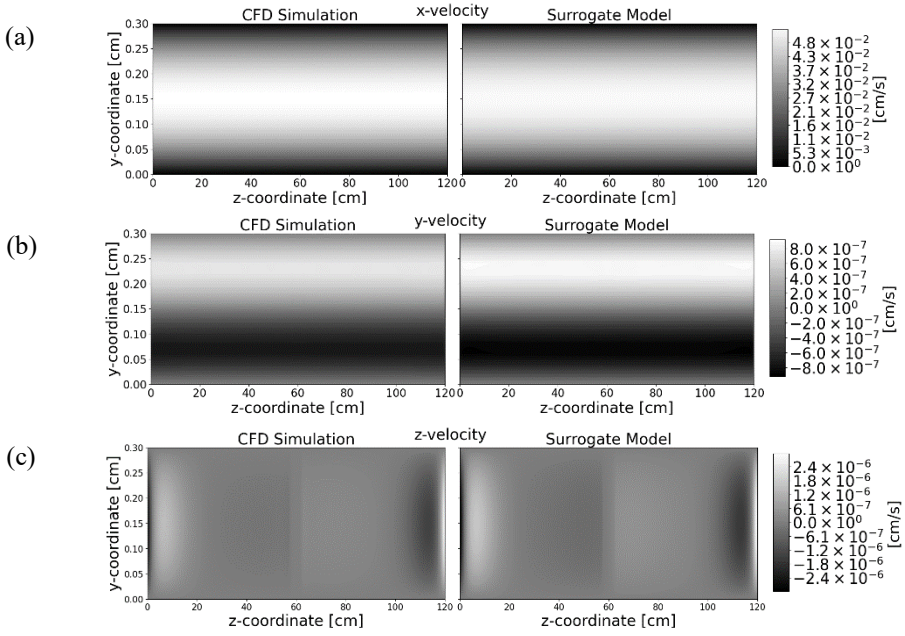

Figure 3. CFD Simulation Result and the Prediction Result of Surrogate Model for a Random Test Sample Data, (η_0, λ, n) = (200, 0.1, 0.5) and t = 0.83 second

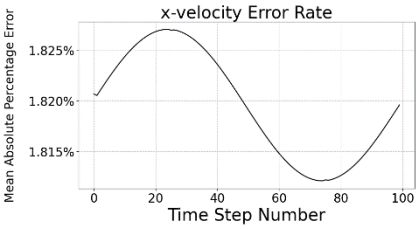

Figure 4. Mean Absolute Percentage Error of x-velocity over Time for a Test Sample Data, (η_0, λ, n) = (200, 0.1, 0.5)

resulting in negligible impact during the actual coating process. The mean absolute percentage errors of the surrogate model, when compared to the CFD simulation, did not exceed 1.830 % over time. The CFD simulation for the coating flow required over 9 CPU hours for a single case, while the proposed model achieved inference for 16 test cases in 0.36 second. The surrogate model, based on POD and DNN, exhibited strong agreement with the CFD simulation and showed significant improvement in inference speed.

5. Conclusion

This work introduced a surrogate modeling approach using POD and DNN for efficient CFD simulation of a slot die coater. Our model demonstrated strong agreement with CFD results, achieving accurate predictions while significantly reducing computation time. The novelty of our work lies in its applicability to real-world industrial processes where input properties may vary. This allows for the prediction of new CFD results based on existing data, eliminating the need to run CFD simulations for every change in input properties. In future work, integrating this research could lead to the development of a unified module encompassing post-coating processes, thereby expanding the scope of application.

References

Li, J., Fleetwood, J., Hawley, W. B., & Kays, W., 2021, From Materials to Cell: State-of-the-Art and Prospective Technologies for Lithium-Ion Battery Electrode Processing, Chemical Reviews, 122, 1, 903-956

Sullivan, J. P., & Bose, A., 2022, On the Connection between Slurry Rheology and Electrochemical Performance of Graphite Anodes in Lithium-ion Batteries, Electrochemistry Communications, 141, 107353

Raissi, M., Perdikaris, P., & Karniadakis, G. E., 2017, Physics Informed Deep Learning (Part I): Data-driven Solutions of Nonlinear Partial Differential Equations, arXiv preprint arXiv:1711.10561

Krishnapriyan, A., Gholami, A., Zhe, S., Kirby, R., & Mahoney, M. W., 2021, Characterizing Possible Failure Modes in Physics-informed Neural Networks, Advances in Neural Information Processing Systems, 34, 26548-26560

Wang, S., Teng, Y., & Perdikaris, P., 2021, Understanding and Mitigating Gradient Flow Pathologies in Physics-informed Neural Networks, SIAM Journal on Scientific Computing, 43, 5, A3055-A3081

Berkooz, G., Holmes, P., & Lumley, J. L., 1993, The Proper Orthogonal Decomposition in the Analysis of Turbulent Flows, Annual Review of Fluid Mechanics, 25, 1, 539-575

Zhang, J., & Zhao, X., 2021, Machine-learning-based Surrogate Modeling of Aerodynamic Flow Around Distributed Structures , AIAA Journal, 59, 3, 868-879

Lee, M., Jung H., Lee, M., Kwak, H., & Nam, J., 2022, Model Fluid for Coating Flows of Li-ion Battery Anode Slurry, Journal of Materials Science, 57, 38, 17935-17945

ESCAPE-34 PSE-2024
European Symposium on Computer Aided Process Engineering
&
Process Systems Engineering

Flavio Manenti, Gintaras V. Reklaitis (Eds.), Book of Abstract of the 34th European Symposium on Computer Aided Process Engineering / 15th International Symposium on Process Systems Engineering (ESCAPE34/PSE24), June 2-6, 2024, Florence, Italy.

Chemical Reaction Neural Networks for the Discovery of Microkinetic Parameters and Reaction Networks for Heterogeneously Catalyzed Reactions – A Training Strategy

Hannes Stagge[a*], Robert Güttel[a]

[a]*Ulm University, Institute of Chemical Engineering, Albert-Einstein-Allee 11, 89081 Ulm*
hannes.stagge@uni-ulm.de

Abstract

Precisely describing dynamic reactor behavior is of increasing importance considering the future need for flexible conversion of renewable energy (e.g. for methane or ammonia synthesis). However, the determination of kinetic parameters for highly accurate transient (microscale) kinetic models is tedious and connected not only to intricate experimental design but also expensive equipment. Furthermore, even the computer aided derivation of parameters from kinetic experimental data still poses a major challenge.

Recently, physically motivated methods of capturing formalized chemical kinetics in artificial neural networks have been published. Most notably the Chemical Reaction Neural Network (CRNN) method proved to be capable of extracting kinetic information from carefully prepared transient simulation or experimental results. However, typical challenges induced by heterogeneously catalyzed reactions have not yet been addressed.

Consequently, in our current contribution we present challenges and limitations of applying CRNN-methodology to pseudo-experimental data with the aim of extracting microkinetic information and link those to the well-known concepts of rate-determining or quasi-equilibrated steps. From the identified limitations, we derive favorable reaction regimes for sampling training data and their effect on the recovered kinetics, which is the basis to design appropriate transient experiments.

Therefore, we propose an extended (heterogeneous) CRNN capable of describing reaction mechanisms catalyzed by solids. The model is trained with virtual data compiled by assuming a combination of fast and slow reactions. Finally, we conclude on the capabilities of heterogeneous CRNNs (hCRNNs).

Keywords: Microkinetics, Neural Networks, Kinetic Modeling, Machine Learning

1. Introduction

The demand for technologies capable of the flexible conversion of renewable energies and the coupling of energy and gas grids (like methanation, ammonia synthesis or Fischer-Tropsch synthesis) is rising. This drives the need for the precise description of reactor behavior in highly transient operating regimes, which in turn requires accurate microscale kinetic models for resolving transient process on catalytic surfaces. The determination of parameters for these kinds of models requires elaborate experimentation, often only enabled by prior experience, expensive analytics and supported by findings from computational chemistry methods like density functional theory (DFT). The whole model development cycle and some current applications are depicted by Motagamwala and Dumesic (2020). With the increasing computational power – already relieving some constraints on this tedious process – the field of machine learning (ML) promises even higher speedups all across the mechanism development cycle.

To help speedup of calculation and parameter identification Barwey and Raman (2021) introduced a neural network formalism for capturing chemical kinetic expressions in matrix vector notation enabling efficient handling within ML frameworks like, e.g., PyTorch. Ji and Deng (2021) used a similar construction (and coined the term Chemical Reaction Neural Network, CRNN) extended by a neural ODE solver to enable detailed kinetic discovery via temporal concentration profiles of multiple homogeneous reaction mechanisms.

Both approaches do not consider the difficulties inherent to heterogeneous reaction mechanisms, where ad- and desorption of reactants occur simultaneously to surface reactions. Specifically, to our knowledge these methods have not yet been linked to the well-established concepts of the rate-determining or quasi-equilibrated steps though from experimentation it is clearly known that the existence of extremely fast or slow reactions in a given reaction network might mask critical pathways to the desired products. Hence, the current state of CRNN models is not yet demonstrated for reaction mechanism being more realistic in heterogeneous catalysis. Consequently, we aim to investigate the influence of the rate differences on CRNN performance and thus identify suitable training strategies to obtain reliable and detailed knowledge about the investigated kinetics.

In our earlier work, we demonstrated a) the wide range applicability and generalizability of microkinetic CRNNs for heterogeneously catalyzed reaction mechanisms emerging from the physically informed network architecture and b) coupling possibilities with common reactor models. These results promise the identification of reaction networks and respective kinetic parameters from readily available transient experimental data, as obtained by periodic transient kinetics method (PTK) presented by Meyer et. al. (2021) or Gäßler et. al. (2022).

2. Heterogeneous CRNNs (hCRNNs)

The underlying structure of the proposed hCRNN is adapted from Ji and Deng (2021) taking advantage of the similarity between the power law and Arrhenius equation for heterogeneous reactions in log-scale and the general mathematical formulation of a single layer in multilayer aNNs (eq. (1)). We propose extending the previous structure by including a more general approach for parametrization of the reaction rate. In addition to the basic structure, our network features parametrization of surface coverage dependency of the Arrhenius expression as well as the inclusion of special kinetic expressions for the adsorption reactions typically parametrized by the initial sticking factor S_0. In eq. (1) the

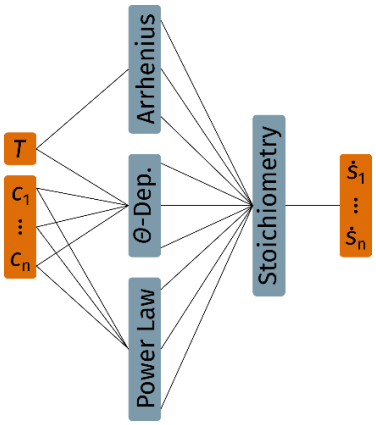

Figure 1: Proposed network architecture. Each box represents a fully connected linear layer.Power law, Arrhenius and coverage dependence layers are further separated intoforward and backward sub-layers acting on their own set of trainable parameters.

rate, r_j, of reaction j depends on temperature, T, via Arrhenius equation (with frequency factor, A_j, activation energy, $E_{A,j}$, and gas constant, R), on surface coverage, Θ_i, of component i (with coverage dependence of activation energy of reaction j, $\varepsilon_{i,j}$) and the surface and gas phase concentrations, c_i, assuming elementary reactions with the order of, $\nu'_{i,j}$. Eq. (2) establishes the connection of species i formation rate $\dot{s}_i$ to all n reactions in the mechanism through the stoichiometric coefficients $\nu_{i,j}$.

$$r_j = \exp\left(\underbrace{\ln(A_j) - \frac{E_{A,j}}{RT}}_{\text{Arrhenius}} + \underbrace{\sum_{i=1}^{m_S} \frac{\varepsilon_{i,j}\,\Theta_i}{RT}}_{\text{Coverage}} + \underbrace{\sum_{i=1}^{m} \nu'_{i,j} \ln(c_i)}_{\text{Power law}} \right) \tag{1}$$

$$\dot{s}_i = \sum_{j=1}^{n} \nu_{i,j}\, r_j \tag{2}$$

Here, we construct a more strongly separated network in the open-source deep learning framework PyTorch. Our architecture aims to make use of clearly interpretable parameter groups for different parts of the microkinetic model such as stoichiometric coefficients, reaction orders, Arrhenius-type parameters, and surface coverage dependency parameters grouping them into their own dedicated layers. Hence, the architecture clearly reflects the structure of eq. (1). An overview of the proposed network architecture is depicted in fig. 1. The main and most physically interpretable hyperparameter to influence learning success is the number of suspected reactions involved in the mechanism. We make extensive use of this hyperparameter and evaluate its influence on the accuracy of the determined kinetic parameters.

3. The influence of rate determining steps in the mechanism

To investigate the influence of reaction rates on training and performance of the hCRNN, a generic but universal Langmuir-Hinshelwood (LH) type microkinetic model consisting of four elementary reactions is constructed, parametrized and used as a benchmark in the

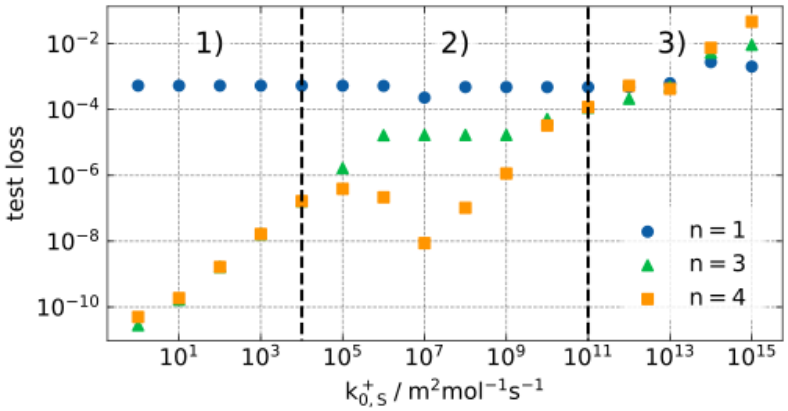

Figure 2: Training result for varying number of presumed elementary reaction steps and surface reaction rate constant $k^{+}_{0,S}$. Notice the three distinct regimes (denoted by 1), 2) and 3)) and the bifurcation and reunification of the branches for $n = 3$ and $n = 4$ presumed reactions.

depicted experiments. As a building block of more complex reaction networks, the LH-mechanism encapsulates reactant adsorption (eqs. (R1) and (R2)) and product desorption (eq. (R4)) as well as a single surface reaction (eq. (R3)), which – depending on their rate constant – can act either as the rate-determining or a quasi-equilibrated step.

$$\mathrm{A} + \star \underset{k_1^-}{\overset{k_1^+}{\rightleftharpoons}} \mathrm{A}^\star \qquad \text{(R1)}$$

$$\mathrm{B} + \star \underset{k_2^-}{\overset{k_2^+}{\rightleftharpoons}} \mathrm{B}^\star \qquad \text{(R2)}$$

$$\mathrm{A}^\star + \mathrm{B}^\star \underset{k_S^-}{\overset{k_S^+}{\rightleftharpoons}} \mathrm{C}^\star + \star \qquad \text{(R3)}$$

$$\mathrm{C}^\star \underset{k_4^-}{\overset{k_4^+}{\rightleftharpoons}} \mathrm{C} + \star \qquad \text{(R4)}$$

Reaction conditions for training data preparation are sampled at constant temperature and random gas- and surface-phase compositions for *all* involved species according to a flat Dirichlet distribution. The so generated dataset consists of 10000 samples at different reaction conditions sampled uniformly from the composition space. To generate the needed composition (c_i) – temperature (T) – formation rate ($\dot{s}_i$) pairs, the latter are calculated according to the presumed LH mechanism at the sampled conditions. Therefore, the rate constant of the surface reaction, $k^{+}_{0,S}$, is varied with fixed ad- and desorption reaction rate constants. This way, we create multiple versions of the dataset corresponding to different surface reaction rates in the mechanism. These cover the dynamic range of the surface reaction being rate determining (slow) up to quasi-equilibrated (fast). This approach represents a highly transient mode of reactor operation far from equilibrium. It should be noted that variation of $k^{+}_{0,S}$ results in differing values for the formation rates $\dot{s}_i$ in the dataset but does not influence the sampled reaction conditions.

Training of the hCRNN is then conducted using the Adam-optimizer with a custom learning-rate decay schedule by minimizing the L2-Norm as a measure for the error between network formation rate prediction and ground-truth mechanistic knowledge. The

number of presumed reactions is varied between 1, 3 and 4. Prior knowledge tells us to expect best results at four presumed reactions matching the number in the ground truth mechanism. As can be observed from fig. 2 the obtained loss (the error between hCRNN prediction and ground truth) behaves differently depending on the order of magnitude of the reaction rate constant of the surface reaction. Three regimes can be identified:
1) Very slow reaction: The surface reaction is too slow to have meaningful impact on overall kinetic behavior; three reactions explain the observed data equally well.
2) Medium fast reaction: The surface reaction is fast enough for the overall behavior to not be explained by only three reactions (see the bifurcation of the branches for $n = 3$ and $n = 4$ reactions) but requires four.
3) Very fast reaction: The surface reaction dominates the reaction network, in the limit for even higher $k_{0,S}^{+}$ one reaction is enough to describe the kinetic behavior.
These results tie in with the known theory of the rate determining step, although they somewhat contradict the experimentalists intuition. As opposed to steady-state kinetic experiments in which quasi-equilibrated steps are virtually invisible to the observer, in the presented transient regime these *fast* steps dominate the dynamics and are therefore easy to identify. Carrying over these results into the design of suitable training regimes hints at the advantages that arise from combining data from both highly transient and steady-state experimental results.

4. Conclusions

This contribution demonstrates that hCRNNs are capable of identifying the number of reactions and determining kinetic parameters for complex mechanisms in heterogeneous catalysis. It is apparent that the reaction regime has a critical impact on the performance of the hCRNN. Identification of all reactions is possible in the isothermal transient regime with no rate limiting or quasi-equilibrated steps, while the significant reaction steps are identified in any case. In our contribution we further investigate this behavior of hCRNNs and present tailored training strategies making use of different data acquisition strategies with the goal of gaining detailed mechanistic knowledge.

References

S. Barwey, V. Raman, 2021, A Neural Network Inspired Formulation of Chemical Kinetics, Energies, 14, 2710.

M. Gäßler, J. Stahl, M. Schowalter, S. Pokhrel, A. Rosenauer, L. Mädler, R. Güttel, 2022, The Impact of Support Material of Cobalt-Based Catalysts Prepared by Double Flame Spray Pyrolysis on CO_2 Methanation Dynamics, ChemCatChem, 14 .

W. Ji, S. Deng, 2021, Autonomous Discovery of Unknown Reaction Pathways from Data by Chemical Reaction Neural Network, J. Phys. Chem. A, 125, 1082–1092.

D. Meyer, J. Friedland, J. Schumacher, R. Güttel, 2021, The periodic transient kinetics method for investigation of kinetic process dynamics under realistic conditions: Methanation as an example, Chem. Eng. Res. Des., 173 , 253–266.

A. H. Motagamwala, J. A. Dumesic, 2020, Microkinetic Modeling: A Tool for Rational Catalyst Design, Chem. Rev. 121, 2, 1049-1076.

X. Su, W. Ji, J. An, Z. Ren, S. Deng, C.K. Law, 2023, Kinetics parameter optimization of hydrocarbon fuels via neural ordinary differential equations, Combust. Flame, 251, 112732.

ESCAPE-34 PSE-2024
European Symposium on Computer Aided Process Engineering
&
Process Systems Engineering

Flavio Manenti, Gintaras V. Reklaitis (Eds.), Book of Abstract of the 34th European Symposium on Computer Aided Process Engineering / 15th International Symposium on Process Systems Engineering (ESCAPE34/PSE24), June 2-6, 2024, Florence, Italy.

Potentials and Limitations of Low-Carbon Steelmaking Process: Iron Ore Reduction with Hydrogen in Shaft Furnace

Abdallah Skaf[a], Ligia Tiruta-Barna[a], Aras Ahmadi[a]

[a] *Toulouse Biotechnology Institute (TBI), Université de Toulouse, CNRS, INRAE, INSA, Toulouse, France*
skaf@insa-toulouse.fr

Abstract

A promising future approach to reducing CO_2 emissions in the metallurgical sector is to reduce iron oxides using renewable hydrogen in a shaft furnace. Here, the potentials and limitations of iron ore reduction with hydrogen at high and low reduction temperatures were studied through two-level dynamic modeling: (i) combined modeling of gas/solid reaction, transfer, and diffusion in porous iron ore pellet, (ii) modeling of the shaft furnace reactor on an industrial scale. A transient one-dimensional reactor model is developed and coupled to the pellet model. In order to predict the conversion and energy performance of the reactor, the conversion and energy efficiency were established on the scale of an industrial reactor for two contrasted operating conditions: (1) at 900 °C, which ensures the complete conversion of iron ore into pure iron with rapid conversion kinetics, (2) at 550 °C, which is more compatible with the use of renewable energy sources for heating.

Keywords: iron ore direct reduction, modeling of gas-solid reaction and diffusion, hydrogen, porous solids.

1. Introduction

Metallurgy is an emblematic energy-consumption process in our society. The reduction of iron oxide to metallic iron, steel, and cast-iron using coal is the process that gave rise to the industrial revolution, clearly taking advantage of the high energy density contained in cheap coal despite its considerable environmental and societal impacts. The production of 1.7 billion tons of steel per year (2017) results in the release of twice as much CO_2 (7 % of global emissions) (*Iron & Steel*, s. d.). The concept of utilizing hydrogen as a reducing agent, as genuinely reviewed in (Spreitzer & Schenk, 2019), is primarily connected to the concern of climate change because the reduction of iron oxide with hydrogen produces water vapor rather than the carbon dioxide produced by the reduction with the carbon monoxide (coal) (Patisson & Mirgaux, 2020). Around 80 % of the world's pre-reduced iron is produced using a gaseous mixture of hydrogen and carbon monoxide as the reducing gas in a shaft furnace. The first production of pre-reduced iron using pure hydrogen is scheduled for 2025. Therefore, our aim is to show the potentials and

limitations of such processes using pure hydrogen at pellet and reactor scale when operating at different operating conditions, such as the reduction temperatures, iron ore pellet size, and water content in the reducing gas.

2. Methods

In the reactor, the various mass and energy transport phenomena are coupled with chemical reactions. In order to predict the process performance, a pellet-scale model is first developed to simulate the various transfer, diffusion, and reaction phenomena. Then, this model is integrated into the global reactor model that simulates the conversion and thermal behaviors at a large scale. The following pellet and reactor models consist of homemade Python scripts.

2.1. Pellet model

The pellet model is based on the progression of a shrinking core by involving simultaneously reaction-diffusion phenomena at each reacting solid layer. This model is commonly applied to situations where a chemical reaction occurs at the surface of a solid material, and over time, the reaction progresses inward, causing the solid core to "shrink" as the reaction front moves deeper into the material. When the reactant transforms into another solid material, leaving behind an unreacted solid, the unreacted shrinking core model (USCM) is applied (Levenspiel, 1998). Since the reduction of iron oxides with hydrogen involves four reactions (R1-4) as a function of temperature, the USCM is extended to consider a wide range of reduction temperatures, from low temperatures (T < 570 °C) where wüstite (FeO) is unstable up to higher temperatures. Consequently, the kinetics of chemical reactions are established separately at low and high temperatures with their respective stoichiometries.

From a chemical reaction perspective, first-order reaction rates (R_i), as shown in Eq. (1), are formulated according to characteristic dimensions, i.e., the radius of the pellet (r_0) and the radius of the corresponding solid layer (r_i), the kinetic constant of reaction (k_i), and the gas concentrations (C_{H_2}, C_{H_2O}). Note that reactions can be reversible depending on the chemical equilibrium constant (K_i). In order to determine the conversion of iron ore pellets, the dynamic evolution of each solid layer is then determined in terms of solid concentration ($C_{s,k}$) as a function of reaction rates and stochiometric coefficients ($\nu_{k,i}$) through Eq. (2).

$$Fe_2O_3 + H_2 \rightarrow 2Fe_3O_4 + H_2O \quad \text{(R1)}$$
$$Fe_3O_4 + H_2 \rightarrow 3FeO + H_2O \quad \text{(R2)}$$
$$FeO + H_2 \rightarrow Fe + H_2O \quad \text{(R3)}$$
$$Fe_3O_4 + 4H_2 \rightarrow 3Fe + 4H_2O \quad \text{(R4)}$$

$$R_i = 3\,\frac{{r_i}^2}{{r_0}^3}\,k_i\left(C_{H_2}(r_i) - \frac{C_{H_2O}(r_i)}{K_i}\right) \quad (1)$$

$$\frac{\partial C_{s,k}}{\partial r} = \sum_{i}^{reactions} \nu_{k,i}.R_i \quad (2)$$

Nonetheless, calculating reaction rates requires knowledge of the pellet's radial gas concentration (C_j). For this purpose, the pseudo-steady-state approach for the gas diffusion is used for each solid layer, as shown in Eq. (3) assuming a spherical pellet:

$$\frac{1}{r^2}\frac{\partial}{\partial r}\left(r^2 D_{eff,j}\frac{\partial C_j}{\partial r}\right) = 0 \tag{3}$$

Where r is the corresponding radius and $D_{eff,j}$ is the effective diffusivity of gas j in the solid layer resulting from Bosanquet's approach (Krishna & Van Baten, 2012). At the pellet boundary condition ($r = r_0$), the diffusion is equal to the amount of mass transfer between the pellet and the bulk gas, as formulated in Eq. (4), where the mass transfer coefficients ($k_{m,j}$) are obtained using Sherwood correlation for spherical pellet (E, 1952).

$$D_{eff,j}\left(\frac{\partial C_j}{\partial r}\right) = k_{m,j}\left(C_{j,bulk} - C_j(r_0)\right) \tag{4}$$

2.2. Reactor model

The reactor model describes the transport, chemical conversion, and thermal effects involved in a countercurrent vertical furnace where cold solid is supplied at the top while the hot gas is injected at the bottom. The model is based on solving the mass and energy conservation equations by including the pellet model (diffusion and reaction with temperature-dependent kinetics). The model is transient and one-dimensional with respect to the height of the reactor. The mass balance equations for all gas and solid components, as well as the energy balance equations for the gas and solid phases are formulated based on the general convection-diffusion equation derived from the general continuity equation as shown in Eq. (5), where the extensity θ consists of the mass fraction for the mass balances and the specific enthalpy for the energy balances (Ranzani Da Costa et al., 2013).

$$\frac{\partial}{\partial t}(\rho\theta) + div(\rho\theta\vec{u}) - div\left(D.\vec{\nabla}\theta\right) = S \tag{5}$$

Where ρ is the density, D the dispersion coefficient, and u the velocity.

The first three terms in Eq. (5) describe the accumulation, the convection, and the diffusion, respectively. S in Eq. (5) is the source term related to the chemical reactions involved both in gas and solid phases. The assumptions used here are: (i) Plug flow is considered for both phases; (ii) The reactor is assumed to be adiabatic; (iii) Uniform pellet temperature, size, and shape at any axial position in the reactor; (iv) Constant bed porosity; (v): Two distinct stoichiometric, at high and low temperatures, coexist in the reactor depending on the temperature profile; (vi): Two types of heat transfer are considered: conduction and convection.

In addition, by assuming an average bed porosity (ε), and by combining the Ergun equation (Wagner, 2008) and the continuity equation in the gas phase, the axial profile of gas velocity (u_g) and pressure were established in the bed.

3. Results and discussion

Although higher reduction temperature results in a higher conversion of iron ore to pure iron (Fig. 1 (a)), studying the apparent conversion kinetics for a single iron ore pellet reveals that an optimal conversion kinetics can be found at a lower temperature (550 °C) (Pescott, 1976). The latter is potentially compatible with alternative low-tech heating solutions using renewable flow energies. Therefore, here the influence of main operating parameters such as hot gas inlet temperature and water vapor content on the conversion and temperature profile was studied to establish the actual conversion and energy efficiency on the scale of an industrial reactor.

Figure 1. shows that based on a water vapor content of 2 % in the inlet gas, when the inlet gas temperature decreases from 900 °C to 550 °C, the conversion decreases from 100 % to 54 % while the energy consumption for heating is reduced by 47 %. In addition, an increase in water vapor content markedly affects the conversion even at high temperatures: no complete conversion for a temperature of 900 °C and 550 °C with a water vapor content of 10 % in the inlet gas.

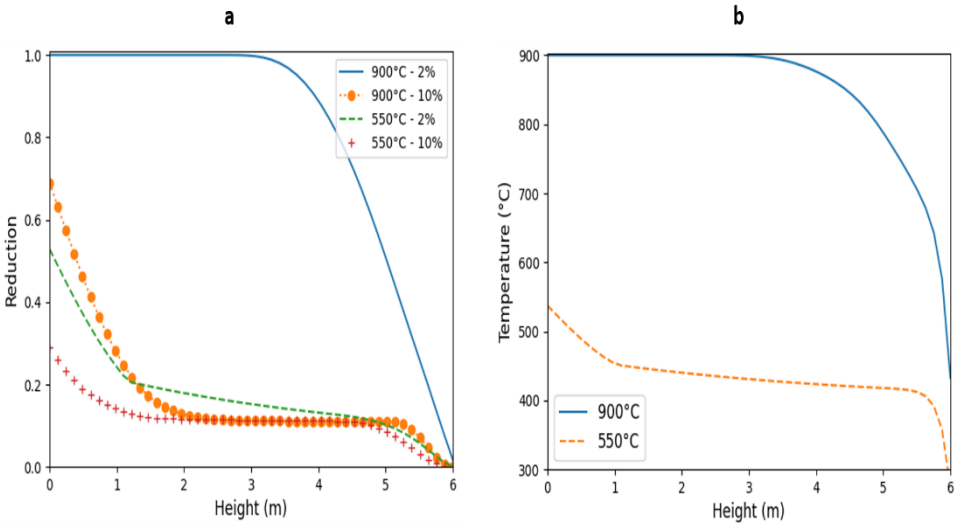

Figure 1. (a): Reduction curves for different inlet gas temperatures and water vapor content. (b): Temperature profile in the reactor for different inlet gas temperatures.

Figure 1. (b) shows that with an inlet gas temperature of 900 °C, the temperature is uniform in the reactor within 3 meters of the gas inlet. The hot gas provides an energy input to compensate the energy required for endothermic reduction reactions with hydrogen. The temperature profile at 550 °C coincides with the shape of the reduction curve at this temperature. In fact, the kinetics are strongly affected at lower temperatures and also by a progressive formation of water vapor through chemical reactions that significantly limit the conversion.

In comparison with the iron oxide reduction performance of a conventional shaft furnace operating with a gaseous mixture consisting mainly of hydrogen and carbon monoxide (50% H_2, 32% CO, 9% CH_4, 4% H_2O, 2% CO_2) : (i) a complete conversion is obtained with a more compact reactor in the case where pure hydrogen is used, this fact due to the more efficient kinetics; (ii) zero CO_2 emissions in a hydrogen reactor since there is no direct CO_2 production; (iii) almost the same order of magnitude of energy consumption is observed (4% smaller energy consumption using pure hydrogen as the reducing agent),

note that the reduction with pure hydrogen is endothermic while in conventional shaft furnace operating with syngas involves also exothermic combustion reactions.

4. Conclusions

The model-based studies provided in this work helped to understand the potentials and limitations of direct iron ore reduction with hydrogen at a real reactor scale. By comparing a reactor fueled with pure hydrogen at 550 °C with the same reactor fueled at 900 °C, the following main observations were made: (i) Although the thermal requirement for heating decreases by 47 % when it operates at 550 °C, conversion drops from 100 % to 54 % for 10 mm iron ore pellets, (ii) temperature profile and conversion are greatly affected at lower temperatures due to loss of conversion kinetics, (iii) the presence of water vapor in the gas becomes the main thermochemical barrier for the final conversion of magnetite to pure iron at lower operating temperatures.

References

E, R. W. (1952). Evaporation from Drops-I and-II. Chem. Eng. Progr, 48, 141-180.

Iron & steel. (s. d.). IEA. Consulté 21 novembre 2023, à l'adresse https://www.iea.org/energy-system/industry/steel

Krishna, R., & Van Baten, J. M. (2012). Investigating the validity of the Bosanquet formula for estimation of diffusivities in mesopores. Chemical Engineering Science, 69(1), 684-688. https://doi.org/10.1016/j.ces.2011.11.026

Levenspiel, O. (1998). Chemical Reaction Engineering. John Wiley & Sons.

Patisson, F., & Mirgaux, O. (2020). Hydrogen Ironmaking : How It Works. Metals, 10(7), Article 7. https://doi.org/10.3390/met10070922

Pescott, E. (1976). Kinetics of the gaseous direct reduction of iron ores in multi-component gas mixtures. Rapport interne de la société British Steel.

Ranzani Da Costa, A., Wagner, D., & Patisson, F. (2013). Modelling a new, low CO2 emissions, hydrogen steelmaking process. Journal of Cleaner Production, 46, 27-35. https://doi.org/10.1016/j.jclepro.2012.07.045

Spreitzer, D., & Schenk, J. (2019). Reduction of Iron Oxides with Hydrogen—A Review. Steel Research International, 90(10), 1900108. https://doi.org/10.1002/srin.201900108

Wagner, D. (2008). Etude expérimentale et modélisation de la réduction du minerai de fer par l'hydrogène.

ESCAPE-34 PSE-2024
European Symposium on Computer Aided Process Engineering
&
Process Systems Engineering

Flavio Manenti, Gintaras V. Reklaitis (Eds.), Book of Abstract of the 34th European Symposium on Computer Aided Process Engineering / 15th International Symposium on Process Systems Engineering (ESCAPE34/PSE24), June 2-6, 2024, Florence, Italy.

Dynamic Model of the Esterification Reaction with Disappearing Second Liquid Phase

Volodymyr Kozachynskyi[a*], Dario Staubach[a], Erik Esche[a], Lorenz T. Biegler[b], Jens-Uwe Repke[a]

[a]*Technische Universität Berlin, Process Dynamics and Operations Group, Berlin, Germany*
[b]*Chemical Engineering Department, Carnegie Mellon University, Pittsburgh, PA 15213, USA*
volodymyr.kozachynskyi@tu-berlin.de

Abstract

Modeling of appearance and disappearance of liquid phases is a challenging task. Methods that predict the phase dis-/appearance in steady state models are usually based on minimization of Gibbs free energy. When such methods are not applicable, graphical methods can be used. These commonly use different modes and switches, which are not supported by most dynamic system solvers. In this work we propose a reformulation of an existing graphical modelling approach that does not require any integer variables or equation switches. The smoothed formulation is used to model an esterification reaction in a batch reactor with liquid phase dis-/appearance. Suggested reformulation of the liquid phase dis-/appearance is robust and can be used with any differential algebraic equation solver.

Keywords: Phase Dis-/Appearance, Liquid-Liquid Equilibria, Dynamic Modelling

1. Introduction

Appearance and disappearance of phases is a challenging aspect for modeling in many chemical engineering applications, particularly of interest for start-up, shutdown or change in operation points of distillation, extraction, and multiphasic reactive systems. There exist different ways to model a dynamic process with vapor-liquid equilibria (VLE) where phases can appear or disappear. Most methods are based on Gibbs free energy minimization, such as the relaxed Karush-Kuhn-Tucker (KKT) approach (Gopal and Biegler, 1999) and usually require solution of an optimization problem to find phase configuration and compositions.
However, whenever a second liquid phase is of interest, as in liquid-liquid (LLE) or vapor-liquid-liquid equilibria (VLLE), Ploch et al. 2018 showed that the KKT approach is not always applicable. They proposed their own hybrid continuous model, which can be categorized as a graphical based approach (Guo et al., 2004). Their modeling approach requires a solver that can handle continuous and discrete variables, a feature, that is not

supported by most integrators of differential equations. An LLE formulation without discrete variables is the focus of this contribution.

2. Methodology

To apply a standard differential algebraic equation (DAE) solver in simulation of a dynamic system, the new, reformulated equation system should consist only of continuously differentiable nonlinear equations. The originally proposed method (Ploch et al., 2019) can be described by an upper and a lower automaton and thus represents a hybrid system. The upper automaton serves as a switch between one and two existing phases. In the lower automaton, the location of the coexisting phase is constrained to one of four possible modes. Contrary to the original formulation, the upper automaton is implemented using complementary conditions (Gopal and Biegler, 1999) with a smoothed maximum function (Eq. 1, Eq. 2) and the lower automaton is reformulated as a nested smoothed minimum function (Eq. 3) (Chen and Mangasarian, 1996).

$$\beta = (\sigma_1 - \sigma_2), \qquad \sigma_1 = \max(0, \sigma_1 - \sigma_2) \tag{1}$$

$$smoothmax(x, y, \epsilon) = \frac{x + y - \sqrt{(x-y)^2 + \epsilon^2}}{2} \tag{2}$$

$$smoothmin(x, y, \epsilon) = \frac{x + y + \sqrt{(x-y)^2 + \epsilon^2}}{2} \tag{3}$$

where σ_1 and σ_2 are two modes that cannot be active at the same time, β is a switching variable indicating existence of a second phase by its sign, and ϵ is a smoothing parameter.

3. Results

To test the new formulation, it is used as a part of a dynamic model that describes the esterification reaction of 1-propanol in batch operation mode. When the reaction is started from the product side, with only water and propyl acetate, a second, water-rich liquid phase exists. After some time, during the hydrolysis reaction 1-propanol and acetic acid are produced, and the second phase disappears. In Figure 1 the simulated trajectory as described above is presented. At the start of the reaction, water and ester separate into two liquid phases, water concentration of both phases is shown as dashed lines. During first four hours 1-propanol and acetic acid are generated, so the height of the second phase start to decrease. After four hours, the second, water-rich liquid phase disappears.

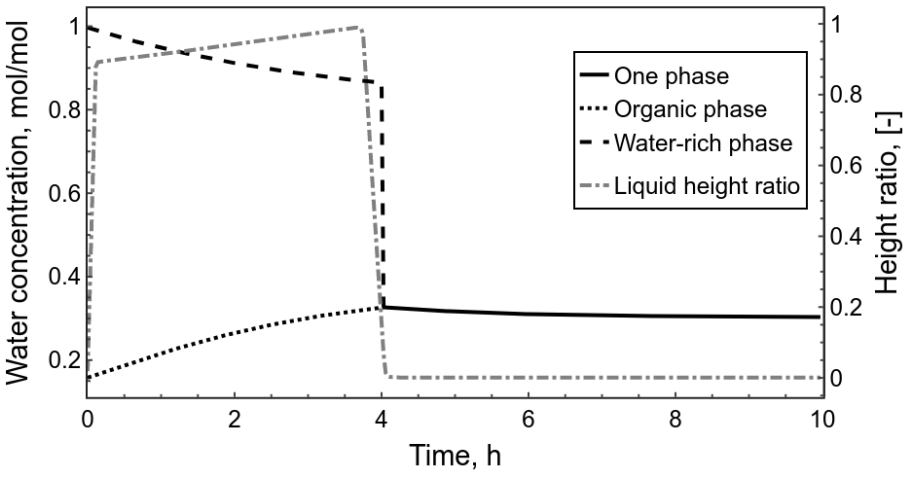

Figure 1: Change of water concentration and liquid height ratio over time

4. Conclusions

Different modelling methods for liquid phase dis-/appearance exist, each having their own advantages and disadvantages. In this work a fully smoothed reformulation of an existing method is proposed. Contrary to the original method, smoothed mode switches can be directly used as part of a system of differential-algebraic equations (DAEs). The dynamic model with phase dis-/appearance is at least once continuously differentiable and can be solved by most DAE solvers. Real experiments are planned to validate the model of the esterification reaction with phase dis-/appearance by comparing the predicted and the measured liquid height ratio of two separated liquids.

Acknowledgement: Funded by the Deutsche Forschungsgemeinschaft (DFG, German Research Foundation) – 466397921.

References

Chen, C., Mangasarian, O.L., 1996. A class of smoothing functions for nonlinear and mixed complementarity problems. Computational Optimization and Applications 5, 97–138. doi:10.1007/BF00249052.

Gopal, V., Biegler, L.T., 1999. Smoothing methods for complementarity problems in process engineering. AIChE Journal 45, 1535–1547. doi:10.1002/aic.690450715.

M. Guo, S. Wang, J.-U. Repke, and G. Wozny, “A simultaneous method for two- and three-liquid–phase stability determination,” AIChE Journal, vol. 50, no. 10, pp. 2571–2582, Sep. 2004, doi: 10.1002/aic.10256.

T. Ploch, M. Glass, A. M. Bremen, R. Hannemann-Tamás, and A. Mitsos, “Modeling of dynamic systems with a variable number of phases in liquid-liquid equilibria,” AIChE Journal, vol. 65, no. 2, pp. 571–581, Nov. 2018, doi: 10.1002/aic.16447.

ESCAPE-34 PSE-2024
European Symposium on Computer Aided Process Engineering
&
Process Systems Engineering

Flavio Manenti, Gintaras V. Reklaitis (Eds.), Book of Abstract of the 34th European Symposium on Computer Aided Process Engineering / 15th International Symposium on Process Systems Engineering (ESCAPE34/PSE24), June 2-6, 2024, Florence, Italy.

Developing a Decision-Support Model for Water and Sanitation Delivery Process in Sub-Saharan Africa: Integrating Environmental Life Cycle Assessment with Economic and Social Models

Brook Tesfamichael,[a,b,*] Ludovic Montastruc,[a] Stéphane Negny[a]

[a] *Université de Toulouse, INP-ENSIACET, LGC (Laboratoire de Génie Chimique) 4, allée Emile Monso, F-31432 Toulouse Cedex 04, France*
[b] *Addis Ababa University, Addis Ababa Institute of Technology, School of Chemical and Bio Engineering, Addis Ababa, Ethiopia*
brook.tesfamichael@aait.edu.com

Abstract

Achieving the Sustainable Development Goals on water and sanitation (SDG 6) is fundamentally important and conditional to realize the other SDGs. However, the achievement of this goal by 2030 is challenging in the Global South, especially in Sub-Saharan Africa (SSA). This is attributed to several challenges, in which weak supply chain network and inappropriate technologies along the water and sanitation supply chain are the major ones. To this end, a decision-support model is developed in this work for selecting the best supply chain network and technologies. After establishing a circular economy-based water and sanitation delivery process and performing an in-depth environmental life cycle assessment (ELCA), a multi-objective optimization model that aims to minimize the ecocost, capital cost and operating cost as well as maximize the job creation of the supply chain is developed.

Keywords: Decision-support model, optimization, water and sanitation, Sub-Saharan Africa

1. Introduction

Several quantitative-based decision support models have been developed so far for supply chains of different goods and services. Nevertheless, there is a limitation of considering the water and sanitation delivery process simultaneously. Rather, many research either focus on the water supply or sanitation process individually. Despite numerous decision support models were formulated by considering the different local-, national- and regional-level cases, none of them taken into account the water and sanitation sector of Sub-Saharan Africa (SSA), as per the author's knowledge. It is difficult to directly adapt and utilize the models developed so far for SSA as the region has its own unique features in the water and sanitation sector, which need to be incorporated in model formulation.
The center of an investigation in the previous water or sanitation related models is either of the economic, environmental or social objectives, not three of them together.

Furthermore, the techniques of environmental life cycle assessment (ELCA), environmental cost accounting, and social audits have been fairly well developed in the models but separately from each other regardless of the interdependence of the three aspects. Moreover, the previous models are largely oriented toward the selection of appropriate technologies (Ddiba et al., 2023) and overlooked the design of the best supply chain network.

Based on the above research limitations, this study intends to develop an optimization-based decision-support model, which integrates the environmental, economic, and social criteria of the water and sanitation process in SSA. In the proposed research, the ELCA, environmental cost accounting, and social auditing will be combined to develop the model. This novel methodology that integrates the three sustainability dimensions will provide strategic decisions, including selecting the best technology and supply chain network for the water and sanitation delivery process of SSA.

2. General structure of the water and sanitation network

The core driver of this study is to deal with the strategic design and planning of water and sanitation delivery process for the SSA region. As a result, a water and sanitation process that takes into account a circular economy approach is developed. The superstructure addressed in this paper is depicted schematically on Figure 1 and the structure is described as follows.

The water supply chain model proposed in this work considers different types of water resources, including rivers, dams, underground water, etc. Then, the raw water from the sources reach to the consumers through two different possibilities. First, it is directly consumed by the consumers without passing through any process, which is the dominant practice in SSA. Second, the raw water goes to a treatment plant with technology *i*. The treatment plant is comprised of one or more technologies, based on the quality of the raw water. The treatment technologies, *i*, considered in this study include preliminary, primary, secondary and tertiary. Once the water is treated and became potable, it is supplied to consumers through a distribution facility with technology *m*. After consuming the water for various purposes, the generated greywater, which is a wastewater from non-toilet plumbing systems such as hand basins, washing, showers and baths, is collected and transferred to sewer wastewater treatment plant.

The sanitation supply chain model proposed in this work considers different types of sanitation technologies *n*, which are broadly classified as improved and unimproved sanitation technologies. The blackwater, which is the waste released from the toilet, is either transferred to sewer wastewater treatment plant with technology *j* or sludge treatment plant with technology *k* depending on the type of sanitation technology used. The greywater and blackwater are treated in the sewer wastewater treatment plant, which has different technologies. Then, the treated water from the sewer treatment plant is either supplied to consumers to utilize for different purposes except drinking, to irrigation uses or discharged to nearby water bodies. On the other hand, the blackwater goes to the sludge treatment plant is treated along with the sludge coming from the water treatment and sewer wastewater treatment plants. To this end, the treated sludge is utilized for composting and anaerobic digestion, whereas the waste liquid generated from the sludge treatment plant is sent to the sewer treatment plant or discharged to the nearby water bodies.

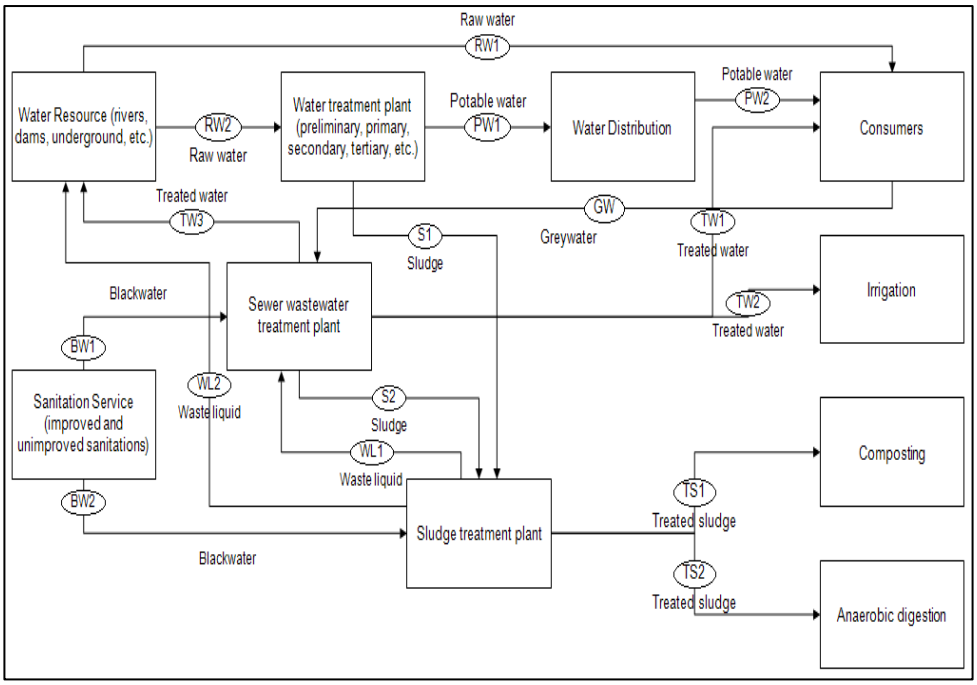

Figure 1: Superstructure of the water and sanitation network

3. Model formulation

A deterministic model is selected since the solution of this model gives decision makers good insights for making better choices. First, a mono-objective optimization model, which intends to minimize the total ecocost (a cost associated with the environmental burden of a product/service on the basis of prevention of that burden) of the water and sanitation supply chain, is developed. Then, an economic model that intends to minimize the investment and operation costs of the supply chain is developed and combined to the previous model, which results in an environmental-economic optimization model. Finally, a model that aims to maximize the job creation along the supply chain is combined to the previous model to result in environment-economic-social optimization model. The general approach for the optimization model formulation is depicted in Figure 2.

4. Case study

The optimization model developed in this study is applied to the water and sanitation sector of Sub-Saharan Africa (SSA) region. The SSA has the lowest global water and sanitation services coverage, in which only 30% and 21% of the region's population uses safely managed drinking water and sanitation services respectively. On top of that, many SSA countries are predicted to show negative and sluggish progress in water and sanitation coverage by 2030 (Zerbo et al., 2021) against the Paris Agreement and 2030 Agenda for Sustainable Development (SDG6). The sluggish and negative progress is associated with several challenges, in which selection of inappropriate water and sanitation technologies is the major one. In SSA, around 30%-60% of the installed water and sanitation technologies and infrastructures are not properly functioning (Bouabid & Louis, 2015), which makes it a prevalent justification for the failure of the water,

sanitation and hygiene (WASH) sector. Beside the failure on the technologies, the inappropriate supply chain network that suits the conditions and needs of the community and the is another challenge for the water and sanitation delivery process in the region.

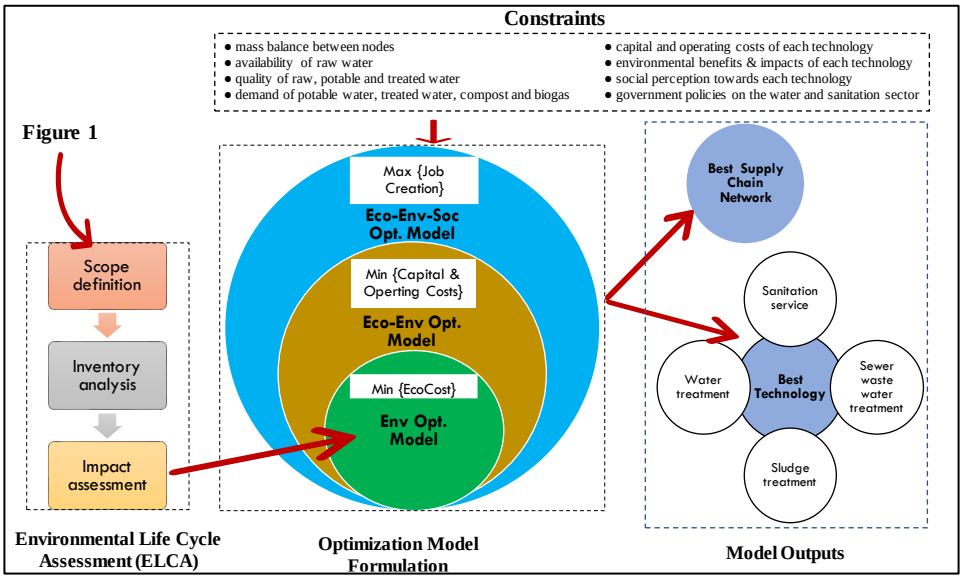

Figure 2: Model formulation approach

5. Conclusion

After establishing a water and sanitation delivery process that considers a circular economy approach and performing an in-depth ELCA, this work developed an optimization-based decision support model. The multi-objective optimization model considers the three pillars of sustainability, namely environment, economic and social, by incorporating objectives of minimizing ecocost, capital cost and operating cost as well as maximizing the job creation of the entire supply chain. The decision support model developed here addresses the major challenges of SSA water and sanitation sector by providing the best supply chain network and water and sanitation delivery technologies that are customized to the circumstances and desires of the SSA community.

Future work will focus on improving the water and sanitation network superstructure, adding other strategic decisions than technology selection and assess the sensitivity of the optimization results to environmental, technical, economic, social and political factors.

References

Bouabid, A., & Louis, G. E. (2015). Capacity factor analysis for evaluating water and sanitation infrastructure choices for developing communities. *Journal of Environmental Management*, *161*, 335–343. https://doi.org/10.1016/j.jenvman.2015.07.012

Ddiba, D., Andersson, K., Dickin, S., Ekener, E., & Finnveden, G. (2023). A review of how decision support tools address resource recovery in sanitation systems. In *Journal of Environmental Management* (Vol. 342). Academic Press. https://doi.org/10.1016/j.jenvman.2023.118365

Zerbo, A., Castro Delgado, R., & Arcos González, P. (2021). Water sanitation and hygiene in Sub-Saharan Africa: Coverage, risks of diarrheal diseases, and urbanization. *Journal of Biosafety and Biosecurity*, *3*(1), 41–45. https://doi.org/10.1016/j.jobb.2021.03.004

ESCAPE-34 PSE-2024
European Symposium on Computer Aided Process Engineering
&
Process Systems Engineering

Flavio Manenti, Gintaras V. Reklaitis (Eds.), Book of Abstract of the 34th European Symposium on Computer Aided Process Engineering / 15th International Symposium on Process Systems Engineering (ESCAPE34/PSE24), June 2-6, 2024, Florence, Italy.

A Smooth and Pressure-Driven Rate-Based Model for Batch Distillation in Packed Columns Using Hold-Time Constraints for Bang-Bang Controllers

Torben Talis[a*], Erik Esche[a], Jens-Uwe Repke[a]

[a] *Technische Universität Berlin, Process Dynamics and Operations Group, Sekr. KWT-9 Str. des 17.Juni 135, Berlin 10623, Germany*
t.talis@tu-berlin.de

Abstract

Batch processes are traditionally operated based on recipes. To replace the recipes and allow for more flexible operation, accurate process models are required for optimization or application of machine learning algorithms e.g., Reinforcement Learning. For optimal operation of real plants with help of model predictive control, the plant-model mismatch must be as small as possible. Available models for distillation in packed columns are insufficiently detailed for this purpose as they do not properly describe the dynamics and are typically not valid from start-up until shutdown. Therefore, we present a smooth and pressure-driven model of a real batch distillation column with a structured packing. We also show how to implement hold-time constraints for bang-bang controllers in continuously formulated systems.

Keywords: pressure-driven, rate-based, batch distillation, hold-time constraints.

1. Model

The proposed model describes the whole batch cycle from start-up to shut-down including inertization for the separation of an ethanol-water mixture as an example system. The phase equilibria are relaxed using methods from (Sahlodin et al., 2016), which allows individual phases to appear or disappear. The system structure does not change, when it transitions from vapor-liquid to vapor- or liquid-only. It is resulting in mathematically feasible, but unphysical, compositions for non-existing phases i.e., they do not need to fulfill the summation term. However, this is inconsequential, because these compositions always get multiplied with hold-ups or flowrates, which are obviously *0*, when the phase does not exist.

The vapor streams are modeled pressure-driven, they are calculated from the pressure differences between the stages. The liquid flow is also modeled rigorously, but here the main driving force is gravity. It is assumed to be a uniform film flow along the packing, with the flowrate being a function of gravity, density, viscosity, and packing specific geometric parameters e.g., surface area and void fraction of the packing. To consider wetting of the packing, the liquid flow is only activated, once the holdup surpasses a

threshold, the dynamic liquid holdup of the packing. This activation is implemented in Eq. 1 to calculate the actual liquid flow, F_{st}^{L},with the binary variable σ_{st}^{L}. Since experimental data for the holdup inside the packing is unavailable for the dynamic case in the open literature. The mentioned threshold is derived from the steady state correlation for total liquid holdup in packed columns at total reflux from (Rocha et al. (1993).

$$F_{st}^{L} = \sigma_{st}^{L} F_{st}^{L,filmflow} \tag{1}$$

The model uses non-ideal thermodynamics. The activity coefficients are calculated with Wilson's g^{E}-Model (Wilson, 1964). To circumvent problems arising from unphysical compositions, the property equations are reformulated, when necessary, e.g., for activity coefficents and density. In Eq. (2), this reformulation is exemplarily shown for the activity coefficient. Here $\gamma_i^{gEmodel}$ and γ_i^{actual} are the activity coefficients calculated from Wilson's equation and the one which is actually used in the system, respectively. γ_i^{dummy} is in this case 1 and $\sigma^{\Sigma x}$ is a binary variable, which is 1 if the liquid phase exists and 0 in case it does not.

$$\gamma_i^{actual} = \gamma_i^{dummy} + \sigma^{\Sigma x} \cdot (\gamma_i^{gEmodel} - \gamma_i^{dummy}) \tag{2}$$

The binary variables inside the model can be expressed by step- or the Kronecker-Delta functions, which are smoothened by sigmoidal or Gaussian functions, respectively. For numerical reasons alternative formulations based on complementarity constraints (Powell et al., 2016) are used in some places.

2. Hold-Time Constraints

The presented model is validated against a real-life plant at TU Berlin. The pressure inside the mini-plant column is controlled by a bang-bang controller: A magnet valve, which is either fully opened or closed, whenever the pressure is above or below the setpoint, respectively, what is typical for lab-scale columns. The switching frequency of real valves is limited. However, in a simple model the valve would flutter rapidly. To mimic the real-life behavior, it is suitable to add hold-time constraints in the model, which force the valve to stay at any position for at least a specified period in time.
Adding these hold-time constraints to a manipulated binary variable, such as the position of a valve or activation of a heater, is trivial in a discretized system, see Eq. 3, especially when discretized with constant time steps. Here u_k is the manipulated variable at timestep k, which may only be altered, if at least N_k timesteps have passed since the last change. N_k depends of the time grid. In equidistant grids this simplifies to a constant N.

$$0 = (u_k - u_{k-1}) \cdot \sum_{n=1}^{N_k} (u_{k-n-1} - u_{k-n})^2 \tag{3}$$

Whilst discretization is beneficial and commonly used in some cases, e.g., for simultaneous optimization; forward integration of the continuously formulated system can still be advantageous in different scenarios, especially simulation. However, here it is non-trivial to add hold-time constraints.
We propose to superpose the switching condition, which is based on the controlled variable with a decaying signal, which is triggered by an actual switch of the manipulated variable, resulting in an oversaturation of the switching signal. Hence, the switching

condition is only considered when the other signal has decayed. A signal flow graph for the exemplary pressure controller is shown in Figure 1.

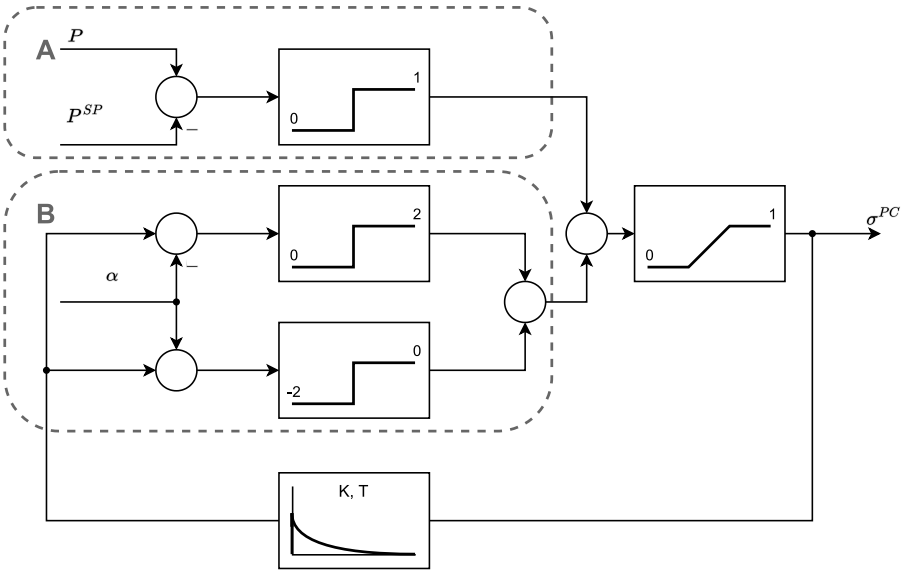

Figure 1: Signal Flow Graph of the proposed pressure controller

The output value of the whole System, σ^{PC}, describes the position of the valve. The output of the DT_1-Element is a signal that peaks in either direction and then moves back to 0, whenever σ^{PC} switches from 1 to 0 or vice versa. To circumvent the need to differentiate the input signal, the DT_1-Element is replaced by a PT_1 and a P element in parallel, which show the same behavior.
Section B takes this signal as an input. If it is in the interval [-α, α], it returns *0*, else it returns *+2* or *-2* depending on the input sign. This signal is added to the output of section A. The subsystem represents a classical bang-bang controller, which returns *1* or *0*, when the difference to the setpoint is positive or negative, respectively. Finally, the sum of the 2 sections is limited to [*0,1*] and represents the output of the whole system. α should be a small value e.g., *0.01* and the parameters for the transfer function can be calculated by Eq. 4, where *t* is the desired hold-time.

$$T = \frac{-t}{log(\alpha)} \qquad (4)$$

$$K = T$$

The described controller can be implemented as a differential-algebraic-equation system (DAE) and the same smoothing techniques as before can be applied.

3. Conclusions

We presented a smooth pressure-driven model of a batch distillation column with structured packing, which can describe the whole batch cycle starting and ending cold and empty, including inertization and phase changes.

Furthermore, hold-time constraints were presented for both discretized, as well as continuously formulated systems.The controller was added to the column model and the resulting DAE system was solved with gPROMS®.

Acknowledgements

This work was funded by Deutsche Forschungsgemeinschaft (DFG, German Research Foundation) – 466380688 – within Priority Programme "SPP 2331: Machine Learning in Chemical Engineering. Knowledge Meets Data: Interpretability, Extrapolation, Reliability, Trust".

References

Powell K., Eaton A., Hedengren J., Edgar T., 2016, A Continuous Formulation for Logical Decisions in Differential Algebraic Systems using Mathematical Programs with Complementarity Constraints, Processes, 4, 7.

Rocha J.A., Bravo J.L., Fair J.R., 1993, Distillation columns containing structured packings: a comprehensive model for their performance. 1. Hydraulic models, Industrial & Engineering Chemistry Research, 32, 641–651.

Sahlodin A.M., Watson H.A.J., Barton P.I., 2016, Nonsmooth model for dynamic simulation of phase changes, AIChE Journal, 62, 3334–3351.

Wilson G.M., 1964, Vapor-Liquid Equilibrium. XI. A New Expression for the Excess Free Energy of Mixing.

ESCAPE-34 PSE-2024
European Symposium on Computer Aided Process Engineering
&
Process Systems Engineering

Flavio Manenti, Gintaras V. Reklaitis (Eds.), Book of Abstract of the 34th European Symposium on Computer Aided Process Engineering / 15th International Symposium on Process Systems Engineering (ESCAPE34/PSE24), June 2-6, 2024, Florence, Italy.

Optimal Control of an Integrated Sorption-Reaction Unit for Ammonia Synthesis

Carl Sengoba[a], Markus Illner[a], Jens-Uwe Repke[a]

[a]*Technische Universität Berlin, Process Dynamics and Operations Group, Straße des 17. Juni 135, Berlin D-10709, Germany*
c.sengoba@tu-berlin.de

Abstract

Long-term chemical storage of renewable hydrogen in ammonia is a potential building block in a carbon-free energy system. An integrated reactive adsorption column for ammonia synthesis may allow for an intensified and flexible process. To investigate this, we present a pseudo-homogeneous pressure-driven phase model representing the integrated unit. Using an operation schedule, the control trajectory is sequentially optimized by means of time-invariant parameters obtaining a single-pass conversion of Y_{H2} = 76 %. Back-reaction of ammonia in presence of the catalyst and the need for a subsequent cryogenic separation unit may however be detrimental to the efficiency of the overall process design.

Keywords: pressure-driven modeling, process intensification, sorption-enhanced catalysis, ammonia production

1. Introduction

Hydrogen will play a crucial role in the transition towards a decarbonized energy system. While its molecular properties (e.g.: density, diffusivity) currently complicate hydrogen storage and transport, ammonia (NH_3) is a viable candidate substance for chemical hydrogen storage. Developing a renewable, resource-efficient, and flexible NH_3 synthesis process is thus desirable to advance the utilization of green hydrogen. The major advantages of process flexibility, required for coping with volatile electricity supply, and increased efficiency (evasion of the limiting chemical equilibrium) could be achieved by cyclic sorption and desorption (Smith, 2021) of the product NH_3 as compared to a recycle in the traditional Haber-Bosch process.

2. Methods

In this study, we employ a dynamic pressure-driven model of a reactive adsorption column. To this end, a (partial differential algebraic equation) PDAE representing the 1-D dynamic pseudo-homogeneous phase model (Palys, 2018) is incorporated by reaction and sorption kinetic models available in the literature (Smith, 2021). Further, a cyclic batch operation schedule is proposed, i.e., a valve activation schedule: pressurization,

reaction/absorption and desorption, which is realised by temporal switching of the boundary conditions at the inlet and outlet as described in the simulation of (pressure swing adsorption) PSA beds (Moon, 2016).

The PDAE is spatially discretized via orthogonal collocation on finite elements to result in a DAE, which permits the usage of gradient-based optimization methods. To handle the expected stiffness of the equation system the gProms® modelling environment is used. The defined operation recipe restricts the control space of the DAE to a set of time-invariant recipe parameters (Löwe, 2001). Based on the developed model, several (optimal control problems) OCPs to maximize the hydrogen conversion, NH_3 purity and the units' productivity are formulated. Thus, the goal is to identify optimal recipe parameters for this recycle-less (i.e., single-pass) NH_3 synthesis reactor.

3. Results and Discussion

To evaluate the potential for improvement in single-pass conversion for the integrated reactor-sorption system, a sensitivity study is performed. Here, the inlet pressure during pressurization p_H and the outlet pressure during desorption p_L are varied from 20-100 bar and 2–12 bar, respectively. The inlet composition is set to a stoichiometric H2/N2 molar ratio along with a uniform temperature over the whole domain of T = 573 K. The results of the simulation campaign are shown in Figure 1.

We calculate a maximum achievable single-pass conversion of the integrated sorption-reaction unit of Y_{H2} = 76 % at a time averaged outlet ammonia molar fraction of $x_{NH3,out}$ = 59 % at p_H = 100 bar and p_L = 2 bar. Integration with a gradient-free optimization algorithm in MATLAB® results in the same, yet trivial, optimal recipe parameters.

The simulations indicate that sorbent material integration enables a single-pass H2-conversion well beyond the chemical reaction equilibrium. Sensitivity studies on both the temperature window and the reaction/sorption kinetic models are conducted to define the performance targets for catalyst and sorbent material development. In general, fast adsorption/desorption kinetics at a high sorbent working capacity allow for a high feed throughput and conversion. However, a large sorption hysteresis (effectively decreasing the working capacity of the sorbent), back-reaction in the presence of the catalyst, and sorbent/catalyst material interactions could occur. All these effects would be detrimental to the conversion performance of the integrated reaction-sorption unit.

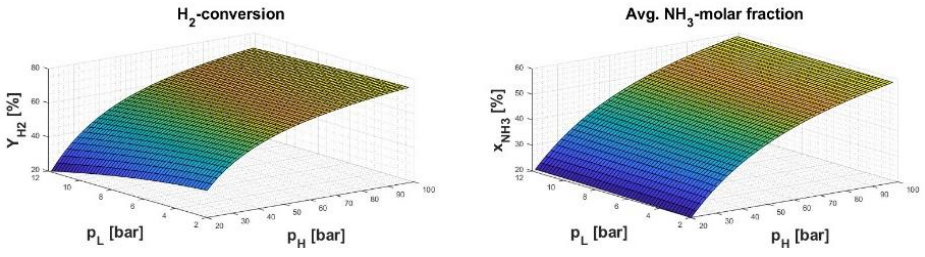

Figure 1. Calculated reactor single-pass conversion (left) and average molar fraction ammonia molar fraction at the outlet (right) for varying inlet (p_H) and outlet pressures (p_L)

4. Conclusions

This study presents a pressure-driven PDAE model for a novel reactive adsorption process for ammonia synthesis. Sensitivity studies regarding both material parameters and the operating window allowed us to examine the achievable conversion, purity and productivity performance of the integrated unit. Restriction of the control space via an operation recipe formulation enabled us to solve an OCP. Mathematical reformulation of the operation recipe is one possible way to render a broader range of numerical optimization methods, e.g., simultaneous methods, applicable to the OCP. Further, the presented model would allow for training of a data-driven regression model, which can be employed in a dynamic real-time optimization (D-RTO) framework.

Including information about the performance from integrated catalyst-sorbent unit experiments to the rate-based model would provide further insight. However, the first OCP studies results already show an encouraging reactor unit performance, in the light of flexible and demand-responsive NH3 production.

Acknowledgement

Funded by the European Union. Views and opinions expressed are however those of the author(s) only and do not necessarily reflect those of the European Union. Neither the European Union nor the granting authority can be held responsible for them. Grant agreement No 101058643.

References

[1]: C. Smith and L. Torrente-Murciano, 2021, Exceeding Single-Pass Equilibrium with Integrated Absorption Separation for Ammonia Synthesis Using Renewable Energy—Redefining the Haber-Bosch Loop. Adv. Energy Mater. 2021, 11, 2003845

[2]: M. J. Palys, A. McCormick, E. L. Cussler and P. Daoutidis, 2018, Modeling and Optimal Design of Absorbent Enhanced Ammonia Synthesis, Processes 2018, 6, 91

[3]: D.-K. Moon, D.-G. Lee and C.-H. Lee 2016, H_2 pressure swing adsorption for high pressure syngas from an integrated gasification combined cycle with a carbon capture process, Applied Energy 2016, 183, 760-774

[4]: https://www.siemens.com/global/en/products/automation/industry-software/gproms-digital-process-design-and-operations.html

[5]: K. Löwe, 2001. Theoretische und experimentelle Untersuchungen über das Anfahren und die Prozeßführung energetisch und stofflich gekoppelter Destillationskolonnen. Ph.D. thesis, TU Berlin, Berlin, Germany

[6]: https://de.mathworks.com/products/matlab.html

ESCAPE-34 PSE-2024
European Symposium on Computer Aided Process Engineering
&
Process Systems Engineering

Flavio Manenti, Gintaras V. Reklaitis (Eds.), Book of Abstract of the 34th European Symposium on Computer Aided Process Engineering / 15th International Symposium on Process Systems Engineering (ESCAPE34/PSE24), June 2-6, 2024, Florence, Italy.

Quantum Computing Application for Mapping Outputs of an Aspen-Python-Activity Browser Interface, Assisted by Support Vector Machines

Ada Josefina Robinson[a*], Viorica Sirghii[a], Stavros Papadokonstantakis[a]

Institute of Chemical, Environmental and Bioscience Engineering
TU Wien,1060 Wien, Austria
ada.robinson@tuwien.ac.at

Abstract

This paper investigates the advancements in Process System Engineering (PSE) by integrating computational methodologies and tools to incorporate next-generation technologies such as Support Vector Machine (SVM) metamodels and Quantum Computing into PSE workflows. We use Python programming language to create an interface that interconnects Aspen Plus and Activity Browser, a graphical user interface for the Brightway2 LCA framework, to accelerate process modelling, simulation, and Life Cycle Assessment (LCA) while bridging the gap between process simulation and environmental impact assessment.

We conduct multiple sensitivity analyses and use the automated interface framework to generate preliminary ReCiPE indicators for LCA. Additionally, we compare the performance of classical Support Vector Regression (SVR) models versus quantum SVR models. We transform classical machine learning models into quantum models using parametrized quantum circuits in Python's scikit-learn and Qiskit packages.

Our preliminary results demonstrate the quantum SVR capabilities to reinforce more efficient, accurate, and sustainable automated process simulation optimization for next-generation process design and assessment approaches.

Keywords: Quantum Computing, Life Cycle Assessment, Support Vector Machine, Machine Learning, Process Simulation

1. Introduction

Process Systems Engineering has become an indispensable and well-established tool for developing, designing, and optimizing chemical processes since its beginnings in the 1970s. Computational methodologies and tools made it feasible to model and simulate complex industrial operations, including traditional chemical processes as well as sustainable ones, enhanced by process intensification. Process simulations are used in the chemical industry to support the entire life cycle of a chemical process, including development, design, construction and operational optimization. Furthermore,

simulations enable a holistic understanding of the environmental impact associated with a product or process by modelling and analysing the environmental effects from raw material extraction to disposal. However, when developing innovative processes, there is currently no single process simulation environment capable of adequately representing all aspects of a process's life cycle. Life Cycle Assessment (LCA) studies and Techno-Economic Analyses often result in numerous trial-and-error phases during technology upscaling, significantly extending time-to-market and costs (Algren et al., 2021).

To effectively integrate process simulation with other applications, such as conducting Life Cycle Assessment (LCA), is a challenging and resource-intensive task due to the way commercial software is integrated into a company's infrastructure. Furthermore, the advancing digitalization within industrial environments demands open interfaces, modularization, and efficient data connections for feasible process modeling, simulation, and optimization. Machine learning and data-driven models are now available and can adapt flexibly to large datasets to analyze the behavior of developing technology at an industrial scale and create scenarios for optimizing environmental factors while meeting higher-level application demands for accuracy, convergence, and speed.

To address the challenge of integrating and switching between these components based on specific application requirements, the utilization of Python can be a potent mean to accelerate process modelling, simulation, and Life Cycle Assessment (LCA) generation through an automated interface (Casas et al., 2020). The Activity Browser is an open-source software for LCA projects within the Brightway framework. It enables Python integration for LCA parameterization, scenario modeling, graph exploration, and other advanced features. This approach effectively bridges the gap that typically exists between process simulation and the assessment of environmental impacts in a streamlined and efficient manner,

Incorporating metamodeling strategies into complex process operations allows us to reduce model complexity and transform it into more manageable algebraic models. One effective way to achieve high accuracy and computational efficiency is by utilizing a Support Vector Machine (SVM) metamodel (Müller et al., 2017). However, the landscape of computational science is rapidly evolving, and a new horizon has emerged with the emergence of Quantum Computing. This presents a unique opportunity to seamlessly integrate quantum machine learning algorithms into the broader framework of metamodeling, optimization and decision-making. Implementing quantum machine learning algorithms could lead to faster training, improved data point separation, and better generalization performance, challenging traditional data science methods. We have decided to investigate the difference in performance between a classical (SVR) and a quantum (QSVR) support vector regression model, using the output data derived from an Aspen – Python – Activity Browser interface designed for simulating a hydrocarbon separation process, serving as an illustrative case study.

For the SVR model we used Python's *scikit-learn* library and for the quantum part *Qiskit* packages for quantum machine learning have been applied (Benedetti et al., 2019).

2. Methods

2.1. Interface Integration

The Aspen-Python-Activity Browser framework is designed in a Jupyter Notebook to ensure flexibility and scalability in its functionality. This framework is the foundation for integrating various software tools and conducting comprehensive analyses (see fig. 2). The simulation section includes an open-source code library that facilitates the integration of simulations developed in Aspen Plus (ten Hagenet al., 2022). In our case study, we focus on the separation and conversion of a hydrocarbon mixture, which involves feed preparation, a DSTWU column, heat exchangers, and an RCSTR and a PLUG reactors to obtain main products (Prod1) and by-products, as shown in a simplified graphical representation in fig. 1. The simulation's inputs and outputs can be defined in this section. Upon linking the simulation, the outputs can be used as inputs for the environmental assessment section, where the process's life cycle assessment (LCA) is modelled upon Activity Browser, a graphical user interface for the Brightway2 open-source LCA framework (Steubing et al., 2020). The environmental section extracts LCA calculations and conducts analyses based on specific environmental metrics and data settings. We consider GWP (kg-CO2-eq/t prod1) and ReCiPe 2016 v1.03 endpoint (E) indicators, utilizing the ecoinvent 3.5 database (Köck et al., 2023).

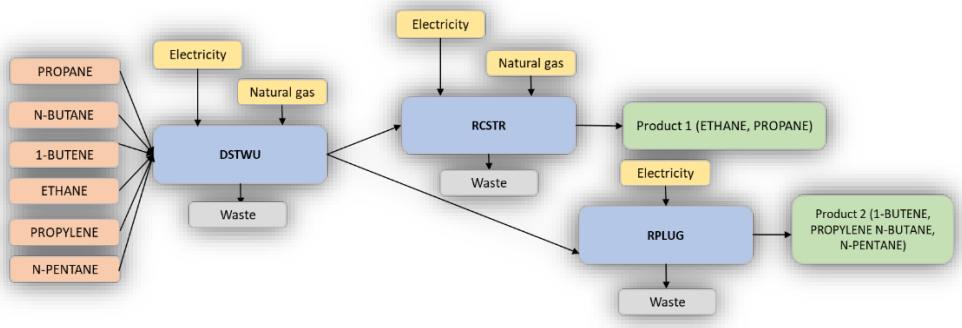

Figure 1 Simplified Process Flowchart for the Separation and Conversion of a Hydrocarbon Mixture comprising Propane, N-Butane, 1-Butene, Ethane, Propylene, and N-Pentane via Distillation (DSTWU) and Conversion (RCSTR and RPLUG) Units, Resulting in Two Distinct Product Streams

2.2. Support Vector Regression

The main goal of regression analysis is to identify the relationship between dependent and independent parameters, in order to predict the target variable. SVR allows for significant improvements in the area of Process Systems Engineering by predicting parameters which play a major role in the decisional processes related to optimization (Pasetto et al., 2022). Predicting environmental impact indicators, such as GWP and ReCiPe, as well as specific operational parameters, like the light key rate within a DSTWU, can play a crucial role in the optimization of industrial processes from an environmental standpoint. This predictive approach aids in the identification of trade-offs among various environmental impact categories and their relationship to the desired product quality and yield. SVR can be applied for linear and non-linear regression problems, by implementing a kernel function such as sigmoid, polynomial or radial basis function (as in our case).

2.3. Quantum Support Vector Regression

The main goal of QSVR is to enhance the performance of classical machine learning regression models, up to the point of outperforming classical methods. The QSVR model developed in our work is based on the quantum kernel method applied on a 2 qubits parametrized quantum circuit (Pasetto et al., 2022).

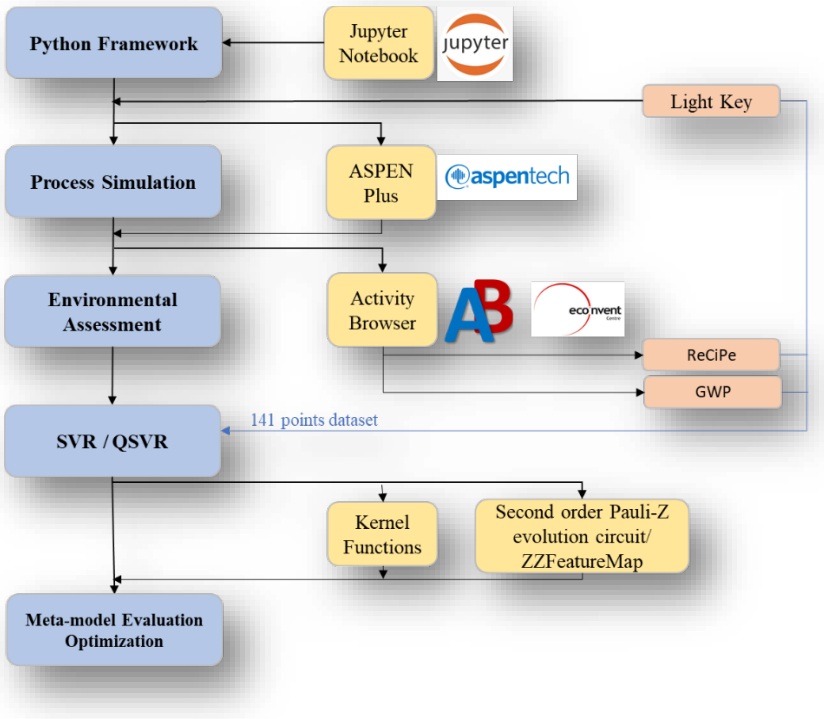

3. Results

3.1. Dataset

The output of the LCA scenario resulted from the Python-Aspen-AB interface has served as the dataset for the modelling task. The training and test datasets consist of 3 variables as follows: Light Key (operation parameter of the DSTWU column) and GWP and ReCiPe, the first one was defined as the label and the next 2 as features (LCA environmental indicators), each with 141 datapoints. These variables were selected because of their strong correlation with the operational process performance under investigation. The light key component often serves as the primary product, and its separation can result in substantial energy consumption. Predicting the behaviour of the light key component can contribute to energy optimization, cost reduction, and mitigating environmental impacts. Furthermore, while GWP helps to identify conditions linked to high global warming potential, ReCiPe can aid in assessing trade-offs among various

environmental impact categories when optimizing product quality and yield. For encoding classical data into quantum space, we have used a second-order Pauli-Z evolution circuit, named as ZZFeatureMap in Qiskit circuit library (Daspal, 2022; Qiskit, 2023). The most efficient model parameters such as data splitting subsets, hyperparameters for both SVR and QSVR, and quantum kernel parameters have been determined empirically. The performance of created models is illustrated in the following subchapters.

3.1.1. Classical SVR

As a first step, the performance of the classical model has been evaluated by comparing test and training accuracies, the coefficient of determination (R^2), and the root mean square error (RMSE) for each of the predicted variables: GWP and ReCiPe, presented in table 1 (Scikit, 2023).

As expected, the classical SVR model performs very well, with a 100% accuracy and minor errors.

Table 1: R^2 and RSME for the classical SVR model

	Accuracy (train)	Accuracy (test)	R^2	RMSE
GWP	1,00	1,00	1,00	0,15
ReCiPe	1,00	0,99	0,99	0,07

Figure 1 illustrates the parity plots between actual and predicted values and as it can be clearly seen, the predicted datapoints are nearly equal to the actual values.

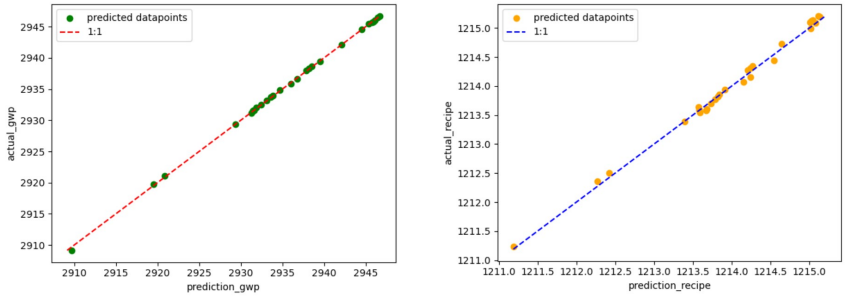

Figure 1: Actual vs predicted target values for the classical SVR model applied on the test subset

3.1.2. Classical SVR vs Quantum SVR

Table 2 displays the comparison of models' accuracy obtained for classical and quantum SVR, applied on both training (subset size = 0,7) and testing (subset size = 0.3) subsets. The performance of QSVR model with quantum kernels is almost equivalent to the classical SVR model. Nevertheless, the current status of QSVR packages proved to be more suitable for the classification problem, rather than the regression problem, therefore only the accuracy has been evaluated at this stage.

Table 2: Models' accuracy for SVR and QSVR

	Accuracy (train)	Accuracy (test)
SVR	0,91	0,89
QSVR	0,89	0,90

The main reason for different accuracy outcomes for the SVR models in Table 1 and Table 2 is due to the fact that different values for random seeds have been tested. The main role of a random seed is to ensure the reproducibility of results and the fact that the code will give the same output after re-running it. As it can be seen, a variation in the initialization parameter has a dominant impact on the classical SVR model performance. At the same time the quantum SVR model does not seem to be affected by changing the random seed value, as in our current QSVR model the random state has been set to qiskit random number generator available in the algorithm utils global package (Qiskit, 2023).

4. Conclusions

The convergence of classical and quantum computing holds immense potential for revolutionizing optimization research across diverse domains. In our work, the performance of two regression models has been compared, one for a classical support vector regression and one for its quantum counterpart. Even though the QSVR does not present a significantly higher performance as compared to classical SVR, the potential of quantum machine learning models should be emphasized as it unlocks the way to exploring its potential for future applications on more complex problems and larger datasets. Furthermore, our ongoing work is dedicated to addressing the challenges of real-time data evaluation and dynamic simulations. Our aim is to facilitate the seamless integration of quantum-enhanced techniques into practical applications in process control, techno-economic analysis, and environmental optimization. This marks a holistic advancement in Process System Engineering and environmental sustainability

References

Algren, M., Fisher, W., Landis, A.E., 2021. Machine learning in life cycle assessment, in: Data Science Applied to Sustainability Analysis. Elsevier, pp. 167–190. https://doi.org/10.1016/B978-0-12-817976-5.00009-7

Benedetti, M., Lloyd, E., Sack, S., Fiorentini, M., 2019. Parameterized quantum circuits as machine learning models. Quantum Sci. Technol. 4, 043001. https://doi.org/10.1088/2058-9565/ab4eb5

Casas, M.G., Andía, J.D., Martos, J.L.G., 2020. ECO2DES: Python Framework for the Eco-Design of Industrial Processes, in: Computer Aided Chemical Engineering. Elsevier, pp. 1987–1992. https://doi.org/10.1016/B978-0-12-823377-1.50332-3

Daspal, A., 2022. OptiPauli: An algorithm to find a near-optimal Pauli Feature Map for Quantum Support Vector Classifiers, in: 2022 IEEE International Conference on Quantum Computing and Engineering (QCE). Presented at the 2022 IEEE International Conference on Quantum Computing and Engineering (QCE), IEEE, Broomfield, CO, USA, pp. 828–830. https://doi.org/10.1109/QCE53715.2022.00133

Köck, B., Friedl, A., Serna Loaiza, S., Wukovits, W., Mihalyi-Schneider, B., 2023. Automation of Life Cycle Assessment—A Critical Review of Developments in the Field of Life Cycle Inventory Analysis. Sustainability 15, 5531. https://doi.org/10.3390/su15065531

Müller, A.C., 2016, Introduction to Machine Learning with Python.

Pasetto, E., Delilbasic, A., Cavallaro, G., Willsch, M., Melgani, F., Riedel, M., Michielsen, K., 2022. Quantum Support Vector Regression for Biophysical Variable Estimation in Remote Sensing, in: IGARSS 2022 - 2022 IEEE International Geoscience and Remote Sensing Symposium. Presented at the IGARSS 2022 - 2022 IEEE International Geoscience and Remote Sensing Symposium, IEEE, Kuala Lumpur, Malaysia, pp. 4903–4906. https://doi.org/10.1109/IGARSS46834.2022.9883963

Qiskit open-source SDK. https://qiskit.org/

Scikit learn open-source. Metrics and scoring: quantifying the quality of predictions. https://scikit-learn.org/stable/modules/model_evaluation.html#regression-metrics

Steubing, B., De Koning, D., Haas, A., Mutel, C.L., 2020. The Activity Browser — An open source LCA software building on top of the brightway framework. Software Impacts 3, 100012. https://doi.org/10.1016/j.simpa.2019.100012
ten Hagen, Richard Wolfgang, 2022, AspenPlus Python Interface (Version 2.1), https://github.com/YouMayCallMeJesus/AspenPlus-Python-Interface/tree/main.

ESCAPE-34 PSE-2024
European Symposium on Computer Aided Process Engineering
&
Process Systems Engineering

Flavio Manenti, Gintaras V. Reklaitis (Eds.), Book of Abstract of the 34th European Symposium on Computer Aided Process Engineering / 15th International Symposium on Process Systems Engineering (ESCAPE34/PSE24), June 2-6, 2024, Florence, Italy.

Quality Modelling in Batch Processes with High Dimensional Output Feedback

Aswin Chandrasekar, Hassan Abdulhussain, Michael R. Thompson, Prashant Mhaskar

Department of Chemical Engineering, McMaster University, Hamilton, Ontario, Canada
mhaskar@mcmaster.ca

Abstract

We present and compare two novel data-driven modelling approaches for batch processes utilizing information from thermal images. Data from a bench scale A rotational molding experimental set up is used to illustrate the approaches. Like most batch processes, the key challenge is to develop a model for quality attributes (such as impact strength and sinkhole area) that are only measurable after batch completion, using non-traditional sensors such as thermal images. We propose and compare multiple approaches 1) where the data from the images is reduced to a lower dimensional space using principal component analysis (PCA), and then a subspace modelling technique is used to derive a dynamic model and an associated quality model, 2) the image data is directly used in the subspace modelling technique to in turn determine the dynamic model and the associated quality model, and 3) the image data and quality model are derived through a Prediction Error Minimization approach.

Keywords: Image-based dynamic and quality modeling, Batch Processes, Thermal images, Non-traditional sensors, Subspace Identification, Prediction Error Minimization

1. Introduction

Most industrial processes, regardless of the domain, have a common target of achieving high quality products. Sometimes, batch operation is preferred, for example, in pharmaceutical, or biochemical applications when the focus is on the quality requirement rather than the quantity of the products. However, due to this reason, coming up with a suitable control routine for the process becomes an important task to maintain consistency in the product quality. Model predictive controllers (MPC) have been conventionally used for many industrial applications. An MPC has an underlying dynamic process model which allows the controller to predict the future of the process and enables it to take the most optimum control action. Arriving at a good model is one of the challenges, especially in processes where there is no first principles model available. An even more pressing challenge and opportunity is the availability of non-traditional sensors such as sounds or images. In such cases, the model development becomes crucial in the eventual effectiveness of the control strategy.

There has been some work in utilizing high dimensional data directly, but most of the image-based modelling has been done in the context of soft sensing applications like monitoring and fault detection (Gopaluni et al. (2020)). Narasingam and Kwon (2017) have applied Dynamic Mode Decomposition (DMDc) directly on spatial CFD data to construct a dynamic model between the inputs and the outputs, which are specific points in the spatial data. In this case, it is safe to assume that the states of the process are present in the high dimensional CFD (Computational Fluid Dynamics) data, and moreover the mapping between the states and the output is known to the authors (i.e., data at specific locations). In most cases, these two assumptions may not hold true. Likewise, Lu and Zavala (2021) have used DMDc on thermal images on a system with multiple heating inputs spread across the spatial field, with the controlled variable being the image itself. Often in processes, one might not have such a high dimensional reference signal, and moreover, the desired target might not be in the form of a setpoint in the first place, but rather for the processed product to meet a certain quality demand. There are other works (Masti and Bemporad (2021)) which combine the reduction of high dimensional data and constructing the dynamic model into one Neural Network model, but these approaches assume high volume of available data. In our case, and in most batch processes, we deal with a limited amount of experimental data and might not have the luxury to run too many experiments considering the material and the energy costs. Considering these issues, we present a general modelling approach to model the process, and present three novel approaches. Data from a Bi-axial Rotational Molding setup, which is a batch process used for manufacturing hollow plastics, is utilized. The system has only one heater as the input. The mold rotates biaxially inside the oven and a thermal imaging camera is placed outside the oven to capture the image of the mold, which is the only continuously measured output of the system. Although the rotation speed is given along with the equipment, the rotation is not perfect and hence the camera cannot be hard-coded to take images at particular instances to get the mold in the frame perfectly. Furthermore, there are two quality variables associated with the molded product; the sinkhole area percentage and the impact strength, which can be measured only through destructive means, only after the experiment is done. It is essential that a model is developed taking into consideration the aforementioned challenges. The proposed modelling approaches are as follows. First, a neural network-based classifier is trained on all the images of a batch, to detect whether the box is in the camera frame. For the images for which the box is detected, the modeling is done in 3 separate ways. In one approach, the high dimensional image data is reduced to a representative (lower dimensional) set of variables which reasonably represent the dynamics of the mold temperature- and/or even more importantly, captures the information necessary to estimate the final product quality. To achieve this, we fit a Principal Component Analysis (PCA) Model on only the images containing the box, to acquire a set of these latent variables. A Linear Time Invariant State Space (LTI SS) model is built between the input and the previously obtained latent variables and a Partial Least Squares (PLS) model is built between the latent variables and the quality measurements. In the second approach, a subsapce model is directly identified using the image data (without reduction), and an associated quality model is identified. Finally, in the third approach, a prediction error minimization approach is utilized to determine the dynamic and quality model simultaneously. We will first present the experimental setup in Section 2 and then present the proposed modelling approaches in Section 3.

2. Process description

A small-scale rotational molding machine is utilized in the laboratory to manufacture plastic molded items. Both the inputs from the single heater coil and the resulting images from the rotational molding setup are supervised and manipulated using LabVIEW and MATLAB programs. A camera, positioned outside the oven, captures images through a narrow opening. High-density polyethylene powder is added to the mold at room temperature, while the oven is pre-heated to 300°C. Then the mold is placed in the oven and is rotated at a steady speed of about 8 RPM. Following the heating phase, the mold is shifted to a cooling chamber. The product, still enclosed in the mold, undergoes air cooling before extraction for subsequent quality testing. Key quality variables in this batch process, namely the sinkhole area and impact strength of the product, are assessed separately after the experiment once the product is obtained.

In the rotational molding process, the degree of sintering is evaluated by examining surface voids. When polymer particles do not undergo complete sintering, the resulting product often displays a noticeable presence of surface voids. To analyze these voids, ImageJ is utilized, employing images of the mold captured by a digital camera. Another crucial quality parameter is the strength of the product, determined through Izod pendulum impact testing. The impact energy of the samples is measured in accordance with the ASTM D256 standard. Additional details regarding these quality variables in the context of this study are available in our earlier work (Chandrasekar et al., 2022).

3. Proposed Modelling Approaches

In this section, we present three modelling approaches to model the dynamics of the process along with the product quality using images. All these modelling approaches have a layered structure, where the first few layers are required to make it implementable in a closed loop setting.

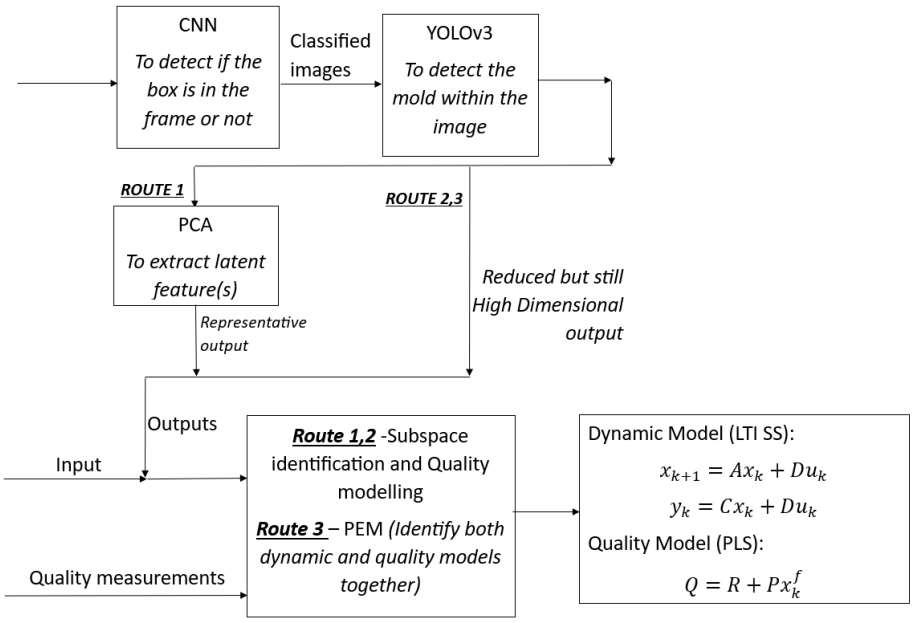

Figure 1

The first layer contains a Convolutional Neural Network (CNN) based classifier to differentiate between images that contain the mold from those that do not. An image, that is classified by the CNN model to contain the mold, goes through another pre-trained, CNN based object detection model (YOLOv3, You Only Look Once by Redmon and Farhadi (2018)), that captures the portion of the image that only contains the mold. This helps in reducing the image upto a certain extent by removing the surroundings, without losing important information related to the dynamics of the process itself. The frame size of the detected portion of image at every time step is set at 40x40. Once this is done, one of the proposed approaches is chosen to complete the modelling process. All the three approaches are shown in Figure 1.

3.1. First Approach

$$T = X * P \tag{1}$$

$$x_{k+1} = Ax_k + Bu_k \tag{2a}$$

$$y_k = Cx_k + Du_k \tag{2b}$$

$$Q = \widehat{R_m} + \widehat{P_m}x[t_{end}] \tag{3}$$

In the first approach, the 40x40 mold-containing image is further reduced by Principal Component Analysis (PCA) (Equation (1)) to a single latent variable which is then used as an output variable along with the heater input while constructing a Linear Time Invariant (LTI) State Space (SS) model (Equation (2)) of an order 2 using subspace identification. A modified version of the deterministic subspace identification algorithm (Moonen et al., 1989) as presented in Corbettt and Mhaskar (2016) that is capable of handling multiple batch data has been used for identifying the state space model. Finally, a Partial Least Squares Regression (PLS) based quality model (Equation (3)) is constructed to link the product quality Q of a batch to the final state $x[t_{end}]$ of that batch, which is obtained from the state space model. Specific details regarding the quality modelling can be found in Mhaskar et al. (2019). The key quality variables of interest are sinkhole area % (Q_1) and the impact strength (Q_2). *T* represents the scores or the latent variables from PCA analysis, *A, B, C, D* are the model matrices for the SS model and finally, the *R* and *P* are the intercept and the coefficient matrices obtained from PLS regression.

3.2. Second Approach

In the second approach however, we directly apply subspace identification taking the 40x40 image as the output and the heater input as the sole input for the LTI SS model. The rest of the approach is similar to the first approach. The only difference is we do not reduce the image using a dimensionality reduction technique like PCA prior to modelling the dynamics.

3.3. Third Approach

Unlike the first two approaches, where subspace identification was used to identify the dynamics between the outputs and the inputs and subsequently a PLS quality model was identified, this approach tries to identify both the dynamic model and the quality model together using Prediction Error Minimization (PEM). In particular, the dynamic model is

identified between the 40x40 image as the output and the heater input as the sole input, and. The optimization formulation used for identifying the models is given below:

$$\min_{A,B,C,D,P,R,x_0(b)} \sum_{b=1}^{n_b} \left((Q_b - \widehat{Q_b})^T * (Q_b - \widehat{Q_b}) + \sum_{k=1}^{n_t} (y_{b,k} - \hat{y}_{b,k})^T * (y_{b,k} - \hat{y}_{b,k}) \right) \quad (4a)$$

$$x_{b,0} = x_0 \quad (4b)$$

$$\hat{x}_{b,k+1} = A\hat{x}_{b,k} + Bu_{b,k} \quad (4c)$$

$$\hat{y}_{b,k} = C\hat{x}_{b,k} + Du_{b,k} \quad (4d)$$

$$\hat{Q}_b = P + R\hat{x}_{b,n_t} \quad (4e)$$

Equation 4a, is the objective function, which minimizes the prediction error of the quality model and the dynamic model. 4b is the initial state of each batch in the data set. Note that the states also have to be estimated as part of the state space model identification. 4c and 4d form the state space model. 4e is the PLS based quality model which related the final state of the batch to the quality of the products obtained in that particular batch.

4. Open Loop Prediction Results

In this section, we compare and tabulate the prediction performance of the proposed approaches in Table 1. All the approaches were trained on 4 batches of data. We can see that the 1st approach performs well in predicting the end product quality from intermediate points during a batch. However, the 2nd approach gives better predictions towards the end of the batch. The PEM approach gives a model that is able to decently predict the qualities during the early stages of a batch and is able to recover the accuracy towards the end of the batch. It must be noted that PEM solves a non-linear optimization, and for this particular problem, the number of variables were found to be around 8000. Hence a good initial guess becomes crucial. The initial guess for the model parameters that were to be identified was used from the 2nd approach. Overall, we can see that all the three modelling approaches are able to sufficiently model the dynamics and in turn, the quality of the product in the batch process.

Table 1

Method	*Single Batch results* Absolute errors in Q_1 and Q_2 for a batch, as seen from different time instances			*All batches* Cumulative MSE
Error in Q_1 and Q_2	*t = 20*	*t = 50*	*t = 80*	*t = End Point*
1st Approach	0.54	0.17	0.95	0.291
2nd Approach	1.61	1.91	2.02	0.043
3rd Approach	3.99	1.37	1.33	0.107

5. Conclusions

In conclusion, this work presents different ways of modelling the quality variables in a batch process when the only available output measurements are high dimensional in

nature. The proposed modelling approaches involve a combination of CNNs, PCA, PLS and LTI SS models to completely account for the process dynamics. In particular, the CNN models were used to detect images containing the mold and cut out the surrounding portions from the image. Then for the 1st approach, PCA is done on the images to reduce the high dimensional image to a single latent variable which can then be used as an output variable along with the input for subspace identification and finally quality modelling. For the 2nd and 3rd approaches, no reduction was done and the whole image was taken in the output space while constructing the LTI SS dynamics model and PLS quality model. Subspace identification and subsequently PLS was used in 2nd approach whereas both the models were jointly identified using PEM in the 3rd approach. The results show that all three approaches are able to sufficiently model the key quality variables of the batch process, hence making them implementable under closed loop control, which is the true objective.

References

Chandrasekar, A., Abdulhussain, H.A., Gritsichine, V., Thompson, M.R., and Mhaskar, P. (2022). Adaptive predictive control algorithm for batch processes: Application to a rotational molding process. Industrial & Engineering Chemistry Research, 61(48), 17572–17581. doi:10.1021/acs.iecr.2c02415.

Corbett, B. and Mhaskar, P. (2016). Subspace identification for data-driven modeling and quality control of batch processes. AIChE Journal, 62(5), 1581–1601. doi:10.1002/aic.15155

Gopaluni, R.B., Tulsyan, A., Chachuat, B., Huang, B., Lee, J.M., Amjad, F., Damarla, S.K., Kim, J.W., and Lawrence, N.P. (2020). Modern machine learning tools for monitoring and control of industrial processes: A survey. IFAC-PapersOnLine, 53(2), 218–229. doi: https://doi.org/10.1016/j.ifacol.2020.12.126. 21st IFAC World Congress.

Lu, Q. and Zavala, V.M. (2021). Image-based model predictive control via dynamic mode decomposition. Journal of Process Control, 104, 146–157.

Masti, D. and Bemporad, A. (2021). Learning nonlinear state space models using autoencoders. Automatica, 129, 109666.

Mhaskar, P.; Garg, A.; Corbett, B. (2019). Modeling and Control of Batch Processes; Advances in Industrial Control; Springer International Publishing: Cham

Moonen, M., De Moor, B., Vandenberghe, L., and Vandewalle, J. (1989). On- And Off-Line Identification Of Linear State Space Models. International Journal of Control, 49(1), 219–232.

Narasingam, A. and Kwon, J.S.I. (2017). Development of local dynamic mode decomposition with control: Application to model predictive control of hydraulic fracturing. Computers & Chemical Engineering, 106, 501–511.

Verhagen, M. and Dewilde, P. (1992). Subspace model identification Part 1. The output-error state-space model identification class of algorithms. International Journal of Control, 56(5), 1187–1210. doi:10.1080/00207179208934363.

Wang, J. and Qin, S.J. (2002). A new subspace identification approach based on principal component analysis. Journal of Process Control, 12, 841–855.

ESCAPE-34 PSE-2024
European Symposium on Computer Aided Process Engineering
&
Process Systems Engineering

Flavio Manenti, Gintaras V. Reklaitis (Eds.), Book of Abstract of the 34th European Symposium on Computer Aided Process Engineering / 15th International Symposium on Process Systems Engineering (ESCAPE34/PSE24), June 2-6, 2024, Florence, Italy.

Prospective Life Cycle Analysis of Green Platform Chemicals Uncovers their Full Environmental Potential

Abhinandan Nabera,[a] Robert Istrate,[b] Antonio José Martín,[a]
Javier Pérez-Ramírez,[a,*] Gonzalo Guillén-Gosálbez[a,*]

[a]*Department of Chemistry and Applied Biosciences, ETH Zurich, 8093 Zurich, Switzerland*
[b]*Institute of Environmental Sciences (CML), Leiden University, 2333 CC Leiden, The Netherlands*
**jpr@chem.ethz.ch, gonzalo.guillen.gosalbez@chem.ethz.ch*

Abstract

Current life cycle assessments (LCAs) of conventional and emerging chemical technologies often neglect future changes in the economy required to meet climate goals, such as those affecting transportation systems and heat and power generation. Disregarding these trends, which will shape the future economy, could lead to less accurate assessments and spurious conclusions. Hence, in this study, we conducted a prospective LCA to understand how future changes in the economy (until 2050) will affect the environmental impact of chemicals, using ammonia as a representative case. To achieve this, we used background data consistent with climate policies aimed at limiting global temperature rise across 26 regions. Our findings reveal that the environmental gap between fossil and green ammonia will significantly increase in the future, with solar-based routes showing the most improvement due to efficiency gains in solar panels and their lower carbon footprint resulting from the decarbonization of the energy mixes used in their manufacture. Overall, this study emphasizes the importance of considering future trends in the assessment of chemical technologies to draw a more comprehensive picture of their environmental potential.

Keywords: climate policies, platform chemicals, prospective life cycle assessment.

1. Introduction

The chemical industry poses a formidable challenge towards decarbonization, primarily due to its heavy reliance on fossil fuels, leading to 5.6 Gt CO_2-eq, accounting for 10% of global GHG emissions (Bauer *et al.*, 2023). Moreover, only one-third of these emissions are direct, with the remaining attributed to energy acquisition and the upstream value chain, highlighting the industry's dependence on global energy systems and supply chains. However, this challenge also presents an opportunity to reduce environmental impacts in chemical production through decarbonization of other key sectors. In recent times, there have been rapid technological advancements in response to decarbonization

challenges and climate policies aligned with the Paris Agreement. In this context, key platform chemicals such as ammonia could play a crucial role in reducing emissions due to their large production volumes and diverse applications. Ammonia plays a pivotal role in the production of fertilizers, ensuring global food security. Currently, 60 to 70% of the ammonia is produced from fossil fuels, leading to emissions of 450 Mt CO_2 y^{-1} (Gabrielli *et al.*, 2023). Several studies have evaluated low-carbon production routes for ammonia from renewable carbon and hydrogen-based feedstocks (D'Angelo *et al.*, 2021; Gomez *et al.*, 2020). These analyses have consistently highlighted the environmental superiority of green routes over their fossil counterparts. However, the majority of them often assume that the foreground system (chemical plant) interacts with the existing energy systems and supply chains, neglecting forthcoming decarbonization efforts, which could lead to less accurate and meaningful assessments. Hence, in this work, we evaluate the environmental impacts of fossil and green ammonia pathways until 2050, by considering expected changes in the power, materials, and transportation sectors under three climate-scenarios: a baseline scenario (3.5 °C), and two scenarios consistent with the 2 °C and 1.5 °C targets, respectively. Furthermore, we highlight the significance of locations in decision-making, by performing a temporal region-specific prospective LCA for 26 regions. Our results show that green ammonia could become more environmentally appealing in the future than originally thought.

2. Methods

In this study, we follow ISO 14040 and 14044 standards (International Standards Organization, 2006) in four phases. Phase one involves defining the goal and scope, where we assess the production of 1 kg of ammonia *via* specific technologies, considering cradle-to-gate impacts from 2020 to 2050 and various climate targets. Phase two includes the inventory analysis, where we use life cycle inventory (LCI) data generated automatically utilizing the IMAGE (Integrated Assessment of Global Environmental Change with IMAGE 3.0, 2014) Integrated Assessment Model (IAM) to evaluate the environmental performance of both fossil and green pathways for ammonia production. This enables us to project potential economic scenarios and provides insights into the environmental impacts based on expected socioeconomic and technological advancements. Specifically, we adopt the middle-of-the-road shared socioeconomic pathway (SSP2) and consider a range of representative concentration pathways (RCPs), including RCP6, RCP2.6, and RCP1.9. RCP6 corresponds to a scenario limiting global temperature rise to 3.5 °C, while RCP2.6 and RCP1.9 correspond to scenarios limiting temperature rise to 2 °C and 1.5 °C, respectively. To generate inventories for prospective LCAs covering the time period from 2020 to 2050, we utilize the *premise* framework (Sacchi *et al.*, 2022). The year 2020 is considered as the reference year for our analysis. Additionally, we perform a regional assessment for the production of these platform chemicals across 26 global regions, considering location-specific temporal dynamics. Phase three involves life cycle impact assessment (LCIA) using IPCC 2013 global warming potentials (GWPs) and Environmental Footprint 3.0 methods to quantify various

impact categories, with a focus on climate change. Lastly, phase four involves interpretation of the results obtained.

3. Results and Discussions

The impact of both fossil and green ammonia will decline in the future, but the environmental gap between them will grow substantially, thus drastically improving the environmental appeal of green ammonia (**Figure 1a**).

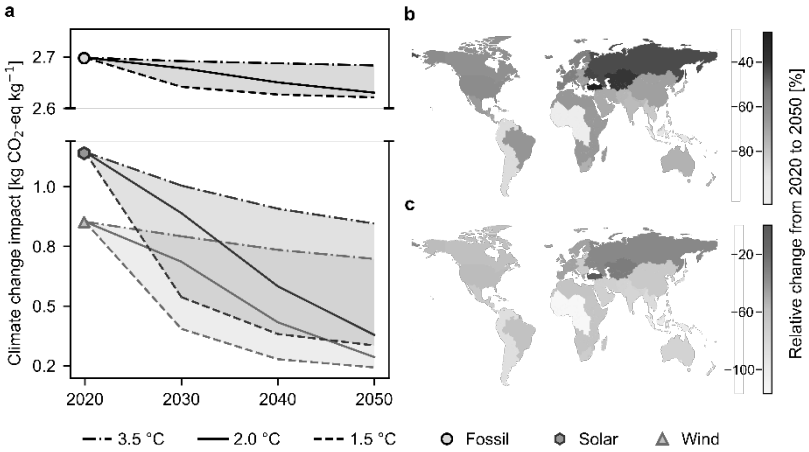

Figure 1 Climate change impacts of ammonia production technologies. **(a)** Global average impacts of fossil, solar and wind-based production from 2020 to 2050 across three scenarios (3.5 °C, 2 °C, and 1.5 °C). Regional analysis under the 2 °C scenario for **(b)** solar and **(c)** wind-based production pathways.

Particularly, under an aggressive climate policy, such as the 1.5 °C scenario, these impacts will decrease significantly, with both the solar and wind-based pathways reducing their impact by 70% in 2050 (compared to 4% in the fossil analogue). Moreover, solar-based routes are projected to compete with, or even outperform, their wind-based counterparts. Under the moderate 2 °C scenario, the impacts of solar and wind-based ammonia routes are projected to decrease by two-thirds compared to their respective 2020 values. In both scenarios, green hydrogen accounted for half of the total impacts in 2020, and its contribution is expected to increase significantly to at least 80% by 2050. Grid electricity played a major role in green ammonia production due to the high-pressure Haber-Bosch process. However, by 2050, this contribution is expected to decrease six-fold due to the anticipated decarbonization of the electricity mix. Even under the baseline 3.5 °C scenario, the green ammonia routes are expected to display significant reductions ranging from 17% to 42%. Furthermore, a regional assessment reveals significant variations in impact reductions for both solar (**Figure 1b**) and wind-based **(Figure 1c**) ammonia production, with African regions demonstrating the highest reductions. This underscores the crucial importance of the location of green facilities in maximizing global benefits. These results indicate that a paradigm shift may occur, *i.e.*, solar-based production routes may demonstrate the highest reduction in climate change impacts over time, approaching the performance levels of their corresponding wind-based counterparts. This nuances previous studies that consistently found wind-based routes to

outperform solar pathways. This is in alignment with investigations indicating that wind turbine performances are plateauing and the most significant improvements in carbon intensity will be derived from the manufacturing and end-of-life recycling of these turbines (Li *et al.*, 2022).

4. Conclusions

In this work, we assess the impact of future economic trends, with a focus on climate policies, on key platform chemicals, using ammonia as a testbed. We conduct this analysis across 26 regions spanning from 2020 to 2050. Our findings reveal that while the impact of both fossil and green routes will decrease, the gap between them will widen, especially under ambitious climate policies. Additionally, we emphasize the significance of facility location in our analysis, as it can significantly influence the results over time. Overall, this work underscores the importance of considering technological advancements, market trends, and regional factors in LCAs of emerging technologies. We hope this study will aid in making informed decisions during the transition towards more sustainable chemicals.

References

Bauer, F., Tilsted, J.P., Pfister, S., Oberschelp, C., Kulionis, V., 2023. Mapping GHG emissions and prospects for renewable energy in the chemical industry. Curr. Opin. Chem. Eng. 39, 100881.

D'Angelo, S.C., Cobo, S., Tulus, V., Nabera, A., Martín, A.J., Pérez-Ramírez, J., Guillén-Gosálbez, G., 2021. Planetary Boundaries Analysis of Low-Carbon Ammonia Production Routes. ACS Sustain. Chem. Eng. 9, 9740–9749.

Gabrielli, P., Rosa, L., Gazzani, M., Meys, R., Bardow, A., Mazzotti, M., Sansavini, G., 2023. Net-zero emissions chemical industry in a world of limited resources. One Earth 6, 682–704.

Gomez, J.R., Baca, J., Garzon, F., 2020. Techno-economic analysis and life cycle assessment for electrochemical ammonia production using proton conducting membrane. Int. J. Hydrog. Energy 45, 721–737.

Integrated Assessment of Global Environmental Change with IMAGE 3.0, 2014. PBL Netherlands Environmental Assessment Agency.

International Standards Organization, 2006. In ISO 14040:2006 Environmental Management--Life Cycle Assessment--Principles and Framework.

International StandardsOrganization, 2006. In ISO 14044:2006 Environmental Management--Life Cycle Assessment--Requirements and Guidelines.

Li, C., Mogollón, J.M., Tukker, A., Steubing, B., 2022. Environmental Impacts of Global Offshore Wind Energy Development until 2040. Environ. Sci. Technol. 56, 11567–11577.

Sacchi, R., Terlouw, T., Siala, K., Dirnaichner, A., Bauer, C., Cox, B., Mutel, C., Daioglou, V., Luderer, G., 2022. PRospective EnvironMental Impact asSEment (premise): A streamlined approach to producing databases for prospective life cycle assessment using integrated assessment models. Renew. Sustain. Energy Rev. 160, 112311.

ESCAPE-34 PSE-2024
European Symposium on Computer Aided Process Engineering
&
Process Systems Engineering

Flavio Manenti, Gintaras V. Reklaitis (Eds.), Book of Abstract of the 34th European Symposium on Computer Aided Process Engineering / 15th International Symposium on Process Systems Engineering (ESCAPE34/PSE24), June 2-6, 2024, Florence, Italy.

A Physics-Guided Data-Driven Model for Capacity Loss Prediction in Lithium-Ion Batteries

Keng-Sheng Lin[a], Chia-Hsi Wu[b], Chia-Hui Kuan[b], Yuan Yao[a*], Hung-Ping Tung[b], David Shan Hill Wong[a], Sheng-Tsaing Tseng[c], Nan-Jung Hsu[c]

[a]*Department of Chemical Engineering, National Tsing Hua University, Hsinchu, 300044, Taiwan, ROC*
[b]*Department of Industrial Engineering and Management, National Yang Ming Chao Tung University, Hsinchu, 300093, Taiwan, ROC*
[c]*Institute of Statistics, National Tsing Hua University, Hsinchu, 300044, Taiwan, ROC*
yyao@mx.nthu.edu.tw

Abstract

In this study, we utilize a physics-guided data-driven approach to model capacity loss in lithium-ion batteries. Spline fitting is used for fitting currently available data, with additional constraints imposed by the physical model. For future data, the extension of the spline fit is governed by the physical model that accounts for reaction diffusion, solid electrolyte interphase growth, and lithium plating. While both the physical model and spline fitting are able to model data across a large capacity range, only the proposed approach can predict degradation over time with a limited amount of data during the period when reaction-diffusion predominates. The ability to detect onset of a fast degradation behavior substantially enhances the accuracy of remaining useful life predictions for batteries and improves battery management systems.

Keywords: lithium-ion battery, capacity loss, reaction-diffusion, lithium plating, physics-guided data driven model

1. Introduction

Modelling and predicting the capacity loss of lithium-ion batteries is a challenging research problem, due to the complexity of loss mechanisms, unit-to-unit variations, and different charge-discharge histories. It is known that capacity loss in a battery can be primarily attributed to the formation the solid electrolyte interphase (SEI) (von Kolzenberg et al., 2020) and lithium plating (Yang et al., 2017). The onset of lithium plating causes rapid, accelerated capacity loss. However, such onset varies from unit to unit and depends on the charging rate. Parameters of physical models must be obtained only after sufficient data on various phenomena has been collected. On the other hand, despite of the prevalence of data-driven models in battery research (Severson et al., 2019), few of them take the underlying physical mechanisms into consideration and hence lacks the ability to predict future decay behaviors. In recent years, physics-guided machine learning has attracted interest in many engineering fields (Williard et al. 2020). In this

study, we will examine the advantage of this approach by modelling the capacity loss data we have collected.

2. Experimental

Commercially available 3350mAh, 18650 cylindrical cells (Panasonic NCR18650B) were used in our experiments. A charge-discharge test chamber (NEWARE, CT-4008T-5V6A-S1) with temperature control was utilized. The chamber temperature was set at 25°C. Charging was carried out at 0.5C, involving a constant current charging process until the battery reached a cut-off voltage of 4.2V, followed by maintaining a constant voltage of 4.2V until the current dropped to 0.02C. The battery was then discharged at 1C. Between each charge and discharge cycle, there was a resting period of 1.5 hours.

3. Physical Model

This study models capacity fade by considering lithium loss due to both the formation of the solid electrolyte interface (SEI) on the negative electrode and lithium plating on the interface between the negative electrode and the separator.

3.1. SEI formation

The SEI is composed of lithium ethylene decarbonate, and the reaction is depicted as follows:

$$2C_2H_4CO_3 + 2Li^+ + 2e^- \rightarrow (CH_2OCO_2Li)_2(\mathrm{s}) + C_2H_4$$

As an electrochemical reaction, the SEI reaction obeys the Butler-Volmer equation, combined with species conservation of diffusion. We can get the differential equation of capacity loss due to SEI formation as depicted in Eq. (1), in which CL_{SEI} is the capacity loss due to SEI formation, t is the cumulative charging time, V is the initial negative electrode void volume, c_{EC}^0 is the bulk concentration of EC, a_s is the specific interfacial surface area of graphite, F is Faraday's constant, $k_{0,SEI}$ is the kinetic rate constant of the SEI reaction, $\alpha_{c,SEI}$ is the cathodic transfer coefficients of the SEI reaction, R is the universal gas constant, T is the absolute temperature, η_{SEI} is the overpotential of SEI the reaction, M_{SEI} is the molar weight of the SEI, D_{EC} is the diffusivity of EC in the SEI, and ρ_{SEI} is the density of the SEI.

$$\frac{\partial CL_{SEI}}{\partial t} = \frac{Vc_{EC}^0}{\frac{2}{a_s F k_{0,SEI} exp\left(-\frac{\alpha_{c,SEI}F}{RT}\eta_{SEI}\right)} + \frac{2M_{SEI}}{F^2 D_{EC}\rho_{SEI}V}CL_{SEI}} \tag{1}$$

3.2. Lithium plating

Lithium plating is an irreversible side reaction occurring in the anode, represented as

$$Li^+ + e^- \rightarrow Li(\mathrm{s})$$

The capacity loss due to lithium plating is given by

$$\frac{\partial CL_{lpl}}{\partial t} = a_s i_{0,lpl} exp\left(-\frac{\alpha_{c,lpl}F}{RT}\eta_{lpl}\right) \tag{2}$$

in which $i_{0,lpl}$ is the exchange current density of lithium plating, $\alpha_{c,lpl}$ is the cathodic transfer coefficient of lithium plating, and η_{lpl} is the overpotential of lithium plating.

3.3. Simplified model

The following assumptions were made to simplify the model:

- Side reactions occur only during the charging phase.

- The rate of SEI formation depends only on the electrolyte solvent concentration, which means that the overpotential of the SEI reaction remains constant.
- The exchange current density of lithium plating is constant
- The overpotential of lithium plating increases linearly with cumulative charging time, and exponential growth in lithium plating becomes prominent only after a period of charging.
- The capacity loss due to the two mechanisms can be integrated independently and is additive.
- The capacity loss can be normalized to the range $[0,1]$ over the time period $[0,\infty)$.

Based on the above-mentioned equations and assumptions, we can derive a simplified model of capacity loss:

$$CL^{phy}(t|\boldsymbol{\beta}) = \frac{tan^{-1}\left(\beta_1\left(\sqrt{1+\beta_2 t}-1\right)+\beta_3\left(e^{\beta_4(t-\beta_5)_+}-1\right)\right)}{(\pi/2)}, \tag{3}$$

where $\boldsymbol{\beta} = (\beta_1, \beta_2, \dots, \beta_5)'$.

4. Physics Guided Spline Fitting

I-spline (Ramsay, 1988), widely used as a spline basis for regression analysis where monotonicity is desired, is defined as

$$I_i(t|p,\mathcal{K}) \equiv \int_{-\infty}^{t} M_i(u|p,\mathcal{K})\, du, \qquad i = 1,2,\dots,N, \tag{4}$$

in which p is the order of the piecewise polynomial, $\mathcal{K} \equiv \{k_1, k_2, \dots, k_{N+p}\}$ is a set of knots in ascending order, and N is the number of free parameters that I-splines having the specified continuity properties. With $p = 1$,

$$M_i(u|1,\mathcal{K}) = \begin{cases} \dfrac{1}{k_{i+1}-k_i}, & for\ \ k_i \le u < k_{i+1}, \\ 0, & otherwise. \end{cases} \tag{5}$$

For $p > 1$,

$$M_i(u|p,\mathcal{K}) = \frac{p\,[\,(u-k_i)\,M_i(u|p-1,\mathcal{K}) + (k_{i+p}-u)\,M_{i+1}(u|p-1,\mathcal{K})]}{(p-1)(k_{i+p}-k_i)}. \tag{6}$$

We fit capacity loss with a linear combination of I-splines:

$$\widehat{CL}(t|\boldsymbol{\delta},\mathcal{K}) = \sum_{i=1}^{N} \delta_i\, I_i(t|p,\mathcal{K}), \tag{7}$$

where $\boldsymbol{\delta} = (\delta_1, \delta_2, \dots, \delta_N)'$ with $\delta_i \ge 0$ are unknown parameters to be estimated. Physics-guided I-spline fits currently available data but is subject to additional constraints imposed by the physical model. To achieve it, for fixed λ and $\mathcal{K}$, the following objective is optimized:

$$\begin{aligned}\left(\widehat{\boldsymbol{\delta}}_{\lambda,\mathcal{K}}, \widehat{\boldsymbol{\beta}}_{\lambda,\mathcal{K}}\right) = \underset{\boldsymbol{\delta},\boldsymbol{\beta}}{argmin} & \sum_{t\in D_{train}} \left(CL(t) - \widehat{CL}(t|\boldsymbol{\delta},\mathcal{K})\right)^2 \\ & + \lambda \sum_{t\in D_{train}} \left(\widehat{CL}(t|\boldsymbol{\delta},\mathcal{K}) - CL^{phy}(t|\boldsymbol{\beta})\right)^2.\end{aligned} \tag{8}$$

Here, $\lambda > 0$ controls the trade-off between the spline fitting and physical model. Finally, the optimal λ and $\mathcal{K}$ are tuned on a grid via the Genetic Algorithm to minimize the validation data loss:

$$(\mathcal{K}^*, \lambda^*) = \underset{\mathcal{K},\lambda}{argmin} \sum_{t\in D_{valid}} \left(CL(t) - \widehat{CL}\left(t|\widehat{\boldsymbol{\delta}}_{\lambda,\mathcal{K}},\mathcal{K}\right)\right)^2. \tag{9}$$

5. Results and Discussions

5.1. Physical Model

Initially, we fit the complete dataset using the physical model through a nonlinear least squares method to validate the model. Figure 1a indicates that the simplified physical model adequately captures the pattern of capacity loss. As mentioned earlier, the growth of SEI can be seen as a diffusion-controlled reaction. Initially, the SEI layer is relatively thin, leading to a faster diffusion rate and a quicker capacity degradation. As the thickness of the SEI layer increases, the rate of degradation gradually slows down. Notably, the capacity loss exhibits a square root correlation with cumulative charging time before 1200h in Figure 1a, aligning with the behavior described by the reaction diffusion model. As the SEI layer thickens, it leads to a linear increase in lithium plating's overpotential over time. Once the SEI layer reaches a certain thickness, it triggers lithium plating. This rapid reaction significantly accelerates the loss of battery capacity with exponential correlation. In Figure 1a, it sharply increases as cumulative charging time reaches 1200 h, indicating the onset of lithium plating. Figure 1b illustrates fitting results of physical models using data from the initial 600 cycles. It seems there's a strong fit in describing the SEI growth phase, but there's no detection of the occurrence of lithium plating behavior. Obviously, the absence of data featuring significant lithium plating hinders the detection of its onset, leading to square root correlation prediction.

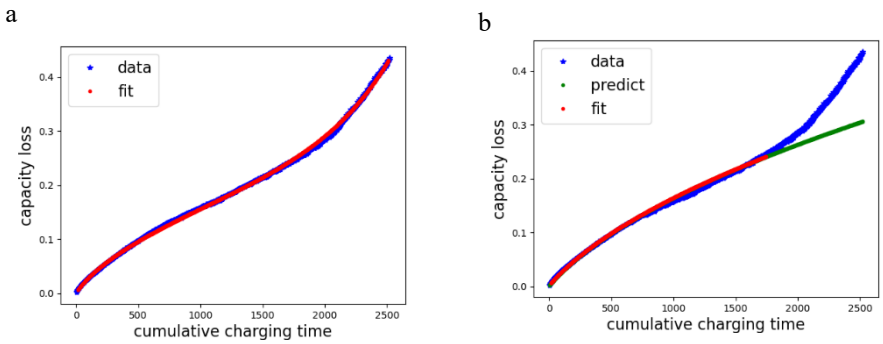

Figure 1: Physical model fitting with full range (left) and 600 cycles (right) of data

5.2. I-spline Fitting

Splines are widely recognized in numerical analysis for their exceptional performance in interpolation. In this section, we first fit the spline model with the full range of data. With a setup featuring 4 equally spaced knot intervals and an order of 4, Figure 2a suggests that the I-spline model effectively captures the pattern of capacity loss through interpolation. Figure 2b illustrates the fitting results of I-spline models using data from the initial 400 cycles as training data and the subsequent 200 cycles for validation. The optimal outcome is achieved with a fourth-order spline and three internal knots. Although I-splines are monotonically non-decreasing, through adjusting weight of each I-spline composing data-driven model can change tendency of the model. As the result of scarce data of lithium plating in training data, the weight of the spline in the last interval is adjust low. In this condition, the model underestimate the capacity loss of follow-up data. In conclusion, the lack of substantial data regarding lithium plating hampers the model's performance in extrapolation.

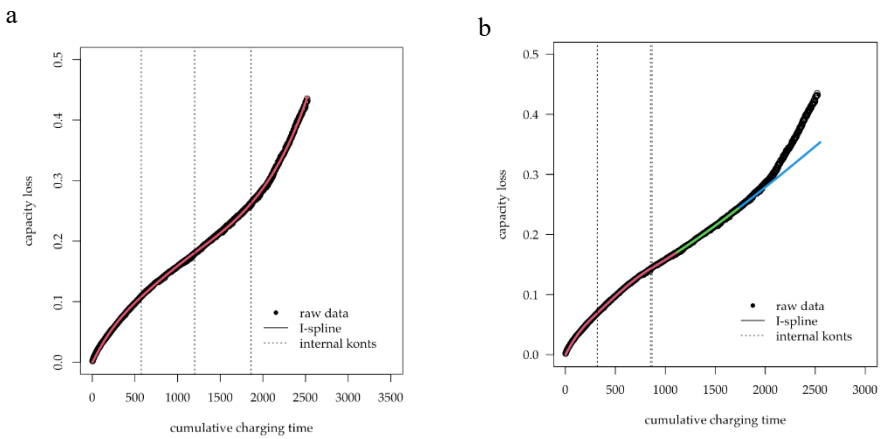

Figure 2: I-spline model fitting with full range (left) and 600 cycles (right) of data

5.3. Physics-Guided I-Spline Fitting

We incorporated a data-driven model into our physical mechanism analysis, utilizing the first 400 cycles as training data and the subsequent 200 cycles for validation. The fifth-order spline with 4 inner knots stands out as the optimal choice due to its minimal loss. The positions of each knot are illustrated by dotted lines along the x-axis. Within this physics-guided data-driven model, Figure 3 predicts the information of the onset of lithium plating that both physical model and I-spline model couldn't achieve. The model adjusts the location of knots to satisfy the physical constrain in validation part. The location of the last internal knot is moved forward, so that the curve can match both data and physical model. It comes out that the physics-guided data-driven model can not only forecast the emergence of the turning point but also accurately track the trajectory of capacity loss.

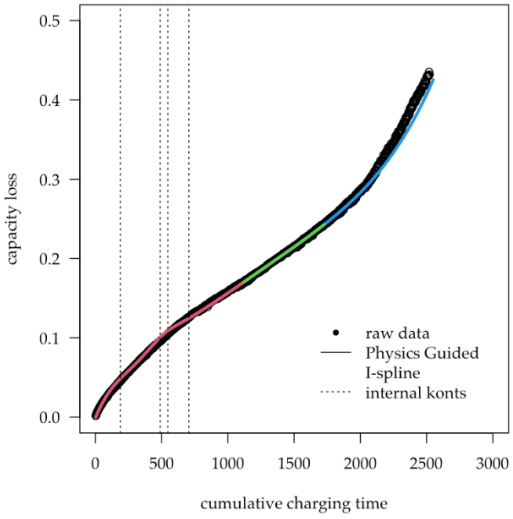

Figure 3: Physical-guided I-spline fitting model fitting with limited range data

6. Conclusions

In this study, we integrate a physical model with a data-driven approach to predict future capacity loss in lithium batteries. The experimental results show that while the physical model can effectively explain the mechanism of capacity loss over time, adequate data is crucial for accurate model parameterization. Otherwise, the physical model fails to detect the onset of lithium plating. Additionally, I-spline, known for its exceptional interpolation performance, shows less favorable results in extrapolation. The physics-guided data-driven model, which integrates spline and physical constraints, comes in handy when training data is insufficient. Consequently, this model predicts capacity loss more accurately than either the physical model or I-spline alone. It showcases significant potential in predicting battery end-of-life and enhancing battery management systems.

Acknowledgment

This work was supported in part by the National Science and Technology Council under project numbers NSTC 111-2634-F-007-010 and NSTC 112-2221-E-007-015.

References

von Kolzenberg L., Latz A. and Horstmann B., Solid–electrolyte interphase during battery cycling: Theory of growth regimes. ChemSusChem, 2020. 13: p. 3901–3910.

Severson, Kristen A; Attia, Peter M; Jin, Norman; Perkins, Nicholas; Jiang, Benben; Yang, Zi; Chen, Michael H; Aykol, Muratahan; Herring, Patrick K; Fraggedakis, Dimitrios; Bazant, Martin Z; Harris, Stephen J; Chueh, William C; Braatz, Richard D. (2019). Data-driven prediction of battery cycle life before capacity degradation. Nature Energy, 4: p. 383-391.

Ramsay, J. O. (1988). Monotone regression splines in action. Statistical Science, 3, 425-441.

Willard, J., Jia, X., Xu, S., Steinbach, M., & Kumar, V. (2020). Integrating physics-based modeling with machine learning: A survey. arXiv preprint arXiv:2003.04919, 1(1), 1-34.

Yang, X. G., Leng, Y., Zhang, G., Ge, S., & Wang, C. Y. (2017). Modeling of lithium plating induced aging of lithium-ion batteries: Transition from linear to nonlinear aging. Journal of Power Sources, 360, 28-40.

ESCAPE-34 PSE-2024
European Symposium on Computer Aided Process Engineering
&
Process Systems Engineering

Flavio Manenti, Gintaras V. Reklaitis (Eds.), Book of Abstract of the 34th European Symposium on Computer Aided Process Engineering / 15th International Symposium on Process Systems Engineering (ESCAPE34/PSE24), June 2-6, 2024, Florence, Italy.

Modelling and Optimization of Ikaite Precipitation for CO_2 Removal Based on Ocean Alkalinity Enhancement

Xuesong Lu, Pranav Thoutam, Aidong Yang
Department of Engineering Science, University of Oxford
xuesong.lu, Pranav.thoutam, aidong.yang@eng.ox.ac.uk

Abstract

In this study, numerical modelling that couples mass transfer and reaction kinetics has been performed on a process designed for ikaite production involving dissolution of calcite and the subsequent controlled precipitation to favour ikaite selective crystallization. Multiple configurations regarding supply of calcite particles and agitation were considered to evaluate energy consumption. Through simulation in COMSOL, the results identified the importance of dissolution and crystallisation over degassing, and the significant influence of calcite particle size and agitation speed on total energy demand, which are to be focused on in the subsequent experimental studies.

Keywords: dissolution, crystallization, ikaite, energy efficiency

1. Introduction

In order to reach the goals of the Paris agreement, it has been considered necessary to remove CO_2 from the atmosphere along with significant reduction of emissions. Oceans have been acting as the natural sink for CO_2. To enhance this process as a way to actively remove CO_2 from the atmosphere, it has been proposed to dissolve suitable minerals in seawater to increase alkalinity, which promotes the dissolution of atmospheric CO_2 to form bicarbonates. Especially, calcite ($CaCO_3$) as a relatively fast dissolving mineral has been suggested for this purpose, which however has already supersaturated the ocean surface, making it impossible to draw down CO_2 from air through its dissolution.

To address this issue, the use of other minerals has been proposed, including particularly hydrated $CaCO_3$ minerals such as ikaite, which can overcome the limitation of calcite and dissolve in seawater naturally, hence fulfilling the purpose of CO_2 removal (Renforth & Henderson, 2017). However, the natural occurrence of ikaite is extremely low, which means that it needs to be manufactured artificially for use in ocean alkalinity enhancement. To understand the feasibility and cost of ikaite manufacturing, the current

work extends an earlier study (Renforth et al., 2022) through process modelling, particularly aiming at quantifying energy consumption of a potentially feasible process.

2. Process configuration and modelling

A COMSOL model consisting of a dissolution reactor, a degasser and a crystallizer was developed to create the ikaite production process (Figure 1), following the configuration and process conditions with constant temperature at 276.15K throughout the system while the dissolution reactor, degasser and crystallizer were maintained at 2, 0.5 and 0.02 bar pressure respectively as proposed by Renforth et al. (2022).

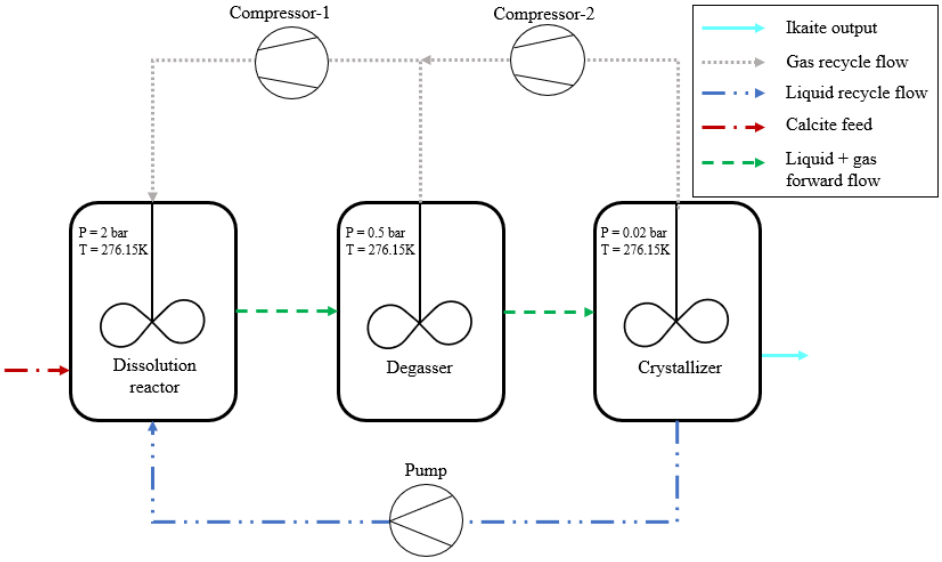

Figure 1. Ikaite production process configuration (Renforth, et al., 2022)

All the three reactors were modelled as stirred tanks, operating in a batch mode. The dissolution reactor was fed with (recycled) CO_2 gas and calcite solid particles to dissolve the latter in water. The dissolution product solution entered the degasser tank where the total dissolved carbon (TDC, including CO_2-aqueous, HCO_3^-, CO_3^{2-}) was partially removed from the solution, with the remaining solution entering the crystallizer. In this final reactor, TDC was further removed due to the pressure difference, and seeded crystallization of ikaite occurs. The evolved CO_2 gas flows from the degasser and the crystallizer were recycled through two compressors back to the dissolution reactor which also received the depleted solution from the crystallizer through a pump.

To model these reactors, calcite particle dissolution was simulated using the particle shrinking model. The chemical reactions depicting calcite dissolution and the aqueous phase reactions were considered following the studies of Plumber and Busenberg (1982) and Cents et al (2005) respectively. The gas-liquid mass transfer followed the same approach in Xing et al (2023). Precipitation of ikaite was modelled using the empirical kinetic equation proposed by Papadimitriou et al. (2014), while the supersaturation and the precipitation constants were calculated according to Strohm et al. (2022). The secondary nucleation and growth equations were utilized in the quadrature method of

moments (QMOM) equations (Wei, et al., 2001) to simulate the ikaite precipitation in COMSOL.

3. Energy Calculations and Simulation Cases

The current study explores the direction of optimization guided by the minimization of energy consumption per unit mass production of ikaite. To calculate energy consumption, the following operations have been considered:

- Compressors for the recycling CO_2 gas flows
- Pumping for water recycle
- Agitation in the stirred tanks
- Grinding for preparing calcite particles

Grinding energy was calculated from the method given by Xing et al (2022), while the energy consumption of the other processes was calculated using standard methods.

Through preliminary simulation tests, it became clear that the degassing process was significantly faster than the other two processes which was therefore excluded in the analysis. The duration of dissolution was potentially affected by both gas-liquid mass transfer and the surface dissolution kinetics. Therefore, its stirring speed (affecting mass transfer) and feed calcite particle diameter (affecting area available for surface dissolution) were chosen as key parameters for analysis. Besides, the stirring speed in the crystallizer, which affects the evolution of CO_2 gas through gas-liquid mass transfer, was also chosen to assess its effect. Table 1 shows all the cases comprising combinations of different settings of these parameters.

Table 1. The configurations considered for the energy modulations.

Case no	Stirring speed in dissolution reactor (RPM)	Stirring speed in the crystallizer (RPM)	Particle diameter (μm)
Case1	60	100	10
Case2	30	30	60
Case3	60	30	60
Case4	30	100	60
Case5	60	100	60
Case6	100	30	60
Case7	100	100	60
Case8	30	60	60
Case9	60	60	60
Case10	60	100	180

4. Results and Discussion

Figure 2 shows the key simulation results of the base case. One can see significant CO_2 dissolution (in the dissolution reactor) and evolution (in the crystalliser) within a very short period of operation, followed by more gradual increase or decrease in TDC caused mainly by the dissolution or crystallisation. In contrast, the concentration of calcium ions changed more evenly. In term of the batch duration, dissolution appeared to consume much longer time than crystallisation. On energy consumption, Table 2 shows the results of the base case.

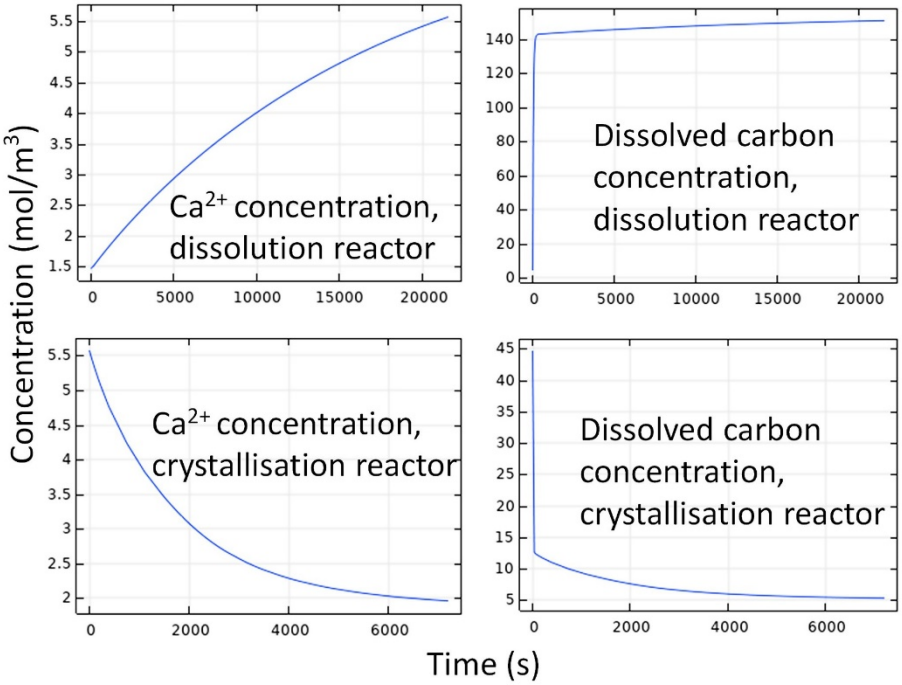

Figure 2. Simulation results of the base case (case 5).

Table 2. Energy consumption during various operations of the base case per kg ikaite.

Operation	Energy Consumption (kJ/kg ikaite)
Compressor1	5.92E1
Compressor2	8.52E2
Agitation in dissolution reactor	5.93E2
Agitation in crystallization	4.05E3
Water pumping	3.62E2
Grinding	3.86E1
Total	5.96E3

The overall energy consumption per one cycle of ikaite production was calculated to be 5.96E3 kJ/kg of ikaite production. Amongst all the operations, agitation was observed to have contributed the highest to the energy consumption followed by compressions.

Figure 3 summarised the energy consumption results of all the simulation cases. It can be seen that the particle diameter has profound influence. Smaller particles, although consuming more grinding energy, lead to a shorter dissolution time and hence lower energy consumption for agitation. A higher stirring speed always leads to the increase in the power required for agitation (while with limited impact on the dissolution rate, not shown) and hence higher energy consumption.

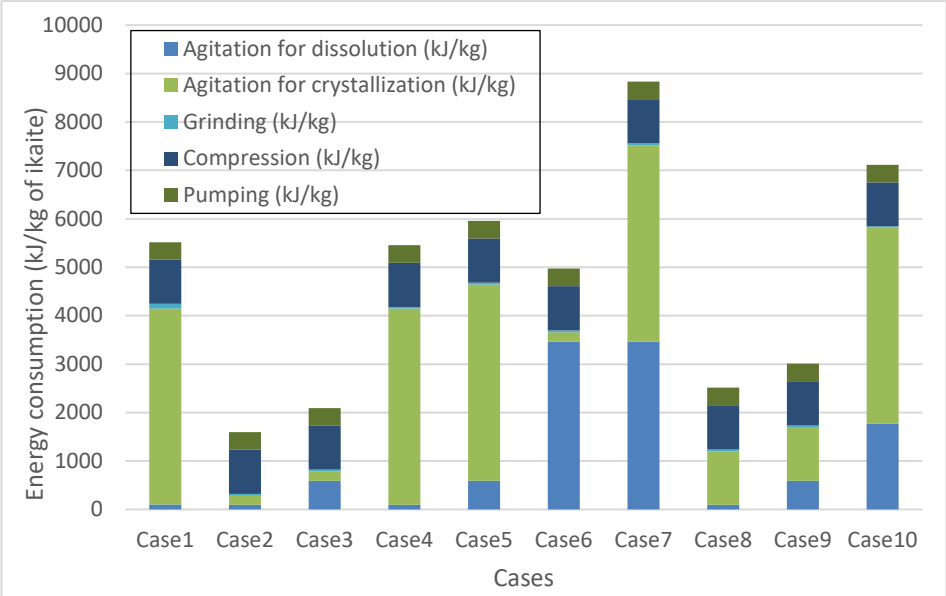

Figure 3. Specific energy consumption by cases listed in Table 1.

Amongst all the cases considered, Case 7, with 100rpm dissolution and crystallizer stirring speeds with 60µm feed particle size was observed to have consumed highest amount of energy with a total of 8.83E3 kJ/kg of ikaite. The minimum energy consumption was observed for the case 2 with 30rpm each with 60µm feed particle size with 1.60E3 kJ/kg of ikaite.

5. Conclusion

This COMSOL based modelling of ikaite precipitation predicted the feasibility of the production of ikaite and identified key parameters for future optimisation in order to reduce energy consumption. More specifically, we observed that the lower stirring speeds would be preferrable, and that using more energy to produce particles at smaller sizes would lead to the reduction of the overall energy demand.

References

Bischoff, J., Fitzpatrick, J. & Rosenbauer, R., 1993. The Journal of Geology, 101(1), pp. 21-33.
Caderbank, P., 1958. Chemical Engineering Research and Design, Volume 36, p. 443.
Caldeira, K. & Rau, G., 2000. Geophysical Research Letters, 27(2), pp. 225-228.
Cents, A., Brilman, D. & Versteeg, G., 2005. Chemical Engineering Science, 60(21), pp. 5830-5835.
Dvorak, B. et al., 1996. Environmental science & technology, 30(3), pp. 945-953..
Edwards, T., Maurer, G., Newman, J. & Prausnitz, J., 1978. AIChE Journal, 24(6), pp. 966-976.
Hughmark, G., 1980. Industrial & Engineering Chemistry Process Design and Development, 19(4), pp. 638-641.
Hu, Y. et al., 2014. Marine Chemistry, Volume 162, pp. 10-18.
Onda, K., Takeuchi, H. & Okumoto, Y., 1968. Journal of chemical engineering of Japan, 1(1), pp. 56-62.

Papadimitriou, S., Kennedy, H., Kennedy, P. & Thomas, D., 2013. Geochimica et Cosmochimica Acta, Volume 109, pp. 241-253.
Papadimitriou, S., Kennedy, H., Kennedy, P. & Thomas, D., 2014. Geochimica et Cosmochimica Acta, Volume 140, pp. 199-211.
Plummer, L. & Busenberg, E., 1982. Geochimica et cosmochimica acta, 46(6), pp. 1011-1040..
Pokrovsky, O., Golubev, S. & Schott, J., 2005. Chemical geology, , 217(3-4), pp. 239-255.
Renforth, P. et al., 2022. Joule, 6(12), pp. 2674-2679.
Renforth, P. & Henderson, G., 2017. Reviews of Geophysics, 55(3), pp. 636-674.
Sjoeberg, E. & Rickard, D., 1984 Chemical Geology, 42(1-4), pp. 119-136.
Stockmann, G. et al., 2018. Applied Geochemistry, Volume 89, pp. 11-22.
Strohm, S. et al., 2022. Chemical Geology, Volume 611, p. 121089.
Tollefsen, E. et al., 2018. Mineralogical Magazine, 82(5), pp. 1119-1129.
Wei, H. et al., 2001. Industrial & engineering chemistry research, 40(23), pp.5255-5261.
Xing, L. et al., 2023. Chemical Engineering Journal, Volume 454, p. 139997.
Xing, L. et al., 2022. Chemical Engineering Journal, Volume 431, p. 134096.

ESCAPE-34 PSE-2024
European Symposium on Computer Aided Process Engineering
&
Process Systems Engineering

Flavio Manenti, Gintaras V. Reklaitis (Eds.), Book of Abstract of the 34th European Symposium on Computer Aided Process Engineering / 15th International Symposium on Process Systems Engineering (ESCAPE34/PSE24), June 2-6, 2024, Florence, Italy.

Pore-Scale Models for Soot and Gaseous Pollutant Conversion in Catalytic Particulate Filters

Ondřej Studeník[a,b], Marie Plachá[a], Martin Isoz[a,b], Miloš Svoboda[c], Petr Kočí[a]

[a] *University of Chemistry and Technology, Prague, Technická 5, Prague, 166 28, Czechia*
[b] *Institute of Thermomechanics, Czech Academy of Sciences, Dolejškova 5, Prague, 182 00, Czechia*
[c] *New Technologies Research Centre, University of West Bohemia, Univerzitní 8, Pilsen 306 14, Czechia*
petr.koci@vscht.cz

Abstract

Tightening emission standards necessitate development and optimization of devices for exhaust gas aftertreatment. Catalytic particulate filter is a multifunctional device that can trap particulate matter (soot and ash) and provide catalytic conversion of gaseous pollutants such as CO, hydrocarbons and NO_x. In the present work, we focus on pore-scale simulations of (i) influence of soot deposits on catalytic conversion of gaseous pollutants and (ii) oxidation of soot deposits during filter regeneration. Pore-scale simulations are performed within a section of the filter wall, 3D reconstructed from X-ray tomography (XRT) images of porous structure including distribution of catalytic material [1]. CO oxidation is used as test reaction. First, we assume uniform soot layer inside the porous wall structure and evaluate its impact on CO conversion. Several different thicknesses of soot layer are compared. In the second approach, we virtually load the same amount of soot deposits using a mechanistic filtration model [2], which results in non-uniform soot distribution, and evaluate again the impact on CO conversion. Subsequently, we introduce a soot oxidation model for the filter regeneration. During oxidation of soot deposits, clusters of particles may detach from the wall and freely travel through wall pores. Such a process can be described with a fully coupled CFD-DEM solver [3], capable of simulating arbitrarily shaped solid particles. The mentioned solver is extended with reactive flows to account for particle oxidation and the related changes in its morphology. All the developed models are implemented in the form of custom-built solvers within the OpenFOAM computational framework.

Keywords: catalytic filters, CFD, OpenFOAM, Automotive exhaust gas aftertreatment

1. Introduction

Present trends in emissions standards and environmental policies further encourage the development of new exhaust gas aftertreatment technologies or optimization of the ones presently available. Catalytic particulate filter is a multifunctional device enabling

catalytic conversion of gaseous pollutants such as CO, hydrocarbons, and NO_x [1]. Furthermore, it removes the particulate matter (soot and ash) from the exhaust [2]. The catalytic filter is designed as a monolithic reactor structured as a cylinder containing parallel channels with alternating plugs at the channel inlet or outlet. Such design forces exhaust gas to flow through the porous channel walls coated with a catalyst. This enables both catalytic conversion of the pollutants and filtration of the particulate matter. Thus, a catalytical filter allows replacing separate catalytic converters and filter by a single device.

Throughout the filtration operation, a layer of particulate matter gradually forms on the wall surface [2]. The soot deposits lead to an increase in filtration efficiency, pressure drop of the filter, and, consequently, a decrease in catalytic activity. The latter phenomenon is due to diffusion limitations presented by soot cake formed on the active sides of the catalyst obstructing the gas flow towards the catalyst's active sides. The filter can be regenerated by oxidation of the soot deposits. In the following text we focus on pore-scale simulations of how soot deposits influence catalytic conversion of gaseous pollutants. We use CO oxidation as test reaction.

2. Methods

The system is resolved with computational fluid dynamics (CFD). To accurately describe the processes occurring within the catalytic filter wall, we need to consider (i) fluid flow through the porous structure of the wall, (ii) diffusion and catalytic reaction of the chemical species present within the passing gas and (iii) enthalpic balance of the given system. Due to the small size of the described wall segment and low concentrations of key reaction component (CO), the system can be considered isothermal. Furthermore, convection, diffusion and reaction processes are simulated in steady state.

2.1. Fluid flow

The Navier-Stokes equations describe the gas flow in the described segment of porous wall, and due to the properties of the given structure and operating conditions, several simplifications might be applied. First, the fixed temperature and low-pressure difference between the inlet and outlet of the wall enables us to consider constant density of the passing fluid. Second, most of the pores present have a characteristic dimension of units of micrometres, resulting in low Reynolds criteria values, enabling us to consider flow laminar. Thus, the momentum balance Eq. (1) and mass balance Eq. (2) written as follows

$$\nabla \cdot (\boldsymbol{u} \otimes \boldsymbol{u}) - \nabla \cdot (\nu \nabla \boldsymbol{u}) = -\nabla \tilde{p} + s \tag{1}$$

$$\nabla \cdot \boldsymbol{u} = 0, \tag{2}$$

where $\boldsymbol{u}$ is fluid flow, $\tilde{p}$ is kinematic pressure ($\tilde{p} = p/\rho$), and ν is kinematic viscosity. The additional source term **s** is applied to additional flow resistance according to the given area e.g, free pore Ω_p soot deposits Ω_s and catalyst Ω_c. The term is defined as following piecewise function

$$s = \begin{cases} \mathbf{0} & in\ \Omega_p \\ \dfrac{\mu}{\kappa_s}\boldsymbol{u} & in\ \Omega_s \\ \dfrac{\mu}{\kappa_c}\boldsymbol{u} & in\ \Omega_c \end{cases}, \tag{3}$$

where κ_s and κ_c are local permeabilities according to Darcys law for soot and catalyst, respectively. Permeability is predicted from the Carman-Kozeny equation [4]. Dynamic viscosity μ is evaluated using the Sutherland equation [5].

2.2. Component diffusion

With the gas flow description presented above, the next step is a description of the mass transport of the individual species (O_2, N_2, CO and CO_2). Ideal gas behavior is assumed and low concentrations of the key reactant (CO) enable consideration of Ficks' laws for volume diffusion. Transport equation for *i*-th species is then

$$\nabla \cdot (\boldsymbol{u} y_i) - \nabla \cdot \left(D_i^{eff} \nabla y_i\right) = \frac{s_i^r}{c_T}, \tag{4}$$

where y_i is the molar fraction of the balanced species, s_i^r is the reaction source term, and D_i^{eff} is effective diffusivity. Its value changes according to domain composition, in a similar manner to the momentum source term (3).

$$D_i^{eff} = \begin{cases} D_i^{Vol} & in\ \Omega_p \\ \dfrac{\varepsilon_s}{\tau_s\left(1/\ D_i^{Vol} + 1/D_{i,s}^{Kn}\right)} & in\ \Omega_s \\ \dfrac{\varepsilon_c}{\tau_c\left(1/\ D_i^{Vol} + 1/D_{i,c}^{Kn}\right)} & in\ \Omega_c\ , \end{cases} \tag{5}$$

where D_i^{Vol} is volume diffusion coefficient [6] and D_i^{Kn} stands for Knudsen diffusion coefficient depending on mean pore size in the given zone. Porosity and tortuosity for the given region are denoted as ε and τ, respectively.

2.3. Catalytic reaction

With the definition of mass transport and treatment of diffusion limitations described above, the treatment of chemical reaction needs to be addressed. In the present simulation, we consider the test reaction, oxidation of CO to CO_2 at the $\mathrm{Pt}/\gamma\text{-}\mathrm{Al_2O_3}$ catalyst as written bellow.

$$CO + \frac{1}{2} O_2 \rightarrow CO_2 \tag{6}$$

The kinetics is described by the steady-state Langmiur-Hinshelwood [7] mechanism for a dual site reaction on the active surface of the catalyst with dominant inhibition by the adsorbed CO:

$$r = k \frac{y_{CO} y_{O_2}}{(1 + K^{inh} y_{CO})^2} \tag{7}$$

Here *k* represents the rate constant for chemical reaction, K^{inh} is the inhibition constant of gas adsorption to the catalyst surface. The temperature dependence given constants is determined by the Arrhenius equation. The rate of chemical reaction is marked as r.
The reaction source term s_i^r is considered only within the catalyst zones

$$s_i^r = \begin{cases} 0 & in\ \Omega_p, \Omega_s \\ \nu_i r & in\ \Omega_c \end{cases}, \tag{8}$$

where ν_i is stoichiometric coefficient for given *i*-th species.
We implemented the models as custom-built solvers in the CFD framework OpenFOAM.

3. Results

In the presented study, we focus on a segment of the channel wall of a catalytic filter with catalyst located within the porous wall structure. The simulation part of the channel model has dimensions of 566 × 200 × 204 µm^3. The computational domain for the given test was prepared directly from digital reconstruction of the XRT scans to stereolithographic description (STL) for both substrate and catalyst. For the generation of the computational mesh, we used snappyHexMesh for the removal of the substrate structure from the domain and prescribe zones with catalyst. Additionally, we used topoSet to prescribe a uniform layer of soot deposits on the free surface, as shown in Figure 1. Both applications are part of the OpenFOAM framework. The presented study is designed to show the combination of the following influences, the thickness of the soot deposit layer (0, 3.3, 6.6, 9.9 µm) channel velocity of the flowing gas (0.05 m/s, 0.1 m/s) and the device temperature (200, 300, 400, 500, 600 °C). Simulations were performed with material and reaction parameters given in Table 1. Composition of the gas entering the wall segment in the simulation was $y_{O_2} = 0.05$, $y_{CO} = 0.001$, and the remaining portion was nitrogen (inert).

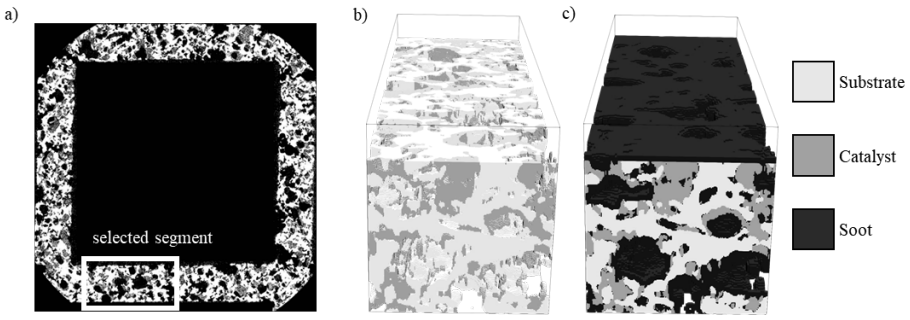

Figure 1. Computational domain: a) slice from the XRT scan of the filter channel with selected segment for the simulation, b) reconstructed STLs for substrate (white) and catalyst (grey), and c) constructed computational domain with added layer of soot deposits (black).

Table 1. Summary of the material and reaction constants applied in the simulations presented (porosity ε, tortuosity τ, mean pore size $\bar{d}_P$, preexponential factor A_0 and activation energy E_a from Arrhenius relation for reaction and inhibition [8,9]).

Structural parameters for materials			Reaction kinetics parameters		
Parameter	Catalyst	Soot	Parameter	Value	Unit
ε [-]	0.3	0.82	A_0	$7.84 \cdot 10^{16}$	mol s^{-1} m^{-3}
τ [-]	3.0	2.50	E_a	$9 \cdot 10^4$	J mol^{-1}
$\bar{d}_P$[m]	$5.0 \cdot 10^{-6}$	$61 \cdot 10^{-9}$	A_0^{Inh}	80	-
			E^{Inh}	$1 \cdot 10^3$	K

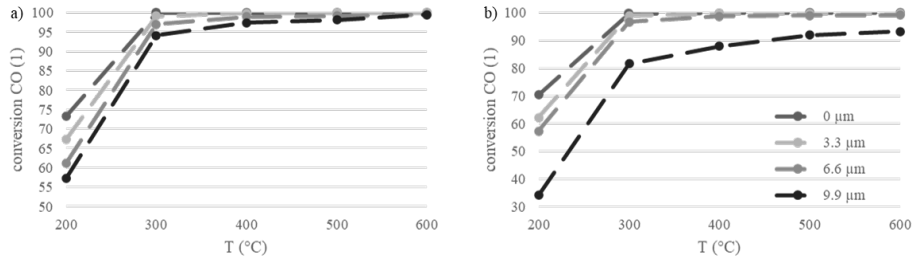

Figure 2. Influence of soot layer thickness on temperature-dependent CO conversion in the simulated segment of the filter wall for superficial gas velocity a) 0.05 m/s, and b) 0.1 m/s.

The results in Figure 2 show an influence of the thickness of the deposited soot layer on the outlet conversion of CO as a function of temperature. For all the tested configurations, the conversion at 200°C is limited by the slow reaction kinetics. The conversion increases readily with temperature and the results suggest complete CO conversion already at 300°C in the case of a clean filter (soot layer thickness 0 µm). The influence of soot deposits is evident – it decreases the CO conversion in all tests by imposing additional diffusion limitation for the access of reactants to the catalytic sites. The diffusion limitation increases with the soot layer thickness. For the lower gas velocity, we notice that full conversion is finally reached at the highest temperature. With the higher gas flow velocity, a decrease in conversion is more severe and a slip of unreacted CO persists up to the highest temperature with the thickest soot layer.

4. Conclusion

In this text we presented theoretical background, methods, and simplification applied for simulation of soot influence onto catalytic conversion of gaseous pollutants in a catalytic particulate filter. Further work that will be presented as a part of our contribution at the conference includes non-uniform soot distribution obtained from mechanistic filtration model as well as a pilot study of soot oxidation model involving CFD-DEM approach.

Acknowledgement

The work was financially supported by the Czech Science Foundation (GA22-12227S), by the institutional support RVO:6138899

References

[1] P. Kočí, M. Isoz, M. Plachá, A. Arvajová, M. Václavík, M. Svoboda, E. Price, V. Novák, D. Thompsett, "3D reconstruction and pore-scale modeling of coated catalytic filters for automotive exhaust gas aftertreatment", Catalysis Today 320, 165-174 (2019).

[2] M. Plachá, M. Isoz, P. Kočí, M. Jones, M. Svoboda, D. Eastwood, A. York, "Particle accumulation model in 3D reconstructed wall of a catalytic filter validated with time-resolved X-ray tomography", Fuel 356, 129603 (2024).

[3] M. Isoz, M. Kotouč Šourek, O. Studeník, P. Kočí, "HFDIB solver coupled with discrete element method for simulations of flows laden with arbitrarily-shaped particles", Computers & Fluids 244, 105538 (2022).

[4] M. Kaviany, Principles of Heat Transfer in Porous Media, SpringerVerlag, New York, 1995.

[5] Sutherland, W., LII. The viscosity of gases and molecular force. The London, Edinburgh, and Dublin Philosophical Magazine and Journal of Science, 1893. 36 (223).

[6] Fuller, E.N., P.D. Schettler, and J.C. Giddings, New method for prediction of binary gas-phase diffusion coefficients. Industrial & Engineering Chemistry 58(5) (1966).

[7] Voltz, S.E., et al., Kinetic study of carbon monoxide and propylene oxidation on platinum catalysts. Industrial & Engineering Chemistry Product Research and Development, 12(4). (1973)

[8] Brilhac, J.-F., et al., Experimental and theoretical study of oxygen diffusion within packed beds of carbon black. Carbon. 38(7),(2000)

[9] M. Dudák, V. Novák, P. Kočí, M. Marek, P. Blanco-García, G. Jones, Prediction of diffusivity and conversion of n-decane and CO in coated Pt/γ-Al2O3 catalyst depending on porous layer morphology, Applied Catalysis B: Environmental (2014)

ESCAPE-34 PSE-2024
European Symposium on Computer Aided Process Engineering
&
Process Systems Engineering

Flavio Manenti, Gintaras V. Reklaitis (Eds.), Book of Abstract of the 34th European Symposium on Computer Aided Process Engineering / 15th International Symposium on Process Systems Engineering (ESCAPE34/PSE24), June 2-6, 2024, Florence, Italy.

Enhanced Technosphere-Wide Life Cycle Assessment of Chemical Systems using Modified Background Data

Margarita Athanasia Charalambous,[a] Romain Sacchi,[b] Gonzalo Guillén-Gosálbez[a,*]

[a]*Institute for Chemical and Bioengineering, Department of Chemistry and Applied Biosciences, ETH Zürich, Vladimir-Prelog-Weg 1, 8093 Zürich, Switzerland.*

[b]*Laboratory for Energy Systems Analysis, Paul Scherrer Institut, Villigen, Switzerland*
gonzalo.guillen.gosalbez@chem.ethz.ch

Abstract

Life cycle assessments of emerging chemical technologies often assume static background data (i.e., secondary supply chain activities connected to the main system under study — foreground activity —), consistent with the current state of the economy. However, the background system within which a process will operate can differ from the one assumed in the environmental database. For example, one may establish a new supply chain with different suppliers or consider future decarbonization and socio-economic trends in the analysis. This work addresses this limitation by adjusting the background data for a more insightful and holistic assessment of the foreground system. We focus on evaluating synthetic diesel fuel in the future, considering projected changes in the technosphere and extending the technological coverage of the background system. To this end, we use inventories from *premise*, a Python library that provides background data consistent with integrated assessment models and includes additional technologies in the background system to model alternative supply chains with which the main technology (foreground system) could interact with. Our findings reveal that modifying the background data can drastically affect the outcome of the LCA analysis. Overall, this work stresses the importance of jointly defining the foreground and background systems to perform more meaningful and accurate LCAs.

Keywords: prospective life cycle assessment, computational LCA, fuel systems, integrated assessment models

1. Introduction

The power, chemical, and transportation sectors are almost entirely powered by fossil fuels today, contributing to 70 % of global anthropogenic greenhouse gas (GHG) emissions in 2021 (IEA 2023). Consequently, there has been a noticeable shift towards sustainable energy systems and environmentally friendly chemical production. At the

core of this transition lies the critical role of environmental assessments, which are essential for guiding policy decisions and experimental work more effectively.

Currently, standard life-cycle assessments (LCAs) retrieve data from life-cycle inventory databases that represent today's economic structure and assume that such data (background data or upstream supply chain data) will remain the same. Moreover, such assessments rely on static and immutable supply chains in the technosphere (e.g., the same suppliers are considered for all the inputs across the supply chain). However, these data are expected to change following future decarbonization and socio-economic trends. Moreover, future supply chains entailing different technological and regional choices could result in different life cycle impacts.

In recent works, some authors defined background LCA data based on the outcome of Integrated Assessment Models (IAMs) scenarios (Mendoza Beltran, 2018). Specifically, Sacchi et al. (2022), introduced *premise*, a tool that generates prospective inventory databases by integrating IAM scenarios. This framework enables the creation of library datasets that use future projections for a more accurate assessment of technologies and future supply chains. Prospective environmental assessments can then use these datasets in their background system when assessing emerging technologies (as foreground activities). However, it is important that full integration between the foreground and background data is accomplished, i.e., technologies in the foreground should also be modeled in the markets used in the background to ensure full consistency. In this regard, the LCA framework Brightway2 (Mutel, 2017) offers an excellent platform to implement changes in the background system that would be very hard to model using standard LCA tools. Here, as a representative relevant case, we evaluate transport fuels under modified background data, finding that the results can greatly vary compared to those assuming a fixed background system. Our analysis highlights the advantages of jointly defining the foreground and background systems for more insightful LCAs.

2. Methodology

We assess the future environmental impacts of the diesel fuel market. The functional unit was defined as 1 MJ of fuel. *premise* is used to create future background data (v.1.5.1), adopting the REMIND (Regional Model of Investment and Development) IAM results consistent with a global atmospheric temperature increase of 1.5 ºC by 2100. The fuel market projected by the IAMs considers fossil, bio-based, and synthetic routes. We increase the technological coverage of synthetic fuel production pathways (i.e., synthetic diesel routes). To this end, we consider four synthetic diesel production pathways where carbon dioxide is captured from the air and hydrogen comes from polymer electrolyte water electrolysis varying the power source (i.e. nuclear, wind, solar, hydro).

Fuel production inventories are modeled with Brightway2 (v.2.4.3). For the diesel scenarios, we assume synthetic Fischer-Tropsch (FT) diesel based on Medrano-García et al. (2022), for carbon dioxide supply, data were retrieved from Keith et al. (2018), and for hydrogen, we follow Bareiß et al. (2019). In this work, we implement the LCA calculations in Python. LCA is performed using the technosphere and biosphere matrix. The technosphere matrix is a square matrix that incorporates all the processes that are present in the economy stored in the columns of the matrix. The rows of the matrix represent the inputs of these processes and are inter-defined in the matrix. Our technosphere matrix incorporates our fuel production inventories, *premise* inventories, and supply chain projections from IAMs. The biosphere matrix includes all the direct emissions or resources consumption of all the processes present in the technosphere.

Matrix modifications and LCA calculations using characterization factors from Brightway2 are performed in Python, using the IPCC 2021 100a as the impact assessment method. Finally, the results are interpreted, and the main conclusions are summarized. As already said, a critical aspect of the analysis is that we vary the background data in a way that is consistent with the foreground system, which we argue is essential particularly when assessing large-scale systems. For example, if one wishes to quantify the impact of e-diesel from captured CO_2 and green H_2 from wind deployed at scale (foreground system), it would be sensible to assume that all the e-diesel in the background would be produced following the same pathway, (or at least deploy such a pathway to some extent) as otherwise, the foreground and background systems would not be consistent with each other, potentially leading to less accurate results.

3. Results and Discussion

Figure 1 shows that global warming impacts of e-diesel, either with *premise* background or with a background fully consistent with the foreground. In Figure 1a, the impacts of synthetic diesel from DAC/nuclear are displayed, for the two cases, as explained before. Modifying the background system to consider the technology studied (in the foreground) can cause notable differences compared to the standard practice (i.e., using the default future background system as provided by premise). Specifically, a 10% difference is found between using consistent background-foreground systems and the premise background in 2050. This demonstrates the importance of incorporating the assessed foreground activity into the background system, especially in the future, where emerging technologies will occupy larger parts of the market. Therefore, in Figure 1b, we compare the emission trajectories of three different e-diesel pathways (DAC/hydro, DAC/solar, DAC/wind) when employed in the market using a consistent foreground-background system. All scenarios show carbon-negative impacts after 2025, while DAC/solar shows the largest global warming impacts through the years with −40 kg $CO_{2eq.}$ MJ^{-1} compared to −55 kg $CO_{2eq.}$ MJ^{-1} of DAC/wind and −78 kg $CO_{2eq.}$ MJ^{-1} of DAC/hydro in 2030. Overall, DAC/hydro performs the best in 2050 with −85 kg $CO_{2eq.}$ MJ^{-1}.

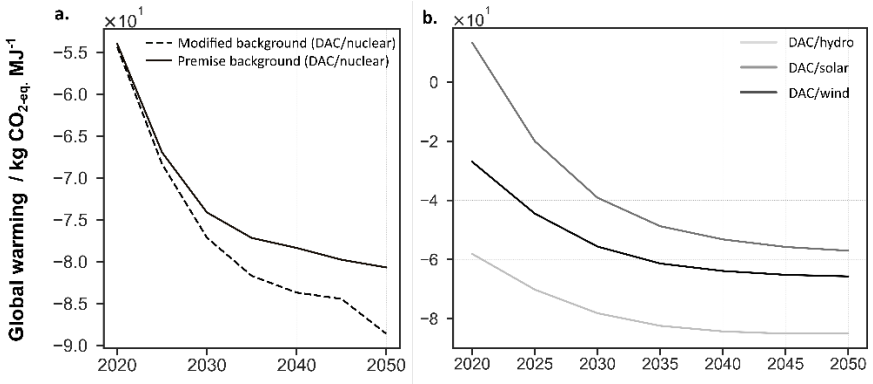

Figure 1: a. Global warming impacts for e-diesel from DAC/nuclear in the diesel market, examining its effects in the foreground and background systems under "Modified background" and "Premise background" scenarios. b. Global warming impacts of three synthetic diesel pathways, (DAC/hydro, DAC/solar, DAC/wind). The trajectories shown here consider a consistent foreground-background system where the diesel market in the background system is modified to consider the synthetic diesel technology assessed in the foreground.

4. Conclusions

In this work, we evaluate the future environmental impacts of synthetic diesel fuel while considering the decarbonization trends outlined by the REMIND IAM, aligning with the Paris Agreement. Additionally, we extend the technological coverage of renewable production pathways considered in the IAM by systematically modifying the technosphere matrix. To our knowledge, this is the first time such fuels are evaluated under future plausible scenarios generated by an IAM with full consistency between the foreground and background data. Notably, we find that the background data can greatly affect the outcome of the analysis, leading in our case study to differences in global warming impact of as much as 10%. Overall, we here stress the importance of adjusting the background data when performing prospective environmental assessments of power and chemical systems.

Acknowledgements

This work was created as part of NCCR Catalysis, a National Center of Competence in Research funded by the Swiss National Science Foundation.

References

IEA, 2023, Energy Technology Perspectives

A. Mendoza Beltran, B. Cox, C. Mutel, DP van Vuuren, D. Font Vivanco, S. Deetman, O.Y. Edelenbosch, J. Guinée, A. Tukker, 2018, When the background matters : using scenarios from integrated assessment models in prospective life cycle assessment, Journal of Industrial Ecology, 24,1, 64-79.

R. Sacchi, T. Terlouw, K. Siala, A. Dirnaichner, C. Bauer, B. Cox, C. Mutel, V. Daioglou, G. Luderer, 2022, Renewable and Sustainable Energy Reviews, 160, 112311.

C. Mutel, Brightway: An Open Source Framework for Life Cycle Assessment, 2017, Journal of Open Source Software, 2 (12), 236

J.D. Medrano-García, M.A. Charalambous, G.Guillén-Gosálbez, 2022, Economic and environmental barriers of CO_2-based Fischer-Tropsch electro-diesel, ACS Sustainable Chemistry & Engineering, 10, 36, 11751-11759.

D.W. Keith, G. Holmes, D. St. Angelo, K. Heidel, 2018, A process for capturing CO_2 from the atmosphere, Joule, 2, 8, 1573-1594.

K. Bareiß, C. de la Rua, M. Möckl, T. Hamacher, 2019, Life cycle assessment of hydrogen from proton exchange membrane water electrolysis in future energy systems, Applied Energy, 237, 862-872.

ESCAPE-34 PSE-2024
European Symposium on Computer Aided Process Engineering
&
Process Systems Engineering

Flavio Manenti, Gintaras V. Reklaitis (Eds.), Book of Abstract of the 34th European Symposium on Computer Aided Process Engineering / 15th International Symposium on Process Systems Engineering (ESCAPE34/PSE24), June 2-6, 2024, Florence, Italy.

Geospatial Modelling and Optimisation of Direct Air Capture and its Energy Supply Options for Cost-Effective Deployment

Marwan Sendi, [a,b] Mai Bui, [b,c] Niall Mac Dowell, [b,c,] Paul Fennell[a,*]

[a]*Department of Chemical Engineering, Imperial College London SW7 2AZ, London, UK*
[b]*The Sargent Centre for Process Systems Engineering, Imperial College London, London SW7 2AZ, UK.*
[c]*Centre for Environmental Policy, Imperial College London, London SW7 2NE, UK. London.*
p.fennell@imperial.ac.uk

Abstract

To meet the emissions reduction targets outlined in the Paris Agreement, removing billions of tons of carbon dioxide from the atmosphere is crucial, particularly for addressing hard-to-abate emissions such as agriculture and aviation. Direct Air Capture and Storage (DACS) stands out as a promising technology for carbon dioxide removal (CDR), owing to its modular design and ease in monitoring, reporting and verification of emissions. However, given its energy-intensive nature, high cost and sensitivity to regional climate variations, optimising its performance is essential. In this study, we introduce a modelling optimisation framework for geospatial assessment of DACS process configurations coupled with different energy sources, considering the impact of both temporal and spatial variations on the techno-economic performance of DACS. The framework is applied to industrial DACS technologies utilising solid sorbents and powered by conventional (i.e., nuclear and natural gas) and renewable (i.e., solar and wind) energy sources. By identifying the least-cost DAC system configurations and their corresponding environmental metrics (such as CO_2 removal efficiency, land requirements, and water footprint) for different regions, our findings offer valuable insights for decision-makers and project developers. This work serves as a guide to identify suitable regions and system configurations for the cost-effective deployment of DACS technology.

Keywords: Carbon dioxide removal (CDR), direct air carbon capture and storage (DACCS), geospatial analysis, techno-economic assessment (TEA), life-cycle assessment (LCA).

1. Introduction

Achieving Paris Agreement emissions targets economically and realistically requires large-scale carbon dioxide removal (CDR) from the atmosphere (Rogelj et al., 2018;

Royal Society and Royal Academy of Engineering, 2018). CDR plays a crucial role in offsetting residual GHG emissions from hard to decarbonise sectors, such as agriculture or aviation. Direct Air Capture and Storage (DACS) emerges as a promising CDR method, offering the advantage of no biophysical limits and enabling immediate CO_2 removal from the atmosphere with permanent storage (Chiquier et al., 2022; Matter et al., 2016; Smith et al., 2016). Additionally, DACS benefits from well-established monitoring, reporting, and verification (MRV) protocols, streamlining the issuance of CDR credits (Mac Dowell et al., 2022). This can attract the necessary investments for rapid technology deployment required to achieve the Paris Agreement targets.

Direct air capture (DAC or DACS when storage is included) is an energy-intensive process. Thus, large-scale DACS deployment would require significant additional demand for low-carbon and cheap energy for the energy transition (Erans et al., 2022). Furthermore, we showed in our previous work that DAC process performance is influenced by regional climate variations, impacted by daily and seasonal fluctuations in ambient air temperature and relative humidity (Sendi et al., 2022).

Building on our earlier findings, this study introduces a geospatial modelling framework to evaluate the techno-economic and environmental performance of various DAC configurations and energy supply options. The goal is to identify the most energy and cost-effective DAC systems based on regional technology performance while accounting for temporal and spatial variations in DAC process performance. We apply this framework to determine the least-cost DAC systems for industrial DAC processes based on amine-functionalised sorbents coupled with different conventional (i.e., nuclear and fossil fuel) and renewable (i.e., solar and wind) energy sources.

2. Methods

We model the solid-based DAC unit based on an industrial DAC unit. In this unit, the adsorption bed, shaped like rectangular frames with a certain thickness, contains the sorbent material. The unique shape of the adsorption bed led us to model it using a combination of detailed 1-D and 2-D adsorption models. The 1-D model is applied when gas flows perpendicular to the bed frame. In contrast, the 2-D model is used when material concentration and temperature variations across the frame's plane influence the process performance. More information regarding the adsorption model is found in our recent publication (Sendi et al., 2022). Additionally, our adsorption model integrates a binary CO_2/H_2O isotherm specifically developed for DAC applications (Young et al., 2021).

The resulting rigorous DAC model yielded a set of partial differential equations, which we discretised using finite volumes. To mitigate non-physical oscillations, we applied the van Leer flux limiter only for the 1-D model, as the 2-D model did not exhibit such oscillations. MATLAB was utilised to implement and solve the resulting time-dependent ordinary differential equations. The rigorous DAC model served as the foundation for constructing simplified surrogate models that describe DAC process performance under varying ambient conditions (i.e., temperature and relative humidity). These surrogate models were then employed to estimate hourly DAC process performance for two adsorption cycle configurations — vacuum-pressure temperature swing adsorption (VTSA) and steam-assisted VTSA (SA-VTSA) — using hourly temperature and relative humidity profiles across different regions.

The regional hourly DAC process data was input into a Mixed Integer Linear Programming (MILP) optimisation model based on the Resource Technology Network

(RTN) framework. This model integrates components related to energy generation, conversion, and storage. Dependent variables that influence the regional techno-economic performance of DAC systems were incorporated, including weighted average capital cost (WACC), solar irradiation, and wind speed. The MILP model, implemented in Pyomo, was solved using CPLEX to identify the least-cost DAC system configuration for different spatial nodes based on regional technology performance. The mathematical formulation of the MILP is shown in Equation 1. Also, the levelised cost of DAC (LCOD) is defined in Equation 2.

$$\begin{aligned} &\textbf{min} \quad \text{total annual system cost } (TAC) \\ &\textbf{s.t.} \quad \text{annual } CO_2 \text{ removal (TAP)} \\ &\qquad \text{mass and energy balance} \\ &\qquad \text{process constraints} \end{aligned} \tag{1}$$

$$LCOD = \frac{TAC}{\mathrm{TAP}} \tag{2}$$

Moreover, key environmental metrics are calculated for the least-cost DAC system, including lifecycle greenhouse gasses (GHG) emissions, water footprint and land requirements. Equation 3 shows how total lifecycle GHG emissions ($TLCGHGE$) is calculated, which is the sum of the annual GHG emissions from different technologies normalised by TAP. Total water footprint and land requirements are calculated using similar equations. Equation 4 defines CO_2 removal efficiency (η^{CDR}) based on $TLCGHGE$. Finally, MATLAB was utilised for visualisation.

$$TLCGHGE = \frac{\sum_t ALCGHGE_t}{\mathrm{TAP}} \tag{3}$$

$$\eta^{CDR} = 1 - TLCGHGE \tag{4}$$

3. Results and discussion

Least-cost DAC system configurations have been identified for different regions based on conventional (i.e., nuclear and fossil fuel) and renewable (i.e., solar and wind) energy sources. **Figure 1**a shows the levelised cost of DAC (LCOD) for the least-cost DAC system supplied by renewable energy with energy storage systems. In this case, the least-cost DAC system configuration is regionally dependent on the DAC regional performance, which is affected by regional climate and weather conditions and the regional availability of renewable energy resources. For instance, regions with high direct normal irradiation (DNI) resources, which also experience drier climates, such as parts of the USA, the Middle East, and Australia, show relatively lower LCOD. This is because DAC energy requirements are lower in drier climates, and in these regions, concentrated solar power (CSP) can provide a relatively cheaper heat source. These results can assist in pinpointing regions where DAC deployment could be economically favourable.

Furthermore, **Figure 1**b showcases an optimised system configuration at specified coordinates. In this example, the optimised system employs the SA-VTSA cycle, utilising CSP for high-temperature (HT) heat generation in the form of high-pressure steam (HPS).

An installed capacity of 2.07 m^2 heliostat mirrors is required to capture 1 $ktCO_2pa$ (kilotons of CO_2 per annum). Normalised energy flows reveal that the CSP needs to generate 3.1 MWh_{th} of HT heat per tCO_2. This HT heat is used to generate electricity for DAC (0.4 MWh_{el} per tCO_2) in steam turbines (ST), which expand HPS to low-pressure steam (LPS). The remaining LPS and HT heat fulfil low-temperature (LT) heat requirements for DAC (2.3 MWh_{th} per tCO_2) in the form of LPS. HT and LT thermal heat storage with installed capacities of 3.58 and 2.49 MWh_{th}, respectively, are needed to increase the DAC plant capacity factor to 93% and lower the system cost. Other environmental performance metrics can also be identified. In this case, the system can produce 0.54 tons of water per tCO_2, have a total land footprint of 25 km^2 per $MtpaCO_2$, and achieve a CO_2 removal efficiency of 93% throughout the project lifecycle.

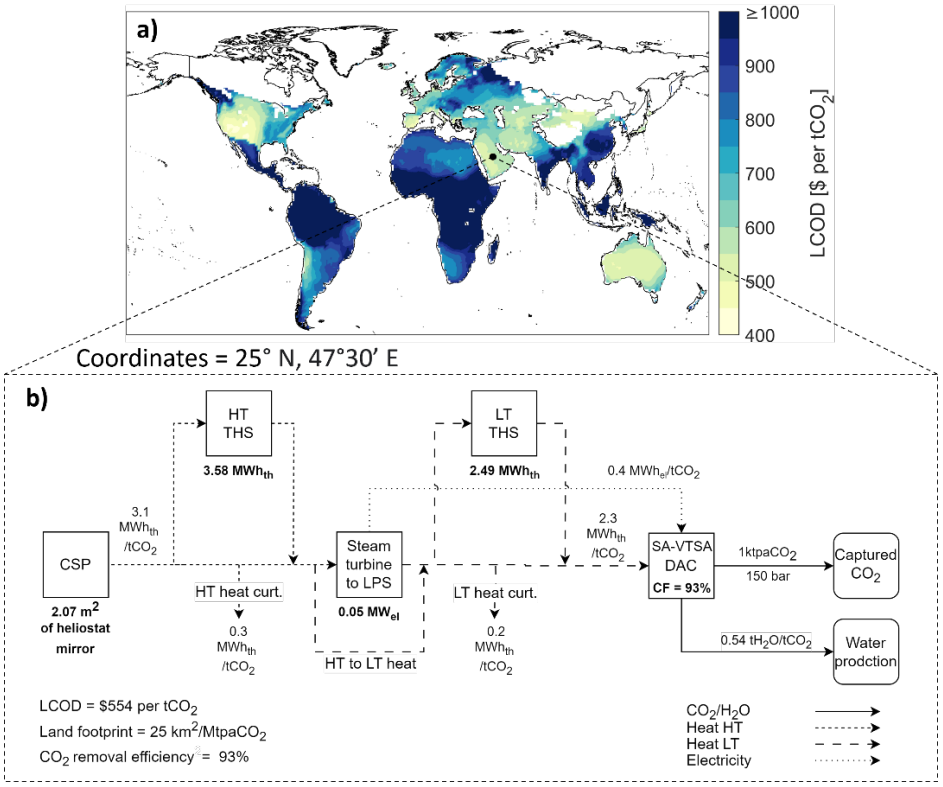

Figure 1 a) regional levelised cost of DAC (LCOD) for least-cost DAC system powered by renewable energy with energy storage. **b)** optimised DAC system configuration for coordinates (25°N, 47°30'E) showing required installed capacity for different technologies and normalised energy flows. **Abbreviation:** concentrated solar power (CSP), thermal heat storage (THS), high-temperature (HT), low-temperature (LT), low-pressure steam (LPS), curtailment (curt.), steam-assisted vacuum-pressure temperature swing adsorption (SA-VTSA), capacity factor (CF), $tpaCO_2$ (tons per annum of CO_2).

4. Conclusions

In this work, we developed a comprehensive framework to evaluate DAC processes and their energy supply, accounting for regional techno-economic performance across various

technologies. This framework considers both spatial and temporal variations in DAC process performance influenced by climate and weather conditions. It serves as an adaptable tool for conducting techno-economic and environmental assessments of different DAC system configurations in diverse regions, facilitating the identification of optimal regional configurations. The insights derived from this research are invaluable for decision-makers and project developers seeking to identify suitable regions and DAC system configurations for the cost-effective deployment of DAC technology.

References

Chiquier, S., Patrizio, P., Bui, M., Sunny, N., & Mac Dowell, N. (2022). A comparative analysis of the efficiency, timing, and permanence of CO_2 removal pathways [10.1039/D2EE01021F]. *Energy & Environmental Science*, *15*(10), 4389-4403. https://doi.org/10.1039/D2EE01021F

Erans, M., Sanz-Pérez, E. S., Hanak, D. P., Clulow, Z., Reiner, D. M., & Mutch, G. A. (2022). Direct air capture: process technology, techno-economic and socio-political challenges [10.1039/D1EE03523A]. *Energy & Environmental Science*. https://doi.org/10.1039/D1EE03523A

Mac Dowell, N., Reiner, D. M., & Haszeldine, R. S. (2022). Comparing approaches for carbon dioxide removal. *Joule*, *6*(10), 2233-2239. https://doi.org/10.1016/j.joule.2022.09.005

Matter, J. M., Stute, M., Snæbjörnsdottir, S. Ó., Oelkers, E. H., Gislason, S. R., Aradottir, E. S., Sigfusson, B., Gunnarsson, I., Sigurdardottir, H., Gunnlaugsson, E., Axelsson, G., Alfredsson, H. A., Wolff-Boenisch, D., Mesfin, K., Taya, D. F. d. l. R., Hall, J., Dideriksen, K., & Broecker, W. S. (2016). Rapid carbon mineralisation for permanent disposal of anthropogenic carbon dioxide emissions. *Science*, *352*(6291), 1312-1314. https://doi.org/10.1126/science.aad8132

Rogelj, J., Popp, A., Calvin, K. V., Luderer, G., Emmerling, J., Gernaat, D., Fujimori, S., Strefler, J., Hasegawa, T., Marangoni, G., Krey, V., Kriegler, E., Riahi, K., van Vuuren, D. P., Doelman, J., Drouet, L., Edmonds, J., Fricko, O., Harmsen, M., . . . Tavoni, M. (2018). Scenarios towards limiting global mean temperature increase below 1.5 °C. *Nature Climate Change*, *8*(4), 325-332. https://doi.org/10.1038/s41558-018-0091-3

Royal Society and Royal Academy of Engineering. (2018). Greenhouse gas removal. In: Royal Society London.

Sendi, M., Bui, M., Mac Dowell, N., & Fennell, P. (2022). Geospatial analysis of regional climate impacts to accelerate cost-efficient direct air capture deployment. *One Earth*, *5*(10), 1153-1164. https://doi.org/10.1016/j.oneear.2022.09.003

Smith, P., Davis, S. J., Creutzig, F., Fuss, S., Minx, J., Gabrielle, B., Kato, E., Jackson, R. B., Cowie, A., Kriegler, E., van Vuuren, D. P., Rogelj, J., Ciais, P., Milne, J., Canadell, J. G., McCollum, D., Peters, G., Andrew, R., Krey, V., . . . Yongsung, C. (2016). Biophysical and economic limits to negative CO_2 emissions. *Nature Climate Change*, *6*(1), 42-50. https://doi.org/10.1038/nclimate2870

Young, J., García-Díez, E., Garcia, S., & van der Spek, M. (2021). The impact of binary water–CO_2 isotherm models on the optimal performance of sorbent-based direct air capture processes [10.1039/D1EE01272J]. *Energy & Environmental Science*. https://doi.org/10.1039/D1EE01272J

ESCAPE-34 PSE-2024
European Symposium on Computer Aided Process Engineering
&
Process Systems Engineering

Flavio Manenti, Gintaras V. Reklaitis (Eds.), Book of Abstract of the 34th European Symposium on Computer Aided Process Engineering / 15th International Symposium on Process Systems Engineering (ESCAPE34/PSE24), June 2-6, 2024, Florence, Italy.

Development of a Solver for CFD-DEM Simulations of Suspensions Containing Arbitrarily Shaped Particles

Martin Kotouč Šourek,[a] Ondřej Studeník,[a] Martin Isoz,[b] Petr Kočí,[a,*] Andrew York[c]

[a]*UCT, Prague, Department of Chemical Engineering, Technicka 5, Praha 166 28, Czech Republic*
[b]*Czech Academy of Sciences, Institute of Thermomechanics, Dolejskova 5, Praha 182 00, Czech Republic*
[c]*Johnson Matthey Technology Centre, Blounts Court Road, Sonning Common, Reading RG4 9NH, United Kingdom*
petr.koci@vscht.cz

Abstract

This research focuses on the pivotal role of suspension flow and its rheological properties in diverse scientific and industrial applications, such as blood cell flow, pneumatic transport, fluidized beds, and catalytic material coating on porous substrates. The study aims to develop a numerical approach using computational fluid dynamics and the discrete element method (CFD-DEM) to investigate suspension behavior under different conditions. A hybrid fictitious domain-immersed boundary method is employed to account for the solid phase, with a unique virtual mesh method designed to enhance contact precision while minimizing computational costs. The developed solver is validated through a suspension rheology case study and applied to simulate the washcoating of a catalytic material into a porous substrate. To comprehensively understand particulate suspensions at the microscopic level, the CFD-DEM model is extended to include interactions between individual particles, considering van der Waals forces, electrostatic interactions, and short-range repulsive forces. The resulting extended CFD-DEM model, accommodating arbitrarily shaped particles and intricate microscopic interactions, offers a comprehensive framework for understanding suspension rheological properties.

Keywords: CFD-DEM, HFDIB, suspension rheology, OpenFOAM.

1. Introduction

Particle suspensions play vital roles in real-life and industrial processes, such as sediment transport, blood cell motion, fluidized beds, and catalytic coating of porous substrates. Numerous experimental and numerical efforts have been dedicated to understanding their behavior (Blazek et al., 2021). While the commonly used Eulerian-Eulerian approach is

computationally efficient, it lacks the ability to capture local fluid-solid interactions and relies on empirical parameters. To address this, the computational fluid dynamics (CFD) coupled with the discrete element method (DEM) in a CFD-DEM approach offers a first-principles-based simulation of suspensions (Sourek and Isoz, 2021).

This paper employs an in-house developed solver based on the hybrid fictitious domain-immersed boundary (HFDIB) method and a level-set-like DEM to study suspension flows. Simulations explore rheological properties with variations in solid phase volume fraction and particle shape. The setup is validated through viscosity estimation for spherical particle suspensions, followed by investigations into non-spherical particles, where experimental data by Mueller et al. (2011) is used for comparison. The solver is also applied to simulate suspension flow through a porous medium, illustrating its potential for studying processes like the washcoating process. Finally, we extended the CFD-DEM model to account for electrostatic interactions between individual particles, providing a more comprehensive understanding of suspension behavior at the microscopic level. This extension enhances the model's accuracy by incorporating additional forces such as van der Waals forces and short-range repulsive forces, bridging the gap between macroscopic rheological properties and microscale phenomena.

2. HFDIB method

At each time step (t), the solid phase distribution is introduced into the computational domain using a discrete indicator function λ, defined as follows:

$$\lambda = \begin{cases} 0 \text{ in } \Omega_f \\ 1 \text{ in } \Omega_s \\ (0,1) \text{ in } \Gamma_{sf} \end{cases} \tag{1}$$

Here, Ω_f represents the portion of the computational domain Ω occupied by the fluid, Ω_s is the portion occupied by the solid phase, and Γ_{sf} is the fluid-solid interface. It's essential to note that this projection may not preserve the sharp edges of particles. The governing equations for the considered flow are based on the standard variant of laminar Navier-Stokes equations for an incompressible Newtonian fluid, including an additional forcing term $\boldsymbol{s}$:

$$\begin{aligned} &\frac{\partial \boldsymbol{u}}{\partial t} + \nabla \cdot (\boldsymbol{u} \otimes \boldsymbol{u}) - \nabla \cdot (\nu \nabla \boldsymbol{u}) = -\nabla \tilde{p} + \boldsymbol{g} + \boldsymbol{s} \\ &\nabla \cdot \boldsymbol{u} = \boldsymbol{0} \end{aligned} \tag{2}$$

Here, $\boldsymbol{u}$ is the fluid velocity, ν is the kinematic viscosity, $\tilde{p}$ is the kinematic pressure, $\boldsymbol{g}$ is the gravitational acceleration, and $\boldsymbol{s}$ is the forcing term constructed to generate a fictitious representation of the solid phase in the computational domain. This modeling approach is commonly known as the hybrid fictitious domain-immersed boundary method, building upon the works of Blais et al. (2016) and Municchi et al. (2017).

3. DEM method

The Discrete Element Method (DEM) serves as a finite difference numerical technique for predicting the motion of independently moving objects within the Lagrangian

framework, treating each solid body individually. At any given time t, the position and angular velocity of each body are described by Newton's second law of motion:

$$m_i \frac{\mathrm{d}^2 \boldsymbol{x}_i}{\mathrm{d}t^2} = \sum_{j=1}^{N} f_i^j, \qquad I_i \frac{\mathrm{d}\boldsymbol{\omega}_i}{\mathrm{d}t} = \sum_{j=1}^{N} \boldsymbol{t}_i^j \tag{3}$$

Here, m_i is the mass of body i, $\boldsymbol{x}_i$ is its centroid position at time t, $\boldsymbol{\omega}_i$ is the angular velocity, I_i and is the matrix of inertial moments. The sums on the right-hand sides encompass all the forces f and torques $\boldsymbol{t}$ acting on body i, respectively.

These equations are numerically solved using the finite difference method, assuming constant translational ($\boldsymbol{a}_i$) and angular ($\boldsymbol{\alpha}_i$) accelerations during each time step. Subsequently, $\boldsymbol{a}_i$ and $\boldsymbol{\alpha}_i$ are employed to calculate incremental changes in the position and rotation of body i.

$$\boldsymbol{a}_i = \frac{1}{m_i} \sum_{j=1}^{N} f_i^j, \qquad \boldsymbol{\alpha}_i = I_i^{-1} \sum_{j=1}^{N} \boldsymbol{t}_i^j \tag{4}$$

For a more in-depth understanding of the DEM implementation, readers are directed to Sourek and Isoz (2021). It is crucial to note that our solver accommodates arbitrarily-shaped particles, allowing for the exploration of particle shape effects on the flow. A comprehensive description of the DEM extension for arbitrarily-shaped solids can be found in Studenik et al. (2022).

4. Simulation results

In our study, we concentrated on simulating the measurement of suspension viscosity, utilizing a computational domain designed to emulate rheometric equipment. The domain comprises a three-dimensional box with two parallel solid plates. In the absence of solid particles, the simulation setup mimics laminar Couette flow. Consequently, we defined a linear velocity profile as an initial condition to facilitate the development of the final velocity profile within the domain. The viscosity estimation itself is based on Newton's law of viscosity:

$$\boldsymbol{\tau} = \nu \frac{\mathrm{d}\boldsymbol{u}}{\mathrm{d}z} \tag{5}$$

here, $\boldsymbol{\tau}$ represents shear stress and $\frac{\mathrm{d}\boldsymbol{u}}{\mathrm{d}z}$ is shear rate. The shear stress acting on the moving wall is obtained using the wallShearStress postprocessing function in OpenFOAM. The suspension composed of spherical particles was specifically chosen for validation purposes. The obtained results were rigorously compared not only against available experimental data but also against widely utilized correlations, specifically Batchelor's (1977), and Krieger's and Dougherty's correlations (1959).

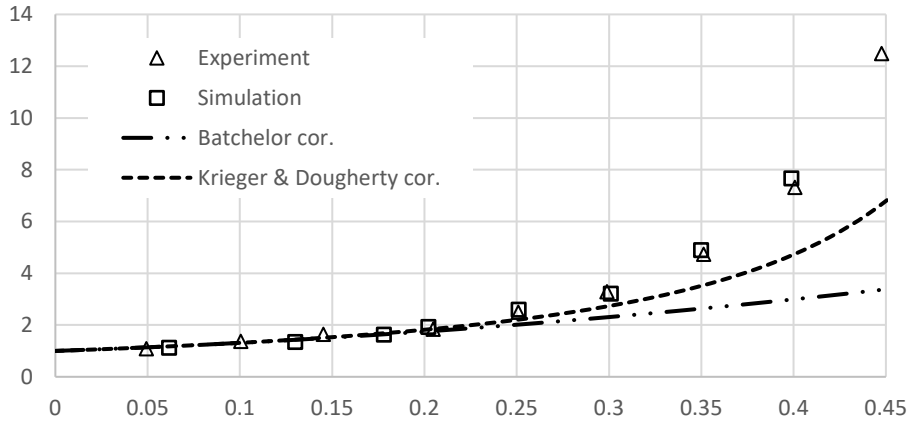

Figure 1: Results of the viscosity study for suspensions made of spherical particles. Trinagles represents experimental data, squares simulation data, dashed line stands for Batchelor´s correlation and dashed-dotted line for correlation by Krieger and Dougherty

In addition to simulating a suspension containing spherical particles, we delved into exploring the influence of particle shape on the apparent viscosity of the suspension. To ensure comparability between our findings and experimental data, we selected particle shapes based on the work of Mueller et al. (2011). This strategic choice allows for a meaningful comparison between the outcomes of our simulations and the corresponding experimental observations.

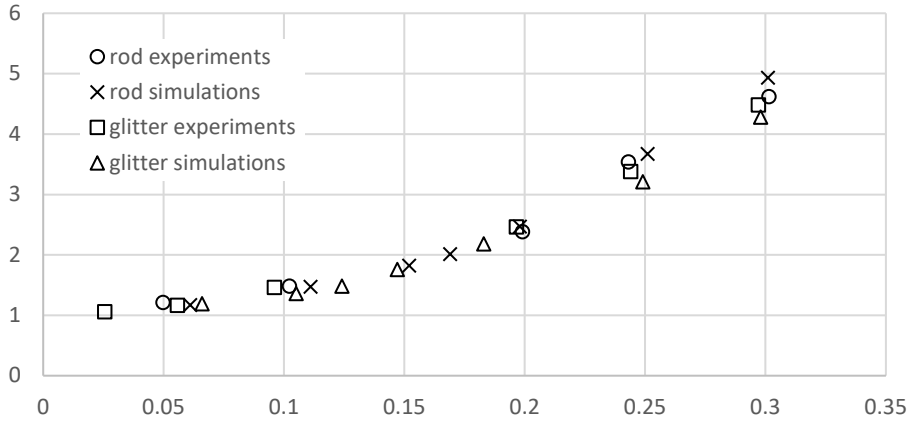

Figure 2: Results for suspensions made of glitter and rod shaped particles. Crosses represents experimental data for rod particles and circles results of the simulations. Triangles stand for experimental data for glitter particles and squares represents results of the corresponding simulations.

The results obtained for suspensions composed of spherical particles exhibit a commendable agreement with both the available experimental data and widely employed correlations. Notably, it is important to highlight that these correlations are typically valid up to a volume fraction of 0.2. However, our simulations extend this scope, showing

consistent agreement with experimental data even at higher volume fractions, specifically up to 0.4. The observed consistency between our numerical estimates and existing data underscores the applicability of our method for conducting numerical investigations on suspensions containing arbitrarily-shaped particles—an area often reliant on experimental approaches.

To demonstrate our solver's real-world applicability, we numerically studied the washcoating process—a crucial step in depositing catalytic material within the porous walls of automotive exhaust gas filters. Following the experimental work by Blazek et al. (2021), we simulated the deposition of catalyst in two different filter sections. Utilizing our CFD-DEM solver, we recreated the washcoating process involving a water-based slurry.

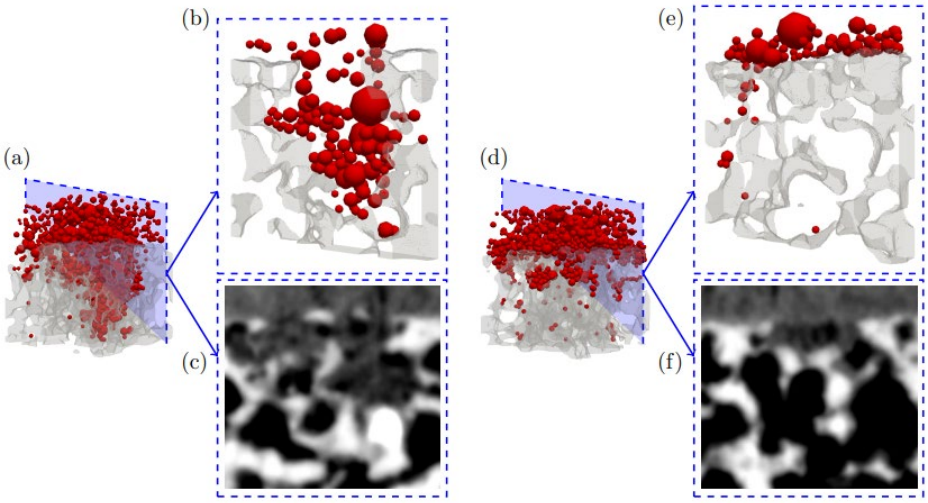

Figure 3: Comparison of the washcoating simulations (a,b,d,e) to the experimental data (c,f) for two different sections of the filter wall: a section with a large pore on (a,b,c) and a closed structure (d,e,f). Color code for the numerical results: grey = wall, red = catalyst. Color code for the experimental data: white = wall, black = void space, grey = catalyst.

The results presented in Fig. 7 offer a qualitative comparison between simulated and experimentally obtained distributions of catalytic particles. Fig. 7a and Fig. 7d provide an overall view of the resulting distributions for structures with a large open pore and a closed structure, respectively. Further insight is gained from a single slice through the structure in Fig. 7b, c and Fig. 7e, f, respectively.

Comparing images (b) and (e) in Fig. 7 highlights the impact of different filter wall morphologies on the final coating distribution. In the section with a large pore, the catalytic material is primarily deposited inside the wall, whereas, in the relatively closed section, the coating is concentrated predominantly on the wall. This observed trend aligns with experimental observations shown in Fig. 7c and Fig. 7f. However, it is noteworthy that a notable difference exists in the spatial arrangement of particles between the simulation and the real sample, with particles in the real sample appearing much more closely packed.

To address this discrepancy, we are incorporating an electrostatic force into our model. This addition aims to simulate the particle interactions more realistically, accounting for the increased proximity observed in the real sample. This enhancement in the model should contribute to more accurate predictions in future washcoating simulations.

5. Conclusions

In conclusion, our study showcases the CFD-DEM solver's versatility in simulating complex particulate suspension behaviors, as demonstrated through successful washcoating process simulations. The qualitative agreement with experiments supports its potential for understanding irregularly-shaped particle systems. Extending simulations beyond typical limits and introducing an electrostatic force enhance the solver's robustness.

Our work establishes a foundation for advancing numerical investigations in suspension dynamics, particularly in applications like the washcoating process. The CFD-DEM solver offers a valuable tool for optimizing particulate processes in diverse industrial and scientific contexts.

Acknowledgement

The work was financially supported by the Czech Science Foundation (22-12227S)

References

G. K. Batchelor, 1977, The effect of brownian motion on the bulk stress in a suspension of spherical particles, Journal of Fluid Mechanics, 83

B. Blais et al., 2016, A semi-implicit immersed boundary method and its application to viscous mixing, Comp. and Chem. Eng, 85

M. Blazek et al., 2021, Washcoating of catalytic particulate filters studied by time-resolved x–ray tomography, Chemical Engineering Journal, 409

I. Krieger and T. Dougherty, 1959, A mechanism for non-newtonian flow in suspensions of rigid spheres, Transactions of the Society of Rheology, 3

S. Mueller et al. 2011, The effect of particle shape on suspension viscosity and implications for magmatic flows, Geophysical Research Letters, 38

F. Municchi and S. Radl, 2017, Consistent closures for Euler-Lagrange models of bi-disperse as particle suspensions derived from particle-resolved direct numerical simulations, Int. J. Heat and Mass Trans., 111

M. Sourek and M. Isoz, 2021, Recent improvements in CFD solver for fully coupled particle-laden flows, Proceedings of the conference Topical Problems of Fluid Mechanics

O. Studenik et al., 2022, Octree-generated virtual mesh for improved contact resolution in CFD-DEM coupling, Proceedings of the conference Topical Problems of Fluid Mechanics

ESCAPE-34 PSE-2024
European Symposium on Computer Aided Process Engineering
&
Process Systems Engineering

Flavio Manenti, Gintaras V. Reklaitis (Eds.), Book of Abstract of the 34th European Symposium on Computer Aided Process Engineering / 15th International Symposium on Process Systems Engineering (ESCAPE34/PSE24), June 2-6, 2024, Florence, Italy.

The Effect Of 3d Printing Process Parameters on Nylon Based Composite Filaments: a Modelling Study

Andras Kaman[a], Miklos Jakab[b], Laszlo Balogh[a], Armand Meszlenyi[a], Attila Egedy[a]

aDepartment of Process Engineering, University of Pannonia, 10 Egyetem str., 8200 Veszprém, Hungary
bDepartment of Materials Engineering, University of Pannonia, 10 Egyetem str., 8200 Veszprém, Hungary
kaman.andras@mk.uni-pannon.hu

Abstract

In recent years, additive manufacturing has become exceedingly popular in industrial applications and scientific studies. The rapid development in this field, especially the slicer and machine software, makes research difficult because these can become obsolete due to software improvements. Another limiting aspect is the lack of knowledge and interest in the 3D printing process and materials; primarily, 3D printing is seen as a tool to achieve some results by researchers. Due to these facts, most studies do not adequately dwell on the 3D printing parameters, making the reproduction of results almost unachievable.

This paper discusses four of the major 3D printing parameters that affect the properties of final products made by chopped carbon fibre filled- and unreinforced nylon filaments; these parameters are the printing temperature, nozzle diameter, layer height, and infill orientation. The family of nylon filaments is mainly used for functional 3D printing, especially in replacing aluminium and steel parts, mainly due to their excellent strength/weight ratio.

The simulation and modelling of tensile tests were carried out in ANSYS Mechanics. Modelling parameters were determined based on the real-life tensile tests carried out beforehand.

Keywords: Additive manufacturing, printing parameters, simulation

1. Introduction

3D printing or additive manufacturing is a rapidly developing field, an increasingly popular topic of scientific studies and research. One of the main reasons for this popularity is the untapped potential it still has due to it being so young compared to other manufacturing techniques, which gives researchers a chance to study the different aspects of additive manufacturing relatively uncontested. However, because it is so new and the

available software and hardware advancements, not to mention the material aspect, are happening in leaps and at a fast pace, it makes the research in this field difficult regarding longevity and repeatability. Another setback is that many researchers are only familiar with 3D printing in a limited capacity.

Material advancements boomed in variety and quality in recent years, such as continuous fibre reinforcement in different thermoplastics that Chen et al. (2021) studied. New high-performance engineering materials appeared and refined; one such material is the family of nylon filaments, especially the chopped carbon fibre-reinforced filaments (Isobe et al., 2018). The nylon filaments became exceedingly popular among 3D printer enthusiasts due to their strength, resistance to substances and UV, printability, high-temperature resistance compared to other available thermoplastic families, and arguably most important of its properties is its low cost. There are two distinct groups that the commercially available nylon filaments fall in, may that be some fibre-reinforced one or unreinforced thermoplastic; these are the nylon 6/66 and the nylon 12 group. Strangely, the nylon 6/66 group is not distinguished between nylon 6 and nylon 66 most of the time; the manufacturers usually state these filaments are nylon or nylon 6/66 since they may be a blend of the two. However, the group of nylon 12 is stated clearly each time by the manufacturer and is usually available for twice the retail price of the other group. Mainly due to its lower price and similar properties, the nylon 6/66 group usage is much more widespread, which is why this thermoplastic group was chosen for the research of this paper.

The simulation of additive manufacturing processes can help to achieve the desired mechanical properties of products, as the process parameters play a crucial role in almost all of them. Saithongkum et al. (2020) made FEM tensile and flexural tests simulations of 3D printed specimens that show one of the most crucial parameters that determine the mechanical properties is the orientation of fibres inside the 3D printed structure. This study's four main parameters are the infill orientation, temperature, nozzle diameter, and layer height. The tensile strength and Young modulus of printed and simulated parts were compared along these four parameters.

2. Materials and methods

When considering the 3D printer that would be adequate for my research purposes, the main requirements were that the printer must be a modular platform for different types of extruders and hotend, and it must also have high-quality mechanical and electrical parts. The ability to run Klipper firmware was crucial as the advanced calibrations it features make the printed parts higher quality with better material deposition. Klipper also makes altering all aspects of the printer and printing process possible. For these reasons, the choice fell on the Rat Rig V-Core 3 400x400, equipped with a Phateus Rapido hotend and orbiter 1.5 extruder for this study. Before printing samples, the following calibrations were carried out: retraction, skew correction, pressure advance, and flow rate. Furthermore, after calibrating the flow rate, a follow-up calibration, including tensile strength tests, was done to ensure that the best possible flow rate is being used while printing samples. ASTM D638 Type I specimen geometry was chosen for the tensile tests as a standard.

For the 3D printing material eSUN ePA-CF with a chopped carbon fiber content of 20 wt% and nylon 6/66 blend as polymer matrix. It is manufactured in Shenzen, China and

is among the most used carbon fibre nylon filaments due to its excellent performance/cost ratio.
For temperature, nozzle diameter, and layer height 4 different values were analysed, while for the infill orientation 2 different values were chosen. These values were the following:
temperature – 240 °C, 260 °C, 280 °C, 300 °C
nozzle diameter – 0.4 mm, 0.6 mm, 0.8 mm, 1.0 mm,
layer height – 25 %, 50 %, 75 %, 100 % (compared to the nozzle diameter used)
infill orientation – 0°, 45°
Furthermore, to reduce the number of specimens needed to be 3D printed an experiment design was carried out.
In order to approximate the values that can be obtained with the adjustment of the studied parameters, a polynomial function was fitted to the measured values in MATLAB.
The simulations of tensile tests were carried out in ANSYS Explicit Dynamics. We specified the material properties; one end of the dog bone-shaped test specimen was fixed in place, while force was applied to the other end.

3. Results

The method of comparing the tensile strength and Young modulus values of simulated and real-life tensile tests was used to evaluate the simulations.
The tensile strength values obtained from MATLAB showed promising similarity except for the four outliers (Figure 1), which showed a significant strength increase compared to their simulated counterparts.

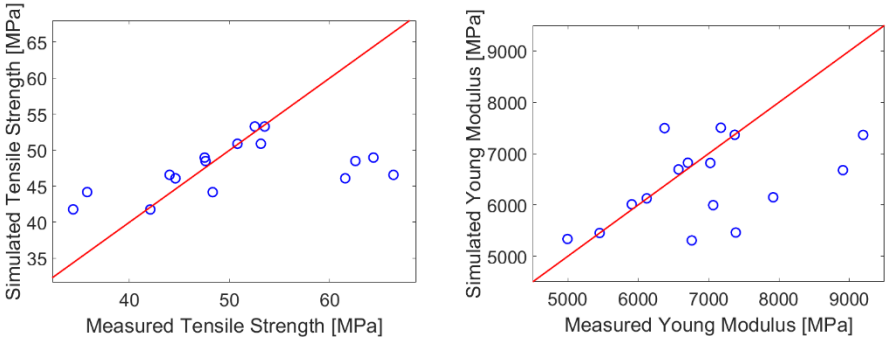

Figure 1: the correlation between the simulated and measured tensile strength/Young modulus values

The same four outliers are also present in the case of Young modulus values (Figure 1); excluding those values, the others show that the values obtained from MATLAB align with measured values. The most influental parameters on strength were the infill orientation ,unsurprisingly considering the nature of the fiber reinforced materials, and the temperature, which can be varied in quite the range as the used material can be printed between 220 – 320 °C with very different results. With the variation of these two parameters the tensile strength values were within a 9-11 MPa range. The nozzle diameter and layer height had a very similar effect on the mechanical properties, with their variance the tensile strength values were between a 5 MPa range. Their effects differed for the Young modulus values, as the most impactful two parameters were the temperature and nozzle diameter, for with their variance the Young modulus values were within a range of 1000-1200 MPa. The layer height had a moderate effect on the Young modulus, with

its variance the values were between a 300 MPa range. Lastly, the infill orientation strangely had no effect on the Young modulus values obtained.

Also, the simulations carried out showed remarkable similarity to the real-life test results, as their stress-strain diagrams showed very similar strength and elongation; however, their dynamic was different. The simulated specimens showed a much more linear stress-strain behaviour, while the real-life specimens only showed linear behaviour at the beginning of the testing until it reached approximately 2/3 of its final tensile strength, where it changed to a logarithmic behaviour until it snapped. In one such comparison the simulated specimen reached 2000 N force with enlongation of 3.9 mm, while the real-life specimen reached a force of 2050 N with 3.8 mm elongation. A maximal principal stress map of a simulated specimen can be seen in Figure 2.

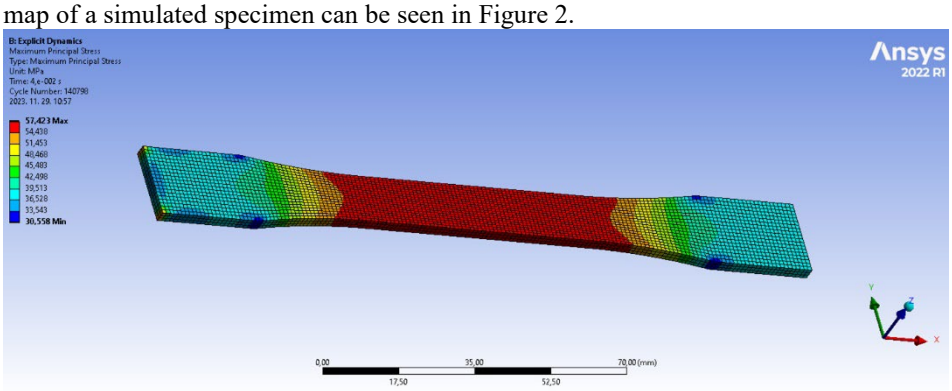

Figure 2.: maximal principal stress map of simulated specimen in ANSYS Explicit Dynamics

4. Conclusions

As the results show, with enough tensile tests, 3D printed parts mechanical properties can be simulated for the examined carbon fibre-reinforced nylon filaments. To manufacture parts with the desired mechanical, be it the highest strength part with little give in terms of elongation or moderate strength but with an elastic failure in order to avoid a catastrophic failure type, these simulations offer a way to credibly predict the properties of an end product without actually printing it first. To achieve this aim, further simulations and real-life tests will be carried out and a boarder range of parameters and material groups will also be studied to further enhance the accuracy of these simulations.

References

1. Chen, Wei & Zhang, Qiuju & Cao, Han & Yuan, Ye. (2021). *Process evaluation, tensile properties, mathematical models, and fracture behavior of 3D printed continuous fiber reinforced thermoplastic composites*, Journal of Reinforced Plastics and Composites. 40.
2. Isobe T., *et al.* (2018). *Comparison of strength of 3D printing objects*
3. *using short fiber and continuous long fiber*, IOP Conf. Ser.: Mater. Sci. Eng. 406 012042
4. Saithongkum, Nathathai & Tuchinda, Karuna. (2020). *Mechanical Properties of 3D Printed Carbon Fiber Composite*, Solid State Phenomena. 304. 15-23.

ESCAPE-34 PSE-2024
European Symposium on Computer Aided Process Engineering
&
Process Systems Engineering

Flavio Manenti, Gintaras V. Reklaitis (Eds.), Book of Abstract of the 34th European Symposium on Computer Aided Process Engineering / 15th International Symposium on Process Systems Engineering (ESCAPE34/PSE24), June 2-6, 2024, Florence, Italy.

Prediction of Life Cycle Inventories for Industrial Waste Treatment Processes from Historical Data using Machine Learning and Physical Models

Sabine Hallamasek,[a] Doğancan Karan,[b] Frank Roschangar,[c] Fabian Stiefel,[d] Judith Fellner,[e] Natalie Egreteau,[e] Moritz Mayer,[e] Hubert Weiser[e] and Alexei Lapkin[a,b*]

[a]*Department of Chemical Engineering and Biotechnology, University of Cambridge, Philippa Fawcett Drive, Cambridge CB3 0AS, UK.*
[b]*Cambridge Centre for Advanced Research and Education in Singapore, CARES Ltd. 1 CREATE Way, CREATE Tower #05-05, 138602 Singapore.*
[c]*Development Sciences, Boehringer Ingelheim Pharmaceuticals, Inc., 900 Ridgebury Road, Ridgefield, Connecticut 06877, USA.*
[d]*Development Sciences, Boehringer Ingelheim Pharma GmbH & Co. KG, Birkendorfer Straße 65, 88397 Biberach, Germany.*
[e]*Boehringer Ingelheim RCV GmbH & Co KG, Doktor-Boehringer-Gasse 5-11, A-1121 Vienna, Austria.*
aal35@cam.ac.uk

Abstract

The treatment of waste effluents from industrial activity is a mandatory task to protect the ecosphere from pollutants. However, the operation of waste treatment systems itself causes environmental impacts, which must be accounted for in life cycle assessment (LCA) studies of industrial processes. The magnitude of the environmental impacts caused by a particular waste treatment process is dictated by the characteristics (composition, physical properties) of the treated waste, since these affect the quantity of consumed process auxiliaries. In this work we leveraged machine learning algorithms and historical process data of industrial waste treatment systems to identify relationships between waste characteristics and process performance. The obtained correlations are shown to enable the calculation of waste-specific impacts of a given treatment system.

Keywords: predictive LCI, machine learning, data-driven regression, waste treatment, green chemistry.

1. Introduction

Every year, enormous amounts of waste are generated by industrial activities, with the chemical industries acting as one of the key players. In 2020, the European Union reported the production of 55 million tons of waste for this sector alone (Eurostat, 2023).

Since the generated waste streams are often heavily contaminated with organic and inorganic process residues, it is imperative that effluents are treated appropriately. Thereby resources can be reused within the technosphere or returned safely to the ecosphere. However, while the treatment of hazardous wastes serves to mitigate the industry's environmental footprint, it must be recognized that waste treatment processes themselves consume resources and release emissions, generating an inherent environmental impact which is attributable to the production process that generated the waste.

The impact incurred by the treatment of a specific waste is dependent on the waste category, which determines the type of required treatment processes, as well as on the exact waste composition, since attributes such as pollutant concentration determine the operational response of a given treatment system in terms of consumed auxiliaries and utilities. Consequently, LCAs of industrial waste treatment systems should consider waste-specific life cycle inventories (LCIs) to obtain reliable impact estimations. However, waste-specific process data for waste treatment systems is not easily obtainable, particularly during early-stage process design, and the availability of waste-specific LCI estimation tools is rather low (Köhler et al., 2007; Seyler et al., 2005; Struijs, 2014). In the absence of waste-specific data, waste treatment LCIs are often estimated using generic datasets from commercial databases (Moreno Ruiz et al., 2022), calculated through time-consuming process modelling, or omitted from the study scope, all of which can introduce significant skew into LCA results. In this work we aimed to close this knowledge gap by developing waste-specific predictive LCI tools for a given waste treatment process from historical process datasets through the application of machine learning techniques.

2. Methods

A data-driven approach was employed to quantify the relationships between waste characteristics and the responses of the investigated waste treatment system. The data was sourced from industry logs of real-time in/on-line monitoring and control measurements, which provide a transparent account of system operation over extended time periods. Logged characteristics of the waste feed (quantity, physical properties) were identified as system inputs, while records of the system's resource and utility consumptions were classified as system outputs. Correlating the system outputs to the variation in waste characteristics was treated as a machine learning regression problem, with the system inputs serving as numerical features.

The presented method builds on the approach taken by Seyler et al. (2005) and Köhler et al. (2007) for the development of waste-specific LCI prediction tools, who conceptualised that every consumption of a waste treatment process can be attributed to one or more specific waste characteristics. However, while previous tools relied on averaged annual production data and required fundamental hypotheses on input-output relationships, this work benefits from access to more granular datasets and the leveraging of machine learning to more accurately model the true impact of multiple waste features on the system's outputs.

The hypothesis was conceptualised on the case study of an industrial wastewater neutralisation system employed by Boehringer Ingelheim. For this purpose, process data logged by the system's control instruments were extracted for the years 2021 and 2022 at 30 second intervals. Data curation and analysis, as well as model screening, training and tuning was implemented in Python.

The available dataset was supplemented with artificial data generated by a physical model emulator to explore its benefits in situations of data scarcity.

3. Case study results

The investigated waste treatment system consisted of unit processes for mixing, pH neutralization and cooling. Accordingly, the waste characteristics that determine the system's operational response were established as waste pH, temperature, and volume. As such, measured values of these quantities were curated to make up the feature space of the regression problem. Equally, the process consumptions that constitute the gate-to-gate LCI for the investigated process were identified as the consumption of neutralizing agents (HCl and NaOH), cooling power (in the form of cooling water and chilling power) and electricity, all of which were regarded as the outputs of the desired machine learning models. Data curation was found to be a crucial stage of the project, revealing limitations and challenges of working with real industrial data.

To determine the relationships between the waste characteristics and process consumptions, the importance of each feature on the magnitude of each consumption was identified via multi-feature single-output regression models on the industrial process data. The obtained fits were used to generate waste-specific LCIs for a range of scenarios ranging from extremely acidic to extremely basic pH, and considering various temperatures and process volumes. For comparison, a non-specific "baseline" LCI dataset was calculated as the process consumptions per m^3 of wastewater treated across the entire measurement period of two years. Benchmarking the waste-specific LCIs against the non-specific baseline inventory, significant differences in predicted process consumptions were observed. This was especially apparent in LCIs generated for wastes of different pH values, where the multi-feature regression models could differentiate waste-specific acid and base consumptions, and thus allocate different environmental impacts for different wastes processed by the system, while also capturing non-intuitive consumptions such as compensation for overshoots in neutralization, which was not captured to the same granularity in the baseline LCI.

4. Conclusions

The symbiotic use of large historical datasets, statistical and physical models yielded a predictive tool that supports the LCA practitioner in the rapid assessment of waste-related emissions. Specifically, the models were able to generate waste-specific LCIs that allow to differentiate between the impacts caused by wastes of different compositions and physical properties. Understanding the influence of waste characteristics on the environmental process impacts is crucial to enable accurate and fair allocation of waste-related process impacts to the waste-generating production processes.

References

Eurostat, 2023. Generation of waste by waste category, hazardousness and NACE Rev. 2 activity. URL https://ec.europa.eu/eurostat/databrowser/view/ENV_WASGEN__custom_2246895/default/table?lang=en (accessed 11.30.23).

Köhler, A., Hellweg, S., Recan, E., Hungerbühler, K., 2007. Input-dependent life-cycle inventory model of industrial wastewater-treatment processes in the chemical sector. Environ. Sci. Technol. 41, 5515–5522. https://doi.org/10.1021/es0617284

Moreno Ruiz, E., FitzGerald, D., Bourgault, G., Vadenbo, C., Ioannidou, D., Symeonidis, A., Sonderegger, T., Müller, J., Dellenbach, D., Valsasina, L., Minas, N., Baumann, D., 2022. Documentation of changes implemented in the ecoinvent database v3.9. Zürich, Switzerland.

Seyler, C., Hofstetter, T.B., Hungerbühler, K., 2005. Life cycle inventory for thermal treatment of waste solvent from chemical industry: A multi-input allocation model. J. Clean. Prod. 13, 1211–1224. https://doi.org/10.1016/j.jclepro.2005.05.009

Struijs, J., 2014. SimpleTreat 4.0 : a model to predict fate and emission of chemicals in wastewater treatment plants. RIVM Rep. 601353005.

ESCAPE-34 PSE-2024
European Symposium on Computer Aided Process Engineering
&
Process Systems Engineering

Flavio Manenti, Gintaras V. Reklaitis (Eds.), Book of Abstract of the 34th European Symposium on Computer Aided Process Engineering / 15th International Symposium on Process Systems Engineering (ESCAPE34/PSE24), June 2-6, 2024, Florence, Italy.

Transparent Design Platform for Flexible Integration and Operation of Waste-to-X Systems

Julie Dutoit[*,a,b], Jaroslav Hemrle[b], Manuela Goulart Maia[b], François Maréchal[a]
[a] *École Polytechnique Fédérale de Lausanne, Industrial Process Energy Systems Engineering (IPESE), Sion, 1951, Switzerland*
[b] *Hitachi Zosen Inova AG, Zürich, 8005, Switzerland*
julie.dutoit@hz-inova.com

Abstract

The design and operation of the next generation of waste management and energy supply systems should ensure the industrial Global Warming Potential (GWP) reduction targets agreed internationally and enable transition towards a circular economy of materials. To that end, quantitatively rigorous assessment of industrial decarbonization and value recovery pathways is critical, while many challenges stem from the range and complexity of involved technologies and engineering domains, variety of possibly conflicting performance criteria, and interaction potential within the system as well as with external interfaces, in the context of uncertain energy supply markets. In this contribution, a versatile simulation and decision support platform is developed for the design and scheduling of municipal solid waste (MSW) treatment technologies from an industrial point of view, including short to long-term energy storage capacity and renewable energy production to offer flexibility in the integration of such systems. The methods aim at simultaneous financial, environmental, and thermodynamic simulation and optimization of modularly complex system models, evaluating unsteady operations and uncertain, time-variant input data. The inferred transparency is reinforced by joining all functionalities into a unique workflow, improving technology development consistency and reliability. This work presents the modeling structure and platform features, demonstrated for the design and system integration of a specific multi-energy case of oxy-enhanced MSW incineration plant.

Keywords: Waste-to-X, Co-optimization, Decision Support Platform, OpenModelica

1. Introduction

Although waste treatment systems have been extensively studied (Niziolek et al., (2017), Puchongkawarin et al., (2020)), a large range of alternative integration strategies, recovery products, and performance criteria specifically for environmental indicators remains to be studied, including uncertainties assessment. Particularly when including intermittent renewable energy production as energy utilities and power grid integration potential, dynamic control and flexible operation of Waste-to-X systems become essential (Abdelghany et al., (2021)). Consequently, industrial waste treatment projects require robust computational tools covering both short-term variability and long-term aspects

(cycling effects, seasonal storage, etc.) to support investment planification via validated digital twins.
This work proposes a flexible and transparent framework for simultaneous process integration and optimal control, detailed financial analysis, and Life-Cycle Impact Assessment (LCIA). A typical system flowsheeting interface is displayed in Figure 1 for the analysis of a specific Waste-to-X system, including oxy-enhanced MSW combustion with flue gas recirculation, flue gas treatment technologies, post-combustion carbon capture, alkaline water electrolysis (AEL), catalytic CO_2 methanation and a selection of heat, cold and power utilities.

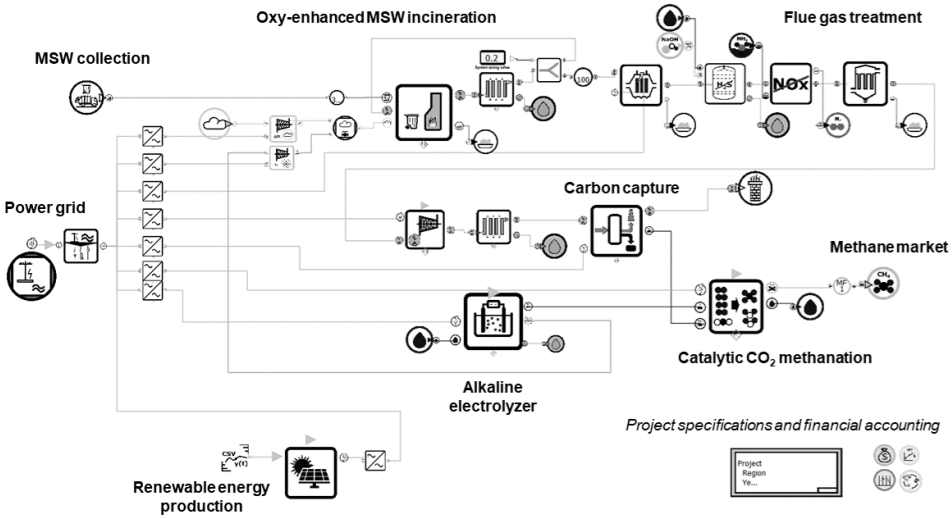

Figure 1: MSW incineration system integrated with carbon capture, alkaline electrolysis, and catalytic CO_2 methanation.

2. Methods

Technology modeling is done primarily in the open-source software OpenModelica (OM) (Fritzson et al., (2020)), implemented in the object-oriented modeling language Modelica for equation-based modeling. A new library of stream definitions and technology models is developed following a set of defined conventions for variable naming, model versioning and documentation (scope, level of abstraction, following Eddy et al., (2012)), and database links. Systematic modeling structures include class attributes of streams, control and energy (heat, exergy) flow structures, as well as consistent accounting and inventory of cash-flows and life-cycle flows. Since the simulation platform is focused on processes and recovery of resources in waste treatment systems, all involved stream definitions include physical state and detailed chemical composition. This respectively enables the understanding of energy flows and contaminants propagation through the system, which is critically important for design of cleaning and feedstock pre-processing stages shown in Figure 1, as well as for evaluation of economic (e.g. quality of products) and environmental impact of the resulting system.
OpenModelica technology models are wrapped in a Python-written environment, forming an interface for input data selection, model compilation and simulation, and selected

results retrieval. Figure 2 leads through these assessment stages, constituting the platform workflow. A single record sheet is used throughout for full traceability of input data, model assumptions and meta-data, including analysis results storage. Workflow functionalities include LCIA, for which the methods follow the ISO14040 norms and use external life-cycle inventory databases for cradle-to-gate activities and End-of-Life assessments.

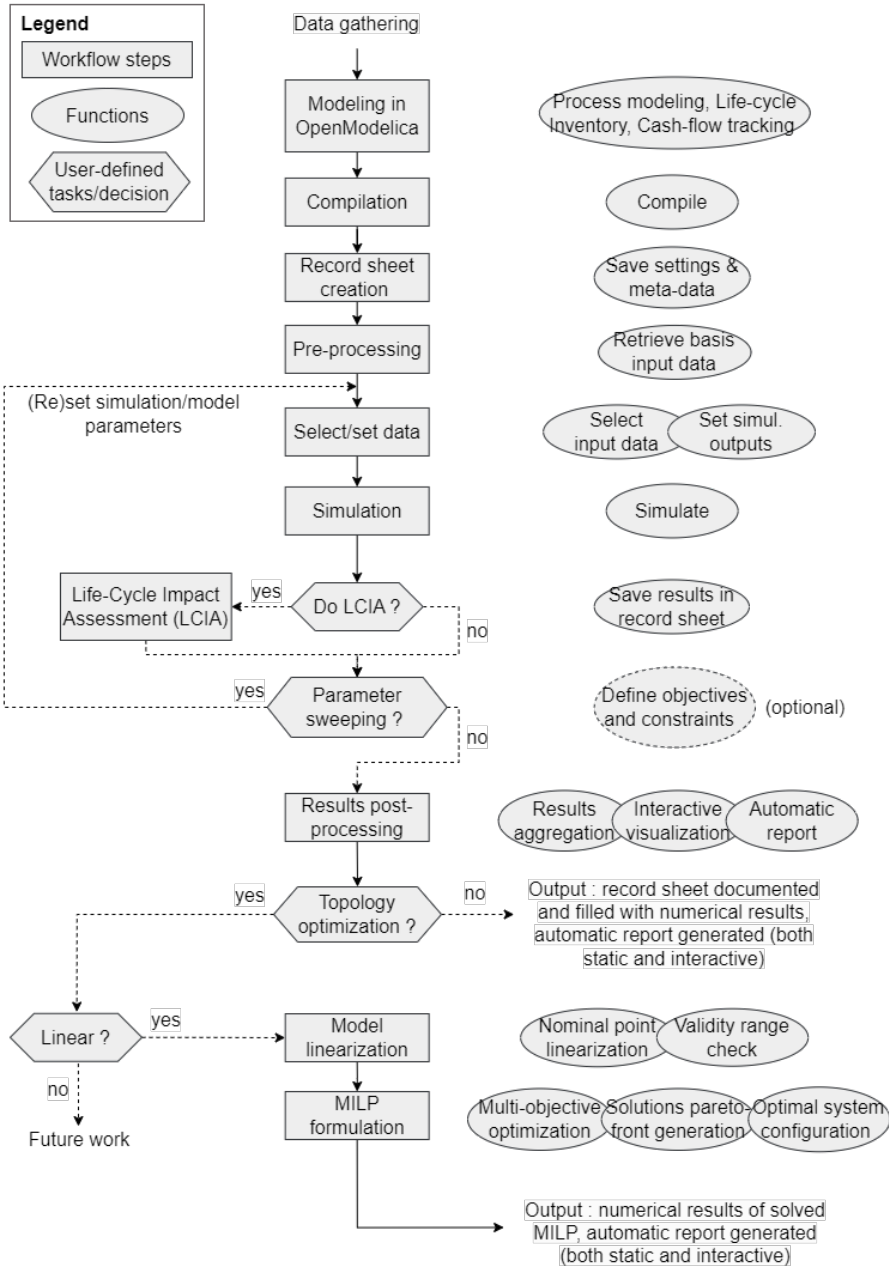

Figure 2: Simulation and optimization workflow functionalities of the computational platform.

The workflow includes 2 functionalities for optimization of the analyzed system based on any combination of thermodynamic/process, economic or environmental indicators (included in Figure 2):

- The model/system parameter sweep modifies simulation input data to evaluate a set of different process conditions or design. Optionally, objectives or constraints on the process characteristics or performance indicators may be formulated, to optimize the system in a derivative-free approach with a genetic, evolutive algorithm (currently implemented with NSGA-II).
- The system topology optimization takes as input a set of technology models from the platform library. Each model in the set is linearized around selected nominal operating point(s), thereby verifying the validity range of the linearization, and generating a new library of black-box technology models. The Mixed-Integer Linear Program (MILP) formulation described by Kantor et al., (2020) is applied to generate Pareto-optimal system configuration solutions through multi-objective optimization.

Computational runtime bottlenecks of the platform are identified and tackled through efficient data handling and software interfacing, avoided model re-compilation, solver outputs selection, and other measures.

3. Illustrative case: extract of typical results

This section illustrates several steps and types of analyses enabled by the workflow. As an example of unit model implementation in the platform, process modeling and validation is demonstrated for the alkaline electrolysis stack model, sub-system of the example case of Figure 1. An electrochemical model of the alkaline electrolyzer stack is built in OM based on the work of Sakas et al., (2022). The parameter sweep optimization workflow is applied to tune model parameters of a proportional-integral (PI) controller of the electrolysis feed lye mass flow, fitting the stack measured temperature reported in literature data. After validation of the AEL stack model with literature data, the input parameters are modified to correspond to the characteristics of an existing demonstration plant stack. The measured stack temperature is compared to the fitted model simulated results in Figure 3, varying in time between hot standby mode and nominal operation temperature as a result of flexible operation.

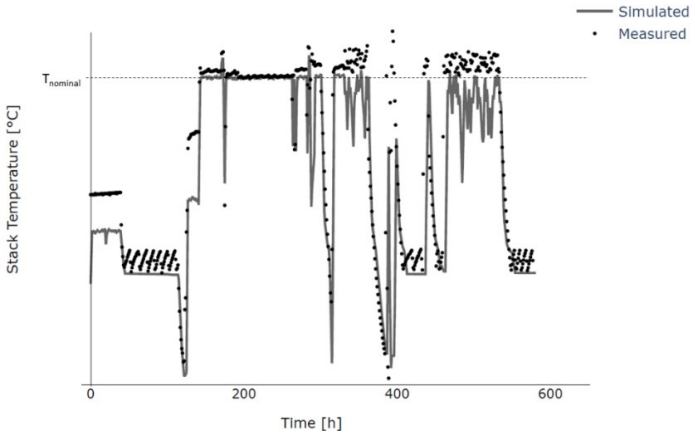

Figure 3: Measured (on an existing demonstration facility) and simulated AEL stack temperature.

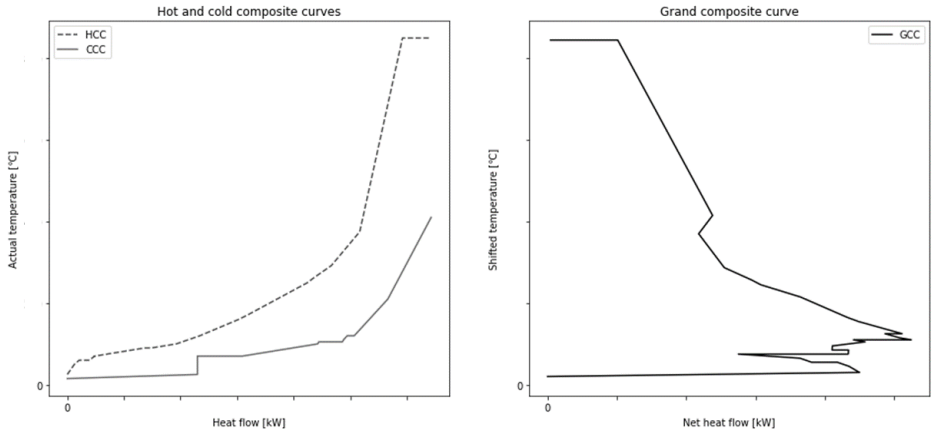

Figure 4: Composite curves for the Waste-to-X system of Figure 1 at nominal operation, equipped with an air-cooling tower. Axis values are kept confidential.

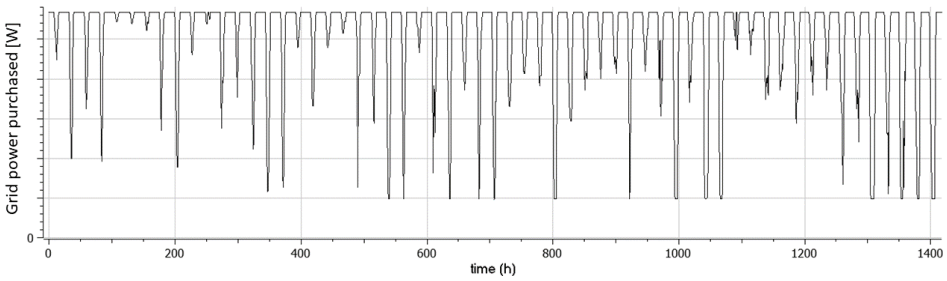

Figure 5: Typical power exchange profile at the power grid connection for 2 months of winter operation.

Systemic analysis of cases such as in Figure 1 includes typically optimal resources integration for the technology system, as well as with external interfaces. As part of the heat and power utilities integration, the results presented here include District Heating Network (DHN) and Water Steam Cycle (WSC). Figure 4 displays the pinch analysis results for heat recovery assessment, with hot and cold composite curves for the entire system of the Figure 1 at nominal operation. It is a snapshot of the heat flows at a given time of the year and does not represent an optimized design. The Minimum Energy Requirement (MER) of the plant in this configuration is composed of cooling requirements only, for which an air-cooling tower is correspondingly sized. The system interaction with the power grid is illustrated with the power exchange at the connection node in Figure 5.

4. Conclusions and perspectives

At current development stage, the described platform has been applied on practical industrial cases, with the benefit of a unique environment covering all aspects of system design and operational strategy optimization in a consistent workflow. Transparency is harnessed in the different analysis stages by systematic modeling practices and structures, documentation and validation, and holistic approaches providing decision-makers with comprehensive performance indicators.

Flexibility of assessment is provided both through the large portfolio of technologies modeled and integration possibilities, and the workflows developed around the simulations to optimize the complex and interlinked systems.
For the specific case study analyzed, further work is needed to modify setpoints on the controllers, but overall accuracy of the simulated results is promising. On the system integration, the potential for improved seasonal integration of heat and power needs to be further investigated to optimize year-round performance for longer term planification of the industrial infrastructure. Forecast capabilities on a range of input (power supply, price and time-dependent emission factor, heat demand, waste composition) may be harnessed to improve the system performance, implementing predictive control in the system operations, and evaluating robustness against deviations. To evaluate a larger technology integration potential via the topology optimization, the model set of Waste-to-X technologies will grow to include more synthetic fuels generation processes, storage units, and other more novel technologies. The MILP formulation will be adapted to include typical days chronology (Blanke et al., (2022)) for more accurate resolution, and a strong focus will be put on the development of algorithms handling the operational strategy within the topology optimization problem, including input parameter uncertainties and model complexity (including surrogation strategies).

References

Abdelghany, M. B., Shehzad, M. F., Liuzza, D., Mariani, V., & Glielmo, L., 2021. Optimal operations for hydrogen-based energy storage systems in wind farms via model predictive control. International Journal of Hydrogen Energy, 46(57), 29297–29313.

Blanke, T., Schmidt, K. S., Göttsche, J., Döring, B., Frisch, J., & van Treeck, C., 2022. Time series aggregation for energy system design: Review and extension of modelling seasonal storages. Energy Informatics, 5(1), 17.

Eddy, D. M., Hollingworth, W., Caro, J. J., Tsevat, J., McDonald, K. M., & Wong, J. B., 2012. Model Transparency and Validation: A Report of the ISPOR-SMDM Modeling Good Research Practices Task Force-7. Value in Health, 15(6), 843–850.

Fritzson, P., Pop, A., Abdelhak, K., Ashgar, A., Bachmann, B., Braun, W., Bouskela, D., Braun, R., Buffoni, L., Casella, F., Castro, R., Franke, R., Fritzson, D., Gebremedhin, M., Heuermann, A., Lie, B., Mengist, A., Mikelsons, L., Moudgalya, K., . . . Östlund, P., 2020. The OpenModelica Integrated Environment for Modeling, Simulation, and Model-Based Development. Modeling, Identification and Control: A Norwegian Research Bulletin, 41(4), 241–295.

ISO, 2006. ISO 14040:2006: Environmental management — Life cycle assessment — Principles and framework. Retrieved August 23, 2023.

Kantor, I., Robineau, J.-L., Bütün, H., & Maréchal, F., 2020. A Mixed-Integer Linear Programming Formulation for Optimizing Multi-Scale Material and Energy Integration. Frontiers in Energy Research, 8. Retrieved December 20, 2022.

Niziolek, A. M., Onel, O., & Floudas, C. A., 2017. Municipal solid waste to liquid transportation fuels, olefins, and aromatics: Process synthesis and deterministic global optimization. Computers & Chemical Engineering, 102, 169–187.

Puchongkawarin, C., & Mattaraj, S., 2020. Development of a superstructure optimization framework for the design of municipal solid waste facilities. Sustainable Environment Research, 30(1), 27.

Sakas, G., Ibáñez-Rioja, A., Ruuskanen, V., Kosonen, A., Ahola, J., & Bergmann, O., 2022. Dynamic energy and mass balance model for an industrial alkaline water electrolyzer plant process. International Journal of Hydrogen Energy, 47(7), 4328–4345.

ESCAPE-34 PSE-2024
European Symposium on Computer Aided Process Engineering
&
Process Systems Engineering

Flavio Manenti, Gintaras V. Reklaitis (Eds.), Book of Abstract of the 34th European Symposium on Computer Aided Process Engineering / 15th International Symposium on Process Systems Engineering (ESCAPE34/PSE24), June 2-6, 2024, Florence, Italy.

Enhancing Systems Models of Pharmaceutical Tablet Manufacturing Using Life Cycle Assessment Approaches

Flora Bouchier[a], Astrid Boje[b], Gavin Reynolds[a]

[a]*Oral Product Development, Pharmaceutical Technology & Development, Operations, AstraZeneca, UK*
[b]*Digital Science, Sustainable Innovation & Transformational Excellence, Pharmaceutical Technology & Development, Operations, AstraZeneca, Sweden*
flora.bouchier@astrazeneca.com

Abstract

Pharmaceutical drug products in the form of tablets are produced via a series of manufacturing steps, transforming powder blends to compacted granules with carefully selected properties such as tensile strength and dissolution time. Typical manufacturing routes include roller compaction and continuous direct compression (CDC). Design of each process step is required to achieve end-product quality for the specific material properties and available equipment, although design decisions are typically made without a quantitative understanding of the impact on product environmental footprint. Using a 'cradle to gate' life cycle assessment (LCA) methodology, a quantitative sustainability comparison has been made between standard oral solid dosage (OSD) form manufacturing platforms. Data from these models has been combined with systems models of the manufacturing processes. These combined models are used to demonstrate the optimisation of processes to meet robust product quality attribute targets whilst identify opportunities to minimise the impact of global warming potential.

Keywords: Pharmaceutical Processing, Tablets, Life Cycle Assessment, Systems Modelling

1. Introduction

Pharmaceutical drug products in the form of tablets are produced via a series of manufacturing steps, transforming powder blends to compacted granules with carefully selected properties such as tensile strength and dissolution time. Typical manufacturing routes include roller compaction and continuous direct compression (CDC). Design of each process step is required to achieve end-product quality for the specific material properties and available equipment. Increasingly, experimental development is complemented by predictive simulations with the aim to support robust process design and optimization with minimal API-, energy- and labour-intensive physical trials. Connected, calibrated mechanistic process models (so-called process digital twins) for multiple manufacturing stages provide an effective system description, enabling

prediction of end-product critical quality attributes as a function of material properties and process settings. As this approach to design becomes more established, the scope of systems modelling can be widened to provide a more wholistic assessment of the end-to-end manufacturing process.

Life cycle assessment (LCA) evaluates the environmental impacts a product has over its lifetime, producing a quantitative measure which can be used to drive sustainable development (Hadinoto, Tran et al. 2022). Using a 'cradle-to-gate' LCA methodology, a quantitative sustainability comparison has been made between standard oral solid dosage (OSD) form manufacturing platforms, roller compaction, direct compression, high shear granulation and CDC.

With the growing focus on sustainability, it is attractive to use systems models as a tool to understand and reduce the environmental cost of pharmaceutical manufacture. As a proof of concept, the LCA methodology and models were incorporated into systems models of tablet manufacturing processes, with a specific example of continuous direct compression presented here. These combined models were used to demonstrate the optimisation of processes to meet robust product quality attribute targets whilst identifying opportunities to minimise the impact of global warming potential.

2. Materials and Methods

2.1. LCA Methodology

A 'cradle-to-gate' approach was used to define the system boundary for the LCA, with the functional unit consisting of the production of 1 kg coated tablets. The scope of the LCA is demonstrated in Figure 1. Life cycle inventory data was sourced from the Ecoinvent database where possible for excipients, auxiliary materials and electricity (Wernet, Bauer et al. 2016). For excipients not available within the ecoinvent database, a similar material with LCI data was used as a 'surrogate'. API contribution was modelled using a value of 1500 $kgCO_2eq/kg$, based on medium emission API data obtained from the Association of the British Pharmaceutical Industry Blister Pack Carbon Evaluation Tool (ABPI and CarbonTrust). Models for each manufacturing platform were analysed using SimaPro 9.4 LCA software (Pré Sustainability B.V.), along with the The ReCiPe 2016 Midpoint (H) V1.05 / World (2010) H calculation method, to calculate the global warming potential (GWP) as the key impact category for this assessment. A generic coated tablet formulation was used for all platforms to measure the influence of process yields alongside non-material sources of GWP. Typical process yields were incorporated into each unit operation, with the impact of yield loss material disposal assessed through a hazardous waste incineration step, sourced the EcoInvent database, modified to account for molecular carbon release being calculated separately, assuming complete combustion.

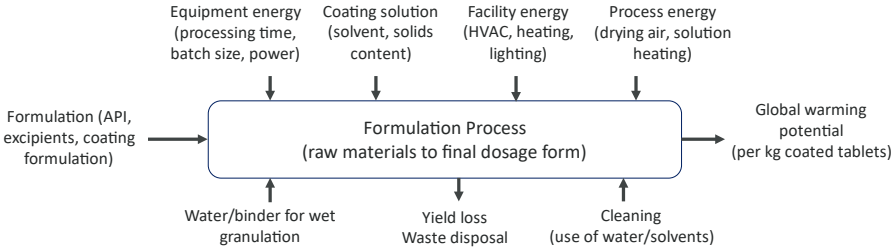

Figure 1 Outline of LCA scope

Energy consumption was assessed both on a unit operation basis, considering unit operation energy requirements, in addition to a facility basis, considering the energy requirement of heating, lighting and air handling within the production facility. Unit operation energy use was calculated using three key methods. The first method relates to equipment where the motor component is the main contribution to power consumption, for example in screw feeders. Assuming that the maximum equipment power is reached at the maximum motor speed, a linear correlation is used to estimate equipment power at given operating parameters. For equipment typically operated at fixed speeds and for a set duration where the major power contributor is torque, such as blenders, a similar method was applied, although maximum power is correlated with maximum load. Finally, for equipment with a heating or drying element, such as coaters, it is assumed that primary energy contribution is required to heat the incoming air. Power use is therefore calculated based on an enthalpy balance of the air, and the subsequent electricity requirement assuming a heater with 100 % efficiency. Facility energy contribution was modelled using a 'building energy intensity' value, calculated using annual electricity meter and building footprint data from a representative OSD manufacturing facility. Space requirements for each unit operation were estimated based on an assumed constant 'dirty room' area, plus a 'clean room' area scaled for relative equipment size and complexity. Facility energy contribution calculated using the building energy intensity and room size, multiplied by processing or cleaning durations, to account for overheads during both stages. Cleaning contribution was built into the models using LCA data from a commercial coater, with solvent use and carbon emissions scaled for other equipment according to relative size and complexity.

2.2. Systems Modelling

Pharmaceutical process design and optimization is increasingly guided by digital activities such as systems modelling. System models are created by the connection of process models for multiple unit operations, connected as in the physical system. This enables simulation of the relationship between material properties and process settings across different process stages, and end-product qualities. Inclusion of LCA models in system models is a natural extension, allowing a more holistic assessment that includes the impact of material and process choices on the sustainability of the overall process.

Here, we demonstrate this approach for the example of a continuous direct compression (CDC) system model for manufacture of 100 mg tablets (Table 1). A number of such CDC system models have been described in the recent literature, for example by García-Muñoz et al. (García-Muñoz, Butterbaugh et al. 2018), Tian et al. (Tian, Koolivand et al. 2021), and Moreno-Benito (Moreno-Benito, Lee et al. 2022). For the purpose of demonstration, the system model was developed in gPROMS Formulated Products (v2023.1.0, Siemens), using the standard model libraries without customization.

Table 1: Tablet composition and LCA contributions

Component	**Mass fraction**	**CO2e per kg**
API	0.200	1500
MCC	0.504	71.69
Lactose	0.231	0.96
Crospovidone	0.050	6.71
Magnesium Stearate	0.015	0.48

The CDC system model (Figure 2) comprises individual material feeders for each component, with API, fillers and disintegrant fed into blender 1, and the ensuing powder

blend combined with lubricant in blender 2. The feeders were modelled as continuously stirred tank reactors with gravimetric screw control and a fixed feed factor of 2 g/rev. Feed factor variability was introduced in the API feeder to assess its impact on the sustainability calculations, whilst variability was neglected for the other feeders. The two horizontal blenders were modelled using the axial dispersion model, with mean residence time calculated based on the total throughput and residence mass. Tablet compression in the tablet press was modelled using the Reynolds (2017) (Reynolds, Campbell et al. 2017) model to calculate tablet porosity and tensile strength, based on generic compressibility properties for the blend. The API content of the tablets was monitored, and the time spent out of specification was recorded to determine the quantity of acceptable material produced during operation. The operating window was defined by excluding the first three residence times to approximate onset of steady state operation and calculating the end time needed to achieve a fixed mass of material. LCA calculations were performed for the material (emissions per kilogram) and the process (emissions due to feeder, blender, and tablet press operation).

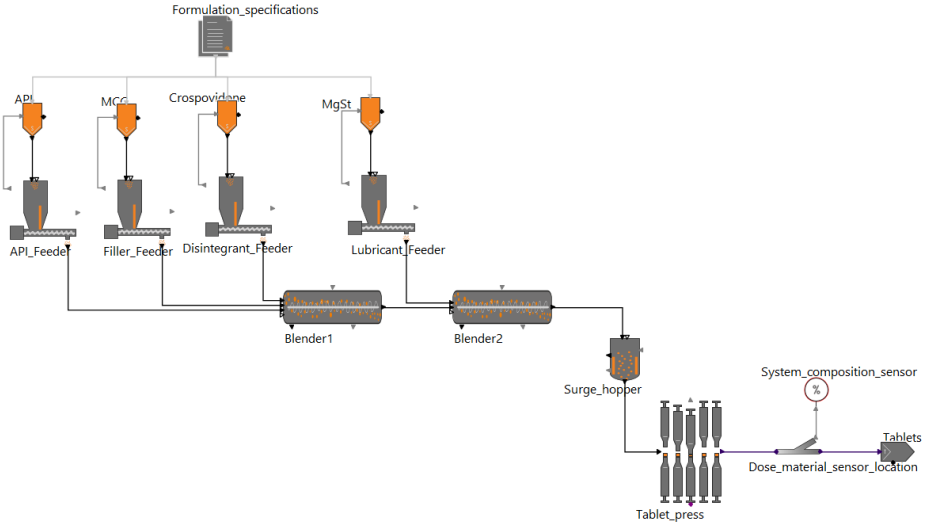

Figure 2: Flowsheet for CDC system model developed in gPROMS Formulated Products 2023.1.0.

3. Results and discussion

3.1. OSD platform comparison

When performing the LCA, all impacts were normalised per kg coated tablets, to allow for comparison to be made across batch sizes. Figure 3 shows the global warming potential added to the baseline formulation contribution for production of one kg of coated tablets across each manufacturing platform and batch size. The results demonstrate that at small batch sizes CDC is the most carbon intensive manufacturing process, although this is highly dependent on batch size, with CDC having the lowest GWP impact at batch sizes above 200 kg. This batch size dependency results from the fixed start up loss assumptions made for process yield, and since API typically has the largest contribution to GWP, increased process yields result in significant GWP reductions. For other platforms, larger batch sizes are favourable for carbon emission reduction as fixed contributions such as cleaning become relatively lower per kg at larger batch sizes.

When assessing batch manufacturing platforms, direct compression has the lowest GWP when compared to granulation processes such as roller compaction. This is largely due to the cumulative effect of additional unit operations on the overall process yield, although in the case of high shear granulation, there is also the influence of the energy intensive drying process.

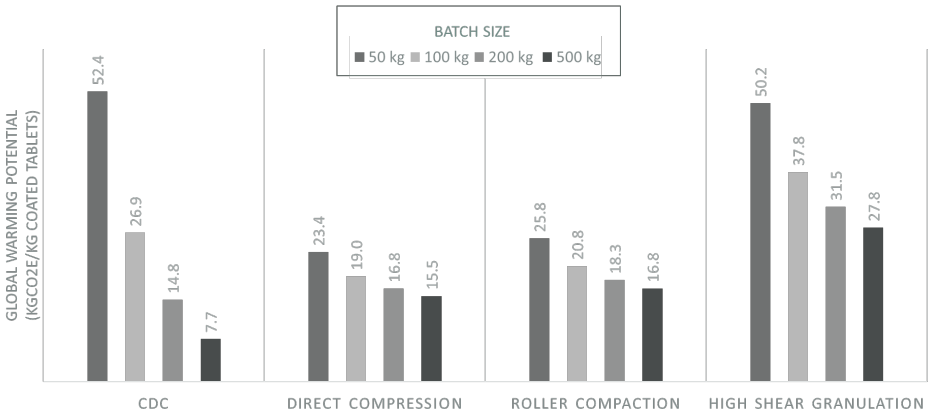

Figure 3 Comparison of global warming potential impacts from different OSD manufacturing platforms and batch sizes. The baseline formulation contribution of 325 kgCO_2eq per kg coated tablets has been removed to allow better visualisation of differences as it is constant for all results.

3.2. System model analysis

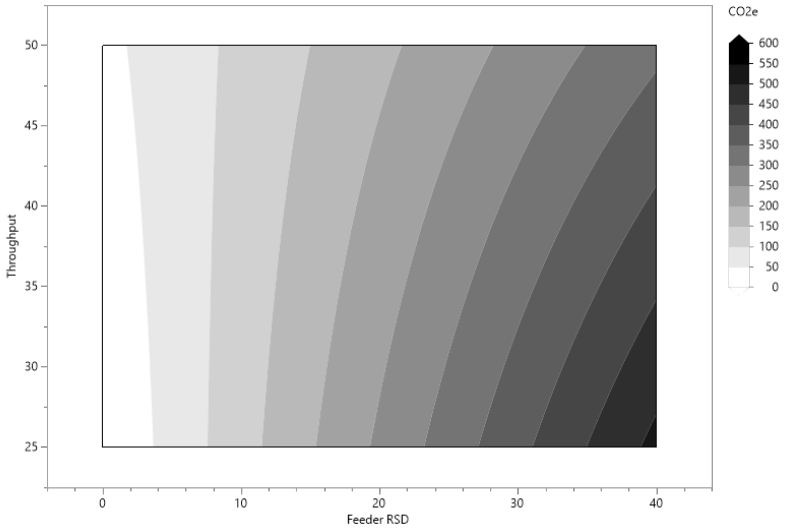

Figure 4 Contour plot of predicted global warming potential (in kg CO2e per kg of formulated tablets) as a function of throughput and feeder variability (RSD). The baseline formulation contribution has been subtracted for visualization.

To illustrate the output from the system model, the influence of the overall process throughput and the RSD of the API feeder on GWP is shown in Figure 4. In this example, the model was run to process the same amount of material (100 kg) across all conditions, with a constant residence mass. The figure shows that the variability from the feeder has

a significant influence on the global warming potential of the product. As the variability in the feeder increases, the composition of the resultant tablets starts to deviate from the control limits, resulting in rejection and therefore an increase in waste from the process. There is also an interaction with throughput observed. At low feeder variability, throughput has very little influence on the global warming potential of the product. In this case, the time to steady state (3 mean residence times) scales resulting in the same mass of wasted tablets (equivalent to 3 residence masses). At low feeder variability there is zero or limited waste from out of specification tablets. At higher feeder variability, a higher throughput typically produces a lower global warming potential. This is due to the overall process running for a shorter period of time and therefore reducing the frequency of composition excursions and rejected tablets. Although additional contributions from the LCA were not included in the system model for this illustration, a higher throughput would also be expected to result in lower facility energy contribution due to a shorter production time.

Further development of the system model can include the addition of factors related to equipment set-up and operation, which would influence the residence mass and therefore the degree of mixing in the process as well as inclusion of additional LCA contributions.

4. Conclusions

A detailed cradle to gate life cycle analysis of pharmaceutical tablet manufacturing has been developed. The LCA methodology has included contributions from raw materials, process equipment energy, facilities, cleaning and waste. This has been used to compare the global warming potential of several typical tablet manufacturing platforms. Data and models from the LCA have been incorporated into a system model of a continuous direct compression process to demonstrate how optimisation of these processes can include a quantitative assessment of the global warming potential of the product. This approach provides an enhanced capability to support the development of more sustainable pharmaceutical manufacturing processes.

References

ABPI and CarbonTrust. "Blister Pack Carbon Evaluation Tool." Retrieved 21/08/2023, from https://www.abpi.org.uk/r-d-manufacturing/abpi-blister-pack-carbon-footprint-tool/

García-Muñoz, S., A. Butterbaugh, I. Leavesley, L. F. Manley, D. Slade and S. Bermingham (2018). "A flowsheet model for the development of a continuous process for pharmaceutical tablets: An industrial perspective." AIChE Journal **64**: 511-525.

Hadinoto, K., T.-T. Tran, A. Chua and W. S. Cheow (2022). "Comparing environmental impacts of direct compaction versus wet granulation tableting methods for drugs with poor flowability by life cycle assessment." Chemical Engineering Research and Design **183**: 439-451.

Moreno-Benito, M., K. T. Lee, D. Kaydanov, H. M. Verrier, D. Blackwood and P. Doshi (2022). "Digital twin of a continuous direct compression line for drug product and process design using a hybrid flowsheet modelling approach." International Journal of Pharmaceutics **628**.

Reynolds, G. K., J. I. Campbell and R. J. Roberts (2017). "A compressibility based model for predicting the tensile strength of directly compressed pharmaceutical powder mixtures." International Journal of Pharmaceutics **531**(1): 215-224.

Tian, G., A. Koolivand, Z. Gu, M. Orella, R. Shaw and T. F. O'Connor (2021). "Development of an RTD-Based Flowsheet Modeling Framework for the Assessment of In-Process Control Strategies." AAPS PharmSciTech **22**: 1-10.

Wernet, G., C. Bauer, B. Steubing, J. Reinhard, E. Moreno-Ruiz and B. Weidema (2016). "The ecoinvent database version 3 (part I): overview and methodology." The International Journal of Life Cycle Assessment **21**: 1218-1230.

ESCAPE-34 PSE-2024
European Symposium on Computer Aided Process Engineering
&
Process Systems Engineering

Flavio Manenti, Gintaras V. Reklaitis (Eds.), Book of Abstract of the 34th European Symposium on Computer Aided Process Engineering / 15th International Symposium on Process Systems Engineering (ESCAPE34/PSE24), June 2-6, 2024, Florence, Italy.

A Comparative Study of ORC Working Fluids Performance in Ultra Low-Grade Waste Heat Recovery from Data Centres

Sai Sudharshan Ravi*, Daniel Alexander Florez Orrego, Shivom Sharma, Francois Merchal

École polytechnique fédérale de Lausanne
sai.ravi@epfl.ch

Abstract

The increasing growth of data centers worldwide has ushered in an era of unprecedented data processing and storage capabilities. As data centers play a pivotal role in the ever-increasing use of cloud computing, social media, and online services in general, their energy consumption continues to rise, accounting up to 1-1.13% of the global electricity demand. Data centers produce low-grade heat. The energy-intensive operations of data centers have spurred a growing interest in waste heat recovery technologies as a means to enhance energy efficiency by usage of this waste heat for electricity generation and district heating. This study examines the waste heat potential of a 5MW data center that primarily employs liquid chip-level cooling to convert waste heat into electricity using an organic Rankine cycle (ORC). By comparing the performances of different working fluids such as R245fa (dry), R134a (wet) and R1234zeE (isentropic) in ORC systems optimized to have the lowest operating cost, this study attempts to understand the operating conditions that maximize the energy savings and improve the Energy Reuse Efficiency (ERE) indicator in datacenters, aiming to reduce the environmental impact.

Keywords: Data Centres, ORC System, Working fluids, System Modelling.

1. Introduction and background

In an era dominated by the unprecedented proliferation of digital data; data centers have emerged as the linchpin of our global information ecosystem. However, the digital renaissance comes with a daunting challenge—the efficient management of the substantial waste heat produced by data centers. The EU has set a goal for the year 2030 in which it aims to reduce the greenhouse gas (GHG) emissions by 40%[1]. A large amount of this could be reduced by reducing the energy consumption of the district heating (DH) systems. Waste heat from the data centres offers the opportunity to reduce the DH load and thereby reducing the overall energy consumption for DH, as discussed by Oro et al (2019)[2]. The heat available from the data centers would still be available during summer when there is not much need for direct heating applications. This heat could then be used to produce electricity by the use of an organic Rankine cycle (ORC). Figure 1 (a) shows a simple schematic diagram of how the waste heat from the data centre can be used to produce work using an ORC. In this study we intend to analyze different working fluids,

which are selected for the case of data centers using a prescreening tool suggested in Kermani et. al (2018)[3], in an ORC superstructure that operates optimally between 5 different pressure levels by optimizing the overall operating cost of the system. The choice of working fluid becomes critical to the ORC's efficiency, as discussed by Herath et. al (2020)[4]. The working fluids are largely classified as dry, wet and isentropic fluids. Figure 1 (b), (c) and (d), show the TS diagram of these fluids along with a simple ORC with superheating for dry, wet and isentropic fluids correspondingly.

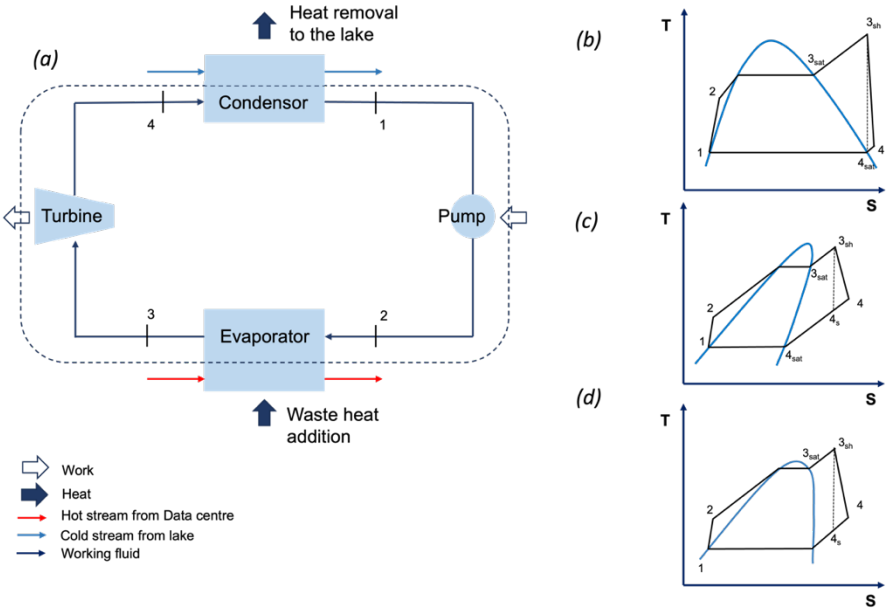

Figure 1 (a) A schematic diagram of simple Organic Rankine Cycle (b) TS diagram for a dry working fluid (c) TS diagram for a wet working fluid (d) TS diagram for an isentropic working fluid

2. Problem Formulation

In this study, we focus on harnessing the potential of R134a (wet), R245fa (dry), and R1234zeE (isentropic) within the context of ultra-low heat recovery applications, specifically in conjunction with a data center's waste heat. Our primary objective is to leverage these three distinct refrigerants, each optimized for heat integration using OSMOSE, a decision support tool, to maximize energy recovery from the data center, maintained at a steady temperature of 85 °C. Complementing this, we utilize lake water as our cold source, with an assumed inlet temperature of 15°C. This temperature differential between the heat source and the cold source forms the crux of our integrated composite curve, allowing us to efficiently extract and convert waste heat into electricity which is then either to partially power the data centre again or integrated to the grid as shown in Figure 2. By focusing on this temperature range, our research seeks to better understand factors that affect ultra-low heat recovery and promote sustainable energy practices within data center operations, as discussed by Montalya et al (2023)[5]. Some of

the key fluid properties of the different fluids chosen for this study are summarised in Table 1

Table 1: Summary of working fluids chosen for ORC. Bell et. al (2014) [6]

	R134a	**R245fa**	**R1234zeE**
Type	Wet	Dry	Isentropic
Boiling Point (^{0}C)	-26.3	14.72	-19.27
Critical Temperature (^{0}C)	101.06	153.86	109.37
Critical Pressure (bar)	40.59	36.51	36.36
Global Warming Potential (GWP100)	3830	3380	-

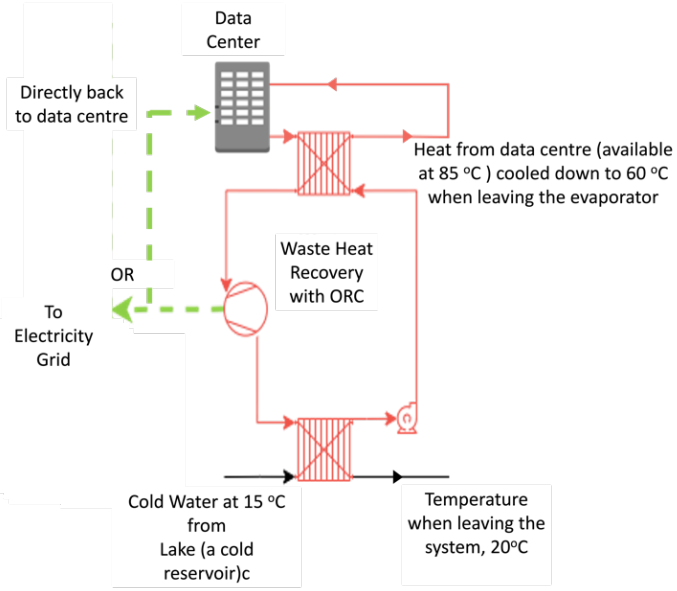

Figure 2 A simplified schematic of the overall process system showing heat removal from the data centre and electricity generation

3. Results and Discussion

By calculating the amount of electricity produced with each of these working fluids, we were able to calculate the efficiency of electricity production in each case. Assuming that the data centre has a power usage effectiveness of 1.58 and a system heat recovery potential of 0.96, we estimated that the heat available to be converted to actual work in the system was only about 3038 kW. The electricity produced and the efficiency is

tabulated in Table 2 below. The efficiencies as calculated here for an ultra-low grade waste heat recovery scenario for the different working fluids, seems to also conform with the findings of Vittorini et al (2019)[7]. and Dai et. al(2009) [8]

Table 2: Efficiency of ORC system with different working fluids

	R134a	**R245fa**	**R1234zeE**
Heat available from system (kW)	3038	3038	3038
Temperature of hot source (°C)	85	85	85
Temperature of cold sink (°C)	15	15	15
Electricity produced (kW)	268.3	270.8	267.5
Efficiency (%)	8.83	8.91	8.8

2.1 Thermal Efficiencies comparison

Furthermore, the efficiencies of these fluids, as delineated in Figure 2 (a), provide critical insights into the thermodynamic characteristics of each working fluid, thereby aiding in the selection of the most suitable medium for waste heat recovery. In the context of waste heat recovery for data centres, thermal efficiency and electric power generation are paramount. A high thermal efficiency signifies the effective utilization of waste heat, reducing operational costs and environmental impact. This is particularly vital for data centres with their energy-intensive operations. The electric power generated by the Organic Rankine Cycle (ORC) system represents a tangible output that can offset electricity consumption within data centres, enhancing their Power Usage Effectiveness (PUE), sustainability and reducing their reliance on conventional power sources, like discussed in Lei et.al (2020)[9]. In this regard, optimizing the thermal efficiency of ORC systems holds significant promise for the efficient and eco-friendly operation of data centres and of the three fluids considered in this study, R245fa like mentioned before, seems to have the most electricity generation for a given amount of heat supplied between these temperature limits.

2.2 Integrated Composite Curves

Integrated composite curves provide a graphical representation of heat exchange profiles in energy systems, revealing temperature pinch points and aiding in optimization. In the context of Organic Rankine Cycles (ORCs) operating between a waste heat source at 85 °C and a cold stream at 20 °C, the integrated composite curves, as depicted in Figure 2 (b), (c), and (d), serve as vital tools for optimizing energy recovery systems. These curves offer a comprehensive visual representation of heat exchange dynamics, enabling the identification of temperature pinch points and facilitating the assessment of energy utilization. Particularly, in the comparison of three distinct working fluids R245fa, R1234zeE, and R134a, it is evident, as illustrated in Figure 2 (b), that R245fa yields the highest power output, underscoring its better performance in this specific application.

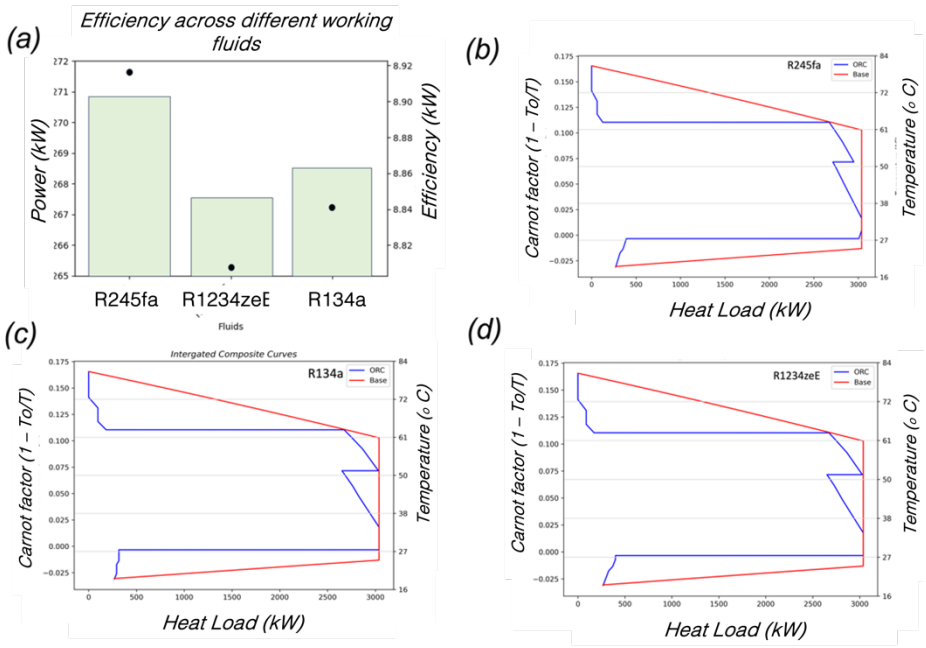

Figure 2: (a) Thermal efficiencies of the ORCs, when using these fluids. Integrated Composite Curves of a (b) R245fa (dry), (c) R134a (wet) and (d) R1234zeE (isentropic) working fluids with in the same temperature bounds

4. Conclusions

In summary, the investigation of three distinct working fluids in the context of waste heat recovery from data centers using Organic Rankine Cycles has revealed their comparative performance. Despite variations in efficiency, these fluids demonstrate nearly equivalent overall efficacy, affording the opportunity to consider other critical factors in the selection process. Such factors encompass environmental impact like the GWP100, specifically in the event of a leakage, as well as the optimization of the system with regard to objective functions extending beyond operational expenses. This study serves as a catalyst for forthcoming research endeavours in the realm of waste heat recovery, advocating a comprehensive approach to decision-making and the exploration of diverse avenues for advancing the sustainability of data center operations. Future research directions may encompass a more profound exploration of the long-term environmental repercussions, system reliability, and multi-objective optimization techniques, contributing to the refinement of working fluid selection and its implementation in waste heat recovery systems.

References

1. Reducing carbon emissions: EU targets and policies | News | European Parliament. https://www.europarl.europa.eu/news/en/headlines/society/20180305STO99003/reducing-carbon-emissions-eu-targets-and-policies (2018).
2. Oro, E., Taddeo, P. & Salom, J. Waste heat recovery from urban air cooled data centres to increase energy efficiency of district heating networks. *Sustainable cities and society* **45**, 522–542 (2019).
3. Kermani, M., Wallerand, A. S., Kantor, I. D. & Maréchal, F. Generic superstructure synthesis of organic Rankine cycles for waste heat recovery in industrial processes. *Applied energy* **212**, 1203–1225 (2018).
4. Herath, H. M. D. P., Wijewardane, M. A., Ranasinghe, R. A. C. P. & Jayasekera, J. G. A. S. Working fluid selection of Organic Rankine Cycles. *Energy Reports* **6**, 680–686 (2020).
5. Montagud-Montalvá, C., Navarro-Peris, E., Gómez-Navarro, T., Masip-Sanchis, X. & Prades-Gil, C. Recovery of waste heat from data centres for decarbonisation of university campuses in a Mediterranean climate. *Energy Conversion and Management* **290**, 117212 (2023).
6. Bell, I. H., Wronski, J., Quoilin, S. & Lemort, V. Pure and Pseudo-pure Fluid Thermophysical Property Evaluation and the Open-Source Thermophysical Property Library CoolProp. *Industrial & Engineering Chemistry Research* **53**, 2498–2508 (2014).
7. Vittorini, D., Cipollone, R. & Carapellucci, R. Enhanced performances of ORC-based units for low grade waste heat recovery via evaporator layout optimization. *Energy Conversion and Management* **197**, 111874 (2019).
8. Dai, Y., Wang, J. & Gao, L. Parametric optimization and comparative study of organic Rankine cycle (ORC) for low grade waste heat recovery. *Energy Conversion and Management* **50**, 576–582 (2009).
9. Lei, N. & Masanet, E. Statistical analysis for predicting location-specific data center PUE and its improvement potential. *Energy* **201**, 117556 (2020).

ESCAPE-34 PSE-2024
European Symposium on Computer Aided Process Engineering
&
Process Systems Engineering

Flavio Manenti, Gintaras V. Reklaitis (Eds.), Book of Abstract of the 34th European Symposium on Computer Aided Process Engineering / 15th International Symposium on Process Systems Engineering (ESCAPE34/PSE24), June 2-6, 2024, Florence, Italy.

Optimal Operation of Multi-Alkaline Electrolyzers in Green Ammonia Production Systems Considering Partial-Load Efficiencies

Bingqian Liu, Catarina G. Braz, François Maréchal

Ecole Polytechnique Fédérale de Lausanne, Valais, Sion, Switzerland

bingqian.liu@epfl.ch

Abstract

The optimal operation of multiple electrolyzers working in parallel poses challenges when modeled as a mathematical programming problem, often introducing numerous auxiliary binary variables. In this paper, we propose a novel formulation that leverages the convex nature of the non-linear performance curve of electrolyzers. This new formulation concisely describes the optimal operation of electrolyzers without compromising accuracy. The results demonstrate the efficient solvability of the novel formulation using off-the-shelf solvers. We have also observed that considering multiple-unit operation enables a more rational use of hydrogen storage, helping to mitigate the need for frequent start-ups of electrolyzers.

Keywords: Optimal operation; green ammonia production system; multiple-unit electrolyzer operation; partial-load efficiency

1. Introduction

A typical green ammonia production plant, as shown in Fig.1, comprises three main components: renewable energy generation, green hydrogen production, and green ammonia production. The system may also be equipped with electric and hydrogen storage. However, the intermittent nature of renewable electricity introduces challenges, causing the load rate of electrolyzers to vary significantly over short periods. Managing the state transfer and partial-load efficiency of multiple electrolyzers in a system remains a difficult task. In the literature, various approaches aim to simplify this challenge, including

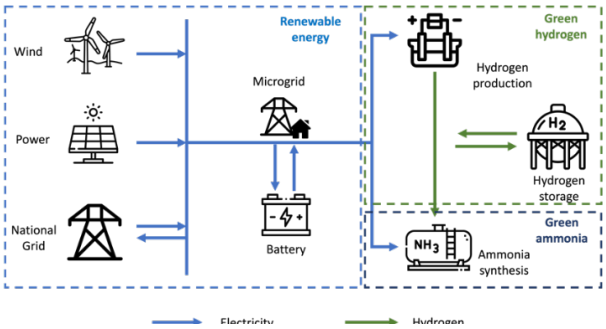

Figure 1. Structure of a green ammonia production system

the aggregation of electrolyzers and linearization of performance curves. In a recent work of Varela (2021), authors proposed to use binary variables in a Mixed-Integer Linear Programming (MILP) model to represent the state of electrolyzers. It is worth noting that the computational burden increases exponentially with the growing number of electrolyzers.

In this paper, we introduce a novel MILP model for optimizing the operation of multiple electrolyzers in the system. First, we apply a piecewise linear approximation to address the non-linear performance curve. Then, by leveraging the convex nature of the performance curve, we represent the states of electrolyzers without using binary variables for each of them. This approach not only provides a more precise description of the operation of the electrolyzer, but also reduces the size of the problem and improve resolution efficiency.

2. Problem Description

2.1. Renewable energy

Renewable energy is generated through existing wind turbines and PV panels in the area. The produced renewable electricity can either be utilized within the system or sold to the grid at a predefined price. Given the intermittent nature of the renewable energy source, the system is allowed to import electricity from the national grid when the renewable energy is insufficient to sustain its operation. The objective of the operational optimization is to minimize the total cost, calculated as the cost of purchasing electricity from the grid subtracted by the revenue generated from selling green electricity to the grid.

2.2. Green hydrogen

At the green hydrogen production stage, the system is equipped with multiple electrolyzers and a hydrogen storage. All electrolyzers are assumed to share the same technical parameters, including capacity, performance curve and starting-up cost. The hydrogen produced can be stored partially in the hydrogen storage and partially directed to the ammonia synthesis unit.

Each electrolyzer has three different states: production, hot stand-by (HSB), and idle. In the production state, an electrolyzer operates above its minimum load rate to generate hydrogen output. The load rate must not fall below the minimum to avoid safety risks. In the HSB state, an electrolyzer consumes a small amount of power to maintain the suitable temperature of the liquid. While it doesn't produce hydrogen in the HSB state, it can switch to the production state within minutes and without extra energy consumption. An electrolyzer is completely turned off in the idle state and doesn't consume any electric power. When it switches to HSB or production state, it needs time and electric power to heat the liquid, so we need to consider a starting-up cost in this case.

The performance curve of an electrolyzer illustrates the relationship between the production rate and electricity consumption. Typically nonlinear, the performance curve exhibits decreasing marginal efficiency as the production rate rises. Therefore, the performance curve forms a convex curve between its minimum and maximum production rate.

2.3. Green ammonia

The green ammonia production stage consists of a cryogenic air separation unit, utilized to extract nitrogen from the air, and a synthesis reactor where hydrogen and nitrogen react to produce ammonia with the assistance of a catalyst under specific temperature conditions. In this paper, we aggregate these components into a unified unit, treated as a

process that consumes electricity and hydrogen to produce ammonia. It's crucial to ensure that the ammonia synthesis unit operates between its working range. The startup time for an ammonia synthesis unit, transitioning from a completely off state to full operation, typically exceeds one day. To maintain the stability of the ammonia synthesis reactor, we assume the ammonia synthesis unit operates continuously within its working range throughout the investigated time horizon.

3. Mathematical model

Parameters	
P_t^{RE}	Available renewable energy in time step t (kWh)
C^{buy}/C^{sell}	Price per kWh of importing/selling electricity to/from the national grid (RMB/kWh)
$Q^{H_2,min}/Q^{H_2,max}$	Minimum/maximum hydrogen production rate of electrolyzers (t)
B	Number of segments used for piecewise linear approximation
a_b/o_b	Slope/intercept of segment b
P^{HSB}/P^{SU}	Fixed electricity consumption of HSB state/starting-up (kWh)
N^{EL}	Number of electrolyzers in the system
η^{elec}/η^{H_2}	Efficiency coefficient of the electricity/hydrogen input of the ammonia synthesis unit
$Q^{NH_3,min}/Q^{NH_3,max}$	Minimum/maximum ammonia production rate (t)
$Q^{NH_3,obj}$	Annual ammonia production plan (t)
Variables	
$P_t^{RE,use}/P_t^{RE,sell}$	Renewable energy for self-use/selling to the grid in timestep t (kWh)
P_t^{grid}	Electricity imported from the national grid in timestep t (kWh)
P_t^{input}	Total electricity consumed by the system in timestep t (kWh)
P_t^{EL}/P_t^{AS}	Electricity consumed by electrolyzers/ammonia synthesis unit (kWh)
$Q_t^{H_2}/Q_t^{NH_3}$	Production of hydrogen/ammonia produced by the system in timestep t
$W_t/H_t/I_t$	Number of electrolyzers in production/HSB/idle state in timestep t
SU_t	Number of starting-up electrolyzers in timestep t
$P_t^{EL,W}/P_t^{EL,S}/P_t^{EL,S}$	Electricity consumption by production-state/HSB-state/starting-up electrolyzers (kWh)
$SoC_t^{H_2}/S_t^{H_2,in}/S_t^{H_2,out}$	Storage level/input mass flow/output mass flow of hydrogen storage
$SoC_t^{elec}/S_t^{elec,in}/S_t^{elec,out}$	Storage level/input energy flow/output energy flow of battery storage

3.1. Objective function

We aim to minimize the total electricity cost of the system. Other operational costs, such as labor and water, are considered constant due to the fixed ammonia production objective.

$$Obj := \sum_{t=1}^{T} \left(C^{buy} P_t^{RE,use} - C^{sell} P_t^{RE,sell} \right) \quad (1)$$

3.2. Constraints

The total electricity consumed by the system and sold to the grid should not exceed the generated renewable energy.

$$P_t^{RE} \geq P_t^{RE,use} + P_t^{RE,sell} \quad (2)$$

The energy balance involves the system's energy consumption, the self-use portion of renewable energy, imported grid electricity, and the utilization of battery storage.

$$P_t^{RE,use} + P_t^{grid} - S_t^{elec,in} + S_t^{elec,out} = P_t^{input} \quad (3)$$

The electricity consumption of the production plant comprises two components: the electrolyzers and the ammonia synthesis unit.

$$P_t^{input} = P_t^{EL} + P_t^{AS} \quad (4)$$

The electricity consumption of the electrolyzers is characterized by a non-linear performance curve, which is approximated piecewise-linearly with B segments. Liu (2021) has proved that in the optimal operation solution, all identical conversion units with convex performance curves in the production state have the same workload. This enables us to aggregate the consumption and production of production-stat electrolyzers as $P_t^{EL,W}$ and $Q_t^{H_2}$. By the nature of the minimization problem, Eq. (5) will yield an equation at the optimal solution.

$$P_t^{EL,W} \geq a_b Q_t^{H_2} + o_b W_t \qquad \forall b \in \{1, \cdots, B\} \quad (5)$$

$$Q^{H_2,min} W_t \leq Q_t^{H_2} \leq Q^{H_2,max} W_t \quad (6)$$

Electrolyzers in the HSB state consume a minimal amount of energy to maintain the temperature of the liquid. Starting up an electrolyzer from the idle state requires additional energy to heat the liquid and prepare the electrolysis conditions.

$$P_t^{EL,S} = P^{HSB} H_t \quad (7)$$

$$P_t^{EL,SU} = P^{SU} SU_t \quad (8)$$

The number of electrolyzers in different states should be consistent with the total number of electrolyzers.

$$W_t + H_t + I_t = N^{EL} \quad (9)$$

The number of units starting up is equal to the decrease in idle units.

$$SU_t \geq I_t - I_{t+1} \qquad \forall t \leq T - 1 \quad (10)$$

$$SU_t \geq 0 \quad (11)$$

The inventory balance constraints for electric storage and hydrogen storage.

$$SoC_t^{H_2} + S_t^{H_2,in} - S_t^{H_2,out} = SoC_{t+1}^{H_2} \qquad \forall t \leq T - 1 \quad (12)$$

$$SoC_t^{elec} + S_t^{elec,in} - S_t^{elec,out} = SoC_{t+1}^{elec} \qquad \forall t \leq T - 1 \quad (13)$$

The electricity and hydrogen consumption of the ammonia synthesis unit.

$$Q_t^{NH_3} = \eta^{elec} P_t^{AS} \tag{14}$$

$$Q_t^{NH_3} = \eta^{H_2}(Q_t^{H_2} - S_t^{H_2,in} + S_t^{H_2,out}) \tag{15}$$

The ammonia synthesis unit should operate within its working range and achieve the total production objective.

$$Q^{NH_3,min} \leq Q_t^{NH_3} \leq Q^{NH_3,max} \tag{14}$$

$$\sum_{t=1}^{T} Q_t^{NH_3} \geq Q^{NH_3,obj} \tag{15}$$

4. Results

We tested the model, as defined in Section 3, on an actual green ammonia production system located in northern China over one year. In this region, we have a wind farm with a generation capacity of 1.5 GW and 15 MW of PV panels. In the hydrogen production stage, there are 150 electrolyzers, each capable of producing a maximum of 83.75 kilograms of green hydrogen per hour. The working range of each electrolyzer is between 50% and 100%, and the nonlinear performance curve, as well as the piecewise linear approximation, is illustrated in the Fig.2. The ammonia synthesis unit can produce a maximum of 75 tons of ammonia per hour and should operate between 10% and 100% of its capacity. The system is also equipped with a 150 MWh battery storage and a 10-ton hydrogen storage tank. The electricity price purchased from the grid is 0.5 RMB/kWh, and the selling price of green electricity is 0.2829 RMB/kWh. We consider a one-year time horizon and the annual production objective is 3.9×10^5 tons.

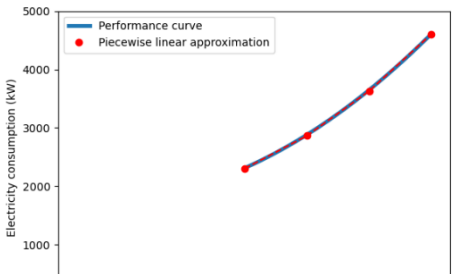

Figure 2. Nonlinear performance curve of electrolyzers and the piecewise linear approximation

The proposed MILP model is optimized with solver CPLEX on a computer with 16GB RAM and Intel i9-12900H CPU. The resolution time is 507 seconds, and the solver returns the optimal solution. In contrast, the model employing conventional binary variables ran out of memory without finding a feasible solution.

The total cost of purchasing electricity from the gird is 1.25×10^8 RMB, and the total revenue from selling renewable energy is 3.92×10^8 RMB, resulting in a total revenue of 2.68×10^8 RMB. The total input of renewable energy for the year is 5274 GWh, of which 1387 GWh is sold to the grid and 3887 GWh is consumed by the system. The self-use rate is 73.7%. Due to the intermittency of available renewable energy, the system also needs to purchase 249 GWh of electric energy from the grid, leading to a grid dependency of 6.4%.

In Fig.3, we illustrate the detailed operation of the system over three consecutive days, from March 7th to March 10th. We observe that there are mainly two periods, on the first day and on the second day, in which the availability of renewable energy is limited. The profile of ammonia production follows the same trend as the availability of renewable energy. Regarding the operation of electrolyzers, we observe that during the long period of limited renewable energy, from 12:00 March 7th to 3:00 March 8th, the optimal operation prefers to switch off the electrolyzers. During the shorter period of limitation, from 18:00 March 8th to 1:00 March 9th, the optimal operation decides to keep electrolyzers in HSB state. The battery storage is charged when sufficient renewable energy is available and discharged when the renewable energy source is limited, resulting in a storage level profile similar to the profile of available renewable energy. The hydrogen storage is utilized in a similar manner, but it is also employed to mitigate frequent starting-up of electrolyzers, as observed from 12:00 March 7th to 3:00 March 8th.

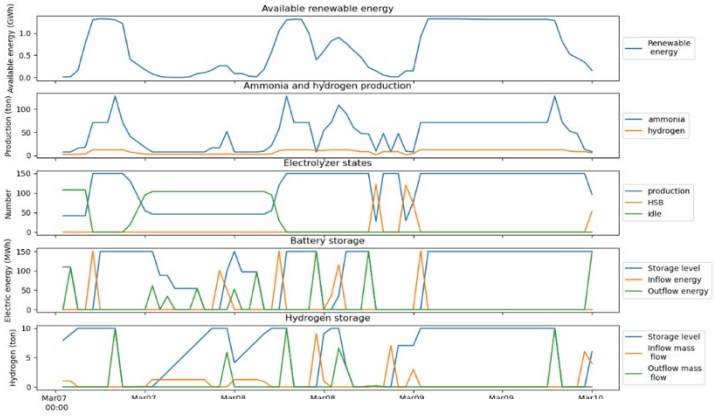

Figure 3. Operation results of three consecutive days

5. Conclusions

In this paper, we developed a novel mixed-integer linear programming model for optimizing the operation of a green ammonia production system. This model considers the partial-load efficiency and state transfer of multiple alkaline electrolyzers. Leveraging the convex performance curve, we establish a priori that all electrolyzers in working state should have the same production rate. Consequently, we can avoid the use of binary variables for each individual electrolyzer, presenting a more concise yet accurate formulation.

The results demonstrate the efficiency of this new model, which can be solved by an off-the-shelf commercial solver in 507 seconds to obtain the optimal operation solution of one year. Furthermore, we have observed that considering the non-linear performance curve and the multiple-unit operation of electrolyzers not only enhances the precision of the model but also allows for a more rational utilization of hydrogen storage in the system, reducing the need for frequent start-ups of the electrolyzers.

References

Varela, C., Mostafa, M., & Zondervan, E. (2021). Modeling alkaline water electrolysis for power-to-x applications: A scheduling approach. International journal of hydrogen energy, 46(14), 9303-9313.

Liu, B., Bissuel, C., Courtot, F., Gicquel, C., & Quadri, D. (2021, February). A hierarchical decomposition approach for the optimal design of a district cooling system. In 10th International Conference on Operations Research and Enterprise Systems (ICORES 2021) (pp. 317-328).

ESCAPE-34 PSE-2024
European Symposium on Computer Aided Process Engineering
&
Process Systems Engineering

Flavio Manenti, Gintaras V. Reklaitis (Eds.), Book of Abstract of the 34th European Symposium on Computer Aided Process Engineering / 15th International Symposium on Process Systems Engineering (ESCAPE34/PSE24), June 2-6, 2024, Florence, Italy.

Numerical Simulation of the L-V Equilibrium within a Stage in a Distillation Column using Cfd

Perla G. Canchola-López[a], Ariadna E. Vázquez-Hernández[a], Jazmín Cortez-González[a], Rodolfo Murrieta-Dueñas[a], Roberto Gutiérrez-Guerra[b], Carlos E. Alvarado-Rodríguez[c]

[a] *Tecnológico Nacional de México/ Irapuato, Ingeniería Química y Bioquímica,; Carretera Irapuato-Silao Km. 12.5, C.P:36821 Irapuato, Guanajuato, MEXICO;*
[b] *Universidad Tecnológica de Leon, Departamento de Sustentabilidad para el desarrollo. Blvd. Universidad Tecnológica 225, Universidad Tecnologica, San Carlos la Roncha, 37670 León, Gto.*
[c] *Departamento de Ingeniería Química, División de Ciencias Naturales y Exactas, Universidad de Guanajuato, Noria Alta S/N, C.P. 36050, Guanajuato, Guanajuato, México.*
jazmin.cg@irapuato.tecnm.mx

Abstract

This work presents the numerical simulation in L -V equilibrium stage in a Sieve plate distillation column using the SPH method. To perform the simulation of the equilibrium stage, periodic conditions in temperature were established. The sizing of the column was performed in Aspen One considering an equimolar mixture of Benzene-Toluene and an operating pressure that guarantees that the cooling water temperature of the condenser is 120°F, the thermodynamic model used was Chao-Seader. With this information, the following was obtained: liquid velocity and vapor velocity per stage, viscosity and density of the mixture, operating pressure and column diameter. The geometry of the stage in the distillation column and the sieve plate were made in SolidWorks. The CFD simulations were performance using DualSPHysics. The results show the effects of sieve plate design on the velocity and temperature distribution in the stage, lead to information to improve the design and efficiency of the stage.

Keywords: CFD, Simulation of Distillation, thermal equilibrium.

1. Introduction

Distillation stands as the most extensively employed unit operation within the field of Chemical Engineering, primarily due to its remarkable capability for product purification. Traditional distillation processes, however, exhibit notable inefficiencies, prompting the exploration of alternative approaches to enhance their thermodynamic efficiency in equipment design and operation. Many of these alternatives have undergone scrutiny through the MESH equations and sequential simulators, while less

attention has been devoted to their modeling with Computational Fluid Dynamics (CFD), mainly due to its inherent complexity. CFD employs methods of either Eulerian or Lagrangian nature. Eulerian methods utilize a mesh for medium discretization, resulting in spatial averages at transfer interfaces between fluids. Noteworthy examples include finite volume and finite element methods, with the former being the preferred choice for simulating hydrodynamics, mass transfer, and momentum within distillation columns (Haghshenas et al., 2007; Lavasani et al., 2018; Zhao, 2019; Ke, 2022). However, this method is not without its drawbacks, encompassing challenges in interface modeling, convergence, and the selection of appropriate turbulence models to simulate turbulent flow.

Conversely, Lagrangian methods afford a detailed view of phenomena at interfaces, discretizing the continuous medium through non-meshed points. This characteristic enables the assessment of flow, concentration, or temperature distribution within a system. Smoothed Particle Hydrodynamics (SPH) emerges as a Lagrangian method that adeptly represents discontinuous media and intricate geometries using particles, avoiding the need for a mesh. It has found applications in modeling diverse scenarios, including microbial growth (Martínez-Herrera et al., 2022), sea wave dynamics (Altomare et al., 2023), and stellar phenomena (Reinoso et al., 2022), showcasing its versatility and robustness. In light of these considerations, this study presents a numerical simulation of a liquid-vapor (L-V) thermal equilibrium stage within a plate distillation column employing the SPH method, specifically examining Sieve and Bubble cap plates. Periodic temperature conditions were imposed to facilitate the equilibrium stage simulation.

2. Methodology

In this work a methodology for the simulation of the hydrodynamics and thermal equilibrium of plate distillation columns is proposed. This methodology consists of 3 stages: rigorous design of the distillation column in Aspen Plus, 3D design of the column - sieve plates and hydrodynamic analysis of the columns using the SPH method. The Aspen Plus simulation results were used as input data for SPH. The 3D design was performed in SolidWorks.

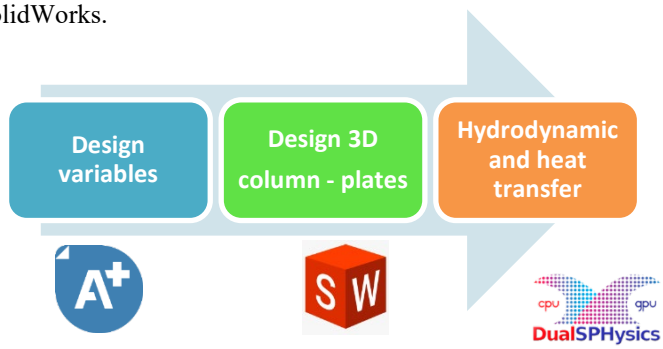

Figure 1. Methodology for the numerical simulation of the hydrodynamics and equilibrium of distillation columns.

2.1. Rigorous design of the distillation column in Aspen Plus

The column's sizing was conducted using Aspen One, considering an equimolar mixture of Benzene-Toluene and an operational pressure guaranteeing a condenser cooling water temperature of 120°F. The thermodynamic model applied was Chao-Seader, and sieve plates were employed. The column featured ten stages, with stage 5 designated for feeding, and both components assumed a 98% purification and recovery rate. This information yielded crucial data, including liquid and vapor velocities per stage, mixture viscosity and density, operating pressure, and column diameter. Three-dimensional CAD files of the distillation column and the sieve and bubble cap plates were developed using SolidWorks. Subsequently, these files were imported into DualSPHysics (Domínguez et. al., 2022) for CFD numerical simulation to ascertain flow and temperature profiles at an equilibrium stage. Stage 6 and 7 were selected for analysis, given their position below the feed stage.

2.2. Column and sieve plate sizing

The 3D design of the column and plates was carried out in SolidWorks. The design parameters used were: column diameter, effective and downspout areas, obtained in Aspen Plus. The distance between plates was proposed to be 0.15m. Stainless steel 316L was chosen as construction material. Figure 1 show, from left to right, the 3D design of the plate, the stage and the initial conditions .

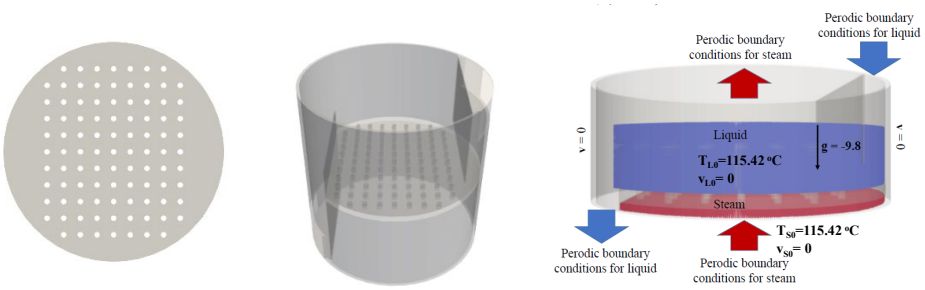

Figure 1. From left to right: 3D Sieve plate design, stage design and initial conditions of simulation.

Table 1. Results of the rigorous simulation of the distillation column in Aspen Plus.

Parameter	Líquid	Vapor
Density (kg/m$^{3)}$	783.8023	4.0206
Viscosity (Ns/m2)	2.5x10^{-4}	9.5x10^{-6}
Temperature (ºC)	105.99	115.42
Mass fraction	0.5886	0.5405
Velocity (m/s)	0.0261	0.0214
Coefficient of thermal diffusivity (m2/s)	7.9247x10^{-8}	
Surface tension	0.018 N/m	0.018 N/m

2.3. Hydrodynamics and heat transfer in SPH

SPH is a Lagrangian, meshless method with applications in the field of Computational Fluid Dynamics. Originally invented for astrophysics in the 1970s (Monagan J, 1992) it has been applied in many different fields, including fluid dynamics (Alvarado-Rodríguez C.E. et al., 2019). The method uses points named particles to represent the continuum and these particles move according to the governing equations in the fluid dynamic. When simulating free-surface flows, no special surface treatment is necessary due to the Lagrangian nature of SPH, making this technique ideal for studying violent free-surface motion. The SPH formalism used in the simulations is reported by (Dominguez et al., 2021) which is set in the DualSPHysics code, in this work only the continuity (Eq. 1), the momentum (Eq. 2) and equation of state (Eq. 3) in the SPH formalism are reported. For this work, the heat equation (Eq. 4) was implemented on the DualSPHysics code to calculate the temperature variation in the stage.

$$\frac{d\mathbf{v}_a}{dt} = -\sum_b m_b \left(\frac{P_a+P_b}{\rho_a\rho_b} + \sum_b m_b \left(\frac{4v_0 \mathbf{r}_{ab}\cdot\nabla_a W_{ab}}{(\rho_a+\rho_b)(r^2{}_{ab}+\eta^2)}\right)\mathbf{v}_{ab} + \sum_b m_b \left(\frac{\vec{\tau}^j_{ab}}{\rho_b{}^2} + \frac{\vec{\tau}^i_{ab}}{\rho_a{}^2}\right)\nabla_a W_{ab}\right)\nabla_a W_{ab} + g\,, \tag{1}$$

$$\frac{d\rho_a}{dt} = -\rho_a \sum_b \frac{m_b}{\rho_b}(\mathrm{v}_b - \mathrm{v}_a)\cdot\nabla_a W_{ab}\,, \tag{2}$$

$$P = B\left[\left(\frac{\rho}{\rho_0}\right)^{\gamma} - 1\right], \tag{3}$$

$$\frac{dT_a}{dt} = \frac{1}{C_p}\sum_b \frac{m_b(k_a + k_b)(r_a + r_b)\cdot\nabla_a W_{ab}}{\rho_a\rho_b(r^2{}_{ab}+\eta^2)}(T_a - T_b). \tag{4}$$

where the subscripts *a* and *b* are denoted for the mean particle "*a*" and the neighbors particles "*b*", v is the velocity, *t* is time, *m* is mass, *P* is pressure, ρ is density, υ_0 is the kinematic viscosity, *r* is the vector position, τ is the stress tensor, $B = c_0{}^2\rho_0/\gamma$, c_0 is and artificial sound speed, and $\gamma = 7$, T is temperature, *k* is the conductivity constant, *Cp* is the heat capacity at constant pressure, and W is the kernel function defined in the SPH method.

This method was implemented for the numerical analysis of the distillation columns under the following considerations: periodic conditions were used to perform the hydrodynamic and equilibrium analysis. Equivalent boundary conditions at zero pressure, P=0, were considered at the exit of the stage. The initial properties of the fluids are shown in Table 1. In all cases, no-slip boundary conditions were considered in the interaction between fluid and boundary particles using the dynamic particle method.

3. Discussion of results

From the results obtained SPH method in the numerical simulations, it is possible to analyze the velocity profile and the temperature profile inside the stage. In addition, it is possible to approximate the time it requires for the stage to reach equilibrium under the initial conditions established.

The simulation was performed with a total of 7,261,750 fluid particles of which 1386940 are bound particles, 4230940 liquid and 1,643,870 are vapor. 60 seconds of real time were simulated. The simulation was completed in a total of 17.5h on the GPU NVIDIA GeForce 3060 of ITESI. In Figure 1 is shown the evolution of velocity field obtained in the simulation. A higher velocity is obtained in the area where the fluid

enters from the downspout, the velocity distribution is not completely homogeneous, however, there are not dominant streamlines in the stage, meaning a good distribution of the flow in the stage. In Figure 3 is shown the evolution of the temperature in the stage which due to the good flow get the equilibrium temperature in the simulated time.

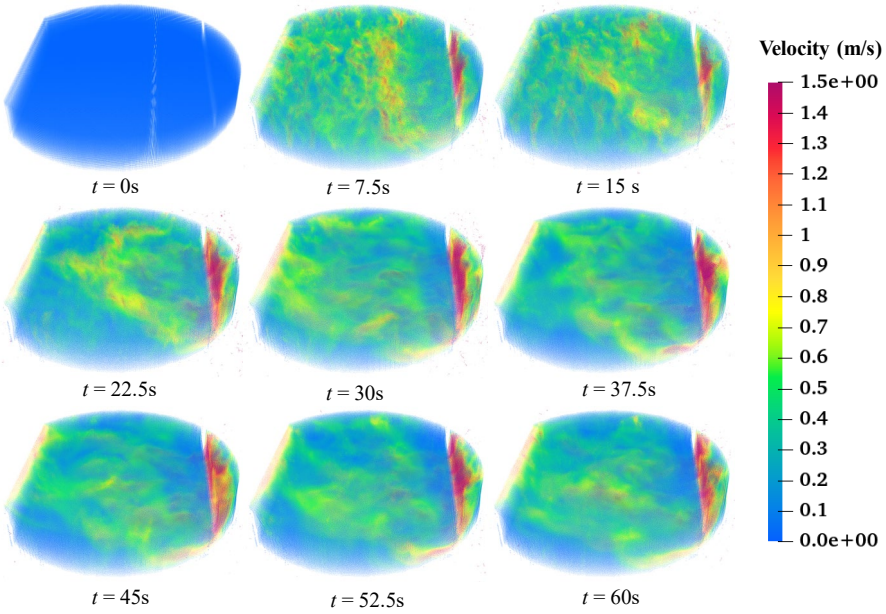

Figure 2. 3D perspective of the velocity field evolution in the stage, each frame correspond to 7.5 seconds.

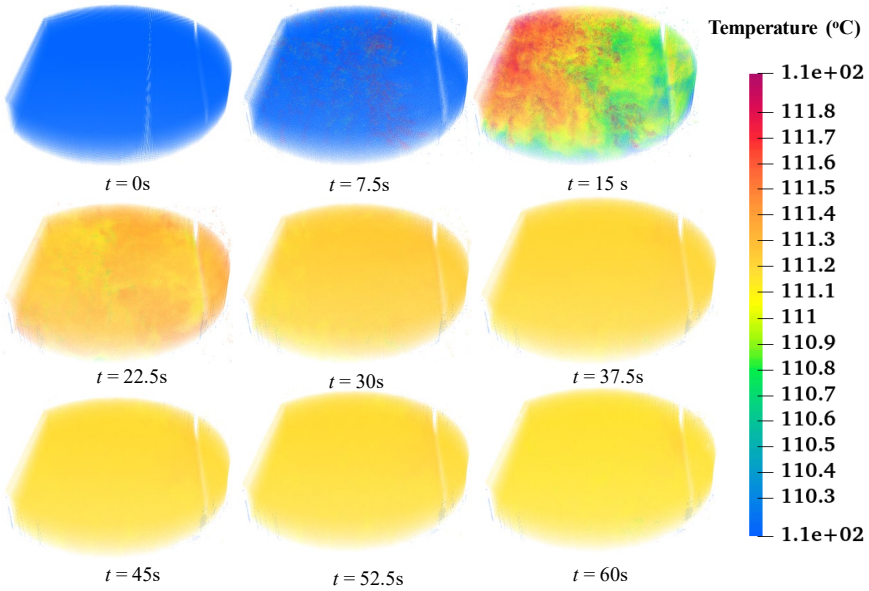

Figure 3. Lateral perspectives of the velocity and temperature fields in the stage., each frame correspond to 7.5 seconds.

4. Conclusions

In this work the CFD numerical simulation of a stage inside a distillation column is presented. The geometry of the column and the plates were made in SolidWorks. Then, the geometries were exported to DualSPHysics to perform the corresponding simulations, based on the parameters obtained with the rigorous simulation in Aspen Plus.

The numerical simulations supply data to analyze the flow and heat transfer in the stage, considering the flow of two faces, steam and liquid, and the change of the temperature of each one. With this data is possible to perform a new methodology to calculate the global heat transfer coefficient in the stage, this parameter could heat to improve the plate design used in the column and to compare between different kind of plates. In summary, the findings underscore the effectiveness of implementing initial and boundary conditions in distillation columns to simulate thermal equilibrium. Furthermore, the SPH method emerges as a potent and versatile tool for conducting numerical simulations of fluid dynamics and thermal equilibrium within distillation columns.

References

Altomare C, Scandura P, Cáceres I, van der A D, Viccione G. 2023. Large-scale wave breaking over a barred beach: SPH numerical simulation and comparison with experiments. Coastal Engineering, 185, 104362. doi:10.1016/j.coastaleng.2023.104362

Alvarado-Rodríguez, C. E., Klapp, J., Domínguez, J. M., Uribe-Ramírez, A. R., Ramírez-Minguela, J. J., & Gómez-Gesteira, M. (2019, March). Multiphase Flows Simulation with the Smoothed Particle Hydrodynamics Method. In International Conference on Supercomputing in Mexico (pp. 282-301). Springer, Cham.

Domínguez JM, Fourtakas G, Altomare C, Canelas RB, Tafuni A, García-Feal O, Martínez-Estévez I, Mokos A, Vacondio R, Crespo AJC, Rogers BD, Stansby PK, Gómez-Gesteira M. (2021), DualSPHysics: from fluid dynamics to multiphysics problems. Computational Particle Mechanics.

Haghshenas Fard, M., Zivdar, M., Rahimi, R., Nasr Esfahani, M., Afacan, A., Nandakumar, K., & Chuang, K. T. (2007). CFD simulation of mass transfer efficiency and pressure drop in a structured packed distillation column. Chemical Engineering & Technology: Industrial Chemistry-Plant Equipment-Process Engineering-Biotechnology, 30(7), 854-861. Martínez-

Herrera, G., Cortez-González, J., Murrieta-Dueñas, R., Uribe-Ramírez, A. R., Pérez-Segura, T., & Alvarado-Rodríguez, C. E. (2022). Smoothed particles hydrodynamics simulations of microbial kinetic in a stirred bioreactor with proximity impellers. Computational Particle Mechanics, 1-13.

Ke, T. (2022). CFD simulation of sieve tray hydrodynamics using openfoam.

Lavasani, M. S., Rahimi, R., & Zivdar, M. (2018). Hydrodynamic study of different configurations of sieve trays for a dividing wall column by using experimental and CFD methods. Chemical Engineering and Processing-Process Intensification, 129, 162-170.

Reinoso, B., Leigh, N. W., Barrera-Retamal, C. M., Schleicher, D., Klessen, R. S., & Stutz, A. M. (2022). The mean free path approximation and stellar collisions in star clusters: numerical exploration of the analytic rates and the role of perturbations on binary star mergers. Monthly Notices of the Royal Astronomical Society, 509(3), 3724-3736.

Zhao, H., Li, Q., Yu, G., Dai, C., & Lei, Z. (2019). Performance analysis and quantitative design of a flow- guiding sieve tray by computational fluid dynamics. AIChE Journal, 65(5), e16563

Martínez-Herrera, G., Cortez-González, J., Murrieta-Dueñas, R., Uribe-Ramírez, A. R., Pérez-Segura, T., & Alvarado-Rodríguez, C. E. (2022). Smoothed particles hydrodynamics simulations of microbial kinetic in a stirred bioreactor with proximity impellers. Computational Particle Mechanics, 9(5), 1017-1029.

ESCAPE-34 PSE-2024
European Symposium on Computer Aided Process Engineering
&
Process Systems Engineering

Flavio Manenti, Gintaras V. Reklaitis (Eds.), Book of Abstract of the 34th European Symposium on Computer Aided Process Engineering / 15th International Symposium on Process Systems Engineering (ESCAPE34/PSE24), June 2-6, 2024, Florence, Italy.

Generation of MINLP Problems for Process Synthesis Using Phenomena-based Building Blocks

Erik Esche[a]*, David Krone[a], Jens-Uwe Repke[a]

[a]*Process Dynamics and Operations Group, Technische Universität Berlin, Str. des 17. Juni 135, D-10623 Berlin, Germany*
erik.esche@tu-berlin.de

Abstract

Formulation and solution of superstructure optimization problems for process synthesis is still challenging. This concerns both the formulation of suitable mathematical models and optimization problems as well as their solution. Here, the focus lies on the formulation and code generation to facilitate subsequent solution. As a novelty, superstructures are generated in MathML / XML form, which are then used to automatically formulated MINLP problems with interfaces to accurate thermodynamic functions. For these large-scale problems, code consistency needs to be addressed early on. MOSAICmodeling's capabilities for processing MathML / XML models are exploited to this end using language specificators for automatic code generation towards target languages and respective frameworks for solution of the MINLP problems. The feasibility of the novel approach is highlighted with an example of a superstructure with phenomena-based building blocks.
Keywords: superstructure, process synthesis, automatic code generation

1. Challenges in Optimal Process Synthesis

Optimal process synthesis requires the formulation and solution of complex optimization problems. An example is the generic network of phenomena-based building blocks as demonstrated by Kuhlmann and Skiborowksi (2017). These problems are typically large and frequently require accurate thermodynamic property information, e.g., to predict vapor liquid equilibria (Krone et al., 2022). This can either be achieved by incorporating the thermodynamic models into the process synthesis problem or by interfacing with external tools. Both cases are challenging during the formulation and implementation of synthesis problems.

For process synthesis problems as in (Kuhlmann and Skiborowski, 2017) and (Krone et al., 2022) there is usually a split between the software used for formulation and solution of the MINLP problem and the tool employed for dedicated solution of thermodynamic equations and properties. The former are typically tools such as GAMS, AMPL, or PYOMO, while the latter are frequently specialized thermodynamic property packages such as Aspen Properties, KBC's MultiFlash, or AmsterChem's TEA, which perform tasks such as determination of the number of phases, computing phase equilibria, etc.

Interfacing between these heterogeneous tools is an error-prone process with disastrous effects for the reliability of results.
MOSAICmodeling (Esche et al., 2017) is a collaborative modeling platform, which follows the paradigm of modelling at the documentation level, i.e., an identity of model formulation and documentation. Models are formulated in MathML / XML, i.e., standardized descriptive markup language, which is flexible and independent of the final implementation in a target language. The backend of MOSAICmodeling instantiates systems according to user specifications regarding index sets and the translation engine converts these instances into programming code (C, C++, Python, Fortran, etc.) or modeling language (GAMS, Pyomo, AMPL, Matlab, etc.). This strategy allows for error-free implementation of models in the form of code but was in the past limited to single language settings.
In the present contribution, we elaborate an approach to exploit the capabilities of the aforementioned thermodynamic property packages for rigorous process synthesis tasks in an error-free fashion. This entails the formulation of synthesis problems as MINLP in MOSAICmodeling with interface definitions for all state variables computed externally. Afterwards, an automatic model decomposition is carried out at the MathML / XML level, which separates the MINLP into two parts: (1) the actual MINLP problem, and (2) the list of required external function calls and their derivatives. These parts are then automatically exported for desired target languages.
Novel decomposition techniques regarding model hierarchy and classifications of variables have been implemented on the MathML / XML level for superstructure problems, which ensures rigor regarding model consistency across heterogeneous target languages.

2. Methodology and Implementation

2.1. Setting
Of interest in this setting are formulations for superstructure optimization problems for general process synthesis which consist of model equations describing at least mass and energy balances for units or phenomena-based building blocks (PBBs), algebraic constraints governing which parts of the superstructure should be activated or deactivated given their connection to others, and an objective function minimizing, e.g., total annualized costs. In general, these types of problems will amount to large-scale MINLP formulations. A specialty in the work of Kuhlmann and Skiborowski (2017), later adapted by Krone et al. (2022) is the inclusion of accurate thermodynamics in these models. Naturally, this leads to a further increase in the computational complexity of the MINLP formulation. To alleviate the situation, Kuhlmann and Skiborowski (2017) suggested outsourcing thermodynamics to an external engine, e.g., Aspen Properties, AmsterChem's TEA, KBC's multiflash, or similar. These external engines ensure solution of the thermodynamic relationships. Nevertheless, setting up the MINLP with external function calls puts an extra burden on the user formulating and solving the overall MINLP.

2.2. Modeling in MathML / XML
In the scope of the here presented work, we exploit the capabilities of the MathML / XML-based model formulation within MOSAICmodeling and extend it towards superstructure problems. During the model formulation of the above described MINLP, all equations and inequality constraints are entered in LaTeX and then automatically translated to MathML. Regarding the thermodynamic function calls, an alternative strategy is pursued. Instead of directly implementing functions or equations, the users

may specify for each that this is to be implemented externally, e.g., in compliance with the CAPE-OPEN standard (COLaN, 2023). For example, in case a liquid phase enthalpy is required, the user specifies as part of an equation system, that this enthalpy is a function of the respective temperature, pressure, and liquid-phase composition. The information is stored in an interface element in XML linking the variables in the equation system to an – as of yet unknown - external engine. In general, this can be done for all thermodynamic properties, which are needed within the model formulation, i.e., enthalpies, entropies, temperatures or pressures of boiling point or dew point, equilibrium coefficients, etc. This way, the model formulation in MathML / XML stays efficient, remains lean, and is still easily understandable to the person formulating the model.

2.3. Model Decomposition and Code Generation

In examples of Kuhlmann and Skiborowski (2017) and Krone et al. (2022), a hierarchical structure is present in the MINLP: A distribution network connects feed nodes and splitters to product nodes and mixers. An example hereof will be given in section 3. Mixer nodes link to individual PBBs and the outlets of PBBs connect to the splitter nodes of the distribution network. The structure is also present in the MathML / XML formulation as model hierarchy. Naturally, the same types of interfaces for thermodynamics reappear everywhere. On all levels of this hierarchy, there may be interfaces to thermodynamic function calls. Also, nonlinear constraints, integer, and continuous variables can appear throughout.

The modeling engine of MOSAICmodeling simultaneously holds a flat version, e.g., all variables numbered globally, as well as a fully hierarchical version, e.g., model equations and variable namings retain hierarchical structure, of the instantiated MathML / XML model while processing it. Instantiated means that the numbers of PBBs, number of components, product nodes, etc., are already confirmed. This dual representation is exploited for code generation and can be of help during the subsequent solution of the MINLP.

First, thermodynamic calls are captured by the modeling engine across all hierarchy levels and two maps are built. The first links the variable namings of the flat to the hierarchical version. The second lists each function call type (boiling point temperature, liquid enthalpy, etc.) and for each instance (i.e., function call) clearly marks all required variables with their type (temperature, pressure, enthalpy, entropy, liquid/vapor composition, boiling point temperature,), their engineering unit (K, Pa, kJ/kmol, etc.), their direction from the perspective of the function call (input or output), and their dimensionality (scalar or vectorial).

Second, the MathML / XML model is decomposed in such a fashion that function values and derivatives can be computed externally and linked back to the occurrences within the hierarchy. This entails a complete separation of the function calls from the rest of the model. The link between both separated parts is based on the hierarchical variables in the MathML / XML structure. Based on the structure of the target code, maps are built for the derivatives either based on the flat (numbering scheme) or the hierarchical variable names. To generate code for the solution of the MINLP, two aspects need to be considered: (1) the environment for the solution and (2) the framework for the external function calls. The translation from MathML / XML form to a target language is governed by language specificators (LS) (Tolksdorf et al., 2019). These can be defined and adjusted by the users and are specified in XML form themselves. In general, an individual LS is required per target language, i.e., AMPL, GAMS, Pyomo, C++, FORTRAN, etc.

For the generation of MINLP problems with external function calls, this is augmented to exploit the hierarchical structure and the aggregation of thermodynamic calls as detailed

above. In practice, this means that the code generation is split between MINLP problem on the one hand side and calls to external functions on the other. The aforementioned maps are used to link these different sides governed by the properties of the target code. For each an LS is set-up to generate the specific, executable code. Further details hereon will be given below.

3. Case Study

3.1. Example Superstructure and Component System

The methodology outlined in section 2 is here presented for a process synthesis problem involving phenomena-based building blocks (Krone et al., 2022; Krone et al., 2023). This is applied on a feed stream of n-pentane, n-hexane, and n-heptane, which is to be separated. The optimization problem consists of 1,303 (in-)equality constraints, 62 binary, and 1,123 continuous variables. The superstructure is depicted in Fig. 1.

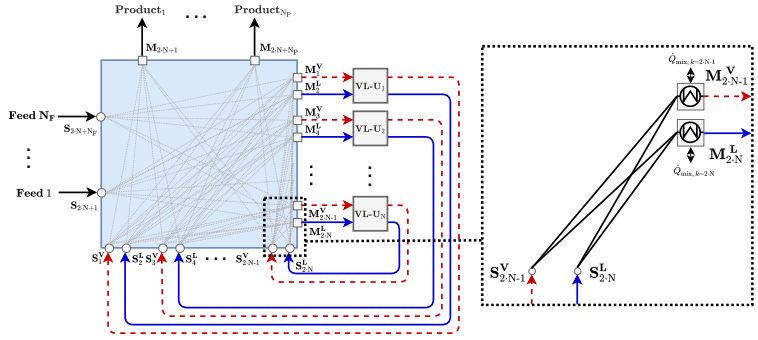

Figure 1. Generic superstructure with vapour-liquid equilibria blocks (VL-U). The left-hand side shows the distribution network with the connected VL-U PBB and the right-hand side a close-up of the connection of splitter nodes to mixer nodes. Red dashed lines signal vapor phase, blue solid lines liquid phase.

The left-hand side shows the distribution network (blue box) with all possible connections between feed, product nodes, splitters, and mixers, as well as the attached PBBs, which here are countercurrent vapor-liquid contactors, depicted as VL-Us (Krone et al., 2023). These could present sections of, e.g., a distillation column. The whole superstructure is implemented in MOSAICmodeling.

3.2. Implementation and Solution of the MINLP

For the solution of the MINLP, GAMS is selected, while the external function calls are implemented using CAPE-OPEN's binary interop architecture (COBIA) (COLaN, 2023). GAMS and COBIA are connected by a dynamic-link library (DLL), which is programmed in C++. On the GAMS side, a solution strategy involving branch & bound algorithms, DICOPT, CONOPT, and IPOPT, is implemented, which is detailed in (Krone et al., 2023). Here, the focus lies on the code generation and connection of GAMS and COBIA. On the GAMS side, our translation engine inside of MOSAICmodeling translates the interface definitions for the thermodynamic function calls into "external equations", see Fig. 2. For this, the mapping between system variables and interfaces for function calls is used and translated into consistent code. In this case, GAMS operates on a numbering scheme regarding external communication, while internally using the hierarchical variable namings. In Fig. 2, the numbers before the multiplication sign are the IDs of each variable for external communication with the DLL, while the strings after the sign are the hierarchical names of the model as translated from MathML into GAMS-

friendly form. For instance, e0s5_p is the pressure of stream 5 and e0e0e2_x_VL_i1_j2 is the liquid mole fraction of component 1 on the second tray of the VL-U 2.

```
exteq1.. 1 =x= 5*e0e1e2_K_VLE_VL_i5_j2 + 1*e0s7_T + 2*e0s7_p + 3*e0s7_x_j1 + 4*e0s7_x_j2;
exteq2.. 2 =x= 10*e0e0e2_h_L_VL_i4 + 6*e0e0e2_T_VL_i4 + 7*e0s5_p + 8*e0e0e2_x_VL_i4_j1 + 9*e0e0e2_x_VL_i4_j2;
exteq3.. 3 =x= 15*e0e0e0s0_h + 11*e0e0e0s0_T + 12*e0s0_p + 13*e0e0e0s0_x_j1 + 14*e0e0e0s0_x_j2;
exteq4.. 4 =x= 19*e0e1e2_K_VLE_VL_i2_j1 + 16*e0e1e2_T_VL_i2 + 2*e0s7_p + 17*e0e1e2_x_VL_i2_j1 + 18*e0e1e2_x_VL_i2_j2;
exteq5.. 5 =x= 23*e0e0e2_h_V_VL_i3 + 20*e0e0e2_T_VL_i3 + 7*e0s5_p + 21*e0e0e2_y_VL_i3_j1 + 22*e0e0e2_y_VL_i3_j2;
exteq6.. 6 =x= 27*e0s5_h + 24*e0s5_T + 7*e0s5_p + 25*e0s5_x_j1 + 26*e0s5_x_j2;
exteq7.. 7 =x= 30*e0e0e2_h_V_VL_i4 + 6*e0e0e2_T_VL_i4 + 7*e0s5_p + 28*e0e0e2_y_VL_i4_j1 + 29*e0e0e2_y_VL_i4_j2;
exteq8.. 8 =x= 33*e0e0e2_h_L_VL_i3 + 20*e0e0e2_T_VL_i3 + 7*e0s5_p + 31*e0e0e2_x_VL_i3_j1 + 32*e0e0e2_x_VL_i3_j2;
exteq9.. 9 =x= 37*e0e0e2_h_V_VL_i2 + 34*e0e0e2_T_VL_i2 + 7*e0s5_p + 35*e0e0e2_y_VL_i2_j1 + 36*e0e0e2_y_VL_i2_j2;
exteq10.. 10 =x= 41*e0e0e2_K_VLE_VL_i1_j1 + 38*e0s4_T + 7*e0s5_p + 39*e0e0e2_x_VL_i1_j1 + 40*e0e0e2_x_VL_i1_j2;
```

Figure 2. Example of automatically generated external equations in GAMS.

On the C++ / COBIA side, a case differentiation needs to be performed. For those cases, where there is a direct match between XML interfaces and CAPE-OPEN specifications little needs to be done: on the C++ side the components need to match the physical components in the CAPE-OPEN specification and the derivatives need to be structured in the correct way to suit GAMS. This is now automatically done by MOSAICmodeling's translation engine. For all other cases, reformulations are required to match CAPE-OPEN-compliant function calls. This implies deriving functional dependencies and derivatives via the implicit function theorem. These need to be derived once and implemented directly in the LS in MOSAICmodeling, which then generates consistent code for each call. Fig. 3 depicts an example of an external function implementation on the C++ side. mylocalThermoObj is a COBIA object. x is the vector of all variables at the interface between GAMS and DLL, f the return vector of residuals for all external function calls, and d the derivative vector.

```
if (icntr[I_Eqno] == 1) {//for the first function
    std::vector<double> composition_liquid = { x[42], x[43], x[44] };
    //External Function for liquid enthalpy calculation
    mylocalThermoObj.setSinglePhasePropResult(enthalpyF, x[30], x[36] * 100000.0, liquid, composition_liquid);
    //std::cout << "this is the h_vapor value: " << mylocalThermoObj.getSinglePhasePropResult(0)  << std::endl;
    f[0] = (x[0] - mylocalThermoObj.getSinglePhasePropResult(0));


    //Derivatives
        //dh/dh
    d[0] = 1.0;
    //dh/dy_j
    mylocalThermoObj.setSinglePhasePropResult(enthalpyF_DmolFraction, x[30], x[36] * 100000.0, liquid, composition_liquid);
    d[42] = -mylocalThermoObj.getSinglePhasePropResult(0);
    d[43] = -mylocalThermoObj.getSinglePhasePropResult(1);
    d[44] = -mylocalThermoObj.getSinglePhasePropResult(2);
    //dh/dp
    mylocalThermoObj.setSinglePhasePropResult(enthalpyF_Dpressure, x[30], x[36] * 100000.0, liquid, composition_liquid);
    d[36] = -mylocalThermoObj.getSinglePhasePropResult(0)*100000.0;//[1/bar]*/
    //dh/dT
    mylocalThermoObj.setSinglePhasePropResult(enthalpyF_Dtemperature, x[30], x[36] * 100000.0, liquid, composition_liquid);
    d[30] = -mylocalThermoObj.getSinglePhasePropResult(0);//[1/K]
}
```

Figure 3. Example of automatically generated C++ and COBIA code for external function calls.

The proposed methodology and described implementation have been tested with a varying number of components (2-3) and number of PBBs (2-6). Consistent, error-free code was generated by the translation engine in MOSAICmodeling for both GAMS and C++. A number of these example MINLP have been successfully solved. At this point we will limit ourselves to showing one cost optimal superstructure which was obtained after 172 h CPU time. Therein, AmsterChem's TEA supplies the thermodynamic properties via COBIA. Fig. 4 shows the result for four vapor-liquid-type PBBs with a fixed number

of five equilibrium stages, which separate a ternary mixture of n-pentane, n-hexane, and n-heptane. The validity of this optimum has been confirmed by comparison with a commercial process simulator. Further details on the optimal solution are published in (Krone et al., 2023).

4. Conclusions

Setting up and solving optimization problems for superstructure-based process synthesis is a challenging task. This is particularly the case when multiple software tools are required to reap the benefits of a state-of-the-art environment for solving MINLPs and efficient implementations for complex thermodynamics. With the here presented solution implemented in the translation and code generation engine within MOSAICmodeling a methodology is available to generate highly complex, large MINLP problems. The proposed procedure can be guaranteed to be error-free regarding code implementation and interfacing of different tools. The results validate the reliability of the decomposition and code generation provided by the novel approach and promise even larger process synthesis applications as a next step. In future work we will extend this approach beyond the GAMS / C++ pair to other frameworks such as Pyomo to interface solvers for generalized disjunctive programming.

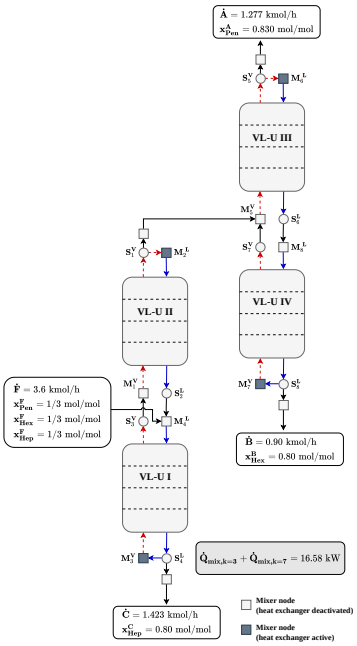

Figure 4. Configuration of four vapor-liquid-type PBB as the optimal design for the separation of an n-pentane, n-hexane, and n-heptane mixture determined via MINLP optimization (published by Krone et al., 2023).

Acknowledgements

This work is funded by the Deutsche Forschungsgemeinschaft (DFG, German Research Foundation) – 523327609.

References

COLaN, 2023, Thermodynamics and Physical Properties interface specification v1.1, https://www.colan.org/specifications/

E. Esche, C. Hoffmann, M. Illner, D. Müller, S. Fillinger, G. Tolksdorf, H. Bonart, G. Wozny,J.-U. Repke, 2017, MOSAIC – Enabling Large-Scale Equation-Based Flow Sheet Optimization, Chem. Ing. Tech. 89, 620–635

D. Krone, E. Esche, N. Asprion, M. Skiborowski, J.-U. Repke, 2022, Enabling optimization of complex distillation configurations in GAMS with CAPE-OPEN thermodynamic models, Comp. Chem. Eng. 157, 107626.

D. Krone, E. Esche, M. Skiborowski, J.-U. Repke, 2023, Optimization-based Process Synthesis by Phenomena-Based Building Blocks and an MINLP-Framework Featuring Structural Screening, *submitted to Comp. Chem. Eng.*

H. Kuhlmann, M. Skiborowski, 2017, Optimization-Based Approach To Process Synthesis for Process Intensification: General Approach and Application to Ethanol Dehydration, Ind. Eng. Chem. Res. 56, 13461–13481.

G. Tolksdorf, E. Esche, G. Wozny, J.-U. Repke, 2019, Customized code generation based on user specifications for simulation and optimization, Comp. & Chem. Eng. 121, 670–684

ESCAPE-34 PSE-2024
European Symposium on Computer Aided Process Engineering
&
Process Systems Engineering

Flavio Manenti, Gintaras V. Reklaitis (Eds.), Book of Abstract of the 34th European Symposium on Computer Aided Process Engineering / 15th International Symposium on Process Systems Engineering (ESCAPE34/PSE24), June 2-6, 2024, Florence, Italy.

Low-regret Decisions for the Steam Supply in the Chemical Industry

Niklas Nolzen[a], Alexander Lademann[a,b], Dennis Roskosch[a], Stefano Moret[a], Hagen Seele[b], Florian Joseph Baader[a], André Bardow[a,*]

[a]*Energy & Process Systems Engineering, Department of Mechanical and Process Engineering, ETH Zürich, Tannenstrasse 3, 8092 Zürich, Switzerland*
[b]*Institute for Technical Thermodynamics, RWTH Aachen University, Schinkelstraße 8, 52062 Aachen, Germany*
abardow@ethz.ch

Keywords: Heat pump, mixed-integer linear optimization, uncertainty analysis, utility system.

Abstract

The decarbonization of the chemical industry requires carbon-neutral steam production either via direct electrification, e.g., using heat pumps, or via indirect electrification, e.g., using green hydrogen. However, due to low technology-readiness levels, the cost and performance of such promising technologies are subject to high uncertainties. This uncertainty prevents the industry from investing, fearing economic regret. This study proposes a method for identifying low-regret decisions based on global sensitivity analysis. Low-regret decisions are defined as an investment in a specific technology that is economically near-optimal in all future scenarios. The proposed method comprises four steps: 1) Uncertainty characterization, 2) Parameter sampling, 3) Identification of low-regret decisions, and 4) Quantification of low-regret decisions. The method is applied to an industrial case study of a multi-energy system. We identify heat pumps and heat storage as low-regret decisions. The proposed method supports the decarbonization of the chemical industry by identifying low-regret decisions as starting points of the transition.

1. Introduction

Decarbonizing the chemical industry requires carbon-neutral steam production since the energy backbone of chemical sites is usually given by steam at different temperature levels. Currently, steam is usually produced at central sites by burning fossil fuels. Promising technologies are available to decarbonize the steam supply, e.g., via direct electrification by power-to-heat or indirect electrification using synthetic fuels, such as green hydrogen (Ruhnau et al., 2019). Today, these technologies are usually more expensive and require major investments. In addition, the decarbonization pathway is affected by substantial uncertainties, e.g., future costs and efficiencies of technologies at low technology readiness levels. As a result, the industry hesitates to take the required

capital-intensive investments, fearing economic regret and lock-in effects. However, the transition to a low-carbon energy system needs to start as soon as possible.
This work presents a method that identifies and quantifies low-regret decisions for multi-energy systems. We define a low-regret decision as an investment in a specific technology that is economically near-optimal in all future scenarios. Thus, investments in low-regret technologies can be taken today to start the transition, while the remaining multi-energy system can be designed later once more information is available.

2. Method

To identify such low-regret decisions, we would, in principle, minimize the expected regret in stochastic optimization or the maximum regret in robust optimization. Each of these problems requires the solution of a two-stage design optimization: the first stage would set the low-regret decision variables, and the second stage adapts the remaining design and operational decisions. However, if uncertainties need to be captured through a large number of future scenarios, the two-stage design optimization is likely too computationally heavy to be solved.
In this contribution, we propose a method to identify low-regret decisions based on global sensitivity analysis (Saltelli et al., 2007). The proposed method comprises four steps: 1) Uncertainty characterization, 2) Parameter sampling, 3) Identification of low-regret decisions, and 4) Quantification of low-regret decisions.

1) **Uncertainty characterization:** The uncertainty of all model parameters is characterized by ranges either based on a literature review or detailed, non-linear process models, following the procedure described in Moret et al. (2017). Therein, parameters are grouped, i.e., parameters with similar uncertainty are assigned the same relative uncertainty range.
2) **Parameter sampling:** The uncertainty analysis draws samples varying all uncertain parameters. The resulting samples are used as input for the design optimization to derive each sample's optimal energy system design.
3) **Identification of low-regret decision:** The most frequently selected components across all system designs are identified as potential low-regret decisions. Note that, in principle, a set of components could also be identified as a low-regret decision.
4) **Quantification of low-regret decisions:** To evaluate the regret, we fix the potential low-regret decision in the design optimization. Subsequently, we re-optimize all regret samples, i.e., all samples in which the identified low-regret components have not been selected in the initial design optimization.
   The economic regret R is quantified for a sample as the difference between the optimal total annualized cost TAC^* and the total annualized cost with the fixed low-regret decision TAC^{lrd}. Here, the maximum cost difference of one sample indicates the maximum regret $R^{\max}$, while the expected regret $\overline{R}$ denotes the average cost increase across all samples. For better interpretability, we introduce the maximum relative regret $R_{\%}^{\max}$, which is the maximum regret $R^{\max}$ divided by the optimal total annualized cost of the respective sample TAC^*. Furthermore, the expected relative regret $\overline{R}_{\%}$ is obtained as the ratio of the expected regret $\overline{R}$ related to the average total annualized cost in case of perfect foresight $\overline{TAC}^{\mathrm{PF}}$.

Table 1: Probability of regret $P(regret)$ as share of regret samples in all samples, average cost increase in case of regret $\overline{TAC}_{\text{loss}}$, maximum cost increase $TAC_{\text{loss}}^{\max}$, expected relative regret $\overline{R}_{\%}$, and maximum relative regret $R_{\%}^{\max}$ for the three identified low-regret decisions (LRD). As a reference, the total annualized cost TAC in case of perfect foresight is $\overline{TAC}^{\text{PF}} = 135.4$ MEuro.

	Components	$\boldsymbol{P(regret)}$	$\boldsymbol{\overline{TAC}_{\text{loss}}}$	$\boldsymbol{TAC_{\text{loss}}^{\max}}$	$\boldsymbol{\overline{R}_{\%}}$	$\boldsymbol{R_{\%}^{\max}}$
		[%]	[kEuro]	[kEuro]	[%]	[%]
LRD-1	$COM_{6\text{ bar}}$	9.6	2668	4487	0.19	3.1
LRD-2	$HS_{6\text{ bar}}$	34.3	39	820	0.01	0.6
LRD-3	$COM_{31\text{ bar}}$	52.1	4349	7054	1.67	5.1

3. Case Study

The method is applied to a case study of an industrial energy system supplying a typical chemical park with time-varying demands for 6-bar steam (1.64 TWh/a), 31-bar steam (1.55 TWh/a), and electricity (2.00 TWh/a) (Bauer et al., 2022) using the SecMOD MILP framework (Reinert et al., 2023). For the global sensitivity analysis, we vary the efficiency, investment, and maintenance costs of all components. Furthermore, we vary the energy prices, the interest rate, the economic payback period, and the energy demands. As a result, the optimization problem comprises 374 uncertain parameters, which are grouped into 53 uncertain parameters. For each group, the uncertainty is characterized. Subsequently, the parameter space is discretized by 30 trajectories, resulting in a total of 1590 samples. These 1590 samples are used to identify low-regret decisions.

4. Results

The case study identifies heat pumps and heat storage as low-regret decisions (Table 1). Specifically, a combined-cycle heat pump for the 6-bar steam line ($COM_{6\text{ bar}}$) with a capacity of 100 MW has no regret in 90 % of the samples. The combined-cycle heat pump comprises a subcritical heat pump and vapor re-compression unit. On the 31-bar steam line, a combined-cycle heat pump with a capacity of 100 MW ($COM_{31\text{ bar}}$) has no regret in 48 % of the samples. This 31-bar heat pump has a higher expected relative regret of 1.67 % and a maximum relative regret of 5.1 %. Furthermore, heat storage ($HS_{6\text{ bar}}$) shows no regret in 66 % of the samples, while both average and maximum relative regrets are low, 0.01 %, and 0.6 %, respectively. The small regret of the heat storage demonstrates the advantage of making the energy system more flexible.

Overall, all identified low-regret decisions for the three components have low expected and maximum cost increases. Thus, the proposed method identifies low-regret decisions for steam supply and can support decision-makers in accelerating the decarbonization of the chemical industry.

5. Conclusions

This study proposes a method to identify and quantify low-regret decisions for multi-energy systems. In this context, low-regret decisions refer to investment decisions that are economically near-optimal across a broad range of future scenarios. The method employs mathematical optimization and uncertainty analysis in four steps.

The method is applied to a case study of a multi-energy system with time-varying demands for 6-bar steam, 31-bar steam, and electricity. Therein, heat pumps and storage are identified as low-regret decisions with minimal overall cost increases.
In summary, the proposed method effectively identifies low-regret decisions for multi-energy systems. Thereby, the method provides valuable support to decision-makers in accelerating the decarbonization of the chemical industry.

Acknowledgments

N.N., F.B., A.B. acknowledge funding by the Swiss Federal Office of Energy's SWEET program as part of the project PATHFNDR. S.M. acknowledges support from the Swiss National Science Foundation under Grant no PZ00P2_202117. H.S. acknowledges support from the German Federal Ministry of Economic Affairs and Energy (ref. no.: 03EN2031A).

References

Bauer, T., Prenzel, M., Klasing, F., Franck, R., Lützow, J., Perrey, K., Faatz, R., Trautmann, J., Reimer, A., Kirschbaum, S., 2022. Ideal-Typical Utility Infrastructure at Chemical Sites – Definition, Operation and Defossilization. Chemie Ingenieur Technik 94 (6), 840–851. 10.1002/cite.202100164.

Moret, S., Codina Gironès, V., Bierlaire, M., Maréchal, F., 2017. Characterization of input uncertainties in strategic energy planning models. Applied Energy 202 (10), 597–617. 10.1016/j.apenergy.2017.05.106.

Reinert, C., Nolzen, N., Frohmann, J., Tillmanns, D., Bardow, A., 2023. Design of low-carbon multi-energy systems in the SecMOD framework by combining MILP optimization and life-cycle assessment. Computers & Chemical Engineering 172 (3), 108176. 10.1016/j.compchemeng.2023.108176.

Ruhnau, O., Bannik, S., Otten, S., Praktiknjo, A., Robinius, M., 2019. Direct or indirect electrification? A review of heat generation and road transport decarbonisation scenarios for Germany 2050. Energy 166, 989–999. 10.1016/j.energy.2018.10.114.

Saltelli, A., Ratto, M., Andres, T., Campolongo, F., Cariboni, J., Gatelli, D., Saisana, M., Tarantola, S., 2007. Global Sensitivity Analysis. The Primer. Wiley.

ESCAPE-34 PSE-2024
European Symposium on Computer Aided Process Engineering
&
Process Systems Engineering

Flavio Manenti, Gintaras V. Reklaitis (Eds.), Book of Abstract of the 34th European Symposium on Computer Aided Process Engineering / 15th International Symposium on Process Systems Engineering (ESCAPE34/PSE24), June 2-6, 2024, Florence, Italy.

Integrated Design of Renewable Fuel and Spark-Ignition Engine

Philipp Ackermann[a], Patrick Burkardt[b], Bastian Lehrheuer[b], Philipp Morsch[c], Karl Alexander Heufer[c], Alexander Mitsos[e,a,d], Stefan Pischinger[e,b], Manuel Dahmen[d]

[a]*Process Systems Engineering (AVT.SVT), RWTH Aachen University, Forckenbeckstr. 51, 52074 Aachen, Germany*
[b]*Chair of Thermodynamics of Mobile Energy Conversion Systems (TME), RWTH Aachen University, Forckenbeckstr. 4, 52074 Aachen, Germany*
[c]*Chair of High Pressure Gas Dynamics (HGD), RWTH Aachen University, Schurzelter Str. 35, 52074 Aachen, Germany*
[d]*Institute of Energy and Climate Research (IEK-10), Forschungszentrum Jülich GmbH, Wilhelm-Johnen-Straße, 52428 Jülich, Germany*
[e]*JARA Energy, Aachen Germany*
m.dahmen@fz-juelich.de

Abstract

Renewable fuels enable high efficiencies in spark-ignition engines. Their combustion properties allow to exploit advanced engine concepts for which conventional gasoline is not suitable, e.g., very high compression ratios and highly boosted conditions. Fuel design can identify such alternative fuels. So far, fuel design utilizes models of engine performance fitted to experiments using moderate engine conditions and conventional gasoline. This work proposes an integrated design approach utilizing an engine model fitted to and validated with measurement data of alternative fuels in an advanced single-cylinder research engine. Constraining volatility related properties, the optimal blend consists of methyl acetate and ethyl acetate and achieves a net indicated efficiency of 44% at high load engine operation. Without property constraints, the optimal blend consists of methyl acetate and methanol and achieves a net indicated efficiency of 45 %. In light of model uncertainties, the results require experimental validation.

Keywords: Renewable fuels, fuel design, integrated product and process design, engine model, engine efficiency.

1. Introduction

Computer-aided product design (CAPD) can identify alternative fuels that enable superior engine performance in specially built engines compared to that of conventional fuels in conventional engines. Typically, such alternative fuels are identified based on physico-chemical fuel properties and, in case of spark-ignition engines, the research octane

number (RON) is used as a proxy for high engine efficiency (Dahmen and Marquardt, 2016, McCormick et al. 2017). CAPD studies for other products, however, suggest that the method can be improved by integrating a model for the product use, for example in solvent design for chemical processes and in working fluid design for energy processes (Muhieddine et al., 2022, Neumaier et al., 2023). In recent years, such approaches have also been applied to fuel design. Specifically, fuels for spark-ignition engines have been designed for maximum engine efficiency, using empirical correlations or a thermodynamic engine model (Gschwend et al., 2019, vom Lehn et al., 2021, Fleitmann, Ackermann et al., 2023). In all these cases, the models contained parameters fitted to engine data of conventional fuels or blends of alternative fuels with conventional fuels. Since models for conventional fuels cannot reliably predict the occurrence of engine knock for alternative fuels, it is uncertain to which extent these models can be used to predict the engine performance of newly designed fuels.

2. Method

We present a CAPD method to design fuels by maximizing the achievable indicated efficiency in a zero-dimensional thermodynamic engine model that was calibrated and validated with experimental data from alternative fuels in a spark-ignition single-cylinder research engine with a compression ratio of 16.4. Importantly, we include ignition delay models derived from kinetic simulations to accurately predict the onset of knock. We maximize the indicated efficiency by optimizing the compression ratio, considering knock and peak pressure limitations. The engine model and optimization are implemented in MATLAB R2020a. To design an optimal multi-component fuel, we then select possible alternative fuel constituents known from previous studies. We enumerate binary and ternary blends and use MATLAB's local optimization solver fmincon to tailor the fuel composition for maximum indicated efficiency, utilizing the engine model with embedded optimization of the compression ratio. To design a fuel that is knock resistant under extreme conditions, we allow compression ratios of up to 20 and set the intake and exhaust pressure to 2 bar. Aiming for proper in-cylinder mixture formation, we constrain volatility-related fuel properties.

3. Results and Discussion

3.1. Fuel Design with Volatility Constraints

The design runs for 12 CPU hours on an Intel® Core™ i5-8500 processor with 16 GB RAM. The optimal blends achieve an indicated efficiency of 44%, which constitutes a relative increase of 17% over the efficiency that conventional gasoline achieves in the simulation with an optimized compression ratio and at an intake pressure of 1 bar. The three top blends contain large shares of methyl acetate and ethyl acetate. As a pure component, methyl acetate violates the upper limit on the enthalpy of vaporization, whereas ethyl acetate violates the lower limit on the bubble point pressure. The mixture balances both properties and thus is feasible regarding the imposed volatility constraints.

3.2. Fuel Design without Volatility Constraints

In a separate design run without volatility constraints, the optimal blend consists of 60 mol-% methyl acetate and 40 mol-% methanol and achieves a slightly higher predicted indicated efficiency of 45%. In the simulation, this blend outperforms its constituents as neat fuels by synergistically combining the charge cooling effect of methanol with the presumably higher knock resistance of methyl acetate. However, it should be noted that

for this binary blend, the change in indicated efficiency as a function of the composition is in the order of magnitude of the fitting error, i.e., the deviation between the experimental data that has been used for model calibration and the model output. Experimental investigations will be necessary to confirm the higher knock resistance of methyl acetate and the synergistic behavior of the blend. Model uncertainties can be caused by the reduced-order modeling approach as well as fuel specific inaccuracies introduced by the choice of sub-models for fuel dependant processes. For example, the used combustion sub-model does not account for the influence of fuel chemistry on the combustion process that influences the pressure trajectory and thus the efficiency. Similarly, the sub-model for the evaporation process influences the temperature trajectory and thus the onset of knock.

4. Conclusions

In conclusion, this study identifies alternative fuel blends for advanced spark-ignition engines. Future work could improve the sub-models for fuel evaporation and combustion processes, as well as quantify the uncertainty. Furthermore, the approach could be extended to design fuels for operation under lean conditions and pre-chamber applications to further increase the indicated efficiency of the engine.

References

M. Dahmen, W. Marquardt, 2016, Model-Based Design of Tailor-Made Biofuels, Energy & Fuels, 30, 2, 1109-1134

R. L. McCormick, G. Fioroni, L. Fouts, E. Christensen, J. Yanowitz, E. Polikarpov, K. Albrecht, D. J. Gaspar, J. Gladden, A. George, 2017, Screening of Potential Biomass-Derived Streams as Fuel Blendstocks for Advanced Spark-Ignition Engines, SAE International Journal of Fuels and Lubricants, 10, 2, 442-460

M. H. Muhieddine, S. K. Viswanath, A. Armstrong, A. Galindo, C. S. Adjiman, 2022, Model-based solvent selection for the synthesis and crystallisation of pharmaceutical compounds, Chemical Engineering Science, 264, 118125

L. Neumaier, D. Roskoch, J. Schilling, G. Bauer, J. Gross, A. Bardow, 2023, Refrigerant Selection for Heat Pumps: The Compressor Makes the Difference, Energy Technology, 11, 4, 2201403

D. Gschwend, P. Soltic, A. Wokaun, F. Vogel, 2019, Review and Performance Evaluation of Fifty Alternative Liquid Fuels for Spark-Ignition Engines, Energy & Fuels, 33, 3, 2186-2196

F. vom Lehn, L. Cai, R. Tripathi, R. Broda, H. Pitsch, 2021, A property database of fuel compounds with emphasis on spark-ignition engine applications, Applications in Energy and Combustion Science, 5, 12, 100018

L. Fleitmann, P. Ackermann, J. Schilling, J. Kleinekorte, J. G. Rittig, F. vom Lehn, A. M. Schweidtmann, H. Pitsch, K. Leonard, A. Mitsos, A. Bardow, M. Dahmen, 2023, Molecular Design of Fuels for Maximum Spark-Ignition Engine Efficiency by Combining Predictive Thermodynamics and Machine Learning, Energy & Fuels, 37, 3, 2213-2229

ESCAPE-34 PSE-2024
European Symposium on Computer Aided Process Engineering
&
Process Systems Engineering

Flavio Manenti, Gintaras V. Reklaitis (Eds.), Book of Abstract of the 34th European Symposium on Computer Aided Process Engineering / 15th International Symposium on Process Systems Engineering (ESCAPE34/PSE24), June 2-6, 2024, Florence, Italy.

Enhanced Fischer-Tropsch E-fuels from Solid Carbon and Captured CO_2

Juan D. Medrano-García[a], Marina T. Chagas[a], Gonzalo Guillén-Gosálbez[a,*]

[a]*Institute for Chemical and Bioengineering, Department of Chemistry and Applied Biosciences, ETH Zurich, Vladimir-Prelog-Weg 1, 8093 Zurich, Switzerland*
gonzalo.guillen.gosalbez@chem.ethz.ch

Abstract

Electro-fuels produced from electrolytic H_2 and captured CO_2 could play a key role in the sustainable energy transition as they could be directly deployed using current infrastructure. However, their high production costs, mainly due to the yet expensive green H_2, could hinder their further adoption. Here we propose an alternative configuration for Fischer-Tropsch e-fuels synthesis based on the coupling of the standard process with a reverse Boudouard (RB) reactor to reduce the H_2 requirements. Using process simulation, optimization, and life cycle assessment (LCA), our results suggest that the integration with the RB reactor could reduce the production costs by as much as 24%. Moreover, considering green H_2 from water electrolysis powered by wind energy, using biochar as feedstock alongside captured CO_2 could reduce the carbon footprint from -6 to -27 kg CO_2-eq per GJ of mixed e-gasoline, e-kerosene and e-diesel products. All in all, the RB reaction helps decrease H_2 usage, closing the gap towards economically competitive e-fuels.

Keywords: reverse Boudouard reaction, carbon capture and utilization, modeling and optimization, process integration, life cycle assessment (LCA)

1. Introduction

Electro-fuels (e-fuels) made with electrolytic H_2 and captured CO_2 share very similar properties with their fossil fuels counterparts (i.e., gasoline, kerosene and diesel) so they could be deployed with minimum changes in current infrastructure. Given that the transport sector was responsible for 21% of anthropogenic CO_2 emitted in 2022, such renewable fuels might be necessary for achieving the climate goals. However, due to the very high cost of electrolytic H_2, e-fuels are currently economically unappealing.
In the Fischer-Tropsch (FT) process using CO_2 as feedstock, CO_2 reduction to CO is carried out before the e-fuels are synthesized via the reverse water gas shift (RWGS) reaction (Medrano-García et al., 2022). This has the drawback of generating water as a by-product, thus consuming costly H_2 (Eq. (1)):

$$H_2 + CO_2 \leftrightarrow CO + H_2O \quad (1)$$

Alternatively, here we explore the integration of the reverse Boudouard (RB) reaction (Lahijani et al., 2015) in e-fuels production, where CO_2 combined with solid carbon at

high temperatures yields CO, thereby reducing the H_2 requirements in the overall process (Eq. (2)):

$$C + CO_2 \leftrightarrow 2CO \quad (2)$$

We study the integration of solid carbon gasification in the synthesis of FT e-fuels from direct air-captured (DAC) CO_2 and wind electrolytic H_2. We use process simulation and optimization, economic analysis and life cycle assessment (LCA) to evaluate two configurations differing in how they achieve the desired H_2/CO ratio of two before the FT reactor: the RWGS or the RB reaction. In addition, we consider two different solid carbon sources for the RB reaction: fossil coal and renewable biochar.

2. Methodology

In order to elucidate the potential benefits of the implementation of the RB reaction in e-fuels synthesis. We study three scenarios: the base case FT process coupled with an RWGS reactor, the base case using an RB reactor with biochar and the same configuration with coal as the solid carbon source.

The base case FT process starts by mixing the H_2 and CO_2 into an equilibrium RWGS reactor to produce the CO required for the e-fuels synthesis. After removing the water produced by condensation, the syngas mixture is sent to the FT reactor. This reactor is modeled using a kinetic model based on the growth factor parameter, where paraffins and olefins up to C_{1000} are considered to be formed (Hillestad, 2015). Then, waxes (C_{22+}) are separated, mixed with additional H_2 and sent to the hydrocracker (HC) reactor, where they are broken down into shorter chain hydrocarbons. This reactor is also modeled using a kinetic model (Bhutani et al., 2006). The lighter fraction of the FT reactor product (C_1 - C_4) is combusted with electrolytic O_2 to produce energy and recycle the CO_2 as feedstock, while the intermediate fraction C_5 - C_{21} is recovered as the main product (e-fuel mixture).

The RB scenario simulation substitutes the RWGS reactor with the RB reactor. Here, CO_2 is mixed with solid carbon and sent to the RB reactor (Dai et al., 2022). Unreacted carbon is recycled and the CO-rich stream is mixed with H_2 and sent to the FT reactor, while the rest of the process remains the same.

The simulation of the FT process is carried out in Aspen HYSYS v11 coupled with MATLAB in order to solve the kinetic models for the reactors. The flowsheet is optimized using the Particle Swarm Optimization (PSO) algorithm from MATLAB in order to minimize the total cost per GJ of e-fuel produced. The LCA is carried out following standard methodologies (ISO 14040/44). We consider a cradle-to-gate assessment using a cut-off attributional approach with a functional unit of 1 GJ of e-fuel. We include all upstream activities (background system), obtained from Ecoinvent v3.5, while the foreground system is modeled from the material and energy balances of the process simulation. The life cycle impact assessment (LCIA) was computed following the ReCiPe 2016 vs1.13 method and using Simapro v9.2.0.2.

3. Results

As shown in Figure 1, the RB configuration outperforms the RWGS in terms of both economics and carbon footprint. Regarding costs, a 24% reduction (from 82 $/GJ to 63 $/GJ of combined e-gasoline, e-kerosene and e-diesel) is observed when integrating the FT process with the RB reactor. Furthermore, the solid carbon source has barely any effect on the cost, as H_2 is still the dominant contribution. This drastic decrease is a

consequence of reducing CO_2 with solid carbon (Eq. (2)) instead of H_2 (Eq. (1)). From these results, we estimate that the minimum cost of H_2 needed for an economically competitive e-fuel production (48 $/GJ) is reduced by 33%, from 3 $ in the RWGS to 2 $/kg of H_2 in the RB configuration.

Regarding the environmental results, a decrease of 341 % (from -6 kg CO_2-eq/GJ to -27 kg CO_2-eq/GJ) in carbon footprint occurs when using biochar as the solid carbon source. This behavior is derived from biochar having lower embedded impacts than DAC CO_2, as it replaces part of the CO_2 as the carbon source for the e-fuels (Eq. (2)). However, an increase to 17 kg CO_2-eq/GJ is observed when using coal, due to the fossil nature of the raw material.

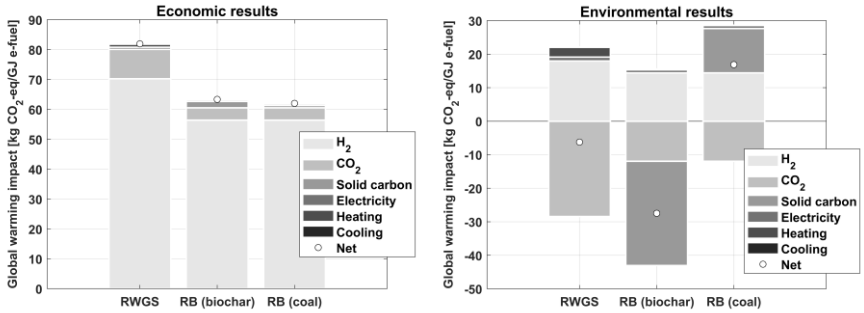

Figure 1. Results of FT e-fuels production under the different CO_2 reduction scenarios.

4. Conclusions

In this work, we studied the RB reaction as an alternative CO_2 reduction pathway in the synthesis of FT e-fuels. Our results show that this integration outperforms the standard RWGS reaction route both economically and environmentally mainly due to a reduction in H_2 usage in the process. Furthermore, the solid carbon source used in the RB dictates the environmental performance of the process but it plays a very minor role concerning the costs. These results promote the benefits of integrating the RB reaction, a well-known and studied reaction system, into e-fuels production by not only closing the economic gap with fossil fuels but also enhancing their already appealing environmental performance even more. All in all, this work paves the path to a cost-competitive energy transition through a more efficient H_2 usage in e-fuels production, with the potential of further facilitating a net-zero transport sector.

References

J.D. Medrano-García, M. A. Charalambous, G. Guillén-Gosálbez, 2022, Economic and Environmental Barriers of CO_2-Based Fischer-Tropsch Electro-Diesel, ACS Sustain. Chem. Eng, 10, 36, 11751-11759.

P. Lahijani, Z. A. Zainal, M. Mohammadi, A. R. Mohamed, 2015, Conversion of the greenhouse gas CO_2 to the fuel gas CO via the Boudouard reaction: A review, Renew. Sustain. Energy Rev., 41, 615-632.

M. Hillestad, 2015, Modeling the Fischer-Tropsch Product Distribution and Model Implementation, Chem. Prod. and Process Model., 10(3), 147–159.

N. Bhutani, A. K. Ray, G. P. Rangaiah, Modeling, Simulation, and Multi-objective Optimization of an Industrial Hydrocracking Unit, Ind. & Eng. Chem. Res., 45, 4, 1354–1372

Huan Dai, H. Zhao, S. Chen, B. Jiang, 2021, A Microwave-Assisted Boudouard Reaction: A Highly Effective Reduction of the Greenhouse Gas CO_2 to Useful CO Feedstock with Semi-Coke, Molecules, 26, 1507.

ESCAPE-34 PSE-2024
European Symposium on Computer Aided Process Engineering
&
Process Systems Engineering

Flavio Manenti, Gintaras V. Reklaitis (Eds.), Book of Abstract of the 34th European Symposium on Computer Aided Process Engineering / 15th International Symposium on Process Systems Engineering (ESCAPE34/PSE24), June 2-6, 2024, Florence, Italy.

Process Design of Hybrid Temperature-antisolvent Crystallization Powered by Machine Learning

Luca Bosetti, Benedikt Winter, Andreas Locher, Lisanne Wittenberg, André Bardow

Energy & Process Systems Engineering, Department of Mechanical and Process Engineering, ETH Zürich, Tannenstrasse 3, 8092 Zurich, Switzerland.

abardow@ethz.ch

Abstract

The chemical industry's pursuit of a net-zero future necessitates energy-efficient separation technologies, with crystallization emerging as a potential solution due to its low energy requirements and ability to achieve high purities. However, the design of crystallization processes is hindered by the need for thermodynamic properties, which are usually obtained through expensive and time-intensive experiments. This study utilizes machine learning, specifically the SMILES to Properties Transformer (SPT) model, originally trained for estimating activity coefficients for vapor-liquid equilibria (Winter et al. 2023), to predict essential quantities for crystallization process development. Focused on the hybrid temperature-antisolvent crystallization of ibuprofen, a pharmaceutical-relevant system, this research showcases a novel design framework that identifies suitable solvents and operating conditions, supporting the efficient and sustainable development of crystallization processes.

Keywords: machine learning, thermodynamic property prediction, sustainable processes, computer-aided process design

1. Introduction

The global transition toward a net-zero economy necessitates the development of highly efficient and sustainable processes. Therein, separating components from complex mixtures has a critical and often economically burdensome role, particularly in the pharmaceutical and chemical sectors (Alder et al. 2016). To address the challenge of developing environmentally and economically favorable separations, computer-aided tools for process design are increasingly used. These tools empower the exploration of a broad space of process alternatives, facilitating the identification of feasible, environmentally friendly, and cost-effective pathways (Papadopoulos et al. 2018).

As a candidate separation technology, crystallization is particularly promising since it is usually operated at or near ambient temperatures while delivering solid products at high purity (Myerson 2002). Within the chemical and pharmaceutical industry, crystallization

frequently serves as a final purification step, as exemplified by the styrene recycling process (Khandelwal 2022). Developing an efficient crystallization process requires a comprehensive understanding of the thermophysical properties associated with pure components and their interactions within mixtures. In particular, crystallization by an anti-solvent relies on accurate activity coefficients as well as enthalpies to achieve optimal process performance. If experimental data are unavailable or too expensive to attain, relying on predictive methods is the only alternative (Watson et al. 2022, Wang et al. 2020). The recent advent of modern machine learning models holds potential to overcome the lack of data requirements. However, the applicability of machine learning models for crystallization process design is currently unclear, although machine learning holds promise in improving design capabilities and promoting the adoption of crystallization as an efficient and sustainable process.

The present study analyzes a hybrid temperature-antisolvent crystallization process, where thermophysical properties are predicted by a machine-learning model (SMILES to Properties Transformer, SPT) (Winter et al. 2022, Winter et al. 2023). The use of a machine-learning algorithm with remarkable performance provides the possibility to systematically screen an extensive number of antisolvents and temperature levels. This screening approach enables the exploration of many process alternatives, which was hardly possible with conventional property prediction methods, and experimentally impossible. The final goal of the application of machine learning to property predictions is to screen many process alternatives, including the molecular degrees of freedom. Such an approach leads us to pinpoint energy-efficient, cost-effective and sustainable solutions, thereby facilitating the transition of the chemical and pharmaceutical industry toward a net-zero future.

2. Methods

Crystallization processes are based on the knowledge of the solid-liquid equilibrium. In crystallization, we define the "solute" as the component that we would like to crystallize, while "solvent" and "antisolvent" as the components that remain in the liquid phase. The expression for solubility can be derived from the chemical potential of the liquid and the solid phases and is most commonly employed in its simplified form as (Watson et al. 2021):

$$\ln(x_{\mathrm{sol}}^{\mathrm{L}}\gamma_{\mathrm{sol}}^{\mathrm{L}}) = \frac{-\Delta H_{\mathrm{sol}}^{\mathrm{fus}}}{R}\left(\frac{1}{T}-\frac{1}{T_{\mathrm{sol}}^{\mathrm{m}}}\right) \qquad (1)$$

where $x_{\mathrm{sol}}^{\mathrm{L}}$ is the liquid-phase molar fraction of the solute, $\gamma_{\mathrm{sol}}^{\mathrm{L}}$ is the liquid-phase activity coefficient, T is the process's operating temperature, $T_{\mathrm{sol}}^{\mathrm{m}}$ is the melting temperature of the solute, and $\Delta H_{\mathrm{sol}}^{\mathrm{fus}}$ is the enthalpy of fusion of the solute. It is worth noting that the liquid-phase activity coefficient depends on the composition of the liquid phase, thus the equilibrium mole fraction $x_{\mathrm{sol}}^{\mathrm{L}}$ is obtained by implicitly solving equation (1).

The melting temperature and the enthalpy of fusion are pure component properties of the solute. Such properties should be known for components that need to be crystallized but are not always available in the early stages of development. Thus, we trained SPT to predict those properties. About 28'000 datapoints have been used as training data for the melting temperature, which were taken from Bradley et al. (2014). For the training on enthalpies of fusion, about 8800 datapoints were taken from Acree and Chickos 2016 and 2017. The activity coefficients are also predicted with SPT, which has been trained on

vapor-liquid equilibrium data from the DDB (Dortmund Databank 2022), and from Brouwer et al. 2021, for a total of 200 000 datapoints for 800 components (Winter et al. 2023).

In the study, we assume a valuable solute dissolved in a solvent: the driving force of the process results from the variation of the temperature of the process, and from the addition of antisolvent to the system. The temperature at which the crystallizer is operated, the molecule used as antisolvent and the quantity of antisolvent used are treated as degree of freedom in the design process. The antisolvents are screened subject to the following constraints:

- the antisolvents should be liquid in a defined temperature range, i.e., $T_{\text{antisolv}}^{\text{boil}} > T_{\max}$ and $T_{\text{antisolv}}^{\text{melt}} < T_{\min}$, with $T_{\min}$ and $T_{\max}$ the minimum and maximum operating temperatures, respectively.
- the selected antisolvent shall not form any liquid phase split with the solvent considered.

For the estimation of the boiling point and of the liquid-liquid equilibrium, the SPT model has been trained to predict Antoine's parameters (Winter et al, *in preparation*), and NRTL parameters, respectively (Winter et al. 2023). Key parameters to target sustainability are the yield of the product, the operation temperature of the reactor, the amount of antisolvent used, and the type of solvents used, according to Alder et al. 2016.

As a case study, we regard ibuprofen as the solute, ethanol as a solvent, and we screen different antisolvents to check for favorable crystallization conditions.

3. Results

The machine learning model SPT has been trained to predict melting temperatures and enthalpies of fusion. The predicted melting temperatures present a mean average error (MAE) of 29.3K for a total of 28'000 pure components, while the MAE for predicted enthalpies of fusion is 5.6 kJ/mol for a total of 8800 components. Experimental measurements should always be used if data are available, but SPT gives the possibility to broaden the design space by predicting properties not available from experiments.
The next step in predicting solid-liquid equilibrium is solving Equation 1 for the mole fraction of the components at equilibrium. The activity coefficients used are those obtained from training on vapor-liquid equilibrium (Winter et al. 2023). The predictions of solid-liquid equilibria for the case study of ibuprofen-ethanol-water are presented in Figure 1 for two temperature levels (solid lines). The dashed lines in Figure 1 refer to the values reported in Watson et al. 2021, who predicted activity coefficients with SAFT-γ Mie.

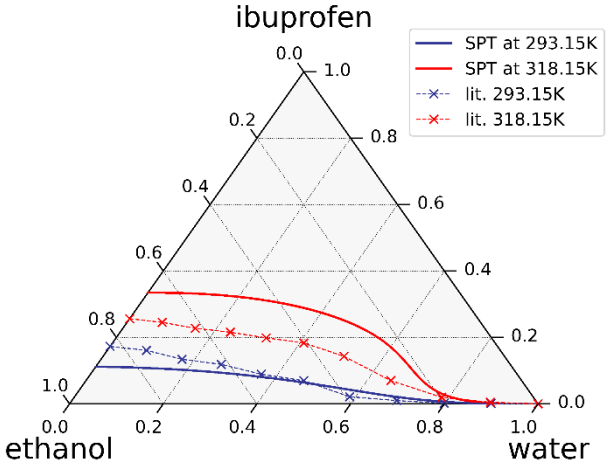

Figure 1. Ternary diagram of ibuprofen-ethanol-water system. The solid lines represent the solid-liquid equilibria at two temperature levels predicted with SPT. The dashed lines represent the corresponding literature data taken from Watson et al. 2022.

The solid-liquid equilibrium lines predicted by SPT correctly capture the temperature trend and the characteristic shape of the concentration profile. It is worth noting that SPT was originally trained on VLE data, so the relatively accurate results of SLE are very promising. Further training of the model on SLE data is expected to increase the accuracy of the predictions, but experimental data for solute-solvent-antisolvent mixtures at different temperatures are rare or not readily accessible.

4. Conclusions

Crystallization processes stand as a promising separation technique, offering innovative solutions to address the evolving demands of the pharmaceutical and chemical industries while striving for sustainability. The successful modeling of a hybrid temperature-antisolvent crystallization process necessitates a comprehensive characterization of the system, particularly the knowledge of the key pure component properties, e.g., melting temperatures and enthalpies of fusion, as well as mixture properties, e.g., activity coefficients.

The application of the machine-learning model SPT to crystallization presents a significant advancement in this context. SPT can be trained for melting properties, specifically melting temperatures and enthalpies of fusion, while also predicting activity coefficients, Antoine's parameters and NRTL parameters. Notably, the solid-liquid equilibria predictions derived from SPT consistently align with the temperature and concentration trends established in the existing literature. This development provides the basis for improved design of crystallization processes.

Acknowledgment: The project leading to this application has received funding from the European Union's Horizon 2020 research and innovation programme under grant agreement No 101036854.

References

Acree, W., Chickos, J. S. (2016). Phase transition enthalpy measurements of organic and organometallic compounds. Sublimation, vaporization and fusion enthalpies from 1880 to 2015. Part 1. C1− C10. *Journal of Physical and Chemical Reference Data*, 45(3).

Acree, W., Chickos, J. S. (2017). Phase transition enthalpy measurements of organic and organometallic compounds and ionic liquids. Sublimation, vaporization, and fusion enthalpies from 1880 to 2015. Part 2. C11–C192. *Journal of Physical and Chemical Reference Data*, 46(1).

Alder, C. M., Hayler, J. D., Henderson, R. K., Redman, A. M., Shukla, L., Shuster, L. E., Sneddon, H. F. (2016). Updating and further expanding GSK's solvent sustainability guide. *Green Chemistry*, 18(13), 3879-3890.

Bradley, J. C., Lang, A., Williams, A. Jean-Claude Bradley double plus good (highly curated and validated) melting point dataset (2014). https://doi.org/10.6084/m9.figshare.1031638.v1, checked on 10/11/2023.

Brouwer, T., Kersten, S. R., Bargeman, G., Schuur, B. (2021). Trends in solvent impact on infinite dilution activity coefficients of solutes reviewed and visualized using an algorithm to support selection of solvents for greener fluid separations. *Separation and purification technology*, 272, 118727.

Dortmund Datenbank (2022). Available online at http://www.ddbst.com/, updated on 2022, checked on 2/6/2022.

Khandelwal, R. (2022). SuRe Styrene: a sustainable process to recover Ultra High Purity Styrene from waste polystyrene via chemical recycling. Sulzer Ltd 2022.

Meys, R., Kätelhön, A., Bachmann, M., Winter, B., Zibunas, C., Suh, S., Bardow, A. (2021). Achieving net-zero greenhouse gas emission plastics by a circular carbon economy. *Science*, 374(6563), 71-76.

Myerson, A. (2002). Handbook of industrial crystallization. Butterworth-Heinemann.

Papadopoulos, A. I., Tsivintzelis, I., Linke, P., Seferlis P. (2018) Computer-Aided Molecular Design: Fundamentals, Methods, and Applications. In: Reedijk, J. (Ed.) Elsevier Reference Module in Chemistry, Molecular Sciences and Chemical Engineering. Waltham, MA: Elsevier.

Wang, J., Zhu, L., Lakerveld, R. (2020). A hybrid framework for simultaneous process and solvent optimization of continuous anti-solvent crystallization with distillation for solvent recycling. *Processes*, 8(1), 63.

Watson, O. L., Jonuzaj, S., McGinty, J., Sefcik, J., Galindo, A., Jackson, G., Adjiman, C. S. (2021). Computer aided design of solvent blends for hybrid cooling and antisolvent crystallization of active pharmaceutical ingredients. *Organic Process Research & Development*, 25(5), 1123-1142.

Winter, B., Winter, C., Schilling, J., Bardow, A. (2022). A smile is all you need: predicting limiting activity coefficients from SMILES with natural language processing. *Digital Discovery*, 1(6), 859-869.

Winter, B., Winter, C., Esper, T., Schilling, J., Bardow, A. (2023). SPT-NRTL: A physics-guided machine learning model to predict thermodynamically consistent activity coefficients. *Fluid Phase Equilibria*, 568, 113731.

ESCAPE-34 PSE-2024
European Symposium on Computer Aided Process Engineering
&
Process Systems Engineering

Flavio Manenti, Gintaras V. Reklaitis (Eds.), Book of Abstract of the 34th European Symposium on Computer Aided Process Engineering / 15th International Symposium on Process Systems Engineering (ESCAPE34/PSE24), June 2-6, 2024, Florence, Italy.

Stability and Fairness in Unconstrained Multi-Actor Heat Integration Problems

Fabian Lechtenberg[a], Antonio Espuña[a], Moisès Graells[a*]

[a]*Department of Chemical Engineering, Universitat Politècnica de Catalunya, Barcelona, Spain*
moises.graells@upc.edu

Abstract

This work explores the application of cooperative game theory to multi-actor heat integration, focusing on unconstrained 3-player situations. A stability proof is given, paving the way for general stability proofs in N-player settings. The findings reveal that stable profit distribution is achievable in collaborative heat integration projects, in the case of unconstrainted integration potential. The study highlights the influence of key parameters on profit allocation, like the minimum temperature difference (ΔT_{min}), emphasizing the need for optimal alignment of efficiency and equity. This research offers crucial insights for process integration decision-makers, promoting sustainable and fair multi-actor collaborations.

Keywords: game theory, multi-actor heat integration, stability proof, profit distribution

1. Introduction

Process Integration (PI) has long been recognized as a key strategy in enhancing the efficiency of resource and equipment usage within the industrial sector. Traditionally limited to intra-company operations, PI has primarily focused on optimizing within a single company's boundaries. Current trends like globalization and the push for more efficient solutions based on industrial symbiosis have shifted the focus towards a broader scope, encompassing resource exchange and equipment sharing across company boundaries. This expansion significantly increases the potential for integration but also introduces the challenge of collaborative dynamics. Questions arise about the existence of **stable** agreements and the **fair** distribution of profits among participants. These concepts are essential to ensure the feasibility of sustainable collaborative relationships within the process industry. As a result, the Process Systems Engineering (PSE) community has started to explore these complexities through the lens of Game Theory.

Notable examples include Hiete et al. (2012) who applied the Shapley Value for profit distribution in a 3-company heat exchange network, Cheng et al. (2014) who used a sequential approach integrating Nash equilibrium for trade price and network structure decisions, and Jin et al. (2018) who incorporated risk factors using a modified Shapley Value to account for uncertainties in coalition stability. These studies have successfully demonstrated the application of cooperative Game Theory concepts in multi-actor process

integration scenarios, providing valuable frameworks for decision-makers to reach sustainable agreements.
However, the stability criterion, which is crucial for rational decision-making, is not addressed properly. While a couple of work such as Jin et al. (2018) illustrate the existence of stable agreements through the core constraints, the novelty of this work lies in the demonstration of a stability proof for a subset of process integration problems.
Furthermore, within the realm of stable profit allocations, the selection of a concrete allocation method is usually not well justified. For instance, the most popular Shapley value is often employed, despite its well-known caveat of not guaranteeing stable allocations. Thus, this work demonstrates the use of alternative methods, and elucidates the impact of process parameters of the PI problem on the outcome.

2. Problem Statement

This study focuses on two key aspects of the 3-player heat integration problem in a cooperative system:

Stability *in the solution of unconstrained 3-player heat integration problems*:
The objective is to prove that a stable profit distribution is always achievable in a 3-player heat integration scenario without integration constraints (e.g. limited total heat exchange area or piping length). This proof is crucial for the theoretical basis of collaborative PI projects, ensuring predictability and stability in profit sharing.

Fairness *of the impact of allocation methods and dependence on the design parameters*:
Following the establishment of stability, the study examines how the minimum temperature difference (ΔT_{min}) affects profit distribution in the PI problem.

3. Stability Proof of 3-Player Unconstrained Heat Integration

A transferable utility (TU) game is defined by a pair $\langle N, v \rangle$ where:

- $N = \{1,2, \dots, n\}$ is a finite set of players
- $v: 2^N \rightarrow \mathbb{R}$ is a characteristic function which assigns a real number to each subset (coalition) of N, representing the total value the coalition can create.

In the context of a 3-player heat integration problem the players can be denoted as $N = \{A, B, C\}$. The characteristic function for the profit allocation case can be written as:

$$v(A) = v(B) = v(C) = 0 \qquad \begin{matrix} v(A,B) = p_{AB} \\ v(A,C) = p_{AC} \\ v(B,C) = p_{BC} \end{matrix} \qquad v(A,B,C) = p_{ABC}$$

Single-player profits are, by definition, zero; p_{AB}, p_{AC}, and p_{BC} are the 2-player profits, and p_{ABC} is the profit of the 3-player grand coalition. For the sake of brevity, the proof of super-additivity is omitted here, but it can be taken for granted that in process integration problems the grand coalition has always the best value, since rejecting the collaboration and returning to the standalone operation is always an option.

The feasible set of profit allocations that satisfy the core constraints can be interpreted as the set of stable allocations where no player has the incentive to deviate from the grand coalition to ensure a better outcome. This property is important to ensure that rational decision-makers will converge towards an outcome which grants them a level of confidence that is required for planning and design decisions. For a 3-player profit allocation situation the conditions for stability reduce to the following set of constraints:

$$x_A, x_B, x_C \geq 0 \tag{1}$$

$$x_A + x_B \geq p_{AB}\ , x_A + x_C \geq p_{AC}, x_B + x_C \geq p_{BC} \qquad (2), (3), (4)$$

$$x_A + x_B + x_C = p_{ABC} \qquad (5)$$

Where x_A, x_B, and x_C are the profits allocated to the players. Equations (1) are the individual rationality constraints, ensuring that no player receives a worse payoff compared to working alone. In a similar fashion, Equations (2) – (4) are the group rationality constraints, ensuring that no subcoalition exists which can distribute the profit to ensure a better payoff to a subgroup of players. Finally, Equation (5) is the efficiency condition, which ensures that exactly the maximum profit of the grand coalition is distributed among the players.

These constraints can be illustrated in a ternary diagram of side length p_{ABC}. Each point within the diagram is an efficient allocation, and if it lies within the area enclosed by the rationality constraints it is a stable allocation. From this diagram, the conditions for the non-existence of stable allocations can be derived.

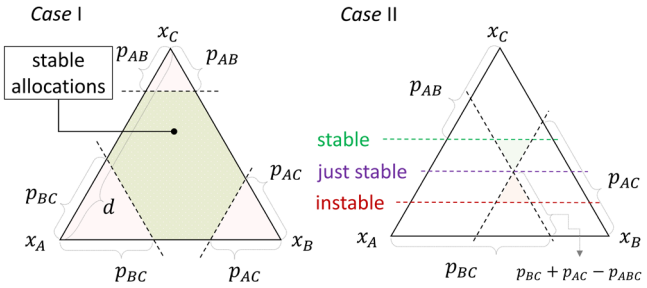

Figure 1. Geometric representation of stability in 3-player profit allocation problems.

Case I:

In the case that $p_{AB} + p_{AC} < p_{ABC}$, $p_{AB} + p_{BC} < p_{ABC}$, and $p_{AC} + p_{BC} < p_{ABC}$ it is evident that the area enclosed by the constraints is a six sided area that contains stable allocations.

Case II:

Assuming that at least for one of the sides (e.g. p_{AC} and p_{BC}) the situation arises that that the sum of the 2-player profits exceeds the profit of the grand coalition (e.g. $p_{AC} + p_{BC} \geq p_{ABC}$) the condition on the profit of the remaining coalition (e.g. p_{AB}) for the non-existence of a stable allocation set can be graphically derived. Figure 1 (right) illustrates this for the case of one side and can be written as:

$$p_{AB} > p_{ABC} - (p_{AC} + p_{BC} - p_{ABC}) \Leftrightarrow 2 \cdot p_{ABC} < p_{AB} + p_{AC} + p_{BC} \qquad (6)$$

For the sake of brevity, this derivation deals with the simplest case of profit determination based on utility cost minimization, considering only a single heating and cooling utility, available at sufficiently high and low temperatures. Denoting the heat balance as shown in Figure 2 the problem can be written for a single company as:

$$\min_{\dot{Q}_z^H, \dot{Q}_z^C \dot{Q}_z} cost = c^{Hot} \cdot \sum_z \dot{Q}_z^{Hot} + c^{Cold} \cdot \sum_z \dot{Q}_z^{Cold} \qquad (7)$$

$$0 = \sum_h \Delta\dot{H}_{h,z}^{Hot} + \dot{Q}_z^{Hot} - \sum_c \Delta\dot{H}_{c,z}^{Cold} - \dot{Q}_z^{Cold} + \dot{Q}_{z-1} - \dot{Q}_z \qquad \forall z \qquad (8)$$

$$\dot{Q}_0 = \dot{Q}_{zmax} = 0 \qquad (9)$$

$$\dot{Q}_z^{Hot}, \dot{Q}_z^{Cold}, \dot{Q}_z \geq 0 \qquad \forall z \qquad (10)$$

Where h is the set of hot streams and c is the set of cold streams available in the company's process system. The set z discretizes the heating and cooling demands $\Delta\dot{H}_{h,z}^{H}$ and $\Delta\dot{H}_{c,z}^{C}$ into z_{max} temperature intervals. The external heating and cooling utilities $\dot{Q}_z^H$ and $\dot{Q}_z^C$ are also discretized into these intervals. In the objective function, these utilities are summed up and multiplied with the respective utility cost c^H and c^C to yield the final utility cost function. The heat transfer of higher temperature intervals to lower temperature intervals is modelled via the variable $\dot{Q}_z$ which is set to zero for the highest and lowest interval, as there are no available streams to receive from or transfer heat to.

A global optimum of this optimization problem exists and will be denoted as $cost^*$. With this, the profit maximization problem of a 2-player coalition can be written as:

$$\max_{\dot{Q}_z^H, \dot{Q}_z^C \dot{Q}_z} \begin{aligned} p_{AB} = cost^{*(A)} - \left(c^{Hot,A} \cdot \textstyle\sum_z \dot{Q}_z^{Hot,A} + c^{Cold,A} \cdot \sum_z \dot{Q}_z^{Cold,A}\right) + \\ cost^{*(B)} - \left(c^{Hot,B} \cdot \textstyle\sum_z \dot{Q}_z^{Hot,B} + c^{Cold,B} \cdot \sum_z \dot{Q}_z^{Cold,B}\right) \end{aligned} \quad (11)$$

$$0 = \textstyle\sum_{hA} \Delta\dot{H}_{hA,z}^{Hot,A} + \dot{Q}_z^{Hot,A} - \sum_{cA} \Delta\dot{H}_{cA,z}^{Cold,A} - \dot{Q}_z^{Cold,A} + \dot{Q}_{z-1}^{(A)} - \dot{Q}_z^{(A)} + \boldsymbol{Q_z^{(A,B)}} - \boldsymbol{Q_z^{(B,A)}} \quad \forall z \quad (12)$$

$$0 = \textstyle\sum_{hB} \Delta\dot{H}_{hB,z}^{Hot,B} + \dot{Q}_z^{Hot,B} - \sum_{cB} \Delta\dot{H}_{cB,z}^{Cold,B} - \dot{Q}_z^{Cold,B} + \dot{Q}_{z-1}^{(B)} - \dot{Q}_z^{(B)} - \boldsymbol{Q_z^{(A,B)}} + \boldsymbol{Q_z^{(A,B)}} \quad \forall z \quad (13)$$

$$\dot{Q}_0^{(A)} = \dot{Q}_0^{(B)} = \dot{Q}_{zmax}^{(A)} = \dot{Q}_{zmax}^{(B)} = 0 \quad (14)$$

$$\dot{Q}_z^{(1)}, \dot{Q}_z^{(2)}, \dot{Q}_z^{Hot,A}, \dot{Q}_z^{Hot,B}, \dot{Q}_z^{Cold,A}, \dot{Q}_z^{Cold,B}, \boldsymbol{Q_z^{(B,A)}}, \boldsymbol{Q_z^{(A,B)}} \geq 0 \quad \forall z \quad (15)$$

This optimization problem introduces coupling variables $Q_z^{(A,B)}$ and $Q_z^{(B,A)}$ which enable the heat transfer between companies A and B as indicated in Equation (12). When forced to zero, the optimization problem can be decoupled into the two subproblems (see also Figure 3). Since these variables are introduced as positive reals, their inclusion may only improve the solution. Denoting the 2-player profit solution as p_{AB}, it can be reasoned that:

$$p_{AB} \geq p_A + p_B \quad (16)$$

For the sake of brevity, here the derivation for the 3-player condition is not formally conducted in full length, but the reasoning can be followed. Introducing player C, counterparts A^*, B^*, and C^*, and the coupling variables $Q_z^{(A^*,B^*)}$, $Q_z^{(B^*,A^*)}$, $Q_z^{(B,C)}$, $Q_z^{(C,B)}$, $Q_z^{(C^*,A)}$, and $Q_z^{(A,C^*)}$ yields a particular structure. This problem may be expressed as summation of the three two player situations (A, B), (C, A^*), and (B^*, C^*). But similar to the reasoning of the two player case, the coupling variables connect these problems to yield, in this case, twice the problem of (A, B, C). This is supported by the idea that the most economical solution to transfer heat from one player to another should be via the least amount of heat exchangers possible. For example, A can directly exchange heat with B, so there is no incentive to go the long way to exchange heat with B^*, which offers the same synergies with A as B. From this, it is possible to derive the relationship of the corresponding 3-player game:

$$2 \cdot p_{ABC} \geq p_{AB} + p_{AC} + p_{BC} \quad (17)$$

Equation (17) is in direct contradiction with the necessary condition for instability derived in Equation (6), proving the proposition.

□

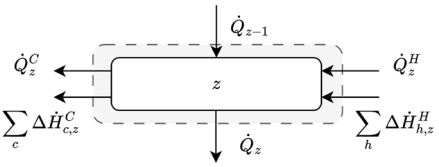

Figure 2. Energy balance for each temperature interval.

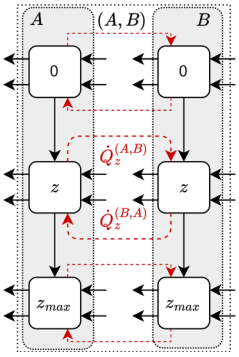

Figure 3. Division of multi-actor heat integration problems into subproblems.

However, if there are constraints on the process integration potential, e.g. via capacity constraints on the equipment that enables the integration, there is no guarantee of stability, as shown for instance in the case of constrained boiler capacity in the work of Lechtenberg et al. (2023).

4. Fairness of Allocation Methods and Design Parameters

With stability as an established baseline, the focus of this section lies on the fairness of allocation methods and the impact of design parameters in process integration on the outcome of profit allocation. The selection of allocation methods poses a significant challenge due to their varying notions of fairness. This is exemplified by the work of Chin et al. (2021), who have proposed and applied different methods in water integration problems. The difficulty lies in choosing the most suitable method from a set of stable allocations, a process akin to multi-criteria decision making (Grierson, 2008). To illustrate this, the problem presented by Jin et al. (2018) has been solved using four different allocation methods, employing the pyCoopGame python package, similar to the approach in Lechtenberg et al. (2023). The results, as shown in Figure 4, reveal significant variations in profit distribution based on the selected method, with each plant showing a preference for a different allocation method.

Additionally, the design parameter ΔT_{min} plays a critical role in determining the optimum balance between utility and investment cost for each company. In the study by Jin et al. (2018), which builds upon Yee and Grossmann et al. (1990), the optimum ΔT_{min} for each company was identified as unusually low (1.5K, 1.2K, and 1.7K). However, when a global ΔT_{min} of 10K was fixed, it led to two main consequences: a very different profit potential, directly resulting from the different compromise, and a biased relative profit allocation among the companies. This effect is demonstrated in Figure 4, which shows how different ΔT_{min} settings impact individual and grand coalition cost: A higher ΔT_{min}, i.e. further away from the optimal individual ΔT_{min}, is associated to a higher collaborative cost saving potential (543×10^3\$ for 15K). Specifying ΔT_{min} closer to the optimum balance, the integration potential of the standalone cases outpaces the collaborative integration potential, resulting in less profit to be shared among the participants (380×10^3\$ for 1K). From this it can be concluded that the coalition formation may, to some extent, make up for inefficient designs derived in the process integration problem. However, from a utilitarian perspective, such inefficiencies should be avoided from the very beginning. Traditionally, exclusively economics are used for decision-making in profit allocation. Future work should investigate how sustainability indicators may be utilized in the collaborative decision-making process to agree upon a definite solution.

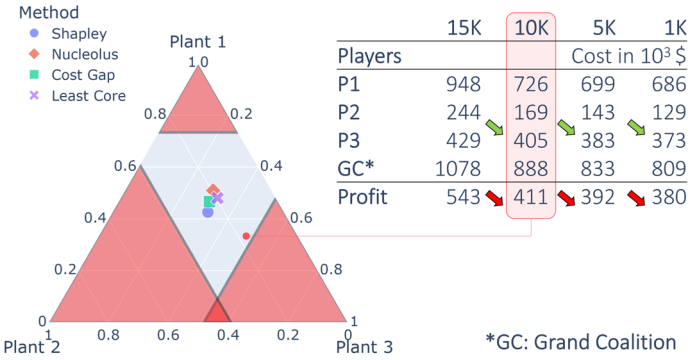

	15K	10K	5K	1K
Players			Cost in 10^3 $	
P1	948	726	699	686
P2	244	169	143	129
P3	429	405	383	373
GC*	1078	888	833	809
Profit	543	411	392	380

Figure 4. Profit allocation methods applied to the problem of Jin et al. (2018). The ternary diagram illustrates the shares of the total profit for the base case. The table shows the standalone and grand coalition cost and profit for varying ΔT_{min}.

5. Conclusions

This study provides a proof for stability in a subset of multi-actor process integration problems. This result is crucial for filling a gap often overlooked in previous research and paves the way for broader future proofs in collaborative profit allocation. Key findings highlight the significance of the ΔT_{min} parameter in determining both absolute and relative profits in process integration. Aligning ΔT_{min} with each participant's optimal level is essential to avoid inefficiencies and ensure fair allocations.

The stability proof offered here instills confidence in multi-actor process integration projects, assuring a degree of predictability and reliability. While the selection of allocation methods requires further research, guiding the choice of integration parameters with process engineering insights can lead to equitable and sustainable solutions, which is essential for the solutions to be accepted and implemented by all stakeholders.

Acknowledgements

Grant PID2020-116051RB-I00 (CEPI) funded by MCIN/AEI/10.13039/501100011033 and by "ERDF A way of making Europe" is fully acknowledged. Fabian Lechtenberg gratefully acknowledges the "Departament de Recerca i Universitats de la Generalitat de Catalunya" for the financial support of his predoctoral grant FI-2022.

References

S.-L. Cheng, C.-T. Chang, D. Jiang, 2014, A game-theory based optimization strategy to configure inter-plant heat integration schemes, Chemical Engineering Science, 118, 60–73

H. H. Chin, P. S. Varbanov, J. J. Klemeš, S. Bandyopadhyay, 2021, Subsidised water symbiosis of eco-industrial parks: A multi-stage game theory approach, Computers & Chemical Engineering, 155, 107539

D. E. Grierson, 2008, Pareto multi-criteria decision making, Advanced Engineering Informatics, 22(3), 371–384

M. Hiete, J. Ludwig, F. Schultmann, 2012, Intercompany Energy Integration: Adaptation of Thermal Pinch Analysis and Allocation of Savings, Journal of Industrial Ecology, 16(5), 689–698

Y. Jin, C.-T. Chang, S. Li, D. Jiang, 2018, On the use of risk-based Shapley values for cost sharing in interplant heat integration programs, Applied Energy, 211, 904–920

F. Lechtenberg, A. Espuña, M. Graells, 2023, Profit Allocation in Industrial Symbiosis Networks: Utility Exchanges, In A. C. Kokossis, M. C. Georgiadis, & E. Pistikopoulos (Eds.), Computer Aided Chemical Engineering, 961–966

T. F. Yee, I. E. Grossmann, 1990, Simultaneous optimization models for heat integration—II. Heat exchanger network synthesis, Computers & Chemical Engineering, 14(10), 1165–1184

ESCAPE-34 PSE-2024
European Symposium on Computer Aided Process Engineering
&
Process Systems Engineering

Flavio Manenti, Gintaras V. Reklaitis (Eds.), Book of Abstract of the 34th European Symposium on Computer Aided Process Engineering / 15th International Symposium on Process Systems Engineering (ESCAPE34/PSE24), June 2-6, 2024, Florence, Italy.

Total Site Integration for Non-Continuous Sites: Leveraging Machine Learning & Mathematical Programming

Timothy Gordon Walmsley,[a*] Keegan K. Hall,[a] Jasper V.M. Walden,[b] Andreja Nemet [c]

[a]*Ahuora – Centre for Smart Energy Systems, School of Engineering, University of Waikato, Hamilton 3240, New Zealand*
[b]*German Aerospace Center (DLR), Institute of Low-Carbon Industrial Processes, Simulation and Virtual Design, Walther-Pauer-Straße 5, Cottbus, 03046, Brandenburg, Germany*
[c]*Faculty of Chemistry and Chemical Engineering, University of Maribor, Smetanova ulica 17, 2000 Maribor, Slovenia*
tim.walmsley@waikato.ac.nz

Abstract

This study explores the enhancement of Total Site Integration (TSI) for non-continuous industrial sites. Utilising a combination of machine learning techniques and mathematical programming, the research innovatively addresses the challenges of defining zones for practical heat recovery. Spatial and temporal clustering methodologies are employed to achieve a more nuanced approach to TSI. The results demonstrate the significant shift in heat recovery and utility targets, highlighting the importance of zoning and the potential of integrating data-driven techniques with engineering principles in TSI practices. Depending on the temporal cluster acceptability, TSI zoning changed the utility targets by 41 % - 143 %, which underscores the criticality of the zoning approach.

Keywords: process integration, non-continuous processing, pinch analysis, total site integration, machine learning, mathematical programming.

1. Introduction

Total site integration (TSI) is a well-known methodology to optimise heat recovery and utility systems across large and multi-plant industrial sites (Klemeš et al., 1997). At its heart, TSI divides a site into discrete zones. The approach then prioritises process-to-process heat recovery within each zone before subsequently capitalising on the utility system to mediate heat recovery inter-zone. Notably, TSI is not confined to the site boundaries (Perry et al., 2008); it can equally extend to potential power, heating, and cooling exchange (Lee et al., 2020) with proximate renewable energy generation, industries, districts, and other community needs (e.g., water desalination).
Dividing a site into zones is non-trivial for many non-continuous industries where the goal is to produce practical heat integration targets. Non-continuous sites must grapple

with their additional intricacies when attempting to apply TSI in practice (Tarighaleslami et al., 2017). Variables such as fluctuating stream temperatures and flow rates, flexibility versus inflexibility of target temperatures, and reliance on hot water utility add layers of complexity. To be viable, TSI strategies for these sites must be conservative to always guarantee operational integrity. Zone segmentation is pivotal in TSI but its praxis is rarely discussed in detail.
This study delves into the adaptation of TSI for non-continuous sites, specifically analysing an industrial hot water system, aided by machine learning techniques and mathematical programming.

2. The challenge of defining zones for total site analysis

Defining zones are an essential part of the praxis of TSI. Zones in TSI refer to defined groups of process streams that are distinct thermal regions within a site. Each zone is characterised by its temperature range and the processes operating within that range. This division helps in identifying the energy deficits and surpluses of different areas within the site. Most studies choose zones based on the operational plant units, applying the logic that intra-plant streams are close together and operationally synchronous. However, in practice, this is only sometimes true and does not assure that the resultant targets and networks meet TSI goals and operational mandates.

2.1. Spatial clustering considerations

Spatial clustering aims to group streams that are located close to each other to avoid the complexities and costs associated with excessive and intricate heat exchanger and piping networks. Spatial locations are three-dimensional positions within a site. Proximity relates to all three coordinates being within a reasonable distance; however, there is no one-size-fits-all and heavily depends on the application. The proximity of sources and sinks is crucial for a system design that is simple, economical, and controllable.
It is common for some streams to spatially exist in two or more zones. For example, a process flow might originate in one zone and then be transported to another for further processing. In such cases, the process flow may require heating or cooling, which could happen in either zone. A decision must be made regarding the heat load allocation between the two zones, which defines the stream temperature at which it crosses the zonal boundary. This temperature can be manipulated to maximise overall heat recovery.
Appropriate spatial clustering often relies on good process knowledge and engineering judgment. A potentially complementary approach is to apply a machine learning approach, such as K-means clustering. Such clustering techniques are data-driven and require specification of the number of clusters (i.e., zones), which is often determined by heuristics, prior contextual information or arbitrary values. As a result, machine learning results provide insight but not definitive answers. Good engineering remains essential.

2.2. Temporal clustering considerations

Most TSI studies assume that streams within the same processing plant are both spatially and temporally aligned. For some industries, this holds; but, not for all. Temporal clustering considerations focus on how well zonal source and sink heat loads match over time. Again, engineers have a significant sway in the praxis of TSI. Solely relying on judgment and experience to decide temporal compatibility, however, can lead to continued inaction.
Machine learning approaches that can support better decision-making are correlation matrix and hierarchical clustering (Müllner, 2011). Both procedures rely on determining the “distance” between each pair of time-series datasets. Distance is often a measure of dissimilarity where a distance of zero means the two series are identical. A challenge with

using plant data is that it may involve similar movement patterns with short time-delays causing them to be slightly out of phase. As a result, techniques such as dynamic time warping (DTW), which is applied in this study, allow for elastic transformations of the time dimension, making it suitable for typical plant data. Using the distances from DTW analysis, hierarchical clustering provides a vantage point of possible temporal clusters depending on an acceptable distance.

2.3. What, therefore, defines a zone in practice?

A zone is a group of streams that are spatially and temporally compatible to allow direct heat integration and retrofit. In praxis for some applications, this will lead to the creation of many additional zones, which will consequentially lower heat integration targets towards more achievable and believe levels.

In defining zones, it is also crucial to distinguish between process streams and utility. Heat integration targets are based on process streams only. However, at times, the identity of a stream can be unclear, especially process water streams that are integrated like a utility. This study makes the distinction between process streams and utility by asking whether the stream flowrate may be manipulated as part of the heat integration network. If the flowrate is determined by a processing unit, it is considered fixed from the perspective of the heat integration network and, therefore, is a process stream.

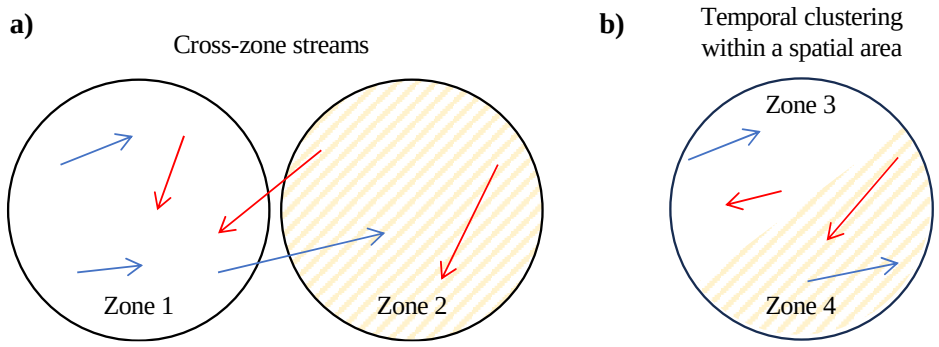

Figure 1. Conceptual views of a) zones where two streams originate in one zone and end in another and b) zoning that meets the requirements of both spatial and temporal compatibility.

3. Methods

The overarching method combines elements of an advanced zonal pinch analysis, total site, and machine learning. Due to space constraints, the presentation of the method is kept to an absolute minimum.

Step 1 – Machine learning for data-driven zoning: Zoning requires a bi-level clustering approach. First, k-means clustering of geolocations provides spatial areas. Second, time-series historical plant data of temperature and volumetric flow rate provide the basis for temporal clustering. However, such measurement data are often incomplete with numerous gaps. This study interpolates to fill in the missing data using a standard third order spline approach from the Pandas library in Python. Given the completer dataset, the required heating duty is calculated, providing the basis for hierarchical clustering using a basic DTW algorithm implemented in Python. Finally, the SciPy library in Python interprets the DTW correlation matrix to perform the hierarchical clustering and draw the dendrogram. By selecting different maximum “distance” (i.e., the measurement of data dissimilarity), various temporal zones are defined and located within the already defined spatial areas.

Step 2 –Zonal and TSI targeting with cross-zone streams: A bi-level optimisation approach is applied where (1) zonal targets are resolved using a modified LP temperature-interval transshipment model (Papoulias and Grossmann, 1983) within (2) a total site optimisation level where cross-zone stream temperatures, splits and an intermediate recovery loop with its associated temperatures are key variables that influence the structure and solution of zonal targets. The transshipment model is implemented in Python using the library GEKKO (Beal et al., 2018) while the outer-level optimisation uses the SciPy library. The objective is to minimise utility use given the constraint of a minimum approach temperature (10°C in this study).

4. Case study

The case study is based on a section of a large non-continuous processing site. Due to confidentiality, the site is not identified. Historical plant data from three spatial areas and their streams form the basis of the case study (Table 1). The median, 90th and 10th percentiles of each data are presented to provide a sense of the variability of the site.

Table 1. Stream data based on 50 days of data at 5-minute intervals. Water grade G3 is the most contaminated and G1 indicates the least contaminated.

Stream	Spatial area	Water grade	Variable	Unit	Median (P_{50})	P_{90}	P_{10}
H1	A2 to A3	G3	T_{supply}	°C	73.0	74.4	70.9
			T_{target}	°C	12.0	-	-
			mc_p	kW/°C	511.1	537.6	474.0
H2	A3	N/A	T_{supply}	°C	116.3	120.0	110.8
			T_{target}	°C	92.0	92.7	91.1
			mc_p	kW/°C	333.6	378.8	278.0
H3	A3	N/A	T_{supply}	°C	81.9	84.9	79.9
			T_{target}	°C	66.5	72.1	63.8
			mc_p	kW/°C	353.9	377.5	265.2
H4	A1	N/A	T_{cond}	C	75.7	77.5	73.4
			Q	MW	39.6	41.8	34.8
C1	A1	G1	T_{supply}	°C	14.9	16.1	14.3
			T_{target}	°C	150.0	-	-
			mc_p	kW/°C	243.3	304.9	243.3
C2	A2	G3	T_{supply}	°C	12.0	-	12.0
			T_{target}	°C	73.0	74.4	70.9
			mc_p	kW/°C	203.5	226.0	166.6
C3	A1 or A2	G3	T_{supply}	°C	12.0	-	-
	to A3		T_{target}	°C	75.0	-	75.0
			mc_p	kW/°C	1041.5	1138.3	846.0
C4	A3	G2	T_{supply}	°C	12.0	-	-
			T_{target}	°C	62.1	68.9	54.2
			mc_p	kW/°C	27.9	28.1	27.7

5. Results and discussion

5.1. Zonal clusters of streams

Both spatial and temporal compatibility are essential for direct intra-process integration to be efficient, economical, and practical. Figure 2 presents the results of a data-driven zoning strategy for TSI praxis.

Figure 2a delineates the temporal dissimilarity (or 'distance') between various streams within the site, with the vertical axis quantifying the DTW distance and the horizontal axis enumerating the streams (H for hot, C for cold). These streams are clustered such that the height at which streams join together in the hierarchical clustering (measured by DTW distance) indicates the order of temporal compatibility. Lower connections imply a greater temporal similarity. The horizontal dash lines are various acceptable distances that will be carried over to determine the zones with both spatial and temporal compatibility, providing a critical piece of information to the TSI targeting model. In Figure 2b, the clusters are demarcated both spatially and temporally. Each zone is characterised by a fusion of temporal clustering with spatial areas. With three spatial areas and two temporal clusters (line A), there is a maximum of 6 zones; however, streams are present in only 5 of the zones.

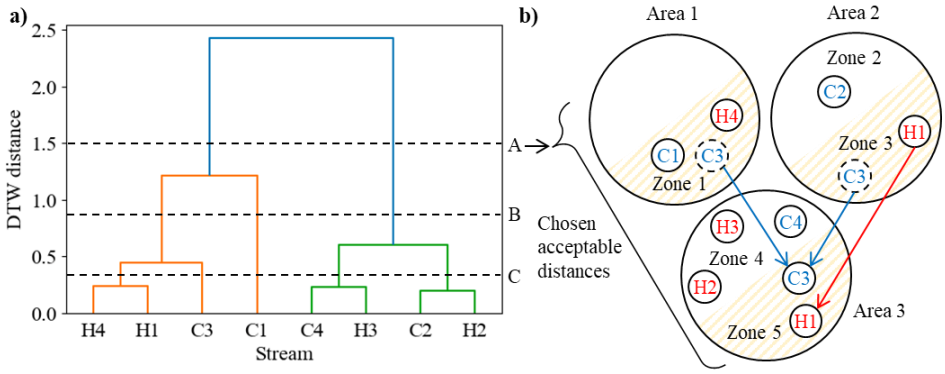

Figure 2. Zoning approach where a) the hierarchical clusters are based on DTW matrix results, showing an example acceptable distance resulting in two temporal zones and b) the spatial areas are each divided into two temporal regions (i.e., six zones) with resulting streams.

The proposed zoning method has been prototyped in Python. It involved 8 streams, resulting in the comparison of 28 possible stream pairs for 14400 time-series entries. On an M2 Macbook Air (8 GB ram), the clustering analysis took 43.5 minutes. Scaling the approach to significantly larger problems will require improved algorithmic and computational efficiency gains. One obvious inefficiency is that it currently analyses spatially incompatible stream pairs. This could be easily avoided in future implementations. Apart from computational efficiency, another challenge is the appropriate interpretation of DTW distance in deciding temporal clusters and how it relates to heat recovery between two streams. As a result, this study analyses multiple possible cluster options. Future work will look to develop a zoning heuristic.

5.2. Total site integration targets

Maximising zonal and total site heat recovery is essential to lowering energy use and saving energy costs. However, targets need to be realistic and achievable in practice to be useful. A key to practical targets is appropriate zoning. Table 2 presents the core results from the bi-level optimisation based on different levels of acceptable temporal dissimilarity. As a result, cases A, B, and C represent differing levels of temporal and

duty alignment. Cases A has 5 zones, B has 6 zones, C has 8 zones. The 'spatial only' serves as a baseline representing TSI performed by an engineer familiar with the plant layout without the explicit optimisation of cross zonal streams and intermediate loops as has been done historically.

Inter-plant heat recovery through the hot water utility system is substantial for this site. Tightening the acceptable temporal dissimilarity of stream-pairs leads to dividing the problem into more zones. More zones, each with less streams, results in less intra-plant heat recovery. However, the reduction in intra-zone heat recovery also gives rise to more opportunities to inter-plant heat recovery. Maximising inter-plant heat recovery requires optimising the temperatures of the hot water utility systems. As part of the outer optimisation layer, an attempt is made to manipulate the upper and lower hot water temperatures to minimise the demand for utility.

Table 2. Total site integration targets based on various temporal "distance" acceptance thresholds.

Zoning basis	Number of zones	Hot utility (MW)	Cold utility (MW)	Intra-plant heat recovery (MW)	Inter-plant heat recovery loop (MW)
Spatial only	3	29.4	1.5	50.8	32.0
A	5	41.6	13.7	45.1	25.5
B	6	48.7	20.8	27.6	35.9
D	9	71.3	43.3	1.4	39.6

6. Conclusions

Incorporating both spatial and temporal data facilitates a sophisticated approach to TSI, mindful of variations across time and space. This could lead to enhanced praxis and uptake of TSI for non-continuous industries. Although targets are gene rally higher as the number of zones increase, their practical achievability and, therefore, acceptability are improved. Future work will look to scale the approach to larger problems, improvement in computational efficiency, and heuristics to better translate the results of the clustering to zoning.

References

L. Beal, D. Hill, R. Martin, J. Hedengren, 2018, GEKKO Optimization Suite, Processes, 6(8), 106.

J.J. Klemeš, V.R. Dhole, K. Raissi, S.J. Perry, L. Puigjaner, 1997, Targeting and design methodology for reduction of fuel, power and CO_2 on Total Sites, Applied Thermal Engineering, 17(8–10), 993–1003.

P.Y. Lee, P.Y. Liew, T.G. Walmsley, S.R. Wan Alwi, J.J. Klemeš, 2020, Total Site Heat and Power Integration for Locally Integrated Energy Sectors, Energy, 204, 117959.

D. Müllner, 2011, Modern hierarchical, agglomerative clustering algorithms, .

S.A. Papoulias, I.E. Grossmann, 1983, A structural optimization approach in process synthesis—II, Computers & Chemical Engineering, 7(6), 707–721.

S. Perry, J.J. Klemeš, I. Bulatov, 2008, Integrating waste and renewable energy to reduce the carbon footprint of locally integrated energy sectors, Energy, 33(10), 1489–1497.

A.H. Tarighaleslami, T.G. Walmsley, M.J. Atkins, M.R.W. Walmsley, P.Y. Liew, J.R. Neale, 2017, A Unified Total Site Heat Integration targeting method for isothermal and non-isothermal utilities, Energy, 119, 10–25.

ESCAPE-34 PSE-2024
European Symposium on Computer Aided Process Engineering
&
Process Systems Engineering

Flavio Manenti, Gintaras V. Reklaitis (Eds.), Book of Abstract of the 34th European Symposium on Computer Aided Process Engineering / 15th International Symposium on Process Systems Engineering (ESCAPE34/PSE24), June 2-6, 2024, Florence, Italy.

Renewable Energy Integration and Waste Heat Valorization in Aluminum Remelting Mills for the Co-Production of Kerosene and Methanol

Daniel Florez-Orrego[a,*], Dareen Dardor[a], Meire Ribeiro Domingos[a], Reginald Germanier[b], François Marechal[a]

[a]*IPESE, Federal Polytechnic School of Lausanne, Rue de l'Industrie 17, 1950 Sion, Switzerland.*

[b]*School of Minas, National University of Colombia, Av. 80 #65-223, Medellin, Colombia.*

daniel.florezorrego@epfl.ch / daflorezo@unal.edu.co

Abstract

The aluminium sector relies on natural gas for the conversion of recycled scrap into new feedstock, which results in substantial atmospheric emissions. Hydric resources are also impacted, as they serve as heat sinks for the waste heat generated during the casting process. Other chemical industries are also responsible for a large production of waste heat, offgas and environmental emissions, which hinders efforts to decarbonize the sector that depend on them. Methanol and transportation fuels production are examples of those industries. Accordingly, there is a significant potential to decarbonize these productive activities via enhanced waste heat recovery and integration of renewable energy sources. The energy integration of aluminium, methanol and fuels production plants within urban areas also offers major advantages in terms of efficient energy utilization and reduced environmental impact, particularly in situations characterized by uncertain supply chains and fluctuating market prices. Biomass gasification offers an alternative carbon source to fossil fuels, and together with electrification, it may help to diversify and decentralize the energy inputs for industries traditionally dependent on natural gas, establishing resilient and sustainable energy pathways. Carbon abatement, power-to-gas and storage systems provide further advantages by mitigating the effects of seasonal availability and prices of electricity and fuel. Yet, the integration of the various energy technologies and industrial facilities calls for a systematic approach to identify optimal options for meeting the energy demands without significantly compromising the operational feasibility. Therefore, in this work, the most cost-effective technologies with minimum investment that meet the energy demands of the aluminium remelting, methanol and fuels production facilities are studied, aiming to upgrade the industrial waste heat available at low temperature to supply an urban center with variable energy needs. Implementing improved integration strategies shows the potential to reduce overall energy consumption, while achieving net-zero CO_2 emissions compared to conventional scenario.

Keywords: Aluminium, Fischer-Tropsch, Methanol, Waste heat, District heating.

1. Introduction

In aluminium, chemicals and fuels production plants, natural gas is typically used either as feedstock or as fuel to supply the heating demands at high temperatures. As a result, the aluminium sector is responsible for about 2% of the global industrial emissions (IA

2021), followed by the methanol production with 1% (Kapoor 2022). Meanwhile, the transportation sector, and more specifically, the aviation sector is a significant contributor to the global greenhouse gas emissions (30%) (Burli 2023), and its impact is expected to heighten in the coming years, considering that global jet fuel consumption is foreseen to be threefold higher than in 2019 (ICAO 2022). In this regard, more efforts should be done to defossilize these critical industrial sectors on which many others rely, including cargo, food packaging, automotive industry, polymers and chemicals synthesis. Methanol is an intermediate molecule for various chemicals production, such as olefins, amines, acetic acid, dimethyl ether and formaldehyde (Domingos 2022); and it can be also used directly or blended with naphtha. Sustainable aviation fuels are drop-in replacements for conventional jet fuel that can be produced from renewable resources, such as biomass and electricity (ICCT 2022). Although less than 0.1% of the jet fuel consumed by commercial airlines is currently composed of sustainable aviation fuels (Adelung 2022), ReFuelEU aviation regulation proposal introduced blending mandates of min. 5% at EU airports by 2030, which is expected to increase by 63% by 2050 (Burli 2023). As for the aluminium, it has innumerable applications in automotive and aerospace industry, food canning, decoration, among others. However, a largely unexploited byproduct of the secondary aluminium production is waste heat, which can be recovered from stack gases generated in the remelting furnaces or from hot water produced in the aluminium casting (Kumar 2022). In fact, since around 90% of the heating requirements of the residential and service sectors can theoretically be covered by process waste heat (Persson 2012), the reuse of waste heat in industrial plants will play an critical role in the defossilization strategy of those sectors (Yu 2018, Clos 2017) and will enable the energy integration with urban energy systems (Stijepovic 2011, Bertrand 2019). The integration of biomass gasification to industrial plants has the potential to achieve overall negative emissions, if combined with electrification and power-to-gas systems, thus adding flexibility to the energy and carbon management approach (Florez-Orrego 2023). However, as the number of decarbonization options increases, a systemic study is necessary to evaluate the most suitable processes and carbon neutral technologies to supply the energy requirements without impacting the operational conditions and process reliability, even under scenarios of seasonal variations of energy inputs prices and demands. A mixed integer linear problem is addressed using OSMOSE platform to maximize waste heat recovery and define the most economically, thermodynamic and environmentally favorable configuration to integrate the aluminium, fuels and chemicals industries to the urban systems.

2. Process description

2.1. Aluminium plant

In the remelting plant, scrap and pure aluminium are processes to produce value-added aluminium coils and other products. In the cast house, the first step consists of preheating pure aluminium sows up to 250°C to dry moisture out before it enters the melting furnace. Therein, scrap aluminium is mixed and the metal is heated up to ~700°C. The molten aluminium is transferred to a holder furnace, which acts as a buffer for the downstream direct chill casting process. In the latter, the aluminium is solidified into ingots by using direct cast chilling with cold water, which can achieve temperatures above 50 °C before discarded to the environment. In the rolling plant, the aluminium ingots are superficially processed in a scalper to remove the outer layer. Next, they go through two parallel pusher furnaces, wherein aluminium ingots are thermally treated (annealing) at 550°C during several hours, before they go through a hot rolling followed by a cold rolling process. In this way, coils with millimeter thickness are mechanically formed consuming a large amount of electricity dissipated as heat. Finally, some of the coils are sent to an annealing continuous line (ACL), where they are chemically and thermally treated using alternating heating and quenching processes. Space heating of the aluminium plant must be also

considered, due to seasonal environmental conditions. The main energy resource for the aluminium processing is fossil natural gas, while diesel is also consumed in some devices and fork lifts. Currently, the casting water containing a large share of the low-grade waste heat from the aluminium production is directly discarded to the environment, but it could be integrated with an anergy (CO_2) district heating network to satisfy the heating needs of the services and residential sector. Fig. 1 shows the integrated energy system, including the aluminium plant, as well as the chemical and fuels production facilities, and the city.

2.2. Chemical and fuel production plants

2.2.1. Biomass conversion system

Biomass moisture is reduced to 10% in a rotary dryer using waste heat and dry biomass is chipped in a mechanical process that consumes 1-3% of biomass energy (Flórez-Orrego 2019). In the gasifier (900°C), biomass is converted into a syngas rich in CO, H_2, CO_2 and CH_4, among other components, using steam as the gasification agent (S/B ratio 0.75). The indirect gasifier operating at atmospheric pressure burns a fraction of the pyrolysis char with air in a second column to supply the energy demands of the endothermic drying, pyrolysis and reduction reactions, thus avoiding the nitrogen dilution of syngas. After the gasifier, the syngas is cooled down to 400 °C and scrubbed with water, in order to remove the impurities and compressed to 35 bar. A water gas shift reactor increases the hydrogen content, at expense of producing more CO_2. The syngas can be used as feedstock for the methanol and the FT liquids plants, whereas the waste heat could be used for combined heat and power production to balance the aluminium and chemical processes demands in a more versatile way than biomass combustion alone.

2.2.2. Methanol plant

The purified syngas is compressed to 90 bar and is heated up by the reactor effluent in a feed-effluent heat-exchanger before it is fed to a methanol synthesis loop. The methanol synthesis occurs in an isothermal reactor operating at 90 bar and 210 °C. The reactor outlet stream is a gaseous mixture of methanol, water and unconverted reactants. This mixture is cooled and flashed twice, first to 30 °C and 45 bar, and then to 3.5 bar, in order to separate the condensable products and the non-condensable reactants (Kiss 2016). The latter are recycled to achieve higher conversions. The condensed stream continues to a distillation column at atmospheric pressure, in which methanol is produced (99% wt.). To avoid the built up of inerts, a fraction of the non-condensable stream is purged.

2.2.3. Fischer-Tropsch liquids plant

The low temperature Fischer-Tropsch reactor with iron catalyst (200-240°C) ensures high selectivity for paraffin and high molecular mass linear waxes. A polymerization reaction yields a large variety of products with different carbon chain lengths, including n-olefins, n-paraffins, oxygenated products, and branched chain hydrocarbons. The selectivity of the products depends on several reaction parameters, e.g. temperature, pressure, catalyst and reactor type. The probability of chain growth via addition of a monomer to the initiator is defined by a chain growth probability (α) given by an Anderson-Schulz-Flory (ASF) distribution. A direct product is diesel-cut, whereas hydrocracking of the waxes yields further kerosene- (C_9-C_{16}) and diesel-cut (C_{15}-C_{20}) mixtures. The hydrocarbons in the naphtha range (C_5-C_{12}) are rather straight chain and need further treatment to increase their branching and achieve high-octane rating (Florez-Orrego 2023).

2.2.4. Other energy technologies

To capitalize on the waste heat available and manage, store and upgrade industrial wastes into value-added products, ancillary technologies, such as reversible water gas shift units, electrolyzer, methanator, supercritical CO_2 cycle, refrigerator, methanol reforming, air separation unit and anergy (CO_2) district heating network are also integrated. Details on the simulation of these energy systems can be found elsewhere (Florez-Orrego 2023).

3. Methods

The process modeling and simulation is performed in Aspen Plus software integrated to the OSMOSE platform, which minimizes the energy requirement of the integrated industrial plants. In this way, low grade waste heat can be reutilized to supply a district heating network or generate power in a supercritical CO_2 cycle. In addition, the implementation of a seasonal power-to-gas approach, including electrolysis, methanation, reverse water gas shift and carbon abatement technologies, allows to manage the time-varying demands and supply. To this end, a multi-time approach has been used to minimize the capital investment of the seasonal energy storage systems (e.g. tanks). The binary y_w and load factor f_w optimization variables in Eqs. 1-4 are used to define the best size and arrangement based on assumed prices of material and energy inputs and CO_2 tax. The best combination of energy technologies has been defined to defossilize industrial applications, such as the aluminum remelting, whereas producing value-added fuels. As for the city demands, typical central European zone city is considered for the assumption of the thermal loads of district heating network, including domestic hot water, space heating, air conditioning and refrigeration (Flórez-Orrego 2022). The integration with the surrounding population has been achieved implementing a novel CO_2 district heating network.

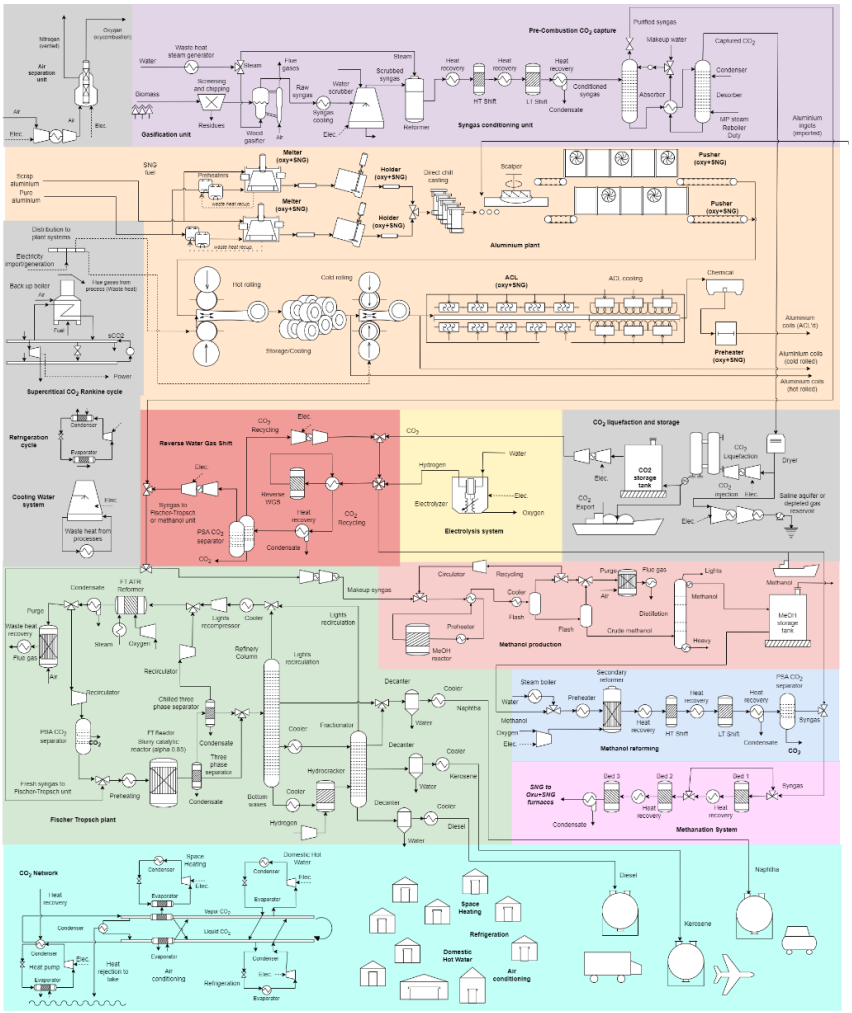

Figure 1. Blocks diagram of the aluminium and chemicals production facility, along with the utility systems (cogeneration, power-to-gas and storage technologies), and the district heating CO_2 network.

$$\underset{\substack{f_\omega,\ y_\omega \\ R_r,W}}{\mathbf{Min}}\left(\sum_{inputs}\left(f\cdot c\cdot m\right)_\omega-\sum_{outputs}\left(f\cdot c\cdot m\right)_\omega+\left(m_{CO_2}\cdot c_{CO_2tax}\right)\pm\left(f_{EE}\cdot c\cdot W\right)_{EE}\right)\cdot N_{h/year}+\left(Z_{equip}\cdot Ann\right) \quad (1)$$

$$\sum_{\omega=1}^{N_\omega} f_\omega q_{\omega,r}+\sum_{i=1}^{N} Q_{i,r}+R_{r+1}-R_r=0 \quad \forall r=1..N \quad (2)$$

$$\sum_{\omega=1}^{N_\omega} f_\omega W_\omega+\sum_{\substack{chemical\\units}} W_{net}+W_{imp}-W_{\exp}=0 \quad (3)$$

$$f_{\min,\omega}\mathrm{y}_\omega \le f_\omega \le f_{\max,\omega}\mathrm{y}_\omega \quad \forall\omega=1..N_\omega \wedge W_{imp}\ge 0,\ W_{\exp}\ge 0 \wedge R_1=0,\ R_{N+1}=0,\ \mathrm{R}_r\ge 0 \quad (4)$$

4. Results and discussion

In this section, selected results for an annual 250 kt/y aluminium processing plant integrated to 4.08 kt/y of diesel, 9.40 kt/y of naphtha, 17.57 kt/y of kerosene (24 MW) and 26.35 kt/y (17 MW) of methanol production sites are discussed. For these production rates, the total biomass energy consumption is 681.77 GWh/y, whereas the total electricity import achieves 1096.52 GWh/y. The diesel consumption in the aluminium plant is 0.23 kt/y. It is worthy to notice that the self-power generation using a sCO_2 cycle for waste heat recovery through the aluminium remelting and the chemical plants is 167.39 GWh/y, which represents around 15% of the total power import. For the sake of comparison, the aluminium plant power consumption is 68.07 GWh/y. Notably, the power demand of the electrolyzer is dominant (1080.76 GWh/y, max. 170 MW), which is explained by the intensive production of hydrogen and the CO_2 conversion to value-added products in a power-to-gas approach. In fact, hydrogen and oxygen production in the electrolyzer amount 19.65 kt/y and 157.20 kt/y, respectively. Oxygen production from an auxiliary air separation unit (24.22 kt/y) is necessary, especially during the winter months, in order to balance the oxygen and hydrogen requirements. In fact, venting of surplus oxygen (77.40 kt/y) and nitrogen (99.55 kt/y) are estimated, even with an intensive oxygen utilization in the oxycombustion furnaces. The CO_2 processed in the reverse water gas shift can be estimated as 95.15 kt/y. Meanwhile, the methanator processes 26.53 kt/y of CO_2 and 4.82 kt/y of hydrogen to yield 134.01 GWh/y of synthetic natural gas, which along with 65.37 GWh/y of synthetic natural gas produced by a methanol reforming unit, supplies the fuel consumption in the oxycombustion furnaces of the aluminium plant. It is worthy to notice that no CO_2 injection or mineralization is necessary, as all the captured and separated CO_2 is processed by the system, and stored to produce value-added products only when the cost of electricity is more favorable during the summer period. A complementary behaviour is observed by the methanol storage tank (see Fig. 2).

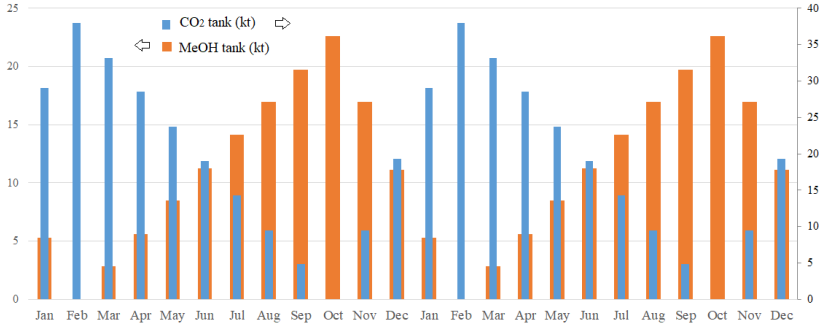

Figure 2. Annual evolution of the storage levels of CO_2 and methanol tanks.

Interestingly, the syngas production for chemicals and fuels production is evenly divided by the reverse water gas shift and the gasification systems, which are respectively 66.40 kt/y and 64.06 kt/y of syngas production, totalizing 130.46 kt/y of syngas. As for the biogenic CO_2 emissions at the gasifier stack (75.12 kt/y), they represent the dominant source of emissions of the integrated energy systems, followed by the also biogenic CO_2 emissions from the offgas flare of the Fischer-Tropsch unit (13.41 kt/y) and the CO_2

emissions from the purge gas flare system in the methanol production unit (3.65 kt/y). The total environmental emissions based on the direct and indirect CO_2 emissions of the integrated system amount 177.50 kt/y. The indirect fossil CO_2 emissions, which arise from the supply chains of the biomass and electricity imports, are estimated as 9.57 and 68.67 kt/y, respectively. In other words, due to an intensive electrification strategy, and considering the emissions intensity of the electricity consumed, a relatively high share of fossil emissions (44% of 177.50 kt/y) could be expected. This fact demonstrates the interrelation between the industrial activities and the need to orchestrate a coordinated decarbonization strategy for all of the energy conversion routes to actually achieve a sustainable net zero target. Provided that the energy inputs are derived from renewable energy resources, the fossil fuel dependency and emissions could be virtually avoided.

5. Conclusions

In this work, via enhanced waste heat valorization and CO_2 management has been proposed to energetically integrate industrial energy systems typically dependent on non-renewable energy resources, i.e. aluminium remelting, methanol synthesis and transport fuel production. Using renewable energy resources, it has been possible to elucidate alternative production routes that enable phasing out fossil fuels utilization, while increasing the electrification, in order to achieve net zero emissions. Yet, indirect emissions still remain the main challenge. In fact, due to intensive electrification, indirect emissions (78 kt/y) related to electricity are expected, but much lower than operating standalone chemical plants.

Acknowledgments

The authors thank Swiss Federal Office of Energy and Suisse Energie for funding the project “Sustainable natural gas (SNG) and aluminium production via biomass gasification and enhanced waste heat recovery in Novelis plant in Sierre City” of the Net Zero Lab consortium.

References

Adelung, S., Dietrich, R. (2022). "Impact of the reverse water-gas shift operating conditions on the Power-to-Liquid fuel production cost." Fuel **317**: 123440.

Bertrand, A. et al. (2019). "Regional waste heat valorisation: A mixed integer linear programming method for energy service companies." Energy **167**: 454-468.

Burli, P., et al (2023). Assessment of successes and lessons learned for biofuels deployment. Lessons learnt in supply chains: Sustainable biomass supply chains for international markets. T. Ekbom, IEA Bioenergy**:** 39.

Clos, D., et al (2017). Enabling Efficient Heat Recovery from Aluminium Pot Gas. Light Metals. A. Ratvik, Springer International Publishing**:** 783-791.

Domingos, M. E. G., et al (2022). "Techno-economic and environmental analysis of methanol and dimethyl ether production from syngas in a kraft pulp process." Computers & Chemical Engineering: 107810.

Florez-Orrego, D., et al. (2023). A systemic study for enhanced waste heat recovery and renewable energy integration towards decarbonizing aluminium industry. ECOS 2023, June 25-30th, Spain.

Florez-Orrego, D., et al (2023). Renewable energy integration and waste heat recovery for the production of sustainable jet fuel and decarbonization of industrial heating applications. AIChE 2023 Annual Meeting, November 5-10, 2023. Orlando (FL), United States.

Flórez-Orrego, D., et al (2022). A systematic framework for the multi-time integration of industrial complexes and urban systems. CPOTE, 20th-23th September, 2022. Warsaw, Poland.

Flórez-Orrego, D., et al (2019). "Comparative exergy and economic assessment of fossil and biomass-based routes for ammonia production." Energy Conversion and Management **194**: 22-36.

IA. (2021). "Aluminium Sector GHG Pathways 2050." 25.03.023, From https://international-aluminium.org/resource/aluminium-sector-greenhouse-gas-pathways-to-2050-2021/.

ICAO (2022). Environmental Report - Innovation for a green transition. Montreal, Canada, International Civil Aviation Organization (ICAO).

ICCT. (2022). "Sustainable aviation fuels: what does real leadership look like?" Retrieved 20.05.2023, from https://theicct.org/publications/renewable-jet-fuel-ghg-lca-2019.
Kapoor, K., et al (2022). Green methanol key to energy transition net-zero plans, S&P Global Commodity Insights - Petrochemicals.
Kiss, A., et al (2016). "Novel efficient process for methanol synthesis by CO2 hydrogenation." Chemical Engineering Journal **284**(15 January): 260-269.
Kumar, R., et al. (2022). A Method for Recovering the Waste Heat to Achieve Overall Energy Conservation in Aluminum Casting Industries. Recent Advances in Energy Technologies. Springer Nature**:** 331-342.
Persson, U., et al (2012). District heating in sequential energy supply. Appl Energy **95**(123-131).
Stijepovic, M., et al (2011). "Optimal waste heat recovery and reuse in industrial zones." Energy **36**(7): 4019-4031.
Yu, M., et al (2018). Waste Heat Recovery from Aluminum Production. Energy Technology 2018, Springer International Publishing**:** 165–178.

ESCAPE-34 PSE-2024
European Symposium on Computer Aided Process Engineering
&
Process Systems Engineering

Flavio Manenti, Gintaras V. Reklaitis (Eds.), Book of Abstract of the 34th European Symposium on Computer Aided Process Engineering / 15th International Symposium on Process Systems Engineering (ESCAPE34/PSE24), June 2-6, 2024, Florence, Italy.

Limestone Calcined Clay Cement (LC3) Concrete Made using Saudi Clays: a Case Study

Marwan Abdulqader,[a] Hammad Raza Khalid,[a,b,*] Mohammed Ibrahim,[c] Saheed Adekunle, [a,b] Mohammed Al-Osta,[a,b] Shamsad Ahmad[a,b]

[a]*Department of Civil and Environmental Engineering, King Fahd University of Petroleum & Minerals, Dhahran 31261, Saudi Arabia*
[b]*Interdisciplinary Research Center for Construction and Building Materials, King Fahd University of Petroleum and Minerals, Dhahran 31261, Saudi Arabia*
[c]*Applied Research Center for Metrology, Standards and Testing, King Fahd University of Petroleum and Minerals, Dhahran, 31261, Saudi Arabia*
hammad.khalid@kfupm.edu.sa

Abstract

The production of Portland cement (clinker) results in an enormous amount of CO_2 emission. Clinker substitution with supplementary cementitious materials (SCMs) is a promising technology for reducing the CO_2 footprint of concrete industry. Substitution of clinker with calcined clays along with limestone results in a ternary blend known as limestone calcined clay cement (LC3). This paper reports the use of local Saudi clays to prepare LC3 concrete. Different clays were sourced from local quarry sites. The collected clay samples were characterized to find their mineralogical composition. Following, clays were crushed, sieved, calcined, and used for clinker substitution along with limestone and gypsum to prepare LC3 samples. Different clay substitution levels were used to prepare a series of LC3 samples. The fresh, mechanical, and durability properties of prepared LC3 samples were studied. The obtained results revealed the potential of Saudi clays to achieve higher clinker replacements (up to 50%).

Keywords: LC3, Calcined clays, Supplementary cementitious materials (SCMs), Clinker substitution, Green cement.

1. Introduction

Portland cement is the main binder in concrete, which has a high CO_2 footprint (Andrew 2017). Efforts are being made to reduce cement content in concrete. A promising and immediate solution is to use supplementary cementitious materials (SCMs) to partially replace cement, as no alternative is currently available to put cement out of the picture (Ahmadi and Shekarchi 2010; Juenger et al. 2019). Different SCMs such as coal fly ash, blast furnace slag, natural pozzolan, and calcined clays can be used for cement replacement up to certain levels. Fly ash is the by-product of coal power generation while slag comes from blast furnaces, and both have limited supplies. Natural pozzolan is available at specific localities. Therefore, the focus of this study is naturally occurring

kaolinite clays which can be calcined at moderate temperature to get good reactivity. Calcined clays are substituted along with limestone powder to make a ternary blend, referred to as LC3. Calcined clays have shown promising mechanical and durability characteristics, desirable for concrete. An increasing number of papers have focused on such clays (Scrivener 2015; Vizcaíno Andrés et al. 2015). In this study, Saudi clays were studied for clinker replacement at different levels. The mechanical and durability properties of concrete made using different clays were studied.

2. Experimental

Two Saudi clay samples, white (WC) and yellow (YC) were collected from the Eastern province of Saudi Arabia. One Ukrainian clay (UC) was also used for the sake of comparison. Collected clay samples were crushed and ground to pass a 150 µm sieve. Following, ground clays were calcined at 850 °C for 3 h to convert kaolin to metakaolin. Type I Portland cement, conforming to ASTM C150, was used. Limestone powder (LSP) was used at a clay-to-LSP ratio of 2:1. A water/binder ratio of 0.4 was used for all the samples. Eventually, the paste samples (25 mm cubes) with clinker substitution levels of 30, 50, and 70 wt.% were made. Samples were cured under water for up to 7, 28, and 90 days, followed by compression testing (Fig. 1). After 28 days of curing, 3 samples from each batch were exposed to a 5% sulfate solution for durability measurements.

Figure 1. Compression testing of paste samples

3. Results and discussion

The compressive strength of all the samples is plotted in Fig. 2. It is evident that the control samples showed higher strength compared to the LC3 samples. The strength of LC3 samples at 50% replacement was about 56, 42, and 40 MPa for white, yellow, and Ukrainian clay, respectively, compared to about 76 MPa for the control sample. Despite the reduction in strength, the achieved strength values of LC3 samples can still give structural-grade concrete. Moreover, this lower strength of LC3 samples was potentially due to the low fineness of clays (particle size < 150 µm) which resulted in lower reactivity. In contrast, cement generally has an average particle size of 45 µm.

The durability of samples against sulfate exposure is shown in Fig. 3. It can be seen that almost all the sulfate-exposed samples showed comparable compressive strength to their

respective control samples (unexposed). This shows the high sulfate resistance of these samples. Hence, clay-substituted binders can be used in sulfate-rich environments.

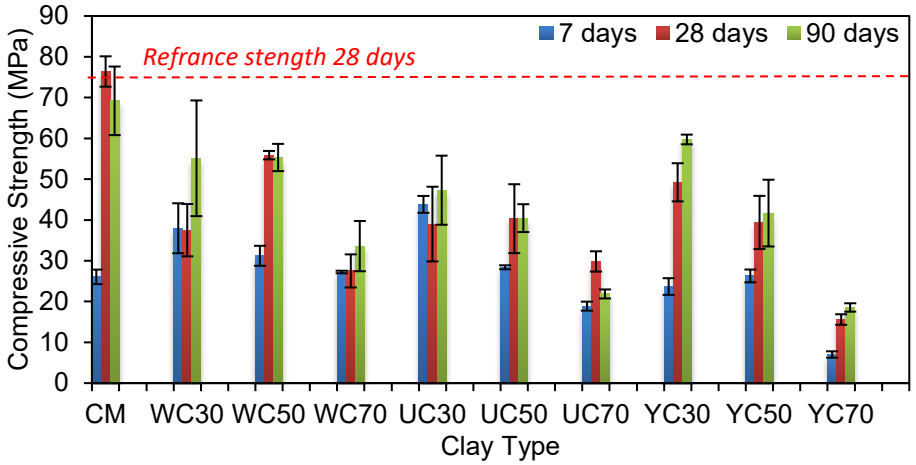

Figure 2. Compression strength of paste samples

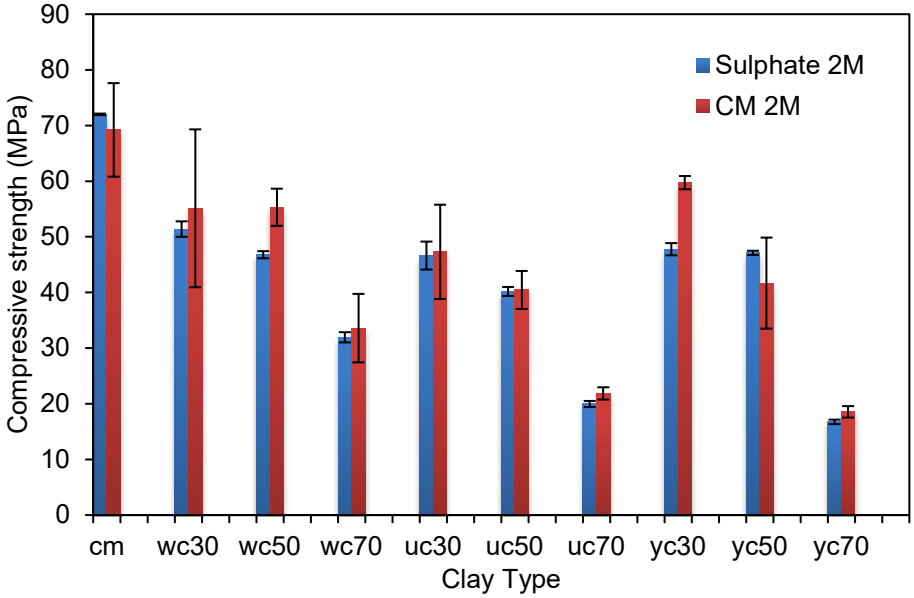

Figure 3. Compression strength of sulfate-exposed paste samples

4. Conclusions

Two Saudi clays were studied in this work to replace clinker partially. Mechanical strength and sulfate resistance were studied. The results have shown that the clay samples have less strength than control samples, potentially due to their low reactivity because of the larger particle size. The reduction in particle size by fine grinding can help in

achieving higher strength. Furthermore, all the samples exhibited high resistance to sulfate exposure.

Acknowledgment

The authors would like to acknowledge the support provided by the KFUPM under grant INCB2314.

References

Ahmadi B, Shekarchi M (2010) Use of natural zeolite as a supplementary cementitious material. Cem Concr Compos 32:134–141. https://doi.org/10.1016/j.cemconcomp.2009.10.006

Andrew RM (2017) Global CO2 emissions from cement production. Earth System Science Data Discussions 1–52. https://doi.org/10.5194/essd-2017-77

Juenger MCG, Snellings R, Bernal SA (2019) Supplementary cementitious materials: New sources, characterization, and performance insights. Cem Concr Res 122:257–273. https://doi.org/10.1016/j.cemconres.2019.05.008

Scrivener K (2015) Calcined Clays for Sustainable Concrete

Vizcaíno Andrés LM, Antoni MG, Diaz AA, et al (2015) Effect of fineness in clinker-calcined clays-limestone cements. Advances in Cement Research 27:546–556. https://doi.org/10.1680/adcr.14.00095

ESCAPE-34 PSE-2024
European Symposium on Computer Aided Process Engineering
&
Process Systems Engineering

Flavio Manenti, Gintaras V. Reklaitis (Eds.), Book of Abstract of the 34th European Symposium on Computer Aided Process Engineering / 15th International Symposium on Process Systems Engineering (ESCAPE34/PSE24), June 2-6, 2024, Florence, Italy.

Analysis and Improvement of Flotation Circuits for Polymetallic Ores

Yordana Flores , Yesica L. Botero , Luis A. Cisternas

Departamento de Ingeniería Química y Procesos de Minerales, Universidad de Antofagasta, Antofagasta, Chile

luis.cisternas@uantof.cl

Abstract

Current mining industry challenges require extracting all valuable elements and treating toxic materials from the ore. One way to achieve these objectives is through flotation plants that process polymetallic ores. The plants design of flotation polymetallic ores usually consists of a sequence of circuits to separate the valuable elements from the gangue without any integration between them beyond the sending of tails or concentrate streams from one plant to another. This work analyzes the integration of these circuits. First, plant design is carried out using optimization to select the best alternative from a set of circuit alternatives. Uniform distribution functions are used to represent recoveries with epistemic uncertainty, and the optimization problem is solved many times to identify a set of optimal solutions. Once this set of optimal designs has been identified, global sensitivity and uncertainty analyses are utilized to identify bottlenecks and improvements. The results showed that these integrated plants' design and analysis would introduce significant improvements in the operation of flotation plants for polymetallic ores. The advantages and challenges of integrated polymetallic ore plants are highlighted.

Keywords: Polymetallic ores, integrated circuits, global sensitivity analysis, improvement

1. Introduction

The mining industry presents critical challenges, given the increased demand for metals, the decrease in grades, the complexity of mining deposits, and the increase in environmental restrictions. This forces to consider extracting all valuable elements and treating toxic materials from the ore. One way to achieve these objectives is through flotation plants that process polymetallic ores. The design of polymetallic ores flotation plants usually consists of a sequence of circuits separating the valuable elements from the gangue without any integration between them beyond sending tails or concentrate streams from one plant to another. Flotation circuits are complex systems with many flotation stages and elements that participate in the system, speaking only of monometallic ore circuits. Using a task superstructure with an origin-destination matrix reduces the solution to the problem significantly (Cisternas et al., 2014). The flotation stage recoveries of stage j of specie i, T_i^j, which are needed to design these systems, are unknown because they

depend on the circuit design. Then, to represent this epistemic uncertainty, a uniform distribution function, $T_i^j \sim U(a,b)$, can be considered. This range of recovery values is sufficient for identifying a set of optimal flotation circuit structures (Cisternas et al., 2015). For the identification, Monte Carlo optimization is applied solving a mixed-integer linear programming (MILP) problem, guaranteeing a global optimum. This way, optimization methodologies can be used for circuits with many species and flotation stages (Calisaya et al., 2016). This design approach was applied by Botero et al. (2024) for the design of polymetallic ore circuits.

To identify bottlenecks in operation and propose additional improvement to polymetallic flotation circuits, global sensitivity analysis (GSA) can be performed, focusing on identifying input variables with the most significant effect on flotation circuit performance. The use of GSA applied to mineral processing has been studied (Lucay et al., 2015; Sepúlveda et al., 2013), and the Sobol-Jansen method has shown the best performance among several methods studied (Lucay et al., 2020). However, all these studies have only been conducted on monometallic ore circuits. This work analyzes the design of integrated flotation circuits for polymetallic ore. The polymetallic ore Kevitsa plant for copper (Cu) and nickel (Ni) is utilized as a case study.

2. Descriptive methodology

The species participating in the polymetallic circuit are chalcopyrite $CuFeS_2$ (Cp), pentlandite $Ni_9Fe_9S_8$ (Pn), pyrrhotite FeS (Po), and non-sulphur gangue (G). The species of interest for the Cu concentrate is Cp, and for the Ni concentrate is Pn. The feed to the flotation circuit is 8.07 t/h Cp, 5.44 t/h Pn, 14.73 t/h Po, and 903.84 t/h G, and the recovery data are presented in Table 1.

2.1. Optimal integrated design

According to the research conducted by Botero et al. (2024) the design strategy of monometallic ores can be applied to the design of polymetallic ores since few optimal structures were found for the circuits studied, given the uncertainty in the stage recoveries. The starting point should be using a superstructure - origin-destination matrix for each concentrate and tail stream based on the existing flowsheet. Then, new stream connections were included, including circuit integration between the Cu and Ni plants. The revenues were used as an objective function, and uniform distribution functions were generated based on plant data. The MILP problem was solved using CPLEX 12.9.0.0 on the GAMS platform.

2.1. Global sensitivity analysis for improvement

GSA was applied to identify the stage recoveries that have a significant effect on the global Cu and Ni circuit recoveries and product grades. The products are the Cu and Ni concentrates. The studied mathematical models of the circuit are obtained by a mass balance representing the stage recoveries by uniform distributions. For the GSA, the Sobol-Jansen method was used, which implements the Monte Carlo estimation of the first-order and total Sobol indices simultaneously (Jansen, 1999; Saltelli et al., 2010). The sensitivity package under R project software was utilized using a random sample of 50,000 data points.

Table 1. Recovery data from the Kevitsa plant flotation circuit (Botero et al., 2024)

Circuit	Stages	Symbol	Cp	Pn	Po	G
Cu	Rougher	R1	0.543	0.112	0.085	0.013
	Cleaner	C11-C14	0.790	0.459	0.530	0.362
	Scavenger	S1	0.401	0.116	0.086	0.028
Ni	Rougher	R2	0.253	0.350	0.272	0.044
	Cleaner	C21-C25	0.174	0.697	0.552	0.385
	Scavenger	S2	0.773	0.844	0.861	0.203

3. Results

3.1. Optimal integrated Cu and Ni flotation design

Figure 1 represents the integral polymetallic flotation circuit obtained to produce Cu and Ni concentrates and a tail. The first flotation circuit, for the production of Cu concentrate, considers a rougher stage (R1), four cleaner stages (C11, C12, C13, and C14), and a scavenger stage (S1). The second flotation circuit, for the production of Ni concentrate, considers a rougher stage (R2), four cleaner stages (C22, C23, C24, and C25), a scavenger stage (S2), and a cleaner-scavenger stage (C21). Observe that the recirculation of a tail stream from the Ni C21 stage to the Cu R1 stage integrates both circuits. This integrated circuit increases the revenue from 261.9 MMUS$/year to 314.9 MMUS$/year, which is a 20% increase.

3.2. Global Sensitivity Analysis (GSA)

The mathematical models utilized for the GSA were the global Cu and Ni recoveries, and Cu and Ni grades, in the polymetallic flotation circuit of Figure 1. These global recoveries were expressed as a function of the stage recoveries, T_i^j. These stage recoveries were given by uniform distribution functions, $T_i^j \sim U(a, b)$, where the constant values a and b were obtained using the data in Table 1 ±0.05. The results are shown in Figures 2 and 3.

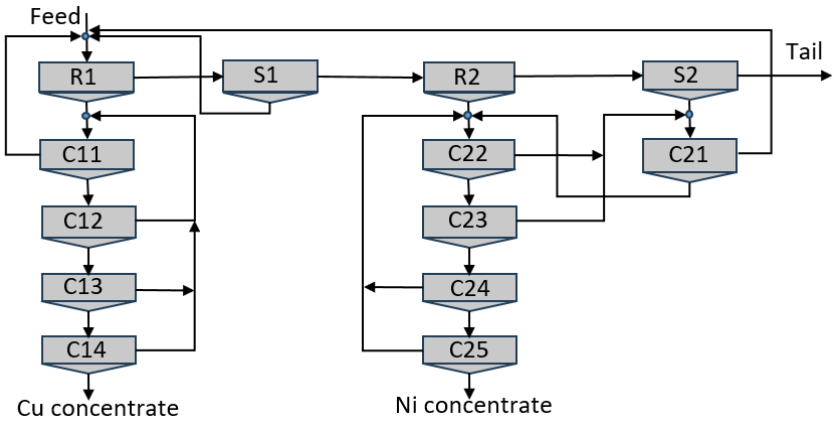

Figure 1. Integrated design of the Cu and Ni -Kevitsa flotation circuits. Modified from Botero et al. (2024).

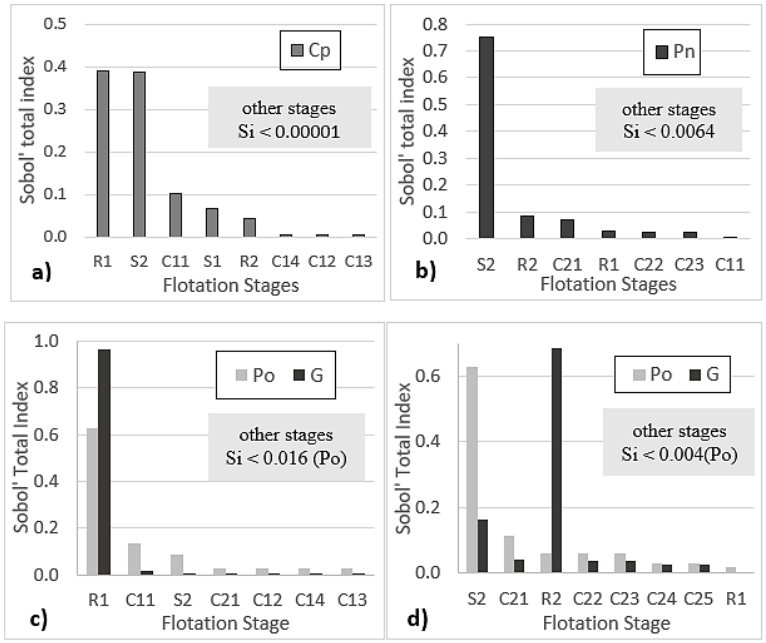

Figure 2. Sobol total index (Si) for global Cu recovery [a) Cp and c) Po, G stage recoveries], and global Ni recovery [(b) Pn and d) Po, G stage recoveries].

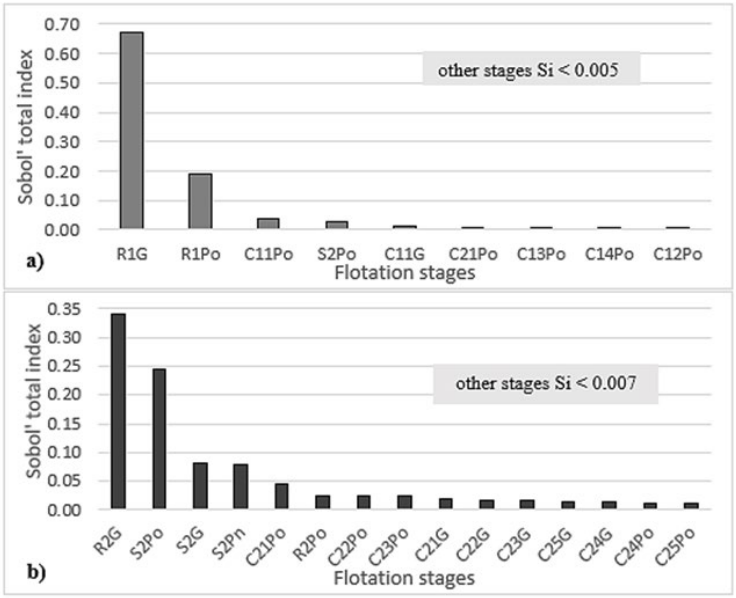

Figure 3. Sobol total index (Si) for the main stage recoveries that influence a) copper grade in the Cu concentrate, and b) nickel grade in the Ni concentrate.

Figure 2a shows the total Sobol index of the T_{Cp}^{j} variables that have the most significant effect on the global recovery of Cp are R1, S2, and C11 stages. This is an exciting result because stage S2 of the Ni circuit has an essential effect on the Cu recovery. Figure 2c

indicates that stage R1 is the most relevant in the global recovery of Po and G species. Figure 2b demonstrates that S2 and R2 stages are the ones that have the most significant effect on the overall recovery of Pn. Figure 2d shows the most important impact of stage S2 on the global recovery of Po and stage R2 for the global recovery of G.

Figure 3a shows that the Po and G recoveries in stage R1 have the most significant effect on the Cu grade. Figure 3b shows that the variables with the most significant effect on the Ni concentrate grade are the G recoveries in stages R2 and S2 and Po recovery in stage S2.

3.3. Improvement of the polymetallic flotation integrated circuit.

According to the GSA of the integral Cu and Ni flotation circuit, better control can be performed in the different flotation stages to increase the recovery of Cp and Pn in stage S2 and decrease the recoveries of Po and G in stages R1 and R2, to guarantee more remarkable global recovery and improvement in the grade of copper and nickel concentrate.

Table 2 shows the revenues, recoveries, and grades of the concentrates of the Cu and Ni in the polymetallic flotation circuit for the original design, the integral design, and the improvement by simulation of this integrated circuit of Cu and Ni, setting values, through flotation criteria, in the stages of most significant effects given in the GSA study, Table 1 (Gray highlighted data changed: $T_{Cp}^{S2} = 0.85$, $T_{Pn}^{S2} = 0.92$, $T_{Po}^{R1} = 0.06$, $T_{G}^{R1} = 0.01$), $T_{Po}^{R2} = 0.2$, $T_{G}^{R2} = 0.02$).

Table 2. Summary of the performance of the original design, integrated design, and improvement after GSA.

Circuit	Revenues	Global recoveries				Concentrate grade		
	MM$US/year	Cp	Pn	Po	NSG	Cu	Ni	Po
Original design								
Cu		66.06	3.40	4.68	0.20	22.98	0.85	8.53
Ni		0.13	75.67	54.28	0.64	0.01	7.76	43.90
Total	261.9							
Optimal integrated design								
Cu		88.18	1.95	5.66	0.05	29.09	0.42	9.79
Ni		0.03	79.31	54.89	0.61	0.00	8.18	45.05
Total	314.9							
Improved integrated design using GSA								
Cu		**91.97**	2.06	0.39	0.04	**30.50**	0.45	6.90
Pb		0.03	**88.03**	54.30	0.50	0.00	**9.60**	45.47
Total	354.0							

The significant improvements of the integral design concerning the original design shown in Table 3 indicate that studies should be carried out to incorporate integration in the design of polymetallic ore flotation circuits. The application of GSA allows increased revenues by 12% and 35% concerning the integrated design and original design, respectively.

4. Conclusions

Integrated designs would considerably improve the design of polymetallic ore circuits. Improvements in the optimal integral circuit operation and identifying bottlenecks can be made with a GSA. Thus, the focus should be on optimizing the operating conditions in those flotation stages that have a more significant effect on improving the recovery and grade of the metal concentrates.

In our case study, an integrated Cu and Ni polymetallic circuit obtained using optimization and the subsequent improvement proposal was analyzed, focusing on the scavenger stage, S2, that has a more significant effect on the global recovery of chalcopyrite and pentlandite, and in decreasing the floatability of pyrrhotite and gangue in R1 and R2 stages to increase the Cu and Ni grades, respectively.

Acknowledgments

This publication was supported by the Agencia Nacional de Investigación y Desarrollo de Chile through ANID/ACT210027 and Fondecyt 1211498 grant.

References

Y. L. Botero, Cisternas, L. A., Demers, I., Benzaazoua, M., 2024, Insights into the design of polymetallic ore flotation circuits, including tailing desulfurization. Minerals Engineering, 205.
D. A. Calisaya, López-Valdivieso, A., de la Cruz, M. H., Gálvez, E. E., Cisternas, L. A., 2016, A strategy for the identification of optimal flotation circuits. Minerals Engineering, 96–97, 157–167.
L. A. Cisternas, L. A., Lucay, F., Gálvez, E. D., 2014, Effect of the objective function in the design of concentration plants. Minerals Engineering, 63, 16–24.
M. J. W. Jansen, 1999, Analysis of variance designs for model output. In Computer Physics Communications (Vol. 117).
F. A. Lucay, Lopez-Arenas, T., Sales-Cruz, M., Gálvez, E. D., Cisternas, L. A., 2020, Performance profiles for benchmarking of global sensitivity analysis algorithms. Revista Mexicana de Ingeniería Química, 19(1), 423–444.
F. A. Lucay, Cisternas, L. A., Gálvez, E. D., 2015, Retrofitting of Concentration Plants Using Global Sensitivity Analysis. In Computer Aided Chemical Engineering (Vol. 37, pp. 311–316).
A. Saltelli, Annoni, P., Azzini, I., Campolongo, F., Ratto, M., Tarantola, S., 2010, Variance based sensitivity analysis of model output. Design and estimator for the total sensitivity index. Computer Physics Communications, 181(2), 259–270.
F. D. Sepúlveda, Cisternas, L. A., & Gálvez, E. D., 2013, Global sensitivity analysis of a mineral processing flowsheet. In Computer Aided Chemical Engineering (Vol. 32, pp. 913–918).

ESCAPE-34 PSE-2024
European Symposium on Computer Aided Process Engineering
&
Process Systems Engineering

Flavio Manenti, Gintaras V. Reklaitis (Eds.), Book of Abstract of the 34th European Symposium on Computer Aided Process Engineering / 15th International Symposium on Process Systems Engineering (ESCAPE34/PSE24), June 2-6, 2024, Florence, Italy.

Economic Nonlinear Model Predictive Control for Flexible Operation of a Reaction-Separation-Recycle Process

Mohammad El Wajeh,[a] Adel Mhamdi, [a] Alexander Mitsos, [a,*]

[a]*RWTH Aachen University, Process Systems Engineering (AVT.SVT), Aachen, Germany*
[*]*amitsos@alum.mit.edu*

Abstract

Economic nonlinear model predictive control (eNMPC) can enable flexible and economically optimal process operation. We apply eNMPC within a virtual environment to an electrified reaction-separation-recycle process actively participating in real-time electricity markets, a subprocess of biodiesel production detailed in our recent work (https://arxiv.org/abs/2308.09537). Employing a mechanistic dynamic model that serves as both the controller model and plant surrogate, we perform a closed-loop case study spanning a 24-hour period with historical electricity prices. The eNMPC strategy results in energy cost savings exceeding 28% compared to optimal stationary operation, yielding similar results to offline dynamic optimization, all while maintaining real-time feasibility.

Keywords: Model predictive control, Demand-side management, Optimal control

1. Introduction

One effective approach for achieving flexible and economically optimal operation of chemical processes is economic nonlinear model predictive control (eNMPC) (Amrit et al., 2013). eNMPC involves solving a dynamic optimization (DO) problem with an economic objective function directly within the controller while considering process models and operational constraints. While researchers have successfully applied eNMPC in various applications, its potential for realizing demand-side management in electrified chemical processes involving reaction, separation, and recycle (RSR) components remains underexplored in the literature. We apply eNMPC in silico to an electrified RSR process, specifically focusing on a simplified version of the biodiesel production subprocess in El Wajeh et al. (2023). We examine a typical demand-response scenario and utilize the same model for both the eNMPC controller and the plant surrogate. For a more comprehensive understanding of the process description and modeling, see El Wajeh et al. (2023). The RSR process flowsheet is illustrated in Figure 1.

2. eNMPC Strategy

We implement the eNMPC strategy by solving online DO problems with a sampling time of 15 minutes over one day. We minimize the process operating cost while penalizing the

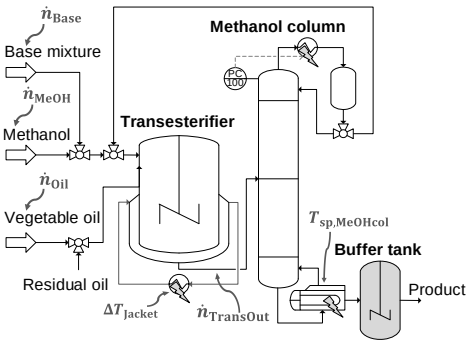

Figure 1. Simplified RSR biodiesel subprocess flowsheet. Controls are indicated by arrows.

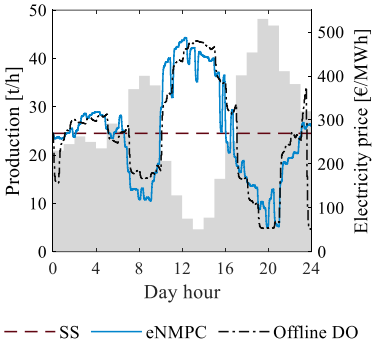

Figure 2. Production rate and electricity price profiles.

control moves and enforcing operational constraints on product purities and level limits. To maintain computationally tractable DO, the control and prediction horizons extend to 10 and 12 hours, respectively. For each optimization iteration, we discretize the controls and constraints at 30-minute and 15-minute intervals, respectively. We implement the model in Modelica and use DyOS (Caspari et al., 2019) to solve the DO problems.

3. Results and Discussion

Figure 2 illustrates the production rates when operating under the eNMPC strategy, as well as for optimal steady-state (SS) and offline DO operations. As expected, with the aid of the buffer tank, the production rate exhibits an inverse relationship with the electricity price profile. Notably, the eNMPC results closely align with the outcomes of the offline DO approach, enabling a heightened degree of operational flexibility when contrasted with the benchmark SS operation. In terms of energy cost savings, both eNMPC and offline DO operations demonstrate substantial benefits, achieving a 28% reduction in costs. Furthermore, the CPU times for solving the DO problems within the eNMPC framework consistently remain below its sampling time, with an average value of 130 seconds, underscoring the real-time feasibility of the eNMPC approach.

4. Conclusion

We demonstrate that eNMPC improves the flexible operation of an RSR process while being real-time tractable. The considered RSR process is a biodiesel production subprocess, wherein buffer tanks decouple different process parts, enabling distributed optimization. Consequently, distributed eNMPC emerges as a promising approach for the optimal flexible operation of the entire biodiesel production process.

References

Amrit R., Rawlings J.B., Biegler L.T. (2013). Optimizing process economics online using model predictive control. Comput. Chem. Eng., 58, 334-343.

Caspari A., Bremen A. M., Faust J., Jung F., Kappatou C. D., Sass S., Vaupel Y., Hannemann-Tamás R., Mhamdi A., Mitsos A. (2019). DyOS - A Framework for Optimization of Large-Scale Differential Algebraic Equation Systems. Computer Aided Chemical Engineering: 29 European Symposium on Computer Aided Process Engineering, Kiss A. A., Zondervan E., Lakerveld R., Özkan L., Eds., 46, 619–624.

El Wajeh M., Mhamdi A., Mitsos A. (2023). Optimal design and flexible operation of a fully electrified biodiesel production process. URL https://arxiv.org/pdf/2308.09537.

ESCAPE-34 PSE-2024
European Symposium on Computer Aided Process Engineering
&
Process Systems Engineering

Flavio Manenti, Gintaras V. Reklaitis (Eds.), Book of Abstract of the 34th European Symposium on Computer Aided Process Engineering / 15th International Symposium on Process Systems Engineering (ESCAPE34/PSE24), June 2-6, 2024, Florence, Italy.

Flexible Hybrid Utility Systems for Industrial Decarbonization

Matthew Taylor,[a] Martin Atkins,[a*] Isuru Udugama,[b] Timothy Gordon Walmsley[a]

[a]*Ahuora – Centre for Smart Energy Systems, School of Engineering, The University of Waikato, Private Bag 3105, Hamilton, 3240, New Zealand*

[b]*Department of Chemical and Materials Engineering, Faculty of Engineering, The University of Auckland, Private Bag 92019, Auckland, 1142, New Zealand*

martin.atkins@waikato.ac.nz

Abstract

To reduce emissions produced due to process heat supply, fossil fuels need to be replaced by renewable fuels in steam boilers. An economical solution may be to utilize renewable electricity and biomass simultaneously to leverage the benefits of both types. This study investigates the economic viability of a dual-fuel boiler system using an industrial case study. Utility system operations were optimized using a Python-based mixed-integer linear programming model, where the minimum operating costs (including fuel and emission components) for all the data points was determined. Under current energy prices, only using coal as the fuel is initially seen as the most cost-effective system. However, as carbon costs increased the dual electrode and biomass system becomes slightly more cost effective. With high price volatility, a hybrid biomass and electrode system would give a 4.9 % cost reduction, as well as a 93.8 % emission reduction.

Keywords: Decarbonization, hybrid utility system, mathematical optimization

1. Introduction

In New Zealand, process heating is largely supplied through non-renewable sources with around 75% supplied by coal and natural gas (Energy Efficiency and Conservation Authority, 2023). Methods of process heat delivery are moving away from fossil fuels, in part due to rising carbon emission costs as well as climate action policy. The New Zealand government is phasing out coal boilers by 2037, prohibiting their usage. Much of the energy used for process heat is used in steam boilers and there are two main renewable alternatives - biomass and electrode boilers using renewable/low carbon electricity. Electrode boilers have high operational costs due to electricity prices and volatility of electrical pricing, whereas biomass boilers have high capital costs (if not retrofitting coal boilers) and potential issues with supply security.

A barrier to decarbonization is uncertainty and risk associated with costs and timeframes resulting in companies deferring investment decisions. Implementing both electrode and biomass boilers together as a hybrid system can reduce the economic barrier (Walmsley

et al., 2023). For hybrid boiler systems, an electrode boiler could operate simultaneously and in a flexible manner with a biomass boiler. In this configuration the biomass boiler would provide baseload steam and the electrode boiler acting as a peaking boiler with rapid response times. In state-of-the-art utility systems, dual-boiler setups tend to have simple operating rules, such as triggers to switch the primary boiler.
The aim of this work is to quantify the economic viability of a price-responsive dual-boiler setup compared to individual boiler types for the same amount of load. To achieve this aim, the study focuses on minimizing the operating cost of different single and dual industrial boiler setups by manipulating which fuel is used, and how much of it is consumed over time. The scope of this study is limited to operating cost optimization, specifically the firing rates of the different boilers in the hybrid system. Future work will look at expanding the scope and move towards a real-time optimization approach.

2. Mathematical Optimization Model

2.1. Model Parameters

The main structure of the optimization model is an equation-based time-slice model where a year's worth of data is split into multiple small slices, and these slices are then solved individually for the minimum cost. The main parameters into the model are the thermal demand, fuel costs, and emission trading scheme costs, with the output of the model being the annual operating cost and annual CO_2 emissions.

2.1.1. Thermal Model

For this work, an industrial case study is used as the basis for the modelling. This is a New Zealand processing plant that currently uses coal boilers as the medium for process heat delivery, but due to confidentiality reasons commercially sensitive details are omitted. One of the major objectives of this work is to understand how the varying electricity spot price can affect the operating cost, which required the thermal demand of the plant to be the same time-step as the spot-price. The thermal model was generated using a previous mass and energy balance, where the heat demand was determined by the change in enthalpy between the water and the steam for each boiler, using on-site sensors. This was then validated against recorded coal usage from the plant. The thermal is shown in Figure 1 as an ordered plot to show the distribution of values. Using this thermal model alongside knowledge of decision-making factors different models and scenarios could be made. Having a specific case study is also important as it establishes a fixed geography of the plant, which can affect many contributing factors, such as fuel price, fuel supply, and electricity prices.

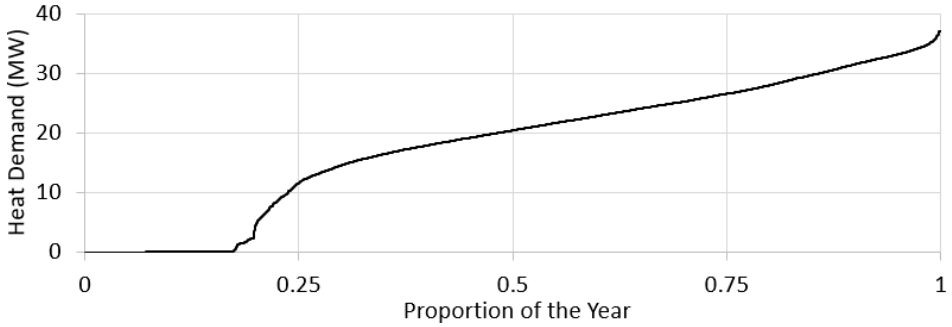

Figure 1: Plant site thermal demand.

2.1.2. Fuel Costs

The main parameters for the optimization are the different fuel costs, which are composed of supply costs and emission trading scheme costs. For the electricity pricing (excluding transmission and distribution costs), this is the trading period (half-hourly) price and applying a general pricing increase factor of 2 %. This increase represents the change in price over time for the average price, based on the location of the plant and plant experience. For the biomass and coal pricings, these were given as starting prices of \$16 NZD/GJ and \$5 NZD/GJ and increasing at 2 % per annum, with the numbers based on the experience of the plant.

2.1.3. Emission Costs

To calculate the emission-based costs both the emission factor and emission unit cost are required. The emission factor represents the relative mass of CO_2 emitted for every unit of fuel consumed. For this work, the emission factors used were 0.083 $t_{CO2\text{-}e}$/GJ for coal, 0.00278 $t_{CO2\text{-}e}$/GJ for biomass, and 0.0167 $t_{CO2\text{-}e}$/GJ for electricity (Ministry for the Environment, 2023a). The electricity emissions factor is an estimate of the average factor over the next 15 years. A price pathway for emissions starting at \$70 NZD/$t_{CO2\text{-}e}$ in 2023 rising to \$144 NZD/$t_{CO2\text{-}e}$ in 2030, and then \$260 NZD/$t_{CO2\text{-}e}$ CO_2 in 2050 was used (Ministry for the Environment, 2023b). A piece-wise linearization was applied to the price pathway. For the optimization of the plant in this study, the final time is set at 2037 (the 2050 pricing helps create the linearization).

2.1.4. Boiler Limits

The boilers in the model have established upper (Q_{UL}) and lower limits (Q_{LL}) that constrain the firing rate, represented by Equation 1. For electrode boilers in the model, the lower limit is set at zero duty (the same as no lower limit) as it has a consistently high efficiency at all partial firing rates.

$$Q_{LL} \leq Q \leq Q_{UL} \tag{1}$$

Solid fuel boilers however have a diminishing efficiency at lower firing rates, so while the partial efficiency model was not used, this was represented by setting the lower operating limit to be half of the upper operating limit. The limits for the boilers are defined based on the current specifications of the boilers in the plant (for the solid fuel boilers) and potential plans (for the electrode boiler). The upper limits are 30 MW for solid fuel boilers, and 12 MW for electrode boilers.

2.2. Optimization Formulation

The optimization is performed using the equation based GEKKO Python package (Beal et al., 2018). For the optimization of a year of data the parameters are defined before solving, with the main parameters being the total fuel cost (C_F) and the limits of the boiler firing rate (Q). For all fuel types, the total cost is made of the supply cost (C_S) and the emission cost (C_E) (based on the emission factor (EF)), shown in Equation 2:

$$C_F = C_S + EF \cdot C_E \tag{2}$$

The firing rate of the boiler is a variable within the model and is the primary aspect that is changed within a timestep. The optimizer will change the duty for each timestep to minimize the operating cost (C_T) while simultaneously meeting the overall demand (Q_T). For an example optimization of a hybrid biomass (denoted by subscript B) and electrode (denoted by subscript E) system, the objective function and demand definition are shown in Equation 3 and Equation 4:

$$min\ (C_T),\ where\ C_T = Q_B \cdot C_{F,B} \cdot z_B + Q_E \cdot C_{F,E} \cdot z_E \quad (3)$$

$$Q_T \leq Q_B \cdot z_B + Q_E \cdot z_E \quad (4)$$

Where z is the binary switch for each boiler that represents the operating state (0 for off, 1 for on). This is used for boilers with a lower limit above 0 MW. The optimization is solved using the GEKKO APOPT solver.

3. Results and Discussion

Five different scenarios are used in this study: coal, biomass, and electrode only, and two hybrid scenarios of biomass/electrode and coal/electrode. Individual boilers give a reference point, whereas the two hybrid scenarios represent potential transition pathways. The main aspect that changes over time is the emission trading scheme pricing, and as the price increases over time, the expectation is that electricity would be the primary fuel in the coal and electrode hybrid and the biomass would be primary fuel in the biomass and electrode hybrid. Figure 2 shows the annual energy costs of the different scenarios at five-yearly intervals. These intervals are capped in 2037, as this is when coal boilers will be phased out in New Zealand, and unable to be used. Comparing coal and biomass as the base fuel, coal-based systems are cheaper to operate due to the low emissions trading scheme pricing. However, if capital costs are not included, then operating an electrode boiler as well as the coal boiler makes the system cheaper than running just the electrode boiler. 2037 is the year where the biomass hybrid system becomes cheaper than the coal hybrid systems, due to the trading scheme making coal supply more expensive than biomass.

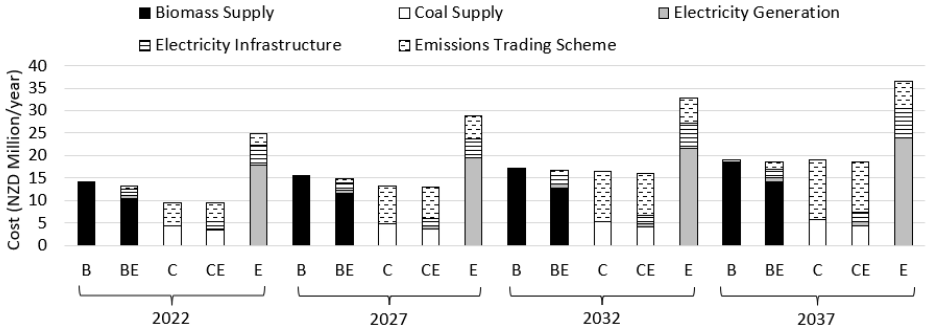

Figure 2: Annual energy costs for the five main scenarios over 15 years.

These results assume that the volatility of the electricity price stays consistent throughout the years. The magnitude is increased by the same 2 % increase factor, but the price volatility stays the same. Volatility (or variance) in this study is the measure of how much the electricity fluctuates away from a recent historical moving average (previous day). To be more realistic, the variance in price is likely to increase because of the addition of more renewable electricity supply into the grid (Electricity Authority, 2022). To investigate this, the model was re-run with new electricity prices, where the variance was increased as a factor of time. The variance was calculated by scaling the difference between actual price (P_A) and the moving average price of the previous day (P_M). The variance increase factor (F) was initially high (20 %) due to the increase not compounding. The main

equation is shown in Equation 5, with P_F representing the new price after scaling. This equation is applied to each price point, repeated for every year since the base year (2022).

$$P_F = P_M + (P_A - P_M) * F \quad (5)$$

The coal hybrid operating cost is recalculated using the new prices, with the results shown in Table 1. With a larger variance on electricity price, the total energy cost decreases because of more periods with a lower electricity price. The constant-variance scenario has a cost reduction of 1.0 %, whereas the increasing variance scenario has a cost reduction of 4.9 %. This means that electrode boiler can be better utilised and meeting the capacity more often. For the scenario without variance, this results in an emissions reduction of 93.8 %, and a reduction of 93.6 % for the high variance scenario.

Table 1: Cost breakdown for different 2037 utility system scenarios.

2037 Scenario	Annual Operating Cost (Million $ NZD)				Annual Emissions (kt CO_2-e)
	Coal/ Biomass	Electricity	Emission Trading Scheme	Total Energy Cost	
Coal Only	5.81	0.00	13.28	19.09	53.95
Coal Hybrid (No Variance)	4.43	2.85	11.23	18.51	42.78
Coal Hybrid (With Variance)	4.11	3.23	10.86	18.20	40.34
Biomass Only	18.59	0.00	0.44	19.03	1.80
Biomass Hybrid (No Variance)	13.45	3.73	1.71	18.89	3.36
Biomass Hybrid (With Variance)	13.15	3.23	1.78	18.16	3.44

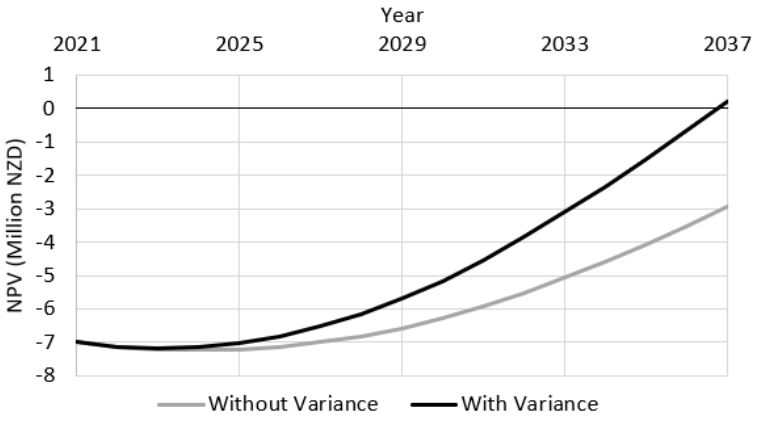

Figure 3: Net present value over time for an implemented 12 MW electrode boiler.

Knowing that variance reduces the operating cost can help with cost justification, as it means the payback period will be shorter. For both the variant and non-variant pricing, the net-present value has been calculated, assuming that an electrode boiler was built in

the starting year (2022). Only the electrode boiler costing was included, as this is closer aligned with the direction of the case study plans. Figure 3 shows this value over time, showing that a variance increase factor of 1.2 (20 % increase) per year is required to make the electrode boiler pay back (assuming the specific parameters of this case study) by 2037. The initial capital cost of the boiler was set at 7 million NZD as an average for the boiler and required infrastructure costing. By not including the variance, the electrode boiler does not pay back before the 2037 mark which can make it harder to justify the decision from an industrial perspective.

3.1. Future Work

The optimization of this study has focused on the time-of-use minimization. However, only the specific firing rate of the boilers has been included in the optimization loop. A future iteration of the optimization should include the boiler capacity as an outer layer. However, this is not a simple process, as the sizing of the boilers has implications on the capital costing, which does not often have linear scaling. Other aspects to investigate would be the costing of individual aspects (like the emission trading scheme, fuel, and electricity costs). These have been assumed as fixed values or linear progressions, but in practice this does not happen. An example is the evolving biomass market within New Zealand, which could cause the fuel cost to increase non-linearly. Finally, better defined installation timelines should be calculated, considering the existing lifespan of coal boilers on-site. The hypothesis would be that if a coal boiler were to reach end-of-life, it should be replaced by a biomass boiler, but there could be value in having the biomass boiler fire coal at a lower efficiency and retrofitting it to biomass after a few years.

4. Conclusion

The optimisation suggests a two-step utility system transition plant (for cost minimisation). Considering higher electricity volatility prices in the future, the recommendation is that first, as soon as practicable, an electrode boiler (12 MW capacity) should be installed next to the coal boiler, reducing annual energy costs by up to 4.9 % and emissions by 25.2 %. Second, the coal boiler would be replaced by a biomass boiler towards 2037, for a total emissions reduction of 93.6 %.

References

L.D.R. Beal, D. Hill, R.A. Martin, J.D. Hedengren, 2018, GEKKO Optimization Suite, Processes, Volume 6, Number 8

Electricity Authority, 2022, Electricity price volatility, https://www.ea.govt.nz/news/eye-on-electricity/electricity-price-volatility-an-emerging-feature-in-an-increasingly-renewable-market/

Energy Efficiency and Conservation Authority, 2023, Energy End Use Database – Key insights and methodology, Wellington, New Zealand. https://www.eeca.govt.nz/insights/data-tools/energy-end-use-database/

Ministry for the Environment, 2023a, Measuring emissions: A guide for organisations, Wellington, New Zealand, https://environment.govt.nz/assets/publications/Measuring-Emissions-Guidance_DetailedGuide_2023_ME1764.pdf

Ministry for the Environment, 2023b, Review of the New Zealand Emissions Trading Scheme: Summary of modelling, Wellington, New Zealand

T. Walmsley, M. Philipp, M, Picón-Núñez, H. Meschede, M. Taylor, F. Schlosser, M. Atkins, 2023, Hybrid renewable energy utility systems for industrial sites: A review, Renewable and Sustainable Energy Reviews, Volume 188

ESCAPE-34 PSE-2024
European Symposium on Computer Aided Process Engineering
&
Process Systems Engineering

Flavio Manenti, Gintaras V. Reklaitis (Eds.), Book of Abstract of the 34th European Symposium on Computer Aided Process Engineering / 15th International Symposium on Process Systems Engineering (ESCAPE34/PSE24), June 2-6, 2024, Florence, Italy.

Reinforcement Learning Combined with Digital Twin Model for Chemical Process Control

Somayeh Mirzaei, Jia-Lin Kang*, Zi Hang Yang

Department of Chemical and Materials Engineering, National Yunlin University of Science and Technology, Yunlin 64002, Taiwan ROC
jlkang@yuntech.edu.tw

Abstract

This study proposes reinforcement learning (RL) combined with a digital twin model to implement an environment for RL training and the stability of process control. The simulated process is established based on a sequence-to-sequence rolling model and an optimization algorithm to build a Model Predictive Control (MPC). The control stability of RL is analyzed using Selective Hydrogenation Unit (SHU) for the separation of C4 and C5 components in the column. Monte-Carlo deep deterministic policy gradient (MC-DDPG) is proposed as RL model and five types of reward functions are designed to reduce the energy consumption of process control. The value of integral absolute error (IAE) for C5 components are reduced by 100% using RL compared to MPC. For C4 components the IAE value using RL decreased by 67% and 80%, respectively indicating that the control effect of RL is better than that of MPC.

Keywords: Reinforcement learning; Digital twin model; StS Rolling prediction; Energy control

1. Introduction

Reinforcement learning (RL) is a subclass of machine learning which an agent learns by interacting with an unknown environment. The agent obtains feedback in terms of a reward from the environment, and it applies this feedback to train itself and collect experience and knowledge about the environment (Naeem, Rizvi et al. 2020, Panzer and Bender 2022). RL needs to interact with the real process for training, but due to the process safety it is not allowed to directly apply the actual process for interactive training. Kang et al. (Kang, Mirzaei et al. 2022) proposed a DDPG model with two-stage training to control the performance of boiler level control. The result showed that compared with DDPG model that directly contracts with online training, the two-stage training DDPG can effectively reduce the number of training. They also proved that control ability of three stages DDPG is better than that of 3E control.
Reinforcement learning can handle continuous or discrete control of single-input single-output systems and multiple-input multiple-output systems, and can perform well in the case of noise in the process control. However, there is not open literature to show that the

simulation results are applied to the actual process for the reinforcement learning process control. Therefore, this study proposes RL combined with a digital twin model to implement an environment for RL training and the stability of process control. This study refers to Yoo et al. (Yoo, Kim et al. 2021) using the Monte-Carlo algorithm to replace the TD-error used in DDPG to update the model, this model is called MC-DDPG. Monte-Carlo deep deterministic policy gradient (MC-DDPG) is introduced as RL model and five types of reward functions are designed to reduce the energy consumption of process control.

2. Methodology

In this study, the real and virtual processes are implemented using Aspen Dynamics simulation and digital twin model, respectively. First, a virtual process is built by digital twin model. Then, the reinforcement learning is combined with virtual process for interactive training. The model is validated using virtual process and then the actual process can be controlled. This process is divided into training and testing parts. A sequence-to-sequence rolling model is used to establish a virtual process. The historical data is input to the encoder. Decoder is comprised the current and future operating and disturbance values. When the reinforcement learning training is completed, the virtual process is tested, analyzed the control results, and then the model is applied to the real process for control.

The architecture and training process of MC-DDPG are shown in Figure 1. The Monte Carlo algorithm is a periodic update, not a single-step update, and the actual reward can be used directly for model training without additional bootstrapping to obtain the real reward. Hence, MC-DDPG needs a set of Actor-Critic network, and Actor and Critic are each an independent ANN network.

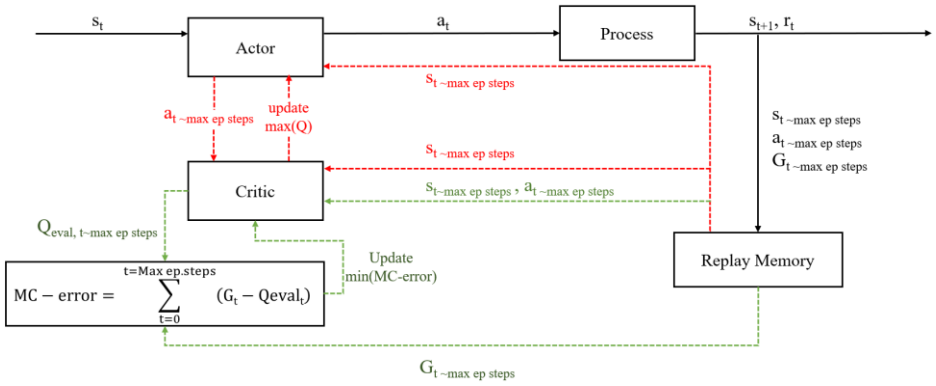

Figure 1. MC-DDPG model used in this study

As shown in Figure 2, the historical data and the operation given by the optimization tool are fed into StS rolling model to predict the result. The model performs online error correction by calculating the error between the actual process data and the predicted model. Hence, the control system has the capability of self-adaptation.

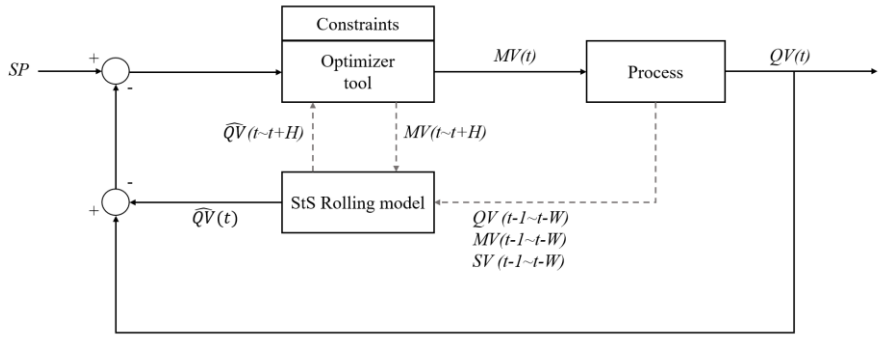

Figure 2. MPC used in this study

Reward functions and integral absolute error (IAE) are used as the basis to evaluate the model control. 5 types of reward functions (Eq. 3-7) are applied to calculate the energy consumption of the process.

Based on Eq. 2, $C5_{loss}$ and $C5_{loss,\ sp}$ indicate the upper product concentration and concentration limitation of output product in column, respectively. $C4_{loss}$ and $C4_{loss,\ sp}$ represent concentration of bottom product and the concentration limitation, respectively. In addition, this study tested each model for 10 rounds, each round simulated 300 time steps, and each time step was simulated for 10 minutes, so each round simulated a total of 3000 minutes.

$$R = R_{conc.} + R_E \tag{1}$$

$$R_{conc.} = \begin{cases} 10, if\ C5_{t,loss} < C5_{loss,sp}\ and\ C4_{t,loss} < C4_{loss,sp} \\ 0 \end{cases} \tag{2}$$

$$R_E = \begin{cases} 2, if\ E_{t-1} > E_t \\ 1, elif\ E_{t-1} > E_t \\ 0 \end{cases} \tag{3}$$

$$R_E = \begin{cases} 10, if\ E_{t-1} > E_t \\ 5, elif\ E_{t-1} > E_t \\ 0 \end{cases} \tag{4}$$

$$R_E = \frac{1}{E_t} \times 4 \tag{5}$$

$$R_E = \frac{1}{W_{C5} \times C5_t + W_{C4} \times C4_t + E_t} \tag{6}$$

$$R_E = \begin{cases} 5, if\ E_t > E_{t,reg.} - 0.005 \\ 0 \end{cases} \tag{7}$$

3. Case study

3.1 Process description

The industrial Selective Hydrogenation Unit (SHU) as a simulated plant was simulated using Aspen Dynamics® to illustrate the effectiveness of the proposed model. The flowsheet is shown in Figure 3. In this study, the quality control of main products including C5 and C4 at the top and bottom of column are investigated. As shown in figure, quality variables of C5 and C4 products are defined as qv_1 and qv_2, respectively.

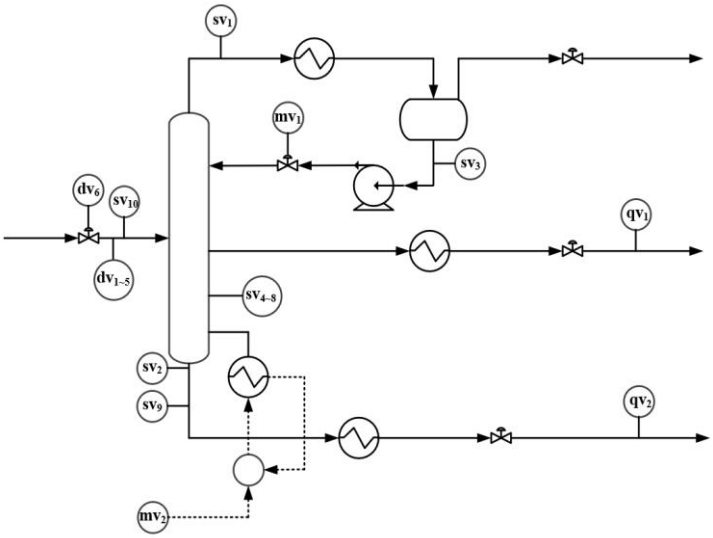

Figure 3. Schematic illustration of SHU process.

4. Result and discussion

4.1 comparison of MPC and RL

Figure 4 indicates control performance of model predictive control and reinforcement learning models in the real process. The result compares the IAE analysis based on C5 and C4 products. The value of IAE for C5 product reduces by 100% using reinforcement learning compared to MPC. The IAE value for C4 product using RL decreases by 67% and 80% respectively, indicating that the control effect of reinforcement learning is better than that of MPC.

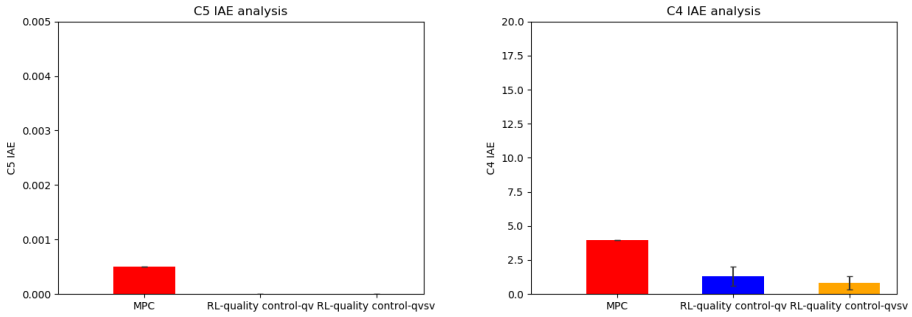

Figure 4. IAE comparison for RL and MPC models

Figure 5 demonstrates IAE value of real case for C5 and C4 products using MPC and 5 types of reward functions considered in this study. It is found that the IAE value for C5 and C4 products using type 3 of reward function is higher than that of MPC models. Therefore, the energy consumption is not considered for type 3.

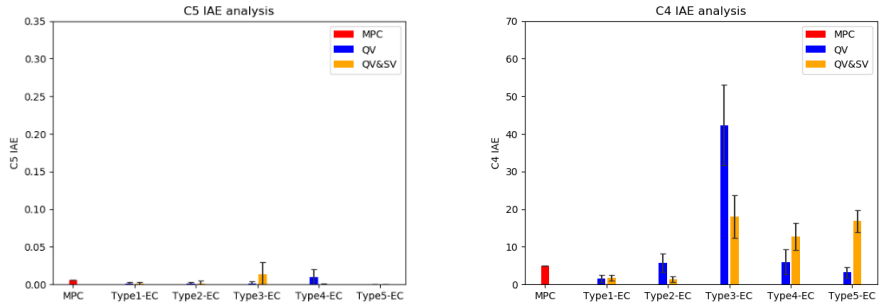

Figure 5. IAE comparison using MPC and different reward functions

Table 1 shows energy consumption reduced using MPC and RL for 4 types of reward functions. It is obvious that type 5 of reward function has the best performance.

Table1. Energy consumption reduced by RL compared to MPC

	Type-1(%)	Type-2(%)	Type-4(%)	Type-5(%)
QV	0.2641	1.0734	0.2058	-0.3945
QV&SV	0.4422	0.4577	-0.5109	-0.4426

4.2 Effect of noise on RL

Figure 6 indicates performance of RL using 3% noise for actual process. IAE value for C5 and C4 products using ±3% noise is slightly higher than that of without noise. These results prove that reinforcement learning can stably control the process when ±3% noise is added to the process. However, the control ability of the model decreases because the information input to the model increases.

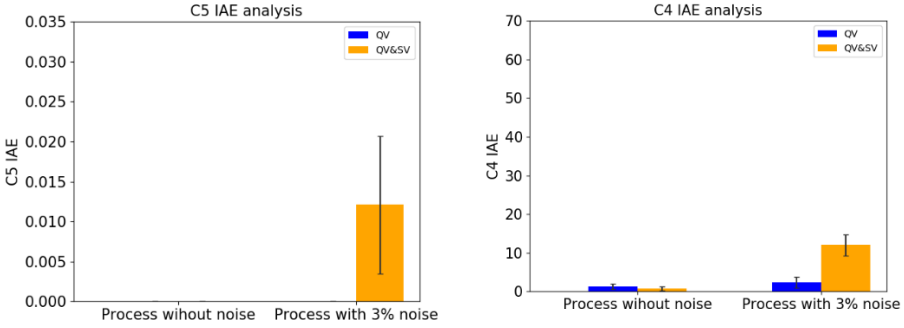

Figure 6. Effect of noise on stability of RL

5. Conclusions

RL needs to interact with the real process for training, but due to the process safety it is not allowed to directly apply the actual process for interactive training. Therefore, this study proposes Monte-Carlo deep deterministic policy gradient (MC-DDPG) as RL model which is combined with a digital twin model to implement an environment for RL training and the stability of process control. Model Predictive Control (MPC) as virtual

process is established based on a sequence-to-sequence rolling model and an optimization algorithm to train the reinforcement learning. StS rolling model is used due to the capability of long-term predictions. MC-DDPG model could perform better than MPC and type 5 of RL was the most stable to reduce the amount of energy consumption. Furthermore, 3% noise could not disturb the RL model stability.

References

Kang, J.-L., S. Mirzaei and J.-A. Zhou (2022). "Robust control and training risk reduction for boiler level control using two-stage training deep deterministic policy gradient." Journal of the Taiwan Institute of Chemical Engineers **130**: 103956.

Naeem, M., S. T. H. Rizvi and A. Coronato (2020). "A gentle introduction to reinforcement learning and its application in different fields." IEEE Access **8**: 209320-209344.

Panzer, M. and B. Bender (2022). "Deep reinforcement learning in production systems: a systematic literature review." International Journal of Production Research **60**(13): 4316-4341.

Yoo, H., B. Kim, J. W. Kim and J. H. Lee (2021). "Reinforcement learning based optimal control of batch processes using Monte-Carlo deep deterministic policy gradient with phase segmentation." Computers & Chemical Engineering **144**: 107133.

ESCAPE-34 PSE-2024
European Symposium on Computer Aided Process Engineering
&
Process Systems Engineering

Flavio Manenti, Gintaras V. Reklaitis (Eds.), Book of Abstract of the 34th European Symposium on Computer Aided Process Engineering / 15th International Symposium on Process Systems Engineering (ESCAPE34/PSE24), June 2-6, 2024, Florence, Italy.

Physics-Informed Neural Networks in Model Predictive Control for Regulating Density in Polymer Blending

*Po-Chun Mao, Yu-Ting Liu, Yuan Yao**
Department of Chemical Engineering, National Tsing Hua University, Hsinchu, 30013, Taiwan, ROC
**Corresponding Author's E-mail: yyao@mx.nthu.edu.tw*

Abstract

Traditional model predictive control (MPC) often relies on linear models, leading to potential inaccuracies when implemented in real-world scenarios with marked nonlinearity, such as grade transitions in chemical processes. In this research, we utilize a physics-informed neural network (PINN) for the dynamic modeling within MPC. By integrating constraints from physical laws during deep neural network training, this method reduces the dependency on vast datasets. Simultaneously, it ensures that the resulting dynamic model possesses a clear physical interpretation and a correct sign of process gain which is essential for the stability of the control system. In the case study, we examine a blending process of two polymer materials. Our proposed method efficiently creates a dynamic and nonlinear process model, even when faced with limited density data for model training. We use this model to virtually regulate density during grade transitions using an MPC strategy, illustrating the its feasibility.

Keywords: model predictive control, physics-informed neural network, deep learning.

1. Introduction

Model predictive control (MPC) is a sophisticated method for process control, designed to manage systems within specific constraints. It has been widely used in chemical industry. However, traditional MPC, based on linear models, often falls short in accuracy, particularly when dealing with nonlinearities common in processes such as grade transitions in chemical plants. To overcome this, integrating neural networks into MPC has been proposed for enhanced nonlinear modelling (Draeger et al., 1995). But the conventional neural networks, while powerful, require extensive training and result in models that lack clear physical interpretation, limiting their practical industrial application.

Our research tackles this challenge by employing physics-informed neural networks (PINN) (Raissi et al., 2019) to build a dynamic model within MPC, using actual factory data. Given the limited availability of data, mostly from steady-state processes, PINN is particularly advantageous. It reduces the amount of data required for training and

improves the model's extrapolation capabilities by incorporating physical laws, making it a more practical solution for real-world industrial applications.
In our case study, we investigate a blending process involving two polymer materials. Here, the key focus is on controlling the post-mixing density, which is regulated by adjusting the ratio of two feed flow rates. This task presents a significant challenge in typical factory settings, where continuous and real-time measurement of product density is difficult. Consequently, during transitions between various product grades, adjustments in the feed flow rate ratio are often based on empirical methods. We established a PINN model, used in conjunction with an MPC strategy, to forecast and virtually regulate density during grade transitions. The results illustrate the feasibility of the proposed method, showcasing its potential to be implemented in real industrial processes.

2. Introduction of the blending process

In this study, our objective was to predict the blending density in a thermoplastic elastomer (TPE) manufacturing process and to establish an PINN-based MPC system. A key goal was to demonstrate the real-world viability of this approach in actual process environments.

The study examines a blending process where two polymer fluids, Component A and Component B, are combined in a mixing tank (as shown in Figure 1). The mixture then passes through a series of reactors before the final density is measured. Due to the lack of real-time density monitoring and adjustment capabilities, operators traditionally rely on their experience to regulate the feed rates of Components A and B during transitions between different product grades.

Table 1 outlines the parameters of the blending process. These include X_{in_A} as a process variable, representing the feed flow rate of Component A (high density), which is determined by the operator, and X_{in_B} as a manipulated variable, denoting the feed flow rate of Component B (low density). X_{out} represents the output flow rate from the mixer. The output density, ρ, is the controlled variable. *PR* indicates the production quantity, while *L* refers to the level in the mixer. Y_1 denotes mass, calculated from *L*. Y_2 represents the ratio of Component A in the mixer, which can be converted into density using empirical formulas.

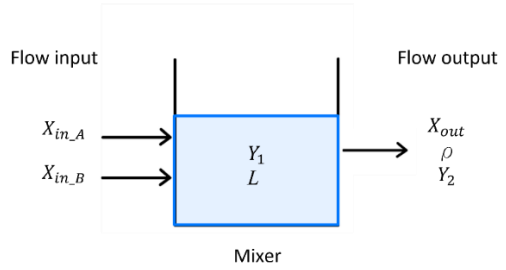

Figure 1. Diagram of blending process in the TPE plant

Table 1. Parameters of the blending process

Parameters	Units	Descriptions
$X_{in\ A}$	Kg/hr	Process variable
X_{in_B}	Kg/hr	Manipulated variable
X_{out}	Kg/hr	Process variable

ρ	Kg/m^3	Controlled variable
PR	Kg/hr	Process variable
L	%	Process variable
Y_1	Kg	Process variable
Y_2	no unit	Process variable

3. Dynamic process model base on PINN

During process modelling, we faced a challenge: the density of the mixture, a crucial product quality variable in the TPE manufacturing process, cannot be measured continuously, resulting in limited label data. Traditional machine learning methods, including most deep neural networks, struggle under such data constraints, often leading to unreliable performance. To overcome this, we chose to employ an PINN, which is designed for supervised learning while adhering to physical laws expressed through differential equations. This approach is particularly suited to addressing data scarcity issues and ensuring physical interpretation of the obtained model.

Figure 2 illustrates the structure of the PINN model. The inputs to this model are $\{X_{in_A}, X_{in_B}, PR, t, \rho_0\}$, where t is the time index and ρ_0 is the initial density at time $t = 0$. The corresponding outputs are $\{Y_1, \rho\}$. The PINN model is designed to involve four hidden layers, each containing 60 neurons. The model was trained using a dataset comprising a small number of on-site data points and 25,000 collocation points, the latter of which were chosen using Latin hypercube sampling (Stein, 1987). The design space was determined by the historical maximum and minimum values of the five input variables. Specifically, the parameter ρ_0 is set to lie within the range of the historical minimum and maximum values of ρ. The utilization of collocation points is particularly effective in reducing the number of required training data points. For the model's architecture, the hyperbolic tangent (*tanh*) function was selected as the activation function, while the Adam algorithm was used for optimization.

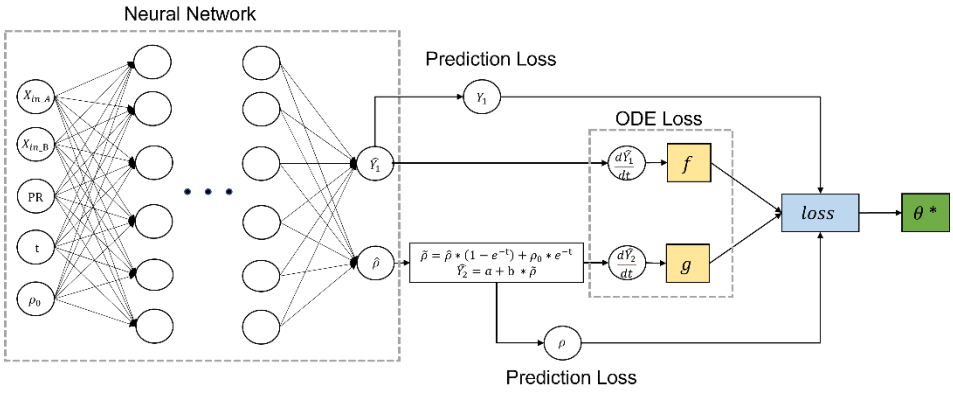

Figure 2. Framework of the proposed PINN model

To define the physical constraints in our PINN model, we formulated a series of ordinary differential equations (ODEs) grounded in the law of mass conservation. (1) represents the overall mass balance, while (2) specifically addresses the mass balance of Component A. (3) is then derived by substituting (1) into (2). We employ equations (1) and (3) to

calculate the ODE losses for the PINN, ensuring that our model adheres to fundamental physical principles. These equations are structured as follows:

$$\frac{dY_1}{dt} = X_{inA} + X_{inB} - X_{out} \quad (1)$$

$$\frac{dY_1Y_2}{dt} = Y_1\frac{dY_2}{dt} + Y_2\frac{dY_1}{dt} = X_{inA} - Y_2X_{out} \quad (2)$$

$$\frac{dY_2}{dt} = \frac{(1-Y_2)X_{inA} - Y_2X_{inB}}{Y_1} \quad (3)$$

Furthermore, the density (ρ) can be converted to the component ratio (Y_2) using an empirical formula, where a and b are known constants.

$$Y_2 = a + b * \rho \quad (4)$$

The loss function of the PINN is composed of four components: two prediction losses and two ODE losses, as depicted in (5) to (11). In these equations, the caret symbol (^) denotes predicted values, i signifies the index of individual sample points, N_R represents the count of on-site data points included in the model training, and N_T indicates the total size of the training set, encompassing both on-site data points and collocation points. The terms f^i and g^i are derived from (1) and (3), respectively. It is noted that the output flow rate values ($X_{out}{}^i$) are only utilized for the calculation of f^i in (9) and are not incorporated into the inputs of the PINN model. To compute the differentials, the automatic differentiation techniques can be employed.

Loss = Prediction loss 1+ Prediction loss2 +λ_1*ODE loss1 +λ_2*ODE loss2 (5)

Prediction loss 1 = $\frac{1}{N_R}\sum_{i=1}^{N_R}((\hat{Y}_1{}^i - Y_1{}^i)^2$ (6)

Prediction loss 2 = $\frac{1}{N_R}\sum_{i=1}^{N_R}((\tilde{\rho}^i - \rho^i)^2$ (7)

ODE loss 1 = $\frac{1}{N_T}\sum_{i=1}^{N_T}(f^i)^2$ (8)

$$f^i = \frac{d\hat{Y}_1{}^i}{dt} - X_{in\_A}{}^i - X_{in\_B}{}^i + X_{out}{}^i \quad (9)$$

ODE loss 2 = $\frac{1}{N_T}\sum_{i=1}^{N_T}(g^i)^2$ (10)

$$g^i = \frac{d\hat{Y}_2{}^i}{dt} - \frac{\left(1-\hat{Y}_2{}^i\right)X_{in\_A}{}^i - \hat{Y}_2{}^i X_{in\_B}{}^i}{\hat{Y}_1{}^i} \quad (11)$$

where the model prediction of ρ is modified from $\hat{\rho}$ to $\tilde{\rho}$ as:

$$\tilde{\rho} = \hat{\rho} * (1 - e^{-t}) + \rho_0 * e^{-t} \quad (12)$$

This modification is crucial to ensure that the predicted density is consistent with the initial condition at t = 0. λ_1 and λ_2 serve as weighting factors that balance the different types of loss functions. Specifically, we have set λ_1 to 0.001 and λ_2 to 1, ensuring an optimal equilibrium between these loss components.

4. PINN-based MPC

Figure 3 presents the layout of the PINN-based MPC. In this setup, the prediction horizon (P) of the MPC is fixed at 6, and the control horizon is set at 1, with each control interval lasting 0.5 hours. At the onset of each grade transition, operators set the desired production quantity and product density targets, denoted as PR_{sp} and ρ_{sp} , respectively. The value of X_{in_A} is then calculated using an empirical formula and held constant with a

zero-order hold. During each control interval k, the predicted product density is represented as $\tilde{\rho}(k+i) = PINN(X_{in_A}, \hat{X}_{in_B}(k+i),\ PR_{sp}, t(i), \check{\rho}_0(k))$, where i ranges from 1 to P. Here, $\check{\rho}_0(k) = PINN(X_{in_A}, X_{in_B}(k),\ PR_{sp}, t(1), \check{\rho}_0(k-1))$ for $k \neq 0$, and $\check{\rho}_0(k) = \rho_0$ for $k = 0$, with ρ_0 being the product density measured before the transition . The variable $\hat{X}_{in_B}$ is the manipulated variable determined by the optimization function (13). During grade transitions, we aim to minimize the Integrated Squared Error, formulated as:

$$X_{in_B}(k+i) = \underset{\hat{X}_{inB}}{argmin} \sum_{i=1}^{P} \left[\rho_{sp} - \tilde{\rho}(k+i)\right]^2 \tag{13}$$

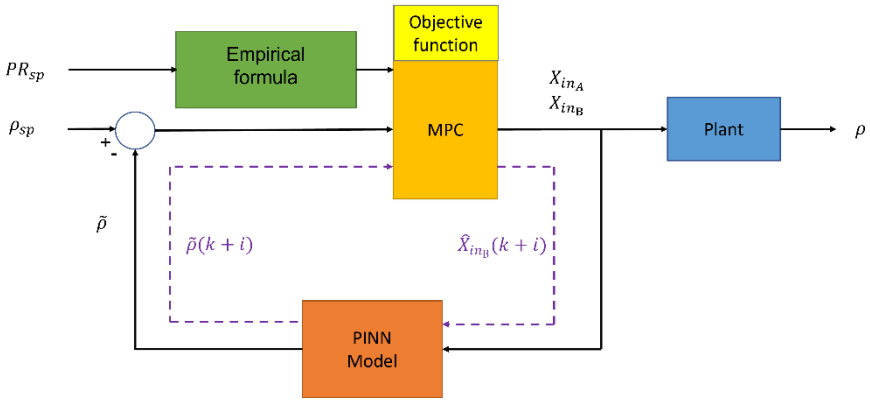

Figure 3. Framework of PINN-based MPC

5. Results and Discussions

Figure 4 displays the coefficient of determination (R^2) and the root mean squared error (*RMSE*) of each on-site data point utilized in the training, validation, and test phases of the PINN model. A total of 150 on-site data points were gathered and distributed across these three subsets in a ratio of 7:1:2.

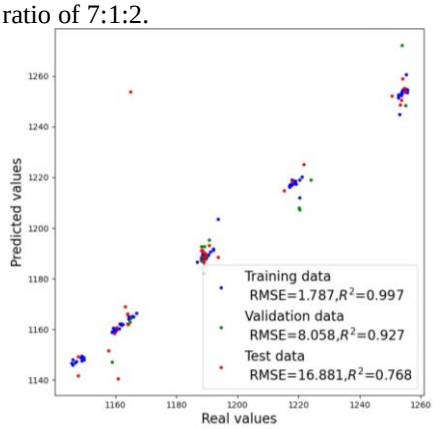

Figure 4. Parity plot between true values and predicted values of product density

Prior to implementing the MPC, control in the case study was executed through a one-step adjustment of both X_{in_A} and X_{in_B}. X_{in_A} was determined using the empirical formula discussed previously, while X_{in_B} was calculated based on the final steady-state mass balance. This approach often led to extended transition times and a considerable

production of off-quality products. Figure 5 illustrates how the proposed PINN-based MPC strategy significantly improves this process. Initially, there is a substantial increase in X_{in_B}, followed by gradual fine-tuning to prevent overshooting and stabilize the control value at its set point. It is evident from the data that our proposed control algorithm notably reduces the transition period and enhances product quality.

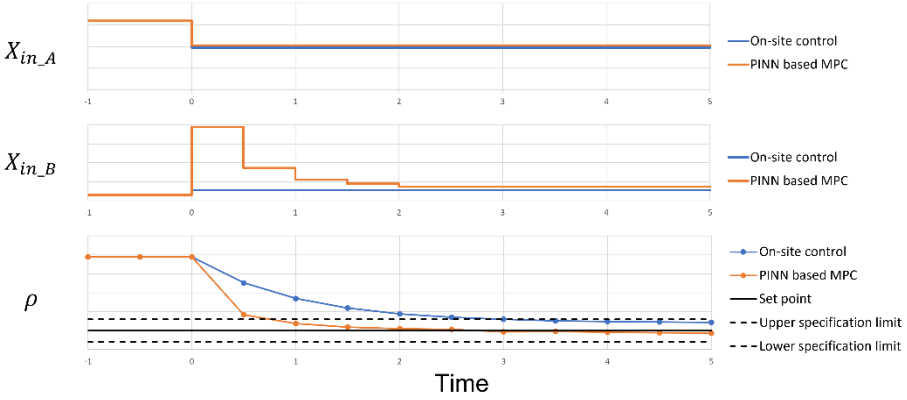

Figure 5. Comparison between the on-site control strategy and the PINN-based MPC in a grade transition

6. Conclusions

In this study, we leveraged a limited dataset of on-site process data to model a blending process using a PINN. The primary objective of this model was to predict product density, serving as a cornerstone for MPC. By integrating physical laws articulated through ODEs and generating collocation points, the PINN model attains commendable predictive accuracy. Comparing to using the mechanistic model only, PINN achieves better predictions by incorporating process measurements in model training. When applied to MPC, this PINN-based control strategy markedly decreases the time needed for grade transitions, thereby enhancing both productivity and product quality.

Acknowledgment

This work was supported in part by the National Science and Technology Council, ROC under project numbers NSTC 112-2221-E-007-015.

References

Draeger, A., Engell, S., & Ranke, H. (1995). Model predictive control using neural networks. IEEE Control Systems Magazine, 15(5), 61-66.

Raissi, M., Perdikaris, P., & Karniadakis, G. E. (2019), Physics-informed neural networks: A deep learning framework for solving forward and inverse problems involving nonlinear partial differential equations, Journal of Computational Physics, 378, 686-707.

Stein, M. (1987), Large sampling properties of simulations using Latin hypercube sampling, Technometrics, 29(2), 143-151.

ESCAPE-34 PSE-2024
European Symposium on Computer Aided Process Engineering
&
Process Systems Engineering

Flavio Manenti, Gintaras V. Reklaitis (Eds.), Book of Abstract of the 34th European Symposium on Computer Aided Process Engineering / 15th International Symposium on Process Systems Engineering (ESCAPE34/PSE24), June 2-6, 2024, Florence, Italy.

Data Depth-based Non-parametric Control Chart for Condition Monitoring of Rolling Element Bearings

I-Yen Wu[a], David Shan-Hill Wong[a], Yu-Jeng Lin[a], Jia-Lin Kang[b]*, Yuan Yao[a]*

[a] *Department of Chemical Engineering, National Tsing Hua University, Hsinchu, 30013, Taiwan, ROC*
[b] *Department of Chemical and Materials Engineering, National Yunlin University of Science and Technology, Yunlin, 64002, Taiwan, ROC*

jlkang@yuntech.edu.tw (Kang); yyao@mx.nthu.edu.tw (Yao)

Abstract

Rolling element bearings play a pivotal role in numerous industrial systems. Therefore, monitoring their condition is essential for ensuring safety and averting equipment failures. In this study, a non-parametric control chart rooted in data depth for the conditional monitoring of bearings was proposed, which transforms the multivariate bearing information into a univariate index by leveraging data sorting and the central tendency of the data cloud. We designate the well-behaved data as located at the centre of this data cloud. Subsequently, a statistic referred to as "rank" is computed for the operational data of the investigated bearing. Based on this rank calculation, we establish a health indicator for the rolling bearings. We have demonstrated the application and feasibility of this method through a case study, successfully using the indicators we created to assess the current condition of the bearings.

Keywords: data depth, condition monitoring, rolling element bearing, control chart

1. Introduction

Given their critical role in various industrial systems, it is essential to monitor the condition of rolling element bearings to ensure safety and prevent equipment breakdowns(Lei, Li et al. 2018). The Shock Pulse Method (SPM)(Zhang, Zhao et al. 2014) serves as a valuable diagnostic tool for rapidly assessing the operational state of these bearings. SPM extracts data from high-frequency vibrations to obtain two primary vibration features, namely LR (Low-Frequency Resonance) and HR (High-Frequency Resonance) which served as the basis for assessing equipment health. However, this health assessment lacks quantitative scaling and requires manual definition to confirm the current health status. In the analysis of bearings conditional monitoring (CM), various vibration characteristics are typically examined. However, it can be challenging to observe equipment health status with multiple variable indicators. Therefore, a reasonable and an intuitive metric should be provided as an indicator of equipment condition.

Principal Component Analysis (PCA) is a widely used tool for multivariate monitoring, including the condition monitoring of rolling element bearings (Ahsan, Mashuri et al. 2018). However, its reliance on the Gaussian distribution assumption often poses a significant challenge in practical scenarios, particularly when the data deviates from this assumed distribution, which is a common occurrence in the condition monitoring (CM) of rolling element bearings. This can lead to misleading results from control charts. To address this, we have developed a nonparametric control chart based on data depth, specifically Tukey depth, which does not require any assumptions about data distributions. This method allows for the creation of a health indicator that accurately quantifies the condition of rolling bearings over time. The effectiveness of this approach is demonstrated through a case study.

2. Methodology

2.1. Data depth

The concept of data depth was first introduced by Tukey et al. (Tukey 1975), highlighting its significance in sorting and analyzing multivariate data. Data depth measures the centrality of multivariate data points in relation to the overall multivariate sample. It adheres to four key properties: 1. affine invariance, 2. maximum value at the center, 3. monotonicity around the deepest point, and 4. vanishing at infinity. Generally, data depth assumes that the data in statistical control follows a p-dimensional distribution function G (referred to as the reference distribution). When G is unknown, an empirical distribution is used, based on the reference sample set $\{x_1, x_2, \ldots, x_m\}$. The reference distribution and sample represent the process in control, i.e. under normal operating conditions.

Various methods exist for calculating data depth, including Mahalanobis depth, Simplicial depth, and Tukey depth. Tukey depth, chosen for its higher breakdown point, measures data points in relation to the centre of the data distribution and considers the distribution across each dimension. The Tukey depth of a data point x under distribution $F(\cdot)$ is defined as follows (Yeh and Singh 1997, She, Tang et al. 2021):

$$TD(F,x) = \inf_{H}\{F(H): H \text{ is a closed halfspace containing } x\} \quad (1)$$

which represents the minimum probability mass carried by any closed halfspace containing the point. The sample version of $TD(F,x)$ is defined by replacing F with F_n, the empirical cumulative distribution function. In the univariate case, the formula simplifies to $TD(F,x) = \min\{F(x), 1\text{-}F(x)\}$. In this study, the qcr package (Flores, Fernández-Casal et al. 2021) is used to calculate the multivariate Tukey depth. A high Tukey depth value implies that the data point is closer to the centre of the data cloud. Conversely, a lower value indicates that the point is more peripheral or potentially an outlier in the dataset.

2.2. r-chart

A distribution-free control chart, as described by Bae et al. (2016), is used to monitor the Tukey depth of each data point. In this study, the r-chart, introduced by Liu in 1995 (Liu 1995), is adopted, which is defined mathematically as:

$$r_G(x) = P\{D_G(y) \leq D_G(x) | y \sim G\} \quad (2)$$

In this formula, x denotes operational data, y represents the reference or "golden" data, and $y \sim G$ indicates that y follows the distribution G. D_G is the data depth, calculated based on (1). If G is unknown, the reference sample $\{y_1,...,y_m\}$ is used instead. The monitoring statistic, or the r value, is then calculated as:

$$r_{Gm}(x) = \frac{\#\{y_j | D_{Gm}(y_j) \leq D_{Gm}(x)\}}{m}. \quad j = 1, \ldots, m \tag{3}$$

where # represents the count function. The value $r_{Gm}(x)$ assesses how closely vector x aligns with the centre of the data cloud formed by the reference sample, by comparing the depth values of x and each point in y. A high probability of x having a greater depth value than those in y suggests that x is likely near the data cloud's centre, resulting in a higher r value and indicating a normal operation. Conversely, a lower probability implies x is likely on the data cloud's edge, leading to a smaller r value and signifying out-of-control data. In the control chart, key thresholds include a centre line of 0.5 and a lower control limit set at α. A statistic below alpha signals an out-of-control process.

3. Case study

This study utilized real-world data from a rolling bearing mounted on an industrial machine. The data was gathered after applying the SPM technique, resulting in multiple variables relevant for the subsequent CM phase. In consultation with equipment experts, a period of "golden data", representing normal operating conditions, was selected to construct control charts. Data collected after this period served as the test set.

Prior to implementing the data depth-based control chart, PCA was used for an initial comparison. The outcomes are illustrated in Fig. 1: Fig. 1(a) displays the Hotelling's T^2 control chart, and Fig. 1(b) shows the *SPE* chart. In these charts, the "golden data" is represented in pink, while other data points are in blue. Notably, a significant number of false alarms are observable during the "golden data" period, attributed to the non-Gaussian nature of the data distribution. Furthermore, a consistent pattern of alarms shortly after the golden data period is seen, contradicting the actual operating conditions of the rolling bearing. Neither the T^2 chart nor the *SPE* chart effectively captures a progressive deterioration trend in the bearing's data.

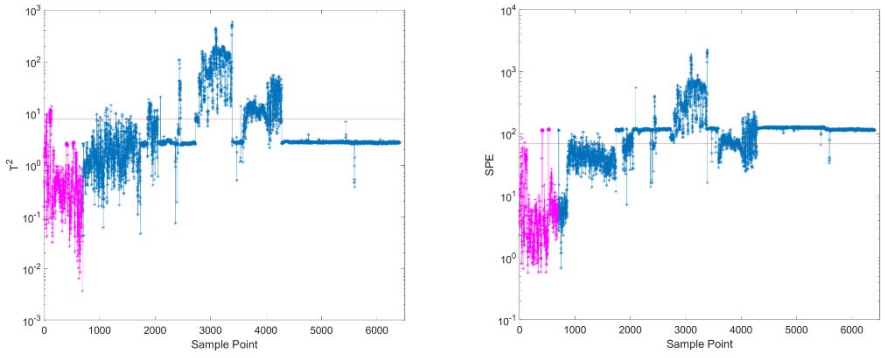

(a) (b)

Figure 1. PCA monitoring results

Subsequently, the proposed method was implemented in the following manner.

1. Reference Sample Selection: The data collected when the bearings are functioning normally and have not experienced failure is identified as “golden data”, serving as the reference sample.
2. Tukey Depth Calculation: The Tukey depth for each data point in the dataset was then calculated.
3. r-chart Construction for Condition Monitoring: An r-chart was subsequently constructed for CM. A process is deemed out of control if the r value falls below the threshold of $\alpha = 0.05$.
4. Minimizing False Alarms with a Moving Window: To further reduce the incidence of false alarms, a moving window approach was adopted. This window consists of n consecutive data points. Based on this window, a health indicator (HI) was formulated using a binomial distribution as shown in equation (4):

$$P(k) = C(n,k) \times p^k \times (1-p)^{n-k} \tag{4}$$

Here, k is the count of data points within the window indicating normal operation, and p (set at 1 - α = 0.95) is the probability of successful operation. $P(k)$ is utilized as the HI, which is interpreted as follows.

- Green Light (Normal Operation): A $P(k)$ value greater than 0.1 suggests normal operating conditions.
- Yellow Light (Caution): A $P(k)$ value between 0.05 and 0.1 acts as a cautionary signal.
- Red Light (Alarm): A $P(k)$ value below 0.05 indicates an alarm, signaling potential issues in the operation.

The r-chart and HI are displayed in Fig. 2(a) and Fig. 2(b), respectively. It is noticeable that the r values of the golden data predominantly converge around an average of 0.5. As time advances and the bearings experience gradual wear, these r values correspondingly decline. This contrasts with the PCA results, where data anomalies appear immediately after the golden data phase. The non-parametric approach, grounded in data depth, facilitates earlier detection of bearing health degradation while effectively minimizing false alarms. Employing this method to develop a health indicator empowers proactive measures against imminent bearing faults.

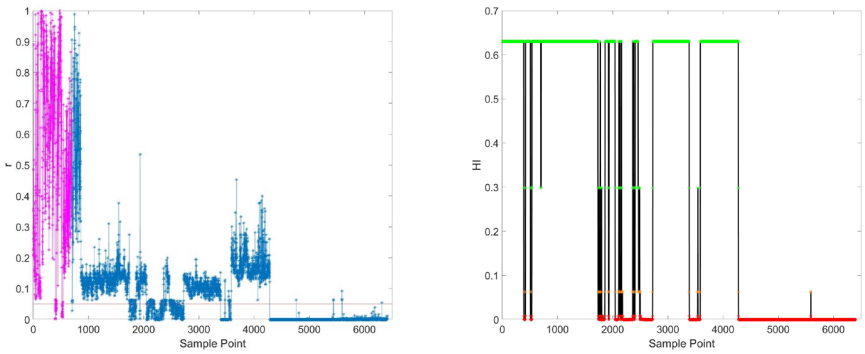

(a) (b)

Figure 2. Data depth-based CM charts

4. Conclusions

In this study, we presented a methodology based on data depth analysis to develop a health indicator for rolling bearings. This method proves particularly effective when dealing with data that does not follow a normal distribution, where traditional PCA for CM may result in inaccuracies. By employing data depth calculation in control charts through a non-parametric approach, this method is not limited by the data's distribution, effectively avoiding the inaccuracies inherent in PCA. The non-parametrically derived health indicator enables earlier detection of bearing health deterioration and significantly reduces false alarms. This innovative approach offers manufacturing facilities a proactive means to foresee and address potential equipment malfunctions.

Acknowledgment

This work was supported in part by the National Science and Technology Council under project number NSTC 112-2221-E-007-105.

References

Ahsan, M., M. Mashuri, H. Kuswanto and D. D. Prastyo (2018). "Intrusion detection system using multivariate control chart Hotelling's T2 based on PCA." Int. J. Adv. Sci. Eng. Inf. Technol **8**(5): 1905-1911.

Flores, M., R. Fernández-Casal, S. Naya and J. Tarrío-Saavedra (2021). "Statistical quality control with the qcr package." R Journal **13**(1): 194-217.

Lei, Y., N. Li, L. Guo, N. Li, T. Yan and J. Lin (2018). "Machinery health prognostics: A systematic review from data acquisition to RUL prediction." Mechanical systems and signal processing **104**: 799-834.

Liu, R. Y. (1995). "Control charts for multivariate processes." Journal of the American Statistical Association **90**(432): 1380-1387.

She, Y., S. Tang and J. Liu (2021). "On Generalization and Computation of Tukey's Depth: Part I." arXiv preprint arXiv:2112.08475.

Tukey, J. W. (1975). Mathematics and the picturing of data. Proceedings of the International Congress of Mathematicians, Vancouver, 1975.

Yeh, A. B. and K. Singh (1997). "Balanced confidence regions based on Tukey's depth and the bootstrap." Journal of the Royal Statistical Society Series B: Statistical Methodology **59**(3): 639-652.

Zhang, X., J. Zhao, J. Kang, H. Li and H. Teng (2014). "Bearing prognostics with non-trendable behavior based on shock pulse method and frequency analysis." Journal of Vibroengineering **16**(8): 3963-3976.

ESCAPE-34 PSE-2024
European Symposium on Computer Aided Process Engineering
&
Process Systems Engineering

Flavio Manenti, Gintaras V. Reklaitis (Eds.), Book of Abstract of the 34th European Symposium on Computer Aided Process Engineering / 15th International Symposium on Process Systems Engineering (ESCAPE34/PSE24), June 2-6, 2024, Florence, Italy.

Transfer Learning across Equipment Scales Can Accelerate Pharmaceutical Tablet Development

Luca Beccaro,[a] Pierantonio Facco,[a] Ranjitkumar M. Dhenge,[b] Marv J. Khala,[b] Fabrizio Bezzo,[a] Massimiliano Barolo[a,*]

[a] *CAPE-Lab – Computer-Aided Process Laboratory, Department of Industrial Engineering, University of Padova, Via Marzolo 9, 35131 Padova PD, Italy*

[b] *GSK, Ware, SG12 0DP, United Kingdom*

max.barolo@unipd.it

Abstract

Roll compaction is pivotal in pharmaceutical tablet manufacturing, but finding the best settings for the operation of a full-scale roller compactor (RC) involves resource-intensive experiments. This is especially challenging during product development, due to limited availability of active pharmaceutical ingredients. To address this issue, a small-scale compactor simulator (CS) is commonly used to save on materials and time. However, the operating conditions that allow one to manufacture a product with assigned specifications in a CS are different from those required to manufacture the same product in a full-scale RC. This study proposes a transfer learning approach enabling one to derive optimal RC settings from experiments carried out on a CS. The proposed methodology effectively captures equipment-scale differences and offers a reliable way to predict RC machine settings, thus allowing for significant time and resource savings.

Keywords: roller compaction, dry granulation, compactor simulator, pharmaceutical tablets

1. Materials, Methods, and Results

Roller compaction is a key unit operation in a dry granulation line, where pharmaceutical powder blends are densified producing a ribbon, by means of the pressure exerted by two counter rotating rolls. Johanson (1965) developed a powder mechanics model describing the compaction process phenomena. The model predicts roll pressure and ribbon solid fraction (SF) from powder physical properties, operating conditions, and roller compactor (RC) geometry. Calibration of the model requires parameter estimation from experimental results. Experimental campaigns on a full-scale RC are lengthy and expensive, also because the required materials may include active pharmaceutical ingredients (APIs), which may not be available in large amounts during product development. To save on time and materials, small-scale compactor simulators (CSs) are used that mimic the roll compaction process through uniaxial compaction using two counter-moving punches (Zinchuk et al., 2004). However, the Johanson model parameters derived from CS experiments are not suitable for modelling an RC, due to pressure differences at equivalent SF values (Reynolds et al., 2010). For this reason, a mass correction factor f_0 has been proposed as a correction to the Johanson model to account for the differences between the two pieces of equipment (Bi et al., 2014).

To understand the differences between the responses of a CS and an RC, and to achieve transfer learning between them, we prepared six formulations including both placebos and APIs. Experiments carried out on all formulations in both pieces of equipment allowed us to estimate the Johanson model parameters for each equipment on each formulation, which in turn allowed us to identify the relevant compression profiles. Figure 1 shows the experimental data obtained for one of the formulations in the CS (triangles) and RC (squares), and the relevant compression profiles fitted by means of the Johanson model (dashed line and dotted line, respectively).

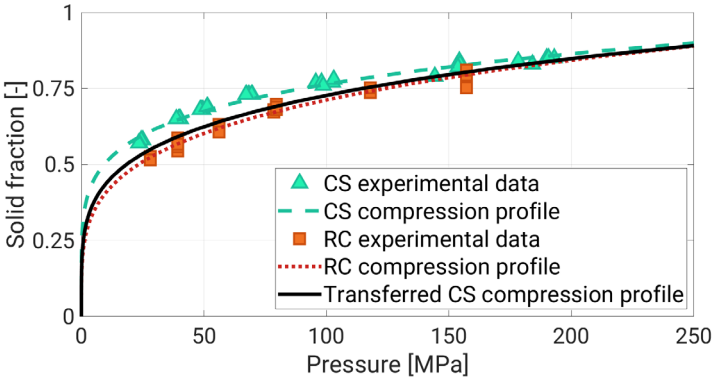

Figure 1. RC and CS compression profiles for one of the formulations investigated.

Clearly, the CS compression profile underestimates the pressure required to achieve the same SF using an RC. This finding holds true for all the formulations investigated. The f_0 parameter represents the link between the compression profiles obtained in different pieces of equipment, and can be used to transfer the operation from one equipment to the other. Whereas f_0 is typically assumed constant in the literature, we found that f_0 can be actually expressed as a generalized nonlinear function F of the roller compaction pressure P_{RC}, namely $f_0 = F(P_{RC})$. Four formulations were used to calibrate the parameters involved in F, and the remaining two formulations were used as validation datasets. Excellent transfer results were obtained in all cases. As an example, Figure 1 shows that the "virtual" RC compression profile (solid curve) obtained by transferring the CS experimental data (triangles) almost perfectly overlaps the compression profile that would be obtained by carrying out the experiments onto the RC directly (dotted line).

2. Conclusions

We presented a transfer methodology to relate the experimental results obtained from two compaction pieces of equipment at different scales and types. Results on six formulations demonstrated the effectiveness of the transfer methodology. The proposed approach enabling significant materials and time savings in pharmaceutical product development, requiring material in order of grams rather than kilograms for the experimental campaign.

References

Johanson, J.R. 1965. A Rolling Theory for Granular Solids. J. Appl. Mech. 32(4), pp.842–848.

Reynolds, G., Ingale, R., Roberts, R., Kothari, S. and Gururajan, B. 2010. Practical application of roller compaction process modeling. Comput. Chem. Eng. 34(7), pp.1049–1057.

Bi, M., Alvarez-Nunez, F. and Alvarez, F. 2014. Evaluating and modifying Johanson's rolling model to improve its predictability. J. Pharm. Sci. 103(7), pp.2062–2071.

Zinchuk, A. V, Mullarney, M.P. and Hancock, B.C. 2004. Simulation of roller compaction using a laboratory scale compaction simulator. Int. J. Pharm. 269(2), pp.403–415.

ESCAPE-34 PSE-2024
European Symposium on Computer Aided Process Engineering
&
Process Systems Engineering

Flavio Manenti, Gintaras V. Reklaitis (Eds.), Book of Abstract of the 34th European Symposium on Computer Aided Process Engineering / 15th International Symposium on Process Systems Engineering (ESCAPE34/PSE24), June 2-6, 2024, Florence, Italy.

A Method of Generating Transition Pathways to a Future Refinery

Yi Zhao,[a*] Pullah Bhatnagar,[a] Hayato Hagi,[b] Bruno Delahaye,[c] François Maréchal[a]

[a]*Industry Process and Energy Systems Engineering, École Polytechnique Fédérale de Lausanne, Rue de l'industrie 17, 1950 Sion, Switzerland*
[b]*TotalEnergies Research & Technology, TotalEnergies OneTech, 76700 Harfleur, France*
[c]*TotalEnergies Hybrid & Storage, TotalEnergies OneTech, 92078 Cedex, France*
[*]*yi.zhao@epfl.ch*

Abstract

In the context of a global imperative for industries to achieve net-zero emissions, this work introduces a methodological framework for establishing possible transition pathways with interim targets aimed at reducing emissions and minimizing costs. The methodology begins by generating different pathways through a multi-period mixed-integer linear programming formula, which takes into account market evolutions such as natural gas prices, renewable energy penetration, and future technology developments. Subsequently, a multi-criteria analysis is applied to select the most promising transition pathways based on predefined key performance indicators (KPIs) and decision metrics. To validate the methodology's effectiveness, a Blueprint oil refinery case study is conducted. The results demonstrate that a net emission reduction over the entire lifespan can be achieved through the implementation of carbon capture and/or electrification technologies at appropriate time steps. The methodology highlights the potential investment decision strategies according to the selected KPI, under predefined assumptions, offering insights for industry stakeholders and policymakers.

Keywords: Transition Pathway, Investment planning, Technology evolution, Refinery.

1. Introduction

The Sixth Assessment report by the Intergovernmental Panel on Climate Change (IPCC) emphasizes the formidable task of limiting the global average temperature rise to 1.5-2°C since 1850, requiring a substantial reduction in cumulative emissions (Masson 2021). While there has been a global effort to achieve net zero, spanning numerous industries and sectors, the significance of optimal transition pathways has not received adequate attention. Industrial sector, responsible for a quarter of global emissions, must evolve to reduce emissions during its lifespan and foster a low-carbon future.
However, determining an optimization pathway for industrial sector faces the following challenges:

- Exhaustive decarbonization options: Overlooking certain potential clean technologies and methods may lead to local suboptimal solutions.
- Market Uncertainty: Fluctuations in costs and the demand for critical utilities, such as natural gas, significantly impact industrial decision-making.
- Technology Evolution: As technology continually evolves, so do associated costs and carbon footprints. A comprehensive understanding of these trends is essential when integrating future technologies.

Valuable research has been carried out in the field of investment planning, including the work of Barkitzi et al. (2012), which emphasizes the advantages of long-term planning for flexibility in decision-making, and Butun et al. (2019), who integrated Investment Planning models into process integration to estimate investment costs of infrastructure demolition at the end-of-life. However, there remains a gap in methodologies tailored to transitional pathways that consider uncertainties and changing tax implications related to emissions. In this work, we present an approach that leverages stochastic optimization addressing uncertainties on markets and future technology costs. This approach facilitates the estimation of the most promising transition pathways based on predefined decision metrics, filling the gap in existing literature and providing a valuable tool for addressing the pressing challenges faced by the industry in the context of climate change mitigation.

2. Methodology

As illustrated in Figure 1, the optimization framework comprises two key sections: a configuration generation section using multi-period mixed integer linear programing (MILP) and a solution ranking section based on selected key performance indicators (KPIs) and decision metrics. During the configuration generation stage, a superstructure is first established combining the industrial sectors and potential decarbonization options with mass and heat integration. This combined superstructure is then solved with a multi-period MILP formula, leading to an unique configuration featuring a collection of decarbonization options that are optimally integrated within the refinery by allowing site-wide heat flows matching.

Multiple market conditions, including electricity price and carbon footprint, natural gas prices and future technology costs are given as incentives to the MILP formula to systematically generate a set of good configurations. In the multi-criterial solution ranking stage, key performance indicators for those different configurations are calculated considering investment planning constraints, including technology construction, resize and decommission. The configurations are then ranked based on the pre-defined decision metrics from the most promising to the least preferred under certain market conditions.

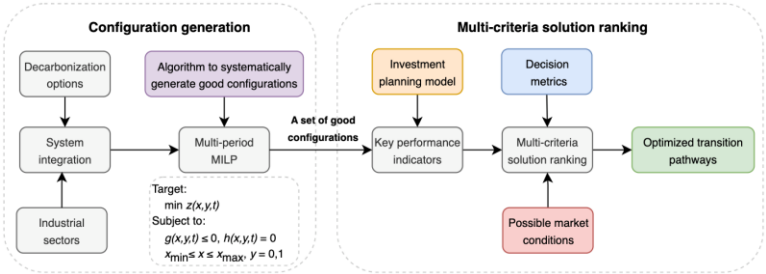

Figure 1. Methodology framework of generating optimal transition pathways. A multi-period MILP formula consists of optimization targets (z), continuous variables(x) and binary variables (y), as well as inequality and equality constraints (g and h).

A systematic method for generating future market scenarios is crucial to produce a diverse range of viable configurations. The transition of an industrial sector is propelled by both exogenous drivers, such as increasingly stringent environmental regulations, and endogenous forces, including decreasing technology and energy costs. In this study, we employed a kinetic evolution model to simulate renewable penetration, future energy costs and decarbonization targets. This kinetic model, also known as the 'S' curve, has been validated by Li et al. (2023) in the field of energy system modeling. As depicted in Eq. (1), with the initial and final states predefined, the model is governed by two critical parameters: *c* and *k*, representing the speed and smoothness of the transition, respectively.

$$S[k,c] = \frac{1}{1+e^{k(c-t)}} \quad (1)$$

By adjusting the values of *k* and *c* (typically *k* ranges from 0.1 to 1 and *c* ranges from 10 to 30 dependent on the initial and final status), a broad spectrum of market conditions and decarbonization targets can be generated. In this stage, the primary focus is not on achieving precise market condition predictions. Instead, we make reasonable assumptions and apply a wide range of possible market conditions to generate a database consisting of a set of viable configurations from which decision-makers can choose. An illustrative example of future market conditions is presented in Figure 2.

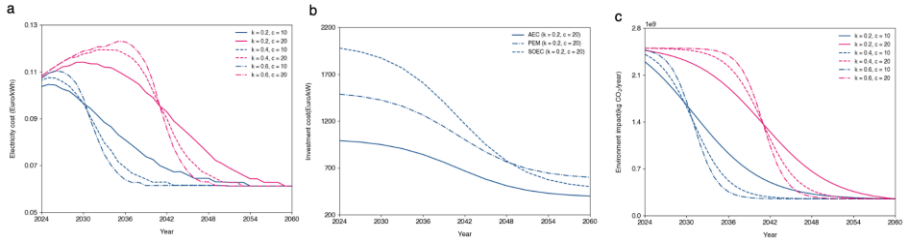

Figure 2. (a) Electricity cost calculated based on renewable penetration evolution under assumptions of final renewable penetration of 90% in 2060 with various *k* and *c* values and electricity technology costs from IEA; (b) Future costs of AEC, PEM, and SOEC electrolysis technologies; (c) Decarbonization targets at different time periods.

An investment planning model was integrated into the multi-period MILP process integration formula to generate diverse transition pathways. For a specific configuration consisting of a set of units with sizes represented as $f_{u,t}$ at the *i*-th year, the net present values of its investment costs encompass both the cost of acquiring new units ($Cinv^{buy}$) and the expenses associated with dismantling these units ($Cinv^{renew}$) when they reach the end of their lifespan for each unit *u* in *U* and each time period *t* in *T* , where *i* is the interest rate considered for the investment (Eq. (4)).

$$Cinv = \sum_{t=1}^{T}\sum_{u=1}^{U}\left(Cinv_{u,t}^{buy} + Cinv_{u,t}^{renew}\right)\cdot\frac{1}{(1+i)^t} \quad (2)$$

Precisely, the investment cost for the initial period is less than 25% of the total investment over the entire project's lifespan.

$$\sum_{u=1}^{U}\left(Cinv_{u,1}^{buy} + Cinv_{u,1}^{renew}\right)\cdot\frac{1}{(1+i)} \le 0.25\cdot Cinv \quad (3)$$

Similarly, the net present value of its operating cost (*Cop*) is calculated in Eq. (4), where t_{op} is the operating time for each time period *t*.

$$Cop = \sum_{t=1}^{T}\sum_{u=1}^{U}\left(Cop_{u,t}\cdot t_{op}\cdot\frac{1}{(1+i)^t}\right) \quad (4)$$

The total system emissions (*Imp*) are quantified by Eq. (5), which calculates the integral of emissions over the entire lifespan.

$$Imp = \sum_{t=1}^{T}\sum_{u=1}^{U}\left(Imp_{u,t}\cdot t_{op}\right) \quad (5)$$

Different solutions are subsequently ranked based on predefined decision metrics, assigning distinct weight factors to the KPIs as outlined in Eq. (6). Weight factors are defined with realistic requirements. In this work, we assign the values w_1 and w_2 as 1, and designate w_3 as the carbon tax factor. This way, different configurations are ranked based on their net present value, which accounts for the costs associated with the implementation of carbon tax.

$$Metrics = w_1 \cdot Cinv + w_2 \cdot Cop + w_3 \cdot Imp \quad (6)$$

To mitigate the impact of uncertainties, we can take into account a range of potential market conditions during the ranking process and select the configuration that exhibits the best overall performance across all these conceivable market conditions.

3. Case study and results

The methodology was validated with the Blueprint refinery model (Cervo et al. 2020), representing the average European refining profile using crude oil as the primary feedstock (Figure 3). The use of public resources and databases may limit specificity for individual industrial stakeholders. However, the framework is designed to enable stakeholders to customize inputs for relevance to their specific requirements. In this context, various options were explored for decarbonizing the current refining assets, such as energy efficiency approaches, clean hydrogen production, renewable energy feedstock, and carbon capture. Each decarbonization option is characterized by its mass balance, heat cascade, investment cost, and carbon footprint. Investment cost data is available in Li et al. (2023), while carbon footprints are sourced from the Ecoinvent database. Table 1 provides a summary of the techno-economic assumptions for these decarbonization options.

Table 1. Techno-economic assumptions of the decarbonization technologies considered in the oil refinery adapted from Li et al. (2023)

Decarbonization option	Assumptions
Gas turbine	Heat efficiency: 55%; Electrical efficiency: 30%; Investment: 2500 €/kW_{eq}
Biogas boiler	Investment cost: not considered; Biogas price: 5 times of natural gas price
Hydrogen recycling	Investment cost: calculated based on compressor and hydrogen purifiers
Heat pump	Carnot efficiency: 55%; Investment: 500 €/MW_{eq} of heat available.
Electric heater	Investment: 300 €/kW_{eq}
AEC	System efficiency: 60%; Operating at 80 °C; Investment: 1000~500 €/kW_{eq}
PEM	System efficiency: 70%; Operating at 80 °C; Investment: 1500~600 €/kW_{eq}
SOEC	System efficiency: 85%; Operating at 800 °C; Investment: 2000~400 €/kW_{eq}
Carbon capture (MEA)	Capture efficiency: 90%; Heat: 3.8 MJ/ton CO_2; Investment: 2 M€/(t/h) CO_2
Carbon capture (Oxy)	Capture efficiency: 95%; 226 kWh/ton O_2, Investment: 0.6 M€/(t/h) CO_2
CO_2 compression	Energy demand: 120 kWh/ton CO_2; Investment: 3500 €/kW_{eq}

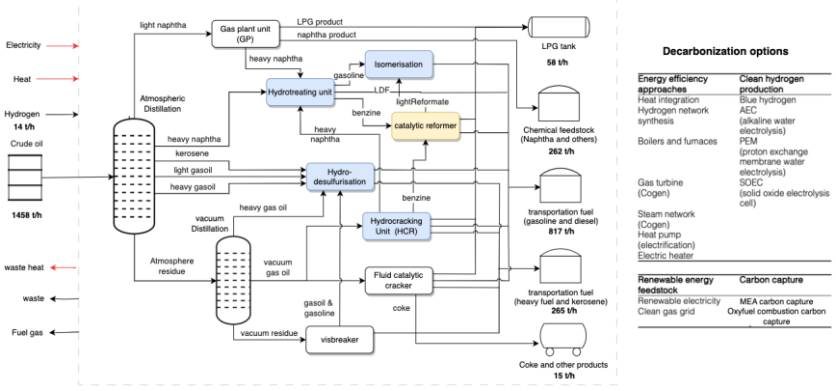

Figure 3. The superstructure of the Blueprint refinery with decarbonization options.

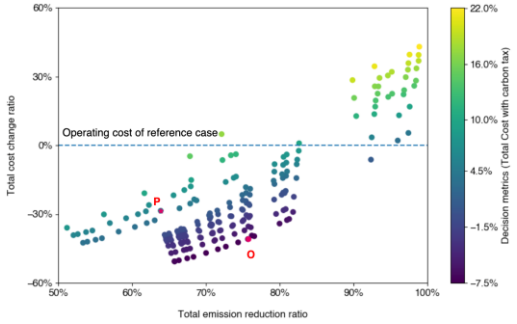

Figure 4: Average net present total cost change ratio against average total carbon emissions reduction ratio over the lifespan of the refinery, considering a market condition with a final renewable penetration of 90%, k = 0.2, and c = 10. Each data point represents a unique configuration. Decision metrics is calculated using Eq. (5).

In this study, 200 different energy market conditions (electricity, natural gas prices and emission constraints) were applied to generate a diverse range of configurations, resulting in a number of unique configurations after sorting and clustering. These unique configurations were subsequently ranked based on selected market scenarios and predefined decision metrics, which are illustrated in Figure 4. A clear trade-off between emission savings and total costs is observed compared to the reference case. The assumption of decreasing natural gas and electricity prices results in a significant number of configurations exhibiting lower total costs than those observed today.

The decision metrics identify configuration *O* as the optimal, with a minimum equivalent total cost reduction of 40%. Figure 5(a) provides insights into investment values and their distribution among different technologies and periods of configuration *O*. The optimizer prioritizes taking actions in the initial period, activating technologies such as carbon capture, hydrogen recycling, and heat pumps. Notably, the heat pump is used to fulfil the heat demand for solvent regeneration in the desorption column. These prompt actions lead to 50% of emission reductions in refineries. Another substantial investment is foreseen around 2050 marked by investments on carbon capture on biogenic emissions to meet zero emission target in 2060 as a negative emission solution. This shift is further illustrated in Figure 5 (b). In this proposed configuration, preference is given to carbon capture technologies. However, it is crucial to acknowledge that carbon capture costs and efficiencies can vary significantly based on the emission source in refineries. Neglecting considerations in this study for CO_2 transportation and storage may result in an overestimation of carbon capture potentials. In our analysis, approximately 40% of onsite carbon emissions were captured and compressed to 110 bars in 2024. However, the downstream treatment could be deemed unrealistic today due to limited infrastructure for utilization and storage. This aspect should be approached with further careful consideration.

When considering a faster transition (higher k value) of renewable penetration, configuration *P* emerges as the better option. Instead of relying on carbon capture, electrification is predominantly observed through green hydrogen production and electric heaters. Solid Oxide Electrolysis Cell (SOEC) outperforms Alkaline Electrolysis Cell (AEC) and Proton Exchange Membrane (PEM) due to its high efficiency and capability to utilize waste heat in refineries for steam generation. With a further decrease in electricity prices and carbon footprints, oxyfuel combustion starts to be applied. However, as a negative emission solution, carbon capture on biogenic emissions continues to dominate post-2050 to offset onsite emissions, achieving zero emission targets in 2060.

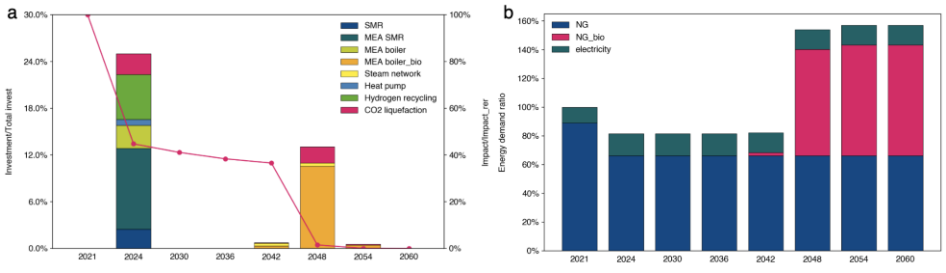

Figure 5: Share of (a) investment of different technologies and (b) natural gas, biogas and electricity imports at different time periods of configuration *O*

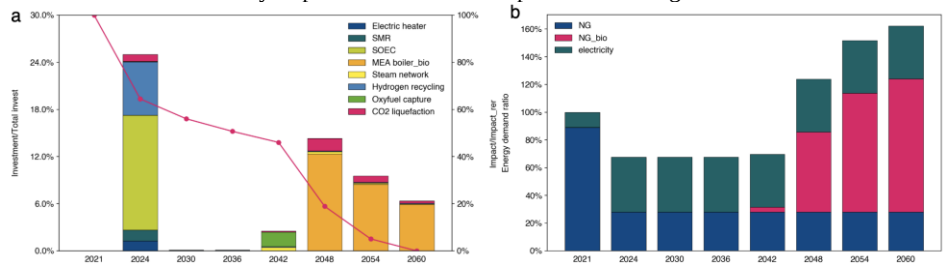

Figure 6: Share of (a) investment of different technologies and (b) natural gas, biogas and electricity imports at different time periods of configuration *P*

4. Conclusions

In this study, we have developed a robust methodology for evaluating investment strategies in the industrial sector, specifically focusing on the generation and selection of optimal transition pathways. This method has been applied successfully to an oil refinery case study, where investment strategies were generated and pathways leading to the minimization of predefined decision metrics under the given hypotheses were determined and analyzed. In comparison to the base case scenario in 2023, the identified pathways prioritized initial investments in carbon capture or electrification technologies according to the selected energy markets assumptions and decision metrics, resulting in a net emission reduction over the entire lifespan of the refinery. Our future work involves more realistic considerations about heat integration constraints than can be encountered in real industrial assets along with completing the superstructure for refinery decarbonization.

References

V. Masson-Delmotte, P.Zhai, A. Pirani, 2021, Climate change 2021, Voulume 2

G.A. Bakirtzis, P.N Biskas, and V. Chatziathanasion, 2012, Generation expansion planning ny milp considering mid-term scheduling decisions, Electric Power Systems Research, volume 86, 98-112

H.Butun, I. Kantor, and F. Marechal, 2019, An optimization approach for long-term industrial investment planning, Energies, Volume 12, no. 21, p.4076.

X. Li, & F., Maréchal, 2023, Deep excavation of the impact from endogenous and exogenous uncertainties on long-term energy planning. Energy and AI, 11, 100219.

H., Cervo, J. H., Ferrasse, B., Descale, and G. Van Eetvelde, 2020, Blueprint: A methodology facilitating data exchanges to enhance the detection of industrial symbiosis opportunities–application to a refinery. Chemical Engineering Science, 211, 115254.

Ecoinvent, Allocation, cut-off by classification, 2021, ecoinvent database version 3.8

ESCAPE-34 PSE-2024
European Symposium on Computer Aided Process Engineering
&
Process Systems Engineering

Flavio Manenti, Gintaras V. Reklaitis (Eds.), Book of Abstract of the 34th European Symposium on Computer Aided Process Engineering / 15th International Symposium on Process Systems Engineering (ESCAPE34/PSE24), June 2-6, 2024, Florence, Italy.

A Novel Process for Blue Hydrogen Production with Molten Carbonate Fuel Cell CO_2 Capture

Federico d'Amore[a*], Luis M.C. Pereira[b], Stefano Campanari[c], Matteo Gazzani[d,e], Matteo C. Romano[c]

[a]*CAPE-Lab – Computer-Aided Process Engineering Laboratory, Department of Industrial Engineering, University of Padova, via Marzolo 9, IT-35131 Padova, Italy*
[b]*Centre Scientifique & Technique Jean Féger (CSTJF) TotalEnergies, Av. Larribau, 64000 Pau, France*
[c]*Politecnico di Milano, Department of Energy, via Lambruschini 4, IT-20156 Milano, Italy*
[d]*Copernicus Institute of Sustainable Development, Utrecht University, CS Utrecht, 3584, the Netherlands*
[e]*Inorganic Membranes and Membrane Reactors, Sustainable Process Engineering, Chemical Engineering and Chemistry, Eindhoven University of Technology, Eindhoven, the Netherlands*
federico.damore@unipd.it

Abstract

H_2 production via steam methane reforming is a mature and cost-effective technology. However, carbon capture and storage is required to decrease its CO_2 emissions. The adoption of molten carbonate fuel cells as means to capture CO_2 from flue gases is attracting scientific interest thanks to their inherent thermodynamic advantage of separating CO_2 while producing electricity. This study investigates and benchmarks the performance of an H_2 production plant equipped with molten carbonate fuel cell for post-combustion CO_2 capture, by proposing a novel configuration where the cell anode is fed with the carbon-rich off-gas from the H_2 separation unit. It emerges that the process can achieve higher capture rates than the reference solvent-based plant: 85-90 % with single cell, 95 % with two-stage cell. Moreover, recycling the carbon-rich off gas to the anode allows for smaller cell area, and potentially lower H_2 production costs compared to the benchmark.

Keywords: Steam methane reformer, Molten carbonate fuel cell, Carbon dioxide capture, Process simulation, Techno-economic modelling.

1. Introduction

H_2 is expected to become a key player in the decarbonisation challenge (van der Spek et al., 2022). The production of H_2 from fossil fuels with CO_2 capture is key to enable large scale production and will be complementary to electrolysis till the electric grid is decarbonised, provided that CO_2 capture is performed according to state-of-the-art and

CH_4 fugitive losses are minimised (Bauer et al., 2022; Pettersen et al., 2022). This work focusses on H_2 production from steam methane reforming (SMR) of natural gas (NG), which is a mature and cost-effective technology (IEAGHG, 2017), coupled with molten carbonate fuel cell (MCFC) for post-combustion CO_2 capture.
In the literature, post-combustion CO_2 capture processes based on MCFC for H_2 plants and other emitters consider NG as fuel for the fuel cell (Consonni et al., 2021). This study proposes a novel configuration (d'Amore et al., 2023), which exploits part of the off-gas from H_2 purification unit as fuel to the MCFC, instead of NG. This configuration keeps a carbon-richer fuel on the MCFC anode side and reduces the flow rate of CO_2 in the SMR to be separated by the MCFC (thus, its area) for a given CO_2 capture rate, with significant beneficial effects in the overall techno-economic performance. Building upon the performance of the novel off-gas feed configuration, it is also assessed how a multi-stage cell configuration with inter-cooling would further improve the process (Spinelli et al., 2014), as it helps decreasing the air dilution at the MCFC cathode inlet and enhances the CO_2 separation efficiency.

2. Methodology

The plants were modelled and simulated in Aspen Plus software by using the Peng-Robinson equation of state, according to the technical assumptions summarised in d'Amore et al. (2023) (Table 1). All chemical reactors were simulated at chemical equilibrium, while the MCFC performance is described through a 0-D model of the polarisation curve taken from Barckholtz et al. (2022).

The reference standalone SMR without CO_2 capture is designed to produce 100,000 Nm^3/h of H_2 (299.5 MW_{LHV}), comprising high temperature water-gas shift (WGS), pressure swing adsorption (PSA), steam cycle (set at 485 °C at 100 bar), and low pressure (LP) steam export (at 6 bar) (Figure 1a). This plant is characterised by an NG-to-H_2 efficiency of 73.5 % and specific CO_2 emissions of 9.29 kg of CO_2/kg of H_2, being the net electric and thermal power outputs equal to 10.4 MW_{el} and 23.2 MW_{th}, respectively. The SMR with post-combustion CO_2 capture with monoethanolamine (MEA) is designed for a CO_2 capture rate of 90 % and a specific heat demand of 3.57 MJ_{th}/kg of captured CO_2 (Figure 1b). This plant is considered as benchmark case for performance and costs comparison with MCFC-based CO_2 capture.

Table 1. Summary of the main input data.

Plant	Component	Parameter	Value	Unit
SMR	Pre-reformer	Steam-to-carbon	3.4	mol/mol
	Reformer	Outlet temperature	890	°C
	PSA	H_2 recovery	90	%
	LP steam	Pressure	6	bar
	HP steam	Pressure/temperature	100/485	bar/°C
MEA	CO_2 separation	Efficiency	90	%
	CO_2 separation	Reboiler duty	3.57	GJ/t CO_2
MCFC	Cathode	Inlet temperature	575	°C
	Cathode	Outlet temperature	645	°C
	Cathode	CO_2 outlet concentration	1	$\%^{mol}$
	Pre-reformer	Inlet temperature	600	°C
	Pre-reformer	Steam-to-carbon	2.1	mol/mol
	Anode	Inlet temperature	600	°C
	Anode	Outlet temperature	645	°C

In the NG-based MCFC (i.e., NGF plant) the SMR flue gases are sent to the MCFC cathode for CO_2 separation. A CO_2 lean stream is produced at the cathode residue and emitted to the atmosphere (Figure 1c). The MCFC anode is fed with pre-reformed NG. The anode residue is sent to a WGS converter. The shifted syngas stream is sent to the low-temperature phase-change purification unit (CPU) to produce a high-purity CO_2 stream and a flow rate that is recycled to the PSA unit downstream the SMR. Differently, in the off-gas-based MCFC (i.e., OGF plant) the MCFC anode is fed with PSA off-gas (Figure 1d). This configuration keeps the carbon-rich fuel on the MCFC anode side and reduces the flow rate of CO_2 in the SMR to be separated by the MCFC (therefore, its area) for a given overall CO_2 capture rate. An additional case (i.e., OGF-2) involves the adoption of two cells in series with inter-cooling to decrease the air dilution at the cathode inlet and enhance the CO_2 separation efficiency for a given cell potential.

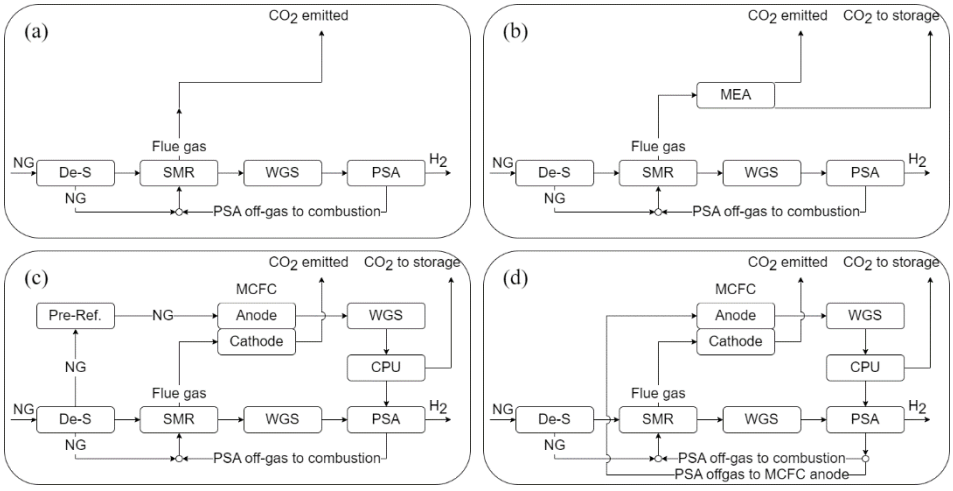

Figure 1. Simplified plant schemes: (a) SMR, (b) SMR with MEA, (c) NGF, and (d) OGF.

3. Results

Even though MCFC-based plants consume more NG with respect to the standalone SMR (between +8 % and +26 %), they also generate a larger low-carbon electricity output (Table 2). Plus, MCFC-based OGF and OGF-2 cases show a better performance compared to MEA solvent-based capture system in a wide range of NG and electricity prices. OGF appears superior to NGF, being the former characterised by higher carbon capture rate (90 % against 85 %), higher H_2 production efficiency (68 % against 59 %), lower specific energy consumption per unit of CO_2 avoided (0.5 against 1.1 MJ/kg of CO_2), and a significantly lower cell area (-43 %). This is due to the higher carbon intensity of the off-gas feed to the OGF cell anode, compared to the NG exploited in the NGF case, which allows reducing the flow rate of CO_2 to be separated by the MCFC for a given CO_2 capture rate. OGF-2 is a particularly competitive configuration, as it can achieve 95 % carbon capture rate with a smaller cell area than OGF (-19 %). This is due to the inter-cooling between cells, which allows reducing the CO_2 dilution resulting from the excess air to be mixed with the flue gas to control the MCFC temperature.

Table 2. Technical performance results.

	SMR	MEA	NGF	OGF	OGF-2
Cell 1 potential [V]	-	-	0.70	0.70	0.65
Cell 2 potential [V]	-	-	-	-	0.60
Util. factor [%]	-	-	75.0 %	75.0 %	70.0 %
CO_2 util. factor [%]	-	-	81.7 %	77.5 %	87.1 %
Total cell area [m^2]	-	-	73123	41615	23605
NG plant inlet [MW_{LHV}]	407.3	407.3	512.4	442.2	439.4
PSA off-gas [MW_{LHV}]	97.1	97.1	90.8	95.0	94.6
Electricity outlet [MW_{el}]	10.4	-12.8	59.1	22.1	19.8
Steam outlet [MW_{th}]	23.2	0.0	21.5	24.6	26.2
Spec. emis. [kg_{CO2}/kg_{H2}]	9.29	0.93	1.75	0.98	0.50
H_2 prod. eff. [%]	73.5 %	73.5 %	58.5 %	67.7 %	68.2 %
Carbon capt. Rate [%]	0.0 %	90.0 %	85.0 %	90.3 %	95.0 %

The economic analysis is based on the assumptions reported in d'Amore et al. (2023). The plants have equivalent operating hours of 8400 h/year, being the electricity and natural gas prices equal to 60 €/MWh and 6 €/GJ, respectively. The results show that OGF and OGF-2 plants exhibit H_2 production costs (1.9-2.2 €/kg of H_2) that are lower than NGF (2.3-2.6 €/kg of H_2) and than SMR with conventional post-combustion CO_2 capture (2.2-2.3 €/kg of H_2). The sensitivity analyses on key economic parameters (e.g., carbon tax, NG cost, electricity price) did not affect the main outcome, i.e., the good economic performance of OGF and OGF-2 (d'Amore et al., 2023). Contrary to the NGF case, the OGF one (and especially the 2-stage configuration) emerges as cost competitive with conventional solvent-based post-combustion capture in the entire range of values explored in the sensitivities.

4. Conclusions

This study highlights the potential of molten carbonate fuel cells (MCFCs) as post-combustion CO_2 capture systems in blue H_2 plants, if fed with off-gas from H_2 purification unit as fuel. The resulting CO_2 capture rate is found equal to 90 % for the single cell configuration and equal to 95 % for the multi-stage cell configuration, against 85 % in the case of natural gas-based anode feed. H_2 production costs are in the range of 1.9-2.2 €/kg of H_2, therefore lower than a traditional natural gas anode feed (2.3-2.6 €/kg H_2), and competitive with solvent-based post-combustion capture (2.2-2.3 €/kg of H_2).

Acknowledgments

This work has been funded by TotalEnergies' R&D Strategic Anticipation Program.

References

T.A. Barckholtz, K.M. Taylor, S. Narayanan, S. Jolly, H. Ghezel-Ayagh, 2022, Molten carbonate fuel cells for simultaneous CO_2 capture, power generation, and H_2 generation, Appl Energy, 313, 118553

C. Bauer, K. Treyer, C. Antonini, J. Bergerson, M. Gazzani, E. Gencer, J. Gibbins, M. Mazzotti, S.T. McCoy, R. McKenna, R. Pietzcker, A.P. Ravikumar, M.C. Romano, F. Ueckerdt, J. Vente, M. van der Spek, 2022, On the climate impacts of blue hydrogen production, Sustain Energy Fuels, 6, 66-75

S. Consonni, L. Mastropasqua, M. Spinelli, T.A. Barckholtz, S. Campanari, 2021, Low-carbon hydrogen via integration of steam methane reforming with molten carbonate fuel cells at low fuel utilization, Adv Appl Energy, 2, 100010

F. d'Amore, L.M.C. Pereira, S. Campanari, M. Gazzani, M.C. Romano, 2023, A novel process for CO_2 capture from Steam Methane Reformer with Molten Carbonate Fuel Cell, Int J Hydrogen Energy, 48, 37366-37384

IEAGHG, 2017, Techno-Economic Evaluation of SMR Based Standalone (Merchant) Hydrogen Plant with CCS

J. Pettersen, R. Steeneveldt, D. Grainger, T. Scott, L.M. Holst, E.S. Hamborg, 2022, Blue hydrogen must be done properly, Energy Sci Eng, 10, 3220-3236

M. Spinelli, M.C. Romano, S. Consonni, S. Campanari, M. Marchi, G. Cinti, 2014, Application of molten carbonate fuel cells in cement plants for CO_2 capture and clean power generation, Energy Procedia, 63, 6517-6526

M. van der Spek, C. Banet, C. Bauer, P. Gabrielli, W. Goldthorpe, M. Mazzotti, S.T. Munkejord, N.A. Røkke, N. Shah, N. Sunny, D. Sutter, J.M. Trusler, M. Gazzani, 2022, Perspective on the hydrogen economy as a pathway to reach net-zero CO_2 emissions in Europe, Energy Environ Sci, 15, 1034-1077

ESCAPE-34 PSE-2024
European Symposium on Computer Aided Process Engineering
&
Process Systems Engineering

Flavio Manenti, Gintaras V. Reklaitis (Eds.), Book of Abstract of the 34th European Symposium on Computer Aided Process Engineering / 15th International Symposium on Process Systems Engineering (ESCAPE34/PSE24), June 2-6, 2024, Florence, Italy.

Rollout of Carbon Capture, Transport, and Storage Infrastructure for Hard-to-abate Industry in Switzerland

Johannes Burger, Paolo Gabrielli, David Yang Shu, Marco Mazzotti, André Bardow, Giovanni Sansavini*

Institute of Energy and Process Engineering, ETH Zurich, 8092 Zurich, Switzerland
sansavig@ethz.ch

Abstract

Climate change mitigation requires a dramatic reduction of greenhouse gas emissions across all sectors, including hard-to-abate industries. Hard-to-abate emissions from industry can be avoided by CO_2 capture, transport, and storage (CCTS), where CO_2 is transported from capture plants to permanent storage sites. However, no CCTS infrastructure is currently deployed in Europe. Therefore, the transition towards a large-scale CCTS infrastructure needs to be properly planned and implemented. Within this context, external factors play a role in the deployment of CCTS supply chains and lead to large uncertainty due to little operational experience for such systems. Here, we investigate the rollout of a Swiss CCTS infrastructure to achieve a net-zero emissions Swiss industry and connect Swiss emitters to a European CCTS infrastructure. We address uncertainty and real-world constraints regarding the rollout of CCTS infrastructure via scenario analysis. Under most scenarios, Swiss CO_2 sequestration targets can be reached, although costs may increase by up to 25%. The delay or limitation of available storage capacity, however, can undermine the sequestration targets.

Keywords: Carbon capture and storage, CO_2 supply chains, hard-to-abate industries, net-zero emissions, CO_2 infrastructure, decarbonization.

Introduction

Strategies to reach national and international climate targets not only demand drastic reductions in greenhouse gas emissions (IPCC, 2022) but also increasingly include carbon capture and storage, as well as carbon dioxide removal for reaching net-zero emission goals (Bundesamt für Energie, 2021). Capturing and storing CO_2 is a viable option to reduce hard-to-abate emissions in the industrial sector, such as cement or waste incineration plants (Paltsev, 2021). However, no infrastructure for CO_2 capture, transport, and storage (CCTS) currently exists in Europe. The transition towards the scale of CCTS required for net-zero emission targets requires fast deployment of large infrastructure systems (IRENA, 2021). This study investigates the cost-optimal rollout of a CCTS supply chain network for Switzerland connected to European CCTS transport routes.

Methods

A linear programming model determines the time-dependent installation and operation of the CCTS infrastructure for Switzerland. More specifically, the optimization model returns the type, location, and size of CO_2 capture, conditioning, and transport technologies, as well as the locations for permanent storage. Furthermore, the input and output streams of technologies, including the CO_2 flow for the installed transport connections are determined. The model minimizes the total annualized costs of the system while complying with annual CO_2 emissions targets and real-world constraints resulting from limitations due to political, societal, or implementation externalities.

The input data to the optimization problem are: (i) current locations and CO_2 emissions of Swiss emitters, (ii) location and capacity of CO_2 storage sites, (iii) efficiency, CO_2 footprint, and investment and operating costs of capture, storage, and transport technologies, (iv) availability of transport technologies between nodes, (v) price and region-specific carbon-intensity of electricity, and (vi) emissions reduction targets for industrial CO_2 emissions. As Switzerland has no large-scale domestic storage and no direct access to the sea, it will require exporting CO_2 through its neighboring countries. In the model, export takes place in Basel where the Swiss infrastructure is assumed to be connected to a European transport route going towards the North Sea. The input data used in the optimization is based on Becattini et al. (2022) and Gabrielli et al. (2022). The constraints of the optimization problem include (i) energy and mass balances, (ii) performance behavior and operating limits of the capture, conditioning, and transport technologies, and (iii) CO_2 emissions limits.

In addition to techno-economic constraints, we include real-world constraints. Although real-world constraints are often neglected, they have a large influence on the deployment speed or even lead to the cancellation of projects (Russel and Bleiker, 2015). The real-world constraints are included as inputs and represent the expectation of how fast a CCTS infrastructure within Switzerland and abroad may develop. The limitations are based on public statements of stakeholders as well as communication with the industry. As the real-world constraints are uncertain, a scenario analysis is used to assess their effect on the Swiss CCTS infrastructure rollout.

The optimization is carried out for the time horizon from 2025 to 2050 and uses a yearly time resolution. We perform a scenario analysis, to investigate the variability in the speed of infrastructure rollout and its effect on the CCTS system. A reference scenario is defined which represents the expected future availability of capture, transport, and storage technologies and their capacities. The reference scenario is the midpoint in the range determined for the real-world constraints. From the reference scenario, additional scenarios are derived which differ in the years when CO_2 capture units, pipelines, or storage sites become available. Furthermore, several unfavorable external conditions are analyzed, namely the lack of foreign pipelines for Swiss emitters to connect to, limited navigability of the Rhine River, unavailability of domestic storage, and an unforeseen shutdown of the closest foreign storage sites.

The cost-optimal infrastructure designs are compared for all scenarios to identify (i) robust design decisions taken across a variety of scenarios and (ii) critical parameters jeopardizing the CCTS rollout.

Results

We identify feasible CCTS network designs for 10 out of the 11 analyzed scenarios with a total cost range of ±25% compared to the reference scenario. The biggest cost reductions

result from the earlier availability of storage capacity. Compared to the reference scenario, earlier storage availability enables shorter overall transport distances because more storage capacity exists close to Switzerland. Additionally, in this scenario, the Swiss storage site is assumed to become available earlier than in the reference scenario. Significant cost savings are realized when a considerable share of the total CO_2 can be stored domestically.

The second largest cost savings are achieved if pipelines can be installed earlier than in the reference scenario. Pipelines are the best mode of transport in an environmental and economic sense (Becattini et al., 2022; Gabrielli et al., 2022). Installing them early reduces the costs and emissions of the CCTS infrastructure, leading to a more efficient and smaller CCTS system to achieve the same CO_2 sequestration targets. The time when pipelines become available is thus a large driver for cost savings. The planning and construction of large pipelines are complex and require coordination among different stakeholders. The process must be initiated immediately to realize potential cost savings.

The only case where the optimization does not produce a feasible result is the scenario where storage site development is delayed, and the storage capacity is limited to a maximum of 5.8 Mt_{CO2}/y compared to 14.3 Mt_{CO2}/y in the reference scenario. The availability of CO_2 storage, both in time and capacity, has the largest effect on the results. On the one hand, early availability of storage capacity enables cost reductions in the long term. On the other hand, failure to secure access to CO_2 storage may cause Switzerland to overshoot its long-term decarbonization targets. As CO_2 storage projects are continuously being announced and developed further (Global CCS Institute, 2022), the availability of storage capacity may depend more on long-term contracts with storage providers and less on the overall availability of injection capacity.

Out of the analyzed parameters, the availability of storage capacity bears the greatest cost-saving opportunity but also the greatest risk for jeopardizing a successful CCTS rollout. Therefore, a Swiss CCTS system designed to meet federal sequestration targets (Bundesamt für Energie BFE, 2021) must ensure the availability of storage capacity. Furthermore, coordinated efforts to construct a pipeline infrastructure must be initiated to enable timely availability of cost- and emission-optimal CO_2 transport.

References

Becattini, V., Gabrielli, P., Antonini, C., Campos, J., Acquilino, A., Sansavini, G., & Mazzotti, M. (2022). Carbon dioxide capture, transport and storage supply chains: Optimal economic and environmental performance of infrastructure rollout. International Journal of Greenhouse Gas Control, 117 (January), 103635. https://doi.org/10.1016/j.ijggc.2022.103635

Bundesamt für Energie BFE. (2021). Energieperspektiven 2050+: Technischer Bericht. Gesamtdokumentation der Arbeiten. Bundesamt für Energie BFE, Bern, Switzerland.

Gabrielli, P., Campos, J., Becattini, V., Mazzotti, M., & Sansavini, G. (2022). Optimization and assessment of carbon capture, transport and storage supply chains for industrial sectors: The cost of resilience. International Journal of Greenhouse Gas Control, 121, 103797. https://doi.org/10.1016/j.ijggc.2022.103797

Global CCS Institute. (2022). Global Status of CCS 2022. Global CCS Institute. https://www.globalccsinstitute.com/resources/global-status-of-ccs-2022/

IRENA. (2021). World Energy Transitions Outlook: 1.5°C Pathway. International Renewable Energy Agency.

IPCC. (2022). Summary for Policymakers. In P. R. Shukla, J. Skea, A. Reisinger, R. Slade, R. Fradera, M. Pathak, A. A. Khourdajie, M. Belkacemi, R. van Diemen, A. Hasija, G. Lisboa, S. Luz, J. Malley, D. McCollum, S. Some, & P. Vyas (Eds.), Climate Change 2022: Mitigation of *Climate Change. Contribution of Working Group III to the Sixth Assessment Report of the*

Intergovernmental Panel on Climate Change (pp. 1–52). Cambridge University Press. https://doi.org/10.1017/9781009157926.001

Paltsev, S., Morris, J., Kheshgi, H., & Herzog, H. (2021). Hard-to-Abate Sectors: The role of industrial carbon capture and storage (CCS) in emission mitigation. *Applied Energy*, *300*(July), 117322. https://doi.org/10.1016/j.apenergy.2021.117322

Russell, R., & Bleiker, C. (2015, December 10). Whatever happened to CCS? *Deutsche Welle*. https://www.dw.com/en/carbon-capture-and-storage-magic-pill-or-chimera/a-18880678

ESCAPE-34 PSE-2024
European Symposium on Computer Aided Process Engineering
&
Process Systems Engineering

Flavio Manenti, Gintaras V. Reklaitis (Eds.), Book of Abstract of the 34th European Symposium on Computer Aided Process Engineering / 15th International Symposium on Process Systems Engineering (ESCAPE34/PSE24), June 2-6, 2024, Florence, Italy.

Enhancing Superstructure Optimization via Embedded Neural Networks in Optimal Process Design for Sustainable Aviation Fuel (SAF) Production

Alexander Klimek[a], Caroline Ganzer[a], Kai Sundmacher[a, b, *]

[a]*Max Planck Institute for Dynamics of Complex Technical Systems, Department of Process Systems Engineering, Sandtorstr. 1, 39106 Magdeburg, Germany*
[b]*Otto von Guericke University, Chair for Process Systems Engineering, Universitätsplatz 2, 39106 Magdeburg, Germany*
sundmacher@mpi-magdeburg.mpg.de

Abstract

Superstructure optimization is suitable for identifying optimal raw materials and process pathways for the production of sustainable aviation fuels (SAFs). Mass and energy balances for the individual processes of the superstructure network are often represented by linear input-output relationships between the feedstocks and products, neglecting nonlinear effects. By embedding surrogates in the form of artificial neural networks (ANNs) within our optimization framework, we achieve a more detailed representation of individual processes. Combined with an adjusted superstructure optimization formulation explicitly including mixtures, we are able to determine not only the optimal process routes but also optimal process parameters (e.g., temperature, pressure) as well as the optimal aviation fuel composition.

Keywords: Sustainable Aviation Fuel, Superstructure Optimization, Surrogate Modeling, Artificial Neural Networks.

1. Introduction

In 2019, the aviation sector emitted over 900 million tons of CO_2-eq, contributing around 10-% of transportation-related greenhouse gases (Vardon et al., 2022). Consequently, the global goal of achieving net zero emissions by 2050 necessitates the defossilization of air transport. Whilst H_2-powered and battery-driven aircrafts may present viable options at small scale and for niche applications, it is expected that long-chain liquid SAFs are crucial at large scale (Freire Ordóñez et al., 2022). Identifying economically viable SAF production pathways in which carbon, hydrogen, oxygen, heat, and electricity are sourced and managed to meet environmental requirements, presents a challenge to the engineering community. Potential system configurations are numerous and difficult to investigate. Various alternatives, such as biomass pathways or captured CO_2 combined with water

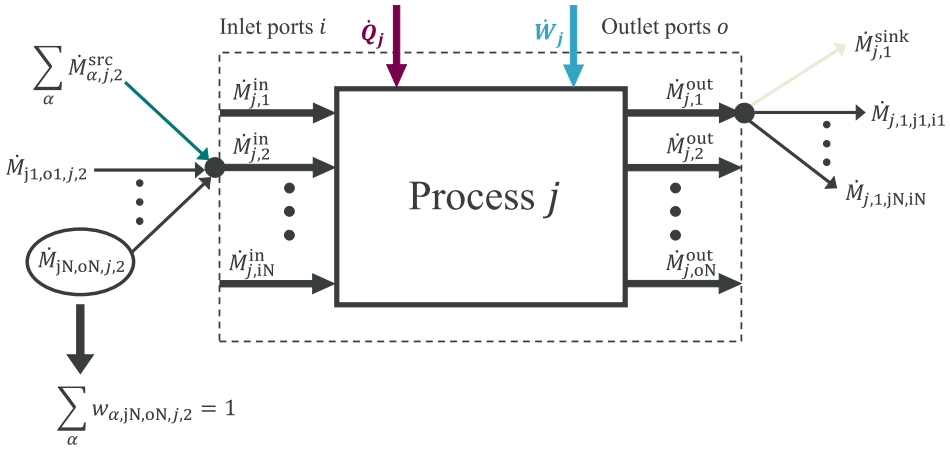

Figure 1: General process representation within superstructure to optimize total mass flows $\dot{M}$ as well as component mass fractions w_α.

electrolysis for syngas production, as well as methanol or Fischer-Tropsch (FT) liquids as intermediates, are possible options and need to be compared systematically.

2. Superstructure optimization approach

Superstructure optimization is frequently employed to determine optimal designs of complex process networks. For this reason, we have set up a SAF production superstructure that includes processes such as biomass gasification, direct air capture (DAC), various electrolysis technologies, autothermal reforming of methane, a reverse water-gas shift process, an acid gas removal plant, CO_2 sequestration, a Fischer-Tropsch process and processes for the production of long-chain hydrocarbons based on methanol. A common problem with conventional superstructure optimization formulations is that they typically consider only pure components (Gonzalez-Garay et al., 2022). Since aviation fuels are mixtures of hydrocarbons, we have developed an adapted formulation that allows mixture compositions to be represented and optimized.

In order to optimize mixture compositions, we model all processes within the SAF superstructure by the general process representation shown in Figure 1. A general process j is modeled as a black box, which can have several inlet ports i and several outlet ports o, allowing operations such as mixing and separating to be included directly. Through the corresponding ports, total mass flows $\dot{M}$ can enter or leave the process j, whereby mass conservation is always satisfied. Total mass flows between the outlet and inlet ports of the various alternatives within the superstructure are used to interconnect all individual processes (e.g., $\dot{M}_{\text{j1,o1},j,2}$). In addition, mass flows can enter the process from outside or leave the process across the system boundaries, which is modeled accordingly by $\dot{M}^{\text{src}}$ and $\dot{M}^{\text{sink}}$. $\dot{Q}$ and $\dot{W}$ describe heat and work (electricity) flows that either leave or enter process j depending on their sign. By adding decision variables for mass fractions w_α for all system components α in each mass flow, component mixtures can be modeled. Partial mass balances of the form

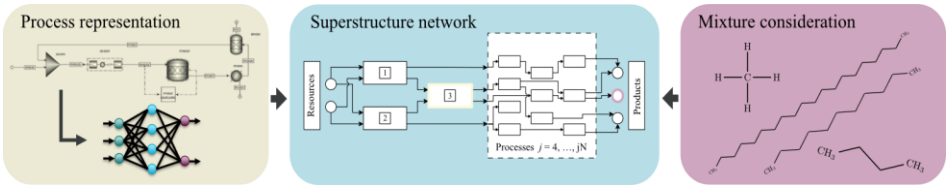

Figure 2: General illustration of the applied methodology, extending superstructure optimization by embedded neural networks and mixture modeling.

$$w^{\text{in}}_{\alpha,(j,i)}\dot{M}^{\text{in}}_{(j,i)} = \sum_{(\tilde{\jmath},o):(\tilde{\jmath},o,j,i)} w_{\alpha,(\tilde{\jmath},o,j,i)}\dot{M}_{(\tilde{\jmath},o,j,i)} + \sum_{\alpha} \dot{M}^{\text{src}}_{\alpha,(j,i)} \qquad \forall (j,i)\,,\alpha, \qquad (1)$$

$$w^{\text{out}}_{\alpha,(j,o)}\dot{M}^{\text{out}}_{(j,o)} = \sum_{(\tilde{\jmath},i):(j,o,\tilde{\jmath},i)} w_{\alpha,(j,o,\tilde{\jmath},i)}\dot{M}_{(j,o,\tilde{\jmath},i)} + w^{\text{sink}}_{\alpha,(j,o)}\dot{M}^{\text{sink}}_{(j,o)} \qquad \forall (j,o),\alpha, \qquad (2)$$

are introduced as equality constraints in the optimization problem in order to describe the connection between the total mass flows and their composition. This formulation allows to consider sustainable aviation fuels composed of hydrocarbons of different chain length and structure. It comes at the expense of quadratic terms in the constraints of the superstructure optimization problem. Together with binary variables for discrete decisions on the installation of processes within the superstructure, the product of mass fraction and mass flow leads to a mixed-integer quadratically constrained programming (MIQCP) formulation. It can be solved to global optimality using state-of-the-art solvers such as Gurobi (Gurobi Optimization, 2023).

3. Artificial neural networks as process surrogates

Another simplification often made in superstructure optimization is that chemical conversions are modeled by linear relationships between raw materials and products, neglecting real non-linear effects. Within such a framework, the operating conditions including temperature, pressure, and conversion of the processes encompassed by the superstructure are fixed in advance and thus cannot be simultaneously optimized (Demirhan et al., 2021; Gonzalez-Garay et al., 2022; Niziolek et al., 2017).

This work enhances traditional superstructure optimization by embedding surrogate models in the form of ANNs into the optimization formulation (Fahmi and Cremaschi, 2012; Henao and Maravelias, 2011). As shown in Figure 2, these ANNs are trained on data generated from Aspen Plus® simulations, correlating component outlet concentrations, electricity, and heat requirements with total mass inflow, inlet concentrations, and reaction conditions of individual processes (Aspen Technology Inc, 2023). For the integration of ANNs, we leverage the Python package OMLT, which facilitates the embedding of machine learning surrogates into Pyomo-implemented optimization problems (Bynum et al., 2021; Ceccon et al., 2022). The main advantage of this approach is that the input-output relationships of the ANNs can be represented as mixed-integer linear constraints through the use of ReLU activation functions, allowing the solution of highly nonlinear mass and energy balances while maintaining an MIQCP

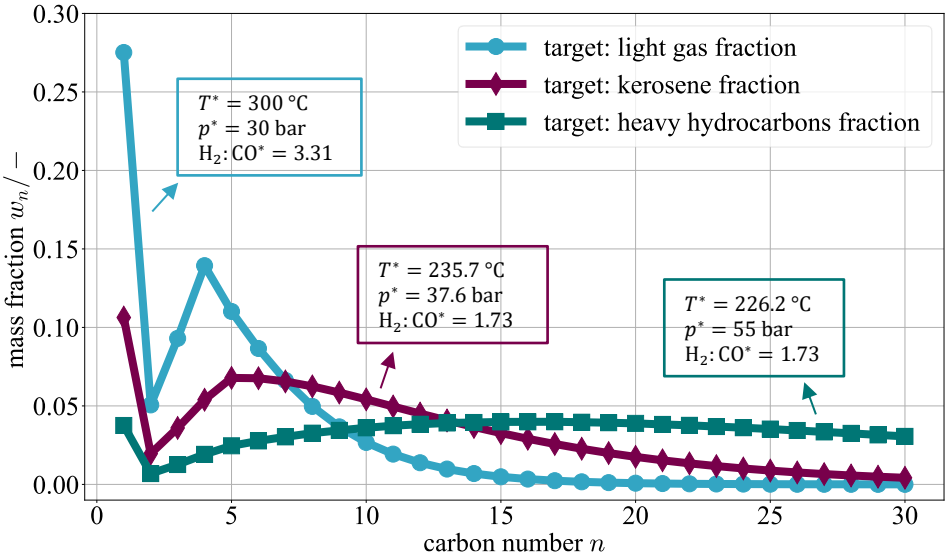

Figure 3: Optimized Anderson-Schulz-Flory (ASF) distribution for C_1-C_{30} n-alkanes calculated via ReLU-ANN as output of the FT process depending on reaction temperature, pressure and syngas composition within the superstructure optimization for different targeted hydrocarbon fractions.

formulation (Grimstad and Andersson, 2019).

For example, we have trained and embedded an ANN that predicts the relationship between reaction temperature, pressure, inlet syngas composition and the distribution of outlet mass fractions for n-alkanes from the FT process (Hamelinck et al., 2004). The FT-ANN, which consists of one hidden ReLU layer with 100 neurons in it, enables a very accurate representation of the outlet mass fraction distribution, but also of the work and heat requirements with an overall R^2 value of 0.99993. Within the superstructure optimization problem, the outlet concentrations of hydrocarbons of different chain lengths can then be calculated as

$$w^{\text{out}}_{C_{11}H_{24},FT,1} = f^{\text{ANN}}_{\text{FT}}(\dot{M}^{\text{in}}_{\text{FT},1}, T_{\text{FT}}, p_{\text{FT}}, w^{\text{in}}_{H_2,\text{FT},1}), \tag{3}$$

where $w_{C_{11}H_{24}}$ exemplifies the mass fraction of n-undecane. Figure 3 illustrates the flexibility of our formulation. We can target the desired kerosene-hydrocarbon fraction in the FT output by optimizing within the constraints on required physical properties. Modeling the hydrocarbons of different chain length and structure as components α of our superstructure provides more detailed information about the SAF composition depending on the selected process route and feedstocks.

4. Conclusions

Different feedstocks such as biomass, CO_2, air and water can be used to produce SAFs via different process routes (e.g., FT pathway, methanol pathway). In order to design optimal SAF production systems, we utilize superstructure optimization and overcome

some of its classical simplifications. By incorporating decision variables for component concentrations in all network flows, the resulting process network designs yield mixtures of hydrocarbons which meet the stringent physical property requirements for SAFs in terms of specific energy, freezing point, viscosity, etc. Important processes are replaced by ANNs representing non-linear relationships between process parameters and inlet and outlet concentrations. As a result, we obtain Pareto-optimal process configurations that enable optimal SAF production with respect to competing objective functions, such as CO_2 emissions vs. cost. Our preliminary results indicate that the use of biomass-based routes provides the best trade-off between specific costs and CO_2 emissions. Under limited availability of biomass, syngas is additionally produced via electrolysis combined with DAC, leading to significantly higher specific aviation fuel costs with a similar CO_2 footprint.

References

Aspen Technology Inc (2023). *Aspen Plus*, https://www.aspentech.com/en/products/engineering/aspen-plus. Accessed 30 November 2023.

Bynum, M. L., Hackebeil, G. A., Hart, W. E., Laird, C. D., Nicholson, B. L., Siirola, J. D., Watson, J.-P., and Woodruff, D. L. (2021). *Pyomo - optimization modeling in Python*, Cham: Springer.

Ceccon, F., Jalving, J., Haddad, J., Thebelt, A., Tsay, C., Laird, C. D., and Misener, R. (2022). "OMLT: Optimization & Machine Learning Toolkit," *Journal of Machine Learning Research*. Volume 23, No. 349: pp. 1–8.

Demirhan, C. D., Tso, W. W., Powell, J. B., and Pistikopoulos, E. N. (2021). "A multi-scale energy systems engineering approach towards integrated multi-product network optimization," *Applied Energy*. Vol. 281, p. 116020.

Fahmi, I., and Cremaschi, S. (2012). "Process synthesis of biodiesel production plant using artificial neural networks as the surrogate models," *Computers & Chemical Engineering*. Vol. 46, pp. 105–123.

Freire Ordóñez, D., Halfdanarson, T., Ganzer, C., Shah, N., Dowell, N. M., and Guillén-Gosálbez, G. (2022). "Evaluation of the potential use of e-fuels in the European aviation sector: a comprehensive economic and environmental assessment including externalities," *Sustainable energy & fuels*. Vol. 6, No. 20: pp. 4749–4764.

Gonzalez-Garay, A., Heuberger-Austin, C., Fu, X., Klokkenburg, M., Di Zhang, van der Made, A., and Shah, N. (2022). "Unravelling the potential of sustainable aviation fuels to decarbonise the aviation sector," *Energy & Environmental Science*. Vol. 15, No. 8: pp. 3291–3309.

Grimstad, B., and Andersson, H. (2019). "ReLU networks as surrogate models in mixed-integer linear programs," *Computers & Chemical Engineering*. Vol. 131, p. 106580.

Gurobi Optimization (2023). *The Leader in Decision Intelligence Technology - Gurobi Optimization*, https://www.gurobi.com/. Accessed 30 November 2023.

Hamelinck, C., Faaij, A., Uil, H. den, and Boerrigter, H. (2004). "Production of FT transportation fuels from biomass; technical options, process analysis and optimisation, and development potential," *Energy*. Vol. 29, No. 11: pp. 1743–1771.

Henao, C. A., and Maravelias, C. T. (2011). "Surrogate-based superstructure optimization framework," *AIChE Journal*. Vol. 57, No. 5: pp. 1216–1232.

Niziolek, A. M., Onel, O., and Floudas, C. A. (2017). "Municipal solid waste to liquid transportation fuels, olefins, and aromatics: Process synthesis and deterministic global optimization," *Computers & Chemical Engineering*. Vol. 102, pp. 169–187.

Vardon, D. R., Sherbacow, B. J., Guan, K., Heyne, J. S., and Abdullah, Z. (2022). "Realizing "net-zero-carbon" sustainable aviation fuel," *Joule*. Vol. 6, No. 1: pp. 16–21.

ESCAPE-34 PSE-2024
European Symposium on Computer Aided Process Engineering
&
Process Systems Engineering

Flavio Manenti, Gintaras V. Reklaitis (Eds.), Book of Abstract of the 34th European Symposium on Computer Aided Process Engineering / 15th International Symposium on Process Systems Engineering (ESCAPE34/PSE24), June 2-6, 2024, Florence, Italy.

CO_2 Capture and Management Strategies for Decarbonizing Secondary Aluminium Production

Dareen Dardor[a,b*], Daniel Flórez-Orrego[a], Meire Ribeiro Domingos[a], Reginald Germanier[c], Manuele Margni[b], François Maréchal[a]

[a,] *Industrial Process and Energy Systems Engineering, Ecole Polytechnique Fédérale de Lausanne, EPFL, Sion 1950, Switzerland.*
[b] *Institute of Sustainable Energy, School of Engineering, University of Applied Sciences and Arts Western Switzerland (HES-SO), Sion 1950, Switzerland.*
[c] *Novelis Switzerland S.A., Sierre 3960, Switzerland*

**dareen.dardor@epfl.ch*

Abstract

The production of aluminium largely depends on the use of fossil fuels, resulting in the emission of significant amounts of greenhouse gases. As the aluminium industry is working towards decreasing its environmental burdens, the elimination of direct emissions from the remelting step becomes increasingly important. This research presents opportunities for decarbonizing secondary aluminium remelting and rolling via optimized carbon capture and abatement routes. Various carbon capture and management strategies for secondary aluminium production sites are developed and evaluated. To this end, process integration and optimization techniques following a mixed integer linear programming (MILP) approach are applied. A blueprint of an aluminium plant is developed, and the integration of several carbon capture and management technologies is modelled. The studied capture options include oxy-combustion, amine-based absorption, membranes, structured solid sorbents, and cryogenic beds. Once captured, the concentrated CO_2 gas stream can be pressurized for pipeline transport or injection, transformed into synthetic natural gas, mineralized into cement additives, or used to produce plastic monomers. A systemic approach was adopted to compare these options in terms of multiple performance indicators. It was found that, up to 80% of the emitted CO_2 can be efficiently captured and utilized. Moreover, additional revenue from mineralized CO_2, olefins, or synthetic natural gas results in a net negative change in operating expenditures of the plant with comparison to continuously emitting the base flows of fossil CO_2. Methanation provides a potential defossilization route when coupled with the use of renewable electricity at the expense of high capital expenditure due to the size of the electrolyzer needed. All these capture and utilization systems are almost three times cheaper than importing green hydrogen for use in aluminium furnaces, a potential solution still under experimental validation in the aluminium sector.

Keywords: Aluminium, Decarbonization, Carbon capture, Cost, Emissions.

1. Introduction

In 2021, the aluminium sector reported a footprint of around 1.17 billion tonnes of CO_2 equivalent, i.e., 2% of global industrial emissions (IAI 2023). Many industries are reliant on the use of aluminium, including but not limited to, aerospace, automotive, beverage can, construction, and renewable energy systems such as solar panels and wind turbines. Secondary aluminium production involves remelting a mixture of scrap and pure aluminium and then rolling it into sheets. This process requires furnaces operating at high temperatures of over 1000°C, the majority of which use fossil based natural gas. While direct electrification could readily provide decarbonization solutions for lower temperature systems; the use of combustible fuels for aluminium remelting furnaces remains the only technically viable solution at large scales. To this end, burning hydrogen fuel is also possible. However, the effect of higher flame temperatures and increased water vapor concentration on product quality are yet to be determined. Hence, a crucial consideration in the industry's current decarbonization plans is the management strategy of CO_2 emissions from burning fossil or synthetic natural gas (SNG). Among the technological solutions for capturing CO_2 are oxy-combustion furnaces, conventional amine-based absorption systems, novel membrane units, structured solid sorbents such as metal organic frameworks (MOFs), and cryogenic routes (Zanco et al. 2021). Captured CO_2 can then be used to manufacture fuels (SNG) or materials (e.g., plastics), mineralized to produce cement additives (such as $CaCO_3$), or stored in geological formations. Figure 1 presents a graphical illustration of the different alternatives considered in this work. These scenarios were defined by combining multiple capture and utilization technologies of interest to the aluminium industry, resulting in more than 20 feasible configurations. Such analysis calls for a systemic study to evaluate competing technologies based on multiple performance indicators. In this study, a CO_2 capture and management strategy is devised for a secondary aluminium production facility, while capitalizing on potential waste heat recovery and system integration opportunities.

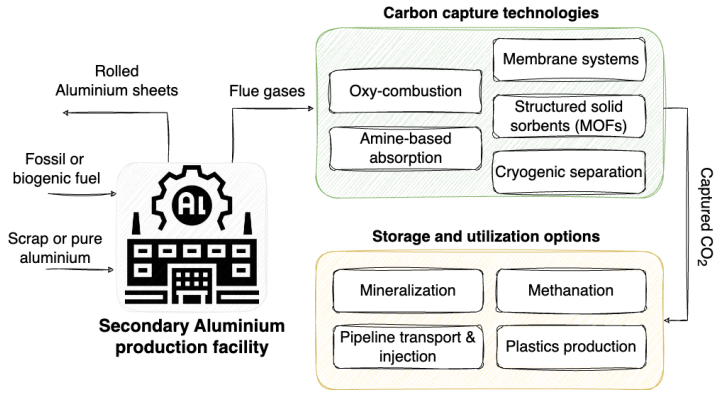

Figure 1: Potential CCUS routes for decarbonizing secondary aluminium production.

2. Methods

An optimization problem for an operating aluminium facility is developed based on minimal incremental costs. Key performance indicators are defined to compare the solutions in terms of thermodynamic, economic, and environmental impact aspects.

2.1. Aluminium process modelling and description of CCUS systems

Figure 2 illustrates a process flowsheet of the secondary aluminium production facility and the CCUS technologies being evaluated. First, pure aluminium is preheated to 250°C.

Subsequently, both pure and scrap aluminium are fed into the melting furnace where they undergo fusion at 660°C, and are superheated to roughly 750°C. Next, the molten aluminium is fed into the direct cast chilling process through the holding furnaces where it solidifies into cast ingots using water as the cooling medium. The ingots are then surface polished in the scalper, annealed at 550°C in pusher furnaces, and rolled into thin sheets. The final treatment step occurs in the annealing continuous line (ACL) where the coils are chemically and thermally treated at approximately 550°C. All plant furnaces emit flue gases containing CO_2, that can be captured and utilized using different technologies. Chemical absorption using amine solvents is one option and consumes 3.6 $MJ_{steam}/kgCO_2$ (Flórez-Orrego et al. 2020). Alternatively, temperature-swing adsorption beds filled with metal organic frameworks (MOFs) can reduce steam consumption down to 0.8 $MJ_{steam}/kgCO_2$ (Lin et al. 2021). Other capture technologies relying on electricity, such as cryogenic separation and membranes, consume 1, and 0.4 $kWh_{EE}/kg\ CO_2$ respectively (Song et al. 2019; Janakiram et al. 2021). In case of oxycombustion, 0.3 kWh_{EE}/kgO_2 for air separation is needed (Nascimento Silva, Flórez-Orrego, and De Oliveira Junior 2019).

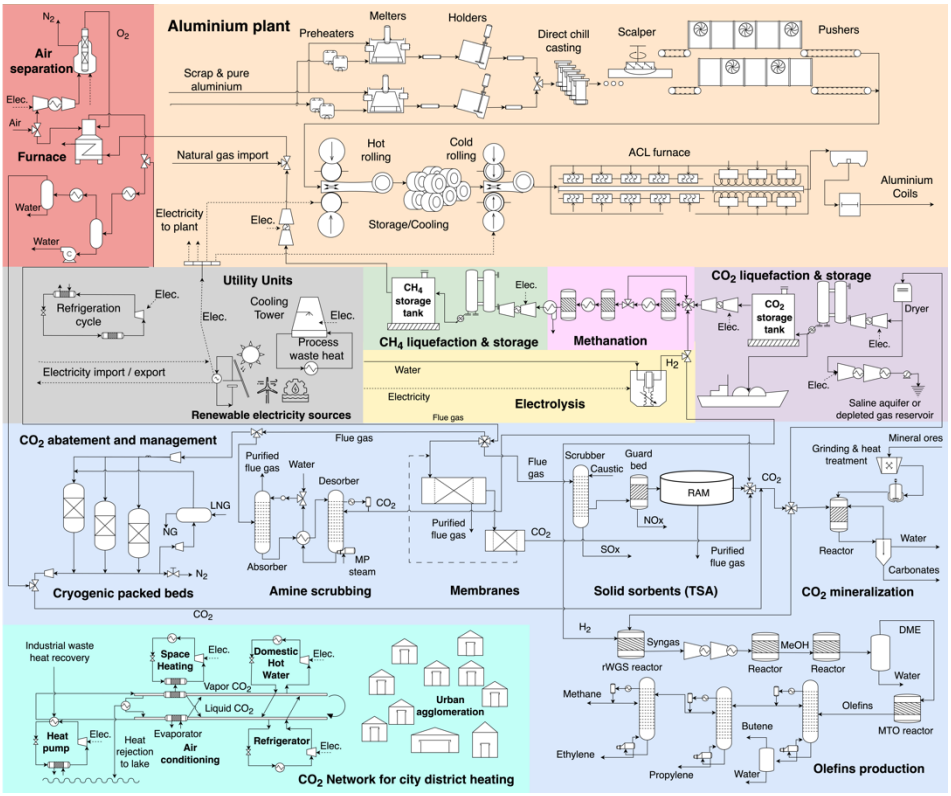

Figure 2: Secondary aluminium production facility and CCUS alternatives.

2.2. Optimization problem definition

Osmose Lua platform developed in the IPESE group at EPFL (Yoo et al. 2015) is used to handle the MILP formulation that minimizes the total cost subject to feasibility constraints, shown in equations (1-6). OSMOSE uses solvers supported by ampl® such as CPLEX or CBC. In this study, the size of the MILPs varied depending on the system configuration from 15 to 35 thousand variables subject to 13 to 34 thousand constraints.

$$min\ Cost_{tot} = \sum_{u \in Units}\left[\sum_{t \in Time}\left(Cop1_u \cdot Y_{u,t} + Cop2_u \cdot M_{u,t}\right) \cdot \Delta t + Cinv1_u \cdot Y_u + Cinv2_u \cdot M_u\right] \quad (1)$$

$$\sum_{w=1}^{N_w} M_w \cdot q_{w,r} + \sum_{i=1}^{N} Q_{i,r} + R_{r+1} - R_r = 0 \quad ; \forall\, r = 1 \ldots . N \tag{2}$$

$$\sum_{w=1}^{N_w} M_w \cdot W_w + \sum_{u \in Units} W_{net} + W_{imp} - W_{exp} = 0 \tag{3}$$

$$Y_{u,t} \cdot Fmin_u \leq M_{u,t} \leq Y_{u,t} \cdot Fmax_u \quad ; \forall u \in Units,\ \forall t \in Time \tag{4}$$

$$R_1 = 0, R_{N+1} = 0,\ R_r \geq 0 \quad ;\ W_{imp} \geq 0,\ W_{exp} \geq 0 \tag{5}$$

Assumed energy prices are: natural gas: 0.07 €/kWh; H_2: 7 €/kg; electricity: 0.15€/kWh (Jan/Feb/Nov/Dec), 0.001€/kWh (other months); and CO_2 tax:120 €/t. Cop1&2 are the fixed and variable operating cost, Cinv1&2 are those of investment cost, qw is the heat load of unit w, R is the heat cascaded from interval r+1 to r, and W is the power import or export. Binary $Y_{u,t}$ and load factor M_u define the existence and size of the utility units.

3. Results and Discussion

Figure 3 presents a high-level summary for the CCUS options under evaluation, and a reference hydrogen case study for comparison. Results indicate that the injection route exhibits the lowest increase in energy load compared to the base case due to the CO_2 compression. This is followed by importing hydrogen from the grid as no capture or utilization energy penalty is incurred. Cryogenic and oxyfuel CO_2 capture methods for injection have a higher energy load than some mineralization pathways due to the larger electricity penalty required for both technologies. Injection is followed by mineralization, which involves electricity consumption for the pretreatment of the mineral ores. The highest energy loads are observed for methanation followed by olefins production because of the electricity required for producing green hydrogen via electrolysis.

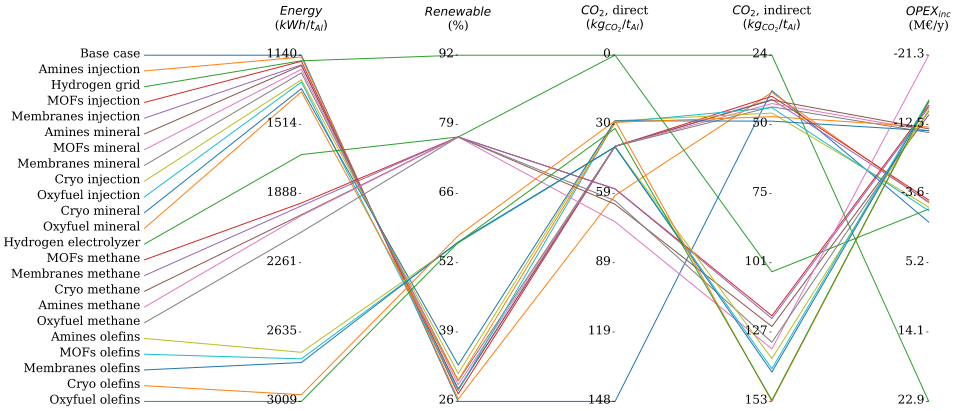

Figure 3: Key performance indicators of competing CCUS options.

Renewability percentage directly reflects the defossilization of aluminium production. The scenario assuming green hydrogen is available in the grid results in the highest renewability of 92 %. This is followed by onsite utilization of captured CO_2 for natural gas production using a Swiss electricity mix, which is 77 % renewable. Next is olefins production at approximately 56 %, where the captured CO_2 and hydrogen from electrolysis are transformed into olefins with a fuel gas byproduct. Finally, injection and mineralization routes still heavily rely on fossil natural gas import resulting in the lowest renewability index. Introducing gasification or importing bio-SNG from the grid to these latter scenarios would substantially increase their renewability indices and result in negative overall CO_2 emissions.

In terms of capture efficiency, almost all routes achieve an 80% reduction in direct CO_2 emissions of the plant. This is lower than efficiencies typically reported for the evaluated capture technologies because of some losses occurring from the plant furnaces during aluminium loading. The capture efficiency of the olefins and methane production routes is slightly lower due to the need for optimized storage systems to supply the plant fuel demands and contain emitted CO_2. An important consideration to account for when utilizing electricity grids are the indirect emissions resulting from that electricity. For some scenarios indirect emissions reach up to 150 $kgCO_2/tAl$, surpassing the emissions of the base case and resulting merely in a scope shifting outcome.

Importing green hydrogen at current prices increases operating expenses (OPEX) by up to 3 times compared to the base case. All the CCUS options provide economic benefits in terms of OPEX compared to the base case. The CO_2 injection route reduces OPEX due to the avoided CO_2 taxes that would be incurred in case emissions continue. The mineralization option also provides a small benefit in operational costs resulting from the value of marketable cement additives. These economic benefits are almost quadrupled in cases of methanation and olefins production due to the higher value of these products compared to simply injecting or mineralizing the captured CO_2.

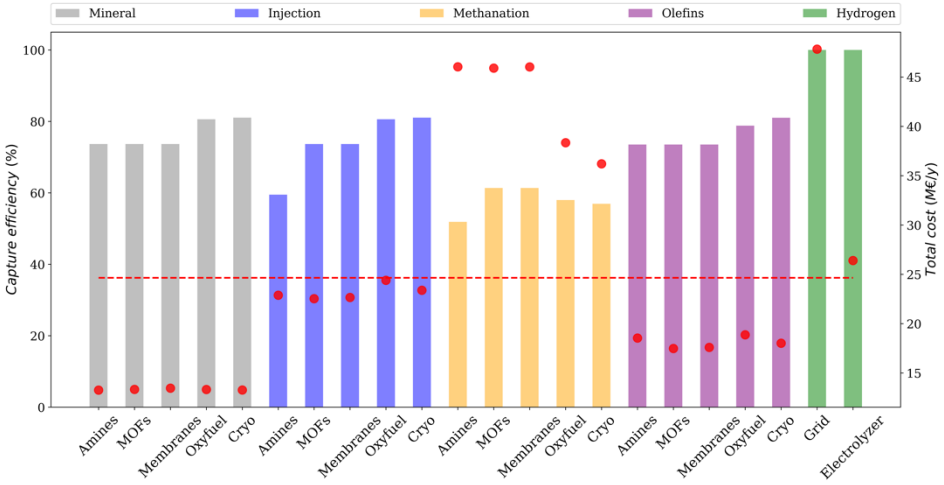

Figure 4: Capture efficiency (left axis, bar plots) and total costs (right axis, red dots) for the CCUS options. Total cost of the base case is indicated with a red dashed line for comparison.

Next, the total annualized costs with relation to capture efficiencies for the evaluated scenarios are presented in Figure 4. Oxyfuel and cryogenic separation almost always achieve the highest capture efficiency, except in the methanation route where additional losses are attributed to storage systems. Mineralization options offer the lowest total cost followed by olefins production due to the added value of products. The total costs of either mineralization, olefin production or injection remain lower than the base case. Methanation is more costly than the base case due to the oversized electrolysis system which needs further optimization. Finally, current green hydrogen prices do not allow economic competition with capture pathways. In this regard, producing hydrogen via electrolysis seems to be more promising. However, technical difficulties summarized in hydrogen storage, higher furnace temperatures, and furnace gas composition currently impede wide application of hydrogen combustion in the aluminium industry.

4. Conclusions

In conclusion, several CCUS pathways were evaluated for decarbonizing a secondary aluminium production facility. Up to 80% capture efficiency is reported for the evaluated technologies. It was found that injection and mineralization pathways sustain the lowest energy consumption penalty (20% higher than the base case). However, these options provide the least operational revenue due to the lower income compared to fuels or chemicals produced in the methanation and olefins routes. In addition, monitoring the indirect emissions of the utilized electricity is crucial for maximizing decarbonization potential and avoiding any scope shifting effects. Complete defossilization is possible if such capture pathways are coupled with the use of renewable electricity. Negative CO_2 emissions are also achievable if SNG of biogenic origin is used in the plant, captured, and transformed via any of the identified utilization options. Finally, burning green hydrogen remains a viable but challenging alternative in both technical and economic aspects compared to the presented capture, storage, and utilization options.

Acknowledgments

The authors would like to thank the Net Zero Lab consortium for funding this work in the context of the project goals of decarbonizing secondary aluminium production.

References

Flórez-Orrego, Daniel, Shivom Sharma, Silvio De Oliveira Junior, and François Maréchal. 2020. "Combined Exergy Analysis, Energy Integration and Optimization of Syngas and Ammonia Production Plants: A Cogeneration and Syngas Purification Perspective." *Journal of Cleaner Production* 244 (January): 118647. https://doi.org/10.1016/j.jclepro.2019.118647.

IAI. 2023. "Greenhouse Gas Emissions – Aluminium Sector." January 25, 2023. https://international-aluminium.org/.

Janakiram, Saravanan, Fabio Santinelli, Riccardo Costi, Arne Lindbråthen, Giuseppe Marino Nardelli, Kris Milkowski, Luca Ansaloni, and Liyuan Deng. 2021. "Field Trial of Hollow Fiber Modules of Hybrid Facilitated Transport Membranes for Flue Gas CO2 Capture in Cement Industry." *Chemical Engineering Journal* 413 (June): 127405. https://doi.org/10.1016/j.cej.2020.127405.

Lin, Jian-Bin, Tai T. T. Nguyen, Ramanathan Vaidhyanathan, Jake Burner, Jared M. Taylor, Hana Durekova, Farid Akhtar, et al. 2021. "A Scalable Metal-Organic Framework as a Durable Physisorbent for Carbon Dioxide Capture." *Science* 374 (6574): 1464–69. https://doi.org/10.1126/science.abi7281.

Nascimento Silva, Fernanda Cristina, Daniel Flórez-Orrego, and Silvio De Oliveira Junior. 2019. "Exergy Assessment and Energy Integration of Advanced Gas Turbine Cycles on an Offshore Petroleum Production Platform." *Energy Conversion and Management* 197 (October): 111846. https://doi.org/10.1016/j.enconman.2019.111846.

Song, Chunfeng, Qingling Liu, Shuai Deng, Hailong Li, and Yutaka Kitamura. 2019. "Cryogenic-Based CO2 Capture Technologies: State-of-the-Art Developments and Current Challenges." *Renewable and Sustainable Energy Reviews* 101 (March): 265–78. https://doi.org/10.1016/j.rser.2018.11.018.

Yoo, Min-Jung, Lindsay Lessard, Maziar Kermani, and François Maréchal. 2015. "OsmoseLua – An Integrated Approach to Energy Systems Integration with LCIA and GIS." In *Computer Aided Chemical Engineering*, 37:587–92. Elsevier. https://doi.org/10.1016/B978-0-444-63578-5.50093-1.

Zanco, Stefano E., José-Francisco Pérez-Calvo, Antonio Gasós, Beatrice Cordiano, Viola Becattini, and Marco Mazzotti. 2021. "Postcombustion CO2 Capture: A Comparative Techno-Economic Assessment of Three Technologies Using a Solvent, an Adsorbent, and a Membrane." *ACS Engineering Au* 1 (1): 50–72. https://doi.org/10.1021/acsengineeringau.1c00002.


ESCAPE-34 PSE-2024
European Symposium on Computer Aided Process Engineering
&
Process Systems Engineering

Flavio Manenti, Gintaras V. Reklaitis (Eds.), Book of Abstract of the 34th European Symposium on Computer Aided Process Engineering / 15th International Symposium on Process Systems Engineering (ESCAPE34/PSE24), June 2-6, 2024, Florence, Italy.

Decomposition Method to Evaluate District Heating/Cooling Network Potential at Urban Scale

Catarina G. Braz*, Raphaël Briguet, Luc Girardin, Bingqian Liu, François Maréchal

Industrial Process and Energy Systems Engineering (IPESE), École Polytechnique Fédérale de Lausanne, Rue de l'Industrie 17, 1951 Sion, Switzerland

catarina.braz@epfl.ch

Abstract

In this work, a tool to design district heating networks (DHN) is presented and applied to the city of Lausanne as a case study. The evaluation of the buildings' heat/cooling demand is performed using a Geographic Information System (GIS) database, built from different public databases, national norms, and real consumption measurements.

In a first approach, the city is decomposed into smaller districts, then heat and cooling demands of each district are determined, and the investment and operational costs of the DHN calculated using a parameterized empirical formula. The costs of the pipes that connect the districts to the heating source are computed by routing the primary network using the Minimum Spanning Tree (MST) algorithm.

This methodology was calibrated for the city of Lausanne, and the influence of the system design and supply/return temperature levels on heat and cooling distribution costs was studied considering the current buildings connected to the DHN.

Keywords: District heating/cooling network, Urban Systems, Geographical database, Sustainable energy supply.

1. Introduction

With approximately 149,000 inhabitants, Lausanne is the 4th largest city in Switzerland in terms of population. In 2020, heat consumed during winter was supplied by the district heat network (25 %) natural gas network (40 %) and fuel oil (35 %) (SiL, 2020).

District heating and cooling are considered to have an important contribution in the transition from the current energy systems to the future energy solutions. 5th generation district heating networks in particular use temperature levels close to ground temperature, minimising thermal losses throughout the grid and having the extra advantage that they can be used for cooling residential buildings with a different type of fluid. The development of DHN into cities has been however hindered by large investment costs.

2. Methodology

2.1. Evaluation of the energy demand of the city of Lausanne

The energy demand was determined using a GIS database (Girardin, 2012) with the stock of buildings in the city of Lausanne. The city is characterized from an energy point of view, using two SIA (Société Suisse des ingénieurs et architects) standards, the SIA 2024 and the SIA 380/1. The first is the standards for *Space usage data for energy and building facilities*, and the second is the standards for *Heat requirements for heating*. The information about the buildings is gathered mainly from three databases:

- **RegBL:** a geographic point containing information like the EGID, affectation, date of construction, number of floors, etc.
- **SwissTLM3D:** 2D polygon representing the footprint of the buildings
- **SwissBuildings3D:** 3D modelling of the buildings, giving information on the orientation of the roofs and area of the facades

The heating demand of a building, $\dot{Q}$, is the sum of the demand for space heating, $\dot{Q}^{SH}$, and the demand for domestic hot water, Q^{HW}. Space heat demand was estimated through a heat balance on the building, as presented in Eq. (1). $\dot{Q}_s$, Q_p, and $\dot{Q}_e$ represent the internal gains from solar irradiation, people, and appliances, respectively. $\dot{Q}_{loss}$ and $\dot{Q}_{vent}$ are the heat losses through the walls and the air renewal, respectively.

$$\dot{Q}^{SH} = \dot{Q}_e + \dot{Q}_p - \dot{Q}_s - \dot{Q}_{loss} - \dot{Q}_{vent} \quad (1)$$

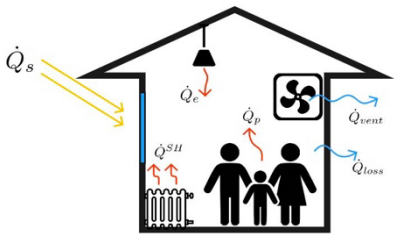

Figure 1 – Heat flows within a building.

2.1.1. Heat consumption validation

The heat consumption in each building was calculated considering the efficiency of the energy system installed, Eq. (2).

$$\dot{Q}_{supply} = \dot{Q}^{SH}_{fuel}/\eta^{SH}_{fuel} + \dot{Q}^{HW}_{fuel}/\eta^{HW}_{fuel} \quad (2)$$

Table 1 presents the efficiencies considered for each energy system.

Table 1 – Heating systems efficiency (Genève, 202).

	Space heating	**Hot water**
Gas boiler	0.86	0.54
Fuel oil boiler	0.86	0.54
DHN	0.95	0.65

The database results were validated using billing data from 2019 provided by the local urban gas and DHN supplier. Since fuel oil is not sold by Lausanne's heat supplier, their value is also an estimation based on the SIA norms. The results of the validation are shown in Figure 2. The database estimated consumption values are very close to the

supplier, with an average deviation of 21, 17 and 5 % for fuel oil, gas and DHN, respectively.

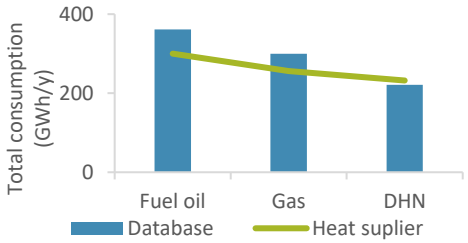

Figure 2 – Estimated total heat consumption compared with the values from the heat supplier.

2.2. Model of the heating network within a district

The modelling of the DHN within a district followed the methodology presented by Briguet (2022), where the estimation of the pipe's length within a given district is based on the area and the number of buildings, assuming that buildings are equidistantly distributed over a given area (Girardin, 2012), Figure 3. Eq. (3) gives the network route length, L for a pair of pipes, in function of the area of the district, A, the number of buildings, n_b, and the shape factor, K. The latter is a coefficient that accounts for the street typology, that had to be calibrated for the city of Lausanne, using the existing DHN.

$$L = (n_b - 1)K\sqrt{A/n_b} \tag{3}$$

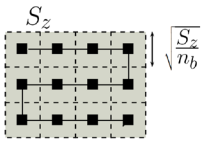

Figure 3 – Representation of the equidistance assumption (Girardin, 2012).

The districts were defined using a meshing algorithm applied in the areas with a connection to the DHN. First, the buildings connected to Lausanne's DHN were selected (Figure 4 (a)), then a mesh with several sizes was applied and the length of pipe within the district was calculated (Figure 4 (b) and (c)). For each mesh size, K was optimized using Excel solver to set the difference between the sum of real pipe length within the districts, and the sum of the lengths calculated by Eq. (3) equal to zero.

This procedure was repeated for meshes with sizes (length of the hexagon faces) between 100 and 300. The results are presented in Table 2. The average relative deviation, $\bar{\sigma}$, was calculated with Eq. (4). The best results are obtained for a mesh with size 125.

$$\bar{\sigma} = \frac{\sum_{i=1}^{N_d} abs(L_{real} - L)/L_{real}}{N_d} \tag{4}$$

The total demand of the network was assumed to be equally distributed among the number of buildings in the district and that there is a linear decrease of the mass flow of heating fluid as the energy is distributed, and, consequently, a decrease of the diameter of the pipe per connection of buildings. Piping costs included a fixed cost that accounts for civil engineering works and a variable that depends on the diameter of the pipe. Total cost was assumed to follow the same linear regression as for the city of Geneva (Henchoz, 2016).

$$c_{pipe} = (5670D + 613) \times L \tag{5}$$

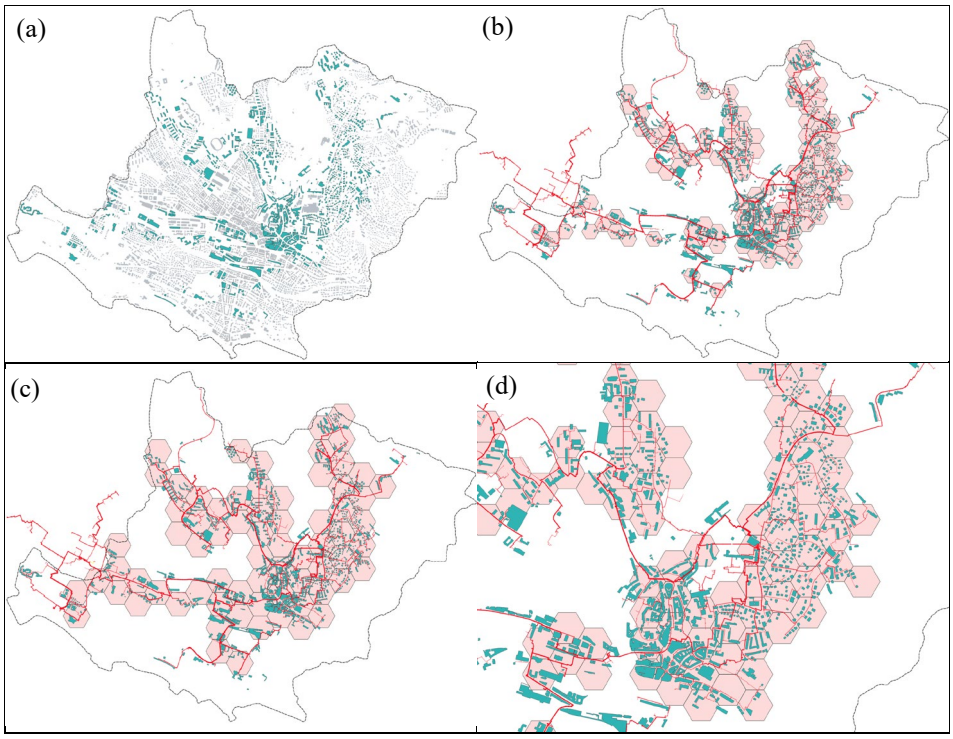

Figure 4 – District definition using a hexagon-shaped mesh. a) Selection of the buildings connected to the DHN. b) Application of a mesh with size 125. c) Application of a mesh with size 200. d) Zoom in on mesh 125. The red line represents the real DHN.

Table 2 – Results per mesh size.

	Area (ha)	***K***	$\bar{\sigma}$ **(%)**
mesh_100	2.6	1.00	56
mesh_125	4.1	0.97	40
mesh_150	5.8	0.93	45
mesh_175	8.0	0.85	53
mesh_200	10	0.80	47
mesh_225	13	0.78	68
mesh_250	16	0.75	64
mesh_275	20	0.75	50
mesh_300	23	0.73	47

2.3. Cost of the district connecting pipes

The routing of the primary network that connects all districts was performed according to the methodology described by Briguet (2022). The path is determined using the MST algorithm, which together with the Python API of *Open Street Map* allows us to obtain the shortest route to connect two geographic points. Once the route taken by the network is calculated, the total cost of the infrastructure, C_p, can be estimated by Eq. (6), Where, $c_{p,i}^{d}$ and c^{c} are the cost of piping in each district and the cost of district connection, respectively.

$$C_p = \sum_i^{N_d} c_{p,i}^d + c^c \quad (6)$$

3. Results

After determining the mesh that best estimates the network length inside the districts, the heating and cooling demands and the cost of DHN pipes within the districts were calculated for a supply/return temperature (T_s/ T_r) of 175/75 °C, Figure 5.

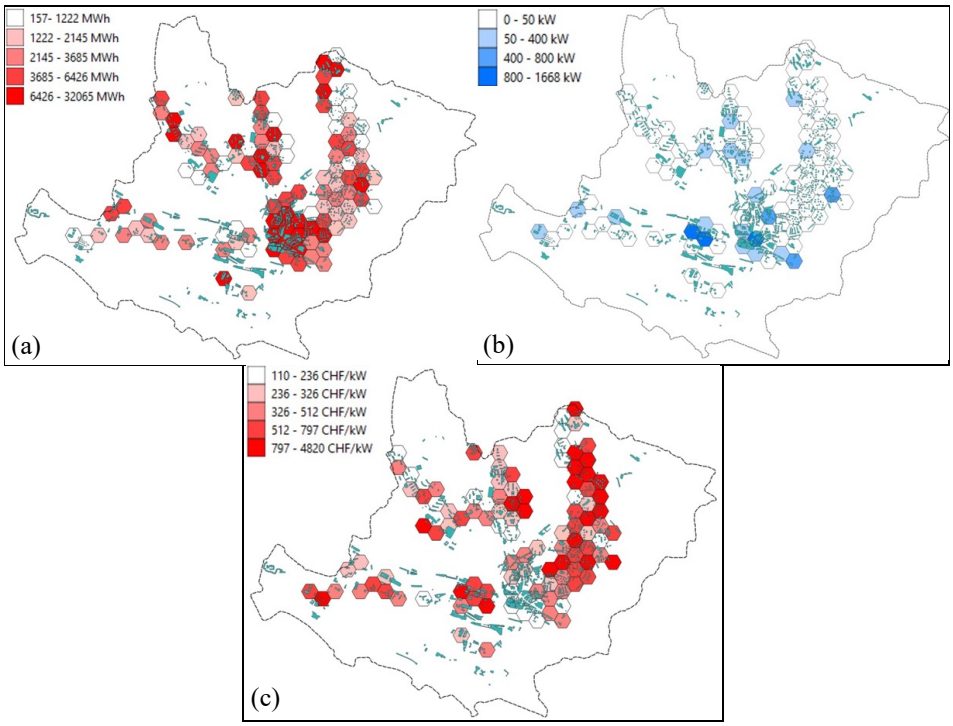

Figure 5 – (a) District heat demand for the buildings connected to the DHN. (b) District power cooling demand. (c) Cost of piping for a temperature level of 175/75 °C.

The districts were connected using the MST described in Section 2.3. As an approximation, it was considered that Pierre de Plan was the only heating source of the city of Lausanne. The results are presented in Figure 6. The total length of the DHN is 218 km, which is very close to the length of the real DHN installed (204 km).

The same methodology was applied to different supply/return temperature levels of the DHN. The results can be seen in Table 3. As expected, the lower the temperature levels, the higher the infrastructure costs due to the need for higher pipe diameters.

Table 3 – DHN infrastructure results for different supply/return temperature levels.

	Total cost of the DHN (MCHF)
T_s = 175 °C; T_r = 75 °C	89.4
T_s = 130 °C; T_r = 70 °C	98.2
T_s = 95 °C; T_r = 70 °C	119.7
T_s = 70 °C; T_r = 50 °C	127.2

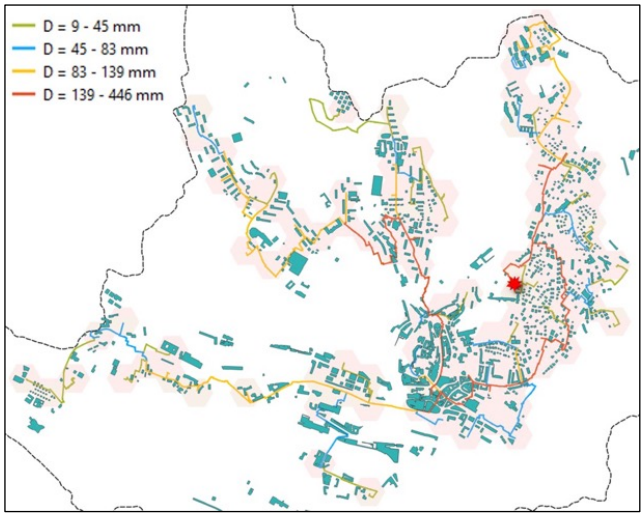

Figure 6 – Results of the DHN routing from Pierre de Plan.

4. Conclusions and future work

In this work, a methodology to assess the investment cost of a DHN has been presented. The methodology was calibrated for the city of Lausanne and validated using real consumption data and the currently installed DHN. In the future, the operation costs of the DHN will be integrated to assess the advantage of decreasing the supply/return temperature levels. Additionally, future scenarios where network coverage is expanded will be studied and the option of centralised or decentralised auxiliary units to operate the network at lower temperature levels, thus with higher exergy and energy efficiency.

Acknowledgements

This research was carried out in the frame of the "UrbanTwin: An urban digital twin for climate action: Assessing policies and solutions for energy, water and infrastructure" project with the financial support of the ETH-Domain Joint Initiative program in the Strategic Area Energy, Climate and Sustainable Environment.

References

2021, SIA 2024/202- Données d'utilisation Des Locaux Pour l'énergie Et Les Installations Du Bâtiment, Collection Des Normes

R. Briguet, 2022, District energy network potentials in a city territory, Master project report

Brüttisellen-Zurich, Marcel Rossi, 2016, SIA 380/1/2016 Besoins de Chaleur Pour Le Chauffage, Collection Des Normes

Genève, 2023, Calculer l'indice de dépense de chaleur admissible : Bâtiment neuf, https://www.ge.ch/node/29458 (accessed 2023-12-01)

L. Girardin, 2012, A GIS-Based Methodology for the Evaluation of Integrated Energy Systems in Urban Area, PhD Thesis

S. Henchoz, 2016, Potential of refrigerant based district heating and cooling networks, PhD Thesis

SiL, 2020, Les SiL en 2021 et 2022, Anual report

ESCAPE-34 PSE-2024
European Symposium on Computer Aided Process Engineering
&
Process Systems Engineering

Flavio Manenti, Gintaras V. Reklaitis (Eds.), Book of Abstract of the 34th European Symposium on Computer Aided Process Engineering / 15th International Symposium on Process Systems Engineering (ESCAPE34/PSE24), June 2-6, 2024, Florence, Italy.

Optimizing Waste-to-Energy Solutions for Circular Plastic Waste Management

Wafaa N. Majzoub[a] and Dhabia M. Al-Mohannadi[a]

[a]*Texas A&M University at Qatar, Department of Chemical Engineering, P.O Box 23874, Education City, Doha, Qatar*

dhabia.al-mohannadi@qatar.tamu.edu

Abstract

This work explores different waste-to-energy (WTE) technologies, including pyrolysis, gasification, and incineration, to achieve Sustainable development goals. A mixed-integer linear programming model is proposed in this study to identify the viable routes for sustainable energy production. Moreover, a new measure of sustainability is proposed to holistically assess all the technologies multi-dimensionally. The Total Sustainability Metric (TSM) encompasses several metrics: energy efficiency, material consumption, water usage, waste generation, emissions, etc. Through a case study comparing various WTE scenarios, initial outcomes spotlight a promising combination of pyrolysis and gasification, delivering sustainable energy with 56% more profitability and over 41% higher sustainability than the base case of incineration. In conclusion, the model offers a swift, systematic approach to pinpointing optimal WTE technologies and holds the promise of resolving plastic waste management and circularity concerns while generating profitable energy solutions.

Keywords: Plastic Waste Management, Sustainability, Chemical recycling

1. Introduction

The urgency to achieve the Sustainable Development Goals (SDGs) drives the escalating emphasis on energy and environmental sustainability. Solid waste management, particularly plastics, is crucial to environmental sustainability due to their nonbiodegradability. The growing plastic production resulted in 139 million metric tons of plastic waste in 2021 (UNEP, 2023). Addressing these concerns, waste-to-energy (WTE) offers a dual benefit by alleviating waste burdens and providing alternative energy sources that align with sustainability objectives. WTE technology presents an eco-friendly avenue to address waste management and energy challenges. The SDGs encompass optimizing lifecycle stages for reuse and recycling using Process System

Engineering (PSE) principles for enhancing circularity and energy efficiency while mitigating costs, emissions, and environmental impact (Avraamidou et al., 2020).

2. Literature Review

Energy recovery through incineration is a promising solution for plastic waste, given its high calorific value and suitability for end-of-life treatment. However, it raises concerns about depleting valuable carbon resources and emitting harmful air pollutants (Nikiema & Asiedu, 2022). Mechanical recycling, while eco-friendly, faces challenges like material quality degradation and labor-intensive processes, hindering plastic circularity (Schyns & Shaver, 2021). Chemical or molecular recycling, including pyrolysis and gasification, gains attention for a circular plastics economy due to their high technology readiness levels (Uekert et al., 2023). Exploring plastic waste management, especially through chemical recycling, supports the transition to a circular economy, reducing costs and pollution. Effective screening methods are crucial for waste-to-energy approaches, with studies employing techno-economic and life cycle assessments for feasibility evaluations. Limited research has delved into optimization models for plastic waste recycling, such as the framework proposed by (Somoza-Tornos et al., 2021) and the superstructure introduced by (Zhao & You, 2021). (Lim et al., 2022) present an optimal strategy for sorting and recycling mixed plastic waste. While previous studies focused on the feasibility of converting plastic waste, there is a need for further exploration, particularly in optimizing primary products from chemical recycling processes such as pyrolysis oil or synthesis gas. Moreover, to measure and design a circular economy, it's essential to establish a metric considering recovered materials' environmental, economic, and social value. Commonly used indicators include the Linear Flow Index (LFI), Material Circularity Indicator (MCI), and Product Circularity Indicator (PCI) based on material flow analysis precisely measuring material circulation but lacks consideration of life cycle emissions and avoided impacts, limiting its ability to represent product sustainability fully. Additional indicators such as material and energy efficiency, feedstock flexibility, and co-product utilization are crucial to individual processes (Supply Chain School, 2019).

This work introduces an innovative screening model that comprehensively evaluates various pathways for plastic waste recycling. Specifically, WTE approaches. This employed framework facilitates sophisticated decision-making by fostering a well-balanced assessment of different plastic recycling technologies. Moreover, to comprehensively assess the sustainability of all alternatives multi-dimensionally, the model introduces a novel metric that integrates various supplementary metrics such as material, energy, and water efficient utilization, waste generation, carbon footprint, economic viability, recyclability, co-product utilization, product quality, and TRL.

3. Methodology

The approach to screening the different plastic waste-to-energy pathways is illustrated in Figure 1.

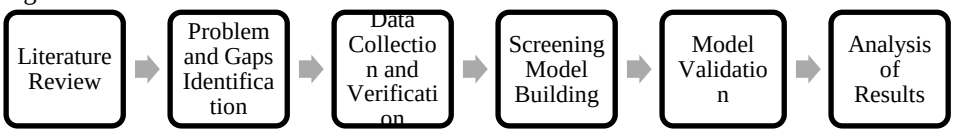

Figure 1. Methodology

4. Mathematical model Formulation

This work focuses on investigating plastic waste in energy technologies. A screening model based on mixed-integer linear programming (MILP) was developed to assess all the alternatives while considering multiple factors. The model's primary objective is maximizing overall profitability and is subjected to various equality and inequality constraints, including material and energy balance, capacity limits, economics considerations, and circularity constraints. The model proposes a set P of possible pathways. The model equations are presented as follows:

$$MAXIMIZE\ \ (Net\ profit) = f(x) \tag{1}$$

Subject to:

$$g_i(x) \leq 0,\ i = 1, \dots, m \tag{2}$$

$$h_j(x) = 0,\ j = 1, \dots, n \tag{3}$$

The net profit and income of the technology is determined as follows:

$$net\ profit = income - Capex - Opex \tag{4}$$

$$income = \sum_i MFR_{out,i} \times Price_i \tag{5}$$

The income is calculated using the output mass flowrate ($MFR_{out,i}$) of the specific product i and the price ($Price_i$) of the product (electricity in this case in \$/kWh). Capex is estimated through regression modeling with piecewise linearization to handle nonlinear data. Opex depends on each pathway's requirements including material, energy, utilities, etc. The overall sustainability is measured by incorporating supplementary metrics such as Material Utilization Indicator (MUI), Energy Utilization Indicator (EUI), Water Utilization Indicator (WUI), Solid-Waste Generation Indicator (WGI), Carbon Footprint Indicator (CFI), Economic viability Indicator (EVI), Co-product Utilization Indicator (CUPI), Recyclability Indicator (RI), Product Quality Indicator (QPI), and Technology Readiness Level Indicator (TRLI). All these indicators are given a specific weight factor (W_f) and collectively form the Total Sustainability Metric (TSM), as shown in Eq. (6) to Eq. (15), respectively. Each individual indicator and the final metric are all normalized on a scale of 0-1, where zero represents the worst-case scenario, and one represents the best-case scenario.

$$MUI_p = Plastic\ waste\ feed\ mass\ flowrate + \sum Mass\ flowrate\ of\ consumables \tag{6}$$

$$EUI_p = \frac{Energy\ required\ by\ pathway\ p,}{Mass\ flowrate\ of\ plastic\ waste\ feed}, \quad \forall p \in P \tag{7}$$

$$WUI_p = \frac{Water\ required\ by\ pathway\ p}{Mass\ flowrate\ of\ plastic\ waste\ feed}, \quad \forall p \in P \tag{8}$$

$$WGI_p = \frac{Mass\ flowrate\ of\ waste\ generated\ by\ pathway\ p}{Mass\ flowrate\ of\ plastic\ waste\ feed}, \forall p \in P \tag{9}$$

$$CFI_p = \frac{CO_{2,equivelent}\ emissons\ by\ pathway\ p}{Mass\ flowrate\ of\ plastic\ waste\ feed}, \quad \forall p \in P \tag{10}$$

$$EVI_p = \frac{Total\ annualized\ costs\ of\ pathway\ p}{Mass\ flowrate\ of\ plastic\ waste\ feed}, \quad \forall p \in P \tag{11}$$

$$CPUI_p = \frac{\sum_i (MFR_{co-product,i,p} \times price_{co-product,i})}{\sum_j (Mass\ flowrate_{main\ product,j} \times price_{main\ product,j})}, \forall p \in P \tag{12}$$

$$RI_p = \begin{cases} 1\ if\ products\ are\ recycable \\ 0\ if\ products\ are\ not\ recycable \end{cases}, \quad \forall p \in P \tag{13}$$

$$PQI_p = \begin{cases} 1\ if\ product\ is\ virgin\ quality \\ 0\ if\ product\ is\ not \end{cases}, \quad \forall p \in P \tag{14}$$

$$TSM_k = W_f \times (MUI_k + EUI_k + WUI_k + WGI_k + CFI_k + EVI_k + CPUI_k + RI_k + PQI_k + TRLI_k), \quad k = 1, \dots, p \tag{15}$$

5. Case Study

Products of waste-to-energy technologies for circular plastic waste management can vary depending on the technologies and processes employed. Generally, waste-to-energy solutions aim to produce energy through electricity generation, heat production, synthetic fuels, steam production, and combined heat and power. The case study considers the production of electricity and fuels through three pathways: pyrolysis, gasification, and energy recovery by direct incineration. The model aimed at achieving maximum economic profit and contribution to the circular economy through the proposed sustainability metric.

Table 1. Case Study Data in $M/y.

No.	Technology	Products	Income	Capex	Opex
P1	Incineration - Base case	Electricity	15.9	1.36	3.6
P2	Gasification + Methanol Synthesis + MTG	Gasoline Propylene	49.7	4.97	23.8
P3	Gasification+ Incineration	Electricity	12.8	6.33	18.6
P4	Pyrolysis	Pyrolysis oil	26.4	3.11	5.5
P5	Pyrolysis + Incineration	Electricity	11.1	4.46	9.0

The case study is scaled based on sources that generate 275 tons per day of mixed plastic waste. Detailed technical are provided in Table 1. Further data and constraints may be formulated and included with the core model as needed for a specific case study to retain the class of the optimization model. The model has been solved with Python 3.10.2 - Pyomo 6.4.0, Gurobi solver 10.0.1. Optimal solutions have been consistently obtained within a few seconds.

6. Results and Discussion

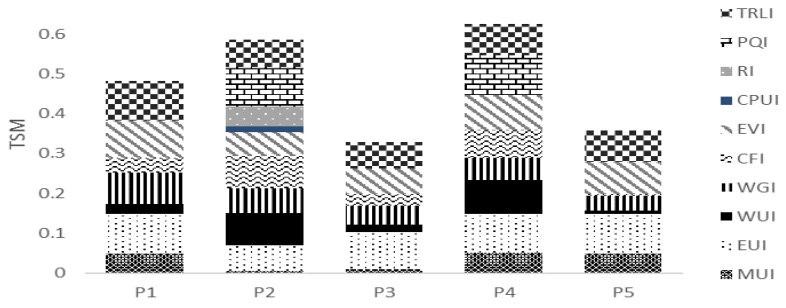

Figure 2. Contribution of Individual Indicators in TSM.

The waste-to-energy pathways (P1 to P5) are evaluated based on a comprehensive set of sustainability metrics, as illustrated by Figure 2, emphasizing that the higher the value is, the better. Among these pathways, P4 (Pyrolysis) stands out as the most sustainable WTE technology, as reflected by the value of TSM, indicating superior overall sustainability and circularity. P2 follows closely, showing strong performance across various indicators. P1 and P5 demonstrate moderate sustainability, while P3 means an overall negative impact. Regarding MUI, P2 demonstrates superior efficiency, while P1 and P5 show higher material usage.

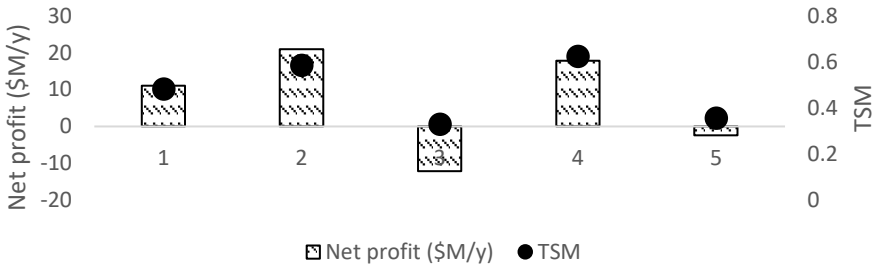

Figure 3. Net profit and TSM for Different Pathways.

Pathway 3 exhibits the most efficient energy utilization (EUI). The most efficient pathways in terms of water are P2 and P4. P3 generates the most waste, while P4 and P2 represent a better performance. CFI is lowest in P3 and P5, indicating the most negligible environmental impact, while EVI is highest in P2, reflecting the lowest cost. P2 is the only pathway that encompasses a valuable co-product, propylene. And that also reflects the better performance in the recyclability metric compared to all alternatives. Lastly, it is noticeable that Incineration for energy recovery is the most mature pathway reflected by the higher TRL value. Figure 3 illustrates the net profit compared to the sustainability metric for all the pathways before using the optimization model and reflecting the trade-offs between economic feasibility and sustainability. Particulary, although P2 is the highest profitable route, it shows lower performance in terms of sustainability compared to P4. Also, although P5 is more sustainable than P3, neither of them is economically feasible.

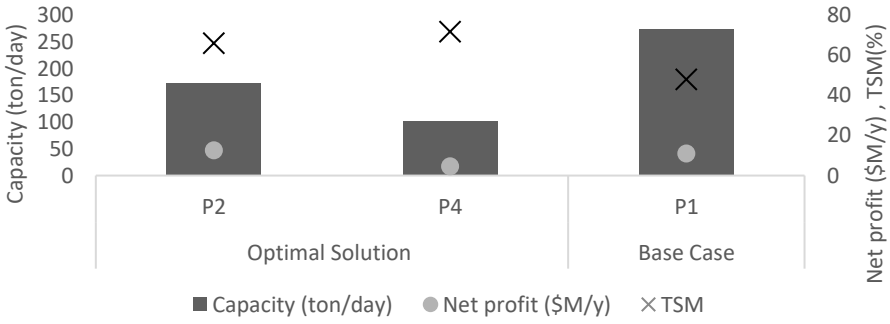

Figure 4. Optimization results

Figure 4 illustrates the optimization results compared to the base case of energy recovery by incineration (P1) for maximizing profitability and sustainability. The base case yields

an annual profit of $11 million, whereas combining the P2 and P4 outperforms, with a total net profit of $M17.2 annually, enhancing the base case's net profit by 57% and improving the base case sustainability by more than 41% offering the highest contribution to the circular economy.

7. Conclusion

The findings of this screening approach suggest that selling pyrolysis fuel oil, represented by P4 and gasoline fuel in P2, holds promise for achieving higher sustainability and circularity in waste-to-energy technologies. Furthermore, assessing individual indicators can provide insights into specific strengths and weaknesses of each pathway. This analysis helps identify pathways that excel in certain aspects, aiding in informed decision-making for sustainable waste-to-energy solutions. This work clarifies the role of technology in the circular economy for authorities to foster a cleaner and more sustainable global economy or, in other words, a sustainable trash-to-cash economy.

8. References

Avraamidou, S., Baratsas, S. G., Tian, Y., & Pistikopoulos, E. N. (2020). Circular Economy - A challenge and an opportunity for Process Systems Engineering. *Computers and Chemical Engineering*, *133*. https://doi.org/10.1016/j.compchemeng.2019.106629

Lim, J., Ahn, Y., & Kim, J. (2022). Optimal sorting and recycling of plastic waste as a renewable energy resource considering economic feasibility and environmental pollution. *Process Safety and Environmental Protection*. https://doi.org/10.1016/j.psep.2022.11.027

Nikiema, J., & Asiedu, Z. (2022). *A review of the cost and effectiveness of solutions to address plastic pollution*. *1*, 3. https://doi.org/10.1007/s11356-021-18038-5

Schyns, Z. O. G., & Shaver, M. P. (2021). Mechanical Recycling of Packaging Plastics: A Review. In *Macromolecular Rapid Communications* (Vol. 42, Issue 3). Wiley-VCH Verlag. https://doi.org/10.1002/marc.202000415

Somoza-Tornos, A., Pozo, C., Graells, M., Espuña, A., & Puigjaner, L. (2021). Process screening framework for the synthesis of process networks from a circular economy perspective. *Resources, Conservation and Recycling*, *164*. https://doi.org/10.1016/j.resconrec.2020.105147

Supply Chain School. (2019). *MEASURING PROGRESS TOWARDS A CIRCULAR ECONOMY: INDICATORS AND METRICS TOOL GUIDANCE*.

Uekert, T., Singh, A., DesVeaux, J. S., Ghosh, T., Bhatt, A., Yadav, G., Afzal, S., Walzberg, J., Knauer, K. M., Nicholson, S. R., Beckham, G. T., & Carpenter, A. C. (2023). Technical, Economic, and Environmental Comparison of Closed-Loop Recycling Technologies for Common Plastics. *ACS Sustainable Chemistry and Engineering*, *11*(3), 965–978. https://doi.org/10.1021/acssuschemeng.2c05497

UNEP. (2023). *Turning off the Tap: How the world can end plastic pollution and create a circular economy. Topic Sheet: Chemical Recycling*. https://doi.org/10.2760/0472

Zhao, X., & You, F. (2021). Waste high-density polyethylene recycling process systems for mitigating plastic pollution through a sustainable design and synthesis paradigm. *AIChE Journal*, *67*(4). https://doi.org/10.1002/aic.17127

ESCAPE-34 PSE-2024
European Symposium on Computer Aided Process Engineering
&
Process Systems Engineering

Flavio Manenti, Gintaras V. Reklaitis (Eds.), Book of Abstract of the 34th European Symposium on Computer Aided Process Engineering / 15th International Symposium on Process Systems Engineering (ESCAPE34/PSE24), June 2-6, 2024, Florence, Italy.

Optimization of Heat Pump and Vapor Recompression Technologies for wide-boiling Mixtures

Armin Rix,[a*] Niklas Paul,[b] Lea Wessner, [a] Daniel Murrenhoff[a]
[a]*Evonik Operations GmbH, Paul-Baumann-Str.1, 45772 Marl, Germany*
[b]*Evonik Oxeno GmbH & Co KG, Paul-Baumann-Str.1, 45772 Marl, Germany*
armin.rix@evonik.com

Abstract

The application of vapor recompression and heat pump technologies to recycle waste heat to the process is straightforward in close-boiling mixtures. Especially in distillation systems with high feed rate and reflux ratio, high energy cost and large compressor cost degression potentials enhance the economic attractiveness. In wide-boiling systems, on the other hand, a high compression ratio may lead to a low coefficient of performance and high cost for electrical energy. In this paper, alternative designs are presented, paving the way to the economic application of vapor recompression and heat pump technology to wide-boiling systems. The design of smart electrification strategies will be a core element on the path to net zero production in the process industries.

Keywords: vapor recompression, heat pump, heat integration, distillation, electrification.

1. Introduction

There are many examples in literature of the successful application of vapor recompression (VR) and heat pump (HP) technologies to recycle waste heat in columns separating close-boiling mixtures. A good overview is given by Jana (2014). Economic designs are possible even in vacuum systems (Rix et al., 2023). To achieve the CO_2-saving goals of the process industries and society as whole, these technologies for effective heat recycling need to be extended to wide-boiling systems. Here, however, large obstacles need to be overcome. Due to the high temperature difference between top and bottom of the column, a high compression ratio, a high compressor duty and a low coefficient of performance (COP) result at first glance. Therefore, new, creative solutions need to be developed, enabling industry to exploit the full potentials of mechanically assisted heat recovery. A simple exchange of existing fossil fueled steam generators by electric boilers would neither be cost-effective, nor could the energy grid supply the vast amounts of still scarce green electricity.

Using practical examples, we show how VR and HP technologies can play an important role in the smart electrification of the process industries even in challenging wide-boiling separations. The guiding principle we follow in this paper is to find creative ways to (at least partially) reduce the temperature lift required for heat recirculation.

To handle the high compression ratios required in wide-boiling systems, multi-stage compressors are employed. A smart utilization of vapors from intermediate compressor stages to heat pre-evaporators, side- and bottom reboilers may substantially reduce the compressor duty. Thus, VR or HP systems may be employed at substantially lower compression ratio and higher COP. However, these interventions are not without consequences on the separation task (Soares Pinto et al., 2011). Sensitivity analysis is employed to evaluate possible advantages of the use of the additional degrees of freedom opened in the design of multi-stage compressors.

2. Wide-boiling distillation systems

2.1. Vapor recompression and heat pump systems for large temperature lift

The compressor duty of any VR or HP system is directly proportional to the temperature lift to be overcome. In columns, this is the temperature difference between bottom and top of the column plus any driving temperature differences for heat transfer. In wide-boiling systems, the large temperature difference leads to compression ratios often exceeding 3. Therefore, two-stage compressor designs as shown in Figure 1 are required to heat the bottom reboiler. Although multi-stage compressor designs require higher capital expenditure, they also offer additional degrees of freedom. We will show, how these may be exploited to optimize the system design and performance.

- The high-pressure condensate formed in the bottom reboiler flashes when its pressure is reduced. Flashing and recycling it to the pressure level of an intermediate compressor stage will lower the flowrate to the first stage and thus the total compressor power.
- Each compressor stage elevates the suction pressure to a certain value, corresponding to a defined condensation temperature. If this temperature is sufficiently high, a part of this intermediate-pressure vapor may be used to heat a side reboiler at a convenient location in the stripping section. A substantial fraction of the total energy demand of the column may thus be recycled at significantly lower temperature lift, lower compression ratio and higher COP than is required for heating the bottom reboiler.
- Most hydrocarbons have hanging log(p),h-diagrams and require superheating to avoid partial condensation during compression. Individual superheating for each stage is recommended.
- Working fluids like methanol or water have a bell-shaped log(p),h-diagram and superheat during compression. To reduce the degree of superheating, high-temperature condensate can be injected into the feed of the second compression stage, reducing its volumetric flowrate, the stage compressor duty, and increasing the overall COP.

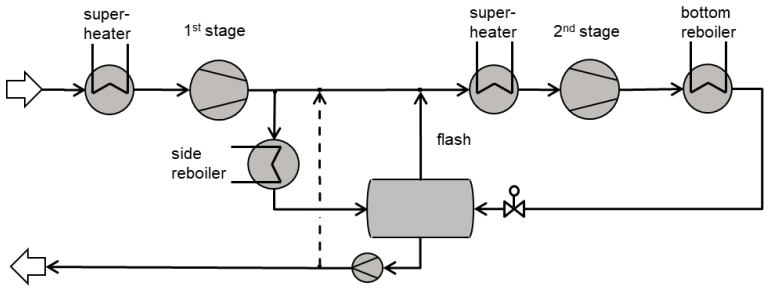

Figure 1: Two-stage compressor with intermediate flash recycle and potential de-superheating.

2.2. Methanol-water separation

Shahandeh et al. (2015) describe a column in operation in a world-scale methanol plant with a capacity of 1 million t/y. The column has 85 trays, operates at 1.2 bar, and is fed with 4,968 kmol/h of a mixture of 69.81 mol-% methanol and 30.19 mol-% water and has a reboiler duty of 107.4 MW. The feed has a vapor fraction of 12 %. Fitting an ASPEN model using NRTL-RK method to plant data, Shahandeh et al. (2015) estimate a tray efficiency of 30 % and use this model for an extended investigation of five different vapor recompression and internally heat-integrated column schemes.

Energy optimization studies should always start with a near-optimum simple column (Rix et al., 2019). There is ample industrial evidence, that well-designed modern trays should reach efficiencies of 70% and higher in the methanol-water system (Yang et al., 2003). Consequently, a sensitivity analysis in ASPEN using 70 % efficiency and 85 trays shows an optimum feed location on tray 75, reducing the energy demand by more than 40 % to 60.3 MW, see Figure 2a).

A next obvious step to further decrease the energy demand is the design of a double-effect heat-integrated column system (Rix et al., 2019). This technology is well established in the Lurgi methanol process (Ott et al., 2012). The light-split reverse (LS-R) configuration (Figure 2b) is chosen. The first column T-20 operates at 1.2 bar, separates almost 60% of the MeOH as overhead product at low reflux ratio and feeds its water-enriched bottom product to the high-pressure column T-30. The pressure of T-30 is raised to 2.8 bar, shifting its condensation temperature to 9 K above the bottom boiling temperature of T-20. It has been shown that this configuration allows heat-integration with the lowest pressure difference between the two columns, thus achieving good thermodynamic efficiency while offering good controllability (Chiang and Luyben, 1988). The energy demand is 35.5 MW, more than 40% lower than the optimized simple column.

Electrification of this separation process is possible using vapor recompression, see Figure 2c. The overhead vapor is fed to a two-stage compressor, which increases its pressure so far, that its condensation temperature is sufficiently high to heat the reboiler. In the base case with a driving temperature difference of 8 K, the COP is 4.6 and the compression ratio of each stage is 2.5 resulting in a total compressor duty of 13.1 MW. Introduction of the hot condensate flash and de-superheating at the intermediate pressure as shown in Figure 1 raises the COP to 5.0 and reduces compressor duty by 1 MW.

We will use this design as a base case and investigate further optimization options.

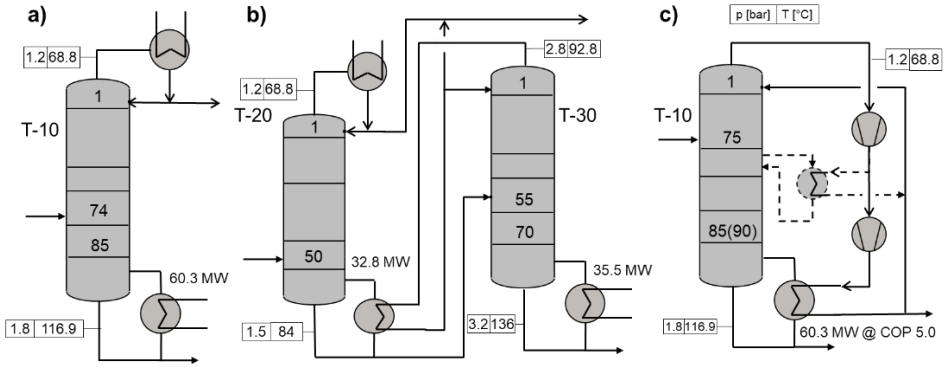

Figure 2: Flow schemes of a) simple column, b) heat-integrated LS-R system and c) vapor recompression with optional side reboiler (broken lines). Pressures and temperatures are given in boxes, relevant tray numbers in columns and heat duties near reboilers.

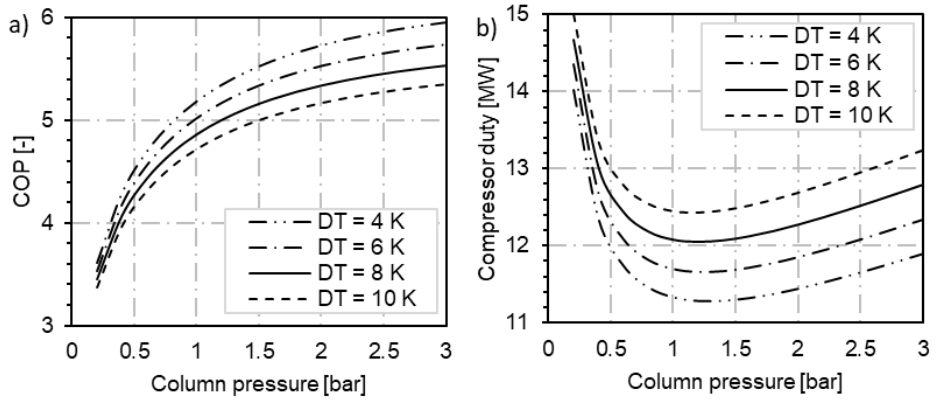

Figure 3: Impact of pressure on performance of VRC. a) Coefficient of performance (COP); b) Total compressor duty (both stages).

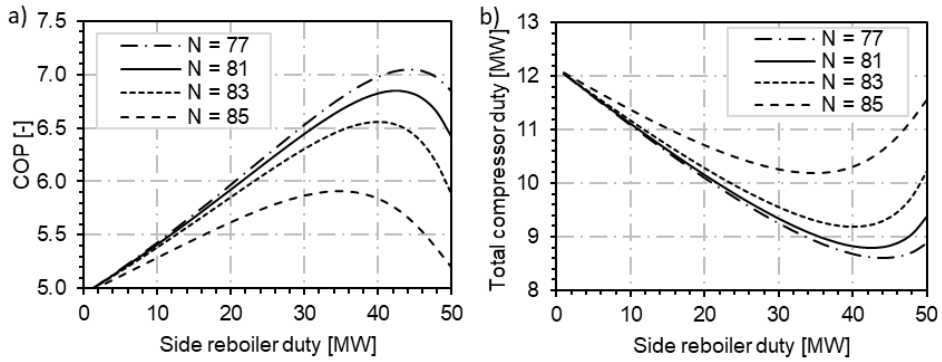

Figure 4: Impact of side reboiler location and duty on performance of VR. a) Coefficient of performance (COP); b) Total compressor duty (both stages).

Figure 3 shows results for a pressure variation at different driving temperature differences DT for heat transfer. Although the COP rises monotonously with pressure, there is a clear minimum of the compressor duty at a column pressure near 1.2 bar. These seemingly conflicting trends are due to the fact, that the separation becomes more difficult at higher pressures, and the energy demand of the reboiler increases. The required compression ratio, on the other hand, decreases, but not fast enough to compensate the first effect. At column pressures lower than ~1 bar, the suction side volumetric flowrate increases drastically, resulting in higher compressor duty. These results show that it is not sufficient to focus on performance indicators alone to judge the merits of design alternatives.

The benefit of introducing the side reboiler shown in broken lines in Figure 2c at different locations is shown in Figure 4. In the columns' stripping section, 5 trays have been added to compensate for changing operating lines (Soares Pinto et al., 2011), increasing the number of trays to 90. The driving temperature difference has been set to 8 K and all calculations have been performed at 1.2 bar.

The closer the side reboiler is located to the feed stage, the higher is its effectiveness. This is due to the distinctive temperature profile below the feed requiring a higher compression ratio in the first compressor stage. The total compressor duty decreases as more duty is shifted from the bottom to the side reboiler. As more methanol is evaporated in the side reboiler, however, the boiling temperature and thus the first stage compression ratio

increases. For each side reboiler location, a clear optimum duty can be seen in Figure 4b. Locating the reboiler at stage 77, 2 trays below the feed, up to 45 MW (i.e., ~75 % of the total energy demand) can be supplied at lower temperature and pressure, thus reducing the compressor duty by almost 40 % from 12 to 8.6 MW. In this operating point, the COP rises from 5.0 to more than 7.0.

Using fossil-based emission factors of 0.2 and 0.366 2 t CO_2/MWh (BAFA, 2023) for steam and electricity, the CO_2-emissions of the three variants shown in -Figure 2 considering 8.600 operating hours/year are a) 103, b) 61 and c) 38 kt/y and are reduced to 27 kt/y using a side reboiler. VR enables the application of green electricity, which results in CO_2-emissions close to zero. A column with vapor recompression designed according to the guidelines given above is currently under construction, enabling the first CO_2-neutral Evonik process. CO_2-savings of up to 30 kt/y are anticipated.

2.3. Debutanizer column

As a further practical example, the debutanizer presented by Luyben (2013) is simulated in ASPEN Plus using the SRK method. The number of stages has been increased from 30 to 40 trays to reduce the basic energy consumption. Figure 5 shows results of a sensitivity analysis varying column pressure from 3 to 9 bar. For VR, there is a clear trend of COP decreasing with pressure, while compressor duty increases. At the optimum operating pressure of 3 bar, the top temperature is only 26 °C, foreclosing the use of cheap cooling media. However, this operating point is made accessible by VR, since the trim condensation can be completely shifted to the pressure side (Luyben, 2019). Increasing the temperature difference from 4 to 12 K increases the compressor duty by 15 to more than 30 %. This large effect clearly shows the strong incentive to employ column internals of low pressure drop and highly efficient heat exchangers in VR and HP systems.

The thick lines in Figure 5 show results for a two-stage HP system with intermediate flash using iso-pentane as the working fluid at 8 K driving temperature difference in both heat exchangers. For column pressures exceeding 4.5 bar, the COP of HP systems exceeds the one of VR systems at the same temperature difference. The strong decline of VR system performance with pressure is due to the fact, that the overhead vapor, a mixture of butanes, approaches its critical pressure more closely at condensation conditions. Consequently, the choice between VR or HP systems depends on the suitability of the thermodynamic properties of the overhead vapor as a good HP working fluid.

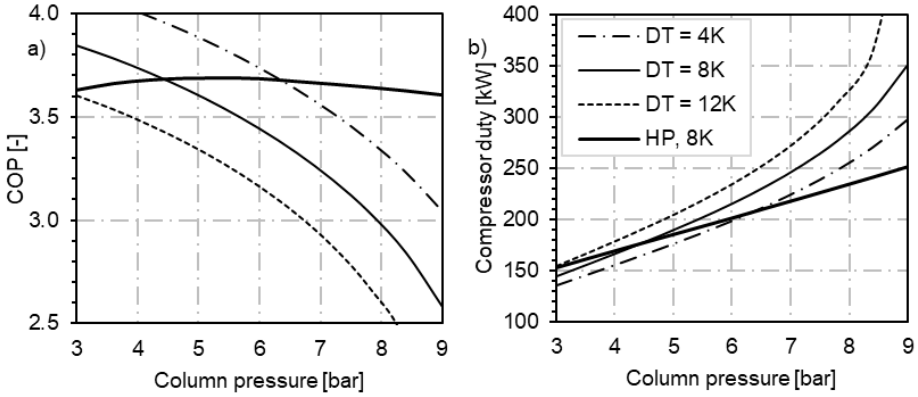

Figure 5: Performance of VR (thin lines) and HP (thick solid line) in the Debutanizer example. a) Coefficient Of Performance (COP), b) compressor duty. Driving temperature difference DT in the integrating heat exchangers as parametric variable.

3. Conclusions

VR and HP technologies are core elements on the path to net zero production in the process industries, increasing the effectiveness of the use of green electricity substituting fossil-based steam. Applying VR and HP to columns separating wide-boiling mixtures faces severe obstacles. To overcome these challenges, creative approaches combining pre-evaporators, side- and bottom reboilers using compressed vapors from intermediate stages of multi-stage compressors may substantially reduce the compressor duty.

VR and HP technologies have been successfully applied to two industrially relevant example columns separating wide-boiling mixtures. Energy optimization studies should start from a soundly designed simple column. Next, options to integrate available waste heat from the site should be considered. Once these low-cost options are exploited, it is time to tackle further optimization using VR and HP systems. To exploit their full potential, they should not be merely treated as an end-of-pipe addition to a pre-existing design. Instead, it is worthwhile to investigate the wider range of operating pressures now attainable. A large effect of driving temperature difference in the integrating reboiler / condenser has been observed. This clearly proves the strong incentive to employ column internals of low pressure drop and highly efficient heat exchangers. In VR and HP systems, internals and equipment design are much more interdependent than in simple columns. An inherent disadvantage of HP systems is, that they need to overcome two driving temperature differences. They should be considered, whenever the direct compression of the overhead vapor has serious drawbacks. These might be close approach to critical conditions at condensation, low suction side density (vacuum), corrosiveness or thermal instability. While challenging in their nature, wide-boiling systems may be successfully tackled using VR and HP systems.

References

BAFA 2023: Bundesamt für Wirtschaft und Energie: Informationsblatt CO2-Faktoren: https://www.bafa.de/DE/Energie/Energieeffizienz/Energieeffizienz_und_Prozesswaerme/Modul4_Energiebezogene_Optimierung/modul4_energiebezogene_optimierung_node.html (accessed December 2023)

T. Chiang, W. L. Luyben, 1988, Comparison of the dynamic performances of three heat-integrated distillation configurations, Ind. Eng. Chem. Res., 27, 99-104

A. K. Jana, 2014, Advances in heat pump assited distillation column: A review, Energy Conservation and Management, 77, 287-297

W.L. Luyben, 2013, Control of a train of distillation columns for the separation of natural gas liquid, Ind. Eng. Chem. Res., 52, 10741-10753

W.L. Luyben, 2019, High-pressure versus low-pressure auxiliary condensers in distillation vapor recompression, Computers Chem. Eng., 125, 427-433

J. Ott, V. Groenemann, F. Pontzen, E. Fiedler, G. Grossmann, D. Kersebohm, W. Weiss, C. Witte, 2012, Methanol, In: Ullmann's Encyclopedia of industrial chemistry.

A. Rix, C. Hecht, N. Paul, J. Schallenberg, 2019, Design of heat-integrated columns: Industrial practice, Chem. Eng. Res. Dev., 147, 83-89

A. Rix, M. Schröder, N. Paul, 2023, Vapor recompression: An interesting option for vacuum columns?, Chem. Eng. Res. Dev., 191, 226-235

H. Shahandeh, M. Jafari, N. Kasiri, J. Ivakpour, 2015, Economic optimization of heat pump-assisted distillation columns in methanol-water separation, Energy, 80, February, 496-508

F. Soares Pinto, R. Zemp, M. Jobson, R. Smith, 2011, Thermodynamic optimisation of distillation columns, Chem. Eng. Science 66, 13, 2920-2934

N. S. Yang, K. T. Chuang A. Afacan, M. R. Resetarits, M. J. Binkley, 2003, Improving the efficiency and capacity of Methanol-Water distillation trays, Ind. Eng. Chem. Res., 42, 6601-6606

ESCAPE-34 PSE-2024
European Symposium on Computer Aided Process Engineering
&
Process Systems Engineering

Flavio Manenti, Gintaras V. Reklaitis (Eds.), Book of Abstract of the 34th European Symposium on Computer Aided Process Engineering / 15th International Symposium on Process Systems Engineering (ESCAPE34/PSE24), June 2-6, 2024, Florence, Italy.

Can Biofuels from Microalgae Become a Sustainable Alternative for the Heavy-Duty Transport Sector?

Richard Cabrera[a], Victor Tulus[b], Jordi Gavaldà[a], Laureano Jiménez[a], Gonzalo Guillén-Gosálbez[b], Carlos Pozo[a]

[a]*Departament d'Enginyeria Quimica, Universitat Rovira i Virgili, Av. Països Catalans 26, 43007 Tarragona, Spain.*
[b]*Institute for Chemical and Bioengineering, Department of Chemistry and Applied Biosciences, ETH Zürich, Vladimir-Prelog-Weg 1, 8093 Zürich, Switzerland*
carlos.pozo@urv.cat

Abstract

In this contribution, we explore how eight different scenarios involving microalgae biofuels could contribute to bringing the heavy-duty transport sector within the boundaries of sustainable operation. These scenarios comprise a variety of configurations, including two different fuel production methods (hydrodeoxygenation and hydrothermal liquefaction), two carbon sources (i.e., carbon dioxide captured from natural gas power plants or directly from the air) and two electricity mixes (i.e., the current mix and a future sustainable mix). The eight scenarios considered are analysed combining Life Cycle Assessment principles with an Absolute Environmental Sustainability Assessment method based on the Planetary Boundaries, adopting a cradle-to-wheel perspective. The selected approach goes beyond greenhouse gas emissions, embracing other impacts on key Earth-system processes and covering the carbon footprint, too. Our findings highlight that microalgae biofuels have significant potential in mitigating environmental impacts compared to the traditional fossil-based heavy-duty transport sector. Notably, pathways utilizing hydrodeoxygenation of microalgae oil and direct air capture with carbon storage demonstrate the potential to decrease the global climate change impact caused by heavy transport by 77%. Additionally, in contrast to standard biofuels, which often require extensive land use, microalgae biofuels also substantially reduce their impact on biosphere integrity.

Keywords: Microalgae biofuels, LCA, planetary boundaries, biosphere integrity

1. Introduction

Currently, the world production of biofuels is mostly based on agricultural crop biomass, causing competition for the available land between fuel and food production (Calvo-Serrano et al., 2019).

This study focuses on the Absolute Environmental Sustainability Assessment (AESA) of various biofuel production scenarios from microalgae, and their use in heavy-duty transport, adopting a cradle-to-wheel perspective (Cabrera-Jiménez et al., 2023). Integrating the principles of Life Cycle Assessment (LCA) and an AESA based on Planetary Boundaries (PBs) (Rockström et al., 2009), we can assert whether technological options are truly sustainable or not, and analysis out of reach of conventional LCA, which can only perform relative assessments. In addition, our analysis extends beyond greenhouse gas emissions to encompass broader impacts on key Earth-system processes related with the PBs.

2. Methodology

The study explores eight transformation scenarios for microalgae-to-biofuels, considering two distinct fuel production methods (hydrodeoxygenation (HDO) and hydrothermal liquefaction (HTL)) and utilizing two carbon sources (natural gas power plants (BLUE) and direct air capture (GREEN)). Additionally, two different electricity mixes are considered, the current one (labeled M2020) and a future sustainable mix (M2040). The integration of byproducts is included across all scenarios. In addition, we also assess the performance of conventional biofuels (i.e., from soybean), and the business-as-usual (BAU) scenario, where diesel is used as fuels for the trucks. In order to quantify the impacts of all these options on the environment, we will use the following methodology.

2.1. Life Cycle Assessment combined with the Planetary Boundaries framework

LCA quantifies the environmental impacts of products, processes, and services over their entire life cycle, covering a wide range of potential damages. This is performed based on four steps for identifying environmental hotspots. In the initial phase, the goal and scope of the study are defined. In this context, we defined the annual world ton-km (tkm/yr) demand for road freight activities as the functional unit to quantify the absolute environmental sustainability of various scenarios for microalgae-based biofuel routes.

The second LCA phase focuses on quantifying the main inputs and outputs (e.g., energy, raw materials, byproducts, and emissions). We exploited mass and energy balance information from prior studies for foreground system activities, such as carbon sequestration, microalgae cultivation, drying, byproduct recovery, fuel production, and combustion. This data was combined with corresponding background activities data to compute life cycle inventories (LCIs) for the modeled scenarios.

Moving to the third phase, the LCA assesses the damage caused by LCIs across various environmental categories. In this case, nine control variables related to seven Earth-system processes were considered as impact categories. Hence, characterization factors developed by Ryberg et al. (Ryberg et al., 2018) were employed to express LCIs in terms of the control variables of the PBs.

When results are interpreted PBs framework, provides absolute thresholds against which to compare environmental impacts. Specifically, limits on control variables are used to define a safe operating space (SOS), i.e., an environmental budget for all anthropogenic activities.

To avoid using downscaling methods for the SOS., we simulate the global anthropogenic impact of the whole economy that would result from replacing the BAU heavy-duty transport sector by an alternative scenario based on biofuels.

3. Results and discussion

The following section summarizes the results obtained for the different scenarios, outlining the environmental impacts associated with distinct pathways of microalgae-based biofuels across different categories. Findings reveal that the current heavy-duty transport sector (i.e., BAU) transgresses the SOS for CO_2 concentration by a factor of 1.11. Similarly, conventional soybean-based biofuels exhibit a considerable transgression of the same boundary, with a factor of 1.41. This is primarily attributed to the substantial climate change impact during soybean oil production. Additionally, soybean farming contributes to change in biosphere integrity, reaching 35% of the whole SOS.

HTL scenarios achieve between 1 and 37% lower carbon footprint than HDO scenarios when M2020 is considered. This superiority stems from the more efficient use of energy and resources in the HTL process, eliminating the need for an oil extraction stage in contrast to HDO. The performance of microalgae-based fuels varies across scenarios, with the most favourable climate change category observed in HDO-GREEN-M2040. This scenario occupies only 25% of the SOS for the climate change PBs (i.e., atmospheric CO_2 concentration and energy imbalance control variables), marking a 77% reduction compared to the BAU scenario.

Notably, biofuels derived from microalgae stand out in terms of high yield per hectare, resulting in minimal impact on land-system change and contributing to lower impacts on biosphere integrity. For instance, when compared to soybean scenarios, the impact is up to 4.1 times lower in the current electricity mix scenario (HDO-GREEN-M2020 vs HDO soybean) and 6.5 times lower considering the 2040 sustainable electricity mix scenario.

4. Conclusions

This study compared eight biofuel production pathways from microalgae for freight road transport, considering various scenarios from a cradle-to-wheel perspective. We assessed the impact of these scenarios on seven Earth-system processes through nine control variables. Our findings reveal that conventional fossil fuels, such as diesel, used in freight road transport are environmentally unsustainable, exceeding the climate change PB by 11%. The alternative of microalgae-based fuels shows promise in mitigating the adverse effects of conventional biofuels, potentially reducing the impact on biosphere integrity by up to six times. However, a carbon-intensive electricity mix combined with carbon sourced from fossil fuels could undermine the potential benefits of microalgae, making it a less favourable option than diesel in terms of climate change (up to two times higher impacts).

References

Cabrera-Jiménez, R., Tulus, V., Gavaldà, J., Jiménez, L., Guillén-Gosálbez, G., & Pozo, C. (2023). Microalgae Biofuel for a Heavy-Duty Transport Sector within Planetary Boundaries. *ACS Sustainable Chemistry & Engineering*, *11*(25), 9359–9371. https://doi.org/10.1021/ACSSUSCHEMENG.3C00750/ASSET/IMAGES/LARGE/SC3C00750_0006.JPEG

Calvo-Serrano, R., Guo, M., Pozo, C., Galán-Martín, Á., & Guillén-Gosálbez, G. (2019). Biomass Conversion into Fuels, Chemicals, or Electricity? A Network-Based Life Cycle Optimization Approach Applied to the European Union. *ACS Sustainable Chemistry and Engineering*, *7*(12), 10570–10582. https://doi.org/10.1021/ACSSUSCHEMENG.9B01115/ASSET/IMAGES/LARGE/SC-2019-01115S_0008.JPEG

Rockström, J., Steffen, W., Noone, K., Persson, Å., Chapin, F. S., Lambin, E. F., Lenton, T. M., Scheffer, M., Folke, C., Schellnhuber, H. J., Nykvist, B., De Wit, C. A., Hughes, T., Van Der Leeuw, S., Rodhe, H., Sörlin, S., Snyder, P. K., Costanza, R., Svedin, U., … Foley, J. A. (2009). A safe operating space for humanity. *Nature 2009 461:7263*, *461*(7263), 472–475. https://doi.org/10.1038/461472a

Ryberg, M. W., Owsianiak, M., Richardson, K., & Hauschild, M. Z. (2018). Development of a life-cycle impact assessment methodology linked to the Planetary Boundaries framework. *Ecological Indicators*, *88*, 250–262. https://doi.org/10.1016/J.ECOLIND.2017.12.065

ESCAPE-34 PSE-2024
European Symposium on Computer Aided Process Engineering
&
Process Systems Engineering

Flavio Manenti, Gintaras V. Reklaitis (Eds.), Book of Abstract of the 34th European Symposium on Computer Aided Process Engineering / 15th International Symposium on Process Systems Engineering (ESCAPE34/PSE24), June 2-6, 2024, Florence, Italy.

Economic Evaluation of the Emerging Electrochemical Nitrogen Reduction to Ammonia Depending on Catalyst Performance

Michael J. Rix[a], Judith Schwindling[a], Alexander Mitsos[c,a,b]*

[a]*RWTH Aachen University, Process Systems Engineering (AVT.SVT), 52062 Aachen, Germany*
[b]*Forschungszemtrum Jülich GmbH, Institute for Climate Research IEK-10: Energy Systems Engineering, 52428 Jülich, Germany*
[c]*JARA-ENERGY, Aachen, Germany*
**amitsos@alum.mit.edu*

Abstract

Electrochemical reduction of nitrogen to ammonia is a promising alternative to the conventional Haber-Bosch process to decarbonize ammonia production. Although there is a lot of work on catalyst development for this novel reaction, there is a lack of concise economic evaluations and rational goals for catalyst development.

Based on an economic evaluation, we estimate production cost based on catalyst performance in terms of achievable Faradaic efficiency at a certain production rate. By relating to benchmark cost, a function mapping Faradaic efficiencies and production rates to reach cost parity is derived, determining the feasible space for catalyst development.

All catalysts reported to date lie considerably below the cost parity curve. Even though recent catalyst developments achieve considerable high Faradaic efficiencies, the production rate remains too low, resulting in the investment cost alone being higher than the ammonia market price.

Keywords: Electrochemistry, Economic Evaluation, Ammonia, Catalyst Evaluation.

1. Introduction

Novel electrochemical reactions can aid in decarbonizing the chemical industry and transition away from using fossil fuels as feedstocks and energy sources (Luh et al., 2018). We evaluate the current status and the potential of the electrochemical nitrogen reduction reaction (eNRR) to ammonia, a novel reaction pathway to synthesize ammonia directly from water and air at near ambient conditions.

In developing these emerging electrochemical technologies, the focus is on identifying and improving suitable catalysts. However, there is a lack of rational goals for catalyst performance. Reported goals state the catalyst performance at one operating point (Soloveichik, 2016). This approach is insufficient as the required performance depends on the operating conditions.

We conduct an economic evaluation of the eNRR process to investigate the catalyst's influence on the performance of the overall process. We estimate production cost based on reaction rate and Faradaic efficiency, quantities reported in catalyst studies, and compare the production cost with benchmark prices. Based on this, we derive a curve mapping required production rates and Faradaic efficiencies to achieve cost parity with the benchmark.

2. Process model

In this work, we focus on evaluating the eNRR and thus model only the electrochemical reactor in more detail. Investigating the influence of downstream processes like product purification is out of the scope of this work. In the electrochemical cell, ammonia is formed at the cathode and the by-product oxygen at the anode. The anode reaction is the same as in alkaline water electrolysis, a mature technology. Therefore, no significant economic impact of an improvement of the anode catalyst is expected, and we focus on the cathode catalyst and the novel reaction. The performance of this catalyst determines the selectivity and reaction rate of the target product ammonia and the side product hydrogen. For a more detailed process description, the reader is referred to a recent literature review by Rezaie et al. (2023).

The levelized cost of ammonia (LCOA) is calculated as the sum of OPEX and annual CAPEX divided by the produced amount of ammonia. The CAPEX for the new process is estimated by transferring the CAPEX for alkaline water electrolysis to the proposed electrochemical reactor as they share the same basic setup.

OPEX of electrochemical processes is mainly determined by the cost of electricity (Hemauer et al., 2023). Additionally, fixed OPEX for operation and maintenance and variable OPEX for the educts are considered.

3. Results and discussion

We evaluate the catalyst studies reviewed by Rezaie et al. (2023) and calculate the respective LCOA at the reported production rate and Faradaic efficiency.

First, the minimal Faradaic efficiency is calculated by setting the investment cost to zero and equalizing the electricity cost with the benchmark price. Following this approach, the minimum Faradaic efficiency and thus the energy efficiency is calculated depending on the cell potential. Some studies achieve Faradaic efficiency higher than the minimal.

Second, the minimal reaction rate is calculated similarly by setting the electricity cost to zero and equalizing the CAPEX and fixed operation and maintenance cost with the benchmark price. All investigated reaction rates lie considerably below the minimal.

Third, we calculate the LCOA based on the experimental data. All results are well above the benchmark price. Even though some studies achieved Faradaic efficiencies higher than the minimal, the production rates and current densities are too low, resulting in capital cost being higher than the benchmark price. Higher production rates are required to reduce production costs considerably and to achieve cost parity.

The production cost calculation conducted in this work depends on the catalyst performance—the achieved Faradaic efficiency at a specific production rate. By equalizing this cost function with the benchmark price, a curve mapping required Faradaic efficiency to the production rate is derived. This curve can be used to evaluate new experimental data and to guide catalyst development towards a competitive process. As

benchmarks to compare the LCOA, the ammonia market price as well as production cost of green ammonia produced via the Haber-Bosch process coupled with water electrolysis are used. Thus, electrochemical ammonia production can be compared to the conventional process and further possibilities to defossilize ammonia production.

4. Conclusion

In this work, we derived a function mapping operation conditions and Faradaic efficiency to achieve cost parity with a benchmark price. Competitive catalysts must reach or outperform the limit defined by this curve. Even though recent catalyst studies show considerable improvement in Faradaic efficiency, the production rates are still too low, resulting in CAPEX being higher than the ammonia market price.

The low reported production rates can be traced back to the nature of the experimental approach focusing on catalyst screening and improving Faradaic efficiencies at low potentials, resulting in low reaction rates. To enable a cost-competitive process, high Faradaic efficiencies at high production rates are required. Thus, catalyst research must transition into aiming for higher production rates.

References

J. Hemauer, S. Rehfeldt, H. Klein, A. Peschel, 2023, Performance and cost modelling taking into account the uncertainties and sensitivities of current and next-generation PEM water electrolysis technology. International Journal of Hydrogen Energy, 48(66), 25619-25634.

S. Luh, S. Budinis, T. J. Schmidt, A. Hawkes, 2018, Decarbonisation of the Industrial Sector by means of Fuel Switching, Electrification and CCS, Computer Aided Chemical Engineering, 43, 1311-1316.

F. Rezaie, S. Læsaa, N. E. Sahin, J. Catalano, E. Dražević, 2023, Low-Temperature Electrochemical Ammonia Synthesis: Measurement Reliability and Comparison to Haber–Bosch in Terms of Energy Efficiency. Energy Technology, 11(10), 2194-4288.

G. Soloveichik, 2016, Renewable Energy to Fuels through Utilization of Energy-Dense Liquids (REFUEL).

ESCAPE-34 PSE-2024
European Symposium on Computer Aided Process Engineering
&
Process Systems Engineering

Flavio Manenti, Gintaras V. Reklaitis (Eds.), Book of Abstract of the 34th European Symposium on Computer Aided Process Engineering / 15th International Symposium on Process Systems Engineering (ESCAPE34/PSE24), June 2-6, 2024, Florence, Italy.

Overpotential Identifiability for Electrode Characterization in Water Electrolysis

J. Raphael Seidenberg[a], Niklas Thissen[b], Anna K. Mechler[b], Dominik Bongartz[c,*]

[a]*Process Systems Engineering (AVT.SVT), RWTH Aachen University, Aachen, Germany*
[b]*Electrochemical Reaction Engineering (AVT.ERT), RWTH Aachen University, Aachen, Germany*
[c]*Department of Chemical Engineering, KU Leuven, Leuven, Belgium*
**dominikbongartz@alum.mit.edu*

Abstract

In water electrolysis, the kinetic overpotential of the oxygen evolution reaction leads to significant energetic losses. To reduce the kinetic overpotential, new electrode materials are frequently investigated. For the characterization of investigated electrodes in terms of performance, the different overpotentials in an experimental setup must be accurately estimated. Estimates of the overpotentials can be obtained by fitting a model of the setup to experimental data. However, the model estimates might have large uncertainty, which needs to be quantified. To this end, we perform parameter estimation and identifiability analysis based on a set-membership approach to determine confidence intervals for the overpotentials. As experimental data, we use chronopotentiometry measurements from a beaker cell setup. The results allow to get an impression of the uncertainty not only of the model parameters but also of the overpotentials themselves and hence of the relative importance of different loss mechanisms.

Keywords: modeling, parameter estimation, uncertainty, electrochemistry, hydrogen

1. Introduction

In water electrolysis, the operating voltage at a certain current, i.e., production rate, is a key factor influencing the system efficiency. The operating voltage is given by the sum of the equilibrium potential and several overpotentials. These represent the voltage losses caused by various phenomena. The kinetic overpotential needed to overcome activation energies required for the oxygen evolution reaction has a large contribution to the total voltage losses (Fabbri et al., 2014). Therefore, new electrode materials are frequently investigated (Wang et al., 2020). These materials are often tested in experimental setups that differ from industrial cell designs. To help transfer results from the experimental setup to industrial cell designs, the different overpotentials must be quantified as accurately as possible from the experimental data. To this end, a model of the experimental system can be used to get an estimate for each overpotential. To get an

impression of how reliable the obtained estimates are, it is desirable to quantify the uncertainty in terms of confidence intervals. This allows to analyze if the uncertainty is sufficiently small, which is a requirement for reliably transferring the results to a model of the industrial cell design.
In this work, we aim at quantifying the uncertainty in parameters as well as overpotentials using methods from the field of identifiability analysis. Identifiability analysis aims at assessing whether parameter values can be estimated uniquely for a given model structure and data set (Guillaume et al., 2019). We adopt the set-membership method used by Jung et al. (2019), which allows to obtain confidence intervals by approximating the feasible parameter set and solving a constrained optimization problem. In contrast to local methods that compute the confidence intervals based on the Fisher information matrix, the method has the advantage that the identifiability analysis is global such that the whole parameter space is considered. The approximation of the feasible parameter set allows the method to be less computationally expensive than when an exact description of the feasible parameter set is used. Using the set-membership method, we derive confidence intervals for both parameters and overpotentials based on chronopotentiometry measurements from a beaker cell setup.

2. Methodology

To obtain confidence intervals for the overpotentials, we investigate an indirect and a direct approach. In the former, parameter confidence intervals are obtained using the set-membership approach described by Jung et al. (2019). The overpotential confidence intervals are then calculated by maximizing and minimizing the respective overpotential at each current density separately and restricting the parameters to be within the priorly obtained parameter confidence intervals. In the case of the direct approach, we directly use a set-membership approach to maximize and minimize each overpotential at each current density separately, while enforcing respective identifiability constraints.
We use experimental measurements for the oxygen evolution reaction at the anode side of alkaline water electrolysis in a beaker cell setup as described in Thissen et al. (2023). In the beaker cell, a reference electrode is used so that the contribution of the anode can be observed independently of the cathode. A 1 cm^2 industry-standard Ni mesh is used as both anode and cathode. Chronopotentiometry measurements at several current densities were conducted in a 30 wt.% KOH solution at 80°C.
We assume that a steady state is reached during chronopotentiometry and hence use a steady-state model to describe the system. The used model is comparably simple and includes a kinetic (η_{kin}) and ohmic overpotential (η_{ohm}). Mass transfer and gas bubble effects are expected to be less pronounced at the present experimental conditions and due to continuous stirring, and are hence neglected. We model η_{kin} using the Tafel equation and the η_{ohm} with a constant resistance. The steady-state model therefore includes three parameters: the ohmic resistance, the exchange current density, and the Tafel slope.

3. Results

The results show that both the indirect and the direct approach can be used to obtain overpotential confidence intervals. While the confidence interval for η_{ohm} is the same for both approaches, the confidence interval for η_{kin} differs significantly and is much tighter for the direct approach. Assuming an experimental noise of 1 mV, the obtained confidence interval for η_{kin} at 1 A/cm^2 is around ±10 mV and ±90 mV for the direct and indirect approach, respectively. While both approaches ensure the fulfillment of the identifiability constraints, the direct approach gives a tighter and therefore clearer picture

of the overpotential confidence interval. The overpotential confidence intervals allow to get an impression of the uncertainty in the overpotential contributions and therefore show how accurately the contribution of the individual loss mechanisms can be identified. In the context of electrode characterization, this allows to analyze how reliable η_{kin} can be estimated.

4. Conclusions

In this work, we show how identifiability analysis can be employed to obtain confidence intervals for overpotentials and therefore analyze the uncertainty in the estimation of overpotentials. A low uncertainty in the estimation of overpotentials is necessary for the results to be reliably transferable from an experimental setup to a model of the industrial cell design. Certain estimates of the overpotentials further allow to assess the contribution of different phenomena (e.g., kinetics and mass transfer) to the overall cell potential and therefore identify levers for potential improvement. In case of a high uncertainty in the estimation of overpotentials, further measurements might help to achieve lower uncertainty. Either way, quantifying the uncertainty is a key first step. Such an approach is expected to be even more relevant when more complex models are used to describe the system and additional overpotential contributions are considered. Furthermore, these methods can be used to estimate overpotential confidence intervals based on different or multiple electrochemical measurements in the future.

References

E. Fabbri, A. Habereder, K. Waltar, R. Kötz, T. J. Schmidt, 2014, Developments and perspectives of oxide-based catalysts for the oxygen evolution reaction, Catalysis Science & Technology, 4(11), 3800–3821.

J. H. Guillaume, J. D. Jakeman, S. Marsili-Libelli, M. Asher, P. Brunner, B. Croke, M. C. Hill, A. J. Jakeman, K. J. Keesman, S. Razavi, J. D. Stigter, 2019, Introductory overview of identifiability analysis: A guide to evaluating whether you have the right type of data for your modeling purpose, Environmental Modelling & Software, 119, 418–432.

F. Jung, F. A. L. Janssen, A. Ksiazkiewicz, A. Caspari, A. Mhamdi, A. Pich, A. Mitsos, 2019, Identifiability Analysis and Parameter Estimation of Microgel Synthesis: A Set-Membership Approach, Industrial & Engineering Chemistry Research, 58(30), 13675–13685.

N. Thissen, J. Hoffmann, S. Tigges, D. A. M. Vogel, J. J. Thoede, S. Khan, N. Schmitt, B. J. M. Etzold, A. K. Mechler, 2023, Industrial-Relevant Conditions in Lab-Scale Analysis for Alkaline Water Electrolysis, Submitted for publication.

J. Wang, Y. Gao, H. Kong, J. Kim, S. Choi, F. Ciucci, Y. Hao, S. Yang, Z. Shao, J. Lim, 2020, Non-precious-metal catalysts for alkaline water electrolysis: operando characterizations, theoretical calculations, and recent advances, Chemical Society Reviews, 49(24), 9154–9196-9154–9196.

ESCAPE-34 PSE-2024
European Symposium on Computer Aided Process Engineering
&
Process Systems Engineering

Flavio Manenti, Gintaras V. Reklaitis (Eds.), Book of Abstract of the 34th European Symposium on Computer Aided Process Engineering / 15th International Symposium on Process Systems Engineering (ESCAPE34/PSE24), June 2-6, 2024, Florence, Italy.

Impact of Industrial Waste Heat Recovery on Heat and Electricity Marginal Costs in an Energy Community

Cédric Terrier*, Dorsan Lepour, François Maréchal

EPFL Valais Wallis, IPESE, Rue de l'Industrie 17, 1950 Sion, Switzerland
cedric.terrier@epfl.ch

Abstract

Sector coupling is seen as one of the keys to improve energy efficiency within urban centers. In this perspective, residential energy system coupled with industrial waste heat recovery via district heating network is a promising solution. However, it also implies the coordination between systems design since a decision taken in one subsystem directly affects the decision-making of other subsystems. The aim of this paper is to demonstrate the sector coupling within an energy community containing an industrial site. The problem is formulated as a renewable energy hub with investment and operation decisions. Each building is modeled individually and the Dantzig-Wolfe decomposition is applied to optimize the district-scale problem. The industrial site is modeled as a heat source with fixed capacity and temperature. The marginal cost analysis demonstrates the spillover effect of waste heat availability on the profitability of PV panels, therefore engendering a self-consumption competition.

Keywords: Renewable energy hub, district heating network, marginal cost, MILP

1. Introduction

The building sector represents 19% of the $CO_{2,\,eq}$ emissions worldwide and is therefore one of the largest contributors to global warming (IRENA 2021). Integrating renewable capacities in the built environment becomes a prerequisite to the energy transition. In this perspective, the European parliament emphasized in 2018 the role of energy communities at promoting a high penetration of renewable energy in urban systems (EU Parliament 2018). They improve the self-consumption of local resources by coupling distributed energy sources and enhance energy efficiency by supplying multiple services to the consumers. Energy communities are usually considered at the neighborhood scale with a majority of residential buildings, therefore neglecting the synergy potential with the industrial sector, responsible for 23% of the $CO_{2,\,eq}$ emissions worldwide (IRENA 2021). It is estimated that industrial waste heat recovery could reduce the energy consumption of cities by up to 26% (Raluca-Ancuta Suciu, 2019). Therefore, besides service coupling, there is as well a need for sector coupling to maximize energy efficiency. The aim of this paper is to analyze energy carriers and sectorial couplings within an energy community composed of a residential area and an industry site. A marginal cost analysis is conducted to understand the dynamics of the system.

2. Methodology

2.1. Overview of the problem formulation

The open-source decision support tool REHO (Renewable Energy Hub Optimizer) is used to model the district energy system (Lepour et al., 2023). The latter is defined as a set of buildings connected to the same low-voltage electricity grid and the same district heating network (DHN). Demands for services, such as space heating and domestic electricity, are evaluated for each building and are supplied by energy conversion units and energy carriers purchased from the utility grids (electricity, gas, heat). The investment into energy units and their operation is optimized with a mixed integer linear programming formulation. At the building scale, the choice of conversion units includes air-water heat pumps, gas boilers, electrical heaters, thermal tanks, lithium-ion batteries and PV panels. When a building is connected to the DHN, the model considers the installation cost of underground pipes and heat exchangers. At the district scales, the energy units include a battery and a centralized heat pump connected to the DHN.

The energy system is constrained by energy and mass balances and heat cascade. Equation 1 represents the energy equilibrium between imports and exports at the building level $\dot{E}^{gr}_{b,l,p,t}$ and energy exchanges with the grids $\dot{E}^{tr}_{l,p,t}$. A positive symbol represents an import of energy and a negative one an export. In addition, capacity constraints are applied to consider the maximal connection power with the grid (Eq. 2). Within the low-voltage grid, buildings are allowed to exchange energy carriers to maximize the self-consumption of renewable energy and respect the capacity constraints.

$$\sum_{b\in B}(\dot{E}^{gr+}_{b,l,p,t} - \dot{E}^{gr-}_{b,l,p,t}) \cdot d_p \cdot d_t = (E^{tr+}_{l,p,t} - E^{tr-}_{l,p,t}) \quad \forall l \in L, \forall p \in P, \forall t \in T \tag{1}$$

$$\dot{E}^{tr\pm}_{l,p,t} \leq \dot{E}^{tr\,max}_{l,p,t} \qquad \forall l \in L, \forall p \in P, \forall t \in T \tag{2}$$

The objective function is the total costs (TOTEX), being the sum of the operating (OPEX) capital costs (CAPEX). The OPEX corresponds to the purchase and sale of energy carriers on the energy layers L (Eq. 3). The CAPEX encompasses fixed and variable investment cost into energy units (Eq. 4). Replacement costs are considered when a unit has to be replaced over the project horizon n. The investment is annualized with an interest rate i. Typical periods (P) are considered to reduce the problem complexity. More details on the problem formulation are given in the following thesis (Middelhauve, Luise, 2022).

$$C^{op} = \sum_{l\in L, p\in P, t\in T} (c^{l,+} \cdot \dot{E}^{tr+}_{l,p,t} - c^{l,-} \cdot \dot{E}^{tr-}_{l,p,t}) \cdot d_p \cdot d_t \tag{3}$$

$$C^{inv} = \frac{i(1+i)}{(1+i)^n - 1} \cdot \sum_{u\in U} b^u \cdot (i^{c1,u} \cdot y^u + i^{c2,u} \cdot f^u) + C^{rep} \tag{4}$$

2.2. Dantzig-Wolfe Decomposition and Linking Constraints

To reduce solving time, the Dantzig-Wolfe decomposition is applied to the original formulation. The latter is split in several small problems fast to solve. Building energy systems are modeled in sub-problems (SPs). They provide system configurations to a master problem (MP) that ensure an optimal integration of the configurations in the

district energy system. The latter considers linking constraints, such as capacity constraints (Eq. 2) and energy balances (Eq. 1) with the grids, as well as energy units at the district scale. The dual values of the linking constraints are inserted in the OPEX of the SPs (Eq. 5) and is similar to a micro-grid tariff of energy. This formulation is a reduced cost. The iteration loop terminates once the reduced cost of all SPs becomes positive, meaning that no additional configuration can improve the MP objective function.

$$C_b^{op,SP} = \sum_{l \in L, \in P, t \in T} (\pi_{p,t} \cdot \dot{E}_{l,p,t}^{gr+} - \pi_{p,t} \cdot \dot{E}_{l,p,t}^{gr-}) \cdot d_p \cdot d_t \qquad \forall b \in B \qquad (5)$$

2.3. District Heating Network Modeling

The DHN cost considers two investments: the costs of pipes and the cost of delivering heat to the buildings, either with a direct heat exchange or with a heat pump. The latter are modeled with fixed and variable costs like the rest of energy units. However, the piping cost follows a highly non-linear function (Eq. 6 and 7). The diameter of the pipes d_b^{dhn} is a square root function of the heat delivered and the length L of the DHN is a decision variable depending on the number of buildings connected to the network. Therefore, to keep the linearity of the model some reformulations are performed by taking advantage of the structure of the Dantzig-Wolfe decomposition. First, the problem is initialized by enforcing the buildings to supply their heating demand from the DHN. The result is an associated piping cost calibrated to the demand of the buildings. These costs are then linearized with fixed and variable costs and used in the SPs. In a second step, the MP collects the SPs configurations, where the DHN heat load of the buildings becomes a parameter. Therefore, it allows the MP to calculate the piping costs based on a linear combination of configurations. Finally, the DHN length between building is assumed constant and is calculated with Eq. 7, where n is the number of buildings and K a shape factor equal to 0.4. More information is available in this thesis (Girardin, 2012).

$$C_b^{pipes} = L_b \cdot (c^1 \cdot d_b^{dhn} + c^2 \cdot y_b^{dhn}) \qquad \forall b \in B \qquad (6)$$

$$L_b = \left(\frac{A^{district}}{n}\right)^{0.5} \cdot (n-1) \cdot K \,/n \qquad \forall b \in B \qquad (7)$$

2.4. Application

The case study is a neighborhood with a mix of 75 residential buildings, offices and industries. Three district heating networks are considered with supply and return temperatures of 80/70°C, 45/35°C and 16/14°C. Water is used as an energy carrier. A geothermal heat pump at the district scale closes the DHN heat balance with a ground source at 8°C. Weather data are clustered in 10 typical days and 2 extreme periods. The electricity retail and feed-in tariffs are respectively 0.25/0.1 CHF/kWh and the natural gas tariff is 0.14 CHF/kWh. These values are taken from the mean tariffs in Switzerland over the last 3 years. Industrial waste heat is modeled by a heat capacity constraint as stated in Eq. 2 and is assumed to be free of charge since the piping costs are already considered. For low and medium temperature DHN, decentralized heat pumps are necessary to elevate the temperature of the heat to the one of the buildings hydraulic systems. The latter is 65°C for old buildings and 41.5°C for recent ones.

3. Results and Discussion

The following analysis looks at the impact of DHN temperatures and waste heat availability on investment and operation design. Figure 1 is showing costs and PV integration as a function of the heat available from the industry, expressed by the ratio between the waste heat power and the heat demand peak power from the district.

Among the three DHN designs, the CAPEX remains relatively constant. Industrial waste heat decreases the capacity of the centralized heat pump, but this investment is relatively low compared to the piping investment. In addition, concerning the low and medium temperature DHN, the need for distributed heat pumps makes the CAPEX decrease negligible (respectively 0.2% and 9.6%). This drop is larger for the high temperature DHN (17.6%) due to the low COP of the heat pump requiring a large capacity.

The analysis is highly contrasting regarding the OPEX. Without waste heat recovery, the high temperature design is twice more expensive than the low temperature one. This is mainly due to the COP of the centralized heat pump, varying by a factor 8. The poor performance of the high temperature DHN is partly compensated by a higher investment into PV panels to access cheap and renewable electricity (Figure 1b). The OPEX and PV penetration are highly sensitive to waste heat availability and the sensitivity increases with the temperature of the DHN. It appears that waste heat and renewable electricity from PV panels are acting like too competing energy sources. Therefore, the highest the exergy content of the waste heat source, the lower the profitability of PV integration. This trend is as well visible from the end use of renewable electricity. Electricity exports are increasing (+12.3%) together with the share of waste heat available due to the low electricity self-consumption within the district. In conclusion, the sector coupling between industry and residential energy system generates a loss of profitability for certain investments, such as the ones in PV panels. It should be noted that the higher the exergy efficiency, the lower are the investment and operation decision change. Therefore, the risks for the residential sector are mitigated.

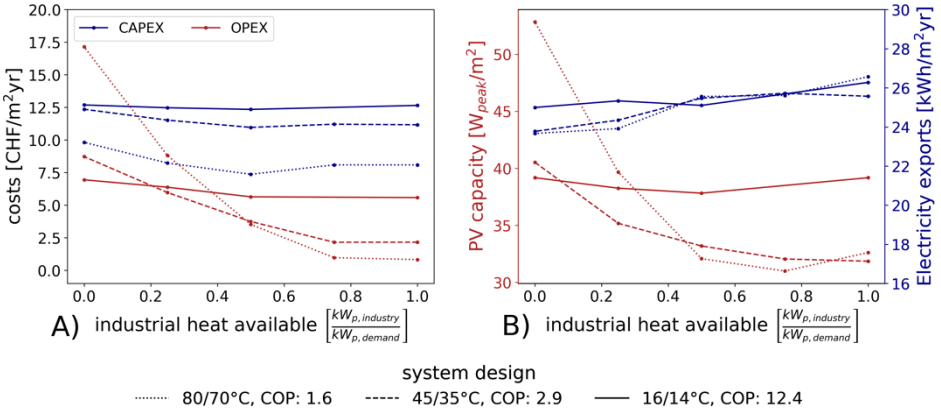

Figure 1: Costs and PV integration metrics with respect to waste heat recovery availability.

Beside reducing computational time, the decomposition approach provides insightful measurements of the system dynamics described previously. The dual values of the energy balances (Eq. 1) are the price signals sent by the district energy system to the buildings. Figure 2 shows their values, being the marginal cost of heat and electricity. Each figure is showing the 10 typical days one after the other. In Figure 2a, no waste heat is available. The marginal cost of electricity oscillates between the retail and feed-in tariff, depending on whether the district is on net import or export of electricity. The synergies between the two energy carriers are clear since the two profiles are highly correlated. The marginal cost of heat considers as well the efficiency of the system since its value is proportional to the COP of the heat pumps, thus to the temperatures of the DHN.

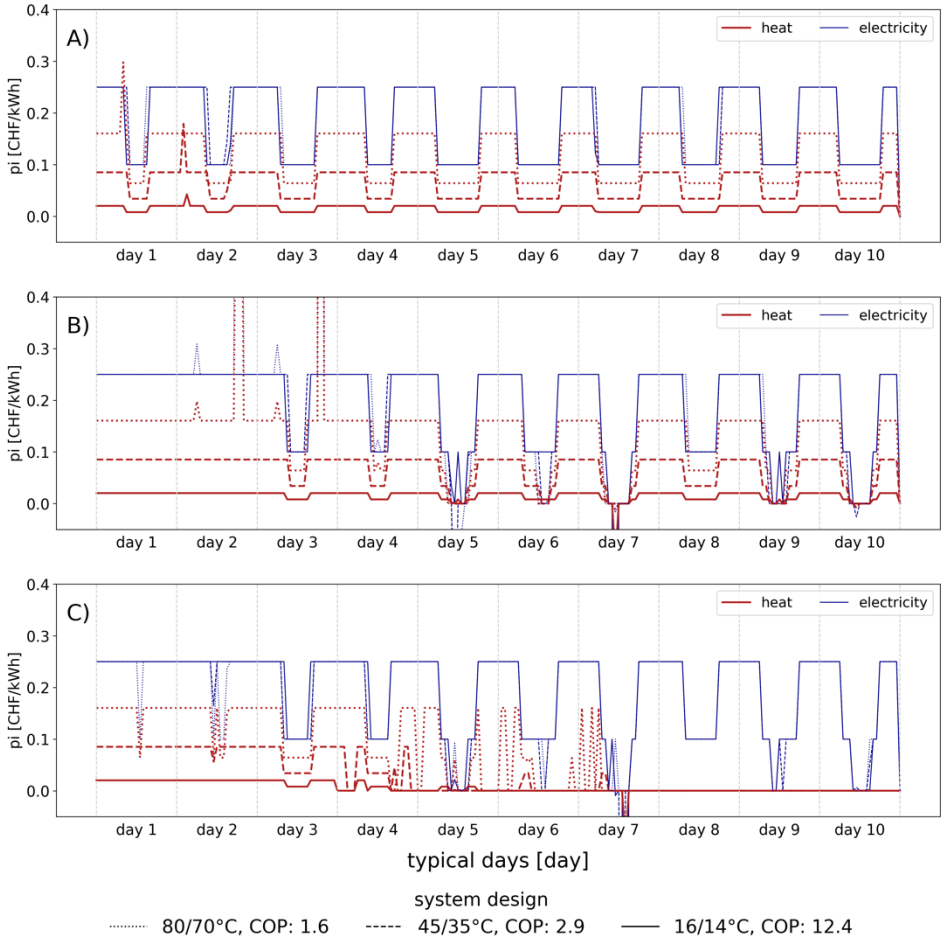

Figure 2: Dual values of the energy and capacity constraints for a) no waste heat, b) no waste heat and electrical capacity of 400 kW, c) $0.5\ \frac{kW_{p,industry}}{kW_{p,demand}}$ waste heat and electrical capacity of 400 kW

The second scenario presented in Figure 2b is similar to the first one, but a capacity constraint of 400 kW has been set on the electricity grid. This constraint decreases the investment into PV panels, therefore making the system net importer over the first two typical days. In addition, the profiles depict positive and negative peaks whenever the

system is reaching the maximal capacity of the electrical grid. It is worth mentioning that for some time steps the electricity marginal cost is negative. It means that the system is decreasing its TOTEX if it consumes more electricity, because it avoids changing configuration.

Finally, a last scenario is built to demonstrate the impact of waste heat recovery (Figure 2c). It possesses the same electrical capacity and has a heat capacity of 0.5 $\frac{kW_{p,industry}}{kW_{p,demand}}$. The electricity marginal cost has a similar profile than in the second scenario. However, the heat profile is uncorrelated to the electricity tariff over the last 4 typical days. This is due to the waste heat competing with renewable electricity, therefore screening the influence of electricity on the heat marginal cost. The outcome is serious. It means that cross-sectorial coupling is reducing cross-energy carrier coupling. In other words, if the waste heat is due to inefficient processes, not only the industry will sell its inefficiency to the residential sector, but it will also reduce the energy efficiency of the residential energy system.

4. Conclusion

The aim of this paper was to demonstrate the sectorial and energy carriers coupling between a residential energy system and an industry delivering waste heat. The energy community is modeled as an energy hub being connected to a district heating network and to electricity and natural gas grids. The Dantzig-Wolfe decomposition is applied on the problem to reduce computational time. This method is based on the use of dual variables. Interestingly, the dual values of the energy balances and grid capacity constraints provide a physical meaning on the dynamics of the system. They inform on the availability of cheap renewable electricity and on the saturation of energy grids. Moreover, they demonstrate the synergies occurring between energy carriers based on the correlation between energy carriers' marginal costs. Without waste heat recovery, the marginal cost of heat is correlated to the one of electricity. However, with the integration of waste heat in the system the correlation between the two drops, especially with waste heat at high temperature. It demonstrates the competition between renewable electricity from the PV panels and waste heat recovery. Therefore, the paper highlights the importance of well-designed sector coupling to prevent a spillover effect of industrial inefficiencies on the residential sector. Further work could be accomplished on the modeling of the industry site and its integration in a nested decomposition accounting for both industrial processes and urban planning in a single optimization.

References

1. Girardin, L., 2012. A GIS-based Methodology for the Evaluation of Integrated Energy Systems in Urban Area. EPFL. https://doi.org/10.5075/epfl-thesis-5287
2. Internation Renewable Energy Agency, 2021. World Energy Transitions Outlook.
3. Lepour, D., Terrier, C., Middelhauve, L., 2023. Renewable Energy Hub Optimizer (REHO).
4. Middelhauve, Luise, 2022. On the role of districts as renewable energy hubs. EPFL.
5. Parliament, E., 2018. DIRECTIVE (EU) 2018/ 2001 OF THE EUROPEAN PARLIAMENT AND OF THE COUNCIL - of 11 December 2018 - on the promotion of the use of energy from renewable sources 128.
6. Raluca-Ancuta Suciu, 2019. Fifth generation district energy systems for low carbon cities. EPFL.

ESCAPE-34 PSE-2024
European Symposium on Computer Aided Process Engineering
&
Process Systems Engineering

Flavio Manenti, Gintaras V. Reklaitis (Eds.), Book of Abstract of the 34th European Symposium on Computer Aided Process Engineering / 15th International Symposium on Process Systems Engineering (ESCAPE34/PSE24), June 2-6, 2024, Florence, Italy.

Equation-Oriented Modeling of a Second-Generation Post-Combustion Carbon Capture Process in the IDAES Platform for Economic Optimization

Ilayda Akkor, [a*] Shachit S. Iyer, [b] John Dowdle, [b] Le Wang, [b] Chrysanthos E. Gounaris [a]

[a] *Carnegie Mellon University, Chemical Engineering Department, 5000 Forbes Ave, Pittsburgh, 15213, USA*

[b] *The Dow Chemical Company, 332 TX-332, Lake Jackson, 77566, USA*

[*] *iakkor@andrew.cmu.edu*

Abstract

A second-generation post-combustion capture process was modeled in the Institute for the Design of Advanced Energy Systems (IDAES) platform to be used for optimization, aiming to improve its economics and to aid its commercial deployment. This equation-oriented model enabled us to find the cost optimal design and operating conditions for varying plant capacities and capture rates. While transitioning this nonlinear model into the IDAES standard can cause some problems with model initialization and scaling, following these modeling principles ultimately led to an interpretable model, with unit models that are compatible with other models in the IDAES library.

Keywords: post-combustion carbon capture, equation-oriented modeling, nonlinear programming.

1. Introduction

Amine scrubbing is a well-established and efficient technology for post-combustion capture (PCC) that can be used to reduce the CO_2 emissions at point sources in the industry. Despite, the research effort aiming to decrease the energy required for capture using new amine solvents and process modifications, one prominent example being the novel Piperazine/Advanced Flash Stripper (PZ/AFS) process (Rochelle et al., 2019), commercial deployment of PCC processes remain limited due to high costs. Therefore, these processes can benefit from process optimization to improve their economic viability, which requires a mathematical model of the process. The Institute for the Design of Advanced Energy Systems (IDAES) platform is a powerful tool to model these kinds of novel processes, which combines a model library with a framework that can handle a variety of optimization problems, such as but not limited to, large scale steady-state and dynamic optimization (Lee et al., 2021). Its core modeling framework leverages Pyomo, an open-source, algebraic modeling language, written in Python (Hart et al., 2011).

2. Modeling in IDAES

In Akkor et al. (2024), we have presented a validated, rigorous, equation-oriented model of the PZ/AFS process that was originally built in Pyomo. In this work, we discuss our experience with transitioning it to an IDAES model. The main units in the model are the absorber and stripper columns, which were modeled in a rate-based fashion, and then discretized using a finite difference method. The non-linear programming (NLP) flowsheet model also includes a heat exchanger network in split flow configuration with two bypasses and a recycle between the columns, resulting in over 8600 variables and constraints, for which we also developed a custom cascade initialization scheme. When transitioning the model for the IDAES platform, a custom packed column model was built to be used for the absorber and stripper columns. Custom property packages were built for the liquid and gas phases containing as components CO_2, H_2O and PZ, as well as N_2 for the absorber side gas phase. These were contributed to the model library in IDAES.

Even though the modeling framework in IDAES leverages Pyomo's capabilities, there are some important differences. The IDAES platform encourages better modeling practices for easier interpretability and reusability of unit models. Furthermore, using this platform has the advantage of gaining access to a comprehensive unit library, where each unit is implemented in a way that makes it compatible to be connected with other units, and to a variety of model diagnostic tools. However, this strict structure can cause problems when transitioning a model to this platform. Since a nonlinear model's convergence is strongly dependent on its initialization, slight changes in the cascade structure while transitioning the model to the IDAES standard, can lead to different results. For instance, in the IDAES platform, the packed column was built as a custom unit model class, which should have its own initialization method. The AFS structure uses this column class and connects it to a flash tank model. The AFS model is therefore initialized on its own first for a chosen set of inlet conditions and only then is connected to the absorber. So, in our implementation, we had to ensure that the column initialization is robust enough on its own to work with other solvent amounts and concentrations after it is initialized. Moreover, in an IDAES model, there should be a complete separation between the unit model and the properties. This separation and the proposed unit model class structure is important so that the unit models are not system specific, however, it does cause some restrictions for the initialization of the model. To avoid introducing variables and constraints related to properties that are not needed in a specific step of the initialization scheme, we used the built-on-demand feature for the property models and disabled/activated the equations referencing said variables within the unit model. A second challenge is with the scaling of the model, which is another important factor for the convergence of an NLP model. The IDAES standard strongly encourages using a base set of units for the properties to ensure unit consistency between models. If the unit selected for a property in the original model was not from this set, then any constraint referencing this variable will have a different scaling in the new implementation. Therefore, manual effort is needed on the user's end to ensure the scaling is the same.

After its transitioning to the IDAES standard was complete, our model was used for optimization to determine the cost optimal design and operating conditions. At the pilot scale, compared to the simulation with nominal design and conditions, it was seen that about 24% yearly savings can be achieved with process optimization. To test the robustness of the model and to investigate commercially-relevant PCC, optimization was

performed also for a variety of different plant capacities, capture targets and with two different flue gas sources, namely coal-fired and natural gas combined cycle (NGCC) flue gases, which have different CO_2 concentrations. Furthermore, whenever the column dimensions were too large to be constructed, two parallel trains—each processing half the flue gas—were evaluated as an alternative. Moreover, with the parallel train configuration, we were able to keep the absorber diameter below the practical limit of 20 meters, with only a slight increase in costs. Finally, it was confirmed that the cost increase between 95% and 99% capture targets was much more significant than the increase between 90% and 95%, as expected when targeting very high capture processes.

3. Conclusions

We built a validated, rate-based, equation-oriented model of a second-generation PCC process. This model was implemented following the IDAES standard to be made open-source, and the custom column model and the property models created were contributed to the IDAES unit library. The model's simulation and optimization capabilities were used for finding the cost optimal design and operating conditions for different plant capacities and flue gas concentrations as well as to get insights on the process design. With the initialization scheme that we developed, we were able to demonstrate the robust convergence of our model under a wide range of different conditions, proving that rigorous modeling and optimization of PCC processes can indeed improve their economics and help their commercialization. This open-source model of the PZ/AFS process can now be used for simulation with different equipment dimensions and operating conditions, for other types of optimization problems or sensitivity analyses.

Acknowledgements

The authors would like to thank Dr. Andrew Le and Dr. Anca Ostace from the National Energy Technology Laboratory for their assistance with using the IDAES platform.

References

I. Akkor, S.S. Iyer, J. Dowdle, L. Wang, C.E. Gounaris, 2024 (to appear), Mathematical Modeling and Economic Optimization of a Piperazine-Based Post-Combustion Carbon Capture Process

W.E. Hart, J.P. Watson, and D.L. Woodruff, 2011, Pyomo: Modeling and Solving Mathematical Programs in Python, Mathematical Programming Computation, 3(3), 219-260

A. Lee, J.H. Ghouse, J.C. Eslick, C.D. Laird, J.D. Siirola, M.A. Zamarripa, D. Gunter, J.H. Shinn, A.W. Dowling, D. Bhattacharyya, L.T. Biegler, A.P. Burgard, D.C. Miller 2021, The IDAES process modeling framework and model library – Flexibility for process simulation and optimization, Journal of Advanced Manufacturing and Processing 3.3 e10095

G.T. Rochelle, Y. Wu, E. Chen, K. Akinpelumi, K.B. Fischer, T. Gao, C. Liu, J.L. Selinger, 2019, Pilot plant demonstration of piperazine with the advanced flash stripper, International Journal of Greenhouse Gas Control, 84, 72–81


ESCAPE-34 PSE-2024
European Symposium on Computer Aided Process Engineering
&
Process Systems Engineering

Flavio Manenti, Gintaras V. Reklaitis (Eds.), Book of Abstract of the 34th European Symposium on Computer Aided Process Engineering / 15th International Symposium on Process Systems Engineering (ESCAPE34/PSE24), June 2-6, 2024, Florence, Italy.

PSEvolve: A Graph-based Solvent Design Framework

Laura König-Mattern[a], Edgar I. Sanchez Medina[b], Anastasia O. Komarova[c], Steffen Linke[b], Liisa Rihko-Struckmann[a], Jeremy S. Luterbacher[c,*], Kai Sundmacher[a,b,*]

[a]*Max Planck Institute for Dynamics of Complex Technical Systems, Process Systems Engineering, Sandtorstraße 1, Magdeburg, 39106, Germany*
[b]*Otto von Guericke University Magdeburg, Chair for Process Systems Engineering, Universitätsplatz 2, Magdeburg, 39106, Germany*
[c]*École Polytechnique Fédérale de Lausanne, Laboratory of Sustainable and Catalytic Processing, Station 6, Lausanne, 1015, Switzerland*

jeremy.luterbacher@epfl.ch, sundmacher@mpi-magdeburg.mpg.de

Abstract

Solvent selection is an essential step during the design of chemical processes, affecting yield, selectivity, environmental impact, and economic feasibility. Here, we present *PSEvolve*, a graph-based genetic algorithm (GA) applicable to a wide range of solvent design problems in chemical engineering. By leveraging graph and valence theory, the GA *PSEvolve* acts on the graph of the molecules, thus exclusively generating structurally feasible molecules. In this way, the chemical space is efficiently explored. In this study, we demonstrate the applicability of *PSEvolve* for lignocellulose fractionation and lignin upgrading. *PSEvolve* is publicly available for use in other molecular design problems.

Keywords: Computer-aided molecular design, Solvent design, Lignin, Biorefineries,

1. Implementation of *PSEvolve*

The Python-based solvent design framework *PSEvolve* employs a GA for the *de novo* design of solvents tailored towards desired properties. For flexible prediction of various target properties, *PSEvolve* can seamlessly include diverse property models, such as neural networks, quantitative structure-activity models, quantitative structure-property models, or group contribution models. Fig. 1 illustrates the interplay between *PSEvolve* and the property models. Based on the property predictions, *PSEvolve* iteratively optimizes a population of molecules by inducing alterations to the solvent structure, such as atom or bond addition, atom or bond deletion, atom or bond substitution, the addition of functional groups or relocation of molecular fragments. Before executing these structural changes, *PSEvolve* predetermines all feasible locations within the molecule by using graph and valence theory so that the algorithm produces exclusively structurally

feasible solvents. Combined with the synthetic accessibility score (Ertl and Schuffenhauer 2009), only solvents that are likely commercially available or easily synthesizable are generated, leading to efficient exploration of the chemical space.

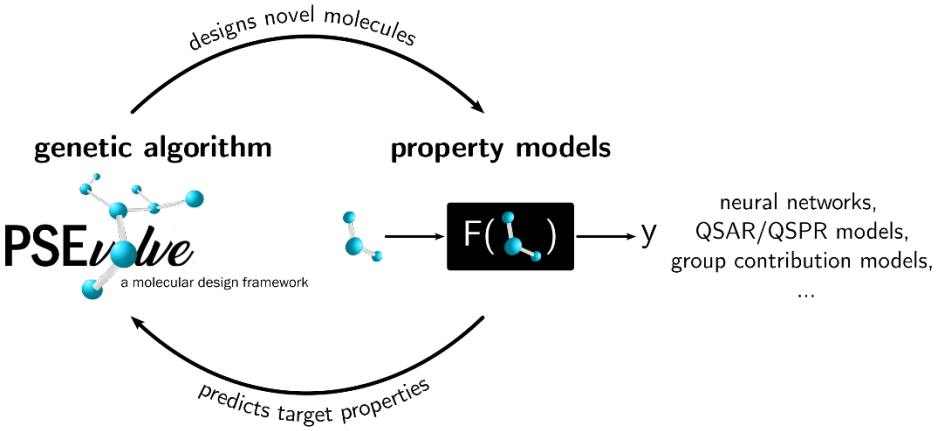

Figure 1: Connection of *PSEvolve* with property models. *PSEvolve* iteratively optimizes molecular structures based on model predictions of the target property.

2. Application to lignocellulose biorefineries and lignin upgrading

Solvent selection for lignocellulose biorefineries and lignin upgrading is a difficult task. Commonly, either toxic solvents with high lignin solubilities (e.g. 1,4-dioxane), or more benign solvents with considerably lower lignin solubilities (e.g. ethanol) are utilized. Therefore, we applied *PSEvolve* to explore alternative solvents for lignin isolation from biomass and lignin upgrading.

Lignin solubility is a critical property in both solvent design problems. Commonly, COSMO-RS is employed for lignin solubility predictions, requiring time-intensive quantum chemical (QC) calculations for each newly designed solvent candidate. To circumvent the QC calculations, we trained a graph neural network (GNN) on COSMO-RS-generated lignin solubility data. Thus, the GNN acts as a surrogate model for COSMO-RS. GNNs gained remarkable attention in recent years, as they provide fast and accurate predictions for various molecular properties, such as activity coefficients (Sanchez Medina et al. 2022; Sanchez Medina et al. 2023), and bioconcentration factors (Sanchez Medina et al. 2021). In this study, *PSEvolve* designed several non-intuitive solvent candidates for aldehyde-assisted lignocellulose fractionation (Shuai et al. 2016) and lignin upgrading based on the GNN-derived lignin solubility predictions.

Additionally, we calculated attributions on the GNN predictions using the integrated gradients method (Sanchez-Lengeling et al. 2020) to elicit structural solvent features that are linked to high lignin solubility predictions. Besides solvents that are frequently applied for lignin dissolution, such as dimethyl sulfoxide, *PSEvolve* designed many so-far unexplored solvents with high potential for application in lignin isolation from biomass and lignin upgrading. Finally, experimental results confirmed high solubilities for different types of lignin in the designed solvents.

3. Conclusions

PSEvolve is a versatile Python framework for tailored solvent design. The seamless integration of various property models expands its applications to a broad range of solvent design problems in chemical engineering. By combining *PSEvolve* with a GNN, we successfully generated several solvents specifically designed for lignocellulose fractionation and lignin upgrading. Experiments confirmed high solubilities for different types of lignin, highlighting the applicability of *PSEvolve* for complex solvent design tasks.

4. Code availability

PSEvolve is publicly available under:

https://git.mpi-magdeburg.mpg.de/pse-group/PSEvolve

References

Ertl P, Schuffenhauer A. 2009. Estimation of synthetic accessibility score of drug-like molecules based on molecular complexity and fragment contributions. J Cheminform. 1(1):8. doi:10.1186/1758-2946-1-8.

Sanchez Medina EI, Linke S, Stoll M, Sundmacher K. 2022. Graph neural networks for the prediction of infinite dilution activity coefficients. Digital Discovery. 1(3):216–225. doi:10.1039/D1DD00037C.

Sanchez Medina EI, Linke S, Stoll M, Sundmacher K. 2023. Gibbs–Helmholtz graph neural network: capturing the temperature dependency of activity coefficients at infinite dilution. Digital Discovery. 2(3):781–798. doi:10.1039/D2DD00142J.

Sanchez Medina EI, Linke S, Sundmacher K. 2021. Prediction of Bioconcentration Factors (BCF) using Graph Neural Networks. In: Computer Aided Chemical Engineering. Vol. 50. Elsevier. p. 991–997. [accessed 2023 Sep 13]. https://linkinghub.elsevier.com/retrieve/pii/B9780323885065501534.

Sanchez-Lengeling B, Wei J, Lee B, Reif E, Wang P, Qian W, McCloskey K, Colwell L, Wiltschko A. 2020. Evaluating Attribution for Graph Neural Networks. In: Larochelle H, Ranzato M, Hadsell R, Balcan MF, Lin H, editors. Advances in Neural Information Processing Systems. Vol. 33. Curran Associates, Inc. p. 5898–5910. https://proceedings.neurips.cc/paper_files/paper/2020/file/417fbbf2e9d5a28a855a11894b2e795a-Paper.pdf.

Shuai L, Amiri MT, Questell-Santiago YM, Héroguel F, Li Y, Kim H, Meilan R, Chapple C, Ralph J, Luterbacher JS. 2016. Formaldehyde stabilization facilitates lignin monomer production during biomass depolymerization. Science. 354(6310):329–333. doi:10.1126/science.aaf7810.

ESCAPE-34 PSE-2024
European Symposium on Computer Aided Process Engineering
&
Process Systems Engineering

Flavio Manenti, Gintaras V. Reklaitis (Eds.), Book of Abstract of the 34th European Symposium on Computer Aided Process Engineering / 15th International Symposium on Process Systems Engineering (ESCAPE34/PSE24), June 2-6, 2024, Florence, Italy.

Absolute Sustainability Assessment of Novel Biobased Chemicals and Materials

Marie J. Jones[a,b]*, Lorenz P. Manker[b], Zezhong John Li[b], Anastasiia O. Komarova[b], Jeremy S. Luterbacher[b], François Maréchal[a]

[a]*Industrial Energy Systems Laboratory, École Polytechnique Fédérale de Lausanne (EPFL), Valais-Wallis, 1950 Sion, Switzerland*
[b]*Laboratory of Sustainable and Catalytic Processing, École Polytechnique Fédérale de Lausanne, 1015 Lausanne, Switzerland*
marie.jones@epfl.ch

Abstract

Biomass is a promising feedstock to source renewable carbon needed to produce biobased chemicals and materials. Whilst the focus has mostly been the development of processes for drop-in replacements of petrochemicals, there is a shift towards the design of new molecules which retain as much biogenic atoms as possible. The Aldehyde-Assisted Fractionation (AAF) of biomass yields functionalized xyloses with high biomass utilization efficiencies. By changing the functionalization of the aldehyde, the properties can be tuned to produce a wide range of products. In this work, we perform an early assessment of the environmental impacts of producing a green solvent and two bioplastics, starting from pure xylose or agricultural wastes. Process inventories, retrieved from Aspen Plus® simulations, are the basis of a cradle-to-grave life cycle analysis, which is further complemented by evaluating the transgression levels of Planetary Boundaries. Whilst a significant reduction of CO_2 footprint compared to petrochemical alternatives can be achieved, especially when starting from non-edible biomass, can be achieved, the absolute sustainability analysis revealed that we remain far from the ecological budget. Our results highlight that a transition to a biobased economy requires changes across the whole chemical industry to decarbonise the utility systems and all the reagents. Prolonged use-phase and efficient recycling are included in the necessary measures to go hand in hand with the development of new molecules designed to improve biomass utilization efficiency.

Keywords: Sustainability, biorefinery, bioplastics, planetary boundaries.

1. Introduction

To keep global warming below 2 ºC above pre-industrial levels, greener production schemes starting from renewable carbon sources have to be adopted by the chemical industry. Lignocellulosic biomass is a promising feedstock to produce biobased fuels, chemicals and materials. A major focus so far has been the development of technologies towards the fractionation and conversion of cellulose into direct petrochemical replacements. However, biomass is a highly oxygenated feedstock

which must undergo several processing steps to yield conventional, carbon-rich, building blocks. Retrofitting biobased molecules to fossil-based molecules thus results in complex processes with low biomass utilisation efficiencies (Manker *et al.*, 2023a). An alternative biorefining strategy is to design molecules retaining as much native-atoms as possible and tune their properties to become functionality substitutes of petrochemicals. One such innovative strategy, relying on aldehydes to stabilize reactive intermediates during the fractionation of lignocellulosic biomass, has recently emerged. In addition to producing a highly digestible cellulose pulp and an uncondensed acetal-stabilized lignin which can be efficiently depolymerized, Aldehyde-Assisted Fractionation (AAF) yields acetal-stabilized xyloses. By using a carboxylic acid-functionalized aldehyde, we can also directly produce a bioplastic precursor, dimethylglyoxylate xylose (DMGX) (Manker *et al.*, 2022), which could substitute petro-based monomers in various polymers, such as PA-8,DGX polyamides (Manker *et al.*, 2023b). Diformylxylose (DFX), a new polar aprotic solvent (Komarova *et al.*, 2021), can be produced in a single-step from agricultural wastes.

To determine the ability of those novel biobased products to be sustainable substitutes to existing petrochemical products, we must assess early the environmental impacts of their production process. Life cycle analysis (LCA) is a necessary starting point but it does not assess the absolute sustainability of a product. The Planetary Boundary (PB) framework offers this possibility, by defining global limits which should not be crossed to avoid destabilising the Earth system. Guillén-Gosálbez and co-workers developed a methodology to link process synthesis with the estimation of the PB transgression levels (Vázquez and Guillén-Gosálbez, 2021) using characterisation factors and economic downscaling. Recent studies on CO_2 utilisation (Ioannou *et al.*, 2023) and the plastic industry (Bachmann *et al.*, 2023) provide guidelines towards absolute sustainability but did not take into consideration new bio-based molecules. In this work, we build upon a comparative LCA of three xylose-derived molecules to assess their transgression levels of PBs, depending on whether they are produced from pure xylose sugars or from raw corn cobs.

2. Materials and Methods

2.1. Process Descriptions

Two alternative feedstocks can be used to obtain 3 products, for which five different processes have been modelled (Figure 1): (1) DMGX from xylose, (2) DMGX from corn cobs, (3) PA-8,DGX from DMGX, (4) DFX from xylose and (5) DFX from corn cobs.

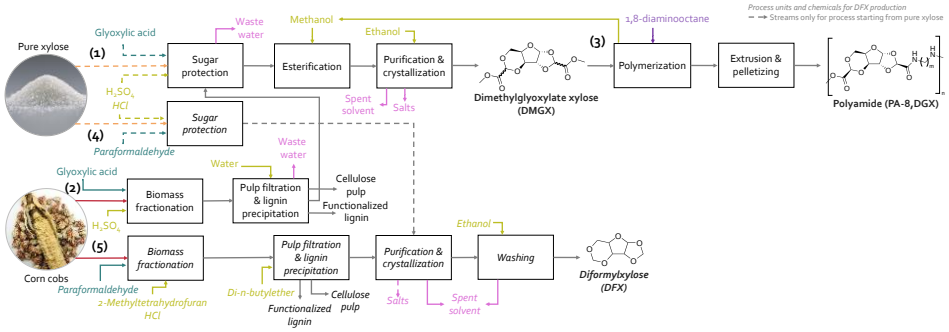

Figure 1 | Block flow diagram of the five processes modelled with Aspen Plus®. Dashed lines indicate streams only for the processes starting from pure xylose.

(1) DMGX from xylose - The production of the bioplastic follows five main steps: the protection of xylose with glyoxylic acid; the esterification of the di-acid with methanol to produce the easily distillable DMGX platform; the separation of DMGX via distillation coupled with solvent recycling and glyoxylic acid recovery by esterification, distillation and hydrolysis; the crystallization of DMGX in ethanol; and the polymerization with a diamine (Manker *et al.,* 2022 and 2023b). Xylose, 50 wt% aqueous solution of glyoxylic acid and sulfuric acid are reacted under reduced pressure to remove the water formed during the reaction, which favors the deprotection reaction. Complete esterification with methanol is then reached and the excess glyoxylic acid is converted with a selectivity of 60 % and 40 % respectively to methyl glyoxylate and methyl dimethoxyacetate. Following neutralization, the methanol is distilled to be recycled. The methyl glyoxylate, methyl dimethoxy acetate, and water are subsequently flashed off using two vacuum flash drums in series. To recover the aldehyde, the vaporised glyoxylates are condensed and hydrolyzed with sulfuric acid as catalyst. The methanol produced during the reaction is stripped to be recycled to the esterification section. The glyoxylic acid and sulfuric acid mixture is also recycled to the protection step. The final polishing steps consist in removing xylose degradation products under high vacuum, and crystallizing DMGX at -20 ºC with ethanol fed at 60 ºC.

(2) DMGX from corn cobs - To produce DMGX from corn cobs, biomass is first fractionated at 110 ºC in a mixture with glyoxylic acid and sulfuric acid. Upon filtration, the solid fraction (51 wt% cellulose) is filtered out. Further washing and neutralisation steps were excluded from this model. Water is added to the filtrate to precipitate the lignin which is also recovered through filtration. To drive the protection reaction, water must be removed in an evaporator with vapour recompression to reduce the heating duty. Xylose protection can then proceed. The evaporated water from the reaction is mixed with the vapour of the feed dryer before recompression. The recovered water is cooled down to be recycled for lignin precipitation. The product stream of the protection reactor then undergoes the same steps as the process developed starting from xylose. Yields up to 83 % based on initial xylan content have been achieved experimentally by Manker *et al.* from which the loading ratios are retrieved (Manker *et al.,* 2022).

(3) PA-8,DGX from DMGX - DMGX can then be polymerized with 1,8-diaminooctane in two steps, the second under vacuum to fully evaporate the methanol released by the condensation reaction. PA-8,DGX, obtained with a yield >98 % from DMGX, is finally extruded and pelletized.

(4) DFX from xylose - DFX is obtained from xylose through acetal protection with paraformaldehyde in 2-methyltetrahydrofuran (2-MeTHF) with sulfuric acid as catalyst. The reactor outlet is neutralized with sodium hydroxide and salts are filtered out. The solvent and produced water are evaporated leading to the crystallization of DFX. Those crystals are further washed with ethanol. Ethanol and residual 2-MeTHF are separated in three distillation columns prior to recycling. The evaporated protection solvent is led to phase separation and then purified in two distillation columns and a flash drum.

(5) DFX from corn cobs - The production of DFX from raw corn cobs requires a biomass pretreatment step where sulfuric acid is substituted by HCl. The solid cellulose is filtered out first. No neutralization of the reaction liquor is needed and instead di-n-butyl ether is added as an anti-solvent to precipitate functionalized lignin. The remaining HCl is evaporated and DFX crystallizes upon removal of the solvent via distillation. Washing with ethanol proceeds similarly to the xylose process but only two distillation columns

and four flash drums are used for purification of ethanol and 2-MeTHF. Overall, isolated DFX yields of 71 mol % and 78 % could be achieved experimentally from pure xylose and corn cobs respectively (Komarova *et al.,* 2021).

2.2. Sustainability Assessment

2.2.1. Cradle-to-grave Life Cycle Analysis

The environmental impacts of the AAF biorefineries are evaluated following the ISO 14040/44 standards. The functional unit is defined as 1 kg of xylose-based product. Emissions are assigned by mass allocation across the by-products (lignin and cellulose pulp). A cradle-to-grave system boundary is adopted following a cut-off attributional approach, where waste treatment is included in the LCA-scope. Data for the background system, including all upstream activities, are retrieved from the Ecoinvent v3.9.1 database using the Python extension Brightway2. We assumed the use of biobased ethanol and methanol. We consider the usage of an electricity mix based on renewable energy sources. The foreground system is modelled using the material and energy flows of the processes simulated with Aspen Plus®, considering heat integration. Two scenarios are developed: a short-term scenario ('Xylose') using purified xylose from edible biomass and a mid-term scenario ('Corn cob') where a supply chain for raw corn cobs is established. The carbon neutrality principle is applied: no carbon credits are assigned to the carbon sequestrated by photosynthesis during the growth of the wood feedstock, but at the end-of-life, the emissions from combustion are set to zero. Since corn cobs are a waste from maize production, its impact is also set to zero. To fill data gaps in the background data, we resort to proxy where available (*e.g.* xylose is modelled as glucose), or we create inventories from Aspen Plus® simulations of upstream activities, such as for 2-MeTHF manufacturing from sugarcane bagasse (Leal Silva *et al.,* 2018).

2.2.2. Transgression Levels of Planetary Boundaries (PB)

Through the EF methodology recommended by the European commission, we quantify 18 LCA indicators, which were related to the 9 PBs and 5 Sustainable Development Goals (SDG) by Sala *et al.* (2020). The transgression level is calculated as the ratio between the estimated impact value and the ecological budget dictated by the PBs. The ecological budget allocated to the product – the safe operating space (SOS) - is estimated via economic downscaling (Vázquez and Guillén-Gosálbez, 2021): we assume that the usefulness of a product is proportional to its market value, therefore to maximize welfare, a product with a higher market size is allocated a bigger share of the global ecological budget. In practice, the SOS is defined as the ratio of market size divided by the world Gross Value Added. In future work, we aim at exploring different downscaling methods, in response to the lack of consensus in the scientific literature. Since xylose-based chemicals do not have a market yet, we assume complete substitution of petrochemicals with similar properties: the polyamide could replace Nylon 6 and DFX is a polar aprotic solvent similar to Dimethylformamide (DMF).

3. Results and Discussions

Designed to reduce CO_2 emissions, the xylose-based products obtained via AAF exhibit a significant reduction in global warming potential (GWP) compared to their fossil-based equivalents (Fig. 2), on a mass basis. More specifically, DFX and DMGX produced from corn cobs could decrease the GHG emissions of their fossil-based counterpart (DMF and PTA) by 67 % and 42 %, respectively. Whilst the protection aldehyde of DMGX (glyoxylic acid) represents the main environmental burden, formaldehyde is less of a

driver in DFX production. Instead, utilities, especially heating, are the main contributor to CO_2 emissions. Through further heat integration and optimisation of the utility system, those energy related emissions are expected to decrease. Using waste lignocellulosic biomass instead of xylose crystals obtained from edible sugars equally plays an important role in decreasing the CO_2 footprint of the process.

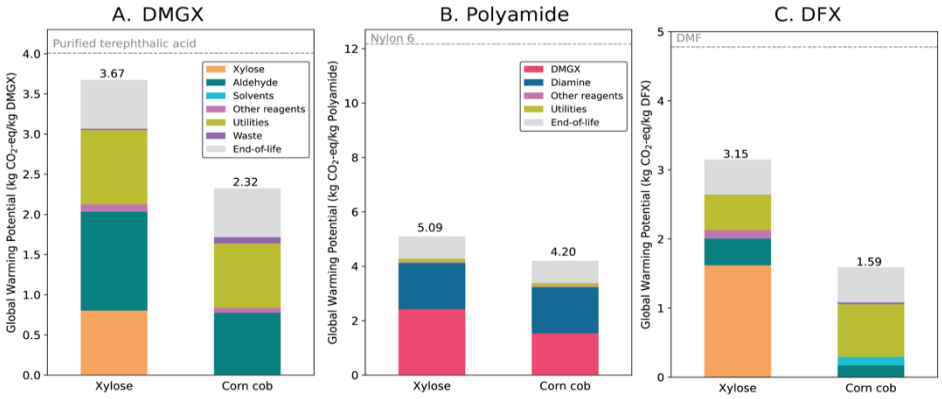

Figure 2 | Cradle-to-grave global warming potential for three xylose-based products.

Despite a significant reduction in the GWP of biobased alternatives, the comparison to fossil-based alternatives tells little about the absolute sustainability of new products. In the case of DFX from corn cobs, the GHG emissions exceed by 20-fold the safe operating space assigned based on the market size of DMF. With biobased chemicals, we also notice a higher transgression level for land and water use, and particulate matter formation due to farming. The effect is even stronger for the process starting from edible sugars. Surprisingly, the route from corn cob leads to the largest transgression, for freshwater ecotoxicity because of the use of di-n-butyl ether as solvent. By identifying it as a burden of high concern, alternative lignin precipitation solvents should be explored.

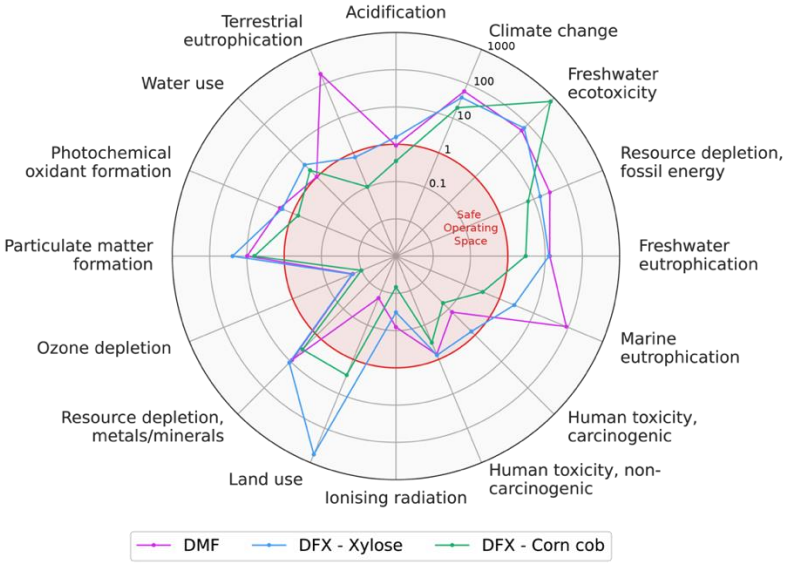

Figure 3 | Transgression levels of the Safe Operating Space for DMF and DFX.

In addition to decarbonization of the whole chemical industry, starting by the utility generation, one of the only technical solutions to stay within the ecological budget is to effectively recycle the products to prolong their life-time and reduce demand. Internalizing the cost for the environmental damages would improve the accuracy of the downscaling method. Introducing mass equivalents for the comparison of different molecules with similar properties or basing the analysis on other functional units (e.g. solvent intensity) would be an interesting area for further investigation.

4. Conclusions

This work aimed at standardizing the sustainability assessment of xylose-based products obtained via acetal-protection. Those novel molecules could enable a significant reduction of CO_2 footprint compared to petrochemical alternatives with similar properties, especially when using waste non-edible biomass as feedstock. However, the absolute sustainability analysis revealed that we remain far from the Safe Operating Space. In addition to decarbonizing both the feedstocks and the utility systems of the chemical industry, prolonged use-phase and efficient recycling appear as necessary measures to stay within our ecological budget. Despite the longer commercialisation times for non-drop-in products due to the inexistence of supply chains, designing new molecules with higher biomass utilization efficiency is a promising avenue to target zero transgression levels of planetary boundaries.

References

M. Bachmann *et al.*, "Towards circular plastics within planetary boundaries", *Nat Sustain*, vol. 6, no. 5, Art. no. 5, 2023.

I. Ioannou, Á. Galán-Martín, J. Pérez-Ramírez, and G. Guillén-Gosálbez, "Trade-offs between Sustainable Development Goals in carbon capture and utilisation", *Energy & Environmental Science*, vol. 16, no. 1, 2023.

A. O. Komarova, G. R. Dick, and J. S. Luterbacher, "Diformylxylose as a new polar aprotic solvent produced from renewable biomass", *Green Chem.*, vol. 23, no. 13, 2021.

L. P. Manker *et al.*, "Sustainable polyesters via direct functionalization of lignocellulosic sugars", *Nat. Chem.*, 2022.

L. P. Manker, M. J. Jones, S. Bertella, J. Behaghel de Bueren, and J. S. Luterbacher, "Current strategies for industrial plastic production from non-edible biomass", *Current Opinion in Green and Sustainable Chemistry*, vol. 41, 2023.

L. P. Manker *et al.*, "Performance polyamides built on a sustainable carbohydrate core", *Nat. Sustain.* (in press).

J. F. Leal Silva, A. P. Mariano, and R. Maciel Filho, "Economic potential of 2-methyltetrahydrofuran (MTHF) and ethyl levulinate (EL) produced from hemicelluloses-derived furfural", *Biomass and Bioenergy*, vol. 119, 2018.

S. Sala, E. Crenna, M. Secchi, and E. Sanyé-Mengual, "Environmental sustainability of European production and consumption assessed against planetary boundaries", *Journal of Environmental Management*, vol. 269, 2020.

D. Vázquez and G. Guillén-Gosálbez, "Process design within planetary boundaries: Application to CO_2 based methanol production", *Chemical Engineering Science*, vol. 246, p. 116891, 2021.

ESCAPE-34 PSE-2024
European Symposium on Computer Aided Process Engineering
&
Process Systems Engineering

Flavio Manenti, Gintaras V. Reklaitis (Eds.), Book of Abstract of the 34th European Symposium on Computer Aided Process Engineering / 15th International Symposium on Process Systems Engineering (ESCAPE34/PSE24), June 2-6, 2024, Florence, Italy.

Evaluating Potential Replacements for Fossil-based PET in Creating a Circular Bio-economy of Packaging Plastics

Jana Lukic[a], Marie J. Jones[a,b*], Antoine Astour[a], François Maréchal[a]

[a]*Industrial Energy Systems Laboratory, École Polytechnique Fédérale de Lausanne (EPFL), Valais-Wallis, 1950 Sion, Switzerland*
[b]*Laboratory of Sustainable and Catalytic Processing, École Polytechnique Fédérale de Lausanne, 1015 Lausanne, Switzerland*

marie.jones@epfl.ch

Abstract

Second-generation bio-refineries rely on the use of waste, non-edible lignocellulosic biomass and can be adapted for the production of highly functionalized plastics, such as PET, or its biobased alternatives with higher production efficiencies, but lower technological readiness levels (TRL). Inherent mass and energy losses are detected at an early stage using the Second-law Thermodynamic Analysis and later complemented with the results of detailed modeling, techno-economic assessment (TEA) and life-cycle analysis (LCA). Trade-offs between currently un-optimized biobased processes and the traditional retrofitting pathways are compared on several levels of modeling complexity with the final goal of assessing the real operation of a biorefinery. Our results highlight the potential in production costs and global warming reduction in the case of new bio-polymers compatible with the biomass structure.

Keywords: circular bioplastic industry, lignocellulosic biomass, PET

1. Introduction

In the near future, the chemical industry will represent one of the main contributors to GHG emissions due to strong reliance on fossil feedstock (Lange et al. 2021). One of the most resource-intensive products of the chemical industry is plastics, whose properties and low cost are irreplaceable to our society (Gabrielli et al. 2023). The shift towards renewable feedstock is required to reduce the fossil fuel depletion, while recycling enables value and properties preservation. Overall potential of the sustainable plastic sector has been assessed in the previous work by Meys et al. 2021 and Bachmann et al. 2023, where the use of CO_2 and biomass as renewable feedstocks are combined with recycling solutions to close the carbon cycle of plastic. However, new technologies with low TRL aren't included in the analysis.

Lignocellulosic biomass offers grand potential of naturally available polysaccharides with high structural similarity to polymers used in packaging applications. New conversion routes that avoid biomass degradation and deoxygenation are expected to result in higher production efficiencies. The work by Manker et al. 2022 portrays successful selective depolymerization of waste biomass to produce xylose-based polyesters (such is PHX (poly(hexylene xylosediglyoxylate)), potential bio-based alternative to rigid polyesters. Their monomer (DMGX (dimethylglyoxylate xylose)) is conceptually compared to the monomers of other bio-based alternatives with intermediate TRL (Manker et al. 2023): PTA (purified terephthalic acid) for bio-PET and FDCA (2,5-furandicarboxylic acid) for PEF (polyethylene furanoate) production.

This work aims at providing the first benchmark for the large-scale production comparison of drop-in polymers (bio-PET) and new molecules (PEF, PHX) obtained from waste lignocellulosic biomass, including traditional biomass treatment by gasification. Only chemo-catalytic routes are considered as the most prominent near-term industrial solutions. Understanding the trade-offs that new technologies are facing in their commercialization and industrial implementation is crucial at the process development stage and requires a robust multi-level methodology (thermodynamic, process and system analysis). The way in which the results change across modeling levels is discussed and justifies the use of computational techniques in order to leverage sustainable processes and support decision making.

2. Methodology

2.1. Thermodynamic Analysis

Second-Law Thermodynamic Analysis is performed in this work by following the changes in chemical exergies across the production routes in focus. Considering chemical transformations with 100% stoichiometric efficiency with all the reagents and products being at ambient conditions, maximum exergy efficiencies are obtained (Weber et al. 2022) to which real processes are always inferior (Müller et al. 2020). Even without considering physical exergy, such analysis serves as a powerful tool in performing comparative studies in cases where processes are of different TRL.

BUE (biomass utilization efficiency) is used as an indicator of atom efficiency for the chemical routes as it represents the percentage of the starting feedstock that ends up in the product structure (Iffland 2015). Main material losses caused by the sub-optimal feedstock valorization are identified. Values obtained from the previous work of Manker et al. 2023 are used in the analysis.

2.2 Process Modelling, Techno-Economic Assessment and Life-Cycle Analysis

Publicly available data from literature and patents (van Putten et al. 2021), (Muñoz De Diego et al. 2013), (Hirsch - Weil et al. 2020), (Masuno et al. 2016), (Hannula and Kurkela 2013), (Manker et al. 2022) has been used to model the processes in Aspen Plus® by extrapolating lab- and pilot-scale conditions to full industrial production. From the mass and energy balances, the capital and operating costs were estimated, for both the process equipment and the auxiliaries (utility generation and waste treatment). The Global Warming Potential (GWP100), expressed in kg CO_2eq/kg of polymer, is used as a sustainability metric to compare the processes. The background inventory is retrieved from Ecoinvent v3.9.1, whilst the foreground data comes from the simulation results. The

functional unit is defined as one kg of polymer and the analysis stops at the factory door ("cradle-to-gate analysis"), since recycling is not yet considered. For multi-output processes, the emissions are allocated, on a mass basis, to other high-value products, such as lignin and cellulose pulp. Regarding biogenic carbon accounting, we follow the conservative approach of carbon neutrality, meaning that no carbon credits are awarded to the biobased products but that upon decomposition, the CO_2 released would be counted as zero.

3. Results and Discussion

3.1.1. Chemical Exergy and BUE Comparison

Each of the four routes is characterized by the change in chemical exergy across its process units (Figure 1). The analysis begins on the level of extracted sugars (glucose in all cases except for PHX which is produced from xylose) and ends with the monomer formation.

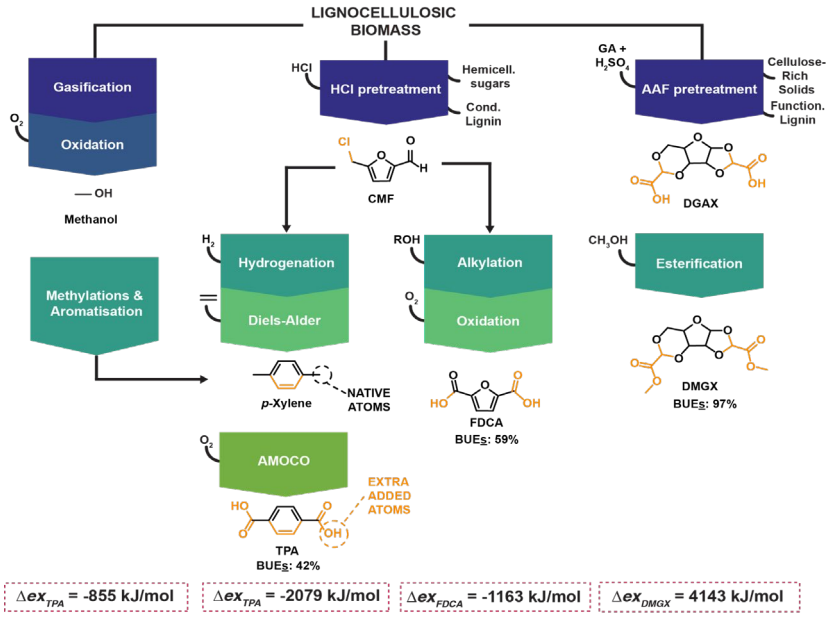

Figure 1:Changes of Chemical Exergy and BUE across the investigated chemical routes; adapted from (Manker et al. 2023)

Negative exergy difference between the starting material and the final product indicates that part of the chemical energy embedded in the starting molecular structure is lost to the environment. This is the case for all synthesis routes except for DMGX, for which additional exergy is required to yield the final product. This result is coherent with the high biomass utilization efficiency achieved by the acetal-protection process: very few biogenic atoms are lost but additional energy must be delivered to the system to drive the protection reaction. From a high-level perspective, energy lost to the environment via atomic rearrangement is wasted, whereas providing extra heat to a process can be done in a controlled manner, thus reducing overall losses. This back-of-the-envelope analysis provides the first argument to the potential of designing biobased molecules retaining as

many biogenic atoms as possible, in contrast to retrofitting biomass to poorly oxygenated petrochemicals.

3.1.2. Process Modeling Results

Process yields and feedstock allocation are presented in the form of Sankey diagrams (Figure 2). The flows are normalized for each process separately and thus, cannot be directly compared across diagrams. Processing steps are represented as dark-gray vertical lines whose height is a size indicator. Their number is related to processing complexity and, in most cases, to the end product yields. For this analysis, the processes are presented as they are reported in literature, thus starting from the waste biomass until the polymer product.

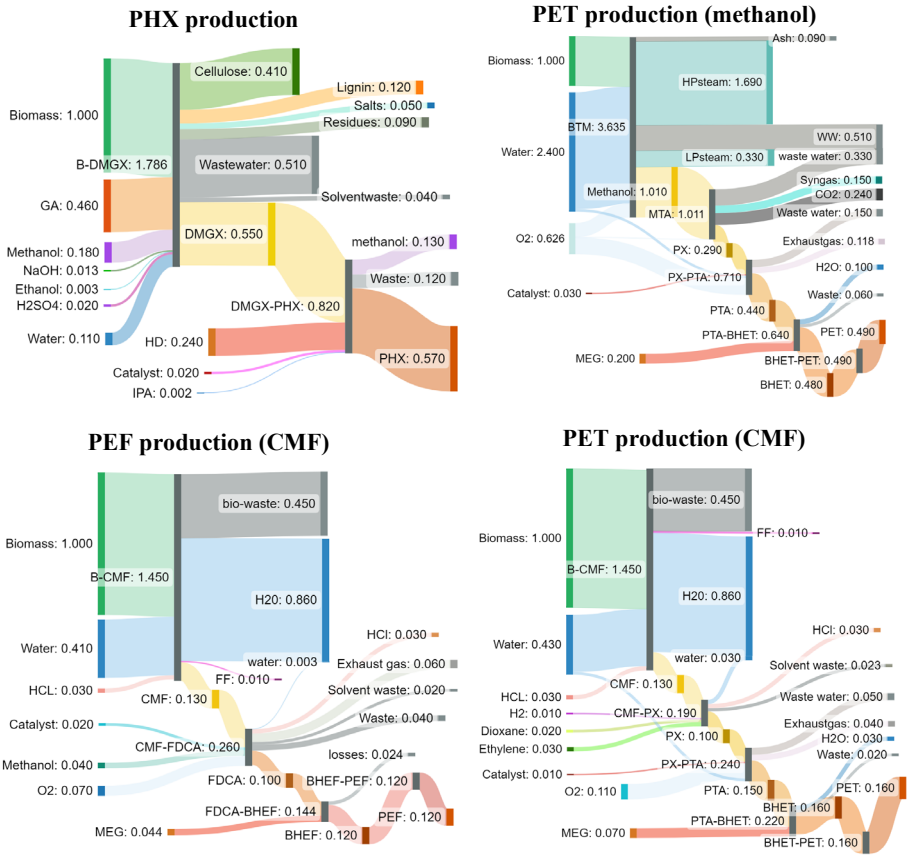

Figure 2: Sankey Flow Diagram - Mass Balance of the analyzed processes

All the routes involved have relatively low material efficiencies, which is in the order of magnitude of second-generation bio-refineries that process recalcitrant lignocellulose structure. The route with the highest product yield and biomass valorization in the form of useful products is the one towards PHX. The routes towards PEF and PET are water- and reagent-intensive and are characterized by an increase in the number of reaction steps. PET formation from methanol is the route with the lowest degree of biomass valorization which comes visible through large amounts of waste formed and the largest material requirements for all the processing steps.

Holistic quantitative assessment of processing routes including both their mass and energy requirements is achieved by translating them into costs and environmental indicators through TEA and LCA. Figure 3 compares the alternatives with respect to the production costs per unit mass of the polymer product (A) and the equivalent CO_2 emissions per kg of all the useful products generated (B). Values presented for PEF and PHX production are subject to a large uncertainty due to scale-up from laboratory or pilot plant results to an industrial scale bio-refinery of 40 ton/h. Another layer of uncertainty to the operating costs is caused by the market price fluctuations.

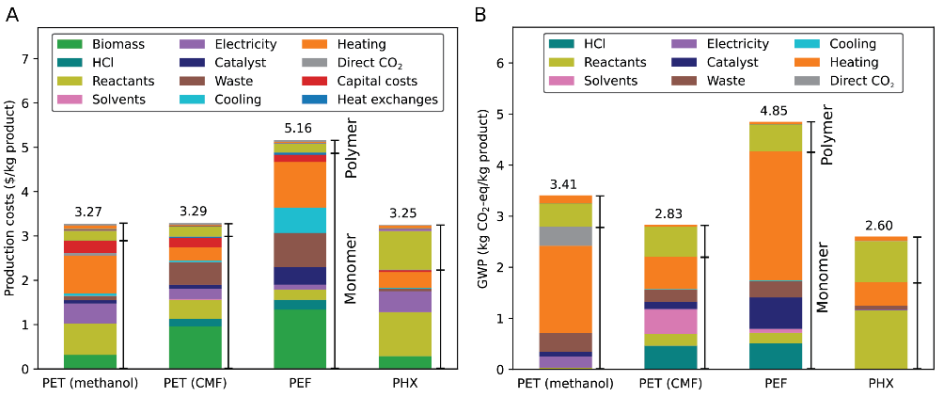

Figure 3: Production costs (A) and Environmental Impact (B) comparison

The most significant contributor to both costs and emissions is monomer production. Material requirements in the form of reagent, feedstock and waste treatment are the most significant cost contributors in all processes, whilst capital expenditures remain in the range of 10 % of the production costs, as expected. PHX production has a substantially different cost distribution compared to conventional gasification route, especially in terms of capital investments. By further optimizing material use in large-scale PHX production, one can envision further reduction in operating costs, which will increase its commercial competitiveness.

The major influence of natural gas in driving the global warming potential across all processes is evident, especially in the case of PEF production. The reason for the excessive heating requirement of PEF compared to PET production through CMF lies in the difference in operating requirements, dilute processing conditions and lower degree of heat integration opportunities. High temperatures required for gasification are on the other hand responsible for high heating demand in PET production through methanol. Key differences in operating conditions between processes arising from the variations in molecular structures are considered as intrinsic process characteristics and are not expected to be overcome by process optimization. Such is the case of PEF whose monomer formation (FDCA) was evaluated potentially more exergy efficient than PTA for PET formation, but experiences additional limitations upon modelling the current production practice.

Some technologies, even though mature, are less likely to be selected in the context of a future bio-refinery due to the high rate of waste formation, energy intensity or even direct CO_2 emissions in the case of gasification. On the other hand, biobased oriented processing is characterized by dilute streams and high material requirements (catalysts etc.) that can

be more easily improved. In order to optimize such processes with substantial yields of high exergy content products and superior degree of feedstock valorization in the form of useful products, process intensification needs to complement the scale-up.

4. Conclusions

This work aimed at portraying the role of each step in the comparative evaluation of emerging industrial solutions towards more sustainable packaging plastics. Rethinking bio-refining in terms of nature-inspired product development instead of retrofitting biomass structure to conventional petroleum-derived structures comes as a key aspect when considering the use of biomass. Mass and energy performance assessed on three different levels (molecule, process and system) in this work justifies such thinking and provides solid proof for pursuing chemically and energetically more feasible routes. Thermodynamic analysis indicates that preserving the native biomass structure in the end product results in the formation of molecules with increased functionalization and chemical exergy content. Detailed process modeling is required to assess the actual process mass and energy efficiencies and shows the difference in cost and emission drivers across processes. It also shows that by continuously optimizing new processes that are more compatible with the biomass structure (energetically and materially), one might become more competitive, whereas for the mature technologies used for the drop-in polymers, such as PET, little room for improvement remains available.

References

Bachmann M., Zibunas C., Hartmann J. et al. "Towards circular plastics within planetary boundaries." *Nature Sustainability*, 2023: 599–610.

Gabrielli P., Rosa L., Gazzani M., Meys R., Bardow A., Mazzotti M., Sansavini G. "Net-zero emissions chemical industry in a world of limited resources." *One Earth* (One Earth), 2023: 2590-3322.

Hannula, I., and E. Kurkela. *Liquid transportation fuels via large-scale fluidised-bed gasification of lignocellulosic biomass.* VTT, 2013.

Hirsch - Weil et al. Methods of Producing Alkylfurans. Patent US 10,618,880 B2. 2020.

Iffland K., Carus M., Baltus D. W., de Bie F. "Definition, Calculation and Comparison of the "Biomass Utilization Efficiency (BUE)" of Various Bio-Based Chemicals, Polymers and Fuels." *Nova Paper 8 on bio-based economy* , 2015.

Lange J.-P. et al. "Towards circular carbo-chemicals – the metamorphosis of petrochemicals." *Energy Environ. Sci.*, 2021: 4358-4376.

Manker L. P., Jones M. J., Bertella S., Behaghel de Bueren J., Luterbacher J.S. "Current strategies for industrial plastic production from non-edible biomass." *Current Opinion in Green and Sustainable Chemistry*, 2023: 2452-2236.

Manker L.P., Dick G.R., Demongeot A. et al. "Sustainable polyesters via direct functionalization of lignocellulosic sugars." *Nature Chemistry*, 2022: 976–984.

Masuno et al. Methods of Producing Para-Xylene and Terephthalic Acid. Patent US 9.260,359 B2. 2016.

Meys R., Kätelhön A., Bachmann A., Winter B., Zibunas C., Suh S., Bardow A. "Achieving net-zero greenhouse gas emission plastics by a circular carbon economy." *Science*, 2021: 71-76.

Müller L. J., Kätelhön A., Bachmann M., Zimmermann A., Sternberg A., Bardow A. "A Guideline for Life Cycle Assessment of Carbon Capture and Utilization." *Frontiers in Energy Research*, 2020.

Muñoz De Diego et al. Method for the Preparation of 2.5-Furandicarboxylic Acid and Esteres Thereof. Patent US 8,519,167 B2. 2013.

van Putten et al. Process For The Conversion of a Solid Lignocellulosic Material. Patent US 2021/0032217 A1. 2021.

Weber J. M., Guo Z., Lapkin A. A. "Discovering Circular Process Solutions through Automated Reaction Network Optimization." *ACS Engineering Au*, 2022: 333–349.

ESCAPE-34 PSE-2024
European Symposium on Computer Aided Process Engineering
&
Process Systems Engineering

Flavio Manenti, Gintaras V. Reklaitis (Eds.), Book of Abstract of the 34th European Symposium on Computer Aided Process Engineering / 15th International Symposium on Process Systems Engineering (ESCAPE34/PSE24), June 2-6, 2024, Florence, Italy.

Modeling the Continuous Production of Monoclonal Antibodies in Perfusion Bioreactors Through a Dynamic Metabolic Flux Analysis (DMFA) Framework

Nikola G. Malinov, Eleftherios T. Papoutsakis, Marianthi G. Ierapetritou*

Department of Chemical and Biomolecular Engineering, University of Delaware, 150 Academy St, Newark, DE 19716, USA
mgi@udel.edu

Abstract

In this work, a comprehensive Dynamic Metabolic Flux Analysis (DMFA) model is developed for monoclonal antibody (mAb) production in Chinese Hamster Ovary (CHO) cell perfusion culture. The framework integrates a kinetic, stoichiometric, and mass balance component to simulate and mechanistically link the temporal evolution of intracellular metabolism to the bioreactor conditions. The framework is calibrated to time-series metabolite data from scale-down semi-perfusion spin tube cultures grown under intensified conditions as a base case training dataset. Subsequent prediction of CHO cell performance in a continuous perfusion bioreactor offers agreement to a subset of measured extracellular species, demonstrating the model's robustness arising from its mechanistic foundation. Perfusion process development and optimization are target model applications.

Keywords: Continuous biomanufacturing, perfusion, dynamic metabolic modeling

1. Introduction

Recombinant mAbs have transformed medicine since the 1980's providing life-saving therapeutics for numerous diseases (Ecker et al., 2015). CHO cells are the preferred mammalian cell platform for mAb production given their robust growth in defined mediums, efficient transfectability, and innate capacity to induce complex post-translational modifications such as N-linked glycosylation (Trill et al., 1995; Wurm, 2004). Fed batch bioreactors have dominated upstream production in bioprocess pipelines. However, increasing global product demand, coupled with the emergence of an ever-expanding biosimilars market, have prompted the industry to transition towards continuous upstream manufacturing achieved through perfusion bioreactors (Walther et al., 2015). The resulting expansive design space and increased operational intensity relative to fed batch pose substantial challenges in the pursuit of continuous upstream bioprocess development and optimization. With respect to mAb production, modeling cell metabolism is imperative to assess nutrient utilization and physiologic objectives

under varying operating setpoints (Reddy et al., 2023). Here, a DMFA framework is established to mechanistically link key parameters of perfusion bioreactors, including media composition, perfusion rate, and bleed rate, to CHO cell metabolism and bioreactor conditions.

2. Materials and Methods

2.1 Semi-Perfusion CHO Cell Cultures

Semi-perfusion cultures of the CHO-K1 VRC01 cell line were seeded at 0.4×10^6 cells mL^{-1} with a starting volume of 9.4 mL in commercial basal media and supplemental L-glutamine in 50 mL vented spin tubes. Cultures were grown in a 5% CO_2 humidified incubator at 37°C, 250 rpm shake speed, 19.05 mm orbital throw, and 90° rocking angle. 1.1 mL of culture broth was sampled every day from day 0 – 3, reducing the working volume to 5 mL by day 3. 0.1 mL of culture was used to quantify cell density, while the remaining 1 mL was centrifuged at 180 g for 5 minutes, 0.22 μm sterile-filtered, and saved for off-line metabolite analysis. On day 3, semi-perfusion at an effective perfusion rate of 1 vvd^{-1} was initiated by centrifuging cultures at 180 g for 5 minutes, removing the supernatant, and resuspending the cell pellet in 5.1 mL of pre-warmed perfusion media formulated to an in-house recipe. 1 mL of the supernatant was saved for metabolite analysis. 0.1 mL of resuspended culture broth was sampled for cell density quantification.

2.2 Analytical Methods

Viable cell density (VCD) was determined via the Trypan Blue exclusion method using a DeNovix CellDrop Fluorescence Cell Counter. Residual glucose, lactate, and ammonia concentrations were measured with a YSI 2950 BioAnalyzer. Amino acid concentrations were analyzed with an OPA/FMOC-derivatization protocol with an Agilent Poroshell HPH-C18 column on an Agilent HPLC 1260 Infinity II system. Daily titer was assessed via Protein A chromatography with a POROS A 20 μm column (4.6 × 100 mm, 1.7 mL) on an Agilent HPLC 1260 Infinity II system.

3. Model Framework Development

The mathematical framework is a structured-unsegregated DMFA model which integrates a kinetic, stoichiometric, and macroscopic mass balance component. The required inputs are the initial extracellular metabolite concentrations, media composition, process conditions, and a robust kinetic parameter set. The model inputs feed to the kinetic component to approximate the growth, death, and metabolite exchange rates. The exchange rates are subsequently incorporated as constraints to the stoichiometric component, functionalized through MFA to assess the intracellular flux distribution. The updated exchange fluxes from the resulting MFA solution are incorporated into the discretized perfusion bioreactor mass balances to predict the concentration of extracellular species at the next timepoint. Iteration over the sequential framework enables dynamic simulation of intracellular metabolism and bioreactor conditions.

3.1 Kinetics

The kinetic component describes the growth, death, and nutrient consumption and metabolite production rates as a function of the time-dependent extracellular concentrations in the bioreactor. The rate equations are formulated according to semi-empirical Monod kinetics, which consider the macroscopic importance of limiting substrates, and the biochemical relationships between nutrients, on cell growth and

energetic functions to yield simple rate expressions. As an example, the growth rate, Eq. (1) and Eq. (2), was derived from the rules of multiple-substrate Monod kinetics and is a function of both limiting and inhibitory species. Time-series metabolite data from semi-perfusion cultures under intensified conditions was assessed to determine the key species, and thereby the form of the kinetic terms, to derive the growth rate expression.

$$\mu = \mu_{max}(\mu_{Glc} + \mu_{Lac})\left(\mu_{Asn} + \mu_{Asp}\right)(\mu_{Gln} + \mu_{Glu})\mu_{Ser}\mu_{Arg}\mu_{Amm,I} \quad (1)$$

$$\mu_i = \frac{\mu_{max,i}[i]}{K_i + [i]} \quad (2)$$

The biochemical relationship between nutrients, such as glutamine and glutamic acid, and their ability to induce diauxic growth, was also considered in the overall growth rate formulation yet omitted here for brevity. In Eq. (1) and (2), μ is the overall specific growth rate, $u_{max,i}$ is the maximum growth rate on species i, K_i is the Monod constant for species i which physically represents the concentration of species i that will sustain half of the maximum growth rate on that substrate. Lastly, $[i]$ is the extracellular concentration of species i in the bioreactor. The death rate is formulated in a similar manner. As an additional example, the rates for essential amino acid consumption are assumed to be proportional to the growth rate, implying that cells will only consume the minimal amount of an essential amino acid necessary to sustain metabolic functions (Chen et al., 2019). 25 rate expressions were derived to encompass the growth, death, and exchange rates of 23 metabolites, yielding a set of 66 kinetic parameters.

3.2 Reduced Metabolic Network

The stoichiometric component is a network of 70 biochemical reactions and 43 metabolites representing the key metabolic pathways in CHO cells. The network was manually curated for prior fed-batch modeling work and includes the pathways for glycolysis, the TCA cycle, essential and nonessential amino acid metabolism, oxidative phosphorylation, the urea cycle, and biomass and antibody synthesis. Reactions for total carbohydrate metabolism, nucleotide synthesis, and lipid synthesis were lumped into the biomass synthesis reaction to reduce the network size. The stoichiometric coefficients for the mAb synthesis reaction were calculated from the amino acid sequence for the VRC01 antibody and include considerations of ATP requirements. The final reduced network has a rank of 43 and a condition number of 18.3. The network ensures physiologically consistent fluxes for the major pathways given the intracellular stoichiometric constraints and provides mechanistic insight towards resource allocation without the need for complex enzymatic rate expressions.

To functionalize the network, the pseudo steady state assumption (Zupke and Stephanopoulos, 1995) is applied to all intracellular metabolites yielding an overdetermined stoichiometric matrix. MFA is employed to solve for the flux value of each reaction and assess the distribution of the metabolic load on the cell at each simulated timepoint, taken as every 0.25 days; the duration over which the fluxes are assumed to remain constant. MFA quantifies the unknown intracellular fluxes, under the constraint of specified exchange fluxes, which can be experimentally determined, and is formulated as a quadratic programming problem, Eq. (3).

$$\begin{aligned} &Min \ \sum_{i=1}^{n=24}\left(\frac{v_i^{calc} - v_i^{meas}(\theta)}{v_i^{meas}(\theta)}\right)^2 \\ &s.t. \qquad \boldsymbol{Sv} = 0 \\ &\boldsymbol{v^{lb}} < \boldsymbol{v_{exchange}} < \boldsymbol{v^{ub}} \end{aligned} \quad (3)$$

v_i^{calc} is the calculated exchange rate of species i scaled to flux units, as determined by solution to Eq. (3), v_i^{meas} is the measured exchange rate as determined by experiment, $\boldsymbol{S}$ is the stoichiometric matrix resulting from steady state mass balances on each metabolite, $\boldsymbol{v}$ is the vector containing both the intracellular and exchange fluxes, and $\boldsymbol{v^{lb}}$ and $\boldsymbol{v^{ub}}$ represent the lower and upper flux bounds on the exchange fluxes respectively. However, within the framework of DMFA, the measured exchange fluxes, v_i^{meas}, are predicted from the kinetic rate expressions described in the previous section and therefore expressed as functions of the kinetic parameters, $\boldsymbol{\theta}$, thus integrating the kinetic and stoichiometric components.

3.3 Macroscopic Mass Balances

The macroscopic bioreactor mass balances on each measured species, link the dynamics between the intracellular and extracellular environments. Perfusion-specific mass balances account for the effect of the perfusion rate, bleed rate, and media composition on the bulk mass transport and cell growth dynamics of the bioreactor. These are three Critical Process Parameters (CPPs) of continuous upstream mAb production which have been explicitly included in the model. To capture all phases of bioreactor operation, the derivative term in the general mass balance is maintained, discretized via forward finite differences, and re-arranged to solve for the extracellular concentration of each measured species at the next time point, Eq. (4).

$$C_{i+1} = \frac{(DC_{feed}+q_i X_{avg})(t_{i+1}-t_i)+C_i}{1+D(t_{i+1}-t_i)} \tag{4}$$

C_{i+1} is the concentration of any species at the next time point, C_i is concentration of any species at the present timepoint, C_{feed} is the concentration of any species in the media, D is the perfusion rate, q_i is the consumption or production rate of any species at the present timepoint, X_{avg} is the average viable cell density between the two timepoints, t_{i+1} is the next time point, and t_i is the present timepoint. The cell bleed, Eq. (5), is simulated as a discrete event to align with its intermittent application during experiments, and the concentration of each measured species after a cell bleed can be predicted accordingly.

$$V_{bleed} = V\left(1 - \frac{X_{sp}}{X_{current}}\right) \tag{5}$$

V_{bleed} is the required bleed volume, V is the bioreactor working volume, X_{sp} is the VCD setpoint, and $X_{current}$ is the presently measured VCD prior to engaging the bleed.

4. Results and Discussion

In addition to prior fed-batch work, time-series metabolic profiles of 24 species from scale-down semi-perfusion CHO cell cultures, as described in Section 2, provided the required data for model development and kinetic parameter estimation. Semi-perfusion cultures were grown without a cell bleed to approximate intensified process conditions characterized by industrially relevant VCDs, corresponding cell-specific perfusion rates (CSPRs), and nutrient depletion.

Intensified semi-perfusion induces a range of metabolic states across the culture duration. Starting from exponential growth coupled with large nutrient consumption rates, the culture approaches fed-batch dynamics ending in reduced net growth with high productivity, indicative of the stationary phase. The mechanistic framework of the model,

provided by the reduced reaction network and mass balances, captures the range of metabolic states with a single set of kinetic parameter values (Figure 1.a).

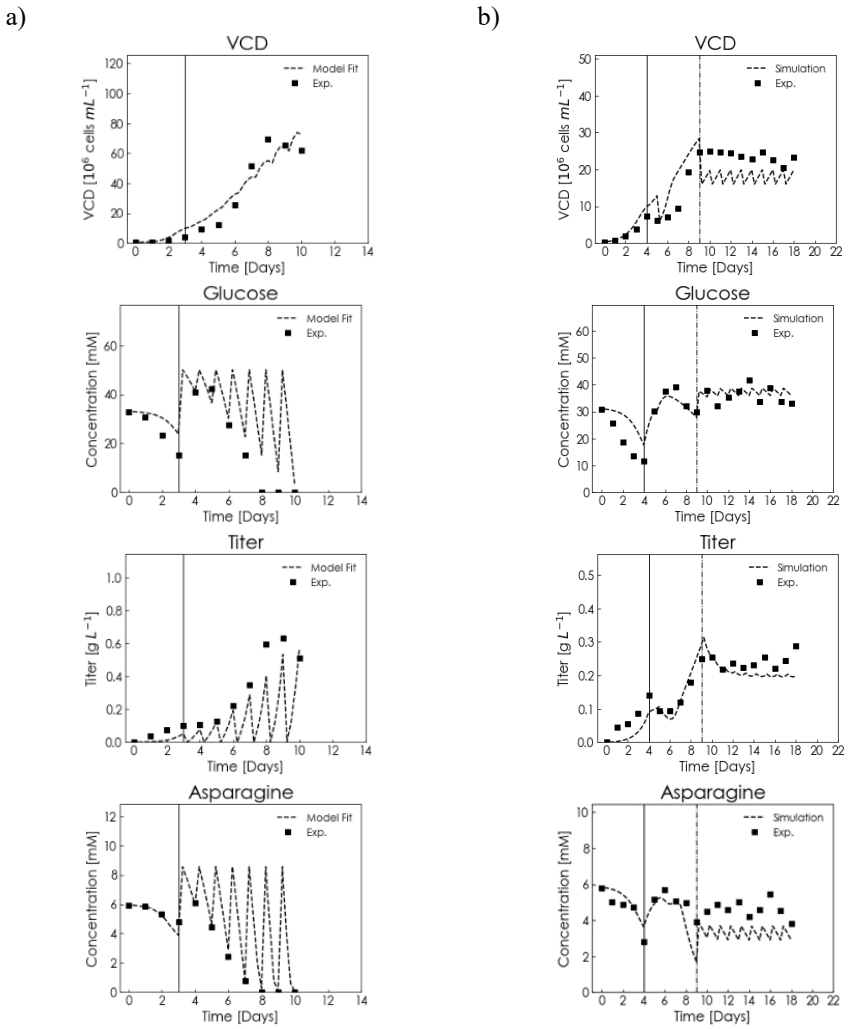

Figure 1. Subset of CHO-K1 VRC01 cell metabolic profiles. a) Scale-down semi-perfusion experimental data and model fits. b) 1 L continuous perfusion bioreactor experimental profiles and model predictions. The solid vertical lines denote perfusion initiation. The dashed vertical line in b) indicates cell bleed initiation.

While calibrated to only a single scale-down semi-perfusion dataset, subsequent model predictions of 1 L continuous perfusion bioreactor dynamics, under similar experimental conditions, followed to assess early performance of model extrapolation. Simulations of cell growth and metabolite profiles under mild process conditions, characterized by a low VCD and sufficient nutrient availability, agreed with previously collected data for a subset of species (Figure 1.b). The agreement between the predicted and experimental profiles can be improved, yet the general trends and magnitudes are maintained, highlighting the robustness of the DMFA framework to two significant differences between the datasets: process dynamics and the ensuing cell metabolic states. The

difference between semi-perfusion, in the form of nearly instantaneous media exchanges, and continuous perfusion coupled with an intermittent cell bleed to control the cell growth rate at steady state, is captured through the mass balance component of the framework. The difference in metabolic states between the two processes, including the range of states observed in semi-perfusion, are explained by the underlying mechanistic foundation of the metabolic network, which provides physiologically meaningful constraints towards intracellular resource distribution.

5. Conclusions

The mechanistic basis of the DMFA framework enables quantitative assessment of CHO cell metabolism across perfusion bioreactor scales and operational modes with a minimal set of required inputs. Future work seeks model application towards process goals of industrial interest. Identification of key nutrients to reduce growth and increase productivity is of primary importance in perfusion bioreactors. Such information can be used to provide insight towards media reformulation and feeding strategies, and subsequently predict the corresponding minimum CSPR, translating to a reduction in operational costs. Increasing the framework's complexity by defining a segregated structure to evaluate metabolic differences between heterogeneous cell populations in the bioreactor over the culture duration is an additional goal of future efforts.

Acknowledgements

The authors express their gratitude for the financial support from the U.S. Food and Drug Administration (FDA) under Award Number U01FD007695, and the Advanced Mammalian Biomanufacturing Innovation Center (AMBIC) under Award Number NSF EEC-2100502.

References

Ecker, D. M., Jones, S. D., & Levine, H. L., 2015. The therapeutic monoclonal antibody market. *Mabs*, 7.9-14.

Trill, J. J., Shatzman, A. R., & Subinay, G., 1995. Production of monoclonal antibodies in COS and CHO cells. *Current Opinion in Biotechnology*, 6(5), 553-560.

Wurm, F. M., 2004. Production of recombinant protein therapeutics in cultivated mammalian cells. *Nature biotechnology*, 22(11), 1393-1398.

Walther, J., Godawat, R., Hwang, C., Abe, Y., Sinclair, A., & Konstantinov, K., 2015. The business impact of an integrated continuous biomanufacturing platform for recombinant protein production. *Journal of biotechnology*, *213*, 3-12.

Reddy, J. V., Raudenbush, K., Papoutsakis, E. T., & Ierapetritou, M., 2023. Cell-culture process optimization via model-based predictions of metabolism and protein glycosylation. *Biotechnology Advances*, 108179.

Chen, Y., McConnell, B. O., Gayatri Dhara, V., Mukesh Naik, H., Li, C. T., Antoniewicz, M. R., & Betenbaugh, M. J., 2019. An unconventional uptake rate objective function approach enhances applicability of genome-scale models for mammalian cells. *NPJ systems biology and applications*, *5*(1), 25.

Zupke, C., & Stephanopoulos, G., 1995. Intracellular flux analysis in hybridomas using mass balances and in vitro 13C NMR. *Biotechnology and bioengineering*, *45*(4), 292-303.

ESCAPE-34 PSE-2024
European Symposium on Computer Aided Process Engineering
&
Process Systems Engineering

Flavio Manenti, Gintaras V. Reklaitis (Eds.), Book of Abstract of the 34th European Symposium on Computer Aided Process Engineering / 15th International Symposium on Process Systems Engineering (ESCAPE34/PSE24), June 2-6, 2024, Florence, Italy.

Retrofitting a Sugar Mill into a Sustainable Biorefinery

Teresa Lopez-Arenas[a,*]

[a]*Departamento de Procesos y Tecnología, Universidad Autónoma Metropolitana – Cuajimalpa, Av. Vasco de Quiroga 4871, Ciudad de México, 05348, Mexico*
mtlopez@cua.uam.mx

Abstract

The purpose of this work is to present the retrofitting of a sugar mill into a biorefinery to diversify the commercialized products, so as to improve the economy and sustainability of the industrial plant. The proposed methodology considers the design, simulation and techno-economic evaluation of a sugarcane biorefinery to produce mainly lactic acid and biofertilizer. From a circular economy perspective, the biorefinery considers the three biomasses generated in a sugar mill: sugarcane juice, molasses and bagasse (a lignocellulosic waste). The study takes into account the availability of raw materials (from the industry in Mexico) to determine the installed capacity of the industrial biorefinery.

Keywords: process design, process modelling, process simulation, biorefinery.

1. Introduction

From a circular economy perspective, the use of both raw materials and waste, as well as the production of high value-added products in a biorefinery, improve the economics of the production process, minimize waste discharge and energy consumption, and reduce dependence on petroleum products. So biorefineries offer new economic opportunities for agriculture and the chemical industry (Fitzpatrick et al., 2010). In particular, retrofitting sugar mills into sustainable biorefineries (see Figure 1) is a potential opportunity, since the Mexican sugar industry has serious operational and profitability problems (Anaya-Reza and Lopez-Arenas, 2018). These industrial facilities provide first (1G) and second (2G) generation biomasses that can easily be converted into value-added products. Among these are sugarcane juice (1G biomass), molasses (byproduct also considered as 1G biomass), and bagasse (2G biomass because it is a lignocellulosic waste).

Regarding the products of a biorefinery, much attention has been paid to bioproducts, that is, those processed through microbial biotechnology. Mainly due to global concerns about energy and environment, which are the main reasons to develop new techniques to produce almost all products through eco-friendly methods. Such as, biofuels, amino acids, organic acids, biopolymers, etc. And of course, with a circular economy approach, secondary byproducts could be steam, electricity, biogas, animal feed, biofertilizer, etc.

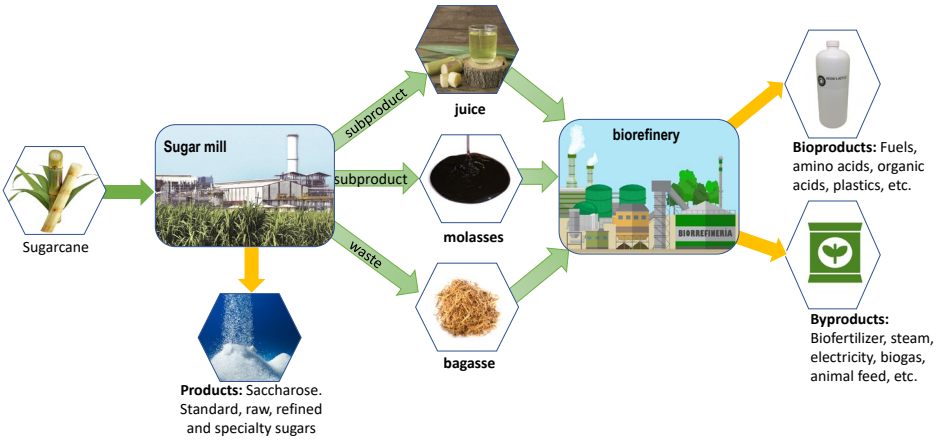

Figure 1. Conceptual design for the retrofitting of a sugar mill into a sustainable biorefinery.

Among the most important bioproducts is lactic acid, since it has wide applications in the pharmaceutical, cosmetic, chemical and food industries; with a world production of $1.6x10^6$ t/y (Fitzpatrick et al., 2010). In addition, it is a precursor with great potential for the production of ecological, biodegradable and biocompatible poly-lactic acid (PLA) polymers. Thus, lactic acid was selected in this work to show the conversion methodology of a sugar mill. While the secondary product is a fertilizer, which is the result of cell culture during the fermentation process of glucose to produce lactic acid.
So, the objective of this work is the retrofitting of a sugar mill, through the proposal of the synthesis, design, simulation and techno-economic evaluation of a sugarcane biorefinery to produce mainly lactic acid and a biofertilizer.

2. Methodology

2.1. Process synthesis
The process stages of the biorefinery are briefly described below.
Raw material conditioning: Each biomass is prepared according to its physical and chemical properties. In the case of juice, a dilution is carried out; and in the case of molasses, impurities are removed, and then molasses is diluted. While bagasse is ground, moistened and diluted. In particular, for bagasse, a steam explosion is carried out as a pretreatment for the structural degradation of the lignocellulosic biomass and the release of sugar polymers from its matrix. Finally, each conditioned biomass is subsequently sterilized for incorporation into the fermenter.

Preparation of culture medium: Tryptone, yeast extract and calcium hydroxide are added as nutrients. This mixture is diluted and heat sterilized to ensure that it is in optimal condition and that there are no contaminants.

Fermentation: The biomass, the culture medium and the microorganism (*L. casei ssp. Rhamnosus*) are added to the fermentation reactor, under isothermal and anaerobic conditions (Anaya-Reza and López-Arenas, 2018). Because microorganism production is inhibited by the lactic acid produced, then calcium hydroxide is added to the fermenter to neutralize the acid, maintaining the reactive mixture at a pH of 5 and forming calcium lactate salts. Upon completion of the fermentation, the output stream is taken to a storage tank.

Purification of the biofertilizer: First, the microorganism is eliminated using a rotating filter. The liquid phase is sent to lactic acid purification. While, the solid phase is sent to a rotary dryer to obtain dry biomass, which will be marketed as biofertilizer.

Purification of lactic acid: The liquid phase separated in the previous stage is sent to an acidifying tank where sulfuric acid is added, since with this the dissociation of calcium lactate is achieved, forming lactic acid and gypsum. The gypsum is removed using a rotating filter, and the lactic acid is recovered using an evaporator and spray dryer. A product with a purity of 55% lactic acid is achieved, which is within the food grade, 50-88% (Alexandri et al., 2019).

2.2. Conceptual Design

The biorefinery conceptual design was implemented in a process simulator (SuperPro Designer), selecting a batch operation mode and considering an annual operation time of 48 weeks. The maximum availability of raw material was determined according to the installed capacity in a sugar mill in Mexico (CONADESUCA, 2022): 3,453,700 t/y of sugarcane juice, 134,160 t/y of molasses, and 910,780 t/y of bagasse; such that the design of the proposed biorefinery is sized. Figure 2 shows the process flow diagrams of the conditioning sections of the three biomasses. While Figure 3 shows the sections of preparation of the culture medium, fermentation, and purification of the biofertilizer and lactic acid.

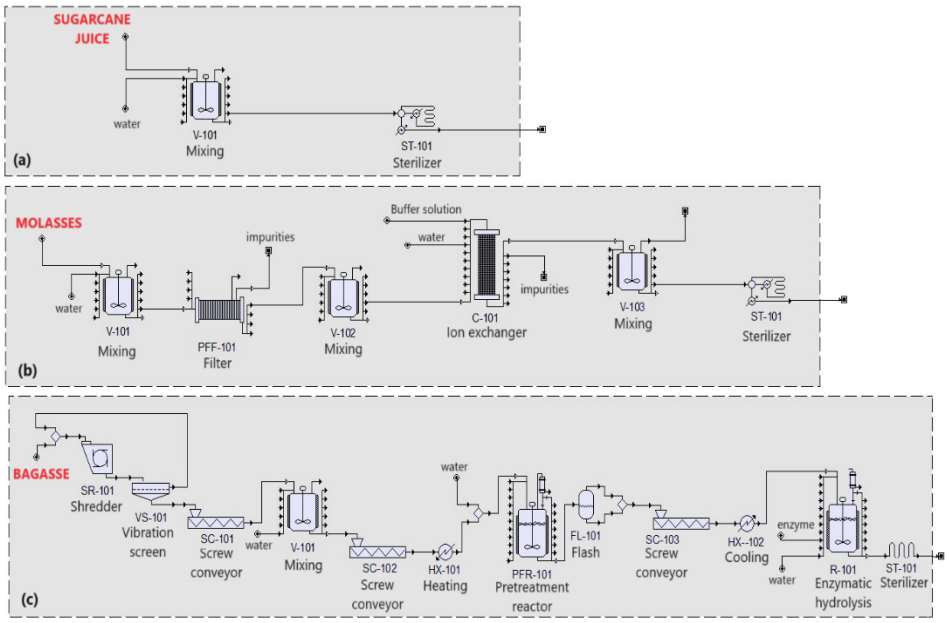

Figure 2. Process flow diagrams of biomass conditioning sections: (a) sugarcane juice, (b) molasses, and (c) bagasse

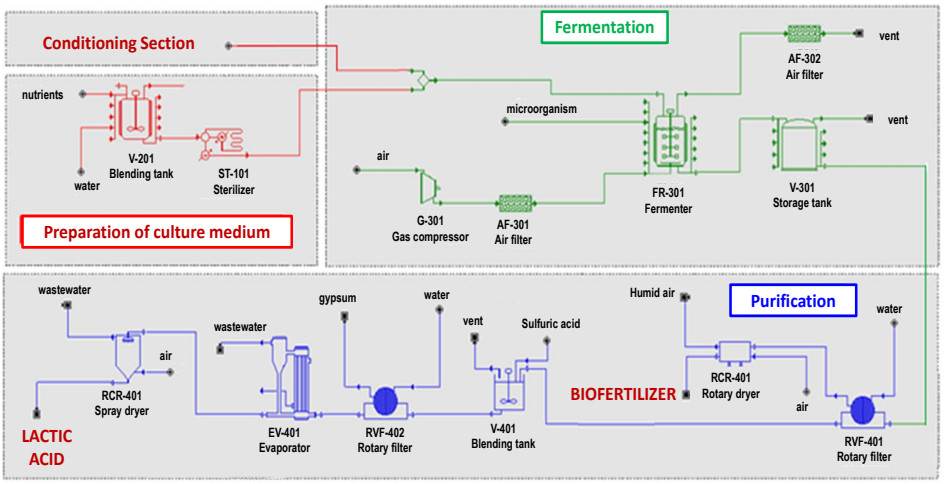

Figure 3. Process flow diagram of preparation of the culture medium, fermentation, and purification sections.

2.3. Biorefinery assessment

The comprehensive evaluation of the biorefinery is carried out considering: (a) technical aspects, verifying the performance, productivity and installed capacity of the process; (b) economic criteria, evaluating the unit production cost, the return on investment and the payback period; and (c) environmental issues, determining water consumption, the heat transfer requirement and energy consumption.

3. Simulation results

Using the modelling and simulation tools of the process simulator, the material and energy balances are calculated, the results of which in turn allow the evaluation of the profitability and environmental impact of each biomass used for the retrofitting of the sugar mill. When carrying out the techno-economic evaluation with the maximum quantity available for each biomass, some designs were not profitable. Therefore, the designs were improved by performing parametric sensitivity analysis: (a) modifying the number of fermentation reactors used in the design (since the reaction stage is a bottleneck), so that by increasing the set of reactors reduces downtime and improves profitability; and (b) varying the amount of biomass fed, so that a design is found that optimizes the efficient use of the equipment and improves the profitability of the process. The optimal profitability results are reported in Table 1 for each case study, noting that:
(i) The technical analysis demonstrates that the production of lactic acid and biofertilizer from the three proposed biomasses is feasible, and the quantity required to achieve the best profitability in each case is determined. It is important to note that profitability is achieved with quantities lower than the limits of each biomass produced in sugar mills.
(ii) Considering that a good profitability is when a rate of return on investment greater than 20% is achieved with a payback period of less than 3 years (Seider et al., 2009), it is observed that, as expected, the best values of profitability are achieved by using the juice followed by molasses, while with bagasse there is no acceptable profitability according the previous profitability definition. However, from a circular economy point of view, even the low profitability values for bagasse (which is a waste) are positive and satisfactory.

(iii) Regarding the environmental issues, it is observed that when sugarcane juice is used, a lower amount of process water is required compared to the other cases of molasses and bagasse. However, the amount of services (water vapor and cooling water) and electrical energy consumption are very similar for all processes.

Table 1. Comprehensive evaluation for the sugarcane biorefinery proposal.

	Biomass			
Concept	Juice	Molasses	bagasse	Units
Technical results				
Raw material consumption	488,070	134,160	298,000	t/y
Lactic acid production	108,753	129,476	236,000	t/y
Biofertilizer production	12,057	13,770	39,563	t/y
Economic results				
Unit production cost	0.73	0.74	1.0125	USD$/kg lactic acid
Return on investment	45.20	39.76	18.44	%
Payback period	2.21	2.51	5.42	y
Environmental results				
Processed water	2.96	9.30	9.15	kg/kg lactic acid
Water steam	14.97	14.47	12.84	kg/kg lactic acid
Cooling water	768.25	746.07	762.19	kg/kg lactic acid
Electric power	0.21	0.20	0.23	kW-h/kg lactic acid

4. Conclusions

The results of this work demonstrate the technical feasibility for the conversion of a sugar mill, being able to expand its marketable products and demonstrating good profitability with short periods of investment recovery. The use of each biomass (sugarcane juice, molasses, or bagasse) has positive aspects and many others to improve, however, their use as tools of change for the conversion of processes focused on linear to circular economies, meet the established requirements in the industry.

References

M. Alexandri, R. Schneider, K. Mehlmann, J. Venus, 2019, Recent Advances in D-Lactic Acid Production from Renewable Resources: Case Studies on Agro-Industrial Waste Streams. Food Technology and Biotechnology, 57, 293-304.

O. Anaya-Reza, T. López-Arenas, 2018, Diseño de una biorrefinería sostenible para la producción ácido láctico a partir de melaza de caña de azúcar. Revista Mexicana en Ingeniería Química, 17, 243-259.

CONADESUCA, Comité Nacional para el Desarrollo Sustentable de la Caña de Azúcar, 2022, https://www.gob.mx/conadesuca.

M. Fitzpatrick, P. Champagne, M. Cunningham, R. Whitney, 2010, A biorefinery processing perspective: treatment of lignocellulosic materials for the production of value-added products. Bioresource Technology, 101, 8915-8922.

W.D. Seider, J.D. Seader, D.R. Lewin, 2009, Product & Process Design Principles: Synthesis, Analysis and Evaluation, John Wiley & Sons, New York.

ESCAPE-34 PSE-2024
European Symposium on Computer Aided Process Engineering
&
Process Systems Engineering

Flavio Manenti, Gintaras V. Reklaitis (Eds.), Book of Abstract of the 34th European Symposium on Computer Aided Process Engineering / 15th International Symposium on Process Systems Engineering (ESCAPE34/PSE24), June 2-6, 2024, Florence, Italy.

Strategies for Renewable Muconic Acid Production from Lignin-based Aromatics through Rational Metabolic Engineering of Pseudomonas Putida KT2440

Pinelopi Marina Politi[a], Ilias Toumpe[b], Stefanos Xenios[a], Konstantinos Mexis[a], Ljubisa Miskovic[b], Vassily Hatzimanikatis[b] and Antonis Kokossis[a*]

[a] *School of Chemical Engineering, National Technical University of Athens, GR 157 72, Athens, Greece*
[a]*First affiliation, Address, City and Postcode, Country*
[b] *Laboratory of Computational Systems Biotechnology (LCSB), Swiss Federal Institute of Technology in Lausanne (EPFL), CH 1015, Lausanne, Switzerland*

akokossis@chemeng.ntua.gr

Abstract

Pseudomonas putida has significant potential as a cell factory, especially for degrading aromatic polymers like lignin, due to its remarkably versatile metabolism. In this work, we devise rational metabolic engineering strategies for producing muconic acid from lignin-based aromatics using the bacterium *Pseudomonas putida* KT2440, focusing on increasing the efficiency and yield of these processes. We develop large-scale kinetic models of *Pseudomonas Putida* KT2440 for biobased cis,cis-Muconic acid (ccMA) production through lignin-related aromatic compounds, such as p-coumarate (pCA), using the ORACLE (Optimization and Risk Analysis of Complex Living Entities) methodology.

The developed large-scale kinetic models are used to derive engineering strategies through Metabolic Control Analysis (MCA) to manipulate the genetic composition of *Pseudomonas putida* KT2440. This study investigates the effects of uncertainty in the operating directions of reactions in the metabolic network on devised metabolic engineering targets. To this end, we study two cases, differing in the direction the phosphoglucose-isomerase (PGI) reaction, an essential step of the glycolysis and gluconeogenesis pathways, operates. We identify target enzymes for the two cases and propose metabolic engineering strategies for each formulation. The analysis of the two cases revealed that our metabolic engineering decisions are strongly affected by the assumptions on the directionality of PGI. Therefore, to devise reliable metabolic engineering targets, interventions that are consistent in the two cases should be considered. This study also allows us to propose future experiments that would reduce the uncertainty in the system and, therefore, improve the reliability of the developed kinetic models.

This research expands our knowledge about the biochemical capabilities of *Pseudomonas putida* through the use of developed large-scale kinetic models of this important industrial host.

Keywords: *Pseudomonas putida* KT2440, Large-scale kinetic models of metabolism, Thermodynamics, Flux Directionality Profile, Metabolic engineering.

Introduction

A promising bacterium for the industrial production of biofuels and biochemicals is *Pseudomonas Putida*, due to its strong ability to tolerate toxic compounds, as well as its capacity to grow on a wide range of substrates. *Pseudomonas putida* can depolymerize high molecular weight (HMW) oligomers, thus making complex aromatic polymers potential substrate candidates. A promising source of renewable carbon for the production of high-value chemicals is lignin, a structural component of plant biomass. Despite being the primary large-volume renewable aromatic feedstock in nature, the transformation of lignin into bioproducts presents a substantial bottleneck due to its intrinsic heterogeneity and resistance to depolymerization (Park et al., 2020). Lignin is currently underutilized and routinely combusted to generate process heat in the paper and pulp industry (Wu et al., 2017).

In the context of lignin valorization, this study focuses on muconic acid, an important chemical intermediate that can be produced from lignin-based aromatics. Muconic acid is suitable for polymerization into biobased polyesters since it can be converted through a single-step hydrogenation process to adipic acid, a common monomer in the production of nylon-6,6 (Vardon et al., 2016). Furthermore, transforming cis,cis-muconic acid into trans,trans-muconic acid via isomerization, followed by subsequent reactions, offers a pathway to generate terephthalic acid, a primary building block for Bio-PET.

Genome-Scale Models (GEMs) of *Pseudomonas putida* have been constructed in the past years, with the most recent one being the iJN1463, consisting of 2153 metabolites, 2927 reactions, and 1462 genes (Nogales et al., 2019). Those models have been used for optimal flux distribution predictions and gene essentiality evaluation. Advancements in computational metabolic engineering have allowed large-scale kinetic models to capture the dynamic metabolic responses of a cell to parameter perturbations (Tokic et al., 2020). However, constructing those models requires experimental datasets to constrain the model's predictions to a physiologically relevant solution space (Miskovic et al., 2015). Several metabolic engineering and bioprocess development studies have been done, focusing on engineering *Pseudomonas putida* toward industrially-relevant MA production from aromatic compounds (Sonoki et al., 2014; Kohlstedt et al., 2022; Almqvist et al., 2021; Kuatsjah et al., 2022; Salvachua et al., 2018).

In this work, we develop a systematic approach to lignin valorization through the strain *Pseudomonas putida* KT2440. We build large-scale kinetic models for two Flux Directionality Profiles (FDPs) of the metabolism of *Pseudomonas putida* and identify enzyme targets for muconic acid overproduction for each FDP.

Methods & Results

For the purpose of this study, the most recent GEM of *Pseudomonas putida* iJN1463, was reduced using redGEM (Ataman et al., 2017), a systematic model reduction framework that produces core networks focused around 8 subsystems of interest: glycolysis,

glyconeogenesis, pyruvate metabolism, TCA cycle, pentose phosphate pathway, β-ketoadipate pathway, the oxidative phosphorylation (ETC) pathway, as well as phenylalanine, tyrosine and tryptophan biosynthesis pathway. We then apply lumpGEM, an algorithm that forms a lumped reaction to accommodate the production of the necessary biomass building blocks (Ataman & Hatzimanikatis, 2017).

The Optimization and Risk Analysis of Complex Living Entities (ORACLE) methodology (Miskovic & Hatzimanikatis, 2010) is used for the analysis of muconic acid production by *Pseudomonas putida* KT2440. Cis,cis-muconic acid production is based on p-coumaric acid uptake of the cell, while cell growth is supported by glucose uptake. For this purpose, two gene knockouts and two reaction additions were performed. The reduced model was further constrained with experimental data of uptake, secretion and growth rates and metabolomics data of media metabolites (Kuatsjah et al., 2022). Thermodynamics-based Flux Balance Analysis (TFBA) (Kiparissides & Hatzimanikatis, 2017; Soh & Hatzimanikatis, 2014) was performed, for which the standard Gibbs free energy of formation (ΔG^o_f) and reaction (ΔG^o_r) were estimated with the Group Contribution Method (Jankowski et al., 2008). The curated reduced thermodynamic model consists of 365 reactions, 307 metabolites and 364 genes.

However, even with integrating available data certain reactions can still operate in either the forward or reverse direction while remaining consistent with the observed physiology. To build the kinetic model, we need to define an explicit directionality for those reactions (Hameri et al., 2019).

We constructed populations of non-linear large-scale kinetic models for 2 selected FDPs. We generated 50,000 stable kinetic models for each FDP, based on 1,000 steady-state solution samples using the SKiMpy (Symbolic Kinetic Models with Python) package (Weilandt et al., 2022). Each kinetic model consists of 2,692 parameters, capturing the complex cellular physiology of *Pseudomonas putida* cells.

Here, we investigate how the directionality assumption of the reaction catalysed by enzyme phosphoglucose-isomerase (PGI) that interconverts glucose-6-phosphate and fructose-6-phosphate affects the predictions of the populated kinetic models. Based on this, we sampled the solution space to determine concentrations and fluxes and developed two kinetic models. We performed MCA (Wang et al., 2004) on these models and identified 17 key enzymes for each FDP that affect the production of catechol, the immediate precursor of muconic acid (Figure 1). Three enzyme targets that have a consistent, positive effect on muconic acid production in the two FDPs, are the ones catalysing NADP biosynthesis, 4-hydroxybenzoate degradation and p-coumarate degradation (Figure 1). The first reaction contributes to the overall production of ADP and NADP energy carriers, whereas the latter two take part in the p-coumaric acid degradation pathway, catabolising our main lignin derivative for muconic acid production, pCA. The directionality in the PGI reaction affects the sign of Flux Control Coefficients (FCCs) for several enzymes, such as reaction GLUPRT participating in the 5-aminoimidazole ribonucleotide biosynthesis pathway. PGI reaction is an essential step of the glycolysis and gluconeogenesis pathways, and it was previously reported that it can operate in both directions (Ebert et al., 2011). Therefore, it is an interesting candidate to investigate its flux directionality effect on muconic acid production.

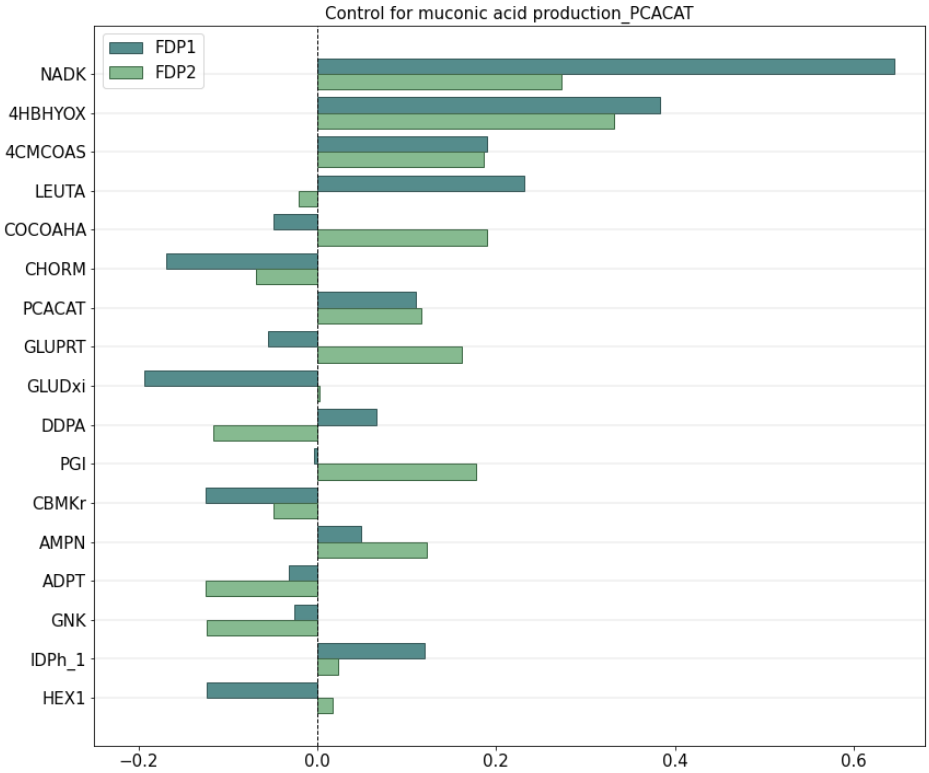

Figure 1. Flux Control coefficients of the production of muconic acid for two different FDPs. Illustration of the top 17 enzymes across the FDPs in terms of absolute control over muconic acid production. The bars correspond to the mean values of FCCs for FDP1, where the directionality of PGI reaction is set forward, and for FDP2 where the directionality of PGI reaction is set backward.

Conclusions

Overall, this project contributes to the advancement of sustainable biobased chemicals and assists in designing future biorefineries. Moreover, the curated genome-scale model of *Pseudomonas putida*, along with the large-scale stoichiometric and kinetic models, are valuable for future biobased chemical research and development. The study's results may also facilitate the exploration of alternative target enzymes and production pathways that increase robustness to lignin-related feedstocks and muconic acid productivity, thereby propelling the field of biobased chemical production forward.

Acknowledgements

This work was conducted as part of an inter-university research collaboration project between the National Technical University of Athens (NTUA) and the Swiss Federal Institute of Technology in Lausanne (EPFL).

The research project was funded by the Hellenic Foundation for Research and Innovation (H.F.R.I.) under the 2nd Call for H.F.R.I. Research Projects to support Faculty Members & Researchers (Project Number: 3817).

References

Almqvist, H., Veras, H., Li, K., Hidalgo, J. G., Hulteberg, C., Gorwa-Grauslund, M., Parachin, N. S., & Carlquist, M. (2021). Muconic Acid Production Using Engineered Pseudomonas putida KT2440 and a Guaiacol-Rich Fraction Derived from Kraft Lignin. *ACS Sustainable Chemistry & Engineering*, *9*(24), 8097–8106.

Ataman, M., Gardiol, D. F. H., Fengos, G., & Hatzimanikatis, V. (2017). redGEM: Systematic reduction and analysis of genome-scale metabolic reconstructions for development of consistent core metabolic models. *PLOS Computational Biology*, *13*(7), e1005444.

Ataman, M., & Hatzimanikatis, V. (2017). lumpGEM: Systematic generation of subnetworks and elementally balanced lumped reactions for the biosynthesis of target metabolites. *PLOS Computational Biology*, *13*(7), e1005513.

Ebert, B. E., Kurth, F., Grund, M., Blank, L. M., & Schmid, A. (2011). Response of Pseudomonas putida KT2440 to increased NADH and ATP demand. Applied and environmental microbiology, 77(18), 6597–6605.

Hameri, T., Fengos, G., Ataman, M., Miskovic, L., & Hatzimanikatis, V. (2019). Kinetic models of metabolism that consider alternative steady-state solutions of intracellular fluxes and concentrations. *Metabolic Engineering*, *52*, 29–41.

Jankowski, M., Henry, C. S., Broadbelt, L. J., & Hatzimanikatis, V. (2008). Group Contribution Method for thermodynamic analysis of complex metabolic networks. *Biophysical Journal*, *95*(3), 1487–1499.

Kiparissides, A., & Hatzimanikatis, V. (2017). Thermodynamics-based Metabolite Sensitivity Analysis in metabolic networks. *Metabolic Engineering*, *39*, 117–127.

Kohlstedt, M., Weimer, A., Weiland, F., Stolzenberger, J., Selzer, M., Sanz, M. A., Kramps, L., & Wittmann, C. (2022). Biobased PET from lignin using an engineered cis, cis-muconate-producing Pseudomonas putida strain with superior robustness, energy and redox properties. *Metabolic Engineering*, *72*, 337–352.

Kuatsjah, E., Johnson, C. W., Salvachua, D., Werner, A. Z., Zahn, M., Szostkiewicz, C. J., Singer, C. A., Dominick, G., Okekeogbu, I., Haugen, S. J., Woodworth, S. P., Ramirez, K. J., Giannone, R. J., Hettich, R. L., McGeehan, J., & Beckham, G. T. (2022). Debottlenecking 4-hydroxybenzoate hydroxylation in Pseudomonas putida KT2440 improves muconate productivity from p-coumarate. *Metabolic Engineering*, *70*, 31–42.

Miskovic, L., & Hatzimanikatis, V. (2010). Production of biofuels and biochemicals: in need of an ORACLE. *Trends in Biotechnology*, *28*(8), 391–397.

Miskovic, L., Tokic, M., Fengos, G., & Hatzimanikatis, V. (2015). Rites of passage: requirements and standards for building kinetic models of metabolic phenotypes. *Current Opinion in Biotechnology*, *36*, 146–153.

Nogales, J., Mueller, J. L., Gudmundsson, S., Canalejo, F. J., Duque, E., Monk, J. M., Feist, A. M., Ramos, J. L., Niu, W., & Palsson, B. Ø. (2019). High-quality genome-scale metabolic modelling of Pseudomonas putida highlights its broad metabolic capabilities. *Environmental Microbiology*, *22*(1), 255–269.

Park, M., Chen, Y., Thompson, M. G., Benites, V. T., Fong, B., Kim, Y., Baidoo, E. E. K., Gladden, J. M., Adams, P. D., Keasling, J. D., Simmons, B. A., & Singer, S. W. (2020). Response of Pseudomonas putida to Complex, Aromatic-Rich Fractions from Biomass. *ChemSusChem*, *13*(17), 4455–4467.

Salvachua, D., Johnson, C. W., Singer, C. A., Rohrer, H., Peterson, D. J., Black, B. A., Knapp, A., & Beckham, G. T. (2018). Bioprocess development for muconic acid production from aromatic compounds and lignin. *Green Chemistry*, *20*(21), 5007–5019.

Soh, K. C., & Hatzimanikatis, V. (2014). Constraining the flux space using thermodynamics and integration of metabolomics data. In *Methods in molecular biology* (pp. 49–63).

Sonoki, T., Morooka, M., Sakamoto, K., Otsuka, Y., Nakamura, M., Jellison, J., & Goodell, B. (2014). Enhancement of protocatechuate decarboxylase activity for the effective production of muconate from lignin-related aromatic compounds. *Journal of Biotechnology*, *192*, 71–77.

Tokic, M., Hatzimanikatis, V., & Miskovic, L. (2020). Large-scale kinetic metabolic models of Pseudomonas putida KT2440 for consistent design of metabolic engineering strategies. *Biotechnology for Biofuels*, *13*(1).

Vardon, D. R., Rorrer, N. A., Salvachua, D., Settle, A. E., Johnson, C. W., Menart, M. J., Cleveland, N. S., Ciesielski, P. N., Steirer, K. X., Dorgan, J. R., & Beckham, G. T. (2016). cis,cis-Muconic acid: separation and catalysis to bio-adipic acid for nylon-6,6 polymerization. *Green Chemistry*, *18*(11), 3397–3413.

Wang, L., Birol, İ., & Hatzimanikatis, V. (2004). Metabolic Control Analysis under Uncertainty: Framework Development and Case Studies. *Biophysical Journal*, *87*(6), 3750–3763.

Weilandt, D., Salvy, P., Masid, M., Fengos, G., Eriksson, R. D., Hosseini, Z., & Hatzimanikatis, V. (2022). Symbolic Kinetic Models in Python (SKiMpy): Intuitive modeling of large-scale biological kinetic models. *bioRxiv (Cold Spring Harbor Laboratory)*.

Wu, W., Dutta, T., Varman, A. M., Eudes, A., Manalansan, B., Loque, D., & Singh, S. (2017). Lignin Valorization: Two Hybrid Biochemical Routes for the Conversion of Polymeric Lignin into Value-added Chemicals. *Scientific Reports*, *7*(1).

ESCAPE-34 PSE-2024
European Symposium on Computer Aided Process Engineering
&
Process Systems Engineering

Flavio Manenti, Gintaras V. Reklaitis (Eds.), Book of Abstract of the 34th European Symposium on Computer Aided Process Engineering / 15th International Symposium on Process Systems Engineering (ESCAPE34/PSE24), June 2-6, 2024, Florence, Italy.

Modelling the Reactive Oxygen Species Initiated Amyloid Aggregation and Inhibitory Action of Chlorogenic Acid

Abdul Majid, Saneev Garg

Department of Chemical Engineering, Indian Institute of Technology Kanpur, Kanpur, Uttar Pradesh, 208016, India
majid20@iitk.ac.in

Abstract

Alzheimer's disease (AD) is a common form of dementia which is closely linked with the reactive oxygen species (ROS) and the abnormal aggregation of amyloid beta (Aβ) protein in the human brain. Aβ protein aggregates to form plaques which deposit across the neurons and lead to neuronal cell death. Thus, Aβ protein is thought to be a major factor for AD pathogenesis. Currently, different strategies are being explored to prevent Aβ aggregation. Seeking therapeutic molecules that could inhibit the aggregation effectively, has been a major research challenge. Chlorogenic acid (CA), considered as an antioxidant, is reported to have an inhibition effect on Aβ aggregation. Herein, a previously reported kinetic model based on free radical polymerisation, assuming ROS as an initiator, is extended and used to study the Aβ aggregation and inhibitory effects of CA. Model parameter tuning is done with the experimental data to estimate the value of new parameter in the model. The simulated results from the model are observed to be in good agreement with the experimental data at a different concentration of CA. The model may also be extended to study the inhibitory effects of other drugs, such as polyphenols and metal chelators, showing a similar kinetic mechanism for inhibition of Aβ aggregation.

Keywords: Kinetic modelling, Aβ aggregation, drug inhibition, Chlorogenic acid.

1. Introduction

Alzheimer's disease (AD) is a common form of dementia characterized by abnormal protein aggregation leading to cognitive disabilities and memory loss (Knowles et al. 2014; Mroczko et al. 2018). The late-onset disease, being more probable than early onset, affects almost 10% of the population above 65 years (Hao and Friedman 2016; Zhou et al. 2004). Currently, at least 50 million people are affected worldwide (Breijyeh and Karaman 2021).

Among the several proposed hypotheses, the amyloid beta (Aβ) cascade hypothesis has gained significant attention in previous few decades (Doig 2018; Rudge 2022).
Aβ proteins are produced by a two-step sequential cleavage of amyloid precursor proteins (APP) which are sometimes cleaved by amyloidogenic pathways responsible for Aβ toxicity (Vijayan and Remya 2019). The hypothesis assumes that the excessive accumulation of Aβ leads to neuronal cell damage (Carrillo-mora and Colín-barenque 2014).

Huge *in vitro* experimental studies have been performed and corresponding mathematical models have been developed to study Aβ aggregation. A traditional mathematical model includes nucleation phase, elongation phase and plateau phase which are observed as a result of nucleus formation, fibril elongation and mature fibril/plaque formation respectively (Ghosh et al. 2010).
Currently, only two types of small molecule drugs, cholinergic inhibitors to cholinesterase enzyme and antagonists to N-methyl d-aspartate (NMDA), have been approved by the Food and Drug Administration (FDA, USA) to treat AD symptomatically (Miculas et al. 2023). The available therapies only temporarily relieve the symptoms and no disease modifying drug has been developed to date which can prevent the disease pathogenesis (Urbanc 2021). Based on the amyloid hypothesis, different strategies are being employed to develop anti-Alzheimer's drugs, with mechanisms of action mainly focusing on reducing the generation of amyloid precursor protein (APP), inhibiting the cleavage of APP by inhibiting the beta and gamma secretase and preventing Aβ aggregation (Miculas et al. 2023; Wu et al. 2022).

Various mathematical models are reported to study the inhibitors' mechanisms of action with Aβ species *in vitro* and to propose possible potential therapeutics. Therefore, a mathematical model is important to study the inhibitory action of molecule inhibitors to find the mechanism and possible therapeutics. Our previously reported kinetic model (Abdul and Garg 2023) was developed to study Aβ aggregation only. The model does not consider the effects of inhibitors and associated mechanisms of action on Aβ aggregation inhibition. The aggregation model is extended to simulate these effects and is the main scope of the current study.
The objective of the current study is to develop a model involving simple ROS initiated free radical polymerisation kinetic equations considering the effects of AD drug on amyloid beta aggregation. In this study, the proposed model deals with amyloid beta aggregation and the inhibitory action of therapeutic molecule, CA, on Aβ40 aggregation. To the best of our knowledge, this is the first ever reported model which studies the inhibition action of drug via free radical mechanism. It may give further insights to develop novel drugs for the treatment of AD.

2. Inhibition Model

To study the inhibitory action of the therapeutic molecule, CA, our previously reported model (Abdul and Garg 2023), originally developed for Aβ aggregation, is further extended. Mancini and co-workers (Mancini and Weaver 2018) investigated that components of coffee (e.g., CA) show inhibitory action on Aβ40 fibrillation using ThT fluorescence. Moreover, Yang and co-workers (Yang and Zheng 2018) reported that CA could inhibit Aβ40 aggregation in a dose dependent manner.

In the extended model, only inhibitory action of CA has been considered. Therefore, a kinetic reaction between CA and Aβ40 monomer has been assumed as CA reacts with Aβ40 monomer and forms a $CA\text{-}M$ (here M represents Aβ40 monomer) molecule as shown below.

$$CA + M \overset{k_m}{\rightarrow} CA\text{-}M \tag{i}$$

Therefore, assuming the elementary reaction mechanism, the equation for monomer concentration (modification of monomer concentration, Equation 3 by (Abdul and Garg 2023)) based on mass balance can be written as follows:

$$\frac{dM}{dt} = -k_i \dot{R}M - k_p M \lambda_0 - k_m M\, CA \tag{ii}$$

where k_m is the rate constant for monomer CA interaction.
Rate equation for CA can be written as follows:

$$\frac{dCGA}{dt} = -k_m M\, CA \tag{iii}$$

Therefore, the extended model consist of a total of 10 simultaneous differential equations, including basic model (Abdul and Garg 2023)(excluding equation for monomer in the basic model), and equations (ii) and (iii).

3. Results and Discussion

3.1. Model tuning and validation

The experimental data (represented by diamonds in Figure 1) for CA inhibition at an initial concentration (CA_0) of 112.9 μM is used to tune the extended model. The previously reported rate parameters ($k_d = 5\times10^{-8}\ s^{-1}$, $k_i = 4.5\times10^{-8}\ M^{-1}s^{-1}$, $k_p = 5.8\times10^{2}\ M^{-1}s^{-1}$, $k_{tc} = 4.8\times10^{1}\ M^{-1}s^{-1}$, $k_{td} \sim 0$) are used and no re-tuning is done except for the added parameter k_m, in the extended model. To solve the set of differential equations *ode23s* solver in MATLAB® is used. Model is tuned to estimate the value of the new parameter k_m. The error function (sum of the square of difference of experimental data model value data) is minimized using a nonlinear least square (LSQNONLIN) solver in MATLAB®. Experimental data shows that monomers (initial concentration of 35 μM) rapidly form fibrils at t ~ 0 with concentration of 17μM. Therefore, setting initial monomer concentration of 35 – 17 = 18 μM, the best fit value of parameter k_m is obtained as $4.8\times10^{-2}\ M^{-1}s^{-1}$. The comparison (Figure 1) between experimental data (diamonds) and the tuned model prediction (solid line) is shown.

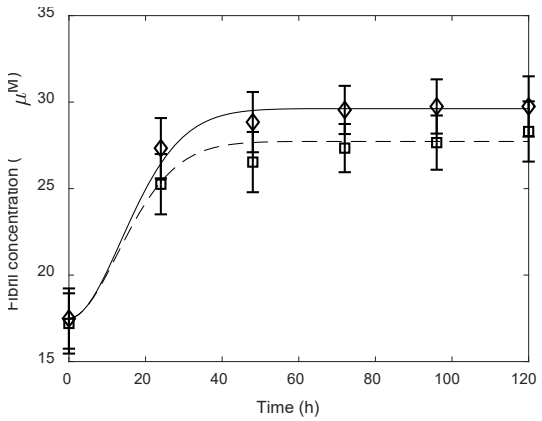

Figure 1. Comparison between model output with experimental data at monomer concentration of 35 μM.

Diamonds and squares show the dose inhibition experimental data at 112.9 and 169.35 μM, respectively. Solid and dashed lines represent the tuned and predicted model output at dose concentration of 112.9 and 169.35 μM, respectively.

Tuned model output is observed to be in good agreement with the experimental data with only one new parameter tuning. It is noted that there is a difference between model output and the initial two experimental data points. This difference is due to only one new added parameter tuning to the model and not tuning the previously reported parameters.

3.2. Model 1 predictions at different CA dose concentration

The experimental data is also available at another initial dose concentration (represented by squares in Figure 1). To analyze the model's reliability, model simulations at an initial CA concentration of 169.35 μM are compared with the experimental data keeping all the parameter (k_d, k_i, k_p, k_{tc}, k_{td}, k_m) values constant. After changing the initial CA concentration only, the comparison between experimental data (Figure 1, squares) and the extended model simulations (Figure 1, dashed line) are shown in Figure 1. It is observed that the model prediction for different initial concentration of CA, without any further re-tuning, agrees well with the reported experimental data.

3.3 Sensitivity of drug concentration and parameter

To check the model robustness, sensitivity analysis of initial drug concentration (CA_0) and associated parameter k_m have been performed on fibril concentration. It is expected that decreasing or increasing CA_0 or k_m should decrease or increase the inhibition effect of drug, respectively. Similar trends can be observed in Figure 2 (**a** is for CA_0 and **b** is for k_m). It can be seen that after changing the CA_0 or k_m by 20% and 180% fibril concentration gets increased or decreased, respectively, as expected.

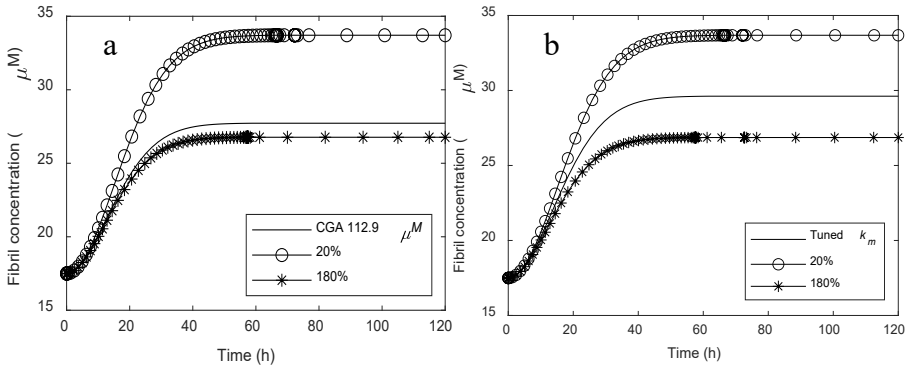

Figure 2. Sensitivity of drug concentration (CA0) and parameter (k_m)

4. Conclusions

In this study an extended model of a basic kinetic model (which solely studies the Aβ aggregation), to study the amyloid beta (Aβ) aggregation and the inhibition effects of chlorogenic acid (CA) drugs on Aβ aggregation is proposed. The CA molecule is reported to have an inhibitory effect on Aβ aggregation. Therefore, mechanisms involving Aβ aggregation inhibition have been incorporated to modify the previously reported model. The extended model requires only one new parameter to fit the reported experimental data. The model predicts the experimental data at different monomer concentrations in good agreement. The approach provides a relatively simple and inexpensive model for studying Aβ aggregation inhibition at different conditions. The model may further be modified to study other inhibitory molecules' effect such as, large molecules (peptide-based) and nanoparticle inhibitors on Aβ aggregation, especially when the molecule is antioxidant (works as a scavenger for ROS). Therefore, the model can be helpful in understanding the mechanism of action between Aβ and drug to develop possible therapeutics for AD in the near future.

References

Abdul, Majid, and Sanjeev Garg. 2023. "Reactive Oxygen Species May Cause Amyloid Beta Aggregation by Free Radical Polymerization Abdul." *Journal of Applied Polymer Science*. Accepted Manuscript.

Breijyeh, Zeinab, and Rafik Karaman. 2021. "Comprehensive Review on Alzheimer'S Disease." *World Journal of Pharmacy and Pharmaceutical Sciences* 10(7):1–28.

Carrillo-mora, Paul, Rogelio Luna, and Laura Colín-barenque. 2014. "Amyloid Beta : Multiple Mechanisms of Toxicity and Only Some Protective Effects ?" *Oxidative Medicine and Cellular Longevity* 2014:1–15.

Doig, Andrew J. 2018. "Positive Feedback Loops in Alzheimer's Disease: The Alzheimer's Feedback Hypothesis." *Journal of Alzheimer's Disease* 66(1):25–36.

Ghosh, Preetam, Amit Kumar, Bhaswati Datta, and Vijayaraghavan Rangachari. 2010. "Dynamics of Protofibril Elongation and Association Involved in Aβ42 Peptide Aggregation in Alzheimer's Disease." *BMC Bioinformatics* 11(SUPPL. 6):1–19.

Hao, Wenrui, and Avner Friedman. 2016. "Mathematical Model on Alzheimer ' s Disease." *BMC Systems Biology* 10:1–18.

Knowles, Tuomas P. J., Michele Vendruscolo, and Christopher M. Dobson. 2014. "The Amyloid State and Its Association with Protein Misfolding Diseases." *Nature Reviews Molecular Cell Biology* 15(6):384–96.

Mancini, Ross S., Yanfei Wang, and Donald F. Weaver. 2018. “Phenylindanes in Brewed Coffee Inhibit Amyloid-Beta and Tau Aggregation.” *Frontiers in Neuroscience* 12(735):1–14.
Miculas, Denisa Claudia, Paul Andrei Negru, Simona Gabriela Bungau, Tapan Behl, Syed Shams ul Hassan, and Delia Mirela Tit. 2023. “Pharmacotherapy Evolution in Alzheimer’s Disease: Current Framework and Relevant Directions.” *Cells* 12(1):1–25.
Mroczko, Barbara, Magdalena Groblewska, Ala Litman-Zawadzka, Johannes Kornhuber, and Piotr Lewczuk. 2018. “Amyloid β Oligomers (AβOs) in Alzheimer’s Disease.” *Journal of Neural Transmission* 125(2):177–91.
Rudge, Jonathan D. Arc. 2022. “A New Hypothesis for Alzheimer’s Disease: The Lipid Invasion Model.” *Journal of Alzheimer’s Disease Reports* 6(1):129–61.
Urbanc, Brigita. 2021. “Cross-Linked Amyloid β-Protein Oligomers: A Missing Link in Alzheimer’s Disease Pathology?” *J. Phys. Chem. B* 125(5):1307–16.
Vijayan, Dileep K., and C. Remya. 2019. “Amyloid Beta Hypothesis in Alzheimer ’ s Disease : Major Culprits and Recent Amyloid Beta Hypothesis in Alzheimer ’ s Disease : Major Culprits and Recent Therapeutic Strategies.” *Current Drug Targets* 20:1–20.
Wu, Tong, Ding Lin, Yaqian Cheng, Senze Jiang, Muhammad Waheed Riaz, Nina Fu, Chenhao Mou, Menglu Ye, and Ying Zheng. 2022. “Amyloid Cascade Hypothesis for the Treatment of Alzheimer’s Disease: Progress and Challenges.” *Aging and Disease* 13(6):1745–58.
Yang, Licong, Na Wang, and Guodong Zheng. 2018. “Enhanced Effect of Combining Chlorogenic Acid on Selenium Nanoparticles in Inhibiting Amyloid β Aggregation and Reactive Oxygen Species Formation In Vitro.” *Nanoscale Research Letters* 13(303):1–9.
Zhou, Weihui, Hong Qing, Yigang Tong, and Weihong Song. 2004. “BACE1 Gene Expression and Protein Degradation.” *Annals of the New York Academy of Sciences* 1035:49–67.

ESCAPE-34 PSE-2024
European Symposium on Computer Aided Process Engineering
&
Process Systems Engineering

Flavio Manenti, Gintaras V. Reklaitis (Eds.), Book of Abstract of the 34th European Symposium on Computer Aided Process Engineering / 15th International Symposium on Process Systems Engineering (ESCAPE34/PSE24), June 2-6, 2024, Florence, Italy.

Benchmarking Deep Anomaly Detection on Real Process Data of a Continuous Distillation Process

Aparna Muraleedharan[a], Fabian Hartung[b,c], Dennis Wagner[b], Marius Kloft[b], Jakob Burger[a*]
[a]*Technical University Munich (TUM) Campus Straubing 94315, Deutschland*
[b]*RPTU Kaiserslautern, Kaiserslautern 67663, Deutschland*
[c]*BASF SE, Ludwigshafen 67063, Deutschland*
burger@tum.de

Abstract

Our work delves into anomaly detection (AD) within the chemical industry, which is vital for maximizing product yields and ensuring operational safety. Over the past decade, many AD methods based on deep machine learning have appeared [1], and they are usually developed, assessed, and compared using artificial process data from the Tennessee-Eastman Process (TEP) [3]. Real chemical processes may exhibit distinct anomalies and dynamics, potentially undermining the effectiveness of methods tailored solely to TEP data. In response, the present work presents findings on AD using deep learning for a continuously operated mini plant in our lab. The dataset, spanning several weeks of operation and encompassing fault-free and faulty operations, serves as the test set for 22 literature methods for AD with deep learning. We compare the performances with prior evaluations on TEP data [2].

Keywords: Machine Learning, Anomaly Detection, Distillation, Data Generation

1. Introduction

Anomaly detection (AD) in the chemical industry is crucial for ensuring safety, maintaining quality standards, reducing costs, complying with regulations, optimizing processes, and, most importantly, preventing potential disasters or environmental damage. In the present work, we focus on AD in continuous chemical processes. Continuous chemical processes are integral to the industry for ensuring efficiency and consistent, high-quality output in a dynamic market landscape. These processes generate time series data, enabling real-time monitoring, predictive maintenance, and the detection of anomalies, thereby facilitating optimized operations and ensuring product quality and safety. For the last three decades, the Tennessee Eastman Process (TEP) has been the benchmark dataset for time-series anomaly detection, including previous works on anomaly detection in chemical processes [4]. Recently, we have published [3] an extensive comparison of 27 anomaly detection methods from the literature for unsupervised AD using a synthetic TEP dataset [32]. The TEP was created and published by Downs and Vogel in 1993 [5] and represents a simulated chemical process rather than

an actual industrial plant; therefore, the respective dataset is a synthetic multivariate time series that does not cover the full spectrum of possible operating scenarios or abnormalities encountered in real-time industrial settings. Since it cannot be guaranteed to simulate every effect of an occurring anomaly and its impact on the whole plant system, we wanted to examine possible performance differences of the models between synthetic TEP data and real-world data.

Therefore, the key challenge is that the availability of chemical data in the public domain could be more extensive. The present work aims to improve this situation and generate experimental data from a continuous distillation plant in TUM Campus Straubing. The experimental data generated is a time series dataset with and without anomalies. Using this data, we tested 22 of the literature mentioned above methods on AD and compared their performance with respective results for the synthetic TEP data.

2. Methods

2.1. Experimental Data Generation

The continuous distillation plant is a mini plant with a capacity of 5t/y feed (Figure 1). Its core is a steel column (operating pressure 1.5 bar). It is controlled and monitored using a LabVIEW system, the primary data collection tool. Multivariate time series data from 17 sensors was collected. The distillation column has one pressure controller, two flow controllers, two level controllers, and two temperature controllers. Six control loops are implemented in LabVIEW, enabling control and operation of the plant. The control strategy within the LabVIEW system offers adaptability for easy adjustments as required.

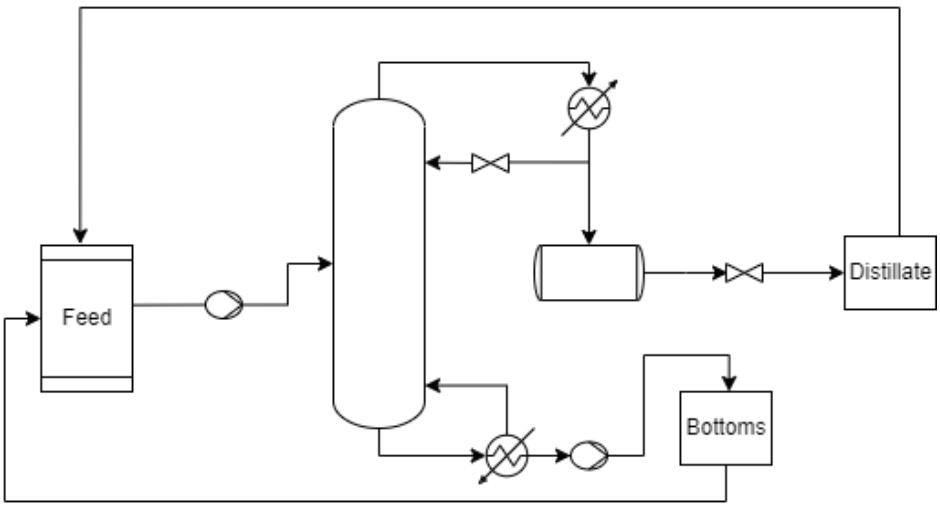

Figure 1: Setup of the continuous distillation plant (steel) for experiments with water

Experiments conducted with a single component water generated time series data spanning 30 days. Choosing water as the sole component streamlined the process by removing the separation aspect and directed the focus toward the overall material balance. Using water also leads to increased safety, enabling the remote and autonomous operation of the plant. Experimental data with and without anomalies were generated and labeled. The labeled data was further used to train, test, and validate anomaly detection methods.

2.2. Anomaly Detection

Advancements in time-series anomaly detection have prominently featured the evolution of unsupervised deep learning methods, notably with the application of sophisticated neural network architectures like recurrent neural networks (RNNs)[6], Long Short-Term Memory Networks (LSTMs)[7], and Variational Autoencoders (VAEs)[8] and various Generative Adversarial Network (GAN)[12] adaptations and operate independently without the need for labeled anomaly instances. Notably, RNNs and LSTMs, lauded for their sequential learning capabilities, excel in capturing extensive temporal dependencies, effectively pinpointing subtle anomalies. Conversely, an AE decodes and reconstructs input data, enabling the identification of deviations by comparing reconstructed sequences to the learned normal patterns. Furthermore, GANs create synthetic data instances and assess their authenticity against the original distribution, proficiently detecting anomalies by discerning disparities between generated and authentic data representations.

These unsupervised deep learning models [9] are trained on patterns representing standard behavior within time series data, allowing them to internalize fundamental structures and representations of regular sequences. Consequently, anomalies reflecting deviations from the learned norms are effectively detected within the data. In our prior work [3], we extensively evaluated and compared 27 unsupervised deep anomaly detection techniques found in contemporary literature for time-series anomaly detection. This thorough assessment gauged their detection accuracies utilizing the synthetic TEP dataset.

Our evaluation involved a comparative analysis of reconstruction-based methods[26], forecasting-based [13], generative methods [8], and hybrid approaches. Detecting anomalies within a time series involves generating anomaly scores[14] for each time step, with detection occurring if the score surpasses a predefined threshold. Commonly used evaluation metrics such as the F1-score [2] and the area under the precision-recall curve (AUPRC) [2] aid us in comprehensively assessing the performance of anomaly detection methods. The F1-score considers true positives, false negatives, and false positives, offering insights into precision and recall. Precision signifies the accuracy of identified anomalies among all flagged instances, while recall measures the model's capability to detect genuine anomalies. The AUPRC provides an overall evaluation of the model's performance across varied thresholds, offering insights into precision for different recall levels. Understanding the associated costs of missed anomalies (false negatives) versus falsely detected anomalies (false positives) in specific use cases is critical, necessitating threshold customization for optimal performance in real-world applications.

The findings [2] indicated that, on average, reconstruction-based methods exhibited superior performance, followed by generative methods, with forecasting-based models demonstrating the least effectiveness in anomaly detection. To substantiate these observations using authentic process data, 22 models underwent training, testing, and validation phases utilizing experimental data derived from a continuous distillation plant operating with water. All methods were trained equally with a training data set of five runs with about 1000 time steps each. The starting phase of the plant was in all data sets removed, and all training data were free of anomalies and normalized. For a better comparison, the hyperparameters were not fixed but optimized with cross-validation, as in our previous evaluation[2] limited to a maximum of 24 hours, to adjust them to this new data set. For this cross-validation, we split the training set into folds of the same size. The training excluded one of these folds, on which we validated the trained model. This process was repeated by switching the folds to have every single one as a validation fold

one time. Therefore, the worst metrics scores for one of those validation folds marked the final score of the used hyperparameters. The ones with the best final score were chosen by repeating this process with different values and combinations of the possible hyperparameters. Afterward, all the optimal trained models were evaluated on a test data set containing ten other runs than the training set with 1,000-11,000 time steps each. These data contain anomalies of varying length and type. Again, for this evaluation, we compared the methods regarding their overall F1-Score and the AUPRC and ranked the average performance of their achieved ranking in both.

3. Results

Table 1: Results of the evaluation of 22 AD methods on real process data with water.

Method	**Method Type**	**F1-Score**	**F1-Score ranking**	**AUPRC**	**AUPRC Ranking**	**Combined Ranking ***
MTAD_GAT[15]	Hybrid	0.9106	1	0.9442	1	1 (21)
LSTM_AE_OCSVM[16]	Hybrid	0.6460	2	0.7435	2	2 (16)
THOC[17]	Hybrid	0.6223	3	0.6702	4	3 (22)
TADGAN[18]	Generative GAN based	0.5893	4	0.6723	3	4 (18)
LSTM_VAE_GAN[19]	Generative VAE based	0.5101	5	0.6445	5	5 (15)
MSCRED[20]	Reconstruction based	0.4519	6	0.6004	6	6 (5)
LSTM_AE[21]	Reconstruction based	0.3484	7	0.4900	7	7 (4)
DONUT[22]	Generative VAE based	0.2464	9	0.4111	8	8 (6)
TKN_AE[23]	Reconstruction based	0.2580	8	0.3831	9	9 (7)
BEATGAN[12]	Generative GAN based	0.2232	10	0.3368	14	10 (1)
DENSE_AE[24]	Reconstruction based	0.1964	15	0.3586	10	11 (3)
GMM_VAE[25]	Generative VAE based	0.2084	11	0.3353	15	12 (13)
UNTRAINED_AE[26]	Reconstruction based	0.1988	14	0.3440	12	13 (10)
LSTM_MAX_AE[14]	Reconstruction based	0.2007	13	0.3386	13	14 (14)
USAD[24]	Reconstruction based	0.1926	16	0.3583	11	15 (12)
OMNI[27]	Generative VAE based	0.2010	12	0.3276	18	16 (8)
STGAT MAD[28]	Reconstruction based	0.1770	19	0.3297	16	17 (19)
LSTM VAE Park[8]	Generative VAE based	0.1864	17	0.3190	19	18 (11)
MADGAN[29]	Generative GAN based	0.1681	20	0.3296	17	19 (20)

Method	Method Type	F1-Score	F1-Score ranking	AUPRC	AUPRC Ranking	Combined Ranking *
SIS_VAE[30]	Generative VAE based	0.1803	18	0.3077	20	20 (9)
TCN_AE[31]	Reconstruction based	0.1387	21	0.3011	21	21 (2)
GENAD[20]	Reconstruction based	0.0812	22	0.2543	22	22 (17)

* The combined ranking obtained with TEP process data is given in brackets.

Table 1 displays the results obtained from the experiments with water. The methods are evaluated using the F1 score, AUPRC score, and a combined ranking based on these two scores with their average placement and score differences. MTAD_GAT, LSTM_AE_OCSVM, and THOC perform the best among all the methods, while SIS_VAE, TCN_AE, and GENAD have the lowest rankings. F1 and AUPRC scores of the methods are lower with the experimental data set than with the TEP data set. The rankings of these methods [2] with the TEP dataset exhibit significant divergence compared to the results obtained from the experimental process data. For the experimental data set, it was found that the hybrid methods perform best. We conject that this is the case because the data amount is limited and combined method architecture is better capable of training the data logic.

4. Conclusions

Hybrid-based deep learning anomaly detection (AD) techniques outperformed others when handling experimental data from the continuous distillation column with a single-component water system. Conversely, despite excelling with TEP data, reconstruction, and generative methods did not demonstrate comparable success with the experimental dataset. We conclude that improving and comparing AD methods using synthetic datasets (like the TEP data) is insufficient to yield high-performance methods for real plants.

All tested AD methods yielded notably low F1 and AUPRC scores on the experimental dataset, suggesting room for improvement by acquiring more process data from the continuous distillation mini-plant. Devising experiments aimed explicitly at generating anomalies that are not easily detectable by a human expert is also a crucial step for more effective training of these methods. It remains a pivotal, challenging aspect for future work. Future work should provide more publicly available experimental and synthetic data from physical modeling [11] and machine learning. We also plan to measure experimental data for the azeotropic distillation of n-butanol and water in future work.

References

1. N. M. Nor et al., 2020, Reviews in Chemical Engineering 36.4, 513–553, DOI: 10.1515/revce-2017-0069
2. F. Hartung et al., 2023, Chemie Ingenieur Technik, in press, DOI: 10.1002/cite.202200238
3. J. J. Downs and E. F. Vogel, 1993, Computers & Chemical Engineering 17.3, 245–255, DOI: 10.1016/0098-1354(93)80018-I.
4. Madakyaru, M., Kini, K.R, 2022, Int. j. inf. tecnol. 14, 3001–3010, DOI: 10.1007/s41870-022-01046-0

5. J. J. Downs, E. F. Vogel, 1993, Comput. Chem. Eng., 17 (3), 245–255. DOI: https://doi.org/10.1016/0098-1354(93)80018-I
6. J.J.Hopfield, 1982, PNAS, 79 (8) 2554-2558. DOI: https://doi.org/10.1073/pnas.79.8.2554
7. S.Hochreiter, J.Schmidhuber, 1997, Neural computation, MIT Press, 9(8), 1735–1780. DOI: https://doi.org/10.1162/neco.1997.9.8.1735
8. M. Soelch, et al., 2016, arXiv:1602.07109. DOI: https://doi.org/10.48550/arXiv.1602.07109
9. L. Ruff, et al., 2018, Proc. Mach. Learn. Res. 2018, 80, 4393–4402.
10. Lyzlova et al., 1979, Russian Journal of Physical Chemistry (Leningrad) 52.3 : 551-555.
11. E. Forte, F. Jirasek, M. Bortz, J. Burger, J. Vrabec, and H. Hasse, 2019, Chemie Ingenieur Technik, 91.3, 201–214. DOI: 10.1002/cite.201800056.
12. B. Zhou et al., 2019, in Proc. of the 28th Int. Joint Conf. on Artificial Intelligence, 4433–4439, DOI:https://doi.org/10.24963/ijcai.2019/616
13. P. Malhotra, L. Vig, G. Shroff, P. Agarwal, 2015, in Proc. of the 23rd European Symposium on Artificial Neural Networks, ES2015-56.
14. A. H. Mirza, S. Cosan, 2018, in Proc. of the 26th Signal Processing and Communications Applications Conf., IEEE, Piscataway,1–4. DOI: https://doi.org/10.1109/SIU.2018.8404689
15. H. Zhao et al., 2020, in Proc. of the 20th Int. Conf. on Data Mining, IEEE, Piscataway, NJ 2020, 841–850. DOI: https://doi.org/10.1109/ICDM50108.2020.00093
16. M. S. Elsayed et al., 2020, in Proc. of the 16th Symposium on QoS and Security for Wireless and Mobile Networks, 37–45. DOI: https://doi.org/10.1145/3416013.3426457
17. L. Shen, Z. Li, J. T. Kwok, 2020, in Proc. of the 34th Int. Conf. on Neural Information Processing Systems, Curran Associates, Red Hook, 13016–13026, Article 1092.
18. A. Geiger, et al., 2020, in Proc. of the 8th Int. Conf. on Big Data, IEEE, Piscataway, 33–43. DOI: https://doi.org/10.1109/BigData50022.2020.9378139
19. Z. Niu, K. Yu, X. Wu, 2020, Sensors, 20 (13), 3738. DOI: https://doi.org/10.3390/s20133738
20. X. Hua et al., 2022, arXiv:2202.04250, 2022.DOI: https://doi.org/10.48550/arXiv.2202.04250
21. C. Zhang et al., 2019, in Proc. of the 33th AAAI Conf. on Artificial Intelligence, AAAI Press, 1409–1416. DOI: https://doi.org/10.1609/aaai.-v33i01.33011409
22. H. Xu et al., 2018, in Proc. of the 27th Int. World Wide Web Conf. DOI: https://doi.org/10.1145/3178876.3185996
23. Jiehui Xu et al.,2022, ICLR, https://arxiv.org/abs/2110.02642
24. J. Audibert et al., 2020, in Proc. of the 26th Int. Conf. on Knowledge Discovery & Data Mining, 3395–3404. DOI: https://doi.org/10.1145/3394486.3403392
25. Y. Guo, W. Liao, Q. Wang, L. Yu, T. Ji, P. Li, 2018, Proc. Mach. Learn., 95, 97–112.
26. S. Kim et al., 2022, in Proc. of the 36thAAAI Conf. on Artificial Intelligence, 7194–7201. DOI: https://doi.org/10.1609/aaai.v36i7.20680
27. Y. Su et al., 2019, in Proc. of the 25th Int. Conf. on Knowledge Discovery & Data Mining, 2828–2837. DOI: https://doi.org/10.1145/3292500.3330672
28. J. Zhan et al., 2022, in Proc. of the 47th Int. Conf. on Acoustics, Speech, and Signal Processing, IEEE, 3568–3572. DOI: https://doi.org/10.1109/ICASSP43922.2022.9747274
29. D. Li et al., 2019, in Proc. of the 28th Int. Conf. on Artificial Neural Networks, Springer, 703–716. DOI: https://doi.org/10.1007/978-3-030-30490-4_56
30. L. Li, J. Yan, H. Wang, Y. Jin, 2021, IEEE Trans. Neural Networks Learn.Syst., 32 (3), 1177–1191. DOI: https://doi.org/10.1109/TNNLS.2020.2980749
31. M. Thill, W. Konen, T. Baeck, 2020, in Proc. of the 9th Int. Conf. on Bioinspired Methods and Their Applications, 161–173. DOI: https://doi.org/10.1007/978-3-030-63710-1_13
32. A. C. Rieth et al., 2017, Additional Tennessee Eastman Process Simulation Data for Anomaly Detection Evaluation, Harvard Dataverse, 2017. DOI: https://doi.org/10.7910/DVN/6C3JR1
33. Ferre, A., Voggenreiter, J., Tönges, Y. et al., 2021, MTZ Worldw 82, 26–31, DOI: https://doi.org/10.1007/s38313-021-0639-x

ESCAPE-34 PSE-2024
European Symposium on Computer Aided Process Engineering
&
Process Systems Engineering

Flavio Manenti, Gintaras V. Reklaitis (Eds.), Book of Abstract of the 34th European Symposium on Computer Aided Process Engineering / 15th International Symposium on Process Systems Engineering (ESCAPE34/PSE24), June 2-6, 2024, Florence, Italy.

A Machine Learning Method to Extract Key Policy Decisions from Energy Transition Scenarios under Uncertainty

Stefano Moret,[a,*] Florian Joseph Baader,[a] Wolfram Wiesemann,[b] Iain Staffell[c] and André Bardow[a]

[a]*Energy & Process Systems Engineering, Department of Mechanical and Process Engineering, ETH Zürich, 8092 Zürich, Switzerland*
[b]*Centre for Environmental Policy, Imperial College London, London, UK*
[c]*Imperial College Business School, Imperial College London, London, UK*
morets@ethz.ch

Abstract

Uncertainties in input parameters, such as fuel prices and energy demands, often lead energy modelers to present large sets of scenarios that are difficult to interpret. Leveraging decision trees, a popular machine-learning technique, we translate the complexity of energy transition studies under uncertainty into a small set of key decisions. Application of our method to an Integrated Assessment Model under uncertainty shows that the global energy transition is primarily determined by choices on heating and industry electrification. Our replicable framework reduces the vast amount of plausible energy system scenarios to a few interpretable storylines and unveils the most important trade-offs in the energy transition.

Keywords: energy planning, uncertainty, machine learning, decision-making.

1. Introduction

Despite the stark reality of climate change as well as the evidence that immediate action is beneficial over a "wait-and-see" strategy, the Intergovernmental Panel on Climate Change's (IPCC) latest report warns that "the pace and scale of what has been done so far, and current plans [to tackle climate change], are insufficient" (IPCC, 2023). This indecisiveness in policy deployment can, at least in part, be attributed to the extreme uncertainties affecting long-term energy planning and decision-making.

Energy system optimization models (ESOMs) can help unravel this complexity and assist policymakers in defining *quantitative* energy transition pathways. While, historically, ESOM studies have focused on generating a single optimal solution, evidence that models' assumptions and input data – such as fuel prices, demands, interest rates, etc. – are highly uncertain (Moret et al., 2017) motivated modelers to consider uncertainty.

However, uncertainty studies often generate hundreds of solutions that are challenging for decision-makers to interpret and act upon (Pickering et al., 2022).

We present a machine learning method to streamline hundreds or thousands of energy system scenarios from uncertainty studies to a few interpretable storylines. The storylines yield *qualitative* descriptions of energy system configurations and are described by urgent policy decisions. Specifically, we show that training decision trees on key outputs of interest of ESOMs allows translating many quantitative energy transition scenarios into a small number of storylines. These storylines are determined by a few policy decisions and, thus, are accessible and interpretable to a broader public.

2. Methods

First, different energy system scenarios are generated by solving a mathematical optimization problem under uncertainty. Given a probability distribution for each uncertain parameter θ, sampling – often Monte Carlo sampling – is performed to obtain N possible realizations of the uncertain parameter vector $\boldsymbol{\theta}$. The energy model is run for each combination of input parameters $\boldsymbol{\theta_i}, i = \{1, \ldots, N\}$, resulting in N energy scenarios. Second, k-means clustering (Hastie et al., 2009) is performed to group these N different scenarios into k clusters (where $k \ll N$) with respect to m outputs of interest $\mathbf{y}$, corresponding to high-level outputs needed to inform decision-makers. k-means clustering is performed using the Python package *sklearn.cluster.KMeans* with default settings, and the number of clusters k is selected using the "elbow method" (Ketchen and Shook, 1996).
Third, a decision tree (Hastie et al., 2009) is trained to identify the key decisions and their effects on the solution space. Decision trees are a supervised machine learning method and, hence, are trained on labeled data. In our case, the labeled data are the N energy system scenarios $\boldsymbol{y_i}$ and the labels $\boldsymbol{c}$ are the cluster numbers assigned by the previous step. The decision tree learns to predict the label c_i given the energy system scenario $\boldsymbol{y_i}$. We limit the number of leaves of the tree to the number of clusters k as, in our numerical experiments, a tree with a number of leaves equal to the number of clusters has high prediction accuracy, i.e., 99% of the data points are correctly assigned to their clusters. Finally, we re-order the energy system scenarios to k clusters according to the rules of the decision tree, i.e., the few points that are predicted wrongly by the decision tree are re-assigned to the other clusters accordingly, making the clustering more interpretable.

3. Results

We apply our method to the global decarbonization pathways under uncertainty studied by Panos et al. (2023), who recently presented the first Monte-Carlo assessment of an integrated assessment model (IAM). Specifically, their study presents 1000 possible global decarbonization pathways generated by sampling 18 uncertain parameters. By applying our method to their published dataset, these 1000 scenarios can be summarized by two key policy decisions: (i) electrification of heating and (ii) electrification of industry (Figure 1). The resulting decision tree has only $k = 3$ leaves, corresponding to three storylines for the global energy transition, illustrating the consequences of each decision. At the root node lies the entire decision space with 1000 scenarios, as presented by Panos et al. (2023), with the radar plots and the open locks indicating the large ranges of variations in the results.

The first decision differentiates between scenarios with low and high shares of electric heating and thereby splits the set of solutions: A low share of electric heating is found to also imply low non-fossil transport and minimal electrification of industry. Moreover, the deployment of renewables is low. On the other side of the tree with a high share of electric heating, the share of non-fossil transport must also be high. As the next key decision, the tree further differentiates between solutions with a low and a high electrification of industry. A high electrification of industry then implies a high deployment of renewables and maximum electrification of heating. The extent to which the resulting storylines rely on renewable energy and sector coupling increases from left to right in Figure 1. Overall, our method breaks down the 1000 Monte Carlo results into a decision- tree with only two key decisions, translating the quantitative output of the IAM study into three storylines corresponding to three actionable policies.

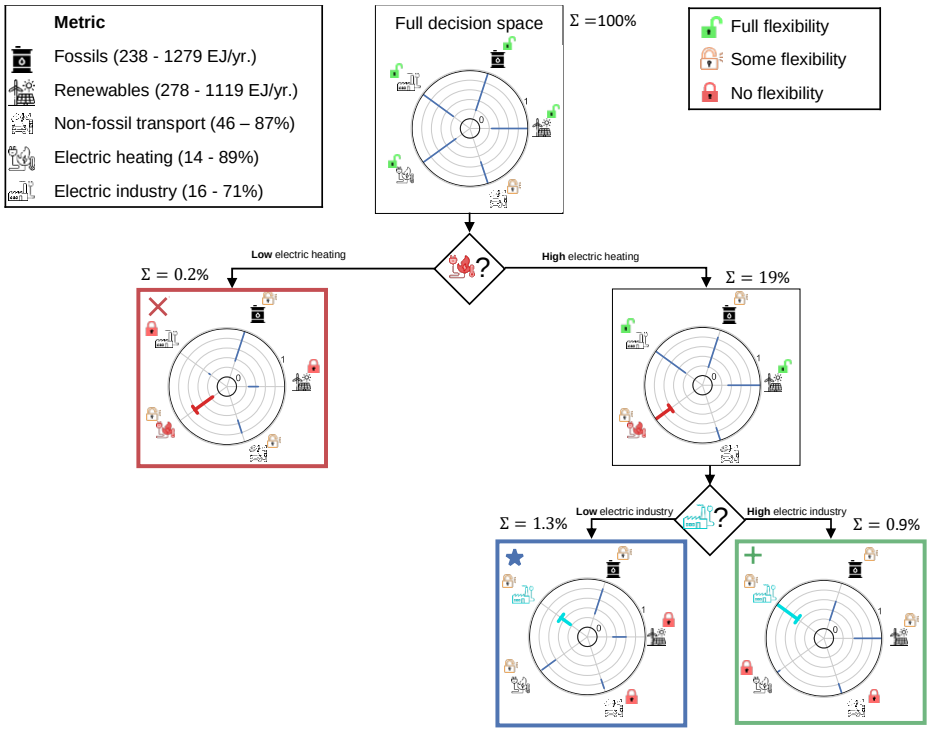

Figure 1: Decision tree translating 1000 scenarios for the global energy transition in 2100 from (Panos et al., 2023) into two key decisions (electrification of heating and industry) along five outputs of interest. The axes of the radar plots are normalized on the range of each output of interest, while the locks indicate the level of flexibility. The volume of the decision space at each node of the tree is expressed by Σ.

4. Conclusions

We present a machine learning method to extract key policy decisions from energy transition scenarios under uncertainty. Application to the global energy transition using an Integrated Assessment Model demonstrates that our method reduces the vast decision

space to a small number of interpretable storylines and critical decisions that must be made to enable this transition. Additionally, we propose a new way to visualize these choices into decision trees, effectively prioritizing decisions and associating each choice with its implied consequences. This analysis unveils the most important interconnection and trade-offs between key policy decisions. These trade-offs (which can be thought of as pivotal policy decisions) are typically hidden both to the user and even to the creators of scenarios, as the volumes of results and high-dimensional solution space obscure 'the wood for the trees'. By combining the strengths of energy systems models and their outputs with the simplicity and clarity of storylines, our tool empowers decision-makers to quickly uncover actionable insights.

Acknowledgments

S.M. acknowledges support from the Swiss National Science Foundation under Grant No. PZ00P2_202117. F.B. and A.B. acknowledge funding by the Swiss Federal Office of Energy's SWEET program as part of the project PATHFNDR.

References

T. Hastie, R. Tibshirani, J. Friedman. The elements of statistical learning: Data mining, inference, and prediction. Springer, 2009

Intergovernmental Panel on Climate Change (IPCC). AR6 Synthesis Report: Climate Change 2023. Technical report, Intergovernmental Panel on Climate Change (IPCC), 2023.

D. J. Ketchen, C. L. Shook. The application of cluster analysis in strategic management research: An analysis and critique. Strategic management journal 17, 441–458, 1996.

S. Moret, V. Codina Gironès, M. Bierlaire, F. Maréchal. Characterization of input uncertainties in strategic energy planning models. Applied Energy 202, 597–617, 2017.

E. Panos, J. Glynn, S. Kypreos, A. Lehtilä, X. Yue, B. Ó Gallachóir, D. Daniels, H. Dai. Deep decarbonisation pathways of the energy system in times of unprecedented uncertainty in the energy sector. Energy Policy 180, 113642, 2023.

B. Pickering, F. Lombardi, S. Pfenninger. Diversity of options to eliminate fossil fuels and reach carbon neutrality across the entire European energy system. Joule 6,1253–1276, 2022.

ESCAPE-34 PSE-2024
European Symposium on Computer Aided Process Engineering
&
Process Systems Engineering

Flavio Manenti, Gintaras V. Reklaitis (Eds.), Book of Abstract of the 34th European Symposium on Computer Aided Process Engineering / 15th International Symposium on Process Systems Engineering (ESCAPE34/PSE24), June 2-6, 2024, Florence, Italy.

The predictive power of NLP models on Perovskite solar cells: BERTforPSC

Naveen Bhati[a,*], Mohammad Khaja Nazeeruddin[b], and François Maréchal[a]

[a]*Industrial Process and Energy Systems Engineering, Ecole Polytechnique Fedérale de Lausanne, Sion, 1951, Switzerland*

[b]*Group for Molecular Engineering of Functional Materials, Institute of Chemical Sciences and Engineering, Ecole Polytechnique Fedérale de Lausanne, Sion, 1951*

**naveen.bhati@epfl.ch*

Abstract

With the advent of ChatGPT, natural language processing (NLP) models have gained tremendous interest from the research community and have been applied to a plethora of scientific domains like batteries, pharmaceuticals, recycling plastics, etc., to obtain insights from the existing corpus of literature, and thus making the process of reading, analyzing, interpreting, and reporting the results shorter and faster. However, the applications of such models are still limited to a few fields in the past, and perovskite solar cells (PSCs) are among them. Recently, PSCs power conversion efficiency climbed the mark of 26.1% in a single junction and 33.7% in silicon/perovskite tandem solar cells, putting them in the leading position of next-generation solar cells. However, optimizing decision variables in terms of materials selection and process conditions requires analysis of the huge database of experiments to draw better insights to make them market-competitive in terms of cost and environmental impacts. In this article, authors have used two state-of-the-art NLP models, BERT and SciBERT, to analyze the corpus of stability data based on experimental datasets and further normalised based on storage and testing conditions to visualize the trends and compare their performance with regression-based models. The insights obtained while employing such models with different kinds of datasets where both alpha-numeric keys are presented as model features are also offered, highlighting the limitations of such models. The efficiency and effectiveness of such models in interpreting the causal relationships and predicting the trends will help in utilizing such models for tackling the challenges of optimizing material-process design problems (MPDP) with available data from literature.

Keywords: Natural language processing, BERT, Machine learning, Perovskite solar cells

1. Introduction

Perovskite solar cells have presented a unique opportunity in the field of PV technologies to have more control over the different aspects of fabrication including the techniques or equipment employed, process parameters used, and materials selection (Huang, 2020) which is not the case with many existing 1st and 2nd generation PV technologies (Singh et

al., 2021). However, this paradox of choice also results in using more nuanced tools and techniques to optimize the overall production of PSCs which not only meets the requirements in terms of efficiency and stability but also emphasizes the design of environmental-friendly and sustainable PV technology for the future (Yoo et al., 2022). Given these possibilities, the amount of experimental work carried out has also presented an opportunity to use state-of-the-art techniques for finding better overall solutions from the myriad of existing possibilities (Jacobsson et al., 2022).

Machine learning and artificial intelligence lie at the forefront of these new techniques that are now used in almost all domains (Sarker et al., 2021). Plenty of work has also been carried out in the domain of perovskite solar cells where the focus of application has varied from individual layer-level characteristics (Liu Y. et al, 2022) to cell (Liu Z. et al, 2022) and module-level characteristics (Ramirez et al., 2023). Lu et al. (2021) and Hu et el. (2022) have discussed the trends in efficiency, bandgaps, V_{oc}, $I_{sc,}$ and stability of PSCs using different kinds of machine learning techniques. However, recently with the advent of transformer-based models, many advanced natural language processing-based algorithms have made a mark in the field of ML/AI-based analysis. BERT (Devlin et al., 2018), XLNet (Yang et al, 2019), and SciBERT (Beltagy et al., 2019) are all different variations of the NLP models based on transformer architecture. ChatGPT (OpenAI) and BARD are among the most advanced ones with the number of parameters greater than one billion. Given these tools at hand, it is important to analyze the effectiveness in dealing with scientific data, especially from the field of material science and optoelectronics. However, since the earlier models are mostly trained on web text and general science it is difficult to expect their high performance on domain-specific tasks (Xie et al., 2023) which is partly because of their limited vocabulary and also lack of embeddings for such specific data.

Here, the NLP models were fine-tuned for the regression tasks of predicting the stability of PSCs by enhancing the vocabulary size of these models with existing perovskite solar cells FAIR (findable, accessible, interoperable, and reusable) dataset (Jacobsson et al., 2022) and are compared with existing regression models. Finally, hyperparameter optimization for all models was carried out to realize the best performance on the dataset.

2. Data and models

In the first part of the article, existing machine learning techniques both linear and non-linear are explored to set the base level of prediction capabilities of these techniques and provide a baseline for comparing the NLP models like BERT. Also, the objective is to predict the continuous values of stability and therefore regression-based analysis was carried out using these models.

2.1. Data cleaning and processing

The data for PSC stability was used based on the analysis presented by Zhang et al. (2022) for the FAIR database which has more than 42000 data points from the experiments and contain data related to the active materials (embedded materials), assisting materials, additives and techniques used for fabricating different layers along with the process parameters for certain cases. Thus, it can be assumed that data for the present analysis is a simulated data based on experiment with physics-based modeling to account for the variations for the storage conditions like temperature, humidity and light exposure. This original dataset contains around 7400 datapoints from 2013 to 2021. Afterwards, the data is cleaned for missing stability values and only data after 2017 is chosen to avoid the bias from the earlier experiments in the field. Also, the data was filtered to represent the most

commonly used perovskite thus avoiding sparse data depending on the light intensity, simulator class, perovskite-inspired structure, perovskite ABX3 structure, single crystal, and cell architecture. In the next step, cleaning of data was based on different layers of the stack, their deposition procedure, the solvent used, synthesis atmosphere, ions composition for perovskite, and additives used such that they represent most of the data. This cleaning procedure is adapted to improve the generalization of models as in other cases it will lead to very high dimensional data. Based on this finally we had 2783 data points which were then cleaned for JV measurement data (missing values for PCE, V_{oc}, $I_{sc,}$ and FF). However, this dataset still has some missing values for certain columns and different amputation strategies were used to treat them while building ML models on top of them. Before that, one-hot encoding strategy is used to treat the categorical data as most of the data exists in terms of the name of elements, compounds, or techniques. In terms of data engineering, a few new columns were also created taking into account the annealing process characteristics like different annealing temperatures, maximum annealing temperature, and total energy absorbed during annealing per unit mass and specific heat as it is related to the phase conversion and might have a good effect on stability. In the end, we have 444 features for our dataset including JV measurement characteristics and stability (TS80 (based on stabilized efficiency at the end of the burn-in-region, Zhang et al. (2022))).

While checking the quality of the dataset, it was found that there were several outliers in terms of stability which were cleaned using the z-score criteria of 3. Even after outliers removal, the data of stability was highly skewed on the right (positive skewed, skewness =9.12) and therefore log transformation was applied to make the data look more normally distributed (skewness=-0.07) which performs better with ML techniques. Also, the cell area values were imputed with the median values. Moreover, the perovskite additives and HTL additives columns were imputed with 'undoped' value. The columns with no variance are removed at this point. Afterward, stratification splitting of data was carried out using the log-transformed stability values so that training (80%) and test data (20%) have values from all kinds of stability regions. Figure 1 shows the variation in stability values with different kind of layers i.e., ETL and HTL in the overall stack.

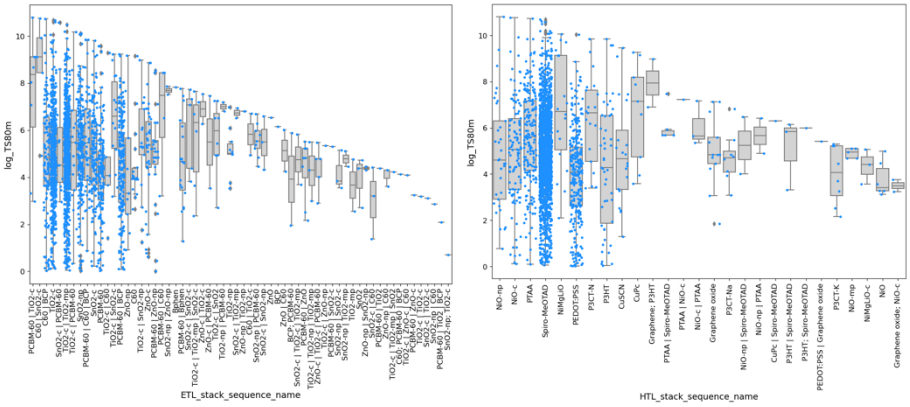

Figure 1: Range of stability values with different a) ETLs and b) HTLs

It shows the range of values possible for any given type of material/stack depending on the other features of the overall cell. During the Pearson correlation check between the features of the dataset, it was found that log_TS80m is highly correlated to TS80 which is basically some kind of direct indication of stability. However, in real-life scenarios, we

would not have access to this data as this is something we would like to predict and therefore all features giving a direct measure of stability are removed. All other features have a lower than 0.22 correlation with the target variable i.e., log_TS80m. A pipeline with an imputation strategy for numerical values using median and standard scaler and one-hot encoding transformation for categorical attributes was used to treat the dataset at this point. Based on these transformations, the final data has 425 columns or features.

2.2. Classical Machine learning models

For ML modeling, initially, a screening is made on a set of 18 models without going for hyperparameter optimization using their default settings. Once models with relatively better performance were found, complete hyperparameter optimization was carried out either using GridSearchCV or RandomSearchCV depending upon the size of the search space to avoid excessive time consumption. For evaluating the models, two metrics were used, RMSE (root mean squared error) and R2 values (coefficient of determination). The models included in the first check included linear regression, decision tree regressor (DTR), random forest regressor (RF), support vector regression (SVM), KNeighbours regressor (KNN), extreme gradient boost regressor (XGB), ridge regressor (RR), lasso regressor, Bayesian regressor (BR), elastic net regressor (ELN), gradient boost regressor (GBR), Adaboost regressor (ADA), multi-layer perceptron regressor (MLP, neural networks), gaussian process regressor (GPR), extra trees regressor (ETR), kernel ridge regressor (KRR), and light gradient boost regressor (LGBM). Data was adapted accordingly to use these different kinds of algorithms/models. Finally, out of the 18 models only 7 were selected for hyperparameter tuning. These models include RF, SVM, XGB, ELN, GPR, ETR, and LGBM. The cross-validation was inherently performed using 5-fold CV in both these hyperparameter tuning methods. The performance of the models on the training and test dataset is shown in Figure 2 for both RMSE and R2 scoring metrics where RF model shows (the best performance in terms of both metrics without overfitting the training dataset (i.e., difference between the performance on 2 datasets is almost same). Here, the RMSE values are based on scaled log-transformed stability data.

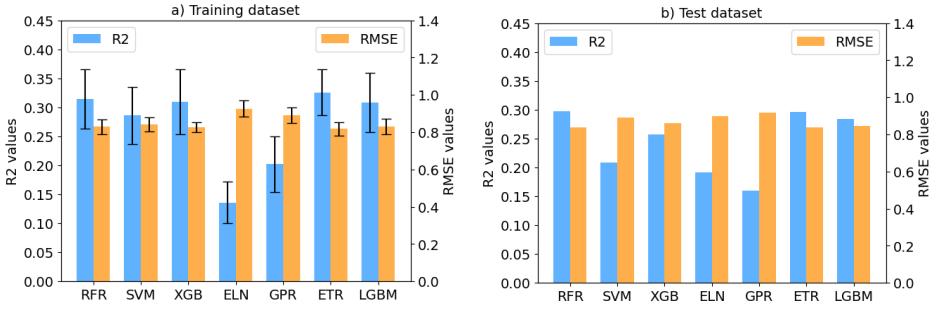

Figure 2: Classical models performance (R2 and RMSE) on a) training dataset and b) test dataset

Based on the best model, the importance of various features was visualized using the recursive elimination method which recursively eliminates the least important features in the dataset. Figure 3 b) shows the relative importance of features where the highest contribution are from the JV measurements followed by energy absorbed, cell area, PSC thickness and maximum annealing temperature. Figure 3 c) shows SHAP analysis to see the nature of effect of these features where it was found that Voc, FF, PCE, Jsc are all positively impacting the stability. Also, the descriptors introduced after feature engineering like energy absorbed and maximum temperature during perovskite annealing are found to have positive impacts on the PSC stability performance.

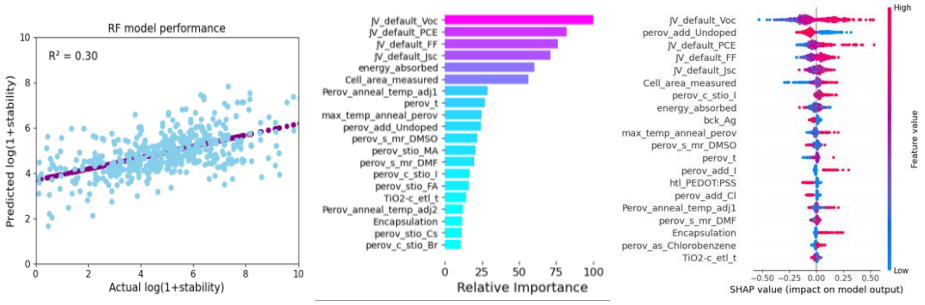

Figure 3: a) RF model performance on test data, b) relative feature importance, and c) SHAP analysis for RF model

2.3. NLP Machine learning models

In this section, two state-of-the-art models, BERT (both cased and uncased) and its variant SciBERT were used to see the performance on the task of stability prediction. In this case, since the models are based on transformer architecture, the starting dataset needs to be treated such that it can be used with these models. As most of the features in the dataset are categorical in nature, they can be directly used without any transformations as they are from the natural language domain. However, the numerical features due to a huge range of scale have to be treated in a manner that it doesn't explode the vocabulary of the models while at the same time providing enough context for creating meaningful embeddings during the training process. To overcome this challenge, the numerical data was converted to scientific form with one decimal precision which significantly reduced the vocab size for all the numbers involved in the dataset. Afterward, the training data and test data (80:20) were created in a similar manner as for above-discussed regression models with log transformation of the target variable. During training both R2 and RMSE metrics were evaluated, however, improvements were made using R2 metrics. Hyperparameter optimization was carried out for learning rates (lr) and batch sizes (B) in grid search manner for BERT variants and random manner for SciBERT. Finally, the best models were selected based on their performance of the test data. With SciBERT, the best performance was found with uncased variant with R2 value as 0.22 (B=64, lr=2e-5) on test data. The tokenization based on SciBERT is shown in the figure below where color of the words are indicative of the relative scores assigned to them using integrated gradient method. For cased and uncased BERT, the best test performances (R2 value) were 0.225 (B=64, lr=2e-5) and 0.23 (B=64, lr=2e-5) which are lower a bit lower than

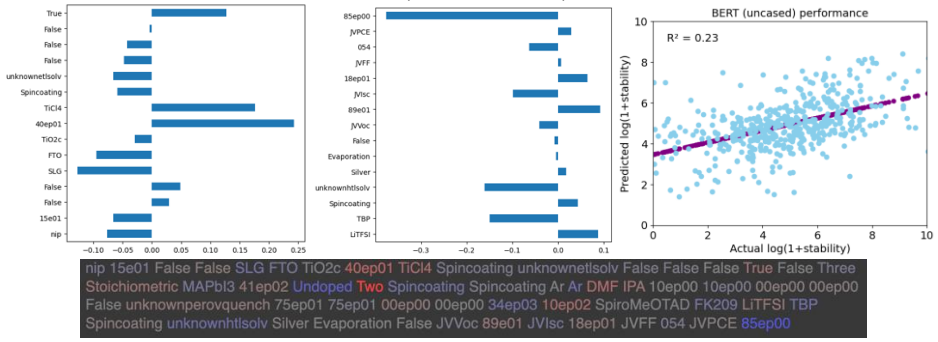

Figure 4: BERT results for relative scores of a) first 15 words b) last 15 words c) test data fitting and d) entire sentence

classical regression models (Figure 3 a)). Moreover, for analyses of the features, scores for each word based on the integrated gradients method are used as shown in Figure 4 a) and b) where the color of words in the sentence corresponds to their relative scores in the final prediction (Fig. 5).

3. Conclusions

Here, the authors have shown how new ML techniques can be used for solving the most pressing challenges of the PSCs and performed an exhaustive study on the different classical regression-based models and state-of-the-art BERT model performance on the dataset of PSC efficiency. It is shown that NLP models can be used to infer information and trends from existing datasets that are already curated rather than training them on a huge corpus of raw data from the literature which can be time-consuming and might have plenty of unnecessary information. Moreover, training on such structured data also allows us to understand and leverage their abilities on datasets created based on critical insights and domain expertise. However, more efforts have to be made on the training part of such models to improve their overall performance in comparison to classical models.

References

OpenAI. (2023). *ChatGPT* [Large language model]. https://chat.openai.com

BARD (2023). Google AI, https://bard.google.com/chat

Zhang, Z., Wang, H., Jacobsson, T.J. and Luo, J., 2022. Big data driven perovskite solar cell stability analysis.

Huang, Y., Liu, T., Liang, C., Xia, J., Li, D., Zhang, H., Amini, A., Xing, G. and Cheng, C., 2020. Towards simplifying the device structure of high-performance perovskite solar cells.

Singh, B.P., Goyal, S.K. and Kumar, P., 2021. Solar PV cell materials and technologies: Analyzing the recent developments. Materials Today: Proceedings, 43, pp.2843-2849

Yoo, J.J., Shin, S.S. and Seo, J., 2022. Toward efficient perovskite solar cells: progress, strategies, and perspectives.

Jacobsson, T.J., Hultqvist, A., García-Fernández, A., Anand, A., Al-Ashouri, A., Hagfeldt, A., Crovetto, A., Abate, A., Ricciardulli, A.G., Vijayan, A. and Kulkarni, A., 2022. "An open-access database and analysis tool for perovskite solar cells based on the FAIR data principles."

Sarker, I.H., 2021. Machine Learning: Algorithms, Real-World Applications and Research Directions.

Lu, Y., Wei, D., Liu, W., Meng, J., Huo, X., Zhang, Y., Liang, Z., Qiao, B., Zhao, S., Song, D. and Xu, Z., 2023. Predicting the device performance of the perovskite solar cells from the experimental parameters through machine learning of existing experimental results.

Liu, Z., Rolston, N., Flick, A.C., Colburn, T.W., Ren, Z., Dauskardt, R.H. and Buonassisi, T., 2022. Machine learning with knowledge constraints for process optimization of open-air perovskite solar cell manufacturing.

Liu, Y., Yan, W., Han, S., Zhu, H., Tu, Y., Guan, L. and Tan, X., 2022. How machine learning predicts and explains the performance of perovskite solar cells.

Hu, Y., H., X., Z., L., Z., T., Y., J., J., B., M., Y., D., X., Z., L., W., J. and C., B., 2022. Machine-Learning Modeling for Ultra-Stable High-Efficiency Perovskite Solar Cells.

Ramírez, E.A., V., J.P., F., A., M., J.F., B., R. and J., F., 2023. Blade-Coated Solar Minimodules of Homogeneous Perovskite Films Achieved by an Air Knife Design and a Machine Learning-Based Optimization.

Xie, T., Wa, Y., H. W., Z., Y., L., Y., L., Q., Wang, S., Kit, C., Grazian, C. and Hoex, B., 2023. Large Language Models as Master Key: Unlocking the Secrets of Materials Science with GPT.

Beltagy, I., L, K. and C., A., 2019. SciBERT: A pretrained language model for scientific text.

Yang, Z., D., Z., Y., Y., C., J., S., R.R. and L., Q.V., 2019. Xlnet: Generalized autoregressive pretraining for language understanding.

Devlin, J., C., M.W., L., K. and T., K., 2018. Bert: Pre-training of deep bidirectional transformers for language understanding.

ESCAPE-34 PSE-2024
European Symposium on Computer Aided Process Engineering
&
Process Systems Engineering

Flavio Manenti, Gintaras V. Reklaitis (Eds.), Book of Abstract of the 34th European Symposium on Computer Aided Process Engineering / 15th International Symposium on Process Systems Engineering (ESCAPE34/PSE24), June 2-6, 2024, Florence, Italy.

Identifying Important Molecular Fragments for Property Predictions by Graph Neural Networks With Explainable AI

Jan G. Rittig,[a] Dominik Goldstein,[a] Manuel Dahmen,[b] Alexander Mitsos[c,a,b]

[a]*RWTH Aachen University, Process Systems Engineering (AVT.SVT), Aachen, Germany*
[b]*Forschungszentrum Jülich GmbH, Institute for Energy and Climate Research IEK-10: Energy Systems Engineering, Jülich, Germany*
[c]*JARA-CSD, Aachen, Germany*
amitsos@alum.mit.edu

Abstract

Graph neural networks (GNNs) have shown great potential for predicting molecular properties. We herein utilize explainable artificial intelligence (XAI) methods to identify molecular fragments, e.g., functional groups, decisive for the GNN prediction of a particular property. We consider both pure component and mixture properties. We systematically search for molecular fragments that are frequently marked as important. We find that the identified molecular fragments comply with available chemical knowledge, therefore providing valuable insights into molecular structure-property relationships.

Keywords: machine learning, molecular modeling, structure-property relationships

1. Introduction

Explainable artificial intelligence (XAI) provides promising methods for extracting chemical knowledge from molecular property data. Machine learning methods, particularly graph neural networks (GNNs), have recently been applied for predicting a variety of molecular properties that are relevant to process systems engineering such as fuel ignition qualities (Schweidtmann et al., 2020), activity coefficients (Sanchez Medina et al., 2023; Rittig et al., 2023), and solubility (Vermeire et al., 2022). While the developed GNNs achieve high prediction accuracies, they typically do not provide explanations for the predicted property values due to their black-box characteristic. Therefore, gaining insight into property predictions made by GNNs is of high interest and is actively investigated, cf. overviews in (Yuan et al, 2022; Wellawatte et al., 2023), with new explainability methods emerging from the field of XAI. However, the focus in molecular applications to date has primarily been on explaining predicted property values for individual molecules, e.g., which molecular fragment of a specific molecule is most influential to the corresponding prediction. Herein, we are also interested in molecular fragments that are frequently marked as important in a diverse collection of molecules.

Thereby, we identify generalizable relations of the molecular structure to a property, i.e., structure-property relationships, from molecular property predictions by GNNs.

2. Explainable AI for Graph Neural Networks

GNNs learn properties directly from a graph representation of molecules, with atoms as nodes and bonds as edges, by encoding the molecular graph through convolutional layers into a molecular fingerprint vector which is then mapped to the property of interest. To find explanations for GNN predictions, we herein investigate two recently introduced XAI methods, the GNNExplainer (Ying et al, 2019) and the Molecular Model Agnostic Counterfactual Explanations (MMACE) method (Wellawatte et al, 2022). The GNNExplainer marks atoms and bonds that are influential for the prediction. The MMACE identifies minimal structural changes that exert a large impact on the prediction. To systematically identify structure-property relationships, we apply the two XAI methods to the molecules in the respective training and testing data sets of the GNN and search for frequently occurring molecular fragments that have a high impact on the predicted property values. Specifically, we aim at the explainability of two of our previously developed GNNs. First, we investigate a GNN for predicting the research octane number (RON) of pure components (Schweidtmann et al., 2020), i.e., a well-established measure for rating the knock resistance of a fuel. Secondly, we consider a GNN for mixture property prediction by the example of activity coefficients of solutes in ionic liquids (Rittig et al., 2023).

3. Results and Discussion

Fig. 1 shows the top molecular fragments identified by the MMACE. On the left, the most occuring molecular fragments are illustrated that lead to increases in RON when added (green) or removed (red) to a fuel molecule. Analogously, on the right, the molecular fragments are shown that result in a higher activity coefficient in ionic liquids on addition to or removal from a solute. In both cases similar structure-property relationships are identified by the GNNExplainer method (not shown here).

For the knock resistance (Fig. 1, left), the MMACE suggests that decreasing the carbon chain length results in a higher RON, which complies with chemical intuition. Likewise, the addition of hydroxyl and carbonyl groups is identified to yield a higher RON. Both groups are well-known to exert strong effects on fuel autoignition and thus knock resistance.

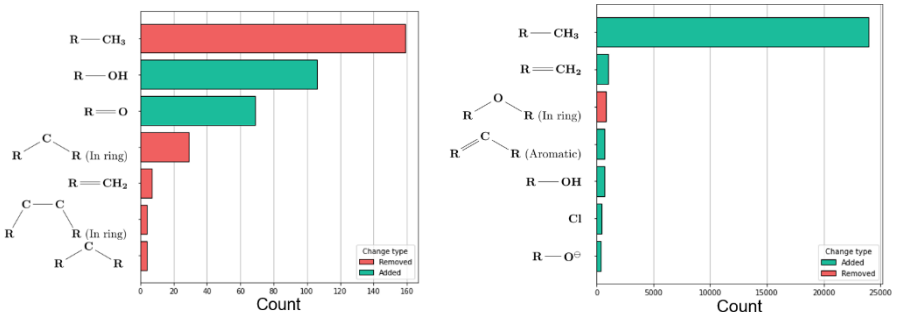

Figure 1. Molecular fragments identified by MMACE resulting in higher predicted values for the knock resistance (left) and the activity coefficient in ionic liquids (right).

In case of the activity coefficient (Fig. 1, right), the polarity of the molecular fragments added to or removed from the solute is recognized to be of high importance for the GNN

predictions. For example, adding non-polar groups, such as methyl and methylene groups, yields higher activity coefficients. Since the polarity is one of the main influences on the type and strength of intermolecular forces (Pfennig, 2004), it is directly related to the activity coefficient and has also been included as input descriptor to activity coefficient prediction models, cf. (Lazzaroni et al., 2005; Sanchez Medina et al., 2023).

We thus find that XAI allows us to identify molecular fragments that provide meaningful chemical insights into structure-property relationships in case of both applications.

4. Conclusion

We utilize XAI methods to extract chemical insights about structure-property relationships from GNNs for molecular property prediction, herein, for research octane number and activity coefficient prediction. We find that the identified molecular fragments comply with available structure-property knowledge. For example, hydroxyl and carbonyl groups as well as increasing lengths of carbons chains are known to exert strong effects on fuel knock resistance. Likewise, for the activity coefficient predictions, the polarity of substructures is known to have a high importance. The systematic explanation of structure-property relationships learned by GNNs thus successfully relates to chemical knowledge and provides promising insights for future investigations. As a next step, it would be interesting to consider interactions of multiple molecular fragments.

References

M. D. Boot, M. Tian, E. J. Hensen, & S. M. Sarathy, 2017, Impact of fuel molecular structure on auto-ignition behavior – Design rules for future high performance gasolines. Prog. Energy Combust. Sci., 60, 1-25.

M. J. Lazzaroni, D. Bush, C. A. Eckert, T. C. Frank, S. Gupta, & J. D. Olson, 2005, Revision of MOSCED parameters and extension to solid solubility calculations. Ind. Eng. Chem. Res., 44(11), 4075–4083.

F. vom Lehn, B. Brosius, R. Broda, L. Cai, & H. Pitsch, 2020, Using machine learning with target-specific feature sets for structure-property relationship modeling of octane numbers and octane sensitivity. Fuel, 281, 118772.

A. Pfennig, 2004, Thermodynamik der Gemische, Springer Berlin, Heidelberg, Germany.

J. G. Rittig, K. Ben Hicham, A. M. Schweidtmann, M. Dahmen, & A. Mitsos, 2023, Graph neural networks for temperature-dependent activity coefficient prediction of solutes in ionic liquids. Comput. Chem. Eng., 171, 108153.

E.I. Sanchez Medina, S. Linke, M. Stoll, & K. Sundmacher, 2023, Gibbs–Helmholtz graph neural network: capturing the temperature dependency of activity coefficients at infinite dilution. Digital Discovery, 2, 781–798.

A.M. Schweidtmann, J. G. Rittig, A König, M. Grohe, A. Mitsos, & M. Dahmen, 2020, Graph neural networks for prediction of fuel ignition quality, Energy Fuels, 34(9), 11395-11407

F. H. Vermeire, Y. Chung, & W. H.Green, 2022, Predicting solubility limits of organic solutes for a wide range of solvents and temperatures, J. Am. Chem. Soc., 144(24), 10785-10797.

G. P. Wellawatte, A. Seshadri, & A. D. White, 2022, Model agnostic generation of counterfactual explanations for molecules. Chem. Sci., 13(13), 3697-3705.

G. P. Wellawatte, H. A. Gandhi, A. Seshadri & A. D. White, 2023, A perspective on explanations of molecular prediction models, J. Chem. Theory Comput., 19(8), 2149-2160.

Z. Ying, D. Bourgeois, J. You, M. Zitnik, & J. Leskovec, 2019, GNNExplainer: Generating explanations for graph neural networks. NeurIPS, 32.

H. Yuan, H. Yu, S. Gui, & S, Ji, 2022, Explainability in graph neural networks: A taxonomic survey. IEEE Trans. Pattern Anal. Mach. Intell., 45(5), 5782-5799.

ESCAPE-34 PSE-2024
European Symposium on Computer Aided Process Engineering
&
Process Systems Engineering

Flavio Manenti, Gintaras V. Reklaitis (Eds.), Book of Abstract of the 34th European Symposium on Computer Aided Process Engineering / 15th International Symposium on Process Systems Engineering (ESCAPE34/PSE24), June 2-6, 2024, Florence, Italy.

Categorical Bayesian Optimization for Indirect Hard Model Selection

Luise F. Kaven[a], Daniel Jungen[a], Jan G. Rittig[a], Alexander Mitsos[a,b,*]

[a]*RWTH Aachen University, Process Systems Engineering (AVT.SVT), Aachen, Germany*
[b]*JARA-SOFT, Aachen, Germany*
amitsos@alum.mit.edu

Abstract

Model-based evaluation of Raman spectroscopy data is routinely conducted by use of indirect hard modeling (IHM). To develop a suitable IHM for a given analyte system, multiple decisions regarding the model settings must be made. These decisions require expert knowledge and exhaustive model development to identify the best suitable IHM for the analyte system. Herein, we propose the application of Bayesian optimization (BO) for the selection of most suitable settings for IHM development. We apply the BO algorithm available in the open-source software package BoFire to support the decision-making in the IHM development process. The results indicate that by leveraging BO, the IHM generation can be significantly accelerated and IHM performance can be exploited.

Keywords: Bayesian optimization, categorical variables, Raman spectroscopy.

1. Introduction

Indirect hard modelling (IHM) constitutes a physically-supported approach that predicts concentrations from spectral data such as near infrared (NIR) or Raman spectroscopy (Alsmeyer et al., 2004). The IHM method represents a multivariate regression technique, enabling concentration predictions of mixtures comprising overlapping component peaks (Alsmeyer et al., 2004, Kriesten et al., 2008). Meanwhile, the method relies on small calibration data sets (Alsmeyer et al., 2004, Echtermeyer et al. 2021). Finding the optimal IHM is a laborious and time-consuming task. Depending on the applied settings and the number of calibration measurements, the model generation can take several minutes. Additionally, the current state-of-the-art software PEAXACT lacks a programmable interface. The generation of an IHMs entails several decisions regarding the model settings. The performance of the IHM, quantified by calculating the coefficient of determination (R2) and root mean squared error of cross-validation (RMSECV) value for each component in the system under consideration, depends highly on the selected settings. Current IHM development often lacks a systematic approach to optimizing the model performance. We propose the strategic development of IHM models using Bayesian optimization (BO) with categorical inputs. BO is an established, efficient, and data-driven optimization method for intricate processes and (costly) experiments. We

leverage BO algorithms that can handle categorical input variables to enhance the IHM development. We benchmark the strategic IHM development via BO with a random sampling of the categories and exhaustive sampling, i.e., creating all possible combinations of model settings.

2. Methods

2.1. Indirect Hard Modeling

Within the development process of IHM evaluation models, several decisions must be made, e.g., regarding the qualitative spectral analysis, pretreatment, and hard model settings. In this work, we consider the choice of type of baseline and standardization for spectral pretreatment and fitting mode as decision variables in the problem setup for IHM development, since they have been shown to highly affect the model performance. As a case study, we develop an IHM for the mixture during the polymerization of *N*-Isopropylacrylamide-based microgels. Hence, the IHM components include the monomer (NIPAM), the polymer (PNIPAM), and the solvent (deionized water).

2.2. Bayesian Optimization Algorithms

BO algorithms that can deal with categorical input variables include the open-source software packages: BoFire, CoCaBo (Ru et al., 2019), GPyOpt, Gryffin (Häse et al., 2021), Nemo-Bo, and NEXTorch (Wang et al., 2021). These software packages differ in the type of surrogate models and acquisition functions and optimization algorithms incorporated. All software packages can deal with continuous, discrete, and categorical type input variables. For BO-supported indirect hard modeling, we use the BoFire software package and compare the performance to random selection of sampling points. Furthermore, the data is approximated by a random forest surrogate model because random forest models are inherently well suited to handle categorical variables.

3. Results

We generated all possible IHM evaluation models with the combinations of settings, resulting in a total of 80 IHMs. In Figure 1, the progression of the objective values (R^2 and RMSECV) over the number of experiments is shown when applying the BoFire software package. Reaching a high R^2 value and a low RMSECV value for each component of the polymer system in the model with a low number of experiments are desirable. Figure 1 shows the 68 experiments conducted after initialization with 12 experiments. Within the first 20 experiments, only two instances with performance decrease (visually detectable by the two spikes in the progression) occur. Overall, it becomes clear that the algorithm follows a strategic approach, as the last experiments are stepwise resulting in a worse performance. Yet, a suitable stopping criterion needs to be defined for future applications of the BO supported method, as based on the exemplary progression of the objective values depicted in Figure 1 different criteria, e.g., number of experiments resulting in similar outcome or a fixed number of experiments to be conducted, would have yielded a different model performance. In contrast, randomly picking IHM settings to test results in high fluctuations of model performances due to the missing strategy. Therefore, the strategic BO-supported approach is preferable.

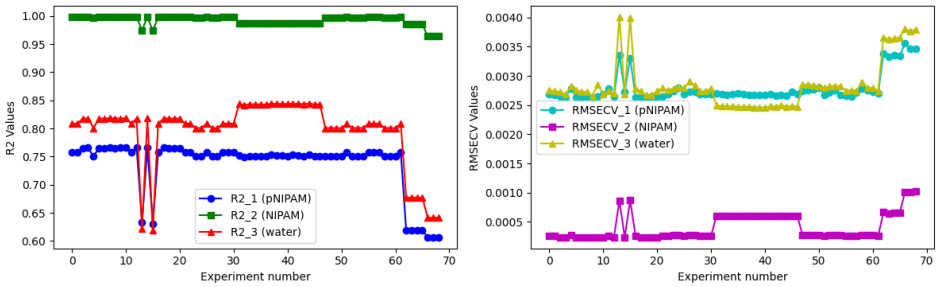

Figure 1 Results of the IHM development supported by BoFire. Left: R^2 objective value for all components in the IHM evaluation model over number of experiments. Right: RMSECV objective value for all components in the IHM evaluation model over number of experiments.

4. Conclusions

In summary, the proposed method involving BO for IHM development allows an efficient decision-making process, focusing on the most relevant model settings for analysis. The findings indicate that BO is promising for selecting IHM settings and could be used in future studies for IHM evaluation of more complex systems involving multiple components and with additionally considered IHM settings, e.g., fingerprint region or number of peaks in deriving pure component models. By supporting the decision-making process in IHM development, the most suitable settings resulting in the best possible model performance can be determined with reduced effort.

References

F. Alsmeyer, H.-J. Koß, and W. Marquardt, 2004, Indirect spectral hard modeling for the analysis of reactive and interacting mixtures, Applied Spectroscopy, 58(8):975–985.

BoFire: Bayesian Optimization Framework Intended for Real Experiments, Github: https://github.com/experimental-design/bofire.

A. Echtermeyer, C. Marks, A. Mitsos, and J. Viell, 2021, Inline Raman Spectroscopy and Indirect Hard Modeling for Concentration Monitoring of Dissociated Acid Species, Applied spectroscopy, 75(5):506–519.

GPyOpt: A Bayesian Optimization framework in python, 2016. Github: http://github.com/SheffieldML/GPyOpt.

F. Häse, M. Aldeghi, R. J. Hickman, L. M. Roch, and A. Aspuru-Guzik, 2021, Gryffin: An algorithm for Bayesian optimization of categorical variables informed by expert knowledge, Applied Physics Reviews, 8(3):031406, Github: https://github.com/aspuru-guzik-group/gryffin.

E. Kriesten, F. Alsmeyer, A. Bardow, and W. Marquardt, 2008, Fully automated indirect hard modeling of mixture spectra, Chemometrics and Intelligent Laboratory Systems, 91(2):181-193.

Nomadic Exploratory Multi-objective Optimisation (NEMO), Python Package: https://pypi.org/project/nemo-bo/.

PEAXACT version 5.8, S-PACT GmbH, Aachen, Germany.

B. Ru, A. S. Alvi, V. Nguyen, M. A. Osborne, and S. J. Roberts, 2019, Bayesian optimisation over multiple continuous and categorical inputs, Github: https://github.com/rubinxin/CoCaBO_code.

Y. Wang, T.-Y. Chen, and D. G. Vlachos, 2021, Nextorch: A design and bayesian optimization toolkit for chemical sciences and engineering, Journal of chemical information and modeling, 61(11):5312–5319, Github: https://github.com/VlachosGroup/nextorch.

ESCAPE-34 PSE-2024
European Symposium on Computer Aided Process Engineering
&
Process Systems Engineering

Flavio Manenti, Gintaras V. Reklaitis (Eds.), Book of Abstract of the 34th European Symposium on Computer Aided Process Engineering / 15th International Symposium on Process Systems Engineering (ESCAPE34/PSE24), June 2-6, 2024, Florence, Italy.

Digital Chemistry – Our path to Versalis Smart Plant

Gabriele Provana[a*],Elvira Fabrizio[a], Alessandra Fidanzi [a],Gianluca Setti[a], Domenico Napoli[b]

[a] *Eni S.p.a Digital & Information Technology,Via Milano 6/8, San Donato Milanese 20097,Italy*
[b] *Eni S.p.a Digital & Information Technology,Via Litoranea Prioloese 39, Priolo 96010,Italy*
**Gabriele.provana@eni.com*

Abstract

Versalis has always considered the adoption of IT technology in industrial plants in synergy with OT technologies as a fundamental factor to ensure effectiveness, efficiency, safety and sustainability in the production processes of its industrial plants. Historically Versalis plants have always been operated with the support of advanced control systems and field data collection systems which are boundary between process systems and management systems. However, in the last 10 years, thanks to the maturity reached by advanced analysis algorithms, AI, IoT systems and integrated collaborative platforms, the design of the "Smart Plant" has been progressively defined. The recent push towards a complete review of the maintenance model, shared with all Eni downstream business, has also further evolved the ambitious reference target.

In Versalis the "Smart Plant" embraces all site and Head Quarter operations processes, and IT and Business functions are working together along our transformation roadmap.

Operation area:

- full operation production systems replatforming with introduction of a single centralized cross-site Industrial Platform:
    - modeling and monitoring of the production process for all different types of production lines both liquid and solid products by integration with field data collection systems and laboratory data system
    - centralized HUB for access to industrial data to support monitoring of production efficiency and plant management, circular economy, CO2, energy management
- machine learning models for advanced analysis of field sensors (recognize faults and operational deviations on critical assets in advance, optimize the process quality parameters, emission monitoring)

- use of High-Performance Computer and specific package for fluid dynamic simulation
- digitalization of on-site logistics processes, warehouses and tanks
- planning support system (production planning and scheduling, turnaround and day by day ordinary maintenance activity planning scheduling and execution)
- digitalization of processes from a paperless perspective (information flows with external government entities such as “ARPA” and “Customs and Monopolies Agency”)
- Digitalization of field operators' activities by mobile devices for remote information and documents access and for manual data collection

Safety area:

- Real-time health and PPE monitoring of operators on field and in confined spaces and digitalization of work permits preparation and authorization process
- Machine learning models for risks predictive alerting

Cyber Security Area: network segregation, system access control enforcement and network traffic continuous monitoring

Keywords: artificial intelligence, machine learning, industrial platform, process digitalization, real-time data, safety, cyber security

1. Digital Chemistry

Our path towards the smart plant is fundamentally based on data valorization to increase productivity, reduce risk and increase plant uptime, process digitalization to ensure operation efficiency, iot technologies to increase safety and best practices adoption to increase cyber resiliency.

1.1. Artificial Intelligence

Versalis has always believed in the potential of data and always considered the adoption of IT technology and artificial intelligence in industrial plants in synergy with OT technologies as a fundamental factor to ensure effectiveness, efficiency, safety and sustainability in the production processes. Historically Versalis plants have always been operated with the support of advanced control systems and field data collection systems which are boundary between process systems and management systems. However, in the last 10 years, thanks to the maturity reached by advanced analysis algorithms, AI, IoT systems and integrated collaborative platforms, the design of the "Smart Plant" has been progressively defined.

Focusing on AI, Versalis journey through machine learning and deep learning models can benefit on Eni AI center of excellence with strong internal skills that oversees market technologies, tests them, and engineers them to encourage agile and at the same time conscious use.

Versalis started with the development, through internal resources of data scientists, of specific use cases and now has a set of engineered environments to develop its own or package-based models [1]. The first machine-learning models were targeted to intercept and predict degradation phenomena in asset performance to increase production capacity and optimize maintenance activities (for example the prediction of cracking furnaces’

coking and runlength for next decoking activity simulation, prediction of furnace vaporizers fouling, root causes analysis of plate fouling and formation of agglomerates phenomena in polythene's reactor, compressor failure prediction). Over the years it has been put in place a cloud platform environment as hub for machine learning, first for R&D [5], then extended to any use cases that leverage field sensors data, with the aim of speeding up and engineering the ingestion, modeling, notification and results sharing phases. At the same time, market solutions, with physical or data driven approaches, were evaluated, and adopted to increase the speed of diffusion by exploiting the knowledge gained in non-specific application areas [3]. The recent emphasis on generative AI has been also treated with a structured approach, starting from understanding the potential of technology, testing it in experimental contexts and conducting assessment sessions of potential application areas from which use cases emerged in terms of training support, maintenance activity on filed support, plant image evaluation, automatic report generation and process trouble shooting support.

1.2. Industrial Platform

The main factors that inspired the rethinking of the industrial operations application portfolio were systems capacity for scalability and flexibility with respect to the corporate structure evolution needs, and the opportunities to improve collaboration and the valorization of data that the new platforms and market solutions can guarantee together with consolidation of some application components geographically distributed.

We designed our model by capitalizing and consolidating features and processes on a centralized, modern and flexible collaborative platform that we recently introduced into our application portfolio, the Dassault Systeme platform (collaborative operation platform COP) by integrating it into a composite architecture with specific domain package and where necessary custom packages developed with a platform as a service perspective. The mantra that guided our choices can be summed up in three words: modernize, centralize and share. In this context, the target model that we have defined and the project streams that we have activated provide:

- implementation in COP of recipes management and production budget, tracking and accounting by consolidating geographically distributed components in the local data rooms
- implementation and consolidation in COP of industrial reporting for production efficiency calculation on a monthly and daily based, extension to energy management and CO2 calculation and near-real-time monitoring of the main plant phenomena
- implementation of an environment for simulation integrated with recipe and margin calculation models to support what-if analyses
- implementation of a custom cloud solution to support tank farm management and digitizing the integration flow with "Customs and Monopolies Agency"
- implementation of a mobile app integrated with COP to support field operations digitalizing data collection and reporting unsafe conditions

The program is very ambitious due to the breadth and relevance of the processes involved and the industrial sites impacted on an international level. It is currently underway and is expected to be completed by 2025 [2].

1.3. New Maintenance model

In the Maintenance area, has been activated a program that aims to increase operational effectiveness and optimize costs through the simplification and digitalization of processes

and the introduction of artificial intelligence capabilities. The scope of the program cuts across the various downstream oil, chemical and power generation businesses and is related to warehouses technical materials optimization and maintenance processes optimization (predictive and prescriptive maintenance, ordinary maintenance, turnaround management). The program consists of 7 project streams to leverage, evolve and share solutions that have proven effective in different businesses and 1 project stream which involves the introduction of a new platform. All the project streams are underway and expected to be completed by the end of 2026 [3].

1.3.1. Maintenance

In the maintenance area the main streams are:

- smart maintenance worker: creation of an integrated maintenance platform that leverages and integrates existing asset integrity systems, field data acquisition systems and ERP system, digitalizing field activities and enabling collaboration between skills
- paperless office: implementation of a custom cloud solution for workflows and documentation digitalization along the maintenance orders creation and accounting process flow
- turnaround coworking tool: preparation of a common multi-business repository for sharing multi-year shutdown plan to intercept potential synergies or related risks
- integrated operation windows: implementation in COP of a sensor monitoring solution for critical assets to intercept operational conditions that can accelerate degradation phenomena and compromise the assumptions underlying the Risk Based Inspection analyzes
- asset performance monitoring: adoption of an artificial intelligence solution for the advanced monitoring of critical static and rotating assets for predictive e prescriptive recognition of failure patterns (failure agent) and deviations from reference operating conditions (anomaly detection agent); the adoption of a market platform based on machine learning technologies allows us to accelerate the roll-out path on the main critical assets on different plants.

As an additional stream we started a study to identify a new platform in the maintenance management system area to support the planning, scheduling and execution processes of ordinary, extraordinary and turnaround maintenance activities.

1.3.2. Asset Performance monitoring focus

The identified solution for advanced asset performance monitoring is package based Aspentech MTELL that has already been successfully implemented in refinery context and deployed on a range of equipment such as furnace, heat exchangers, pumps, columns, compressors, reactors & boilers. The package that combines physical and data driven approach and offers different type of agent that allow you to choose the right one based on your maintenance strategy:

- rules based, best for simple monitoring: monitor sensor and calculated sensor data in real time to trigger alerts when data points are out of bounds
- conditions based, best for rapid response: correlate sensor and calculated sensor data with usage to trigger alerts for degradation that is occurring

- first principle based, best for assessing degradation: physics-driven calculations to assess asset degradation based on pre-defined criteria
- machine learning, best for predicting degradation: proven, pre-selected pattern recognition algorithms to predict asset degradation based on embedded domain knowledge
- brind your own model, best for unique use cases: custom-created algorithms by citizen data scientists for advanced / unique use cases

We are in a roadmap to deploy the solution on the main Versalis over the next 2 years starting from the main critical asset and process, based on a value map with measurable critical success factors that covers production gain, environmental gain, maintenance and inspection planning optimization.

1.3.3. Material and spare parts warehouses

In the warehouse management area, the main streams are:

- warehouse dashboard: implementation of a shared monitoring environment for the technical materials and spare parts warehouse stock to improve single business control and enable cross-business synergies in the use of surplus materials
- warehouse automation: adoption of a market package specialized in the automation of inbound, outbound and inventory processes of technical materials and spare parts using RFID, BARCODE, QRCODE technology integrated with the company ERP

1.4. Digital Safety

The safety of operators on field has always been a priority for Eni and Versalis and therefore over the years different technologies have been tested and adopted to support the prevention and mitigation of risks connected to the activities carried out by internal and third-party personnel at our plants. Also, in this area, the interventions are divided into different streams:

- electronic work permit: we developed an Eni application, to support the process of compiling, managing and archiving work permits with the aim of increasing control and monitoring of all the risks connected to the process, prevent interference between different maintenance teams operating in the same area, digitize work permit documentation, with easier archiving, retrieval and tracking of information
- smart safety: use of wearable devices and algorithms able to detect dangerous situations in real time through specific use cases for monitoring the use of personal protective equipment, monitoring access to restricted areas, automatic "man down" notification, SOS requests, management of system emergencies with automatic counting at the safe point and geolocation in the plant
- safety pre-sense: application of natural language processing and machine learning models to predict possible risk situations through advanced analysis of the amount of security events recorded in the central Eni repository to generate alerts from weak signals or recurring situations of danger and enable a new approach to incident prevention and improvement of recording and analyzing safety data and the possibility of increasing prevention through targeted actions; in this context, an experiment is underway to extend the scope of analysis also to process data to correlate them with incidents (e.g. maintenance interventions in the plant)

The roll-out program in Versalis plants is underway and specific KPIs are calculated to ensure the maximum possible benefit in terms of safety of personnel in the field [4].

1.5. Machine Learning HUB

The potential that arises from the use of advanced analytics models in operations, R&D and HSE has pushed us to set up a cloud environment on which to quickly and easily implement models for different use cases [5].

The characteristics of the environment we have implemented are:

- enhance the representative and collaborative capacity of analyzes between functions through advanced, real-time and mobile data visualization tools
- design an enterprise solution for the ingestion, modeling, notification and sharing phases of plant monitoring via machine learning
- already opened near-real-time field and laboratory data integration and further data sources ready to set up ensuring scalability

More specifically, in the hub we created models based on machine learning technology:

- models for optimizing the quality of production processes through real-time data monitoring from process data, laboratory data and other unstructured data sources
- ARMA models predicting the value of the main emission parameters for cracking furnace and polymer plant to be capable to monitor these parameters even in case of dedicated sensor fault.

1.6. Cyber Security OT

The growing threat represented by cyber risks led us to activate a broad enforcement program across all industrial sites aimed to enforce the resilience of OT systems.
An assessment study completed in the past have allowed us to set up a program with a risk-based approach which is divided into the following intervention guidelines applied according to a model consistent with the mapped risk cluster:

- business continuity system enforcement and cyber active monitoring probes
- network segregation enforcement between process network connected with industrial control system and office network connected to filed data acquisition system
- data acquisition system hardening and continuous lifecycle management of industrial control system

2. References in the text

3. Conclusions

The digital chemistry vision contributes and aligns with Versalis's strategy aimed at maintaining technological and industrial leadership to maintain a positioning in the market of high added value applications, be a completely sustainable and diversified company and contribute to achieving the goal of carbon neutrality.

References

[1] Setti G., LightHouse Brindisi Project, Versalis
[2] Napoli D.,Versalis Industrial System Evolution , Versalis
[3] Autuori A., Full Potential New Maintenance Model, Versalis
[4] Napoli D., Digital Safety Program Versalis, Versalis
[5] Rovati G., R&D Machine Learning Hub, Versalis

ESCAPE-34 PSE-2024
European Symposium on Computer Aided Process Engineering
&
Process Systems Engineering

Flavio Manenti, Gintaras V. Reklaitis (Eds.), Book of Abstract of the 34th European Symposium on Computer Aided Process Engineering / 15th International Symposium on Process Systems Engineering (ESCAPE34/PSE24), June 2-6, 2024, Florence, Italy.

De-Novo Generation of Synthetic Copolymers with Graph-to-String Variational Autoencoder

Gabriel Vogel[a], Paolo Sortino[b], Jana Marie Weber[a,*]

[a]*Delft Bioinformatics Lab, Department of Intelligent Systems, Delft University of Technology, Van der Maasweg 9, Delft 2629 HZ, The Netherlands*
[b]*Deptartment of Computer Engineering, University of Palermo, Palermo, Italy*
j.m.weber@tudelft.nl

Abstract

Synthetic polymers are a key material class in many applications with importance to our society, such as plastics and novel energy materials. This causes an increasing demand for new synthetic polymers with superior properties. However, due to their complex hierarchical and highly versatile structure, the theoretical design space for polymers is large. Generative polymer design is a promising approach to accelerate polymer materials discovery and reduce experimental screening costs. Yet, generative polymer design is still in its infancy with most previous approaches focusing on generating the repeating units of polymers without additional structural information. Here, we present our recently published graph-to-string variational autoencoder (VAE) that builds upon a recent polymer graph representation including stoichiometries and chain architectures of monomer ensembles. The model enables de-novo generation of copolymer structures including the monomer stoichiometry and chain architecture. In this work, we demonstrate three different sampling strategies to generate novel polymers, namely sampling from noise, around a seed polymer, and through interpolation between two polymers. All methods generate novel polymers not found in the training data, mainly through new monomer combinations and novel monomer chemistries. Sampling around seed molecules and interpolation between molecules illustrate how variations in the latent space change the generated polymers.

Keywords: generative molecular design, synthetic polymers, variational autoencoder, transformers, graph neural network

1. Introduction

De-novo generative design of molecules is an increasingly popular approach to intelligently design molecules in-silico, reducing experimental screening time and costs. Generative models are commonly trained on a large corpus of molecular data and facilitate the generation of promising novel molecular structures which can then be synthesized in the lab. Yet, compared to the small molecule world, generative synthetic polymer design is still in its infancy. One reason is the overall small amount of available, accessible, and sufficiently detailed polymer data (Amamoto, 2022; C. Kim et al., 2018; Otsuka et al., 2011). Second, unlike for small molecules, the definition of a machine-

readable data representation that accurately corresponds to the final polymer material is difficult (Amamoto, 2022; Hatakeyama-Sato, 2022; Yan & Li, 2023). This results from the stochastic nature of polymers and their different structural levels reaching from monomer chemistry over monomer composition and stoichiometry to chain architecture and linking structure, visualized in Figure 1.

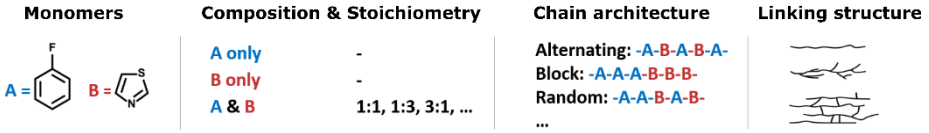

Figure 1: Structural levels of polymers: Monomers, combination of monomers and stoichiometry, chain architecture, and chain linking structure

Most previous works on generative design of polymers focuses mainly on generating single polymer repeating units with little or no information about the higher-order structural levels (S. Kim et al., 2023; Ma & Luo, 2020). In this work, we demonstrate our recently published graph-to-string variational autoencoder (VAE) (Vogel et al., 2023), a generative model that has been trained on polymer representations that include the stoichiometry of the monomer ensemble and the chain architecture of the polymer (Aldeghi & Coley, 2022). The model encodes the training data to a continuous numerical latent space that can be used to generate novel copolymers including the monomer stoichiometry and chain architecture. We demonstrate three different sampling strategies in the model's latent space, namely sampling from noise, around a seed molecule and through interpolation between known molecules. Finally, we discuss the implications of the sampling results for future work.

2. Methods

2.1. Representations and Data

The model is trained on the dataset published by (Aldeghi & Coley, 2022), which is built upon the polymer space of (Bai et al., 2019). The dataset comprises combinations of eight A-monomers with 682 B-monomers with the stoichiometries 1:1, 1:3, and 3:1 and three chain architectures (alternating, random, block), leading to a dataset of 42966 copolymers. Additionally, we augment the dataset by allowing B-B copolymers with the same selection of stoichiometries and chain architectures, as described in Vogel et al. 2023. We work with the polymer graph representation introduced by Aldeghi & Coley, 2022 together with an equivalent string format, both including the information about stoichiometry and chain architecture. Further information regarding the polymer representations can be found in (Vogel et al., 2023).

2.2. Model

We use our recently published model to encode the polymer graph to a latent representation $\mathbf{z_x}$ with latent dimension 32 and to decode it to the corresponding polymer string. As shown in Figure 2, in the encoding step the model utilizes a graph neural network to learn the mean $\boldsymbol{\mu_x}$ and standard deviation $\boldsymbol{\sigma_x}$ of the data which is then reparametrized using a gaussian prior. The decoder is based on the transformer architecture, using the latent representation through encoder-decoder attention and

through concatenation with the token embeddings. More details on the model architecture and training hyperparameters are provided in the original paper (Vogel et al., 2023).

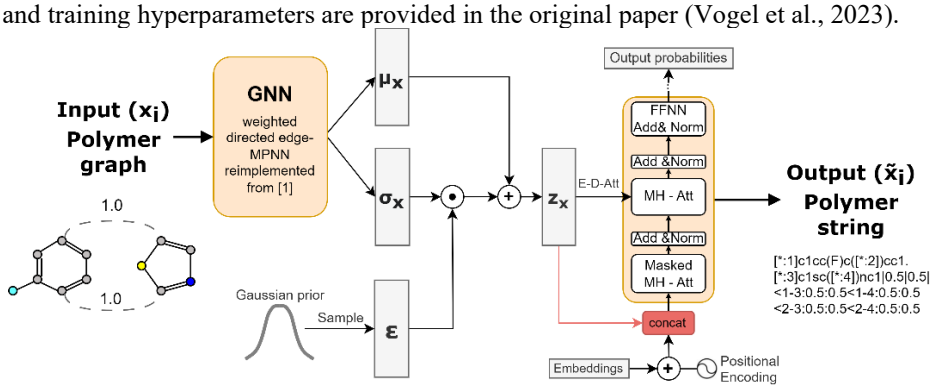

Figure 2: Simplified overview of Graph-to-string VAE model for synthetic polymer design (Vogel et al., 2023). Polymer graphs are encoded in a wDMPNN (Aldeghi & Coley, 2022) to learn $\boldsymbol{\mu_x}$ and $\boldsymbol{\sigma_x}$ which are then reparametrized to the latent representation $\mathbf{z_x}$. The latent representation is fed to a Transformer decoder that decodes the equivalent polymer strings.

2.2.1. Sampling: from noise, around seed, and using interpolation

In this work, we demonstrate de-novo generative design of synthetic polymers using three different sampling techniques. First, novel polymers can be generated by sampling latent vectors from Gaussian noise $\boldsymbol{z_{n\_gaussian}}$ and decoding these using the trained model. Second, we sample novel polymers around a given seed molecule, i.e. by repeatedly adding noise $\boldsymbol{n}$ (of latent dimension 32) elementwise to a seed latent vector $\boldsymbol{z_s}$, leading to $\boldsymbol{z_{s+n}}$. Lastly, we interpolate between molecules, i.e. between two latent codes for two known molecules $\boldsymbol{z_{m1}}$ and $\boldsymbol{z_{m2}}$. One can take the mean or interpolate in a stepwise manner. In this work, we create ten interpolated latent codes $\boldsymbol{z_{i,m1\rightarrow m2}}$, by interpolating elementwise in equidistant steps between the two latent codes of the known molecules. For instance, let latent dimension one be 0.2 for $\boldsymbol{z_{m1}}$ and 0.75 for $\boldsymbol{z_{m2}}$, then the interpolated values of latent dimension one $z_{1,i,\mathrm{m1}\rightarrow\mathrm{m2}}$, would be $\{0.25, 0.3, 0.35, \ldots, 0.7\}$ for the respective interpolated latent vectors $\boldsymbol{z_{i,m1\rightarrow m2}}, i \in \{1, 2, 3, \ldots, 10\}$.

3. Results and Discussion

In the following, we show the results of de-novo generation of synthetic polymers focusing on the three proposed sampling techniques. Moreover, we discuss how the monomer chemistries, stoichiometry, and chain architecture change when changing the latent codes of polymers.

3.1. Sampling from gaussian noise

We use the model to sample 16000 polymers from gaussian noise leading to polymers with 77 % novelty (percentage of polymers not in training set), 40 % diversity (percentage of unique polymers), and >99 % validity (polymer string corresponds to a valid molecule). Further, when investigating the novelty per structural category, we observe 10.9 % novel B monomer chemistries and 2.3 % novel A monomer chemistries. We observe no novel stoichiometries and chain architectures, meaning that the model is currently limited to generating the classes found in the training data. Thus, the overall novelty is introduced through novel monomers and novel combinations of structural components. This indicates that structural categories with a higher variation in the training

data lead to higher novelty during sampling, demonstrating the necessity to diversify the dataset in all structural categories in future efforts.

3.2. Sampling around a seed molecule

Figure 3 shows example molecules when sampling 512 times around a seed molecule by repeatedly adding noise to the seed latent code $\boldsymbol{z_s}$. We observe variation from the seed molecule in all structural levels, i.e. monomer A, monomer B, stoichiometry, and chain architecture. Also, there are several instances of sampling the seed molecule itself (in this example 3 out of 512). The level of noise can be varied, with less noise leading to less changes from the seed molecule. Figure 3b reveals that, for this example, the structural level that is varied the most when adding noise is monomer B, followed by monomer A, stoichiometry, and the chain architecture. The higher variation in monomer B is expected, since the diversity in the training data is the highest. As already mentioned in Section 3.1, we also find novel B-monomers and few novel A-monomers (not present in the dataset) indicated as the red hatched bar in Figure 3b.

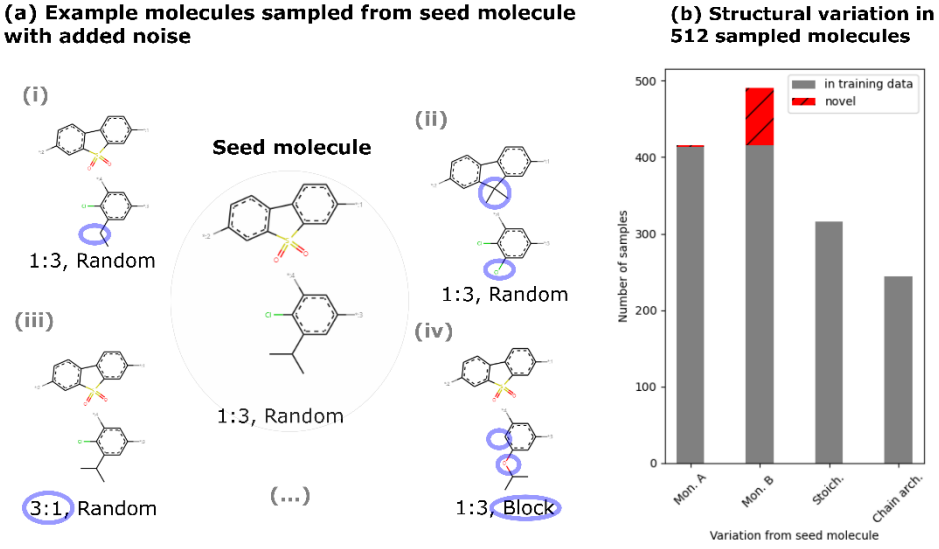

Figure 3: Sampling around a seed molecule. (a) Different structural categories (monomer A, monomer B. stoichiometry, and chain architecture) are varied. (b) The bar chart shows how often out of 512 samples the respective structural categories are varied from the seed molecule. The red (hatched) bars indicate novelty in the respective structural category.

3.3. Interpolation between molecules

Figures 4a and 4b show examples of the interpolation path between two copolymers, where monomer A is depicted in the upper part and monomer B in the lower part. The interpolation pathway reveals that the different structural levels transform stepwise from the start molecule to the end molecule. Furthermore, we observe that the stoichiometry and chain architecture change less frequently, yet altering the latent code sufficiently leads to a structural change in the decoded polymer. On the contrary, the monomers change already for smaller variations of the latent vector throughout the interpolation, especially monomer B, as expected based on the diversity of monomer B in the dataset. Notably, all polymer intermediates in Figure 4 are not found in our dataset and are novel, valid copolymers. The novelty of intermediates in Figure 4a is only due to novel

combinations, meaning that all monomers in this interpolation path are found in the dataset. In the example in Figure 4b we also observe novel monomers, in line with novel A and B monomers found when sampling around seed molecules (see Figure 3b).

In both examples, we see that heteroatoms (no C or H) and functional groups play a key role how the monomers change. Heteroatoms like S, F, Cl, N, and O determine whether polymers are encoded in similar regions in the latent space. For instance, in Figure 4b, the start molecule contains four oxygen atoms, while the end molecule does not contain any. Throughout the interpolation path, the oxygen atoms are disappearing in the decoded molecules. Similarly, the end molecule contains a chlorine atom, while the start molecule does not. In the middle of the interpolation part a chlorine atom appears, changing its position in the polymer between the two monomers until reaching the end molecule. This behavior is desirable, since functional groups such as chloride or nitro groups determine the properties of the polymer and therefore polymers with the same functional groups should be close in latent space.
Furthermore, all sampled polymers are conjugated copolymers, in line with the chemical space that the model is trained on which consists of conjugated copolymers used as photocatalysts (Bai et al., 2019).

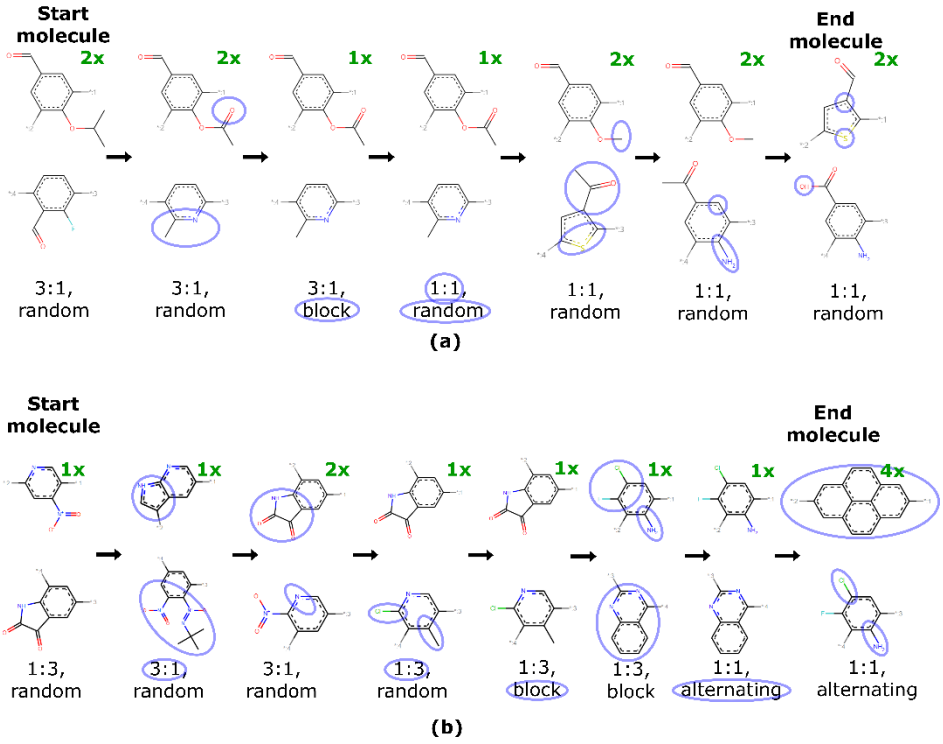

Figure 4: Two examples of interpolation paths between two polymers showing sequential changes in monomer A (upper molecule), monomer B, stoichiometry and chain architecture. Changing parts of the polymer compared to the previous step are highlighted in blue circles. The green number indicates for how many steps this polymer is decoded on the interpolated path.

4. Conclusions

We developed a model for de-novo generative design of synthetic copolymer structures including monomer chemistries, stoichiometry and chain architecture. Our approach increases the level of information about the polymer, enabling the generation of polymer structures that represent the polymer material more accurately. Here, we demonstrate with three sampling techniques how the model can be used to generate novel copolymers and show that novelty is introduced by new combinations of known structural levels, novel monomer chemistries and the combination of the two. Moreover, in this work we show that polymers with similar functional groups and heteroatoms are encoded in similar regions of the latent space. Prospectively, with an increased diversity of the dataset on all structural levels, we envision a model that can generate novel and diverse polymer structures, including, for instance, novel stoichiometries.

References

Aldeghi, M., & Coley, C. W. (2022). A graph representation of molecular ensembles for polymer property prediction. Chemical Science, 13(35), 10486–10498.

Amamoto, Y. (2022). Data-driven approaches for structure-property relationships in polymer science for prediction and understanding. Polymer Journal, 54(8), 957–967.

Bai, Y., Wilbraham, L., Slater, B. J., Zwijnenburg, M. A., Sprick, R. S., & Cooper, A. I. (2019). Accelerated Discovery of Organic Polymer Photocatalysts for Hydrogen Evolution from Water through the Integration of Experiment and Theory. Journal of the American Chemical Society, 141(22), 9063–9071.

Hatakeyama-Sato, K. (2022). Recent advances and challenges in experiment-oriented polymer informatics. Polymer Journal, 1–15.

Kim, C., Chandrasekaran, A., Huan, T. D., Das, D., & Ramprasad, R. (2018). Polymer Genome: A Data-Powered Polymer Informatics Platform for Property Predictions. The Journal of Physical Chemistry C, 122(31), 17575–17585.

Kim, S., Schroeder, C. M., & Jackson, N. E. (2023). Open Macromolecular Genome: Generative Design of Synthetically Accessible Polymers. ACS Polymers Au.

Ma, R., & Luo, T. (2020). PI1M: A Benchmark Database for Polymer Informatics. Journal of Chemical Information and Modeling, 60(10), 4684–4690.

Otsuka, S., Kuwajima, I., Hosoya, J., Xu, Y., & Yamazaki, M. (2011). PoLyInfo: Polymer Database for Polymeric Materials Design. 2011 International Conference on Emerging Intelligent Data and Web Technologies, 22–29.

Vogel, G., Sortino, P., & Weber, J. (2023, November 3). Graph-to-String Variational Autoencoder for Synthetic Polymer Design. AI for Accelerated Materials Design - NeurIPS 2023 Workshop.

Yan, C., & Li, G. (2023). The Rise of Machine Learning in Polymer Discovery. Advanced Intelligent Systems, n/a(n/a), 2200243.

ESCAPE-34 PSE-2024
European Symposium on Computer Aided Process Engineering
&
Process Systems Engineering

Flavio Manenti, Gintaras V. Reklaitis (Eds.), Book of Abstract of the 34th European Symposium on Computer Aided Process Engineering / 15th International Symposium on Process Systems Engineering (ESCAPE34/PSE24), June 2-6, 2024, Florence, Italy.

Representation Learning for Flowsheets: Generating Structures for Process Synthesis

Antonio Rocha Azevedo[a,b], Tahar Nabil[c], Valentin Loubière[b], Benoît Valentin[c], Romain Privat[a], Thibaut Neveux[b], Jean-Marc Commenge[a,*]

[a]*Université de Lorraine, CNRS, LRGP, F-54000 Nancy, France*
[b]*EDF R&D Chatou, 6 quai Watier, 78400 Chatou, France*
[c]*EDF R&D, Boulevard Gaspard Monge, F-91120 Palaiseau, France*
jean-marc.commenge@univ-lorraine.fr

Abstract

The research for the optimal flowsheet is a key part of process synthesis. However, optimization at a structural level is difficult due to its discrete nature, and current approaches may not guarantee a good exploration of possibilities. A continuous structural domain could be useful for systematizing this research and exploration.

In this work, a machine learning model is trained to develop a continuous representation for flowsheets: every process can be turned into a point in space, and points in space can be translated back into processes. The model's capability of generating new processes from random points in space is assessed. Results show that, although capable of grouping similar processes together, in clusters, it may not always propose structurally feasible flowsheets. Dataset generation and hyperparameter finetuning could also be improved before the model is coupled with process synthesis approaches.

Keywords: Process Synthesis, Machine Learning, Artificial Intelligence, SFILES

1. Introduction

In process synthesis, finding the optimal flowsheet for a given application is challenging, and it may be difficult to explore the realm of possibilities. While heuristics can be used for proposing relevant alternatives, they may miss better, less intuitive ones. Superstructural (see Mencarelli et al. (2020)) and generative approaches (see Nabil et al. (2022)) search a wider range of processes, but may not ensure a systematic exploration of the domain of feasible structures – which is difficult to represent mathematically. In contrast, mapping the discrete space of process flowsheets to a continuous one could prove useful, since optimization exploration techniques could be applied.

The goal of this work is to develop a model that learns a continuous, vector-space representation of process flowsheets, from which new ones can then be sampled. In this space, it is desired that two similar processes be found close to each other, while two very different flowsheets should be further apart. The motivation behind this objective is to eventually use this model to systematize the research of the optimal flowsheet – since a continuous space would yield a better way to analyse and quantify the exploration of

alternatives, and enable the use of sampling and optimization strategies for proposing new ones.
This work takes inspiration from the paper by Gómez-Bombarelli et al. (2018), in which a Variational Autoencoder was used to develop a continuous representation for molecular structures – being used for running property optimization directly in the continuous space. Here, their publicly available codes were adapted for flowsheets, with a few additions for improving model learning efficiency.

2. Representation Learning Model

2.1. Representation Learning and the Variational Autoencoder
Representation Learning is a branch of Machine Learning that attempts to automatically identify patterns and features in raw data – and develop efficient representations for it.
The Variational Autoencoder (VAE) is a deep learning model composed of two separate parts: an encoder and a decoder. The encoder is a dimensionality reduction model, that transforms an input (in our case a flowsheet) into a representation vector (also called a "latent" vector); while the decoder tries to reconstruct the original input from said vector. While each of these parts are used separately, for different purposes, they are trained as a single model: the VAE receives an input and tries to reconstruct it, passing through a latent space of smaller dimension (which forces the model to learn an efficient representation). The model relies solely on the similarities between flowsheets to learn.
The "variational" label, put simply, entails that noise is added to the encoded vector during training to improve learning, and that the loss (i.e., the objective function used for training the model) is composed of a reconstruction term and a regularization term. The former ensures that the model is capable of translating points from the latent space back into the correct processes; the latter forces the data to be close together in the latent space, improving the continuity of the representation. In practice, the VAE is probabilistic in nature, a property that yields attractive generative capabilities.

2.2. Input: SFILES notation
To train a Neural Network (NN) with process structures, it is necessary to convert them into a format that can be understood by the model (a matrix). To bridge this gap, the SFILES 2.0 notation (Vogel et al., 2023a) for representing process structures is used. It mirrors the SMILES standard used for molecules (used by the molecular VAE authors) and represents flowsheets as a string of "words" (or, more generally, "tokens") making the task analogous to a Natural Language Processing problem – which is well-studied in the Machine Learning field. A token may represent an equipment or special symbols (such as recycles and branches). When all tokens relevant to the problem are listed, each one can be associated to a ("one-hot") vector. The string of tokens thus becomes a sequence of vectors, which makes up the model's actual input.

2.3. Output: decoding strategy
Because of the discrete nature of the problem, the flowsheet is decoded one word at a time. At each step, the model outputs a probability for each word and picks that step's word randomly, according to those probabilities. Then, this token is used as an input for decoding the next one, and so on. While other probabilistic decoding strategies are possible (see Vogel et al. (2023b)), this step-by-step sampling was kept for simplicity. This means that the model's performance is probabilistic. Because of this, when evaluating the model, encoded vectors will be run multiple times through the decoder, and results will be presented according to this number of "decoding attempts". For comparison, a "greedy", deterministic, strategy will also be used: in it, the token with the

highest probability is picked at each step. An illustration of the complete VAE is shown in Figure 1.

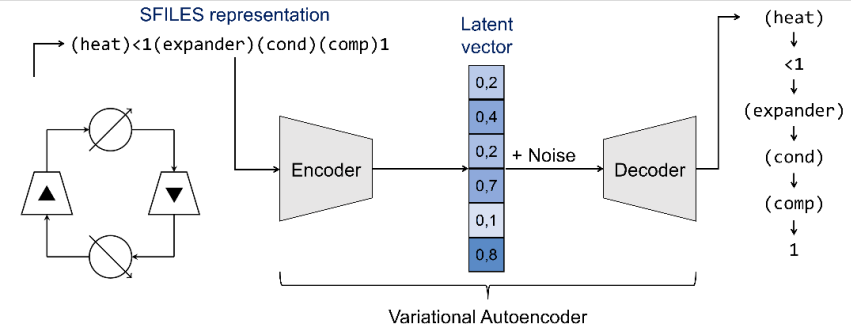

Figure 1: Illustration of a VAE and example of a process represented as a SFILES string.

3. Case Study: Thermodynamic Cycles

3.1. Methodology

To train the model, a dataset of around 300,000 randomly generated thermodynamic cycles is used with a 90 %/10 % training/validation split. These processes are composed of 7 different types of equipment: compressors, turbines, heaters, coolers, integrated heat exchangers, stream splitters and mixers. All flowsheets are *structurally* feasible – they are closed cycles and equipment connectivity is respected – but they are not necessarily well-performing or logical from a thermodynamical standpoint. This dataset stems from the works by Nabil et al. (2023) and was kindly provided by the authors. An extra dataset (hereinafter "test" dataset) with 100,000 cycles was created by one of the generative AI models mentioned in the referenced paper and is used for further analysis.

The VAE's *process* reconstruction accuracy (i.e., the fraction of correctly reconstructed processes in a set) for each dataset is used for verifying if the model was able of learning and generalizing. Note that the reconstruction of a given process is considered as a failure as long as at least one token is incorrectly decoded in the sequence. Token-wise accuracies (the fraction of correctly decoded tokens in the set) are also presented for discussion. To analyse the model's capacity of generating new flowsheets, points will be randomly sampled from the latent space and decoded. The fraction of valid (structurally feasible SFILES), unique, and new (not present in the training dataset) flowsheets will be used for quantifying performance.

Since the model is given multiple decoding attempts, it is necessary to define which decoded flowsheet will be assigned as final. Here, the methodology used by the molecular VAE's authors is adapted, for taking feasibility into account. After a point is decoded multiple times, each process is screened for feasibility. Then, each one is re-encoded into latent space, using the encoder part of the VAE (without adding noise to the result). Finally, the valid process which is the closest to the sampling point is chosen as the "assigned" decoding. This methodology is illustrated in Figure 2.

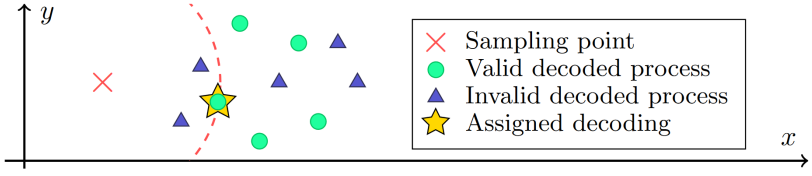

Figure 2: Illustration of the structure assignment methodology for a point in latent space (2D in this example). The final decoding is the valid process which is closest to the point.

3.2. Results

3.2.1. Reconstruction accuracies

Models with different numbers of latent space dimensions were trained for a total of 40 epochs. They will be referenced as a function of their dimensionality (e.g., model 100D has a 100-dimensional latent space). Because GPU acceleration was not possible, training times were a limiting factor, and most hyperparameter values were kept as default (e.g., the dimension size of 196 was the default). As mentioned in section 2.1, the model is trained with a regularization term. Following the molecular VAE's authors' recommendation, the weight of this term is increased during training, following a sigmoid curve. Here, its value is varied from 0.001 at epoch 21 to 0.999 at epoch 31 (steeper than default values, because of the long training times). Table 1 shows results for the best two models, for the epoch (training iteration) with minimal validation loss.

Table 1: Reconstruction accuracies for the best two models.

		Reconstruction accuracy		
Model	**Decoding type**	**Training**	**Validation**	**Test**
100D	Greedy (token-wise)	98.5 %	98.3 %	87.8 %
	Greedy (process-wise)	85.7 %	84.3 %	45.4 %
	10 attempts (process-wise)	87.2 %	86.3 %	45.8 %
196D	Greedy (token-wise)	98.3 %	98.2 %	87.0 %
	Greedy (process-wise)	80.5 %	79.5 %	42.0 %
	10 attempts (process-wise)	86.3 %	85.6 %	45.0 %

As expected, the models achieve better accuracies with more attempts (since greedy decoding is deterministic, it represents one decoding). Since process reconstruction fails if at least one token is incorrectly decoded, very high token-wise accuracies are needed to achieve good process-wise accuracies. It is observed that the 100D model achieves slightly better reconstruction accuracies than the 196D. However, the former peaks at epoch 23, while the latter peaks at epoch 25, when the regularization weight is higher (though not yet 1). Model 196D is thus expected to have better latent space properties. Because of the steep variation of the regularization weight, a harsh deterioration of validation accuracy and loss were observed after the best epoch, from which the models did not recover by the end of training. For smaller dimensions, the drop in accuracy is greater and the recovery is much worse – which is shown in Table 2, where validation *process* reconstruction accuracies (10 decoding attempts) are presented for both the best and last epochs. Although the 196D model should have better latent space properties by the last epoch (40), which has a smaller regularization loss, it proved much worse for generating *feasible* flowsheets from the latent space. For this reason, only the best epoch models were kept for the next analyses.

Table 2: Evolution of validation process reconstruction accuracy (10 decoding attempts) according to latent space dimension and epoch.

		Reconstruction Accuracy	
Model	**Best epoch number**	**Best epoch**	**Last epoch**
20D	22	70.7 %	0.00 %
50D	23	83.0 %	0.25 %
100D	23	86.3 %	0.31 %
150D	22	83.2 %	13.1 %
196D	25	85.6 %	77.5 %

Finally, it is observed that test accuracies are much worse than training and validation's, which was expected since the test set was generated in a different way (likely containing flowsheets that do not resemble the ones in the training set). This indicates that the model has trouble to generalizing beyond its training distribution.

3.2.2. Latent space analysis

Ten thousand points were sampled from the latent space and decoded according to the methodology described in section 3.1. Table 3 presents the proportion of valid; valid *and* unique; and valid, unique *and* new processes decoded from the sampling. Note that these values consider only the 10,000 *assigned* decodings, and not the total number of decoded SFILES (10,000 times the number of decoding attempts).

Table 3: Sampling results for the best models.

		Process Percentages		
Model	**Decoding attempts**	**Valid**	**Unique**	**New**
100D	Greedy	17.7 %	17.7 %	17.0 %
	10 attempts	41.5 %	41.5 %	40.5 %
	100 attempts	72.4 %	72.3 %	71.2 %
196D	Greedy	21.9 %	21.8 %	20.9 %
	10 attempts	52.3 %	51.8 %	50.4 %
	100 attempts	84.6 %	83.2 %	81.5 %

It is observed that the 196D model has better sampling results, as expected from its better latent space properties and despite 100D's slightly better reconstruction accuracies. It is observed that the models are not always capable of decoding valid SFILES from arbitrary points in space: processes will often include equipment with more (or less) connections than they should, or not be cyclical (necessary in this case study's application). The proportion of valid decodings can be improved by increasing the number of decoding attempts, but this only means that *at least one* feasible process was generated, out of all attempts. This indicates that the model may struggle to find other similar and feasible processes around the same point. When analyzing the decoded processes in latent space, it is seen that the decoded SFILES are found in clusters, rather than being evenly spaced, as illustrated in Figure 2. An example of processes decoded from a same point is shown in Figure 3.

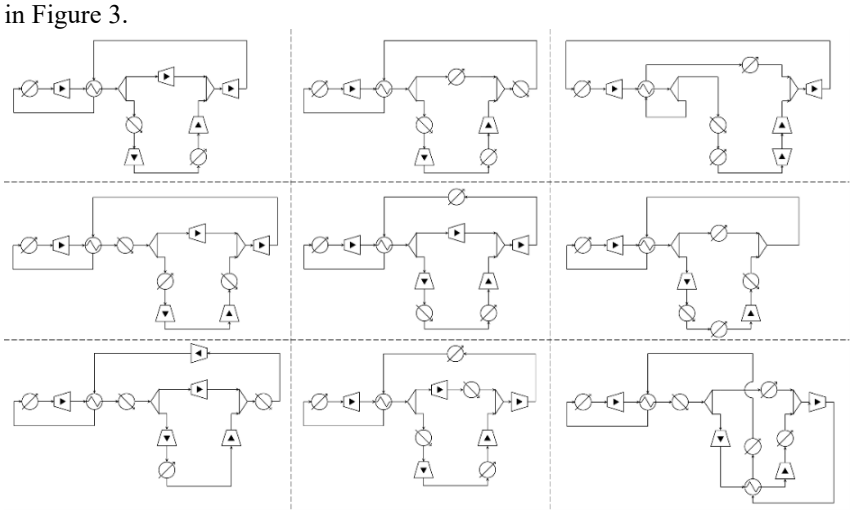

Figure 3: Example of processes sampled from a same point in latent space.

The choice of picking the closest valid process from the sample coordinates as the assigned decoding can be the subject of discussion, especially since the encoder and the decoder are used separately. When running multiple decoding attempts, a natural option would be to pick the SFILES decoded the most often, which should relate to the decoder's confidence – the distance serving as a tiebreaker. Also, depending on the intended use, multiple – if not all – valid decoded processes can be taken into consideration.

3.3. Limitations

Language-based notations may allow multiple ways of representing the same flowsheets. Even if a canonical representation is defined, it is hard to guarantee that similar processes will always have similar token-by-token representations. This may cause the model to have two representations for the same process in different parts of the latent space.

The use of directed graphs would be more adequate, but graph generative models are far more complex than language-based ones. A possible middle ground for this application could be to use a graph representation as an input for the encoder, while keeping the SFILES notation for the decoder's output.

4. Conclusions

In this work, the development of a continuous representation for process flowsheets is studied. It is observed that the model can generate new, valid flowsheets from the representation space, and that similar structures can be found next to each other. However, performance can still be improved: in some cases, only one feasible process was decoded in 100 attempts, while it would be desired that multiple feasible, similar processes could be sampled from a same region.

Training data generation must also be improved. Since the generated processes do not need to be simulated, data generation is inexpensive. However, the time needed to train the model was not. Adapting the model for GPU acceleration would allow the use of more data and hyperparameter optimization.

Future works could seek to improve model performance and to use its generation capabilities to feed generative approaches, to allow a more efficient exploration of alternatives. Following the molecular VAE paper, the model could also be coupled with performance data, and running optimizations directly in latent space could be tested.

References

R. Gómez-Bombarelli, J. N. Wei, D. Duvenaud, J. M. Hernández-Lobato, B. Sánchez-Lengeling, D. Sheberla, J. Aguilera-Iparraguirre, T. D. Hirzel, R. P. Adams, A. Aspuru-Guzik, 2018, Automatic Chemical Design Using a Data-Driven Continuous Representation of Molecules, ACS Central Science, 4, 2, 268–276

L. Mencarelli, Q. Chen, A. Pagot, I. E. Grossmann, 2020, A review on superstructure optimization approaches in process system engineering, Computers & Chemical Engineering, 136, 106808

T. Nabil, J.-M. Commenge, T. Neveux, 2022, Generative Approaches for the Synthesis of Process Structures, In Y. Yamashita & M. Kano (Eds.), Computer Aided Chemical Engineering, 49, 289–294, Elsevier

T. Nabil, M. Noaman, T. Morosuk, 2023, Data-driven structural synthesis of supercritical CO2 power cycles, Frontiers in Chemical Engineering, 5

G. Vogel, E. Hirtreiter, L. S. Balhorn, A. M. Schweidtmann, 2023a, SFILES 2.0: an extended text-based flowsheet representation, Optimization and Engineering, 24, 4, 2911–2933

G. Vogel, L. S. Balhorn, A. M. Schweidtmann, 2023b, Learning from flowsheets: A generative transformer model for autocompletion of flowsheets. Computers & Chemical Engineering, 171, 108162

ESCAPE-34 PSE-2024
European Symposium on Computer Aided Process Engineering
&
Process Systems Engineering

Flavio Manenti, Gintaras V. Reklaitis (Eds.), Book of Abstract of the 34th European Symposium on Computer Aided Process Engineering / 15th International Symposium on Process Systems Engineering (ESCAPE34/PSE24), June 2-6, 2024, Florence, Italy.

Pyomo.DoE: Facilitating Collaborations using Model-Based Design of Experiments in the Pyomo Ecosystem

Alexander W. Dowling

Chemical and Biomolecular Engineering, University of Notre Dame, Notre Dame, USA
adowling@nd.edu

Abstract

Identifying impactful solutions for global grand challenges often requires concerted research efforts that span molecular, material, device, systems, and infrastructure length-scales and transcend disciplines. In this contribution, we argue predictive multiscale mathematical models, often grounded in scientific theories, provide principled approaches to realize molecular-to-systems engineering. Using a membrane example, we present a tutorial on science-based data analytics including nonlinear regression, practical identifiability, parameter uncertainty quantification, and model-based design of experiments (MBDoE). Next, we provide a tutorial on how to use Pyomo.DoE to perform MBDoE for parameter precision optimization in the open-source Pyomo ecosystem. We conclude the best practices for using models at advance collaborations across disciplines (i.e., outside process systems engineering).

Keywords: data science, nonlinear regression, digital twins, membrane science, software engineering

1. Mathematical Modeling Facilitates Collaboration

Sustainability is considered a "wicked problem" (Lönngren and Van Poeck 2021) because of the complex interdependencies between social, natural, and engineered systems. These problems thus require interdisciplinary teams and new modeling strategies to consider complex interactions across molecular, material, device, process, and infrastructure scales (Eugene, Phillip, and Dowling 2019). Informed by our recent in collaborations ranging from water treatment (Eugene, Phillip, and Dowling 2021), refrigerant recycling (Befort et al. 2023), and additive manufacturing (K. Wang et al. 2023), we argue predictive mathematical models are a critical important tool for bridging length and timescales as well as disciplines.

2. Tutorial on Science-based Data Analytics

Through a short tutorial on membrane modeling, we show systematic steps for building, training, and validating mathematical models, illustrated in Figure 1.

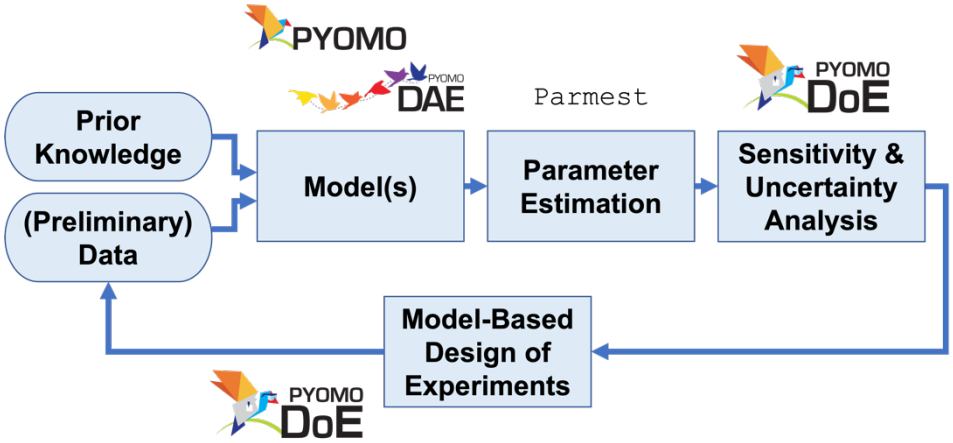

Figure 1. Science-based modeling workflow adapted from literature (Franceschini and Macchietto 2008; J. Wang and Dowling 2022) in the Pyomo ecosystem. Starting with preliminary data and prior knowledge, the modeler postulates one or more mathematical models grounded in engineering science. Physically meaningful parameters in these models are estimated via nonlinear optimization. Sensitivity and uncertainty analyses determine which parameters are estimable from the available data. Optionally, statistical information criteria can facilitate model selection. Finally, model-based design of experiments recommends the next most valuable measurements to discriminate between candidate models or increase parameter precision or both.

Diafiltration is a membrane staging technique to efficiently separate charged molecules, with current applications focused on valuable products such as proteins and buffer exchange (Ouimet et al. 2022). Motivated by the ongoing global transportation electrification, we contemplate optimizing diafiltration cascades for lithium-ion battery recycling (Harper et al. 2019). We previously showed how molecular-to-systems optimization using science-based mathematical models facilitates systematic evaluation of trade-offs in membrane system design and sets quantitative materials property targets for new applications (Wamble et al. 2022). However, this analysis was predicated on mathematical models for membrane transport.

Motivated by this goal of designing new membrane materials and systems using predictive science-based models, we share how the synergies between data analytics (e.g., dynamic modeling, nonlinear parameter, Fisher information analysis) and transport experiments (e.g., sensor design for time-series measurements) led to the new Diafiltration Apparatus for high-Throughput Analysis (DATA) technique for higher throughput membrane characterization (Ouimet et al. 2022). Using the DATA framework as a motivating example, we present a tutorial on science-based data analytics:

1. Postulating a dynamic model to describe changing concentrations as rejections as a function of time,
2. Using weighted nonlinear regression to balance prediction errors across three experimentally measured quantities,
3. Performing estimability analysis to demonstrate the importance of diafiltration experiments which sweep a large concentration range,
4. Using model-based design of experiments (MBDoE) to identify the operating regions with the most information (Liu et al. 2022).

Our tutorial shows how these data science tools directly inform apparatus design and experiment optimization, ultimately leading to predictive science-based mathematical models with quantified parametric uncertainty.

3. Pyomo.DoE and Model-based Design of Experiments (MBDoE)

Open-source tools, including Pyomo and Pyomo.DoE (J. Wang and Dowling 2022), enable model-based data analysis in Python while exploiting state-of-the-art nonlinear optimization solvers. In summary, MBDoE first sequentially determines the best experiments to discriminate between a set of candidate mathematical models (Olofsson et al. 2019). Then, in parameter precision mode, MBDoE sequentially recommends experiments to reduce parameter uncertainties (Franceschini and Macchietto 2008). Recently MBDoE algorithms have been combined with automated experiments (Pankajakshan et al. 2023) to establish digital twins (Kuchemüller, Pörtner, and Möller 2021). Pyomo.DoE helps Pyomo users automatically formulate and solve MBDoE for parameter precision optimization problems. In this contribution, we provide a tutorial for specifying models in Pyomo.DoE. We conclude by summarizing ongoing development activities for Pyomo.DoE.

4. Conclusions and Key Contributions

Through the membrane example, we show how science-based data analystics, especially MBDoE, provides a framework to characterize transport properties of membranes 10x faster than conventional experiments. Moreover, this example provides a tutorial on key data analytics tools.

While MBDoE is a powerful paradigm, it requires expertise in mathematical modeling, optimization, and statitics. To reduce these barriers, we are developing Pyomo.DoE, a package for MBDoE within the popular Pyomo modeling ecosystem.

References

Befort, Bridgette J., Alejandro Garciadiego, Jialu Wang, Ke Wang, Gabriela Franco, Edward J. Maginn, and Alexander W. Dowling. 2023. “Data Science for Thermodynamic Modeling: Case Study for Ionic Liquid and Hydrofluorocarbon Refrigerant Mixtures.” *Fluid Phase Equilibria* 572 (September): 113833. https://doi.org/10.1016/j.fluid.2023.113833.

Eugene, Elvis A., William A. Phillip, and Alexander W. Dowling. 2019. “Data Science-Enabled Molecular-to-Systems Engineering for Sustainable Water Treatment.” *Current Opinion in Chemical Engineering*, Energy, Environment & Sustainability: Sustainability Modeling ● Reaction engineering and catalysis: Green Reaction Engineering, 26 (December): 122–30. https://doi.org/10.1016/j.coche.2019.10.002.

———. 2021. “Material Property Targets to Enable Adsorptive Water Treatment and Resource Recovery Systems.” *ACS ES&T Engineering* 1 (8): 1171–82. https://doi.org/10.1021/acsestengg.0c00046.

Franceschini, Gaia, and Sandro Macchietto. 2008. “Model-Based Design of Experiments for Parameter Precision: State of the Art.” *Chemical Engineering Science*, Model-Based Experimental Analysis, 63 (19): 4846–72. https://doi.org/10.1016/j.ces.2007.11.034.

Harper, Gavin, Roberto Sommerville, Emma Kendrick, Laura Driscoll, Peter Slater, Rustam Stolkin, Allan Walton, et al. 2019. “Recycling Lithium-Ion Batteries from Electric Vehicles.” *Nature* 575 (7781): 75–86. https://doi.org/10.1038/s41586-019-1682-5.

Kuchemüller, Kim B., Ralf Pörtner, and Johannes Möller. 2021. “Digital Twins and Their Role in Model-Assisted Design of Experiments.” In *Digital Twins: Applications to the Design*

and Optimization of Bioprocesses, edited by Christoph Herwig, Ralf Pörtner, and Johannes Möller, 29–61. Advances in Biochemical Engineering/Biotechnology. Cham: Springer International Publishing. https://doi.org/10.1007/10_2020_136.

Liu, Xinhong, Jialu Wang, Jonathan A. Ouimet, William A. Phillip, and Alexander W. Dowling. 2022. "Membrane Characterization with Model-Based Design of Experiments." In *Computer Aided Chemical Engineering*, edited by Yoshiyuki Yamashita and Manabu Kano, 49:859–64. 14 International Symposium on Process Systems Engineering. Elsevier. https://doi.org/10.1016/B978-0-323-85159-6.50143-3.

Lönngren, Johanna, and Katrien Van Poeck. 2021. "Wicked Problems: A Mapping Review of the Literature." *International Journal of Sustainable Development & World Ecology* 28 (6): 481–502. https://doi.org/10.1080/13504509.2020.1859415.

Olofsson, Simon, Lukas Hebing, Sebastian Niedenführ, Marc Peter Deisenroth, and Ruth Misener. 2019. "GPdoemd: A Python Package for Design of Experiments for Model Discrimination." *Computers & Chemical Engineering* 125 (June): 54–70. https://doi.org/10.1016/j.compchemeng.2019.03.010.

Ouimet, Jonathan A., Xinhong Liu, David J. Brown, Elvis A. Eugene, Tylar Popps, Zachary W. Muetzel, Alexander W. Dowling, and William A. Phillip. 2022. "DATA: Diafiltration Apparatus for High-Throughput Analysis." *Journal of Membrane Science* 641 (January): 119743. https://doi.org/10.1016/j.memsci.2021.119743.

Pankajakshan, Arun, Solomon Gajere Bawa, Asterios Gavriilidis, and Federico Galvanin. 2023. "Autonomous Kinetic Model Identification Using Optimal Experimental Design and Retrospective Data Analysis: Methane Complete Oxidation as a Case Study." *Reaction Chemistry & Engineering* 8 (12): 3000–3017. https://doi.org/10.1039/D3RE00156C.

Wamble, Noah P., Elvis A. Eugene, William A. Phillip, and Alexander W. Dowling. 2022. "Optimal Diafiltration Membrane Cascades Enable Green Recycling of Spent Lithium-Ion Batteries." *ACS Sustainable Chemistry & Engineering* 10 (37): 12207–25. https://doi.org/10.1021/acssuschemeng.2c02862.

Wang, Jialu, and Alexander W. Dowling. 2022. "Pyomo.DOE: An Open-Source Package for Model-Based Design of Experiments in Python." *AIChE Journal* 68 (12): e17813. https://doi.org/10.1002/aic.17813.

Wang, Ke, Minxiang Zeng, Jialu Wang, Wenjie Shang, Yanliang Zhang, Tengfei Luo, and Alexander W. Dowling. 2023. "When Physics-Informed Data Analytics Outperforms Black-Box Machine Learning: A Case Study in Thickness Control for Additive Manufacturing." *Digital Chemical Engineering* 6 (March): 100076. https://doi.org/10.1016/j.dche.2022.100076.

ESCAPE-34 PSE-2024
European Symposium on Computer Aided Process Engineering
&
Process Systems Engineering

Flavio Manenti, Gintaras V. Reklaitis (Eds.), Book of Abstract of the 34th European Symposium on Computer Aided Process Engineering / 15th International Symposium on Process Systems Engineering (ESCAPE34/PSE24), June 2-6, 2024, Florence, Italy.

Predicting CO_2 Solubility in Solvent Mixtures using Graph Neural Networks

Ulderico Di Caprio[a], Min Wu[a], Emine Kayahan[b], Florence Vermeire[c], Tom Van Gerven[d], Peter Hellinckx[e], Steffen Waldherr[f] , Mumin Enis Leblebici[a,*]

[a]*Center for Industrial Process Technology, Department of Chemical Engineering, KU Leuven, Agoralaan Building B, 3590 Diepenbeek, Belgium*
[b]*Biomimetics Group, Division of Mechatronics, Biostatistics and Sensors (MeBioS), Department of Biosystems, KU Leuven, Willem de Croylaan 42, 3001 Leuven, Belgium*
[c]*Chemical Reactor Engineering and Safety (CREaS), Department of Chemical Engineering, KU Leuven, Celestijnenlaan 200F, 3001 Leuven, Belgium*
[d]*Process Engineering for Sustainable Systems, Department of Chemical Engineering, KU Leuven, Celestijnenlaan 200F, 3001 Leuven, Belgium*
[e]*Faculty of Applied Engineering, University of Antwerp, Groenenborgerlaan 171, 2000 Antwerp, Belgium*
[f]*University of Vienna, Molecular Systems Biology (MOSYS), Department of Functional and Evolutionary Ecology, Faculty of Life Sciences, 1030 Vienna, Austria*
muminenis.leblebici@kuleuven.be

Abstract

The anthropogenic CO_2 emissions reinforce the global warming phenomena. Post-combustion absorption is the most mature technology to reduce the CO_2 footprint. In the last decade, many solvent blends have been developed and tested to improve the process efficiency. However, testing such solvent blends relying only on laboratory experiments is expensive and laborious. Computational screening represents a viable solution for this challenge. A reliable model to predict the absorption performance of CO_2 in solvent blends is needed to achieve this task. Graph neural networks (GNNs) are a machine learning technique that correlates a graph structure with its properties through a learned molecular representation. They have shown significant capabilities in correlating the physic-chemical properties of a mixture with the molecular structures of its components. This work aims to build and analyse a model correlating the chemical composition of a mixture with its CO_2 solubility using GNN. The model considers the molecular structure of the components in the mixture, their concentrations, and other process parameters (i.e., process temperature and CO_2 concentration in the gas) as input variables. The model output is the CO_2 molar fraction within the liquid at equilibrium. Several model configurations were tested, and the most performant one employed three graph attention layers with an embedding size of 16. The final model returned a mean absolute percentage error and a root mean squared error of 26.86% and 0.011 on the entire test set, and 22.34% and 0.011 on test data involving only new molecular structures.

Keywords: CO_2 capture, Graph neural networks, QSPR relationship, Solvation.

1. Introduction

Global warming is one of the main challenges humanity is facing. It is enforced by anthropogenic CO_2 emissions. Many technologies are available to reduce carbon footprint; the most mature is post-combustion capture (Bui et al., 2018). This solution employs chemical solvents to absorb the CO_2 molecules in a flue-gas stream. The state-of-the-practice employs aqueous monoethanolamine (MEA) solutions at 30%wt. as the absorbent liquid. The chemistry of the solvent significantly affects the efficiency of the process; for this reason, many studies focus on the experimental investigation of novel solvent blends, investigating the CO_2 absorption capacity of both organic and ionic liquids (Aghel et al., 2022). Solvent design is a promising way to improve the efficiency of such a process; however, the experimental investigation of the solvent mixtures is very time-consuming and laborious. Digital solvent screening represents a viable solution for this challenge. However, a reliable model to predict the absorption performance of CO_2 in solvent blends is needed to achieve this task. The absorption properties of the solvent blend are connected to the chemical properties of the mixture components; therefore, correlating these two properties is the most promising way to achieve the modelling task. In amine blends and non-ionic solvents, absorption is typically driven both by chemical and physical mechanisms. Consequently, modelling such behaviour is challenging. In recent years, machine learning (ML) techniques have shown outstanding capabilities in predicting solubilities (Vermeire et al., 2021). They rely on experimental data of a given system to predict its behaviour and performance in given scenarios. More specifically, graph neural networks (GNNs) are an ML technique that correlates a graph structure with its properties through a learned molecular representation. Such a modelling technique has already been applied to predict the CO_2 solubility in ionic liquids (Jian et al., 2022). Many studies are available in the literature correlating the molecular structure of non-ionic liquids with absorption properties using ML techniques, such as Orlov (2021) and Orlov (2022). However, to the best of our knowledge, the literature lacks studies considering mixtures between organic components and water and the process conditions (i.e., temperature and CO_2 partial pressure in the flue gas) employing GNNs. This work aims to fill this gap by proposing a modelling methodology which applies GNN to predict the CO_2 solubility in non-ionic liquids. The model considers a mixture of up to two organic components and their concentration in water at different process conditions.

2. Methodology

The data to train the network was obtained from literature and involved mixtures of organic liquids with up to two organic components. Overall, the dataset contained 1902 data points involving 25 unique organic molecules. Each data point contains the chemical structure of the organic components and their mass fraction, the mass fraction of water, the absorption temperature, the equilibrium CO_2 partial pressure and the molar fraction of the dissolved CO_2 within the absorbent liquid.

All the information was used as network input except the molar fraction of the dissolved CO_2, which was used as model output. The information about the chemical structure was coded into molecular graphs through SMILES. The following properties characterised each node of the graph: 1) whether the atom is a hydrogen bond acceptor, 2) if the atom is in a ring and the dimension of the ring it is in, 3) the number of lonely pairs, 4) electronegativity, 5) atomic number and 6) hybridisation. All the node features were reported as continuous variables. The following properties characterised each edge

between the nodes: 1) the bond type (i.e., single, double, aromatic), 2) whether the bond is in a conjugated system, 3) whether the bond is in a ring, and 4) the bond length. All the edge features were reported as continuous variables except for the bond type, which was reported as a one-hot encoding. In addition, each molecular graph was characterised using the physical properties of the molecules, namely: 1) total number of hydrogen bond acceptor sites on the molecule, 2) total number of hydrogen bond donors on the molecule, 3) total number of hydrogen within the molecule, 4) total number of carbon within the molecule, 5) total number of oxygen within the molecule, 6) total number of nitrogen within the molecule, 7) total number of sulphur within the molecule, 8) total number of rotatable bounds within the molecule, 9) molecule topological surface area, 10) molecular radius, 11) molar mass. The physical molecular information was included to support the information obtained from the molecular graph. This information could be learned from the molecular graph; however, this would require a more complex graph layer structure. Therefore, an explicity of physical molecular information was added to the network to improve the efficiency of the model training. The node, bounds and molecular properties were obtained using RDKit, a cheminformatics toolkit. In order to test the network performance, part of the dataset was held out from the training and used as the test set; it contained 566 data points. All the data points referred to 2-methylpiperizine (2MPZ) were used in the test set. Such a part of the test set comprised 42 data points. Additionally, to evaluate the performance under process conditions, random data points involving mixtures containing monoethanolamine (MEA), methyldiethanolamine (MDEA) and piperazine (PZ) were included in the test set. The training set was employed for the network hyperparameter identification and its training, while the test set was never used in the training; it was used only to evaluate the performance of the final model following the model hyperparameter identification and training step.

Figure 1 reports the structure of the employed network. The information from the molecules was extracted using graph convolutional layers. This work tested two convolutional layers: the one reported by Kipf and Welling (2017) and Veličković et al. (2018). Now on, the former is referred to as GCN and the latter as GAT. The training involved their implementations included in PyTorch Geometric 2.2.0 and employed the default settings. The information obtained from the convolutional layer was embedded in arrays using average and maximum pooling for each molecule. Such operators get the average and the maximum values over each matrix column returned by the convolutional layers. In addition, a further array was employed, including molecular information calculated via RDKit. The three arrays were concatenated, generating an array that is molecule-specific. After that, the molecule-specific arrays of the two organic components were multiplied by their mass fraction and summed. The obtained array was used as input to a multilayer perceptron (MLP) with the process conditions to calculate the dissolved CO_2 amount. Prior to the usage in the MLP, the following scaling techniques were applied to the input: the molecular features were standardised, the temperature input was normalised in the range [0,1], and the CO_2 pressure was firstly logarithmically scaled and then normalised in the range [0,1]. The MLP comprised two hidden layers, the first containing 20 nodes and the following 5 nodes. The layer had many nodes as the input, and the output layer contained only one output neuron. The internal activation functions were rectified linear units, while the output node employed a sigmoid function. The activation functions were found by manual grid search.

The number of graph layers, the type of graph layers and the embedding size were chosen using a grid search. The identification of the network hyperparameters was performed using a 10-fold cross-validation. Each fold contained mixtures with at least one molecule not included in the other folds; this way, the score on the test folder represents the model

performance when dealing with unknown molecular structures, and the network selection is more reliable. A full-factorial investigation was performed involving two graph layers (i.e., GCN and GAT), three sizes of the molecular embedding (i.e., 16, 32 and 64) and three amount of graph layers (i.e., 1, 2 and 3). The network showing the lower median values of the mean squared error on the validation folds was selected. All the networks were trained using Adam optimiser for 500 epochs with a learning rate of $3 \cdot 10^{-3}$.

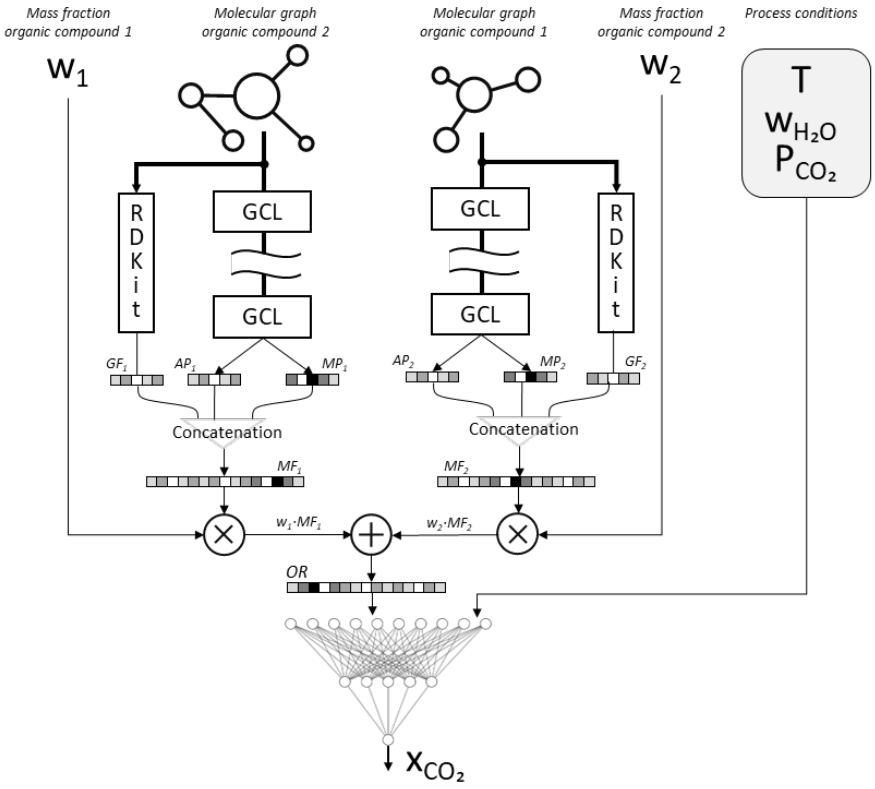

Figure 1. Structure of the employed Graph Neural Network. In this figure: Graph Convolutional Layers (GCL), Average Pooling (AP), Mean Pooling (MP), Molecular Features (MF), Graph feature (GF), Organic representation (OR).

The network showing the best performance in the 10-fold cross-validation was trained on the entire training set, applying ensemble learning over 30 networks. Each network was trained on the entire train set with different initial guesses of the model weights. The results of the 30 networks were averaged and re-scaled to the original output values scale.

3. Results and discussion

Among the various networks, the most performant one on the 10-fold cross-validation employed a structure containing three graph attention layers per molecule, with a molecular embedding size of 16. Figure 2 reports the performance of this model, including the parity plots and the metrics on the test set. The root mean squared error (RMSE) and the mean absolute percentage error (MAPE) were employed.

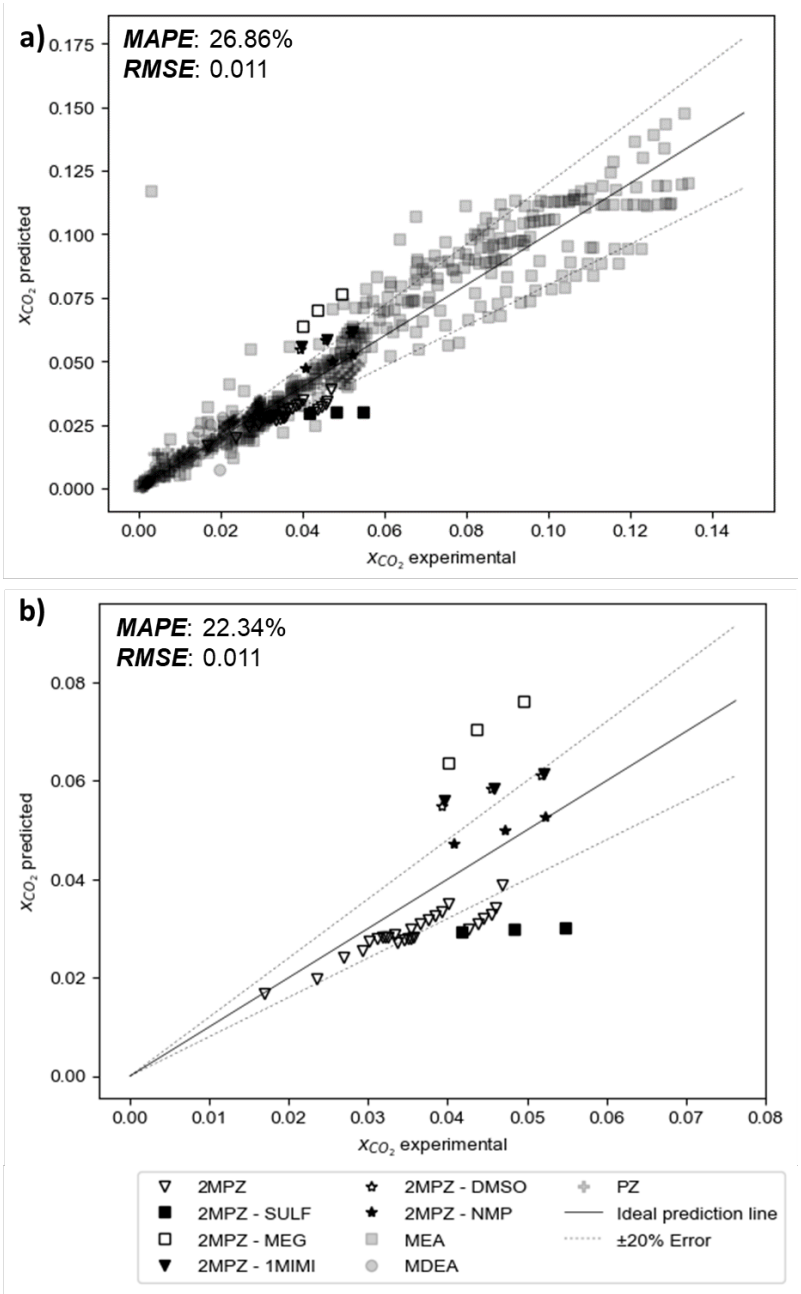

Figure 2. Parity plot and metrics of the model on the test set. a) Model performance on the entire test set. b) Model performance on the test molecules not included in the train set. The abbreviations are as follows: 2-methylpiperizine (2MPZ), sulfolane (SULF), ethylene glycol (MEG), 1-methylimidazole (1MIMI), Dimethyl sulfoxide (DMSO), N-methyl-2-pyrrolidinone (NMP).

Figure 2a reports the performance of the model on the entire test set. In this case, the predictions are made both on molecules not included in the training set and on those

included in the training set but at different process conditions. In this case, the model returns a MAPE value of 26.86% and a RMSE of 0.011. In addition, most of the points related to the molecules already included in the train set fell in the range ± 20%. This result highlights the prediction accuracy of the model over the process conditions.
Figure 2b reports the model accuracy on molecules it was not trained on. In this figure, only the points related to the 2MPZ are included. The model showed a MAPE of 22.34% and a RMSE of 0.011 in these conditions. From the figure, it is possible to assess how most of the points are within the error range of ± 20% when the organic blend is composed of only 2MPZ or 2MPZ-NMP. However, the predictions significantly diverge for all the other mixtures. The training data included points involving the other molecules within the organic part with 2MPZ; however, they included MEA or MDEA instead of 2MPZ. We hypothesise that this is related to the fact that both MEA and MDEA do not include cyclic structures in the molecule and have only one nitrogen atom in their structure; on the other hand, 2MPZ have a cyclic structure and includes two nitrogen atoms. However, further investigations are required to prove this hypothesis.

4. Conclusions

In this work, we obtained a model estimating the CO_2 solubility within an organic mixture, given the molecular structure of the components and the process conditions. The model was obtained employing graph neural networks. The model generalisation capabilities were evaluated on unseen molecular structures and process conditions. In both cases, the trained model showed acceptable prediction accuracy with a mean absolute percentage error of 26.88% on the overall test set and 22.34% on the test set, including only unseen molecular structures.
A continuation of this work would be a more systematic investigation of further network structures to improve the model accuracy since some bias toward some input variables is reported. In addition, a further improvement would be assessing the estimation of other physical parameters affecting the capture process efficiencies.

References

B. Aghel et al., 2022, Review on CO2 capture by blended amine solutions, International Journal of Greenhouse Gas Control, 119, 103715
M. Bui et al., 2018, Carbon capture and storage (CCS): the way forward, Energy & Environmental Science, 11, 1062-1176
Y. Jian et al., 2022, Predicting CO2 Absorption in Ionic Liquids with Molecular Descriptors and Explainable Graph Neural Networks, ACS Sustainable Chemistry & Engineering, 10, 50, 16681–16691
T.N. Kipf and M. Welling, 2017, Semi-Supervised Classification with Graph Convolutional Networks, arXiv, 1609.02907
A.A. Orlov et al., 2021, Chemoinformatics-Driven Design of New Physical Solvents for Selective CO2 Absorption, Environmental Science & Technology, 55, 22, 15542–15553
A.A. Orlov et al., 2022, Computational screening methodology identifies effective solvents for CO2 capture, Communications Chemistry, 5, 37
P. Veličković et al., 2018, Graph Attention Networks, arXiv, 1710.10903
F.H. Vermeire and W.H. Green, 2021, Transfer learning for solvation free energies: From quantum chemistry to experiments, Chemical Engineering Journal, 418, 129307

ESCAPE-34 PSE-2024
European Symposium on Computer Aided Process Engineering
&
Process Systems Engineering

Flavio Manenti, Gintaras V. Reklaitis (Eds.), Book of Abstract of the 34th European Symposium on Computer Aided Process Engineering / 15th International Symposium on Process Systems Engineering (ESCAPE34/PSE24), June 2-6, 2024, Florence, Italy.

Adversarial Attacks on Demand Side Management of a Grid-Scale Battery Storage

Eike Cramer [a*]

[a] *RWTH Aachen University – Process Systems Engineering (AVT.SVT), Forckenbeckstraße 51, 52074 Aachen, Germany*
eike.cramer@alumni.tu-berlin.de

Abstract

This work investigates the effects of adversarial attacks on the combined decision-making process of electricity price forecasting and optimization-based demand side management (DSM). At the example of a grid-scale battery, this work shows how attackers can induce significant changes in system operation by adding targeted modifications to the input data of the decision-making process. Furthermore, this work proposes a black-box approach using empirical emulators (adversarial surrogate models) of the decision-making process. The proposed attack leads to significant changes in the DSM schedules and the obtained profits, even for small perturbations of the input data.

Keywords: Demand side management, electricity price forecasting, machine learning, adversarial attacks, safety

1. Introduction

The process systems engineering (PSE) community is and has been at the forefront of developing algorithms for optimization-based DSM for flexible process operation, which can achieve cost savings in the energy- and chemical industries (Ave et al., 2018; Baader et al., 2020). Solving DSM problems typically requires solving large-scale optimization problems, which use predictions of electricity price data as parameters (Morales et al., 2014).

The success and increased application of machine learning-based decision making in DSM and other PSE disciplines increases the risk of malicious interference from outside parties. Most machine learning algorithms used in DSM do not consider the threat of adversarial attacks, i.e., data corruption aimed at deteriorating machine learning model outputs (Xu et al., 2020). This work investigates the vulnerability of flexibly operated industrial processes to such adversarial attacks. Opposed to the known threat of hackers, adversarial attacks are data-based attacks that implement attacks without access to the operation itself. Attack design methods, such as the fast gradient sign method (FGSM) (Goodfellow et al., 2015), rely on the sensitivity information of the machine learning model with respect to its input features to generate adversarial noise that is added to the original data. Such adversarial noise patterns can either pursue a targeted attack, i.e., aiming to induce specific predictions or untargeted attacks, i.e., forcing predictions that are as far from the correct output as possible (Xu et al., 2020).

At the example of a grid-scale battery, this work showcases the effects of adversarial attacks on the decisions made in optimization-based DSM. The grid battery operators aim to return a profit by trading on the day-ahead electricity market. As the actual prices are unknown, the full decision-making process consists of electricity price forecasting and solving a DSM optimization problem. As in most real-world applications, neither the forecasting model nor the DSM optimization model are publicly available. Therefore, this work proposes to train an emulating regression model of the full decision-making process of electricity price forecasting and optimization via a black-box attack scheme. This type of process emulating model is referred to as adversarial surrogate model (ASM) throughout this work. Using gradients of the ASM, the attacker designs minimal perturbations to the residual load forecasts that aim to deteriorate the trading decisions and lead to financial losses.

The trading decisions of the battery operators are made using a linear scheduling model. The optimization problem is solved using electricity price forecasts from state-of-the-art forecasting models such as LASSO regression and artificial neural networks (ANN) that use residual load forecasts as their input features (Trebbien et al., 2023). The results show how minimal changes in the input data can induce significant financial losses to the operation of the electricity storage. Thus, data-based adversarial attacks pose a threat to comparable decision-making processes in the energy- and chemical industries.

2. DSM of a grid-scale battery and multi-period electricity price forecasting

This Section introduces the DSM case study and the multi-period electricity price forecasting scheme. Note that this Section states the models for completeness. The attacker has no access to of knowledge of the scheduling or the forecasting model.

2.1. DSM of a Battery Storage

This work investigates the DSM of a grid-scale battery. The battery operation aims to return a profit by trading on the day-ahead market. Problem (P) shows the optimization problem to determine the optimal trading decisions. The problem considers a 1200 kWh storage capacity, and the formulation is adapted from previous work (Cramer et al., 2022) and general formulations for day-ahead trading (Morales et al., 2014). The formulation assumes a constant efficiency $\eta = 0.9$ for charging and discharging, making Problem (P) a linear optimization problem.

$$
\begin{aligned}
&\max_{W_t^{in}, W_t^{out}} \sum_{t=1}^{24} P_t^{DA}\left(W_t^{out} - W_t^{in}\right)\Delta t \\
&s.t. \quad SOC_t = SOC_{t-1} - \frac{1}{\eta} W_t^{out} - \eta W_t^{in} \\
&\qquad 0 \leq SOC_t \leq SOC^{max} \\
&\qquad SOC_{t=24} = SOC_{t=0} \\
&\qquad 0 \leq W_t^{out} \leq W^{max} \\
&\qquad 0 \leq W_t^{in} \leq W^{max}
\end{aligned}
\tag{P}
$$

In Problem (P), W_t^{in} and W_t^{out} are the trading decisions for the t-th hour, W^{max} is the maximum (dis-)charging rate, SOC_t is the state of charge at hour t, P_t^{DA} is the day-ahead

price at the hour t, and Δt is the trading interval of 1h. Generally, the battery will charge during low-price hours and discharge during high-price hours. The problem solves efficiently using the *gurobi* optimization software.

2.2. Multi-period electricity price forecasting

The decision-making process uses multi-period forecasting to predict the electricity price based on day-ahead residual load forecasts, which are the most important features for day-ahead electricity prices (Trebbien et al., 2023). The multi-period approach matches the structure of the day-ahead markets where all 24-time intervals are set at the same time. The general form of the multi-period forecasting is a multivariate regression problem that reads:

$$\boldsymbol{P}^{DA} = T(\boldsymbol{W}^{DA}_{res.\ load}) \tag{1}$$

Here, $\boldsymbol{P}^{DA}$ is the vector of day-ahead electricity prices, $\boldsymbol{W}^{DA}_{res.\ load}$ are the residual load forecasts, and T is a multivariate regression model. To implement the multivariate regression, this work uses a linear regression model with a LASSO penalty, a fully connected ANN, and a convolutional ANN (TCN). All regression models are implemented using the Python-based machine learning library *TensorFlow*.

3. Black-box attacks using adversarial surrogate models

This Section proposes an approach to fitting an emulator to the full decision-making process for DSM. The ASM is used to compute sensitivities that provide quantitative information to design adversarial noise.

3.1. Emulating decision-making processes via adversarial surrogate models

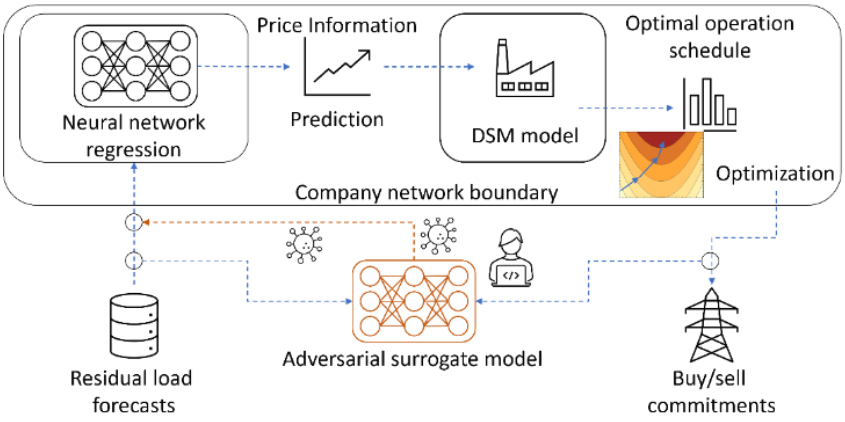

Figure 1 Concept of the adversarial surrogate model (ASM). EPF and DSM models are inside the secure company boundary. The ASM is trained to emulate the full decision-making process.

The individual steps of the decision-making process are unknown to external attackers, i.e., the attacker does not know the EPF model nor the DSM model. Furthermore, the EPF takes place within the secure company network and, thus, the prices forecasts cannot be intercepted by the attacker. Instead, the attacker only knows the input and output data. For the considered case, this assumption is reasonable as the final DSM decisions are the target values of the attacks and the input data consists of the most widely used input data for electricity prices forecasting, i.e., the residual load forecasts (c.f. Section 2.2 for details). This work proposes a black-box attack strategy based on what this work calls an

adversarial surrogate model (ASM). Thus, the attack only has to intervene with the data pipelines to and from the company instead of the infiltrating the company network itself. Figure 1 shows the ASM scheme. The ASM is trained on the residual load forecasts and the buy/sell commitments of the company under attack. The evaluation of the ASM then reads:

$$\widehat{\boldsymbol{W}}_{buy,sell} = ASM(\boldsymbol{W}^{DA}_{res.\ load}) \tag{2}$$

Here, $\widehat{\boldsymbol{W}}_{buy,sell}$ are the ASM prediction of the trading decisions. In the following, the ASM provides gradient information that describes how the decisions of the company change based on changes to the input data, i.e., the residual load forecasts.

3.2. Heuristic attack target for the design of adversarial attacks

Adversarial attacks allow for either targeted or untargeted attacks (Xu et al., 2020), i.e., attacks that pursue a specific target or randomly worsen the outputs, respectively. This work proposes a dampening heuristic to design targeted attacks. Following the intuition that a constant operation is worse than a flexible operation based on variable electricity prices, the proposed dampening attack aims to force trading decisions towards a constant. This work uses the simple yet effective fast gradient sign method (FGSM) (Goodfellow et al., 2015) to compute adversarial noise patterns that are added to the original input data:

$$\widetilde{\boldsymbol{W}}^{DA}_{res.\ load} = \boldsymbol{W}^{DA}_{res.\ load} + \epsilon \cdot sign\left(\nabla \mathrm{MSE}\left(ASM(\boldsymbol{W}^{DA}_{res.\ load}), \overline{\boldsymbol{W}}_{buy,sell}\right)\right) \tag{3}$$

Here, $\widetilde{\boldsymbol{W}}^{DA}_{res.\ load}$ is the adversarially modified data, ∇MSE is the gradient of the MSE loss function, $\overline{\boldsymbol{W}}_{buy,sell}$ is the historical mean of the trading decisions, and ϵ is a scaling parameter called attack rate (Goodfellow et al., 2015).

4. Results

This Section investigates the effects of the black-box attack proposed in Section 3 to the grid-scale battery problem presented in Section 2. In particular, Section 4.1 shows the how the attacks affect the operational schedules and Section 4.2 shows the statistics of the changes in profits for different attack rates and the three different regression models. This Section only considers attacks on the full decision-making process as the individual components like the EPF and the DSM models are unknown to the attacker, i.e., the attacker cannot evaluate the effect of the attack on the EPF performance or the sensitivity of the DSM model to the electricity prices directly.

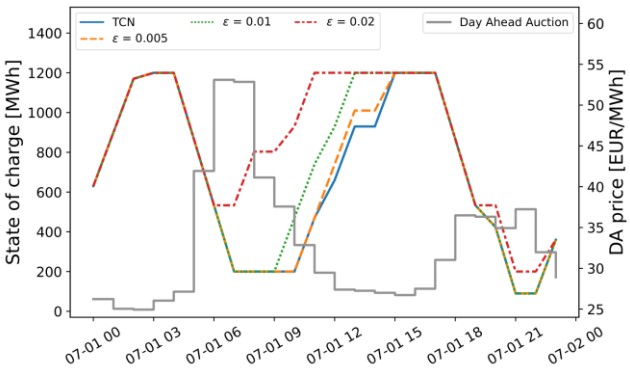

Figure 2 Changes of the scheduling decisions for attack rates $\epsilon = 0.005$, $\epsilon = 0.01$, $\epsilon = 0.02$ in relation to the actual day-ahead electricity price on July 1st, 2019.

4.1. Storage schedules

Figure 2 shows the schedule of the grid-scale battery storage on July 1st, 2019, for different attack rates. The figure relates the actual day-ahead electricity price with the

state of charge schedule of the battery storage. The blue line labeled TCN shows the battery operation schedule obtained with the forecasts from the TCN without any perturbations. The schedule clearly shows how the battery is charged in the early morning between midnight and 4 am, when the electricity prices are low, and discharged between 5 am and 7 am, when the electricity prices peak. A similar cycle then repeats later in the day. With increasing attack rates, the operation of the electricity storage changes to less favorable schedules. In particular, the recharging, which previously started around noon and continued during the low-price hours of the afternoon, now starts earlier when the electricity prices are still high. For instance, for an attack rate of $\epsilon = 0.02$, the battery is charged between 6 and 7 am when the electricity price is at its peak. The schedules shown in Figure 2 highlight how small perturbations to the input data can lead to significant and harmful changes in the scheduled operation of the grid-scale electricity storage.

4.2. Profits

Ultimately, the adversarial attack in this work aims to turn the profitable operation of the battery storage to lower profits or even losses. Figure 3 shows the mean and variance bands of the profits obtained via DSM of the battery storage. The profits are computed for results for each day in 2019 and attack rates between 0 and 1 to obtain representative statistics.

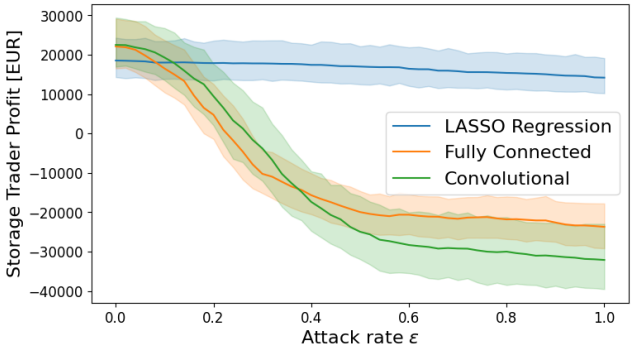

Figure 3 Profits obtained in DSM of the grid scale battery storage for the three forecasting models and attack rates between 0 and 1.

The results show decreasing profits for all three forecasting models. However, the decline in profits obtained with LASSO regression is significantly slower compared to the two neural networks, where the profits decrease quickly and even lead to losses. The drop of in profits confirms the observation from Figure 2 that the proposed black-box attack leads to a deterioration of the decisions made by the optimizer in Problem (P). The LASSO regression is fitted using a regularization of the scale parameters of the linear regression. Thus, the LASSO prediction is dominated by its bias term, i.e., a constant that is not affected by the adversarial attack. Therefore, the LASSO regression model is more robust towards the attacks. Meanwhile, the neural networks include many scaling parameters making the impact of small perturbations more significant. Notably, the profits obtained with LASSO forecasts without any attacks are significantly lower compared to the two neural networks. Hence, a trade-off occurs between the accuracy of the electricity price forecast and the robustness towards adversarial attacks.

5. Conclusions

This work considers a case of an adversarial attacker aiming to attack the combined decision-making process of EPF and DSM. In the considered case, the attacker has no access to the individual models and cannot intervene with any intermediate state of the decision-making process. The main proposal of this work is an ASM that emulates the decision-making process by training a regression model on the inputs and outputs of the

decision-making process; the residual load forecasts that form the basis of the price forecasts and the decisions made via the optimization problem.

The results of the grid-scale battery case study show that small perturbations based on targeted gradient information can lead to significant damage in DSM. Notably, the attacker can design and implement the black-box attack without accessing the company's internal network directly. Instead, the data pipelines to and from the company need to be monitored and only the input data must be modified. Thus, the proposed attack poses a potential threat to the profitability of companies practicing DSM and additional work is required to develop defensive strategies.

Acknowledgments

The author gratefully acknowledges the financial support of the Kopernikus project SynErgie 3 by the Federal Ministry of Education and Research (BMBF) and the project supervision by the project management organization Projektträger Jülich.

References

Ave, G. D., Harjunkoski, I., & Engell, S. (2018). Industrial Demand Side Management Formulation for Simultaneous Electricity Load Commitment and Future Load Prediction. In *Computer Aided Chemical Engineering* (Vol. 44, pp. 1237–1242). Elsevier B.V. https://doi.org/10.1016/B978-0-444-64241-7.50201-9

Baader, F. J., Mork, M., Xhonneux, A., Müller, D., Bardow, A., & Dahmen, M. (2020). Mixed-Integer Dynamic Scheduling Optimization for Demand Side Management. In *Computer Aided Chemical Engineering* (Vol. 48, pp. 1405–1410). Elsevier B.V. https://doi.org/10.1016/B978-0-12-823377-1.50235-4

Cramer, E., Paeleke, L., Mitsos, A., & Dahmen, M. (2022). Normalizing flow-based day-ahead wind power scenario generation for profitable and reliable delivery commitments by wind farm operators. *Computers and Chemical Engineering*, *166*. https://doi.org/10.1016/j.compchemeng.2022.107923

Goodfellow, I. J., Shlens, J., & Szegedy, C. (2015). Explaining and harnessing adversarial examples. *3rd International Conference on Learning Representations, ICLR 2015 - Conference Track Proceedings*, 1–11.

Morales, J. M., Conejo, A. J., Madsen, H., Pinson, P., Zugno, M., Grigoroudis, E., & Siskos, Y. (2014). Integrating renewables in electricity markets - Operational problems. In *Springer* (Vol. 205). https://doi.org/10.1007/978-1-4614-9411-9

Trebbien, J., Gorjão, L. R., Praktiknjo, A., Schäfer, B., & Witthaut, D. (2023). Understanding electricity prices beyond the merit order principle using explainable AI. *Energy and AI*, *13*, 100250. https://doi.org/10.1016/j.egyai.2023.100250

Xu, H., Ma, Y., Liu, H. C., Deb, D., Liu, H., Tang, J. L., & Jain, A. K. (2020). Adversarial Attacks and Defenses in Images, Graphs and Text: A Review. *International Journal of Automation and Computing*, *17*(2), 151–178. https://doi.org/10.1007/s11633-019-1211-x

ESCAPE-34 PSE-2024
European Symposium on Computer Aided Process Engineering
&
Process Systems Engineering

Flavio Manenti, Gintaras V. Reklaitis (Eds.), Book of Abstract of the 34th European Symposium on Computer Aided Process Engineering / 15th International Symposium on Process Systems Engineering (ESCAPE34/PSE24), June 2-6, 2024, Florence, Italy.

Determining the Feasible Region of Non-Linear Dynamic Process Models for Optimization Through Data-Driven Regression with Classification

Torben Talis,[a] Gerardo Brand Rihm,[a] Raoul Heese,[b] Erik Esche,[a] Michael Bortz,[b] Jens-Uwe Repke[a]

[a]*Technische Universität Berlin, Process Dynamics and Operation Group, Str. des 17. Juni 135, Berlin 10623, Germany*
[b]*Fraunhofer Institute for Industrial Mathematics (ITWM), Fraunhofer-Platz 1, Kaiserslautern 67663, Germany*
t.talis@tu-berlin.de

Abstract

Surrogate models from machine learning have no guarantees regarding extrapolation. However, they will also predict results in areas where the original model is known to be infeasible. Classifiers can be used to model the boundary of the feasible region. Here, classifiers are analysed and extended towards dynamic systems. A rigorous, dynamic model is sampled in different ways and the feasible region is identified by data-driven classifiers. The suitability of different architectures is evaluated for the case study of a flash separation unit. The most suitable classifier will be used to improve real time optimization using surrogate models by preventing faulty extrapolations and forcing all points of the solution to be in the feasible region.

Keywords: imbalanced classification, data-driven models, feasible region, dynamic systems.

1. Introduction

Chemical processes can be described by complex nonlinear dynamic models. These models have a limited feasible region, e.g., a common flash unit model is only valid in two-phase region or a distillation column model is only defined in the proper fluid dynamic operation area. Hard and hidden constraints like these are included in the formulation of first principles models. However, the computational cost of these models often prohibits their application in real time optimization. In contrast, data-driven surrogate models are fast to evaluate, but there is typically no information on the region of validity included in the model. Hence, these models return results even for points outside the feasible region, which are obviously bad extrapolations. Real plant operation is frequently performed close to these bounds, so information on the feasible region should be added to the surrogate models. Similar has been done before for steady state models by e.g., (Penteado et al., 2020). (Schweidtmann et al., 2022) use a classifier to identify the boundaries of a training dataset und use this as the region of validity for their

surrogate model. The actual feasible region of the process is not investigated. However, the method is applied for optimization on a dynamic model. We focus on exploring the feasible region of the rigorous model and matching the surrogate model's region of validity to it. This enables safe operation close to the bounds. For this, it is mandatory to incorporate data of non-converging trajectories into the training dataset.

2. Methods

In this study we use a rigorous model of a flash unit with non-ideal thermodynamics, depicted in Fig. 1, to first generate data and then investigate the suitability of the following classifier architectures: random forest, k-nearest neighbors, and balanced bagging classifier (Guillaume Lemaître et al., 2017). The rigorous model is only valid in the two-phase region and is described in more detail in (Brandner et al., 2023). Different cases are investigated, where scenarios for heat flux and feed composition are generated by a step or a pseudorandomized sequence. These signals have a wide spread, so the simulation diverges at the end of almost all simulation scenarios, whenever the system leaves the two-phase region. However, this results in highly imbalanced datasets with a lot of valid points (along the time series) and only very few points describing the boundary of convergence and beyond (typically the last point of such a time series). 28 datasets with 3 different sampling rates (10 / 100 / 1000 s^{-1}) are investigated. The share of non-converging points amounts to 0.8, 0.1, and 0.01 %, respectively for the three sampling rates. For the classification, four different sets of features are selected: (i) the states x (T, p, x^B, y^D), (ii) x and the controls u (Q, x^F), (iii) x and gradient information dx, (iv) x, u, and dx. For ease of implementation, the gradient of the systems internal energy and the component hold-ups were used instead of the before mentioned states. Although, it might be less intuitive, the system is fully described by this information. All datasets are then split into 80% training and 20% test data, while keeping the same ratios of the two classes in both sets and are used to train different classifiers. Tab. 1 shows the truth table for the models. The geometric mean score (g-score), which is the geometric mean of sensitivity and specificity (Eq. (1)), was used to score their performance.

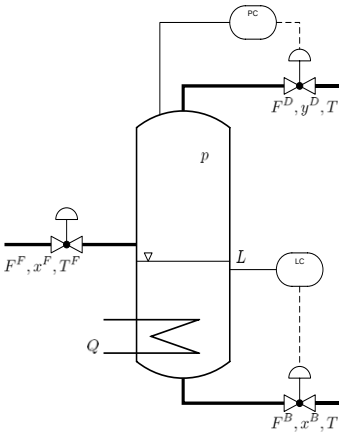

Figure 1: Flowsheet of the flash unit with controls Q and x^F

$$g = \sqrt{\frac{TP}{TP + FN} \cdot \frac{TN}{TN + FP}} \tag{1}$$

Table 1: Truth table for classifier

	Classifier predicts non-convergence	Classifier predicts convergence
Rigorous model does not converge	TP	FN
Rigorous model converges	FP	TN

3. Results and Discussions

There are eight datasets with a timestep of 0.001, and each 10 with a timestep of 0.01 and 0.1. The mean, as well as the min and max value of the g-score of all datasets are shown in Fig. 2 for four different architectures (3-nearest-neighbors (3-NNC), 5-nearest-neighbors (5-NNC), random-forest (RFC), and balanced-bagging classifier (BBC)) against the four different feature sets. The results show that in general a higher sampling rate renders the classification problem more difficult and thus leads to a worse classification accuracy. However, while the classification metric is better for small sampling rates, the actual bounds of the feasible region cannot be described accurately in these cases. In contrast to the classic k-NN- and RFC classifiers, the BBC is an ensemble method, that makes use of the undersampling technique and was specifically developed for imbalanced datasets. The achievable g-scores are much better than with the other architectures and the metric seems to be surprisingly independent of both the timestep and the selected features.

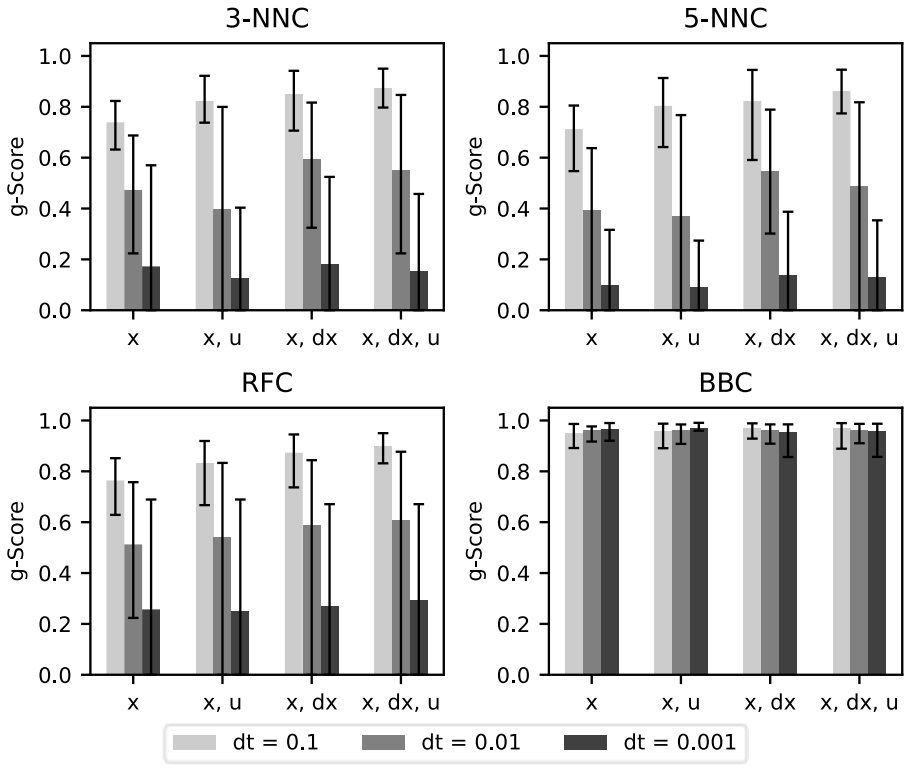

Figure 2: Comparison of different classifier architectures. Mean, min, and max value of all datasets for different feature sets.

4. Conclusions

In a case study, we evaluated the suitability of different data-driven classifiers for describing the feasible region of a dynamic model of a flash separation unit. Different sampling rates and classification techniques have been analyzed and compared. Of the investigated model architectures, the balanced bagging classifier is best in predicting,

whether the rigorous model is solvable at a given state. To the best of our knowledge this is the first instance of a classifier used for describing the feasible region, instead of the valid range of training data. We consider the present work a proof of concept for dynamic models in general. This classifier will subsequently be used in combination with a data-driven regression model, to guarantee feasibility of the solutions of optimization problems.

Acknowledgement

This work was funded by Deutsche Forschungsgemeinschaft (DFG, German Research Foundation) – 466380688 – within the Priority Programme "SPP 2331: Machine Learning in Chemical Engineering. Knowledge Meets Data: Interpretability, Extrapolation, Reliability, Trust".

References

Brandner D., Talis T., Esche E., Repke J.-U., Lucia S., 2023, Reinforcement learning combined with model predictive control to optimally operate a flash separation unit In: M.C.G.E.P. Antonios C. Kokossis (Ed), 33 European Symposium on Computer Aided Process Engineering, Vol 52, Elsevier, 595–600.

Guillaume Lemaître, Fernando Nogueira, Christos K. Aridas, 2017, Imbalanced-learn: A Python Toolbox to Tackle the Curse of Imbalanced Datasets in Machine Learning, Journal of Machine Learning Research, 18, 1–5.

Penteado A.T., Esche E., Weigert J., Repke J.-U., 2020, A Framework for Stochastic and Surrogate-Assisted Optimization using Sequential Modular Process Simulators In: 30th European Symposium on Computer Aided Process Engineering, Vol 48, Elsevier, 1903–1908.

Schweidtmann A.M., Weber J.M., Wende C., Netze L., Mitsos A., 2022, Obey validity limits of data-driven models through topological data analysis and one-class classification, Optimization and Engineering, 23, 855–876.

ESCAPE-34 PSE-2024
European Symposium on Computer Aided Process Engineering
&
Process Systems Engineering

Flavio Manenti, Gintaras V. Reklaitis (Eds.), Book of Abstract of the 34th European Symposium on Computer Aided Process Engineering / 15th International Symposium on Process Systems Engineering (ESCAPE34/PSE24), June 2-6, 2024, Florence, Italy.

AI-powered Framework to Predict Environmental Impacts of Organic Chemicals via Retrosynthesis

Shaohan Chen, Tim Langhorst, Benedikt Winter, Johannes Schilling, André Bardow*

ETH Zurich, 8092 Zurich, Switzerland
abardow@ethz.ch

Abstract

The transition toward a sustainable chemical industry relies on the ability to quantify the environmental impacts of chemical production. Life cycle assessment (LCA) is a holistic method that quantifies the environmental impacts of chemical productions across multiple impact categories. However, conducting a thorough LCA study is challenging in the early process design stages due to limited LCA data availability. This work estimates LCA data of organic chemicals by designing a pathway-resolved framework using machine-learning-based retrosynthesis. Our method automatically predicts the life cycle inventories (LCI) and the corresponding environmental impacts solely using SMILES codes of target chemicals as the input. We verify this framework with a benchmark dataset of 136 organic chemicals, including industrially validated LCIs. The results show that our framework can accurately predict LCIs and the environmental impact of all impact categories. Our framework thus allows for filling data gaps in LCA databases for early-stage process design and accelerates the transition toward a sustainable chemical industry.

Keywords: Environmental impacts, predictive LCA, retrosynthesis, machine learning.

1. Introduction

Integrating environmental impacts at the early stages of process design is essential for fostering a sustainable chemical industry. Life cycle assessment (LCA) is a standardized method that comprehensively quantifies potential environmental impacts across various impact categories, such as climate change and toxicity (ISO 14040). However, current LCA databases only cover a limited number of chemicals, necessitating tedious LCA work to assess any other chemicals. These LCAs require extended life cycle inventory (LCI) data that quantify the material and energy requirements needed to produce the target chemical. This data is challenging to acquire during the early stages of process design (Chebaeva et al., 2021).

To mitigate the lack of LCA data, two types of methods have been developed to predict the environmental impacts of chemical production: 1) machine-learning-based (ML-based) methods and 2) stoichiometry-based methods. ML-based methods, for example, Kleinekorte et al. (2023), usually use molecular descriptors as the input. The resulting

accuracy is limited because of data scarcity for training, and the input ignores the actual conversion pathway. Stoichiometry-based methods, for example, Langhorst et al. (2023), integrate chemical synthesis details from literature but are, therefore, also time-consuming and labor-intensive. In particular, the impacts of the reactants need to be known so that the data problem is only shifted to them.

To bridge the gap between the two types of pioneering methods, we design a pathway-resolved machine-learning framework to automatically estimate LCIs and the corresponding environmental impacts of organic chemical production. For this purpose, we integrate an ML-based retrosynthesis tool (Schwaller et al., 2020).

2. Method

Our pathway-resolved ML-based framework predicts the LCI data required to produce a specific chemical and its reactants. The LCI data is used subsequently to calculate the environmental impacts. The framework consists of three modules to ensure reliable environmental impact predictions for chemical production (see Figure 1):

1. First, an ML-based retrosynthesis tool (Schwaller et al., 2020) provides possible synthesis pathways and potential precursors to produce the target chemicals.
2. Second, this synthesis pathway data is analyzed by an optimization model to determine the stoichiometric coefficients of the reactants and possible byproducts. Thereby, we know the stoichiometries along the full predicted synthesis pathway.
3. Lastly, the reaction equations along the predicted synthesis pathway are used for stoichiometric estimation methods to predict the LCIs of producing the target chemical. To calculate the environmental impacts, the LCIA scores of reactants are taken from available LCA databases. For reactants not available in the considered LCA databases, we use feedforward neural networks with a similar structure as the one proposed by Wernet et al. (2008) to predict proxy LCIA scores of the reactants.

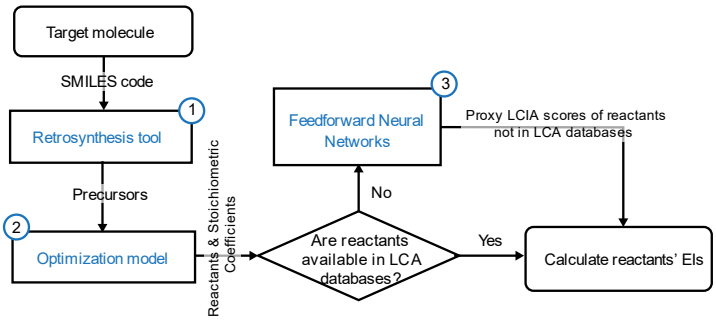

Figure 1. Flow chart of the proposed pathway-resolved ML-based framework to predict reactants' environmental impacts (EIs).

3. Results

Our pathway-resolved ML-based framework is verified by comparing the predicted LCIs and the estimated environmental impacts with a benchmark dataset of 136 organic chemicals (Langhorst et al., 2023). This dataset includes industrially validated LCIs for each chemical. As an underlying LCA database, we use Ecoinvent version 3.5 (Wernet et al., 2016) and the ReCiPe (H) V1.13 method (Huijbregts et al., 2017). Since the

retrosynthesis tool mainly identifies the reactions along the synthesis pathways, we focus our analysis on the predicted reactants' environmental impacts.

In our dataset, our framework identifies 60 chemicals with predicted reactants sourced entirely from the Ecoinvent database. For the remaining 76 chemicals, for which the reactants are not fully listed in the Ecoinvent database, the framework calculates proxy LCIA scores via neural networks.

For the 60 chemicals with reactants in Ecoinvent, Figure 2 exemplifies the predicted reactants' environmental impacts on global warming impact (GWI) and freshwater ecotoxicity potential (FETPinf). This analysis distinguishes between two groups of chemicals: those for which our framework predicts the same synthesis pathways as the one in the benchmark dataset and those for which an alternative pathway is predicted.

Our framework performs remarkably regarding Spearman's rank correlation coefficient when the predicted pathways are the same as in the benchmark, 0.93 for the GWI and 0.99 for the FETPinf, respectively. The corresponding mean absolute percentage error (MAPE) is 0.11 for the GWI and 0.12 for the FETPinf, respectively. The MAPE is between 0.11 and 0.16 for all 18 impact categories.

The validation is not possible in cases where an alternative synthesis pathway is predicted since this difference does not imply an incorrect prediction. Manual analysis of the predicted pathways using SciFinder shows that 89% of them exactly match the ones in the existing literature. The presented framework is transparent by providing the details on the assumed pathways.

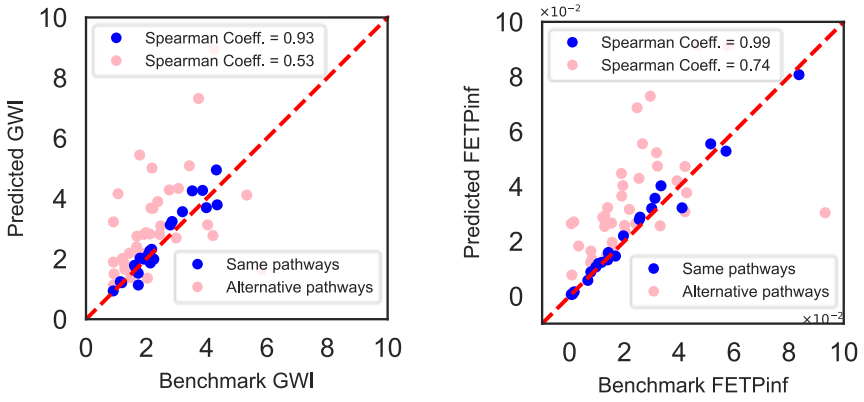

Figure 2. Predicted reactants' environmental impacts compared to the benchmark reactants' environmental impacts. Left: global warming impact (GWI), right: freshwater ecotoxicity potential (FETPinf). Blue dots indicate chemicals for which our framework predicts the same synthesis pathways as considered in the benchmark dataset. Pink (light) dots represent chemicals for which our framework predicts synthesis pathways different from those in the benchmarks.

These results demonstrate that our framework can reliably predict the LCIs for organic chemical production, accurately estimate the environmental impacts when the predicted synthesis pathways match the benchmark, and predict reasonable alternative pathways in a transparent manner for the LCA practitioner to check and verify.

4. Conclusions

This work proposed a pathway-resolved framework using ML-based retrosynthesis to predict the environmental impacts of organic chemical production by using the SMILES code of the target chemical as the only input. Our framework provides transparent information on synthesis pathways, stoichiometric coefficients of the predicted chemical reactions, and the estimated byproducts.

The results show that our framework can accurately predict LCIs and the environmental impact of all impact categories. Due to the transparent modelling of the synthesis pathways and LCIs of chemical productions, the framework can be adapted for specific LCA databases, LCIA methods, and system models. Our framework thus allows for filling data gaps in LCA databases for early-stage process design and accelerates the transition toward a sustainable chemical industry.

Acknowledgments

This work is part of the Usorb-DAC Project supported by a grant from The Grantham Foundation for the Protection of the Environment to RMI's climate tech accelerator program, Third Derivative. It is also partly funded by the LIFE Klimastiftung and the ETH Zurich Foundation.

References

[1] ISO 14040, *Environmental management - Life cycle assessment-Principles and framework*; International Organization for Standardization, 2006.

[2] N. Chebaeva, M. Lettner, J. Wenger, J. P. Schöggl, F. Hesser, D. Holzer, and T. Stern (2021). Dealing with the eco-design paradox in research and development projects: The concept of sustainability assessment levels. *Journal of Cleaner Production*, *281*, 125232.

[3] J. Kleinekorte, J. Kleppich, L. Fleitmann, V. Beckert, L. Blodau, and A. Bardow (2023). APPROPRIATE Life Cycle Assessment: A PROcess-Specific, PRedictive Impact AssessmenT Method for Emerging Chemical Processes. *ACS Sustainable Chemistry & Engineering*.

[4] T. Langhorst, B. Winter, D. Roskosch, and A. Bardow (2023). Stoichiometry-Based Estimation of Climate Impacts of Emerging Chemical Processes: Method Benchmarking and Recommendations. *ACS Sustainable Chemistry & Engineering*, *11*(17), 6600-6609.

[5] P. Schwaller, R. Petraglia, V. Zullo, V.H. Nair, R.A. Haeuselmann, R. Pisoni, C. Bekas, A. Iuliano, and T. Laino (2020). Predicting retrosynthetic pathways using transformer-based models and a hyper-graph exploration strategy. *Chemical science*, *11*(12), 3316-3325.

[6] G. Wernet, S. Hellweg, U. Fischer, S. Papadokonstantakis, K. Hungerbühler (2008). Molecular-structure-based models of chemical inventories using neural networks. *Environmental science & technology*, *42(17)*, 6717-6722.

[7] G. Wernet, C. Bauer, B. Steubing, J. Reinhard, E. Moreno-Ruiz, and B. Weidema (2016). The ecoinvent database version 3 (part I): overview and methodology. *The International Journal of Life Cycle Assessment*, *21*, 1218-1230.

[8] M. A. J. Huijbregts, Z. J. N. Steinmann, P. M. F. Elshout, G. Stam, F. Verones, M. D. Vieira, A. Hollander, M. Zijp, and R. van Zelm (2017). ReCiPe 2016 v1.1: a harmonized life cycle impact assessment method at midpoint and endpoint level report I: characterization [RIVM Report 2016 -0104a]. *National Institute for Public Health and the Environment RIVM*, 2016-0104.

[9] SciFinder. Chemical Abstracts Service, n.d. https://scifinder.cas.org (accessed November 8, 2023).

ESCAPE-34 PSE-2024
European Symposium on Computer Aided Process Engineering
&
Process Systems Engineering

Flavio Manenti, Gintaras V. Reklaitis (Eds.), Book of Abstract of the 34th European Symposium on Computer Aided Process Engineering / 15th International Symposium on Process Systems Engineering (ESCAPE34/PSE24), June 2-6, 2024, Florence, Italy.

Fast Fourier Transform-Based Synthetic Method for Chemical Process Data Augmentation and Fault Classification

Jie-Ning Chen,[a] Jia-Lin Kang,[b*] Yuan Yao[a*]

[a]*Department of Chemical Engineering, National Tsing Hua University, Hsinchu, 30013, Taiwan, ROC*
[b]*Department of Chemical and Materials Engineering, National Yunlin University of Science and Technology, Yunlin, 64002, Taiwan, ROC*
jlkang@yuntech.edu.tw; yyao@mx.nthu.edu.tw

Abstract

Faults in industrial processes can lead to significant financial losses and severe safety concerns. Thus, timely identification of faults is crucial. Fault classification, usually based on supervised machine learning approaches, uses historical process data to extract fault characteristics and classify them accurately. However, the limited availability of fault data in real-world plants hampers effective model training, as conventional supervised learning depends on sufficient training data. Consequently, creating synthetic fault data that captures the temporal evolution of variable trajectories can be a viable solution to enrich the dataset. In this study, we proposed a synthetic method using Fast Fourier Transform (FFT) to generate fault data, applied to the Tennessee Eastman Process (TEP) dataset to augment fault data and improve classification accuracy. Besides, we use the gradient boosting classifier as our classifier to determine whether our synthetic fault data can assist the detection post fault occurred by comparing the testing accuracy of the classifiers training with and without fault data augmentation. The case study results illustrate the feasibility of the proposed method.

Keywords: fast Fourier transform, fault classification, imbalanced data, data augmentation.

1. Introduction

In chemical industry operations, it is essential to maintain the normal functioning of process variables, including the concentration, temperature, and flow rates of materials flowing into and out of each unit. This is crucial for achieving mass production and preventing malfunctions. Fault classification, typically reliant on supervised machine learning techniques, plays a significant role in enhancing fault detection and diagnostics. This approach leverages historical process data to accurately identify and categorize fault characteristics. However, a major challenge in this approach is the dependency on extensive training data, which is often scarce in real-world plants due to the infrequent nature of historical fault occurrences (Jiang and Ge, 2020). Consequently, generating

synthetic fault data to augment the training dataset emerges as a practical strategy to improve the accuracy of fault classification.

Industrial processes involve the operation of multiple units and the interaction of diverse components, resulting in process data that is typically represented as multivariable time series. Generally, the emergence of a process issue is not attributable to the abnormality of a single variable. Consequently, it is essential to generate synthetic fault data that accurately reflects the temporal evolution of faults. The generative adversarial network (GAN) is a popular method for dataset augmentation, prized for its ability to generate a wealth of data from random noise. However, training GAN models can be challenging due to the min-max competition between the generator and the discriminator. Often, the discriminator rapidly outpaces the generator, leading to the latter's underperformance and a tendency to produce overly conservative data outputs (Klopries and Schwung, 2024). This imbalance can be particularly problematic when generating time series data akin to industrial process data, as GANs may struggle to capture the temporal evolution of the series, instead generating data that represents an average of the entire series.

we introduce a novel data synthesis method utilizing the fast Fourier transform (FFT) to address the challenges associated with augmenting multivariable time series data. By applying FFT, we transform our time series fault data into the frequency domain. This transformation reveals the amplitude compositions of sinusoidal waves across various frequencies, simplifying the analysis process. We then generate synthetic fault data by applying the Inverse Fast Fourier Transform (IFFT) to these processed frequency-domain data, effectively reconstructing time series data that retain the essential characteristics of the original faults.

2. Methodology

2.1. Fast Fourier transform-based data synthesis method

FFT is an algorithm designed to compute the discrete Fourier transform (DFT) with enhanced efficiency. It transforms data from the time domain into the frequency domain (Rapuano and Harris, 2007). The DFT is mathematically represented as shown in Eq. (1), where W denotes $e^{-j\frac{2\pi}{N}}$, with N being the size of the data set. In this equation, $X(k)$ represents the frequency domain data obtained post-transformation, while $x(n)$ corresponds to the original time domain data collected at sampling time n.

$$X_i(k) = \sum_{n=0}^{N-1} x_i(n) W^{kn},\ k = 0,1,\dots,N-1;\ \ i = \text{fault or normal} \tag{1}$$

$$\Delta X(k) = X_{fault}(k) - X_{normal}(k) \tag{2}$$

$$X'_{fault}(k) = \Delta X(k) + X'_{normal}(k) \tag{3}$$

$$x_{synthetic}(n) = \sum_{k=0}^{N-1} X'_{fault}(k) W^{-kn} \tag{4}$$

The framework of the proposed fault data synthesis method is depicted in Figure 1.The process initiates by applying FFT to each process variable, as per Eq. (1). This step transforms the data from the time domain ($x_{\text{fault}}(n)$ or $x_{\text{normal}}(n)$) to the frequency domain ($X_{\text{fault}}(k)$ or $X_{\text{normal}}(k)$). Next, we analyse the differences between normal and fault operation data in the frequency domain (Eq. (2)), identifying what termed “waveform variations” ($\Delta X(k)$). These variations not only describe the disturbance post fault occurs but also capture the evolution of the fault. Subsequently, we randomly overlay these waveform variations onto other normal operation data sets in the frequency domain ($X'_{normal}(k)$), as depicted in Eq. (3). This procedure generates the frequency

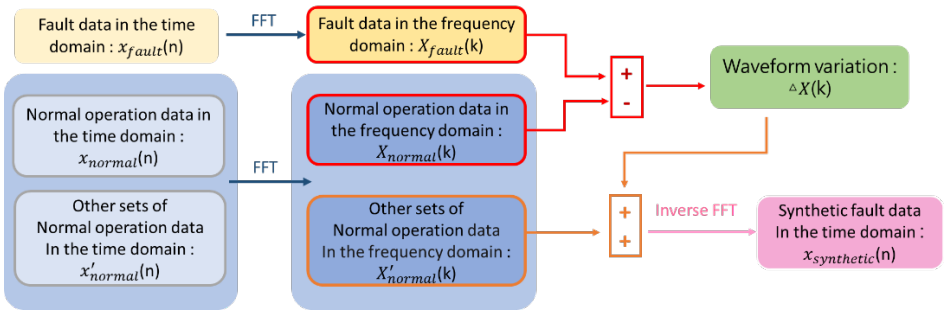

Figure1. The flow chart of our fault data synthetic method based on FFT

compositions for synthetic fault data ($X'_{fault}(k)$). The final step involves applying inverse FFT (as per Eq. (4)) to convert these compositions back into the time domain, resulting in synthetic fault data ($x_{synthetic}(n)$) that aligns in the same format with the original process data.

2.2. Gradient boosting

After integrating the measured process data with the synthetic fault data, we employ gradient boosting (Friedman, 2002) as the classifier for fault classification. Gradient boosting is a powerful algorithm that sequentially combines multiple "weak learners" to form a stronger model. Each learner in the sequence is trained using the residual errors from the previous model as its target. The optimal model we aim to construct can be described by Eq. (5), where F represents the cumulative model, with the subscript m denoting the sequence of the models. The term h refers to the new model being trained, which will be added to F, and ρ is a small positive coefficient, typically ranging between 0 and 1.

$$F_{m+1} = F_m + \rho h_m \tag{5}$$

Let y_i represent the observed value and $\hat{y}_i$ is the predict value from the model F_m. The objective of gradient boosting is to fit the new model h_m to the residuals of F_m (as shown in Eq. (6)). This approach allows each new model to correct the errors made by the previous models, progressively improving the overall accuracy of the classifier.

$$residual = y_i - F_m(x_i) = y_i - \hat{y}_i \tag{6}$$

In our study, we utilized decision trees as the weak learners within the gradient boosting framework, while the total number of weak learners was chosen to be 100. The loss function selected for optimization is the multinomial deviance. We set the learning rate at 0.01 to ensure gradual model improvement. During the boosting process, a maximum of 52 features were randomly chosen at each split for every tree, providing a balance between diversity and model complexity. Additionally, we constrained the size of each decision tree by limiting the number of nodes to a maximum of 21.

3. Case Study

3.1. Tennessee Eastman Process

The Tennessee Eastman process (TEP) (Rieth et al., 2017) dataset was used as the case study to illustrate the feasibility of the proposed method. The TEP encompasses five key units: a reactor, a product condenser, a vapour-liquid separator, a recycle compressor, and a product stripper. The dataset encompasses 21 distinct types of faults, including step changes, random variations, slow drifts, sticking, and some unknown types. A

comprehensive description of each variable and fault type is available in reference (Downs and Vogel,1993). In each run, there are 52 variables recorded over 500 sampling points, with the exception of fault 6. Fault 6 involves a shutdown occurring 6 hours after the fault onset, resulting in a total of 140 sampling points. Faults are introduced after an hour of normal operation. Consequently, the initial twenty sampling points represent normal operational conditions, while the subsequent 480 points correspond to data during the fault condition.

3.2. Fault data synthesis by FFT

We applied FFT to the TEP dataset for the purpose of synthesizing fault data. Given that FFT is designed to process one variable at a time, we systematically applied FFT to the data of each variable sequentially. To account for the fact that the frequency components identified by FFT can vary with different lengths of input data, we implemented a moving window approach. This approach involved slicing the data using a window of 50 sampling points and a step size of 10 sampling points. The next step involved calculating the waveform variations for each fault type. This was achieved by subtracting the amplitude composition of the normal operational data from that of the fault data. We then integrated these waveform variations with the amplitude compositions of normal operational data, which had not been previously used in the waveform variation calculation, to create new amplitude compositions representative of the faults. Finally, we generated time-series synthetic fault data by applying inverse-FFT to these newly formed amplitude compositions.

In this study, we assumed that the known historical data for each fault type was represented by the first run of data in the TEP dataset. In this context, 140 sampling points were available for fault 6 and 500 sampling points for other fault types as well as normal operational data. To generate the synthetic fault data, five runs of normal operational data were randomly selected.

3.3. Classifier training

Before training the classifier, the process data was standardized and then pre-processed by applying a moving window technique which involves a window length of 20 sampling points and a step size of 1 sampling point. Consequently, for each run of normal operation data, this process yielded 461 data windows. For fault 6, which has a shorter duration, we obtained 101 data windows. For other fault types, we generated 181 data windows representing the transition state and 261 windows for the steady state. The first ten hours of data following a fault occurrence was categorized as transition data, with the subsequent data classified as steady state. For training purposes, we included all windows of transition data and a selection of 90 windows from the steady state data. For testing, we used all available data windows.

In terms of training the classifier, we initially used five runs of normal operation data and one run of data for each fault type, prior to data augmentation. Post-augmentation, we enriched the training dataset with an additional 10 runs of synthetic data for each fault type.

4. Results And Discussions

For data visualization purposes, we projected both the original fault data from the TEP dataset and the synthetic fault data into a common coordinate system defined by three principal component axes: pc1, pc2, and pc3. First, we represented each run of fault process data as a single point in the PCA score plot. This was done to assess whether the

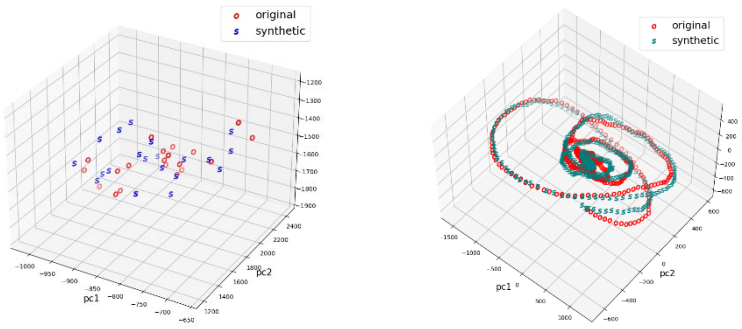

(a) (b)

Figure 2. PCA score plot of fault 7:
(a) each point represents one run; and (b) each point represents one window

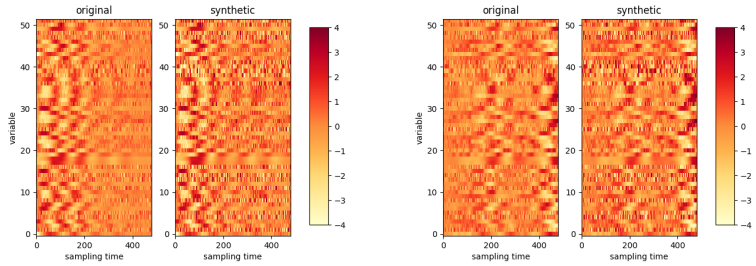

(a) (b)

Figure 3. Heatmaps comparing original and synthetic fault data:
(a) fault 1; and (b) fault 8

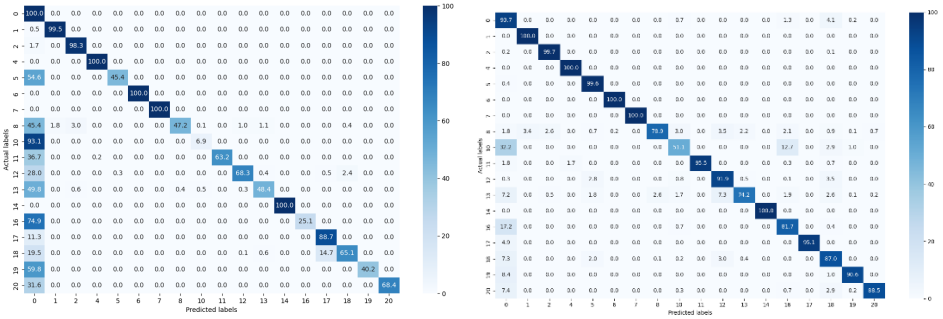

(a) (b)

Figure 4. Confusion matrices of classification accuracy (%):
(a) before and (b) after data augmentation

overall information and diversity of our synthetic fault data were comparable to that of the original fault data. The results, as depicted in Figure 2 (a), indicated that the distributions of most synthetic faults closely resembled those of the original faults. This similarity demonstrates the effectiveness of our method in capturing the essential characteristics of faults while maintaining diversity. Subsequent analysis involved representing each moving window of data as a point in the PCA score plot. This approach allowed us to determine whether our synthetic data successfully captured the temporal evolution of fault trends. The results, shown in Figure 2 (b), revealed that our synthetic fault data closely followed the trajectory of the original fault data, indicating our method's capability to replicate fault trends in time series relationships.

We also evaluated our synthetic data using heatmaps, which visually represent the numerical fluctuations of the 52 variables through color variations. The results indicated that the numerical fluctuations in our synthetic fault data closely mirrored those in the original data, confirming the successful extraction of fault trends (Figure 3).

To ascertain the impact of our synthetic data on fault classification effectiveness, we trained two gradient boosting classifiers. The first classifier was trained using the original, imbalanced TEP dataset, while the second was trained with our augmented dataset, which included the synthetic data. The results demonstrated a significant improvement in testing accuracy, from 75.08% to 91.40%, before and after data augmentation, respectively. This marked improvement, as shown in Figure 4, validates the efficacy of our data augmentation approach in addressing the challenges posed by imbalanced datasets in fault classification problems.

5. Conclusions

In this study, we investigated the effectiveness of time series data augmentation in chemical industrial processes, particularly focusing on datasets with imbalanced fault distribution, and examined whether the inclusion of generated data could enhance fault classification accuracy. We applied FFT to analyse the waveform compositions of various faults and generate synthetic fault data, the characteristics of which were visualized using PCA score plots and heatmaps. These visualizations demonstrated that the synthetic data successfully captured the dynamic and sequential properties of the fault progression over time. Additionally, the overall variable fluctuations in the synthetic data closely mirrored those in the original dataset, encompassing both the transition and steady states following a fault occurrence. To quantify the impact of data augmentation on fault classification, we compared the confusion matrices of classifiers trained with and without the augmented data. These comparisons clearly showed that the inclusion of the synthetic data led to a significant improvement in classification accuracy.

Acknowledgement

This work was supported in part by the National Science and Technology Council under project numbers NSTC 112-2221-E-007-015

References

Downs, J.J. and E.F. Vogel, A plant-wide industrial process control problem. Computers & chemical engineering, 1993. 17(3): p. 245-255.
Friedman, J.H., Stochastic gradient boosting. Computational statistics & data analysis, 2002. 38(4): p. 367-378.
Jiang, X. and Z. Ge, Data augmentation classifier for imbalanced fault classification. IEEE Transactions on Automation Science and Engineering, 2020. 18(3): p. 1206-1217.
Klopries, H. and A. Schwung, ITF-GAN: Synthetic time series dataset generation and manipulation by interpretable features. Knowledge-Based Systems, 2024. 283: p. 111131.
Rapuano, S. and F.J. Harris, An introduction to FFT and time domain windows. IEEE instrumentation & measurement magazine, 2007. 10(6): p. 32-44.
Rieth, C.A., et al., Additional tennessee eastman process simulation data for anomaly detection evaluation. Harvard Dataverse, 2017. 1: p. 2017.

ESCAPE-34 PSE-2024
European Symposium on Computer Aided Process Engineering
&
Process Systems Engineering

Flavio Manenti, Gintaras V. Reklaitis (Eds.), Book of Abstract of the 34th European Symposium on Computer Aided Process Engineering / 15th International Symposium on Process Systems Engineering (ESCAPE34/PSE24), June 2-6, 2024, Florence, Italy.

Discovering the Origin of Catalyst Performance and Degradation of Electrochemical CO2 Reduction Through Explainable Artificial Intelligence

Ung Lee[a]*, Daeun Shin[b] Hakan Karasu[a], Dahye Won[a] Jonggeol Na[b]

[a] *Clean Energy Research Center, Korea Institute of Science and Technology, 5, Hwarang-ro 14-gil, Seongbuk-gu, Seoul, 02792, Republic of Korea*
[b] *Department of Chemical Engineering and Materials Science, Ewha Womans University, Seoul 03760, Republic of Korea*

Abstract

Catalyst degradation poses a substantial hurdle for the commercialization of electrochemical CO2 reduction, leading to diminished activity and selectivity. The significant experimental cost associated with catalyst characterization limits the in-depth understanding of this degradation. Machine learning has emerged as a promising tool to bypass these costly procedures, though its limited interpretability has often complicated its application. This study introduces an interpretable machine learning framework capable of accurately predicting catalyst conditions using linear sweep voltammetry (LSV) in sub-seconds, while also shedding light on identifying the origins of catalytic degradation. Based on a comprehensive dataset of 5236 LSV experiments, a convolutional neural network was trained and demonstrated superior predictive capabilities for total current and faradaic efficiency. The insights derived from the model are further elucidated through explainable artificial intelligence (XAI), pinpointing key degradation factors. To validate the XAI interpretation, surface analysis experiments were conducted, underscoring the reliability of the proposed approach. This novel framework offers potential applications in various catalytic processes, battery degradation, and chemical process monitoring, indicating its potential for rapid and reliable performance monitoring.

ESCAPE-34 PSE-2024
European Symposium on Computer Aided Process Engineering
&
Process Systems Engineering

Flavio Manenti, Gintaras V. Reklaitis (Eds.), Book of Abstract of the 34th European Symposium on Computer Aided Process Engineering / 15th International Symposium on Process Systems Engineering (ESCAPE34/PSE24), June 2-6, 2024, Florence, Italy.

Monte Carlo-Free Radioactive Particle Tracking Technique

Ghazaleh Mirakhori,[a,b] Jocelyn Doucet,[c] Bruno Blais,[a] Jamal Chaouki[b*]

[a]*Research Unit for Industrial Flows Processes (URPEI), Department of Chemical Engineering, Polytechnique Montreal, Stn Centre-Ville, Montreal, H3C 3A7, Canada*
[b]*Process Engineering Advanced Research Lab (PEARL), Department of Chemical Engineering, Polytechique Montreal, Stn Centre-Ville, Montreal, H3C 3A7, Canada*
[c]*Pyrowave Inc, Montreal, H2N 2B7, Canada*
jamal.chaouki@polymtl.ca

Abstract

Radioactive particle tracking (RPT) is a non-intrusive method to measure the velocity profiles in single and multiphase systems. It tracks a radioactive particle by measuring the γ-rays it emits using NaI scintillation detectors positioned around the reactor (Alghamdi et al., 2022). Traditionally, this method relies on a mathematical model that incorporates Monte Carlo simulations to establish the relationship between radiation intensity and particle positions. The model requires three unknown inputs for every detector. These parameters are obtained through a calibration procedure which includes manually placing the particle at multiple known positions and solving an optimization problem to identify the model parameters (Zambonino and Santos, 2023). RPT has some limitations. It assumes a uniform attenuation coefficient for the system, which may not fully represent complex multiphase reactors. The model is also sensitive to detector and calibration point positioning, leading to a build-up of reconstruction error if these quantities are not known with great accuracy. In this work, we introduce a novel approach that bypasses the need for calibration prior to reconstructing the tracer particle's position in RPT experiments. We implement a collaborative robot (cobot) to move the tracer particle inside the volume of interest, recording the exact position of the particle in time. The freedom to program a robotic arm enables strategic volume sampling, extensive data accumulation, and the creation of a dataset linking positions to detector counts. Instead of following the conventional calibration process to determine unknown parameters in the mathematical model, we utilize this dataset to train an Artificial Neural Network (ANN) model. The model predicts the particle position by analyzing the received photon counts from each detector surrounding it. Therefore, this ANN model can reconstruct the particle positions free from the limitations and artifacts typically associated with the mathematical model. Consequently, it yields lower prediction errors when compared to traditional methodologies. Due to these improvements, RPT will be able to accommodate larger-scales multiphase reactors, facilitating the design and scale up procedures.

Keywords: Radioactive Particle Tracking, Artificial Neural Networks, Robotics

1. Methodology

1.1. Database generation

We use a Doosan cobot (A0912) mounted on a fixed pedestal. The cobot carries a tracer particle attached to the tip of a metallic rod, held securely by a custom in-house-developed gripper. Its operation is managed through a controller, which itself is controlled by a computer executing a Python script.
We program the cobot in a way that moves the tracer within the specified volume, passing through hundreds of positions and mapping the entire volume. The cobot logs the position of the tracer along with the corresponding time throughout the entire experiment at determined time intervals. While the cobot is in movement and on an entirely distinct system, we capture the photon counts at each 10 ms interval using scintillation detectors strategically positioned around the volume.
The RPT hardware starts recording photon counts data slightly before the robot's movement. Both systems operate on different clocks and different temporal scales, necessitating an external synchronization. To effectively organize these positions and their associated photon counts into dataset for training the ANN model, a post-processing procedure is required.

1.2. Data post-processing for database generation

The post-processing of raw data comprises three steps:

- Time delay calculation: to find the time delay between the two systems, we establish a handshake protocol. We specify one detector to communicate with the cobot. The cobot places the particle in front of the detector at a distance of 20 cm. Subsequently, the cobot moves the particle toward the detector's face at a constant velocity. Following this approach, the cobot then returns the particle to its initial position. The reciprocating motion of the robot leads to the generation of two peaks in both the RPT signal and particle position. By aligning these two peaks, we can determine the lag between the two systems.
- Smooth out the noise: because of the quantized nature of γ-rays, the radiation emitted by the radioactive tracer particle exhibits continuous intensity fluctuations over time. We apply a 1st order Savitzky–Golay filter to smooth out the noise from the signal.
- Time step synchronization: the alignment of the position and photon counts datasets is essential due to their distinct time intervals. The goal is to calculate photon counts data at the instants which the cobot recorded the positions. To accomplish this, we utilize the time steps from the cobot dataset and employ a nearest interpolation technique to determine the photon counts at these specific time steps.

1.3. ANN for position reconstruction

ANN is comprised of interconnected neurons organized into layers: the input layer, hidden layers, and output layer. The input layer incorporates photon counts received by the array of detectors at each time step. The hidden layers consist of nodes designed to capture the non-linearity between the input and output (Bibeau et al., 2023) which is the spatial position of the tracer particle at each time step, including the coordinates x, y, and

z. The details of the chosen architecture for the back calculation of the particle position from the photon counts data can be found in Table 1.

Table 1 Architecture summary of the ANN model

Parameter	Value
Number of hidden layers	5
Number of neurons in each hidden layer	256, 128, 64, 32, 16
Hidden layers activation function	tanh
Optimizer	Adam
Error function	MSE
Learning rate	0.00001
Batch size	50000
Number of epochs	6000

2. Results and discussion

We sample a cube with dimensions measuring 6 × 6 × 6 cm, surrounded by a configuration of 8 detectors. In this experiment, we used a sealed Scandium source with an activity of 125 μCi. The cobot guides the particle through 300 sampling points within the cube. While transitioning from one point to another, we capture data on photon counts. Figure 1 shows the configuration of the cube in surrounded by scintillation detectors.

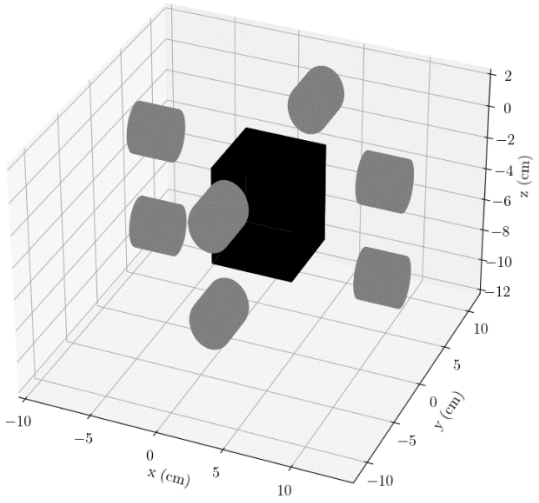

Figure 1 Detector configuration around the sampling volume

We evaluate the accuracy of the position reconstruction algorithm across various datasets using performance metrics, including Mean Absolute Error (MAE) and Standard Deviation (SD) for each directional component in the x, y, and z directions, as well as the Mean Euclidean Distance Error (MEDE). We train the ANN model with part of the experimental dataset (70%) and test it with the rest of the dataset (30%) until the point that it doesn't overfit the data.

Moreover, to demonstrate the model's performance, at the end of the sampling step, the robot moves the tracer particle in a spiral trajectory, and we subsequently reconstruct this path using the trained model.

Table 2 Position reconstruction performance indices

	MAE (mm)	SD (mm)	MEDE (mm)
x	0.4	0.3	1.2
y	0.4	0.3	
z	0.9	0.7	

Table 2 shows the performance metrics corresponding to 8100 reconstructed positions inside a 3D spiral path within the sampled cube's volume. Figures 2 and 3 illustrate the spiral path from the actual movement of the robot alongside the reconstructed path via ANN implementation.

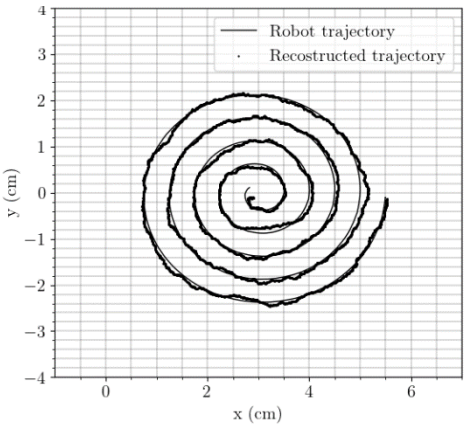

Figure 2 xy plane view of spiral reconstructed trajectory

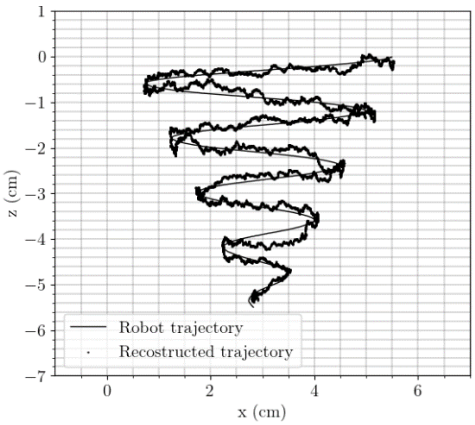

Figure 3 xz plane view of spiral reconstructed trajectory

3. Conclusion

This work introduces Monte Carlo-free RPT. We employ a cobot to establish a database, linking hundreds of thousands of positions within the volume of interest to the corresponding photon counts recorded by strategically positioned scintillation detectors surrounding the volume. Using this massive dataset, we train an ANN model to reconstruct the radioactive particle motion in an RPT experiment.

To validate this method, we reconstruct 8100 points along a 3D spiral. A thorough comparison with the actual cobot-recorded positions shows a significant improvement in reconstruction accuracy, MEDE of 1.2 mm, compared to recent experimental works in the literature, 3.84 mm, (Yadav et al., 2020).

Our dynamic data sampling, in contrast to static or time-averaged approaches, closely mimics real experimental conditions, contributing to a more realistic representation of photon count during the experiment. Furthermore, the validation procedure also uses the dynamically sampled data.

It's also worth mentioning that this innovative approach improves operator safety by eliminating the need for manual calibration and minimizing contact with radioactive particles.

References

A. A. Alghamdi, T. M. Aljuwaya, A. S. Alomari, M. H. Al-Dahhan, 2022, Geant4 simulation for radioactive particle tracking (rpt) technique, Sensors, 22, 1223.

S. S. Zambonino, R. Santos, 2023, Sas geant4 application and machine learning algorithms for radioactive particle tracking, Radiation Physics and Chemistry, 111056.

V. Bibeau, L. Barbeau, D. C. Boffito, B. Blais, 2023, Artificial neural network to predict the power number of agitated tanks fed by cfd simulations, The Canadian Journal of Chemical Engineering.

A.Yadav, T. K. Gaurav, H. J. Pant, S. Roy, 2020, Machine learning based position-rendering algorithms for radioactive particle tracking experimentation, AIChE Journal, 66, e16954

ESCAPE-34 PSE-2024
European Symposium on Computer Aided Process Engineering
&
Process Systems Engineering

Flavio Manenti, Gintaras V. Reklaitis (Eds.), Book of Abstract of the 34th European Symposium on Computer Aided Process Engineering / 15th International Symposium on Process Systems Engineering (ESCAPE34/PSE24), June 2-6, 2024, Florence, Italy.

Renewable Energy Hub Optimizer (REHO) – A Comprehensive Decision Support Tool for Sustainable Energy System Planning

Dorsan Lepour[a], Cédric Terrier[a], Joseph Loustau[a], François Maréchal[a]

[a]*EPFL, Rue de l'industrie 17, Sion 1950, Switzerland*
dorsan.lepour@epfl.ch

Abstract

The transition to sustainable energy systems in the face of growing renewable energy adoption and electrification is a complex and critical challenge. The Renewable Energy Hub Optimizer (REHO) emerges as a powerful decision support tool designed to investigate the deployment of energy conversion and storage technologies in this evolving landscape. REHO leverages a Mixed-Integer Linear Programming (MILP) framework combined with a Dantzig-Wolfe decomposition to simultaneously address the optimal design and operation of energy communities, catering to multi-objective considerations across economic, environmental, and efficiency criteria. This paper introduces REHO and highlights its key features and contributions to the field of sustainable energy system planning.

Keywords: Renewable Energy Community, MILP, Multi-Objective Optimization, Open-Source.

1. Context

Cities around the world are moving towards increasing the penetration of local energy harvesting and storage capacities to render their energy consumption more sustainable and less dependent on a geopolitical context. Intensification of renewables deployment is witnessed in the past decade and keeps continuing, leading to important techno-economic-social trade-offs in energy strategy. This transition blurs the boundaries between demand and supply and creates new types of stakeholders. Adopting a district-level approach for energy system planning seems thus particularly relevant, as it promotes the valorization of endogenous resources and enables economies of scale while preserving local governance (Heldeweg, 2020). The emergence of the concept of renewable energy communities is a clear example of this growing interest for energy planning at the neighborhood scale (Dóci, 2015). Energy communities are expected to play a pivotal role in the ongoing energy transition by fostering decentralized, sustainable, and community-driven approaches to energy production and consumption. Through the collaborative efforts of residents, utilities, and institutions, they offer a techno-economic

framework to support the paradigm shift from centralized energy systems to a distributed and district-level model (Caramizaru, 2020).
Optimizing an energy community at the district-level is a complex and computationally intensive task due to its network structure and interdependent decision variables. Facing this problem, a common method is to fix some degrees of freedom through assumptions and scenarios based on expert knowledge (Reynolds, 2019; Pickering, 2019). Many studies in literature assumes energy demand profiles (Murray, 2020) or predetermines the energy system configuration (Chakrabarti, 2019; Alhamwi, 2018; Kramer, 2017). The issue with such assumptions is the consideration of energy carriers to be delivered instead of energy end use demands to be satisfied. By assuming a priori some investment decisions into energy capacities, the solution space is reduced, and such model does not unveil the full potential of energy communities. However, modeling subsystems as entities embedded in a larger system should reveal the interdependency of the decision-making and exploit the main benefits of energy communities to coordinate decisions both at the building and district-level.
In addition to addressing the need for a more holistic problem statement, another notable gap in the existing research pertains to the limited generalizability of findings. A predominant trend in the literature involves the examination of singular case studies, within a specific neighborhood. While certain authors have explored the overarching implications of local residential systems, their investigations predominantly hinge on building-level energy systems (Stadler, 2019; Kotzur, 2020).
This gap has motivated the development of Renewable Energy Hub Optimizer (REHO), a comprehensive decision support tool for energy system planning at the district-level, considering simultaneously diverse end use demands, multi-energy integration, and buildings interactions.

2. Districts as energy hubs

The energy hub concept (Mohammadi, 2017) is used to model an energy community where multi-energy carriers can supply diverse end use demands through building units and district units optimally interconnected and operated.

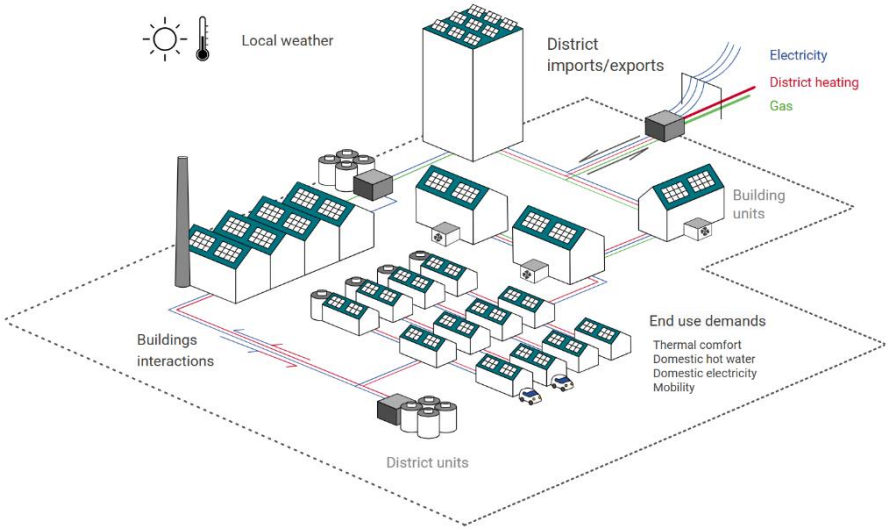

Figure 1: District energy hub model in REHO.

Figure 1 displays the input data necessary to characterize a district-level energy hub to be optimized with REHO:

- the geographic boundaries of the considered territory;
- the end use demands, resulting from the building stock and local weather;
- the technologies available and their specifications regarding cost, life cycle, efficiency;
- the endogenous resources;
- and the energy market prices for district imports and exports.

The optimal solution minimizing the specified objective function will then be fully characterized by the decision variables defining the energy system configuration. These decision variables are the installed capacities of the building and district units among the available technologies, their operation throughout a typical year, and the resulting energy flows (buildings interactions and district imports/exports).

3. The REHO package

3.1. Model foundations

REHO exploits the benefits of two programming languages to explore the solution space defined by the district energy hub input data. Figure 2 illustrates the tool architecture:

- The data management structure is written in Python and used for input parameters preprocessing, and decision variables postprocessing.
- The optimization model is written in AMPL, encompassing objective functions, modelling equations, and constraints at building-level and district-level.

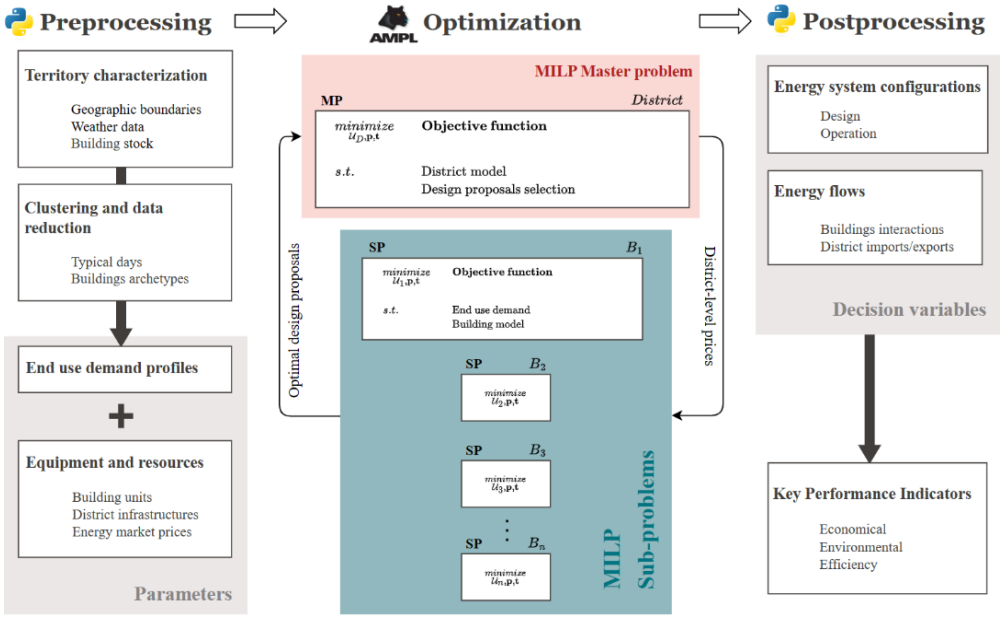

Figure 2: Diagram of the REHO architecture.

3.1.1. Data reduction

The task of optimally designing and scheduling energy systems with a high share of renewable energies is complex and computationally demanding. REHO includes machine learning techniques to cluster yearly input data. The model operates in the conventional way with typical periods **p** of 24 timesteps **t**, but it can be freely adapted to a finer or coarser granularity as required.

3.1.2. MILP formulation with decomposition

A Dantzig-Wolfe decomposition is applied on the district-level problem to define a master problem (MP) and one sub-problem (SP) for each building. Linking constraints allow the problem to iteratively converge to the solution minimizing the global objective function: the MP sends optimal district-level prices to the SPs, which in turn send back optimal building-level design proposals. The building-level optimization model is based on Stadler (2019) and the decomposition methodology is described in Middelhauve (2022).

3.2. Embedded features

3.2.1. Multi-Service Consideration

REHO encompasses a wide range of end use demands, including thermal comfort (heating and cooling loads), domestic hot water, domestic electricity, mobility, and information and communication technologies needs.

3.2.2. Multi-Energy Integration

REHO incorporates various energy sources and networks, such as electricity, fossil fuels, biomass, biofuels, district heating and cooling networks, and hydrogen. This holistic approach ensures a comprehensive representation of the energy landscape.

3.2.3. Multi-Scale Capabilities

REHO's flexibility spans various scales, from individual buildings to entire districts. The district-scale optimization feature capitalizes on synergies between buildings, allowing them to function as an energy community and enabling energy and financial flows between buildings. In addition, such an approach opens the possibility of deploying district-level infrastructures.

3.2.4. Multi-Objective Optimization

REHO’s versatility extends to multi-objective optimization, accommodating objectives related to economic (capital and operational costs), environmental (life cycle analysis and global warming potential), and efficiency criteria. Epsilon constraints provide fine-grained control, enabling decision-makers to explore trade-offs and identify Pareto fronts.

3.2.5. PV orientation

Given the pivotal role of photovoltaic (PV) systems in the energy transition, their optimal deployment is of paramount importance and must consider the specific characteristics of the building morphology, the local solar irradiance, and the grid curtailment restrictions. REHO integrates the deployment of solar panels on roofs and facades, with the possibility to take into consideration the orientation of surfaces.

3.2.6. Electric mobility

REHO enables the integration of electric vehicles into neighborhoods, including the possibility of smart charging, unidirectional or bidirectional. The fleet of electric vehicles can thus be used to provide an energy storage service.

3.2.7. Grid constraints

As the electrification of diverse sectors gains momentum, the demands placed on the electricity grid are expected to further escalate. The existing electrical grid, originally designed for centralized power generation and unidirectional energy flows, now faces new demands and complexities. REHO allows for the consideration of the local grid specifications, through line and transformer capacities, or peak power shaving and curtailment measures.

3.2.8. District heating and cooling

REHO enables the deployment of district heating and cooling networks, with consideration of several heat transfer fluids and distribution temperatures. Infrastructure costs are also incorporated, based on the topology of the considered neighborhood.

3.2.9. Open-source and interoperability

REHO is available as an open-source and collaborative Python library, supported by comprehensive documentation. It is deployed as a PyPI package, boasting its capability to interface and exchange information with other tools.

4. National-level case study

By providing the relevant input data regarding energy needs and endogenous resources, investigations on energy communities can be carried out in a wide range of urban territories. Such real-world applications demonstrate the significance of REHO's capabilities and its potential to shape resilient and sustainable energy systems.

The interoperability of REHO also enables extensive studies. As a demonstration, it was combined with the QBuildings GIS database (Loustau, 2023), allowing for the optimization of Switzerland's entire building stock comprising 2.6 million entities. REHO can run over the 17,844 districts of the country – where is district is defined as the batch of buildings deserved by the same MV/LV transformer (Gupta, 2021).

As an example of the investigation results, Figure 3 displays the gradual electrification and integration of renewables for Switzerland, and the expected performance in terms of annual costs. The values reflect the weighted average of the building stock surface area.

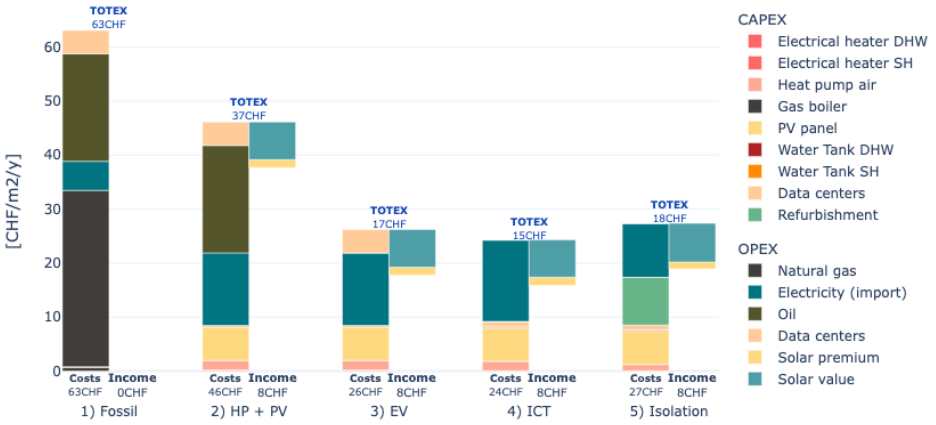

Starting from an energy system based on fossil fuel to satisfy the residents end use demands, the costs are likely to drop by 41% when integrating heat pumps combined with PV panels, and to 73% when enabling electric vehicles. Considering the integration of decentralized data centres into the building stock further stimulates synergies within the neighbourhoods and sets the cost reduction at 76%. Finally, the investigation regarding building isolation shows that an improvement of the thermal envelope translates to staying within a similar range of annual costs, while considerably reducing the demand for heat. These findings could serve as an encouraging benchmark contributing to energy planning towards net zero carbon cities in 2050.

5. Conclusion

Energy communities are poised to play a pivotal role in the generation, distribution, and management of renewable energy resources. In this context of evolving energy landscape, REHO stands as a versatile and indispensable tool for stakeholders in the renewable energy transition. Its MILP framework, consideration of diverse end-use demands, multi-energy integration, multi-scale adaptability, and multi-objective optimization drive informed decision-making in energy system planning.

Relevant links

REHO package: https://pypi.org/project/REHO/
REHO documentation: https://reho.readthedocs.io/en/main/

References

Alhamwi Alaa et al. “Modelling urban energy requirements using open source data and models”. Applied Energy 231 (Dec. 2018), pp. 1100–1108. ISSN: 03062619.

Caramizaru, Aura. “Energy communities: an overview of energy and social innovation.” European Commission - Joint Research Centre for Policy Report, 2020.

Chakrabarti Auyon et al. “Optimisation and analysis of system integration between electric vehicles and UK decentralised energy schemes”. Energy 176 (June 2019), pp. 805–815. ISSN: 03605442.

Dóci Gabriella, Vasileiadou Eleftheria, Petersen Arthur. “Exploring the transition potential of renewable energy communities”. Futures, Volume 66, 2015, Pages 85-95, ISSN 0016-3287.

Gupta Rahul, Sossan Fabrizio, and Paolone Mario. “Countrywide PV hosting capacity and energy storage requirements for distribution networks: The case of Switzerland”. Applied Energy (Jan. 2021), p. 116010. ISSN: 03062619.

Heldeweg Michiel, Saintier Séverine. “Renewable energy communities as ‘socio-legal institutions’: A normative frame for energy decentralization?”. Renewable and Sustainable Energy Reviews, Volume 119, 2020, 109518, ISSN 1364-0321.

Kotzur Leander and al. “Bottom-up energy supply optimization of a national building stock”. Energy and Buildings 209 (Feb. 2020), p. 109667. ISSN: 03787788.

Kramer Michael, Jambagi Akhila, and Cheng Vicky. “Bottom-up Modeling of Residential Heating Systems for Demand Side Management in District Energy System Analysis and Distribution Grid Planning”. 2017, p. 8.

Loustau Joseph, Lepour Dorsan, Terrier Cédric, and Maréchal François. “Clustering and typification of urban districts for energy system modelling”. Proceedings of the 36th International Conference on Efficiency, Cost, Optimization, Simulation and Environmental Impact of Energy Systems (June 2023).

Middelhauve Luise. “On the role of districts as renewable energy hubs”. PhD thesis. EPFL, 2022.

Mohammadi et al. “Energy hub: From a model to a concept – A review”. Renewable and Sustainable Energy Reviews 80 (Dec. 2017), pp. 1512–1527.

Murray Portia, Carmeliet Jan, and Orehounig Kristina. “Multi-Objective Optimisation of Power-to-Mobility in Decentralised Multi-Energy Systems”. Energy 205 (Aug. 2020), p. 117792. ISSN: 03605442.

Pickering B. and Choudhary R.. “District energy system optimisation under uncertain demand: Handling data-driven stochastic profiles”. Applied Energy 236 (Feb. 2019), pp. 1138–1157. ISSN: 03062619.

Reynolds Jonathan and al. “Operational supply and demand optimisation of a multi-vector district energy system using artificial neural networks and a genetic algorithm”. Applied Energy 235 (Feb. 2019), pp. 699–713. ISSN: 03062619.

Stadler Paul. “Model-based sizing of building energy systems with renewable sources”. PhD thesis. EPFL, 2019.


ESCAPE-34 PSE-2024
European Symposium on Computer Aided Process Engineering
&
Process Systems Engineering

Flavio Manenti, Gintaras V. Reklaitis (Eds.), Book of Abstract of the 34th European Symposium on Computer Aided Process Engineering / 15th International Symposium on Process Systems Engineering (ESCAPE34/PSE24), June 2-6, 2024, Florence, Italy.

Globally Optimal Scheduling of an Electrochemical Process via Data-Driven Dynamic Modeling and Wavelet-Based Adaptive Grid Refinement

Chrysanthi Papadimitriou, Tim Varelmann, Christian P. Schröder, Andreas Jupke, Alexander Mitsos*

RWTH Aachen University, Process Engineering (AVT), Aachen, Germany
amitsos@alum.mit.edu

Abstract

Flexible operation of an electrochemical recovery process of succinic acid can potentially yield economic benefits. We conduct experiments on the process and retrieve data for data-driven dynamic modeling. We then perform offline dynamic scheduling with discrete-time Hammerstein-Wiener (HW) models to obtain the globally optimal process schedule. We acknowledge the high computational requirements of the solution approach and propose a wavelet-based adaptive grid refinement algorithm for global optimization (GO) (AGRAGO), which employs a refinement criterion based on Lagrangian multipliers. AGRAGO is implemented in our in-house software for deterministic GO, MAiNGO. It is, then, used to automatically allocate the available control parameters in the grid to provide superior solutions in less CPU time. We demonstrate the applicability of AGRAGO and observe improved results compared to uniform control sampling while still detecting high computational expenses for dynamic GO. Overall, global dynamic scheduling (GDS) with AGRAGO leads to 14.1% economic savings.

Keywords: electrochemical acid recovery, demand-side-management, global dynamic scheduling, Hammerstein-Wiener model, adaptive grid refinement

1. Introduction

Optimal process scheduling provides economic savings to electricity-intensive processes (Mitsos et al., 2018). When process dynamics are time-relevant to electricity price fluctuations, they are accounted for to ensure schedule accuracy, resulting in a dynamic optimization (DO) problem (Bhatia and Biegler, 1996). Although typically solved with local optimization methods or model simplification techniques (Dias and Ierapetritou, 2019), optimal dynamic scheduling is often applied to complex processes necessary to be considered to avoid intractable scheduling objectives (Yang et al., 2014). Nonconvex global dynamic optimization (GDO) is considered among others (Floudas and Gounaris, 2009) by Kappatou et al. (2022), who introduce an approach of deterministic GDO using a HW nonlinear process model. The optimization problem is solved after control parametrization and time discretization using ODE relaxations (Singer and Barton, 2004)

and a branch-and-bound (B&B) algorithm. The high computational demands of the method favor grid refinement approaches (e.g., Chen et al., 2012) that optimally decide on the control discretization to use fewer optimization variables (DoFs) and reach high-quality solutions. Schlegel et al. (2005) introduce an adaptive refinement algorithm based on wavelets to solve continuous-time DO problems sequentially. Schäfer et al. (2020a,b) extend their work to quasi-steady-state scheduling problems introducing a refinement criterion based on Lagrangian multipliers.

We here give a summary of our latest work (Papadimitriou et al., 2023), where we perform GDS to a downstream electrochemical process of succinic acid recovery (Schröder et al., 2022) using HW models (Kappatou et al., 2022) trained on experimental data. To reduce the computational expenses, we then propose a wavelet-based adaptive grid refinement algorithm for GO (AGRAGO), applicable to DO problems, based on previous works (Schlegel et al., 2005; Schäfer et al., 2020a,b), which we include in our software for deterministic GO, MAiNGO (Bongartz et al., 2018).

2. Data-driven dynamic modeling

We focus on a downstream process (Fig. 1) of bio-based succinic acid recovery (Schröder et al., 2022) as a promising candidate for scheduling application. We perform experiments on the first electrolysis cell and obtain data on the power consumption (model output) over the process molar throughput (model input) by applying current density variations while reaching full acid protonation. The data are used to identify a single-input, single-output HW model. Discrete-time dynamics and an ANN trained on the H function are used to decrease computational expenses. The model uses a 4th- (H,) and a 2nd-degree (W) polynomial, and a 4th-order LTI. The resulting model fitting is 95 % (*1 - NMSE*).

3. Deterministic global dynamic scheduling

We consider the scheduling problem of flexible operation of the process of Fig. 1 to adjust the molar throughput (**u**) leading to varying power consumption levels (**y**) while reaching a fixed daily acid production under one-day hourly changing German spot electricity prices of February 7, 2023. The problem is formulated, according to Kappatou et al. (2022), as a GDO problem, and is solved for a piecewise constant control parametrization and varying control time series - discretization (n), using MAiNGO (Bongartz et al., 2018)). The ANN relaxations are provided by MeLOn (Schweidtmann and Mitsos, 2019).

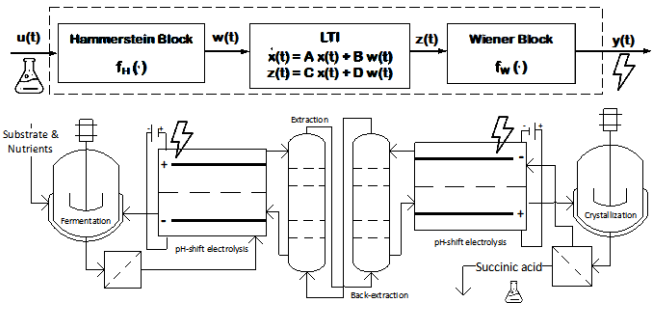

Figure 1. Succinic acid recovery process flowsheet (Schröder et al., 2022) and Hammerstein-Wiener (HW) process model representation. The HW model consists of a linear dynamic block (LTI) placed between two nonlinear static blocks (H and W).

The results indicate an overall increasing objective value improvement and an exponential scaling of the computational expenses over the number of control discretization points (n). The latter poses limits to the real-time applicability of the method, considering a 12-hour gap between price announcement and implementation. The highest economic benefit of the solution accepting this limit is 13.1 %. The corresponding schedule gives the dynamic process response to the price fluctuations.

4. Wavelet-based adaptive grid refinement algorithm for global optimization (AGRAGO)

We propose an adaptive control grid refinement algorithm for GO (AGRAGO) based on discrete wavelet transformations (Schlegel et al., 2005; Schäfer et al., 2020a,b) for full exploitation of the price fluctuations while decreasing computational expenses or equivalently using fewer DoFs. AGRAGO works iteratively (Fig. 2); first performing (D)GO given a certain control grid, then post-processing the optimization results evaluating the coefficient values and the Lagrangian multipliers associated with the deactivation and activation, respectively of a coefficient to, last, construct the grid of the next iteration. The algorithm terminates heuristically.
AGRAGO is integrated into MAiNGO (Bongartz et al., 2018) for automatic refinement and, in contrast to previous works, allows for application to a wide selection of problems, including GDS. It, additionally, incorporates the concept of *batches* (subhorizons of the same power-of-two grid intervals) to allow matching setpoint and problem parameter (i.e., price) changes and suggests GO in the space of the original control parameters rather than the wavelet coefficients (Schäfer et al., 2020b). The adaptations improve the results in terms of objective value and CPU time, respectively.

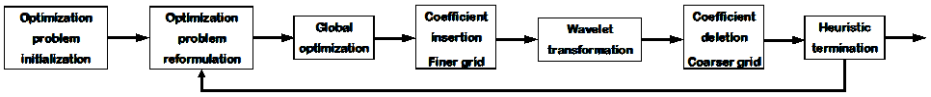

Figure 2. Simplified graphical representation of AGRAGO.

We solve the problem using AGRAGO, similar to Section 3, considering three *batches* and a set of equality constraints related to the coefficients' deactivation. We note a similar computational scaling and improved savings for the same n compared to uniform control sampling. AGRAGO exhibits high savings for only a few DoFs (1.7 % higher compared to equidistant sampling for five n). The best solution achieved with AGRAGO respecting the computational time limitations gives 14.1 % savings. The resulting optimal schedule suggests higher benefits from lower production during the high and medium prices and more flexible adjustments during the lower prices to fulfill the daily production demand.

5. Conclusions

We perform experimentation and data-driven dynamic modeling for an electricity-intensive process for electrochemical acid recovery. We consider the flexible operation of the process for participation in a day-ahead electricity market and solve the dynamic optimization problem to global optimality. We note the high economic savings attained and the high computational demands of the approach. We propose a wavelet-based adaptive grid refinement algorithm for global optimization (AGRAGO) for automatic control discretization refinement applied to global dynamic scheduling. AGRAGO

application results in higher savings, reached in less computational time and an overall economic gain of 14.1 %.

References

T. Bhatia, L.T. Biegler, 1996, Dynamic optimization in the design and scheduling of multiproduct batch plants, Industrial and Engineering Chemistry Research, 35, 7, 2234–2246.

D. Bongartz, J. Najman, S. Sass, A. Mitsos, 2018, MAiNGO - McCormick-based Algorithm for mixed-integer Nonlinear Global Optimization, http://permalink.avt.rwth-aachen.de/?id=729717.

W. Chen, K. Wang, Z. Shao, L.T. Biegler, 2012, Chapter 11: Direct Transcription with Moving Finite Elements, Control and Optimization with Differential-Algebraic Constraints, 233-252.

L.S. Dias, M.G. Ierapetritou, 2019, Optimal operation and control of intensified processes - challenges and opportunities, Current Opinion in Chemical Engineering, 25, 82-8.

C.A. Floudas, C.E. Gounaris, 2009, A review of recent advances in global optimization, Journal of Global Optimization, 45, 3-38.

C.D. Kappatou, D. Bongartz, J. Najman, S. Sass, A. Mitsos, 2022, Global dynamic optimization with Hammerstein–Wiener models embedded, Journal of Global Optimization 84, 321–347.

A. Mitsos, N. Asprion, C.A. Floudas, M. Bortz, M. Bonvin, A. Caspari, P. Schäfer, 2018, Challenges in process optimization for new feedstocks and energy sources, Computers & Chemical Engineering, 113, 209-221.

C. Papadimitriou, T. Varelmann, C. Schröder, A. Jupke, A. Mitsos, 2023, Globally optimal scheduling of an electrochemical process via data-driven dynamic modeling and wavelet-based adaptive grid refinement, Optimization and Engineering, 1-39.

P. Schäfer, A.M. Schweidtmann, P.H. Lenz, H.M. Markgraf, A. Mitsos, 2020, Wavelet-based grid adaptation for nonlinear scheduling subject to time-variable electricity prices, Computers & Chemical Engineering 132, 106598.

P. Schäfer, A.M. Schweidtmann, A. Mitsos, 2020, Nonlinear scheduling with time-variable electricity prices using sensitivity-based truncations of wavelet transforms, AIChE Journal, 66, 10, e16986.

M. Schlegel, K. Stockmann, T. Binder, W. Marquardt, 2005, Dynamic optimization using adaptive control vector parameterization. Computers & Chemical Engineering 29, 8, 1731-1751.

C. Schröder, M. Gausmann, A. Jupke, 2022, Markt- und Stromsystem, Managementsysteme und Technologien energieflexibler Fabriken, Energieflexibilität in der deutschen Industrie, 2, 297-316.

A.M. Schweidtmann, A. Mitsos, 2019, Deterministic global optimization with artificial neural networks embedded, Journal of Optimization Theory and Applications,180, 3, 925–94.

A.B. Singer, P.I. Barton, 2004, Global solution of optimization problems with parameter-embedded linear dynamic systems, Journal of Optimization Theory and Applications, 121, 613–646.

Z. Yang, K. Li, A. Foley, C. Zhang, 2014, Optimal Scheduling Methods to Integrate Plug-in Electric Vehicles with the Power System: A Review, 47, 8594-8603.

ESCAPE-34 PSE-2024
European Symposium on Computer Aided Process Engineering
&
Process Systems Engineering

Flavio Manenti, Gintaras V. Reklaitis (Eds.), Book of Abstract of the 34th European Symposium on Computer Aided Process Engineering / 15th International Symposium on Process Systems Engineering (ESCAPE34/PSE24), June 2-6, 2024, Florence, Italy.

PULPO: A Technosphere-Wide Lifecycle Optimization Package

Fabian Lechtenberg[a], Robert Istrate[b], Antonio Espuña[a], Moisès Graells[a], Gonzalo Guillén-Gosálbez[c*]

[a]*Department of Chemical Engineering, Universitat Politècnica de Catalunya, Barcelona, Spain*

[b]*Institute of Environmental Sciences (CML), Leiden University, Leiden, Netherlands*

[c]*Department of Chemistry and Applied Bioscience, Institute for Chemical and Bioengineering, ETH Zurich, Zurich,Switzerland*

gonzalo.guillen.gosalbez@chem.ethz.ch

Abstract

Life cycle optimization (LCO) couples multi-objective optimization with life cycle assessment (LCA). It is often carried out by adding LCA-based linear equations to the mathematical formulation, which are parameterized with data retrieved from environmental databases. While the mathematical model is used to optimize the foreground system (i.e., the system of decisions over which the modeller has a degree of control), its influences on the parameters of the background system (i.e., the system which provides inputs to the foreground such as electricity or transport) are omitted in this approach. The main limitation of this approach is that it does not allow to optimize decisions in the background system (i.e., those activities in the supply chains of the main processes in the foreground system). Moreover, in large-scale assessments, technological changes in the foreground will affect the background, making LCO less accurate unless full integration between optimization and LCA is attained. To overcome these shortcomings, this work introduces PULPO, a novel framework integrating mathematical optimization with LCA. Building upon open-source tools, PULPO allows for concurrent optimization of foreground and background decisions, accounting for feedback loops between them. A case study on sustainable methanol production demonstrates PULPO's effectiveness in designing constrained and coupled global supply chains considering a range of impact categories.

Keywords: methanol, supply chain, carbon capture and utilization, open-source

1. Introduction

In Process Systems Engineering, LCA indicators have been integrated into process and supply chain optimization problems to quantify trade-offs between economic and environmental performance, facilitating sustainable decision-making (Ferdous et al., 2023). However, process modeling & optimization and LCA are often combined offline, that is, LCA data expressed via eco-vectors representing the impact linked to mass and energy flows in the foreground (e.g., 1 kWh, 1 kg of chemical) are retrieved

from environmental databases and incorporated into mathematical models as parameters. Here, the mathematical model represents the foreground system (e.g., chemical plant, supply chain) over which we have a certain level of control (i.e., through the optimization of the decision variables). Meanwhile, LCA data denote the background system (surrounding activities providing inputs to the foreground system) that is often assumed to be fixed during optimization. This approach omits feedback loops between both systems. For example, when optimizing the power system of a country, the carbon footprint of power technologies will depend on the composition of the power mix, which needs to be decided by the optimization model. In the process systems realm, the optimization of a supply chain model including degrees of freedom such as capacity and planning decisions may constitute the foreground decisions. The static environmental indicators obtained from the background (surrounding activities such as electricity, transport, storage etc.) parameterize the linear LCA-based equations in the model.

Following the traditional offline integration, such a model would assume fixed carbon footprints of the power technologies, omitting the coupling between foreground and background activities. Moreover, using fixed background data provides limited insights into how changes in the Technosphere, in which the foreground system is embedded and with which it displays strong links, will affect the outcome of the environmental analysis.

In a seminal work, Kätelhön and coworkers introduced the Technology Choice Model (TCM) for optimizing technology choices in production systems (Kätelhön et al., 2016), which, so far, used aggregated unit processes in the underlying linear programming approach, omitting potential feedback effects between the choices made across the product supply chain. Inspired by this work, here we present a framework to carry out Technosphere-wide optimizations attaining full integration between optimization and LCA. This is achieved through the development of PULPO, a user-friendly open-source tool which instantiates and solves user defined LCO problems, integrating, opposed to the original TCM approach, complete Life Cycle Inventory (LCI) databases instead of aggregated unit processes.

2. Methodology

Here we introduce PULPO (*Python-based User-defined Lifecycle Product Optimization*). This innovative framework forges a direct link between mathematical optimization and LCA. PULPO seamlessly integrates full LCI databases in the optimization problem, enabling the concurrent optimization of both foreground and background systems. Figure 1 illustrates the implemented flow of information and connectivity to other packages. To define the optimization problem, the user is required to establish several key components. First, the functional unit that represents the production system's primary output. Second, the objective function based on a selected method for evaluating environmental impacts. Third, the potential process choices, which could involve technological or geographical decisions across supply chains in the Technosphere. Lastly, additional constraints shall be imposed, like limits on production capacity or the availability of resources.

Utilizing the data management features of the "brightway2" package (Mutel, 2017), users have the flexibility to include new processes into the LCI database. These LCIs are extensive and serve as the foundational framework for constructing the superstructure optimized in PULPO. Such a superstructure is tailored based on the user-defined options and limitations. The PULPO package encapsulates all this data into

a “pyomo” optimization model (Bynum et al., 2021), which can be solved with open-source solvers, e.g., HiGHS, or through integration with proprietary software like GAMS.

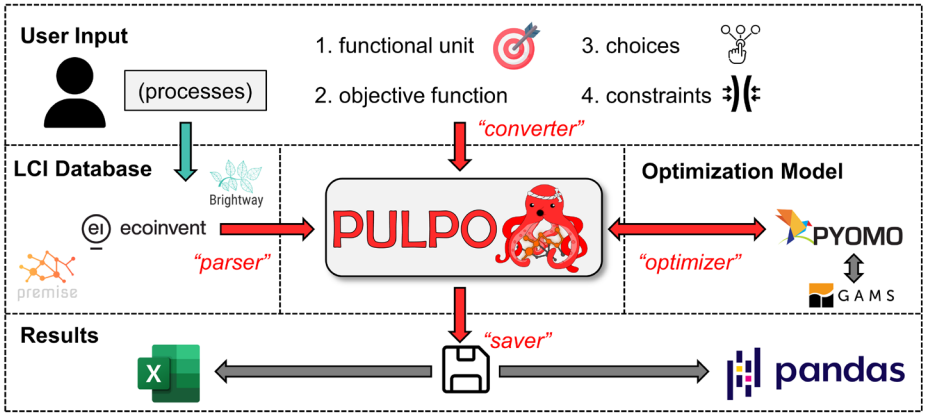

Figure 1. PULPO information and workflow.

The underlying optimization framework, inspired on the TCM approach (Kätelhön et al., 2016), is summarized in (OP1). A noteworthy conceptual extension is the “$slack$” vector, which enables the direct specification of final supply instead of final demand values, an issue which has been previously addressed via an auxiliar optimization problem (Meys et al., 2021).

$$\min_{s.t.\ s,slack} \ Q \cdot B \cdot s$$

$$A \cdot s = f + slack \qquad \text{(OP1)}$$

$$s_j^{low} \leq s_j \leq s_j^{high} \qquad \forall\, j$$

$$0 \leq slack_i \leq slack_i^{high} \qquad \forall\, i$$

Where the notation used is as follows: A is the rectangular Technosphere matrix, B is the Biosphere matrix, Q is the matrix containing the characterization factors of the lifecycle impact assessment method, s is the scaling vector, f is the final demand vector, s_j^{low} and s_j^{high} are the upper and lower limits on the production quantities (capacity limits) of processes j respectively, and $slack$ is the newly introduced vector containing decision variables for the case of specifying final supply instead of final demand values. The $slack_i^{high}$ vector is zero for all products i which have a defined final demand and takes a big constant value for those products where the final supply is specified. This notation follows the computational structure of LCA elaborated by Heijungs and Suh (2002).

PULPO is available on GitHub, Zenodo (Lechtenberg, 2023) and PyPI. In an example provided as a jupyter notebook in the open repository, a case study optimizing the German power mix is presented. Using the ecoinvent 3.8 cutoff system, the share of lignite, coal, wind and nuclear power is optimized. In the unconstrained case, the global warming potential is minimized when relying exclusively on nuclear power. Using the ReCiPe human health indicator as objective, PULPO identifies wind power as most suitable option. Here, capacity constraints alongside the supply chain are introduced.

We note that optimizing the mix following a standard LCO approach (i.e., the background data is not updated during the optimization) leads to an overestimation of the total impact by about 8% due to the omission of feedback loops between the foreground and background systems.

3. Results and Discussion

PULPO was utilized to explore the role of carbon capture and utilization (CCU) in sustainable methanol production, analyzing its interplay with the electricity market. The goal and scope of this LCO is to decide on the optimal portfolio of methanol pathways in a set of locations considering region- and scenario-specific performance metrics and constraints. For demonstration purpose, the minimization of the global warming potential (GWP) is used as the objective function.

The functional unit is the production of 100 Mt of methanol, as well as regional final supply values for electricity as projected by an integrated assessment model (IAM). In order to enforce these final supply constraints, the previously mentioned slack variables were utilized. We select the 1.5 °C and 3.5 °C temperature increase scenarios of the REMIND IAM and use the corresponding background databases based on the ecoinvent 3.8 cutoff system model generated by "premise" v.1.8.1 (Sacchi et al., 2022) as backbone for the superstructure.

These LCIs contain datasets for methanol production via direct-air capture (DAC) based methanol but do not implement them in the markets because this option is not considered in the IAM. Precisely, the IAM only considers steam methane reforming for methanol production, which we refer to as the business as usual (BAU). Additionally, we added inventories for point-source capture (PSC) based methanol, as well as the necessary inventories for retrofitting fossil thermal powerplants with carbon capture to supply the CO_2. The choices that the optimizer must take involve the selection of the optimal technology (BAU, DAC, or PSC) in the 12 regions of the IAM. If PSC is selected, a lower-level choice on the retrofitting of the available fossil thermal powerplants (coal and natural gas) must be taken.

The potential of CO_2-based methanol production routes heavily relies on the availability of green hydrogen, which in turn hinges on the availability of low-carbon electricity. Thus, shifting from the BAU practices to these new technologies implies the need for expanding power production capacities. In order to assess only a marginal deviation from the IAM baseline, we introduce a constraint on the power capacity expansion in each region.

With these configurations, the two scenarios have been optimized for a range of electricity capacity constraints. Figure 2 illustrates the results for a total GWP reduction of 50 Mt CO_2e. Comparing the amount of additional power capacity needed to reach this target underlines the pressing need to decarbonize the power sector for the hard-to-abate sectors to tag along in the quest for sustainability. The base case, aligning with a 3.5 °C scenario, requires an additional 417 TWh of electricity annually, whereas the 1.5 °C scenario reduces this need to 223 TWh.

Additionally, the transformation in the chemical sector is less extensive. In the 3.5 °C scenario, 50.4 Mt of fossil methanol needs replacement with carbon-capture alternatives, compared to only 23.0 Mt in the 1.5 °C scenario. This result does not suggest the chemical sector should wait for the power sector's progress. Instead, it emphasizes the need to prepare for the transition by developing suitable infrastructure and technology to meet or surpass these targets.

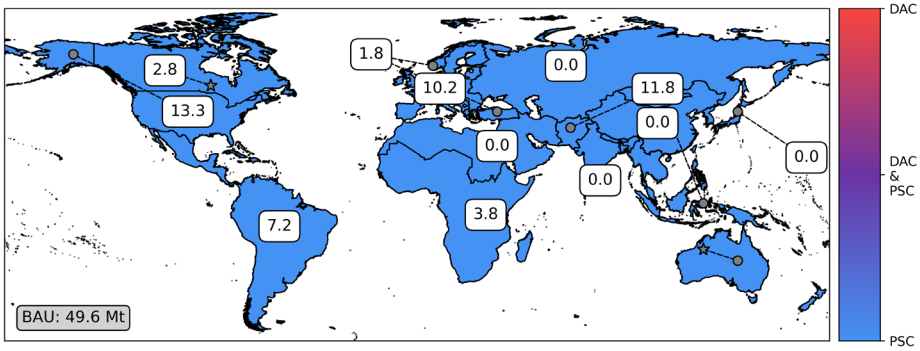

(a) Base (3.5°C)

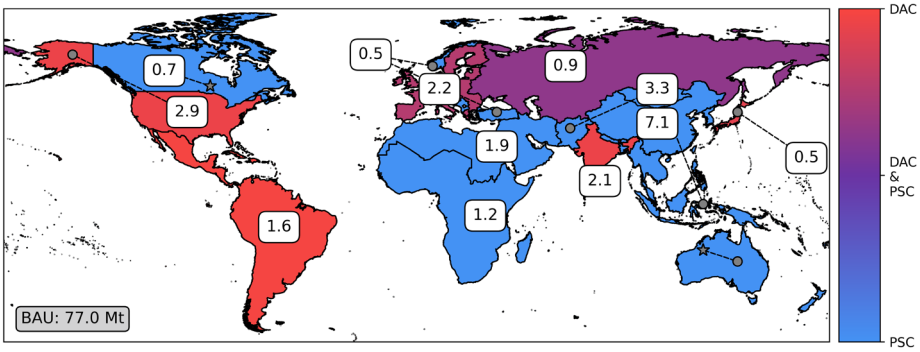

(b) PkBudg500 (1.5°C)

Figure 2. Optimized global methanol supply chains in 2040 for a (a) 3.5 °C temperature increase and a (b) 1.5 °C temperature increase scenario. Both systems reduce the total GWP by 50 Mt CO_2e. Methanol production quantities are indicated in each region (boxes) and the share of the technology employed (color). DAC: direct-air capture; PSC: point-source capture, BAU: business as usual (fossil based).

Our use of PULPO in this study provides detailed technological and regional insights, as depicted in Figure 2. In the 3.5 °C scenario, regions with more decarbonized grids face greater pressure to implement PSC for CCU, explained by the limited number of regions where PSC can outperform BAU. Consequently, electricity production capacities in these regions increase by 2.1 %. In the 1.5 °C scenario, this pressure decreases due to universally decarbonized grids, allowing better GWP performance from PSC and DAC compared to BAU. The maximum regional increase in electricity production capacity observed is 0.4 %. These geographically distributed results are strongly linked to the electricity constraint included in the optimization problem.

Notably, compared to the 3.5 °C scenario, the 1.5 °C scenario employs DAC based methanol production. This can be explained by the fact that some regions like South America and Europe have grids with a very low fossil share. Consequently, they fail to provide sufficient CO_2 for green methanol, making DAC necessary to cover the carbon source requirements.

Leveraging the comprehensive data in the LCIs, this assessment was enabled by PULPO's ability to integrate the entire database as a superstructure. Furthermore, the impact of optimizing power mixes by retrofitting with carbon capture technologies

plays a crucial role in ensuring an accurate and coherent assessment. Although less pronounced, the assessment also implicitly considers additional feedback effects originating from changes in the chemical sector.

4. Conclusions

PULPO represents a significant leap forward in merging mathematical optimization with LCA. Its integrated approach enables more precise and insightful analysis of technological and regional options in production systems. By accommodating dynamic changes within the Technosphere, PULPO enhances the accuracy and relevance of environmental impact assessments, particularly in the context of large-scale, impactful socio-economic decisions. This framework opens new avenues to support sustainable decision-making in Process Systems Engineering, building bridges with the Industrial Ecology community currently working on LCA.

Acknowledgements

Grant PID2020-116051RB-I00 (CEPI) funded by MCIN/AEI/10.13039/501100011033 and by "ERDF A way of making Europe" is fully acknowledged. Fabian Lechtenberg gratefully acknowledges the "Departament de Recerca i Universitats de la Generalitat de Catalunya" for the financial support of his predoctoral grant FI-2022. This publication was created as part of NCCR Catalysis (grant number 180544), a National Centre of Competence in Research funded by the Swiss National Science Foundation.

References

M. L. Bynum, G. A. Hackebeil, W. E. Hart, C. D. Laird, B. L. Nicholson, J. D. Siirola, D. L. Woodruff, 2021, Pyomo—Optimization Modeling in Python, Springer International Publishing

J. Ferdous, F. Bensebaa, N. Pelletier, 2023, Integration of LCA, TEA, Process Simulation and Optimization: A systematic review of current practices and scope to propose a framework for pulse processing pathways, Journal of Cleaner Production, 402, 136804

R. Heijungs, S. Suh, 2002, The Computational Structure of Life Cycle Assessment, Springer Netherlands

A. Kätelhön, A. Bardow, S. Suh, 2016, Stochastic Technology Choice Model for Consequential Life Cycle Assessment, Environmental Science & Technology, 50(23), 12575–12583

F. Lechtenberg, 2023, flechtenberg/pulpo: PULPO Release v1.0.0, Zenodo

R. Meys, A. Kätelhön, M. Bachmann, B. Winter, C. Zibunas, S. Suh, A. Bardow, 2021, Achieving net-zero greenhouse gas emission plastics by a circular carbon economy, Science, 374(6563), 71–76

C. Mutel, 2017, Brightway: An open source framework for Life Cycle Assessment, The Journal of Open Source Software, 2(12), 236

R. Sacchi, T. Terlouw, K. Siala, A. Dirnaichner, C. Bauer, B. Cox, G. Luderer, 2022, PRospective EnvironMental Impact asSEment (premise): A streamlined approach to producing databases for prospective life cycle assessment using integrated assessment models, Renewable and Sustainable Energy Reviews, 160, 112311

ESCAPE-34 PSE-2024
European Symposium on Computer Aided Process Engineering
&
Process Systems Engineering

Flavio Manenti, Gintaras V. Reklaitis (Eds.), Book of Abstract of the 34th European Symposium on Computer Aided Process Engineering / 15th International Symposium on Process Systems Engineering (ESCAPE34/PSE24), June 2-6, 2024, Florence, Italy.

Methodology for Qualitative Analysis of Atmospheric Carbon Dioxide Removal through Mineralization Technologies

Corre Soline [a*], Dimitrova Zlatina [b], Harambat Fabien [b], Zoughaib Assaad

[a] *EPFL, 17 route de l'industrie, 1950 Sion, Switzerland*
[b] *Stellantis, 2bd de l'Europe, 78300 Poissy, France*
soline.corre@epfl.ch

Abstract

This article focuses on comparing qualitatively using a decision-aid method technological solutions to address climate change, such as Carbon Capture and Storage (CCS) technologies. The research explores technological-based CCS solutions and has revealed a wide range of available technologies for CCS, each with varying efficiency and global capacity. Factors influencing the selection of CCS technologies include price, energy efficiency, environmental impact, and societal acceptance. Given the lack of a global methodology for comparing different CCS technologies, this article develops a qualitative methodology, inspired by certification standards and regulatory frameworks. Following this methodology, a qualitative analysis of mineralization technologies is presented. Enhanced rock weathering (ERW) applications in agricultural lands, oceanic/coastal environments, and underground storage of CO_2 via mineralization are explored. The criteria are applied to assess the state-of-the-art research. The results show that ERW on agricultural lands and underground storage of CO_2 via mineralization are mature and qualitatively suitable under certain conditions, while ERW in oceanic and coastal environments requires further research. The study suggests improving the decision-aid method by incorporating new key performance indicators based on economic, life cycle assessment, and thermodynamic analyses of various CCS methods.
Keywords: carbon dioxide, enhanced rock weathering, qualitative analysis.

1. Introduction

CCS technologies can be classified into two categories: the nature-based solutions, with methods of afforestation/reforestation, peatland, and the technological-based solutions, such as direct air capture (DAC) or point-source capture, combined with storage, enhanced rock weathering (ERW) on agricultural lands or coastal/oceanic areas, and biochar. Each of these technologies has its limits and needs to be carefully thought, with not only their feasibility but also their integration into their environment. Their efficiency and worldwide capacity differ, for example for the ERW on agricultural lands techniques and biochar the potential is estimated at 0.5 to $2GtCO_2y^{-1}$, for soil organic carbon sequestration it varies from 0.5 to 5 $GtCO_2y^{-1}$ (Beerling et al., 2020). To decide which technology to choose amongst the different available, criteria such as price, energy

efficiency, environmental impact, and acceptance of the technology at different levels (global, local) have to be taken into account. The question now is how to compare the different technologies on such diverse criteria, considering that there is no global methodology existing to compare them. Trying to complete this methodological shortcoming, this work presents a qualitative decision-aid method, based on certification standards (Arcusa et al., 2022), on the emerging laws from the European Parliament (European Parliament, 2022), and on societal analysis (Selma et al., 2014). To illustrate the decision-aid method, that can be used on every CCS technology, it is applied in this work to mineralization.

2. Definition of the decision-aid method

The decision-aid method, illustrated in Figure 1, helps in tracking through four simple steps whether a proposed technology is qualitatively viable or not. The first step, "the technology avoids any social and environmental harm", verifies that the project does not provoke any social or environmental harm. It ensures compliance with basic human rights and laws, avoids socially and environmentally sensitive areas, and prevents the generation of any social or environmental harm. The second step states that "it is possible to estimate the CO_2 removals and prove the permanence of the storage. The categories of impact from the Life Cycle Assessment (LCA) are considered in the estimation". This step applies to the development phase of the project (thinking phase), where estimation and previous analysis of potential impacts are made. It entails estimating CO_2 removals using a robust and clear calculation methodology, undergoing peer review. The estimation process considers all impacts, aligning with the principles of LCA (such as global warming potential, ozone depletion, eutrophication, acidification, depletion of abiotic resources, water and land use, and ecotoxicity). It is also based on "permanence", which requires demonstrating permanent reductions in GHG emissions and proving the absence or reversal of such emissions. The third step requires the validation of the following sentences: "It is possible to measure and monitor the quantity of carbon removed and stored during the duration of the project, by the authors and by a third-party auditor. No double counting is ensured". This step is linked to the ongoing phase of the project: the measures done during the project, by the authors or by a third-party auditor. The concept of "measurability and monitoring" is used to emphasize the importance of transparent and demonstrated measurement practices and strong monitoring throughout the project's duration. These practices should be carried out by a trusted local player. "Verifiability" is another crucial indication, that necessitates professional verification of the project by tird-party auditor (preferably with specific accreditation). The verification process occurs from the starting date and is repeated, with publicly available audit results. Finally, the notion of "ownership and unicity" ensures that no double counting occurs, and the ownership of credits is enforceable. If the first three criteria are not validated, further research and improvement of the technology to validate the criteria must be carried out. The fourth step stipulates that "there is a strong societal acceptance of the technology proposed, based on the institutional link (confidence with local institutions) and governance robustness (transparency, public consultation) on a local scale and acceptability of the technology on a global scale". If it appears to be incomplete, the project should be modified or further explanation towards citizens should be conducted. To maintain the "governance robustness", the project should have strong overall program

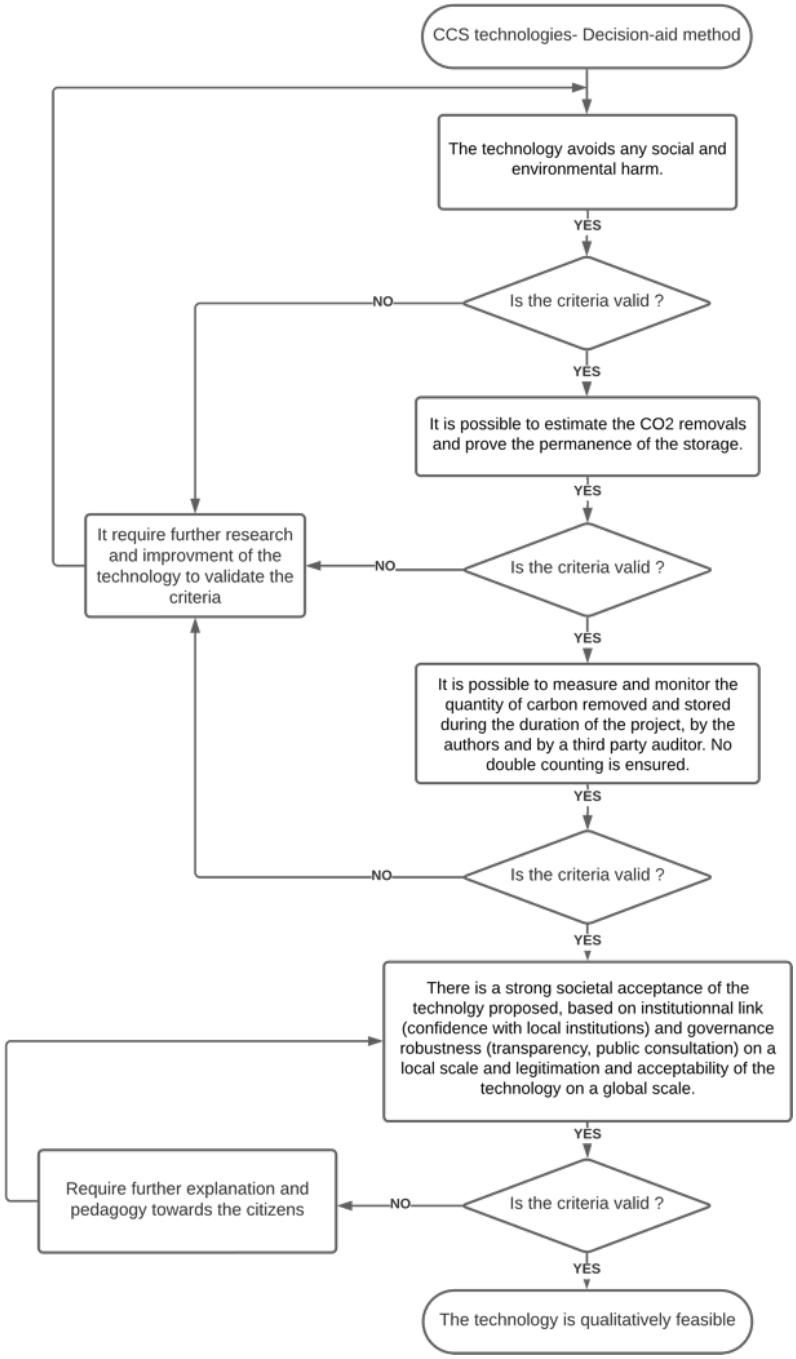

Figure 1: Decision-aid qualitative methods of CCS technologies.

governance, transparency regarding the project's progress, and public consultation. A complaints appeal policy should be in place, and the project's methodologies and registry design should operate independently from commercial activities. Lastly, "institutional

link" highlights the importance of integrating the project into the local institutional ecosystem.

3. Mineralization technologies

ERW is an inorganic carbon sequestration technique with the capacity to store CO_2 for over 100,000 years (Beerling et al., 2020). It is used on agricultural lands and oceanic areas. ERW works according to the following steps: crushed silicate rock is spread in soil or on coastal environments/ocean and dissolves, liberating base cations (as Mg^{2+}, Ca^{2+}). These cations generate alkalinity that draws down CO_2 from the atmosphere by forming principally carbonate ions. There is an increase in the seawater alkalinity resulting in additional CO_2 uptake from the atmosphere, occurring also with ERW on agricultural lands, as some of the minerals are washed to the ocean via soil drainage waters.
Storing underground via mineralization the CO_2 already captured in large quantities consists of injecting underground (in reactive rocks, such as mafic and ultramafic rocks) CO_2 dissolved in water, requiring twenty-five tons of water for one ton of CO_2 injected (Delerce and Oelkers, 2022). The solution reacts with reservoir rocks to trap CO_2 in the form of carbonate minerals. Solubility trapping occurs immediately, and most of the CO_2 injected reacts and reaches a stable form within two years (Snæbjörnsdóttir et al., 2020).

4. Analysis of the mineralization technologies with the decision-aid method

4.1. Analysis of ERW on agricultural lands

The step one of the decision-aid method, "avoiding social and environmental harm", faces a lack of knowledge in the actual state of the art that impeaches to fulfil it. The main risk is the contamination of lands, crops, and groundwaters with heavy metals and toxic substances, such as nickel and chromium, present in the rocks (Schuiling and Krijgsman, 2006). Moreover, the project leaders should be careful that there is no trade-off between carbon sequestration and crop production, as ERW could decrease the organic carbon content in soils and threaten food security (Lehman and Possinger, 2020). Then, the local impact of mines to extract the rocks is also to be analysed via an LCA study, as it destroys locally the environment. Another provenance of rocks (via industrial alkaline waste) would reduce this impact (Castro-Amoedo et al., 2023). Therefore, the criteria "Avoiding Social and Environmental harm" require further investigation and mitigation to be sure that there is no risk at all. Concerning step two, the estimation of the storage permanence, the storage has been established with the state-of-the-art study, that attests that once mineralized the carbon is stable and trapped for geological time spans (Beerling et al., 2020). The estimation of the carbon removal, and its validation will depend on the method proposed to assess the quantity of CO_2 that will be captured. Concerning step three, e. g. the measurability and the monitoring of carbon removal during the project, it seems possible to extend and realize a proper estimation method, verifiable by a third party. Samples of rocks can be analysed before the spreading and after a few months to assess the quantity of carbon removed. Step four, or governance robustness and institutional link have not been established yet, due to a lack of regulation of this specific practice.

4.2 Analysis of ERW on coastal environments and oceans

The criteria one, avoidance of social and environmental harm, has not been fulfilled. It is due to a lack of knowledge over the possible addition of toxic substances in the ocean as nickel and its impact on marine ecosystems. The impact of the increase in rates of some metals as Mg^{2+}, Si, $Fe^{2+,}$ and Ni^{2+} has to be assessed as well (Bach et al., 2019). The local impact of mines to extract the rocks is also to be analysed via an LCA study, as it destroys locally the environment. Concerning step two, e.g. estimation of the CO_2 removal and the

permanence of the storage, it is impeached by the occurrence of secondary reactions, making olivine dissolution's effectiveness in CO_2 sequestration under oceanic conditions uncertain (Montserrat et al., 2017). This aspect requires further investigation. To finish with, the LCA must be carefully conducted, as the small size of grains required to achieve effective mineralization requires a consequent energetic consumption (Hangx and Spiers, 2009). Step three is not validated as well: at this stage, it is impossible to monitor (due to the absence of an indicator) or even estimate the quantity of atmospheric CO_2 effectively captured. Furthermore, the possible co-reactions make it impossible to statute on the permanence of the storage (Montserrat et al., 2017). Concerning step four, the potential of toxicity of this technology and the knowledge gaps could impeach societal acceptance (Bach et al., 2019). No law concerning ERW in oceanic areas has been stated in Europe as far as we are aware. There is a high risk of social contestations if the beaches turn green due to the dispersion of olivine. To be qualitatively feasible, this technology thus requires further investigations on a scientific level, treating all the subjects mentioned before.

4.3 Analysis of CO_2 underground storage via mineralization

This technology has been judged as avoiding any social or environmental harm, as there is no risk of CO_2 leakage during storage (Delerce and Oelkers, 2022). Step one is therefore completed. The major blocking point is the decarbonized electricity required for the DAC and the need for a huge amount of fresh water. Due to these needs, this technology can be achieved in Iceland mostly, however, it is critical for other countries. Concerning step two, it is considered that a proper estimation of the quantity of carbon removed could be established before the project with models and calculations. The permanence of the project has been validated through the state-of-the-art study, attesting that carbon dioxide is mineralized and stable for geological time spans (Delerce and Oelkers, 2022). Furthermore, for step three, the measurability and monitoring can be achieved easily according to the CO_2 captured and then injected underground. This step is verifiable by a third part. To finish, as underground carbon storage can be criticized and impeached by local protests (O'Neill et al., 2012), it has not been established whether the social acceptance criteria (step four) is fulfilled or not. This point might require further investigations concerning the implantation of the technology in new areas. The global conclusion is positive at the state-of-the-art level of research.

5. Conclusions

Different mineralization technologies for CCS have been examined and a qualitative methodology to compare them has been proposed. This methodology includes criteria such as social and environmental impacts, storage permanence, measurability, and monitoring, as well as social acceptance. For ERW on agricultural lands, several criteria have been met, but uncertainties remain regarding the potential risks of soil and crop contamination by metals present in the rocks. The question of the impact on food production should also be considered. Social acceptance and specific regulations are still in development. Coastal and marine ERW faces uncertainties related to secondary reactions and requires scientific research on this point. Aspects related to measuring the quantity of captured CO_2 and the permanence of storage remain to be clarified. Moreover, potential toxicity and social risks related to the dispersion of rocks on beaches require further study. Underground CO_2 storage via mineralization appears promising but faces challenges related to the availability of decarbonized electricity and fresh water in certain regions. It seems to address major concerns related to social and environmental impacts, including the avoidance of CO_2 leakage. The decision on which technology to prioritize among various CCS options requires a thorough evaluation based on criteria such as cost,

energy efficiency, environmental impact, thermodynamic indicators, and social acceptance. The qualitative decision-aid method presented here provides a first step toward a more comprehensive assessment. Clear regulations and standards are imperative to guide the choice of CCS technologies and ensure responsible implementation.

References

Arcusa, S. and Sprenkle-Hyppolite, S., 2022. Snapshot of the Carbon Dioxide Removal certification and standards ecosystem (2021–2022). *Climate Policy*, *22*(9-10), pp.1319-1332.

Bach, L.T., Gill, S.J., Rickaby, R.E., Gore, S. and Renforth, P., 2019. CO_2 removal with enhanced weathering and ocean alkalinity enhancement: potential risks and co-benefits for marine pelagic ecosystems. *Frontiers in Climate*, *1*, p.7.

Beerling, D.J., Kantzas, E.P., Lomas, M.R., Wade, P., Eufrasio, R.M., Renforth, P., Sarkar, B., Andrews, M.G., James, R.H., Pearce, C.R. and Mercure, J.F., 2020. Potential for large-scale CO_2 removal via enhanced rock weathering with croplands. *Nature*, *583*(7815), pp.242-248.

Bouckaert, S., Pales, A.F., McGlade, C., Remme, U., Wanner, B., Varro, L., D'Ambrosio, D. and Spencer, T., 2021. Net zero by 2050: A roadmap for the global energy sector.

Castro-Amoedo, R., Granacher, J., Abou Daher, M. and Maréchal, F., 2023. Integrating CO_2 Mineralization in Industrial Clusters: The Benefits of Material and Heat Integration. *Proceedings of FOCAPO/CPC*.

Delerce, S. and Oelkers, É.H., 2022, January. Le potentiel du stockage géologique du CO_2 par minéralisation. In *Annales des Mines-Responsabilité et environnement* (No. 1, pp. 57-62).

Delerce, S., Marieni, C. and Oelkers, E.H., 2023. Carbonate geochemistry and its role in geologic carbon storage. *Surface Process, Transportation, and Storage*, pp.423-477.

European Parliament, 2022. A union certification framework for carbon removals. *EU legislation in progress*, pp.1-8.

Hangx, S.J. and Spiers, C.J., 2009. Coastal spreading of olivine to control atmospheric CO_2 concentrations: A critical analysis of viability. *International Journal of Greenhouse Gas Control*, *3*(6), pp.757-767.

Lehmann, J. and Possinger, A., 2020. Removal of atmospheric CO_2 by rock weathering holds promise for mitigating climate change.

Montserrat, F., Renforth, P., Hartmann, J., Leermakers, M., Knops, P. and Meysman, F.J., 2017. Olivine dissolution in seawater: implications for CO2 sequestration through enhanced weathering in coastal environments. *Environmental Science & Technology*, *51*(7), pp.3960-3972.

O'Neill, R.N. and Nadaï, A., 2012. Risque et démonstration, la politique de capture et de stockage du dioxyde de carbone (CCS) dans l'Union européenne. *VertigO-la revue électronique en sciences de l'environnement*, *12*(1).

Roelich, K. and Giesekam, J., 2019. Decision making under uncertainty in climate change mitigation: introducing multiple actor motivations, agency and influence. *Climate policy*, *19*(2), pp.175-188.

Schuiling, R.D. and Krijgsman, P., 2006. Enhanced weathering: an effective and cheap tool to sequester CO_2. *Climatic Change*, *74*(1-3), pp.349-354.

Selma, L., Seigo, O., Dohle, S. and Siegrist, M., 2014. Public perception of carbon capture and storage (CCS): A review. *Renewable and Sustainable Energy Reviews*, *38*, pp.848-863.

Snæbjörnsdóttir, S.Ó., Sigfússon, B., Marieni, C., Goldberg, D., Gislason, S.R. and Oelkers, E.H., 2020. Carbon dioxide storage through mineral carbonation. *Nature Reviews Earth & Environment*, *1*(2), pp.90-102.

ESCAPE-34 PSE-2024
European Symposium on Computer Aided Process Engineering
&
Process Systems Engineering

Flavio Manenti, Gintaras V. Reklaitis (Eds.), Book of Abstract of the 34th European Symposium on Computer Aided Process Engineering / 15th International Symposium on Process Systems Engineering (ESCAPE34/PSE24), June 2-6, 2024, Florence, Italy.

Systematic Comparison of Flowsheet Optimization Options: Surrogate Modelling vs. Genetic Algorithms vs. Bayesian Optimization

Caroline Ganzer[a*], Kai Sundmacher[a,b]

[a]*Max Planck Institute for Dynamics of Complex Technical Systems, Department of Process Systems Engineering, Sandtorstraße 1, 39106 Magdeburg, Germany*
[b]*Otto von Guericke University, Chair for Process Systems Engineering, Universitätsplatz 2, 39106 Magdeburg, Germany*
cganzer@mpi-magdeburg.mpg.de

Abstract

This project aims to systematically compare options for flowsheet optimization. Surrogate modelling, genetic algorithms, Bayesian optimization, and combinations of them can be used to approach the black-box optimization task which arises from complex process simulation. There are trade-offs in computational effort, number of hyperparameters, reliability in reaching global optima, etc. The goal is to categorize existing methods, evaluate the performance of the algorithms, and synthesize guidelines on which algorithms to use depending on the flowsheet, objective, and dimensionality.

Keywords: surrogate modelling, Bayesian optimization, genetic algorithms, flowsheet optimization, derivative-free optimization, gradient-free optimization

1. Background

Process modelling with flowsheet simulators is a powerful, established tool for process design. When the formulation of the simulation is equation-based, optimization of the flowsheet can be solved with deterministic, gradient-based optimization algorithms. In many cases, however, gradients are not available from these simulations, calling for derivative-free optimization (DFO). Further, they frequently exhibit high computational cost, resulting in the need to limit the number of function evaluations. One established method to approach this task is surrogate modelling. A data set is generated from the simulation, which is then used to train a surrogate model, such as an artificial neural network (ANN). As the structure of the surrogate model is known, deterministic optimization is used to optimize over the surrogate model. Alternatively, genetic algorithms (GA) can be applied to flowsheets. It is a heuristic technique which uses evolving generations of testing points to iterate closer to optimal solutions. Recently, Bayesian optimization (BO) has gathered attention, and has been applied to flowsheet optimization (Sanchez Medina et al., 2021a). BO utilizes a surrogate model, often a

Gaussian process (GP) model, and an acquisition function to estimate where sampling would reveal the most information. Many variations and even combinations of these methods exist (Sanchez Medina et al., 2021a, Sanchez Medina et al., 2021b). They vary in their accuracy, workflow complexity, computational effort, number of and sensitivity with respect to hyperparameters, ability to deal with constraints, and behavior at higher dimensions (degrees of freedom).

It is not obvious which type of DFO is appropriate or optimal depending on the flowsheet. Among the options, surrogate modelling has been a major focus (McBride and Sundmacher, 2019). The data requirement of effective ANN training can be a restrictive factor. GA tends to be applied much less frequently, but can be favored for multi-objective optimization (Shafiee et al., 2017). This can be helpful for chemical engineering applications, where there are often conflicting objectives such as efficiency, yield, cost, energy consumption, environmental impact. Its conception as heuristics-based may present a disadvantage. BO appears most helpful when function evaluations, i.e., simulation runs, are particularly expensive, but it comes at higher computational cost itself (van de Berg et al., 2022).

2. Methodology

We are evaluating the various options for flowsheet optimization, using ASPEN for flowsheet simulation. We plan to assemble a collection of DFO methods applicable to flowsheets as well as a set of different flowsheets, e.g., methanol synthesis from (green) H_2 and CO_2. Appropriate methods such as early stopping are utilized for training the surrogate models to ensure prediction accuracy and prevent overfitting. The set of flowsheets is designed deliberately diverse, with variation in types and number of unit operations as well as presence and number of recycles. Then the parameters characterizing the algorithms and the flowsheet optimization tasks can be varied and the performance of the algorithms can be estimated.

3. Conclusions

We expect trade-offs between the techniques in computational effort, number of hyperparameters, reliability in reaching global optima, etc. Further, the algorithms' behavior at increasing number of degrees of freedom, and for varying objectives will be examined. Can some algorithms deliver adequate performance without the need to carefully adapt them to the flowsheet and tune the hyperparameters? What is the trade-off between adaptability and complexity? The goal is to categorize existing methods, evaluate the performance of the algorithms, and synthesize guidelines on which algorithms to use depending on the flowsheet, objective, dimensionality, and other factors.

References

E. I. Sanchez Medina, D. F. Rodriguez-Vallejo, E. A. del Rio-Chanona, K. Sundmacher, and P. Petsagkourakis, 2021a, Multi-objective Bayesian optimization of process flowsheets using trust regions and quality set metrics, 2021 AIChE Annual Meeting.

E. I. Sanchez Medina, D. F Rodriguez Vallejo, B. Chachuat, K. Sundmacher, P. Petsagkourakis, and E.A. del Rio-Chanona, 2021b, Acyclic modular flowsheet optimization using multiple trust regions and Gaussian process regression, Computer Aided Chemical Engineering, 50: 1117–1123.

K. McBride and K. Sundmacher, 2019, Overview of surrogate modeling in chemical process Engineering, Chemie Ingenieur Technik, 91(3):228–239.

A. Shafiee, M. Nomvar, Z. Liu, and A. Abbas, 2017, A new genetic algorithm based on prenatal genetic screening (PGS-GA) and its application in an automated process flowsheet synthesis problem for a membrane based carbon capture case-study, Chemical Engineering Research and Design, 128:265–289.

D. van de Berg, T. Savage, P. Petsagkourakis, D. Zhang, N. Shah, and E. A. del Rio-Chanona, 2022, Data-driven optimization for process systems engineering applications. Chemical Engineering Science, 248:117135.

ESCAPE-34 PSE-2024
European Symposium on Computer Aided Process Engineering
&
Process Systems Engineering

Flavio Manenti, Gintaras V. Reklaitis (Eds.), Book of Abstract of the 34th European Symposium on Computer Aided Process Engineering / 15th International Symposium on Process Systems Engineering (ESCAPE34/PSE24), June 2-6, 2024, Florence, Italy.

The Role of Biomass in the Swiss Energy Transition: Low-Regret Strategies for an Uncertain Future

Gabriel Wiest,[a] Gianfranco Guidati,[b] Adriana Marcucci,[b] André Bardow[a] and Stefano Moret[a,*]

[a]*Energy and Process Systems Engineering, Department of Mechanical and Process Engineering, ETH Zürich, Tannenstrasse 3, 8092 Zürich, Switzerland*
[b]*Energy Science Center, ETH Zürich, Sonneggstrasse 28, 8006 Zürich, Switzerland*
morets@ethz.ch

Abstract

Biomass is a versatile resource and, thus, can support the net-zero energy transition in various sectors. However, the limited availability of biomass requires careful allocation and prioritization of its usage. Making good choices in energy system planning becomes challenging when considering future uncertainties. This study introduces a method that streamlines this decision process and identifies low-regret strategies for long-term energy system planning under uncertainty. We apply this approach to biomass usage in Switzerland's energy system. Our analysis results in four potential biomass strategies. Evaluating the strategies in detail suggests that prioritizing biomass for fuel production reduces the expected regret while focusing on bio-methane production results in the lowest worst-case regret.

Keywords: strategic decision-making, energy systems, biomass, uncertainty, low-regret

1. Introduction

Biomass plays a central role in transitioning to net-zero energy systems, capturing CO_2 during growth and achieving negative emissions when combined with carbon capture and storage. Recent sector-specific studies identify biomass as a cost-effective and versatile resource to decarbonize heating and electricity supply (Ozolina et al., 2022), aviation (Bergero et al., 2023), or the production of chemicals (Meys et al., 2021). However, the limited availability of sustainable biomass prohibits simultaneously satisfying the demands across all these sectors.

Thus, deciding how to utilize the limited biomass resources in the energy system requires strategic prioritization. This decision must be made today to enable a rapid energy transition and mitigate the worst effects of climate change. This planning task relies on uncertain scenarios of future energy demands, fuel prices, and technology costs (Moret et al., 2017). As the optimal solution for one scenario may prove sub-optimal for another, the challenge lies in identifying strategies that yield minimal regret over the set of all possible realizations.

2. Method

The goal of our method is to identify strategies with minimal regret. In the first step, *outputs of interest* from the energy systems model, e.g., the installed capacity of technologies, are selected. Next, applying latin hypercube sampling (McKay et al., 1979) to the uncertain input parameters, we generate N different scenarios $s \in \Omega = \{s_1, \ldots, s_N\}$. Each scenario, corresponding to a different uncertain parameter sample, is then optimized in the energy system model. The potential solution space is obtained by computing the previously chosen outputs of interest. Using k-means clustering, this space is grouped into k clusters. Following the approach by Baader et al. (2023), a decision tree is trained on the outputs of interest to predict the corresponding cluster. The resulting leaves of the tree are denoted as *strategies* $I = \{1, \ldots, k\}$. Ω_i is the subset of Ω for which strategy i is optimal.

Next, we calculate the regret for the scenarios where strategy i is not the optimal choice: Each scenario $s \in \Omega \setminus \Omega_i$ is reoptimized while enforcing strategy i, resulting in the cost $C_{i,s}$. Taking the difference between the cost $C_{i,s}$ and the cost of the optimal strategy C_s^{opt}:

$$R_{i,s} := C_{i,s} - C_s^{opt} \quad \forall i \in I, \forall s \in \Omega \setminus \Omega_i \tag{1}$$

the *regret* $R_{i,s}$ of strategy i in scenario s is obtained. Note that, by construction, $R_{i,s}$ is always non-negative. Repeating this computation for all scenarios $s \in \Omega \setminus \Omega_i$ results in a distribution of regrets for strategy i. Last, for each strategy, the mean and maximum of its regret distribution, together with the probability of regret P^{regret}, are computed.

3. Case study

We model the Swiss energy system using the open-source whole-energy system framework Energyscope (Limpens et al., 2019) and, for the first time, extend it to include all the possible biomass conversion pathways. Specifically, we consider four types of biomass resources: wood, animal manure, green waste, and fresh sewage sludge. On the demand side, we include the supply of residential and industrial heat, electricity, and mobility. In addition, we integrate the production, demand, and recycling of essential chemicals and plastics based on Meys et al. (2021).

The 27 technologies that use biomass as a resource are grouped by their products into eight categories: Low-temperature heat; high-temperature heat; combined heat and power; fuels; hydrogen; natural gas; charcoal; and chemical products.

The eight outputs of interest of our case study are defined as the amount of energy from biomass that flows into each one of the above categories.

To apply our method, we simulate N = 1000 different scenarios. We identify the required number of clusters k by applying the "elbow method" (Ketchen et al., 1996) concluding on using k = 4 clusters. This choice is in agreement with psychological studies suggesting that for maintaining interpretability and effective communication no more than three to five alternatives should be presented to decision-makers (Cowan, 2001).

4. Results

In all scenarios, we do not observe significant use of biomass (<1 GWh) for production of chemicals or low-temperature heat. Thus, both outputs of interest are discarded from further analysis. Based on the remaining six outputs of interest (energy flow of biomass

into high-temperature heat; combined heat and power; fuels; hydrogen; natural gas; and charcoal), the decision tree is trained (Fig. 1) following the method by Baader et al. (2023). At each node of the tree, a radar plot indicates the level of flexibility with respect to each output of interest. Starting from the entire solution space at the top, including all $N = 1000$ scenarios and hence showing full flexibility across each output of interest, every decision on a given output of interest influences the potential of the remaining ones, thus constraining the solution space. For example, choosing a high use of biomass for fuel production significantly lowers the availability of biomass for all other usages except cogeneration of heat and power.

At the bottom of the tree, we end up with four leaves, which are cost-optimal strategies for biomass usage for different regions of the input space: Strategy 1 focuses on using the available biomass to produce bio-methane, Strategy 2 primarily produces hydrogen and high-temperature heat, Strategy 3 centers around generating biochar, and Strategy 4 focuses on using biomass to produce liquid fuels.

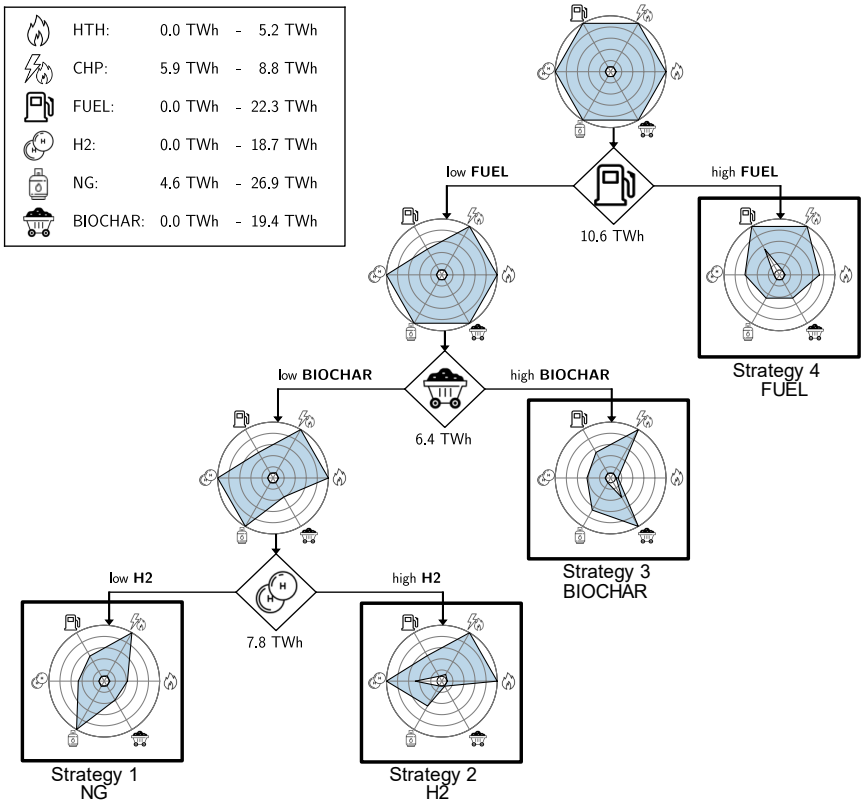

Figure 1: Decision tree on six of the outputs of interest: high-temperature heat (HTH), combined heat and power (CHP), diesel/kerosene (FUEL), hydrogen (H2), bio-methane (NG), and charcoal (BIOCHAR), identifying four potential strategies for the use of biomass in the Swiss energy system.

Only the use of biomass for combined heat and power is present in all strategies independently of the decisions. The reason is that, in all scenarios, the only energy flow into this category is given by all available manure being used in biogas motors.

Thus, the energy flow into combined heat and power in our model solely depends on the amount of available manure.
In the next step, we enforce the strategies for the scenarios where they are not optimal and reoptimize the model. Using Eq. (1), the regret distributions for the four strategies are computed, and the results are summarized (Tab.1).
The regrets among the individual strategies differ considerably: The minimal *expected regret* P^{regret} x R^{mean} results from producing fuels (Strategy 4), followed by bio-methane (Strategy 1), hydrogen (Strategy 2), and biochar (Strategy 3). While Strategy 4 clearly stands out with respect to most metrics in Table 1, if the objective is to minimize the *worst-case regret* R^{max}, bio-methane and hydrogen are preferred over fuel production from biomass. Thus, there is not the one biomass strategy that performs best in all measures. Depending on whether the objective of the decision-maker is minimizing the *expected* or the *worst-case regret*, the preferred strategy differs. Furthermore, the sensitivity of the regret of a strategy with respect to the inputs, especially those controllable by the decision-maker, could give valuable insights for the decision process. By ensuring these inputs remain within certain limits potential worst-case scenarios could be avoided.

Table 1: Results from the regret analysis of the biomass strategies in units 10^6 €. The lowest values of regret are highlighted in bold.

Regret	**Strategy 1 Methane**	**Strategy 2 Hydrogen**	**Strategy 3 Biochar**	**Strategy 4 Fuel**
$R_i^{mean} := \underset{s}{\text{mean}}(R_{i,s})$	256	425	580	**174**
$R_i^{max} := \underset{s}{\max}(R_{i,s})$	**781**	877	1,517	962
$P_i^{regret} := \frac{\#(\Omega \setminus \Omega_i)}{\#\Omega}$ in [%]	90.5	91.1	85.5	**32.9**
P_i^{regret} x R_i^{mean}	232	387	496	**57**

5. Conclusions

Guiding the energy transition under uncertainty requires the synthesis of multiple plausible scenarios, which is challenging due to the volume and complexity of options resulting from uncertainty studies. Our replicable method streamlines the solution space of an optimization under uncertainty problem, highlighting the key strategies with their potential regret.
We identify four potential strategies for the usage of biomass in Switzerland that are optimal for different regions of the input space. Our analysis reveals that the strategy focusing on using biomass to produce fuels results in the lowest expected regret, while having a high production of bio-methane has the lowest worst-case regret.
Our approach of identifying potential strategies and quantifying their regrets can easily be generalized to other fields of energy system planning. It enhances the accessibility of uncertainty-related results for policymakers, thus encouraging informed decision-making.

Acknowledgment

G.W. and S.M. acknowledge support from the Swiss National Science Foundation under Grant No. PZ00P2_202117.

References

F. Baader, S. Moret, W. Wiesemann, I. Staffell, A. Bardow, 2023. Streamlining Energy Transition Scenarios to Key Policy Decisions. arXiv:2311.06625.

C. Bergero, G. Gosnell, D. Gielen, S. Kang, M. Bazilian, S. J. Davis, 2023. Pathways to net-zero emissions from aviation. Nature Sustainability 6, 404–414.

D. J. Ketchen, C. L. Shook, 1996. The Apllication of Cluster Analysis in Strategic Management Research: An Analysis and Critique. Strategic Management Journal 17(6), 441-45.

G. Limpens, S. Moret, H. Jeanmart, F. Maréchal, 2019. EnergyScope TD: A novel open-source model for regional energy systems. Applied Energy 255, 113729.

M. D. McKay, R. J. Beckman, W. J. Conover, 1979. A Comparison of Three Methods for Selecting Values of Input Variables in the Analysis of Output from a Computer Code. Technometrics 21(2), 239–245.

R. Meys, A. Kätelhön, M. Bachmann, B. Winter, C. Zibunas, S. Suh, A. Bardow, 2021. Achieving net-zero greenhouse gas emission plastics by a circular carbon economy. Science 374 (6563), 71–76.

S. Moret, V. C. Gironès, M. Bierlaire, F. Maréchal, 2017. Characterization of input uncertainties in strategic energy planning models, Applied Energy 202, 597-617.

S. A. Ozoliņa, I. Pakere, D. Jaunzems, A. Blumberga, A. Grāvelsiņš, D. Dubrovskis, S. Daģis, 2022. Can energy sector reach carbon neutrality with biomass limitations? Energy 249, 123797.

ESCAPE-34 PSE-2024
European Symposium on Computer Aided Process Engineering
&
Process Systems Engineering

Flavio Manenti, Gintaras V. Reklaitis (Eds.), Book of Abstract of the 34th European Symposium on Computer Aided Process Engineering / 15th International Symposium on Process Systems Engineering (ESCAPE34/PSE24), June 2-6, 2024, Florence, Italy.

Automating Life Cycle Assessment from Chemical Process Simulations

Lukas Spiekermann,[a] Hitesh Sewani,[a] Sebastian Lochmann,[a] Samuel Hummel,[a] Johannes Schilling,[a] Luca Bosetti,[a] Benedikt Winter,[a] Jan Seiler,[a] Sangwon Suh,[b] André Bardow[a*]

[a]*Energy & Process Systems Engineering, Department of Mechanical and Process Engineering, ETH Zürich, Tannenstrasse 3, 8092 Zurich, Switzerland.*

[b]*Bren School of Environmental Science and Management, Bren Hall, 2400 University of California, Santa Barbara, CA 93117, USA.*

abardow@ethz.ch

Abstract

Advancing sustainability requires knowledge on the environmental impacts of chemicals. For this purpose, life cycle assessment is the preferred method, but usually carried out by manually extracting data from process simulation software and transferring data to life cycle assessment software. This process is very labor-intensive and error-prone.
Here, we bridge the gap between process simulation and life cycle assessment by automated data extraction from process simulators to life cycle assessment software. Our tool currently links the process simulators Aspen Plus, Aspen HYSYS, and AVEVA Process Simulation to the open-source tools Brightway/Activity Browser for life cycle assessment. The tool is exemplified using openly available case studies and simulation files for bio-based and CO_2-based processes. Simulation studies can be combined to, e.g., integrated CO_2 capture and utilization chains within life cycle assessment software.
Our tool directly integrates process simulations results into life cycle inventory databases with easy workflows and could thereby enable the generation of more life cycle assessments of chemical processes.

Keywords: chemical process simulation, life cycle assessment, automated data extraction, life cycle inventory

1. Introduction

Life cycle assessment (LCA) of chemical processes is a crucial part of process development (Hungerbühler et al., 2021). Often, LCA is performed subsequent to process development and simulation (Köck et al., 2023). Today, the LCA computation relies on manual data handling for transferring simulation results to life cycle assessment software and requires deep process knowledge (Köck et al., 2023). This approach is labor-intense and error-prone (Azzaro-Pantel et al., 2022) and might neglect flows that seem irrelevant but substantially contribute to environmental impacts (Rosental et al., 2020).

However, the workflow of LCA for chemical processes offers the potential for standardization, as many chemical processes follow a logic of converting feedstocks to products, byproducts, and waste with the help of utilities and solvents (Hungerbühler et al., 2021). Therefore, streamlining the workflow can significantly ease and accelerate the LCAs of chemical processes.
In this work, we establish a bridge between process simulation and LCA by introducing an automated data extraction tool that connects the process simulation software Aspen Plus (Aspen Technology Inc., 2019a), Aspen HYSYS (Aspen Technology Inc., 2019b), and AVEVA Process Simulation (AVEVA Group plc, 2023) with the LCA software Brightway (Mutel, 2017). Our tool simplifies the integration of standard software and methodologies in process systems engineering with the tools essential for LCA. Automating data processing accelerates the LCA process, facilitating the integration into larger systems and limiting the possibility of data transfer errors.

2. Methods

Our tool streamlines the connection of process simulation to LCA. For this purpose, we connect common process simulators with the open-source Python-based software package Brightway (Mutel, 2017), a well-established and widely adopted tool within the academic LCA community. Furthermore, integration into Brighway allows the use of the open-source LCA tool Activity Browser, which offers an intuitive graphical interface for conducting additional calculations and managing databases and results (Steubing et al., 2020). By using Python as a shared programming language across both process simulation and LCA domains, we ensure a unified and cohesive approach to our implementation. A graphical user interface guides the user through the workflow, from flowsheet extraction to life cycle inventories (LCIs) and life cycle impact assessment (LCIA).

In its current implementation, our tool supports the process simulation software Aspen Plus (Aspen Technology Inc., 2019a), Aspen HYSYS (Aspen Technology Inc., 2019b), and AVEVA Process Simulation (AVEVA Group plc, 2023), which are common software in chemical process simulation both in academia and industry (de Beer and Depew, 2021). The only input to the extraction tool is a simulation file of a chemical process, which is evaluated and from which all mass and energy streams are extracted.

After extracting process simulation results, the next step involves linking the process streams with the corresponding activities in life cycle assessment databases to calculate environmental impacts. Typically, life cycle inventory databases such as ecoinvent (Wernet et al., 2016) or GaBi (Sphera Solutions Inc., 2023) are used. The process streams are either linked to direct emissions to the environment or linked to activities further down the supply chain, which causes underlying environmental impact. The stream-linking step requires manual user input and is hard to automate since specifications are needed for the exact locations, energy mixes, or modeling assumptions, e.g., options for waste treatment. However, the user is assisted by a graphical interface providing process streams and life cycle inventory activities next to each other in one combined interface for easy linking. Furthermore, the user is provided with stream information and can further modify the process data. Finally, all process streams are linked to inventory activities as the final step of the life cycle inventory analysis (LCI).

Starting from the LCI, the life cycle impact assessment (LCIA) is calculated automatically to determine the potential environmental impacts of the investigated process.

Furthermore, the contribution of the streams to the overall impacts in various impact categories is evaluated. The contribution analysis allows for identifying hotspots that might require further process development. Finally, LCI and LCIA results can be exported and used further in other simulations. As the results are stored within Brightway, newly developed processes can be integrated and evaluated in larger supply chains.

3. Case Study

The robustness of our automated data extraction and LCA tool is tested by assessing literature case studies. These studies encompass a spectrum of processes, including bio-based conversion, CO_2 capture, and CO_2 utilization, for which simulation files are readily available online together with the corresponding publication or provided as example files for the process simulation software. Moreover, these studies provide access to life cycle inventories, LCA results, and/or techno-economic analysis (TEA) findings, offering a data source for validation. The simulation files were taken from the literature with no further modification. In particular, the simulations used different unit sets or stream definitions.

We demonstrate the possibilities arising from the full integration capabilities of our tool by combining multiple simulation files from three different software tools into one larger LCA study. The combination shows the potential for data handling without manual data transfer or manipulation. We combine the amine-based CO_2 flue gas capture by Adams et al. (Adams et al., 2014, Adams, 2017) implemented in Aspen Plus with water electrolysis provided as AVEVA Process Simulation example (AVEVA Group plc, 2023) as feedstocks for the CO_2 hydrogenation to methanol implemented in Aspen HYSYS (Vázquez and Guillén-Gosálbez, 2021) (see Figure 1).

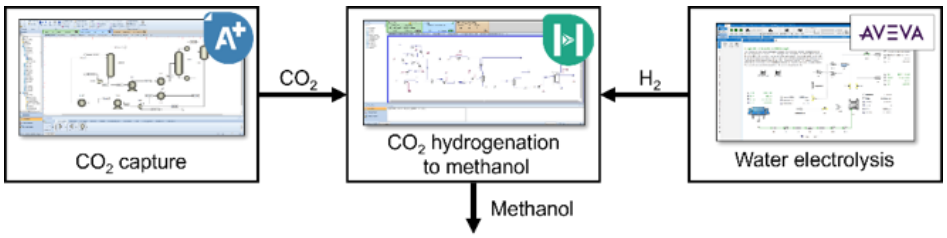

Figure 1: Simulation files automatically combined to generate the life cycle inventory for the CO_2 hydrogenation to methanol including CO_2 capture and water electrolysis.

Our demonstration is executed using the ecoinvent 3.9.1 database (cutoff system model) (Wernet et al., 2016) and the environmental footprint methodology 3.1 (Andreasi Bassi et al., 2023) as life cycle inventory database and life cycle impact assessment method, espectively. For the simplicity of demonstration, only the available ecoinvent processes for the US are used, and no further modeling of feedstock or utility systems is performed.

4. Results

The case study demonstrates the automated integration of multiple case studies into one larger supply chain for which LCA results are automatically computed. The tool determines the total climate change impacts of methanol production to 22.7 kg_{CO2eq}/kg_{MeOH}. The relative contributions to climate change impacts for methanol production are shown in Figure 2.

The tool allows for the identification of hotspots further down the supply chain and across the integrated flowsheets. Here, the major hotspot is the electricity demand for hydrogen production. In this case study, electricity is assumed to be taken from the US-average electricity grid. This assumption leads to the high climate change impacts of methanol.

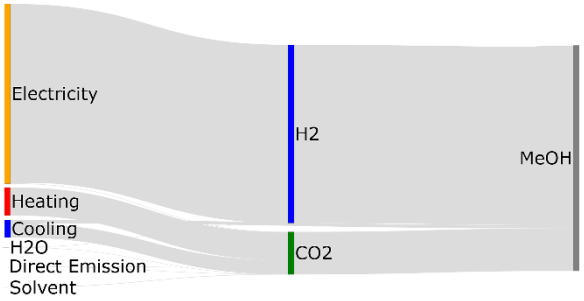

Figure 2: Relative contribution to climate change impacts for the CCU pathway to methanol by integrating the flowsheets in Figure 1.

Integrating our tool with standard software facilitates the transfer of results and the incorporation of individual processes into supply chains within the Brightway framework. Therefore, the impact of flowsheet changes on the LCA results of whole value chains can be evaluated automatically.

5. Conclusions

This work presents an automated data extraction tool for connecting process simulation software and life cycle assessment software. The tool showcases its capabilities by automatically integrating case studies from the literature into a comprehensive supply chain. Data handling and the calculation of environmental impacts are automated, and hotspots in the process can be identified easily.

Our methodological approach allows for the direct integration of LCI results into databases, promoting user-friendly workflows. This approach holds the potential to mitigate data gaps within life cycle inventories of chemical supply chains, facilitating more comprehensive LCAs of chemical processes. Furthermore, our tool aids the integrated development and environmental assessment of chemical processes.

Acknowledgments

This publication was created as part of NCCR Catalysis (grant number 180544), a national Centre of Competence in Research funded by the Swiss National Science Foundation.

References

K. Hungerbühler, J.M. Boucher, C. Pereira, T. Roiss, M. Scheringer, 2021, Chemical Products and Processes (Springer International Publishing, Cham, Switzerland)

B. Köck, A. Friedl, S. Serna Loaiza, W. Wukovits, B. Mihalyi-Schneider, 2023, Automation of Life Cycle Assessment-A Critical Review of Developments in the Field of Life Cycle Inventory Analysis, *Sustainability* 15(6), 5531

C. Azzaro-Pantel, M. Madoumier, G. Gésan-Guiziou, 2022, Development of an ecodesign framework for food manufacturing including process flowsheeting and multiple-criteria decision-making: Application to milk evaporation, *Food and Bioproducts Processing* 131, 40–59

M. Rosental, T. Fröhlich, A. Liebich, 2020, Life Cycle Assessment of Carbon Capture and Utilization for the Production of Large Volume Organic Chemicals, *Front. Clim.* 2, 586199

Aspen Technology Inc., 2019a, Aspen Plus (Burlington, MA, USA)

Aspen Technology Inc., 2019b, Aspen HYSYS (Burlington, MA, USA)

AVEVA Group plc, 2023, AVEVA Process Simulation (Cambridge, UK)

C. Mutel, 2017, Brightway: An open source framework for Life Cycle Assessment, *JOSS* 2(12), 236

B. Steubing, D. de Koning, A. Haas, C. L. Mutel, 2020, The Activity Browser — An open source LCA software building on top of the brightway framework, *Software Impacts* 3, 100012

J. de Beer, C. Depew, 2021, The role of process engineering in the digital transformation, *Computers & Chemical Engineering* 154, 107423

G. Wernet, C. Bauer, B. Steubing, J. Reinhard, E. Moreno-Ruiz, B. Weidema, 2016, The ecoinvent database version 3 (part I): overview and methodology, *Int J Life Cycle Assessment* 21(9), 1218–1230

Sphera Solutions Inc., 2023, GaBi Database. , https://sphera.com/life-cycle-assessment-lca-database/. Accessed 27 October 2023

T. A. Adams, Y. K. Salkuyeh, J. Nease, 2014, in Reactor and process design in sustainable energy technology, ed. F. Shi (Elsevier, Amsterdam, The Netherlands), p. 163–231

T. A. Adams, 2017, New: Simulation Files Database. (PSE Community.org - The World Community for Chemical Process Systems Engineering Education and Research), https://psecommunity.org/new-simulation-files-database. Accessed 5 June 2023

D. Vázquez, G. Guillén-Gosálbez, 2021, Process design within planetary boundaries: Application to CO2 based methanol production, *Chemical Engineering Science* 246, 116891

S. Andreasi Bassi, F. Biganzoli, N. Ferrara, A. Amadei, A. Valente, S. Sala, F. Ardente, 2023, Updated characterisation and normalisation factors for the Environmental Footprint 3.1 method (Publications Office of the European Union, Luxembourg, Luxembourg)

ESCAPE-34 PSE-2024
European Symposium on Computer Aided Process Engineering
&
Process Systems Engineering

Flavio Manenti, Gintaras V. Reklaitis (Eds.), Book of Abstract of the 34th European Symposium on Computer Aided Process Engineering / 15th International Symposium on Process Systems Engineering (ESCAPE34/PSE24), June 2-6, 2024, Florence, Italy.

Smoothing the Chaos: Addressing Chaotic Behavior in Energy System Models through MILP Stabilization

Jonas Schnidrig[a*,b], François Maréchal[b], Manuele Margni[a]

[a] *HES-SO Valais Wallis, CIRAIG, Sion, Switzerland.*
[b] *Ecole Polytechnique de Lausanne, IPESE group, Sion, Switzerland.*
jonas.schnidrig@hevs.ch

Abstract

In MILP energy system modeling, chaotic behaviors frequently emerge because of the integer and linear nature of the problem, complicating the interpretability and utility of the model outputs. Such volatility has already been observed in equivalent solutions in previous works due to the symmetry of the problem definition [1–3]. Still, it can notably be observed in nonsymmetrical global energy system models while applying parametrization of penetration of various technologies, for example, high-altitude photovoltaic (PV) systems in the Swiss energy landscape, where equivalent solutions from the point of view of the objective function exist but are distinguished in the activated constraints and thus by the energy system configuration. The present study introduces an innovative methodology to stabilize the parametrization of technology penetration scenarios to address this. The technique is engineered to enable a more "smooth" and predictable energy system evolution when subjected to various penetration configurations, all within a mixed-integer linear programming (MILP) framework, thus opening the door to identifying equivalent solutions to an optimization problem.

Utilizing the MILP energy system modeling framework EnergyScope [4–6], the research presents a novel, simple, and linear contribution by introducing an additional stabilization term into the model's objective function. This stabilization term is constructed to capture the absolute variation in the size of installed technologies between consecutive model runs, thus adding a term minimizing the configuration changes to the objective function. The challenge of weighting this contribution without penalizing the primary objective function value is assessed by assessing the impact of the latter scaling on the generated, thereby enriching the analysis and robustness of the model's output.

From a results standpoint, the study delineates the specific conditions that lead to optimal stabilization, culminating in a smooth transition of energy system configurations from one scenario to another. The implemented methodology significantly enhances the identification of vertices in the solution space, allowing for a more nuanced understanding of critical configurations within that space.

Moreover, the study extends its applicability by employing the stabilization methodology to the Swiss energy system's trajectory toward 2050, a system envisioned to be both energy-independent and carbon-neutral. In this context, the methodology displayed its utility in providing nuanced insights into the penetration scenarios of high-altitude PV. These insights are crucial for policymakers and stakeholders, offering actionable steps to meet energy transition indicators effectively. The methodology stabilizes the parametrization. It provides a sophisticated tool for evaluating energy transition indicators, catalyzing more robust and reliable energy system modeling.

Keywords: Mixed-Integer Linear Programming, Parametrization Stabilization, Equivalent solutions, Energy System model, Energy Transition

1. Introduction

1.1. Context

Modeling energy systems through mixed-integer linear programming (MILP) is pivotal in shaping our understanding and approach to the evolving energy landscape. In the quest for sustainable and efficient energy solutions, MILP models are instrumental in evaluating and strategizing energy system transitions. However, these models often encounter a significant hurdle: chaotic behaviors arising from their integer and linear problem structures. This complexity is not only a characteristic of symmetrical problems [1–3], but also manifests in non-symmetrical global energy system models. A notable example is the parametrization of technology penetration, such as high-altitude photovoltaic (PV) systems in the Swiss energy landscape. Here, equivalent solutions, in terms of objective function outputs, diverge in their activated constraints, leading to varying energy system configurations.

1.2. Literature Review

The inherent volatility in MILP energy system modeling, particularly regarding technology penetration, has been a focal point of previous research. While the literature addresses the equivalent solutions arising from symmetrical problems, a gap exists in understanding and managing the chaotic behavior in non-symmetrical models. The EnergyScope framework [4–6] has been instrumental in this domain, offering a basis for developing more robust and nuanced models. However, the challenge of stabilizing parametrization in such models, especially in varied technology penetrations, has not been comprehensively addressed. This gap points to the need for a methodology that stabilizes the model outputs and enhances the interpretability and utility of these models in planning and decision-making processes.

1.3. Problem Statement

The primary challenge in MILP energy system modeling is the stabilization of parametrization under different technology penetration scenarios. The unpredictability and complexity inherent in these models hinder their effectiveness in guiding the transition to sustainable energy systems. This research aims to introduce an innovative methodology to address this challenge. The proposed technique is designed to add a stabilization term to the objective function of the MILP model, aiming to minimize configuration changes between model runs.

This approach facilitates a smoother, more predictable transition in energy system configurations, enhancing the model's reliability and applicability. The methodology's effectiveness will be demonstrated through its application to the Swiss energy system,

aiming for energy independence and carbon neutrality by 2050. By providing a more stabilized approach to modeling, the research offers a path toward more effective planning and implementation of energy transition strategies, catering to the needs of policymakers and stakeholders in the energy sector.

2. Methods

This research employs a mixed-integer linear programming (MILP) approach to stabilize the parametrization of technology penetrations in energy system modeling. The proposed methodology introduces a novel objective function that includes a stabilization term, aiming to reduce the variance in technology configuration between model iterations n and $n-1$.

Adapting the modeling framework EnergyScope[6], the optimization problem is enhanced by adding a stabilization term, such as the objective function (Eq. 1), which seeks to minimize the total cost $\boldsymbol{C_{tot}}$, subject to a stabilization factor ϵ that influences the change in technology size $\boldsymbol{\Delta F_n}$ between successive iterations.

The total cost (Eq. 2) is the sum of the investment cost of the technologies-specific investments c_{inv} multiplied by the technology annualization factor (τ), and maintenance costs c_{maint} for each technology i, in addition to the operational costs c_{op} for each resource j in each time period t.

The end uses $\boldsymbol{EU}$ for each layer l and time period t is defined by the technology utilization $\boldsymbol{F_t}$ adjusted by the technology efficiency η including the storage technology flows $\boldsymbol{F_t^+}$ and $\boldsymbol{F_t^-}$ (Eq. 3).

The technology size $\boldsymbol{F}$ is determined by the reference size f_{ref} and the number of units $\boldsymbol{N}$ installed, which is an integer value (Eq. 4).

Technology sizes are constrained by their minimum and maximum feasible sizes f_{min} and f_{max} (Eq. 5).

Technology Ξ, in this case study, PV EHV is integrated via the penetration parameter ξ_n, which increases monotonically, thus varying the technology installed between $f_{min}(\Xi)$ and $f_{max}(\Xi)$ (Eq. 6).

The change in technology size $\boldsymbol{\Delta F_n}$ is the absolute difference between the sizes in consecutive runs (Eq. 8), ensuring non-negativity (Eq. 9).

$$\min_{\mathbf{F},\mathbf{Ft},\xi_n} \boldsymbol{C_{tot}} + \epsilon \cdot \boldsymbol{\Delta F_n} \tag{1}$$

s.t.

$$\boldsymbol{C_{tot}} = \sum_i \left(c_{inv}(i) \cdot \tau(i) + c_{maint}(i)\right) \cdot \boldsymbol{F}(i) + \sum_j \sum_t c_{op}(j,t) \cdot t_{op}(t) \cdot \boldsymbol{F_t}(j,t), \quad \forall\, i \in TECH, j \in RES, t \in PERIODS \tag{2}$$

$$\boldsymbol{EU}(l,t) = \sum_i \boldsymbol{F_t}(i,t) \cdot \eta(i,l) + \sum_l \boldsymbol{F_t}(l,t) + \sum_s \left(\boldsymbol{F_t^+}(s,l,t) - \boldsymbol{F_t^-}(s,l,t)\right), \quad \forall\, l \in LAYERS, t \in PERIODS, i \in TECH, j \in RES, s \in STO - TECH \tag{3}$$

$$\boldsymbol{F}(i) = f_{ref}(i) \cdot \boldsymbol{N}(i), \qquad \forall\, i \in TECH, N(i) \text{ integer} \tag{4}$$

$$f_{min}(i) \leq \boldsymbol{F}(i) \leq f_{max}(i), \qquad \forall\, i \in TECH \tag{5}$$

$$\boldsymbol{F}(\Xi) = f_{min}(\Xi) + \xi_n \cdot \left(f_{max}(\Xi) - f_{min}(\Xi)\right), \quad \forall\, \xi_n > \xi_{n-1}, \xi_0 = 0 \tag{6}$$

$$\boldsymbol{\Delta F_n}(i) \geq \sum_i \left(\boldsymbol{\Delta F_n^+}(i) + \boldsymbol{\Delta F_n^-}(i)\right) \geq 0, \quad \forall\, n > 0, i \in TECH \tag{7}$$

$$\boldsymbol{\Delta F_n^+}(i) - \boldsymbol{\Delta F_n^-}(i) = \boldsymbol{F_n}(i) - f_{n-1}(i), \quad \forall\, \boldsymbol{\Delta F^{\pm}} \geq 0, n > 0, f_0 = 0, \qquad i \in TECH \tag{8}$$

3. Results

Upon applying the stabilization methodology to the EnergyScope MILP framework, distinct operational configurations were observed under consistent high-altitude photovoltaic (PV) penetration levels. The analysis was conducted by parametrizing the PV penetration within the Swiss energy system model from 0 to 20 GW. The model was also run in reverse to ensure the identification of distinct solutions, from 20 GW down to 0. Notably, despite the different starting points and directions of parametrization, the total cost (primal objective function value) remained constant for equivalent levels of PV penetration.

Figure 1 highlights two technology configurations, wind, and PV, exhibiting this phenomenon. The solid lines represent the initial scenario of increasing PV penetration, while the dashed lines depict the reverse parametrization. It is observed that, at any given level of PV penetration, the total cost remains the same between scenarios, indicating the presence of equivalent solutions within the optimization problem.

Adding the stabilization term allows for the identification of these equivalent solutions, offering a strategy to avoid abrupt changes in suggested technology configurations—commonly referred to as "technology jumps"—that may arise from the inherently chaotic nature of the model. By stabilizing the parametrization process, the model can adhere to a particular set of solutions, lending consistency and predictability to planning the evolution of the energy system.

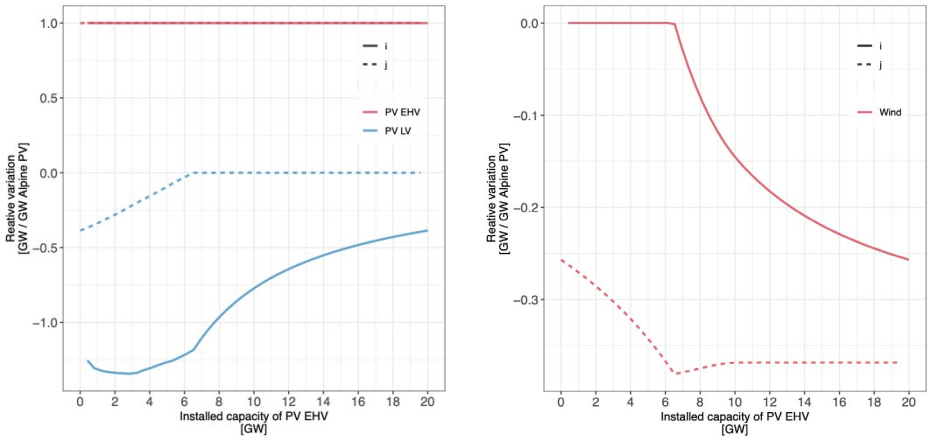

Figure 1: Comparison of relative variation of installed PV and Wind technologies under PV EHV parametrization.

4. Conclusion

The study's findings indicate that the proposed stabilization methodology effectively identifies equivalent solutions within the MILP framework for energy system modeling. This outcome is pivotal for energy system planners and policymakers, providing a more stable and reliable foundation for making technological investments and system configuration decisions.

Stabilizing the parametrization process and adhering to consistent solutions amidst equivalent options is particularly beneficial for managing the dynamic and complex interactions within energy systems. This approach enhances the robustness of the model and simplifies the interpretation of results, thereby contributing to more informed and strategic energy planning.

In conclusion, the stabilization methodology introduced in this research offers a significant step forward in energy system modeling. Mitigating chaotic behaviors and revealing equivalent solution spaces allows for a more deliberate and systematic approach to the transition toward sustainable and resilient energy systems.

The exploration of the stabilization methodology in MILP energy system modeling has opened avenues for future research, particularly in addressing the challenges associated with the stabilization term and identifying equivalent solutions.

The first challenge lies in thoroughly assessing the influence of the stabilization term, denoted as epsilon ϵ, which in our study was set equal to the solver's mipgap. Future investigations need to determine the optimal calibration of ϵ to balance between stabilization and the primary objective of minimizing costs. This could involve sensitivity analyses or the development of heuristic methods to guide the selection of ϵ based on model dynamics and the specific characteristics of the energy system under study.

The second challenge is devising a systematic approach to identify and enumerate the different equivalent solutions that the model yields at the same cost level. Using integer cuts presents a promising method to differentiate between these solutions. Adding integer cuts after each solution is found allows the model to explore alternative configurations, thereby mapping the landscape of equivalent solutions more comprehensively. This method could unveil hidden patterns and dependencies within the model structure, enriching our understanding of the solution space and aiding in strategic decision-making. Both challenges underscore the need for ongoing refinement of the stabilization methodology to enhance its applicability and effectiveness in energy system modeling.

References

(1) Ashouri, A.; Fux, S. S.; Benz, M. J.; Guzzella, L. Optimal Design and Operation of Building Services Using Mixed-Integer Linear Programming Techniques. *Energy* **2013**, *59*, 365–376. https://doi.org/10.1016/j.energy.2013.06.053.

(2) Maravelias, C. T.; Grossmann, I. E. A Hybrid MILP/CP Decomposition Approach for the Continuous Time Scheduling of Multipurpose Batch Plants. *Comput. Chem. Eng.* **2004**, *28* (10), 1921–1949. https://doi.org/10.1016/j.compchemeng.2004.03.016.

(3) Westerlund, J.; Papageorgiou, L. G.; Westerlund, T. A MILP Model for N-Dimensional Allocation. *Comput. Chem. Eng.* **2007**, *31* (12), 1702–1714. https://doi.org/10.1016/j.compchemeng.2007.02.006.

(4) Li, X.; Damartzis, T.; Stadler, Z.; Moret, S.; Meier, B.; Friedl, M.; Maréchal, F. Decarbonization in Complex Energy Systems: A Study on the Feasibility of Carbon Neutrality for Switzerland in 2050. *Front. Energy Res.* **2020**, *8*, 549615. https://doi.org/10/gjgz7v.

(5) Moret, S.; Codina Girones, V.; Bierlaire, M.; Maréchal, F. Characterization of Input Uncertainties in Strategic Energy Planning Models. *Appl. Energy* **2017**, *202*, 597–617. https://doi.org/10.1016/j.apenergy.2017.05.106.

(6) Schnidrig, J.; Cherkaoui, R.; Calisesi, Y.; Margni, M.; Maréchal, F. On the Role of Energy Infrastructure in the Energy Transition. Case Study of an Energy Independent and CO2 Neutral Energy System for Switzerland. *Front. Energy Res.* **2023**, *11*. https://doi.org/10.3389/fenrg.2023.1164813.

ESCAPE-34 PSE-2024
European Symposium on Computer Aided Process Engineering
&
Process Systems Engineering

Flavio Manenti, Gintaras V. Reklaitis (Eds.), Book of Abstract of the 34th European Symposium on Computer Aided Process Engineering / 15th International Symposium on Process Systems Engineering (ESCAPE34/PSE24), June 2-6, 2024, Florence, Italy.

Assessing the Contributions of Process Integration Towards the United Nations Sustainable Development Goals

Safeer Hafeez, Elizabeth J. Abraham, Dhabia M. Al-Mohannadi*

[a]*Department of Chemical Engineering, Texas A&M University at Qatar, Education City, PO Box 23874, Doha, Qatar*

dhabia.al-mohannadi@qatar.tamu.edu

Abstract

The latest UN Sustainable Development Goals (SDGs) progress report states that we are currently on track to achieve only 12% of the targets. One of the many reasons for this situation is the disconnect between the policy space where the SDGs are and the technical space where some promising solutions to achieve the SDGs exist. One such solution is process integration (PI) which is an essential tool for creating a circular economy where the utilization of energy and resources, and the environmental impact of industrial processes are minimized while boosting economic growth. However, PI research currently lacks the inclusion of social aspects, an important third pillar of sustainability, in optimization problems which is mostly due to a lack of social indicators. Therefore, this work aims to bridge the gap between the policy and technical spheres by evaluating the contributions of PI towards the UN SDGs via a bibliometric analysis of PI literature and reviewing social and sustainability indicators that can be utilized in future research. The analysis revealed that PI contributes to 70% of the SDGs, including all the goals in the economic and environmental pillars of sustainability, and 38% of the goals in the social pillar.

Keywords: process integration, sustainable development goals, circular economy, industrial symbiosis, sustainability indicators

1. Introduction

The 2030 Agenda for Sustainable Development, established in 2015 by all nations, outlines a global commitment to achieving peace and prosperity for both people and the planet (UN, 2015). Comprising 17 Sustainable Development Goals (SDGs), it addresses a spectrum of issues with set targets for accomplishment by 2030 (UN, 2015). Despite progress, a recent SDG progress report reveals a sobering reality: only about 12% of goals are on track, approximately 50% are off track, and around 30% have stagnated or regressed from the 2015 baseline (UN, 2023). The multifaceted nature of SDGs demands collaboration among governmental bodies, NGOs, the private sector, communities, and research centres. However, a significant hurdle lies in the disconnect between policy and technical spheres, hindering the realization of technical solutions' full potential. Process

integration (PI), a key solution for fostering a circular economy, exemplifies this challenge.

Circular economy (CE) involves minimizing primary energy and virgin resource consumption by maximizing energy and material recycle and recovery at the macro-level (Geissdoerfer et al., 2017). Several studies have explored CE's potential contributions to SDGs across various industries, including construction, and food (Hassoun et al., 2022; Ogunmakinde et al., 2022; Schroeder et al., 2019). Zooming into the micro-level, industrial symbiosis (IS) emerges as a critical component of CE, facilitating the exchange of resources between industries to minimize overall wastage while maximizing profits (Lawal et al., 2021). PI, a well-established IS-enabling tool, optimizes resource use through resource integration. Several tools for PI have been developed for various applications. The original graphical pinch analysis technique for heat exchanger network design (Townsend & Linnhoff, 1983), has been extended to wastewater minimization (Wang & Smith, 1994), integration of renewable energies (Alizadeh Zolbin et al., 2022), and financial planning for energy conservation projects (Roychaudhuri et al., 2017). Mathematical programming models have also advanced to solve increasingly complex optimization problems, like multi-objective resource integration for industrial clusters (Ahmed et al., 2021), multi-period optimization for CO_2 emissions reduction planning (Al-Mohannadi et al., 2016), and integrated design of waste management systems using P-graph (Fan et al., 2020). PI has even been expanded to the macro-scale with a framework combining elements of PI, IS and CE to increase circular flows in processes, industries and economies (Walmsley et al., 2019).

PI is essential in addressing contemporary global challenges such as energy transition, climate change and sustainable development, which asserts the critical role of PI in achieving the SDGs. As such, there is a need to bridge the gap between the policy and technical spheres to enable greater adoption of PI by assessing the capacity of PI tools and applications to tackle the SDGs and proposing social and holistic sustainability metrics to be used in future research.

2. Methodology

A bibliometric analysis was conducted to map the contributions of PI research to the SDGs. Bibliometric analysis is a quantitative literature review methodology used to explore and map the scientific knowledge of a select domain in existing literature by utilizing large volumes of unstructured data. The scope of this study is to analyze the literature on PI that explicitly identifies the sustainability contributions of their work. As such, the Web of Science database was used to search for publications that contained “process integration” and “sustainable” or “sustainability” in their title, abstract, or keywords. The query retrieved 484 publications, which was narrowed down to 325 most relevant papers after careful review.

A keyword matching exercise was carried out to assign to each paper the SDGs that it contributed towards. This was done by first selecting the relevant keywords for each SDG in the context of PI using the exhaustive search queries developed by Aurora Universities Network as a guide (Vanderfeesten et al.). The presence of these SDG keywords was then checked in the keywords and abstracts of the 325 selected papers. The SDGs 4 (education), 5 (gender equality), 10 (reduced inequalities), 16 (peace and justice) and 17 (partnership for the goals) are not included in this analysis because the keyword search for them gave no matches. Keyword mapping allowed us to determine: 1) how many papers contributed towards each SDG, and 2) how often each pair of SDGs were addressed in the same paper.

3. Results and Discussion

The network map generated from the keyword matching exercise is shown in Figure 1. The map visualizes the relative contributions of the papers towards the SDGs and the relationship between the SDGs in the context of PI research. The keywords pertaining to SDG 12 (responsible consumption and production) were the most common in our set of papers, followed in order by SDG 8 (decent work and economic growth), SDG 13 (climate action) and SDG 7 (affordable and clean energy). These SDGs are also the most interlinked, with an average of 75 papers contributing towards each pair of these four SDGs. However, the interrelation between the SDGs is high in general, with all SDGs commonly addressed alongside the others in most papers. For example, despite being mentioned in only 21 papers, SDG 11 (sustainable cities and communities) is still addressed alongside ten of the total eleven other SDGs in this study. This shows that the SDGs are interlinked and complement each other with respect to PI applications. Overall, Figure 1 exhibits the broad-spectrum impact of PI on the SDGs identified within our small collection of PI publications.

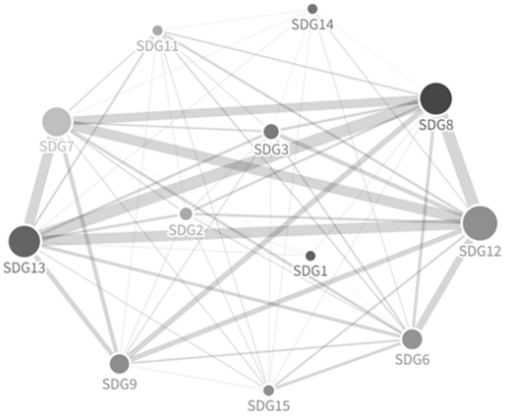

Figure 1: Network map of the SDGs addressed in the set of papers used in this study. Relative size of each node represents the number of papers that contained the keywords of the SDGs in their abstract or author keywords. Relative thickness of lines represents the number of papers that contained keywords of both SDGs connected by the line.

The contributions of the PI publications can also be visualized by the three pillars of sustainable development, namely social, economic and environmental. The pillars are interconnected, and so are the SDGs, which is why some of the SDGs can be categorized within multiple pillars. However, we simplify and categorize the SDGs within the pillars as shown in Figure 2 (Costanza et al., 2016). The greatest contribution is towards the economic pillar because the SDGs and subsequent targets within this pillar have many direct implications for industry. This is a promising outcome for governments as it proves PI can contribute towards economic growth and sustainable development simultaneously. Within the environmental pillar, SDGs 13 (climate action) and SDG 6 (clean water and sanitation) prove to be significant within PI research, with several applications in emissions minimization, development of biorefineries, and water networks optimization, among others. However, there is a need to incorporate the impacts on life below water (SDG 14) and life above land (SDG 15) in PI research.

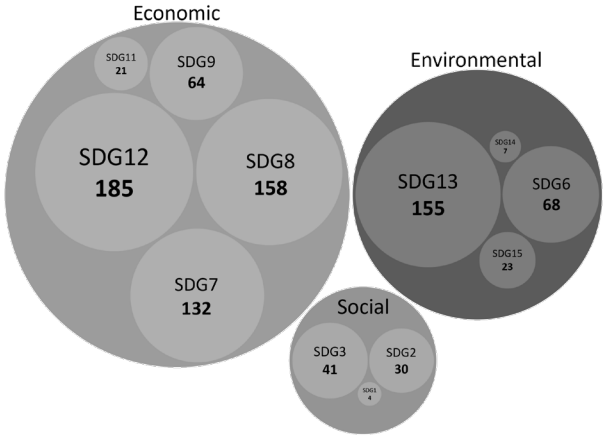

Figure 2: Categorization of the contributions of PI research towards the SDGs by the three pillars of sustainability and the number of papers addressing the respective SDGs.

The contributions identified in PI literature towards the social pillar are relatively lacking, despite the many indirect impacts of PI on these SDGs due to the contributions to economic and environmental pillars. This can mainly be attributed to the fact that social indicators are not widely used in PI research, and that PI doesn't directly impact some of the social issues that the SDGs address like education (SDG 4), gender inequality (SDG 5), and peace and justice (SDG 16). Nevertheless, there are opportunities to contribute to SDG 1 (end poverty) via efficient and equitable allocation of resources and economic development, SDG 2 (end hunger) by optimizing food production, processing and distribution systems, SDG 3 (Good health and wellbeing) by minimizing pollution, SDG 10 (reduced inequalities) and SDG 17 (partnership for the goals) via multi-stakeholder partnerships and technology transfer. However, to capture the contributions of PI to these SDGs and to optimize processes for sustainability, there is a need to utilize social indicators and holistic sustainability metrics.

The most notable work in this regard was by El-Halwagi with the development of the Sustainability Weighted Return on Investment Metric, or SWROIM (El-Halwagi, 2017). This metric allowed the integration of conventional profitability calculations with an aggregate of multiple sustainability indicators, which can include social indicators. SWROIM was extended to incorporate safety indicators like hazard parameters (Guillen-Cuevas et al., 2018). While safety is a very important social aspect, it fails to represent the broader societal impacts that the SDGs aim to improve. To that end, the SDG framework itself provides a set of indicators for each goal which can be used to evaluate and benchmark the sustainability performance of an optimization problem. Also, the approach developed by Rafiaani et al. can be used to identify the most relevant social indicators for sustainability assessment (Rafiaani et al., 2020). They used a multi-criteria decision-making tool empirically determine relevant indicators to assess social impacts of a CCU operation. Furthermore, a comprehensive review by Messmann et al. covers a wide range of social indicators, including social objective functions and constraints in supply chain optimization which can also be utilized in PI (Messmann et al., 2020). Therefore, the need to assess the social impacts in future PI research can be met by utilizing the available social indicators and aggregate sustainability metrics.

4. Conclusions

PI tools like pinch analysis, multi-objective optimization and p-graph have found a broad range of applications in industry and infrastructure, providing a basis for the holistic design and operations of process systems. From our analysis, it is evident that utilizing PI tools can contribute towards achieving 70% of the UN SDGs. However, several barriers exist that hinder greater implementation of PI in industry stemming from the following three main factors:

1) Resistance to change due to risk averse mindset.
2) Confidentiality and reliability concerns.
3) Increased complexity.

These barriers can mostly be overcome by greater cooperation between industries, government and researchers. Firstly, there needs to be more follow up studies and publications on successful PI implementation projects to increase awareness about the environmental, economic and social benefits of PI. Also, future research should include broader sustainability indicators including social and other SDG indicators to provide a holistic picture of the sustainability contributions of the work. To overcome confidentiality and reliability issues, industrial partnerships to establish central operations for integrated plants could be a solution. Additionally, an independent government platform could be developed for planners and policymakers to have access to the data for industrial planning and identification of PI opportunities. Targeted policies can also incentivize industries to become more resource efficient. Enforcing a carbon or GHG emissions tax and stricter wastewater regulations will incentivize industries to reduce their emissions via carbon and water integration. Economic incentives like tax breaks or subsidies for sustainable integrated industries or industrial parks could be provided based on sustainability ratings like LEED or GSAS developed for the construction industry by the US Green Building Council and Gulf Organization for Research & development, respectively. Indicators based on water and raw material recycling, energy recovery, abated emissions, jobs creation, employee and community satisfaction, and incident rate can be used to assess the environmental and social impacts of industries for the rating.
In order to realize the potential of PI in establishing a circular economy and contributing towards the UN SDGs, there needs to be greater cooperation between the enablers in the policy and technical spheres. With this paper, we bridge that gap by highlighting the contributions of PI towards the SDGs for policymakers and identifying the need to broaden the scope of PI for researchers by assessing the sustainability and SDG implications of future work.

References

Ahmed, R. O., Al-Mohannadi, D. M., & Linke, P. (2021). Multi-objective resource integration for sustainable industrial clusters. *Journal of Cleaner Production*, *316*, 128237.

Al-Mohannadi, D. M., Alnouri, S. Y., Bishnu, S. K., & Linke, P. (2016). Multi-period carbon integration. *Journal of Cleaner Production*, *136*, 150-158.

Alizadeh Zolbin, M., Tahouni, N., & Panjeshahi, M. H. (2022). Total site integration considering wind /solar energy with supply/demand variation. *Energy*, *252*, 123928.

Costanza, R., Daly, L., Fioramonti, L., Giovannini, E., Kubiszewski, I., Mortensen, L. F., Pickett, K. E., Ragnarsdottir, K. V., De Vogli, R., & Wilkinson, R. (2016). Modelling and measuring sustainable wellbeing in connection with the UN Sustainable Development Goals. *Ecological Economics*, *130*, 350-355.

El-Halwagi, M. M. (2017). A return on investment metric for incorporating sustainability in process integration and improvement projects. *Clean Technologies and Environmental Policy*, *19*(2), 611-617.
Fan, Y. V., Klemeš, J. J., Walmsley, T. G., & Bertók, B. (2020). Implementing Circular Economy in municipal solid waste treatment system using P-graph. *Science of The Total Environment*, *701*, 134652.
Geissdoerfer, M., Savaget, P., Bocken, N. M. P., & Hultink, E. J. (2017). The Circular Economy – A new sustainability paradigm? *Journal of Cleaner Production*, *143*, 757-768.
Guillen-Cuevas, K., Ortiz-Espinoza, A. P., Ozinan, E., Jiménez-Gutiérrez, A., Kazantzis, N. K., & El-Halwagi, M. M. (2018). Incorporation of Safety and Sustainability in Conceptual Design via a Return on Investment Metric. *ACS Sustainable Chemistry & Engineering*, *6*(1), 1411-1416.
Hassoun, A., Prieto, M. A., Carpena, M., Bouzembrak, Y., Marvin, H. J. P., Pallarés, N., Barba, F. J., Punia Bangar, S., Chaudhary, V., Ibrahim, S., & Bono, G. (2022). Exploring the role of green and Industry 4.0 technologies in achieving sustainable development goals in food sectors. *Food Research International*, *162*, 112068.
Lawal, M., Wan Alwi, S. R., Manan, Z. A., & Ho, W. S. (2021). Industrial symbiosis tools—A review. *Journal of Cleaner Production*, *280*, 124327.
Messmann, L., Zender, V., Thorenz, A., & Tuma, A. (2020). How to quantify social impacts in strategic supply chain optimization: State of the art. *Journal of Cleaner Production*, *257*, 120459.
Ogunmakinde, O. E., Egbelakin, T., & Sher, W. (2022). Contributions of the circular economy to the UN sustainable development goals through sustainable construction. *Resources, Conservation and Recycling*, *178*, 106023.
Rafiaani, P., Dikopoulou, Z., Van Dael, M., Kuppens, T., Azadi, H., Lebailly, P., & Van Passel, S. (2020). Identifying Social Indicators for Sustainability Assessment of CCU Technologies: A Modified Multi-criteria Decision Making. *Social Indicators Research*, *147*(1), 15-44.
Roychaudhuri, P. S., Kazantzi, V., Foo, D. C. Y., Tan, R. R., & Bandyopadhyay, S. (2017). Selection of energy conservation projects through Financial Pinch Analysis. *Energy*, *138*, 602-615.
Schroeder, P., Anggraeni, K., & Weber, U. (2019). The Relevance of Circular Economy Practices to the Sustainable Development Goals. *Journal of Industrial Ecology*, *23*(1), 77-95.
Townsend, D. W., & Linnhoff, B. (1983). Heat and power networks in process design. Part II: Design procedure for equipment selection and process matching. *AIChE Journal*, *29*(5), 748-771.
UN. (2015). *Transforming our world: the 2030 Agenda for Sustainable Development*. United Nations Department of Economic and Social Affairs. Retrieved October 2023 from https://sdgs.un.org/2030agenda
UN. (2023). *Progress towards the Sustainable Development Goals: Towards a Rescue Plan for People and Planet*. https://sdgs.un.org/sites/default/files/2023-04/SDG_Progress_Report_Special_Edition_2023_ADVANCE_UNEDITED_VERSION.pdf
Vanderfeesten, M., René, O., & Spielberg, E. Search Queries for Mapping Research Output to the Sustainable Development Goals (SDGs). *5.0*.
Walmsley, T. G., Ong, B. H. Y., Klemeš, J. J., Tan, R. R., & Varbanov, P. S. (2019). Circular Integration of processes, industries, and economies. *Renewable and Sustainable Energy Reviews*, *107*, 507-515.
Wang, Y. P., & Smith, R. (1994). Wastewater minimisation. *Chemical Engineering Science*, *49*(7), 981-1006.

ESCAPE-34 PSE-2024
European Symposium on Computer Aided Process Engineering
&
Process Systems Engineering

Flavio Manenti, Gintaras V. Reklaitis (Eds.), Book of Abstract of the 34th European Symposium on Computer Aided Process Engineering / 15th International Symposium on Process Systems Engineering (ESCAPE34/PSE24), June 2-6, 2024, Florence, Italy.

Data-driven Epidemic Inference Through Decomposition of Large-scale Nonlinear Optimization Problems

Laurens R. Lueg[a], Michael L. Bynum[b], Carl D. Laird[a]*, Lorenz T. Biegler[a]

[a]*Chemical Engineering Department, Carnegie Mellon University, Pittsburgh, PA, USA*
[b]*Sandia National Laboratories, Albuquerque, NM, USA*
claird@andrew.cmu.edu

Abstract

The COVID-19 pandemic has demonstrated that a systematic understanding of the dynamics of infectious diseases is crucial to reduce their impact on a population. To this end, the use of epidemiological models has proved effective for both parameter estimation and epidemic control problems. In this work, we formulate a compartmental epidemic model on a US national scale with county-level granularity and fit relevant spatio-temporal parameters to data collected during the early stages of the COVID-19 pandemic. Conventional, serial solvers struggle to solve large-scale, nonlinear optimization problems such as this within reasonable time limits. Instead, we exploit the problem's structure to apply a Schur complement decomposition. This allows for the computationally most expensive operation in an interior point method, the computation of the step direction, to be parallelized. We demonstrate promising scaling properties of this method when applied to large-scale epidemic inference problems on a moderately-sized parallel computer.

Keywords: large-scale nonlinear optimization, parallel computing, decomposition, epidemic modeling

1. Introduction

The outbreak of the COVID-19 pandemic had an unprecedented impact across the world. Significant excess deaths, stress on medical infrastructures and sustained economic fallout were amongst the most acute direct consequences. Toward the goal of guiding public health responses, epidemiological models are an important tool to understand the dynamics of infectious diseases and plan mitigation strategies accordingly. In this work, we present efficient computational approaches to solve large-scale parameter estimation problems arising from epidemic models.

2. Methodology

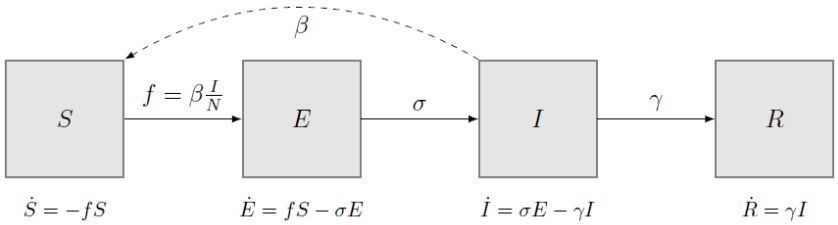

Figure 1: SEIR model for a single population. Rectangles depict the compartments, solid arrows, the movements of individuals between them. The dashed arrow visualizes contact between compartments, leading to transmission of the disease.

Compartmental models have proved effective in describing the spread of various infectious diseases (Rock et al., 2014). The population is divided into compartments, which represent different stages of a disease, i.e., susceptible (*S*), exposed (*E*), infectious (*I*) or recovered (*R*). The dynamics of individuals between compartments over time are determined by the contact, incubation, and recovery rates (β, σ and γ, respectively), which may vary across time and space. For a visualization of this dynamic model for a single population see Fig. 1.

In this work, we applied a large-scale, model-based approach to estimate epidemic model parameters based on policy-related descriptors. To reflect the spatial heterogeneity in the US, separate epidemiological compartments are defined on a county level. Interaction between counties is modeled using information on mobility patterns, in this work we use census data on commuting flows (US Census Bureau, 2020). The contact rate parameters for each county are defined as piecewise-constant functions, depending on the implementation of public health responses, such as mask mandates, over time in each county. Additional terms accounting for demographic or seasonal factors are possible. This defines a large-scale, nonlinear system of ordinary differential equations with ~10^4 differential state variables (epidemiological compartments for ~3000 counties in the US), discretized over a time horizon of several months. The parameters of this model are fitted to case data collected during the beginning of the COVID-19 pandemic.

Optimization problems such as this are usually solved using interior point algorithms. Serial implementations struggle to solve problems of this scale within reasonable time limits. Instead, we exploit the problem's structure to apply a Schur complement decomposition (Kang et al., 2014). This allows for the computationally most expensive operation in an interior point method, the computation of the step direction, to be parallelized. The epidemic model at hand is amenable to this decomposition, as there are only a few shared variables between counties, i.e., the factors associated with the effect of different non-pharmaceutical interventions (NPIs) on the local contact rates. Below, the promising scaling properties of this method are demonstrated.

3. Results

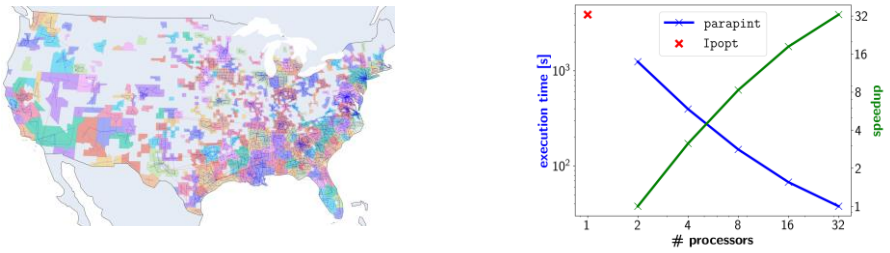

(a) (b)

Figure 2: (a) Map of counties considered for national scale model. Shading is based on the spatial decomposition of counties for parallelization. (b) Strong scaling of parallel Schur complement method. Speedup computed relative to two core execution. Solution time using *Ipopt* solver is shown for serial case.

The parameter estimation problem was solved simultaneously for 1900 counties in the US (see Fig. 2a) over the first 170 days of the pandemic. The full 3142 counties of the US were not considered because those with fewer total cases than 0.1% of the county population during this period were discarded. All parameters other than β were fixed to common values from literature (Yang et al., 2021). Three NPIs were included in the model: mask mandates, school closings and stay-at-home orders, with state-level implementation dates taken from the sources listed in Yang et al. (2021). All tests were performed using an x86 machine with 32 cores, each with a clock rate of 3.3 GHz. The parallel Schur complement method was applied to this problem using the *parapint* package (Rodriguez et al., 2023). The scaling of the solution time with an increasing number of parallel processors was observed, with results shown in Fig. 2b. In our model, each of the NPIs considered in this work reduced the contact rate by 11-15% when implemented in the respective counties. These values are reasonably close to statistical estimates listed in other works (Yang et al., 2021), but come with yet unquantified confidence intervals stemming from both model and measurement uncertainty.

4. Conclusion

We use a dynamic compartmental model for COVID-19 with county-level granularity, which considers inter-county infections through commuters and quantifies the effect of non-pharmaceutical interventions (NPIs) on the contact rate between individuals. The parallel Schur complement method was applied to solve this large-scale nonlinear programming problem on a US national scale, with significant speedup when using 32 cores, compared to the serial state-of-the-art solver *Ipopt* (Wächter and Biegler, 2006). The qualitative results suggest that the implementation of NPIs had an adverse effect on the spread of COVID-19. Uncertainty quantification for these results remains as future work.

Acknowledgements

Sandia National Laboratories is a multi-mission laboratory managed and operated by National Technology & Engineering Solutions of Sandia, LLC (NTESS), a wholly owned subsidiary of Honeywell International Inc., for the U.S. Department of Energy's National Nuclear Security Administration (DOE/NNSA) under contract DE-NA0003525. This written work is authored by an employee of NTESS. The employee, not NTESS, owns the right, title and interest in and to the written work and is responsible for its contents. Any subjective views or opinions that might be expressed in the written work do not necessarily represent the views of the U.S. Government. The publisher acknowledges that the U.S. Government retains a non-exclusive, paid-up, irrevocable, world-wide license to publish or reproduce the published form of this written work or allow others to do so, for U.S. Government purposes. The DOE will provide public access to results of federally sponsored research in accordance with the DOE Public Access Plan.

References

J. Kang, Y. Cao, D. P.Word, and C. D. Laird, 2014. An interior-point method for efficient solution of block-structured nlp problems using an implicit schur-complement decomposition. Computers & Chemical Engineering, 71:563–573.

K. Rock, S. Brand, J. Moir, and M. J. Keeling, 2014. Dynamics of infectious diseases. Reports on Progress in Physics, 77(2):026602.

J. S. Rodriguez, R. B. Parker, C. D. Laird, B. L. Nicholson, J. D. Siirola, and M. L. Bynum, 2023, Scalable parallel nonlinear optimization with pynumero and parapint. INFORMS Journal on Computing, 35(2):509–517.

United States Census Bureau, 2020 Census Results, retrieved in July 2023. URL: https://www.census.gov/data/tables/2020/demo/metro-micro/commuting-flows-2020.html

A. Wächter and L. T. Biegler, 2006, On the implementation of an interior-point filter line-search algorithm for large-scale nonlinear programming, Mathematical programming, 106:25–57.

B. Yang, A. T. Huang, B. Garcia-Carreras, W. E. Hart, A. Staid, M. D. Hitchings, E. C. Lee, C. J. Howe, K. H. Grantz, A. Wesolowksi, et al., 2021, Effect of specific non-pharmaceutical intervention policies on sars-cov-2 transmission in the counties of the united states. Nature communications, 12(1):3560.

ESCAPE-34 PSE-2024
European Symposium on Computer Aided Process Engineering
&
Process Systems Engineering

Flavio Manenti, Gintaras V. Reklaitis (Eds.), Book of Abstract of the 34th European Symposium on Computer Aided Process Engineering / 15th International Symposium on Process Systems Engineering (ESCAPE34/PSE24), June 2-6, 2024, Florence, Italy.

Feasibility Analysis of Dimethyl Ether-based International Renewable Energy Supply Chain

Chong Wei Ong,[a] Sheng-Chi Lien,[a] Tsai-Wei Wu,[b] Cheng-Liang Chen[a]*

[a]*Department of Chemical Engineering, National Taiwan University, No. 1, Sec. 4, Roosevelt Rd., Taipei 106319, Taiwan (R.O.C.)*
[b]*Department of Frontier Science for Advanced Environment, Graduate School of Environmental Studies, Tohoku University, 468-1 Aramaki Aza Aoba, Aoba-ku Sendai, Miyagi, Japan, 980-8572*
**CCL@ntu.edu.tw*

Abstract

To tackle the urgent global challenge of climate change and the unequal distribution of renewable resources, a transition plan toward sustainable, low-carbon energy systems is imperative. This study introduces an international renewable energy supply chain leveraging dimethyl ether (DME) as an energy carrier. In pursuit of the 2050 net-zero carbon emissions target, this supply chain establishes a connection between two nations: one abundant in renewable energy resources as an energy-exporting country and the other lacking such resources as an energy-importing country. In the exporting country, renewable energy is harnessed for electrolysis to produce hydrogen (H_2). Due to the high costs associated with H_2 in terms of transportation and storage, using DME as an energy carrier for H_2 enhance the feasibility of implementing this supply chain. Consequently, DME is synthesized from H_2 and captured CO_2 and transported to the importing country via shipping. Upon reaching the importing country, two viable methods for DME utilization emerge. The first option involves converting DME back into H_2 via steam reforming process, which can then be employed in fuel cells for electricity generation. The second option entails introducing DME as fuel into oxy-combustion CO_2 power plants, generating electricity. Simultaneously, the resultant CO_2 is captured and transported to the exporting country for DME synthesis. This research assesses the feasibility of both application approaches, considering engineering, economic and environmental aspects. Furthermore, simulations and analyses of the chemical processes are carried out, along with the economic evaluations of these processes, electrolysis, fuel cells and transportation. Lastly, the costs of DME, H_2 and green electricity in the importing country are evaluated to analyse the feasibility of this supply chain. The current result show that the cost of imported electricity is USD 135.42/MWh_e with an electricity conversion rate between both regions is 30.8% (=4.358/14.145), and the carbon emission of this supply chain using solar and wind power are 0.190 and 0.069 t/MWh_e respectively.

Keywords: Dimethyl ether, Energy carrier, Hydrogen fuel cells, Oxy-combustion, International renewable energy supply chain

1. Introduction

To address the urgent global challenge posed by climate change and the uneven distribution of renewable resources, it is crucial to implement a transition plan towards sustainable, low-carbon energy systems. Countries such as Australia and Saudi Arabia (Wang et al., 2023), which possess abundant natural resources, have the capacity to generate significant amounts of renewable energy. This surplus energy can be efficiently transformed into green hydrogen (H_2) through electrolysis and stored for future use. However, the transportation of H_2 is costly (Brändle et al., 2021). Therefore, to provide a cost-effective alternative, the international renewable energy supply chain relies on chemical energy carriers, which include H_2, methanol (MeOH) (Dalena et al., 2018), ammonia (NH_3) (Hasan et al., 2021), dimethyl ether (DME) (Catizzone et al., 2021) and methylcyclohexane (MCH) (Matsuoka et al., 2017). These carriers can be transported to energy-importing nations like Japan and Germany (Wijayanta et al., 2019), as depicted in Figure 1. Subsequently, these carriers can be used directly or converted into H_2, facilitating the transfer of renewable energy between countries.

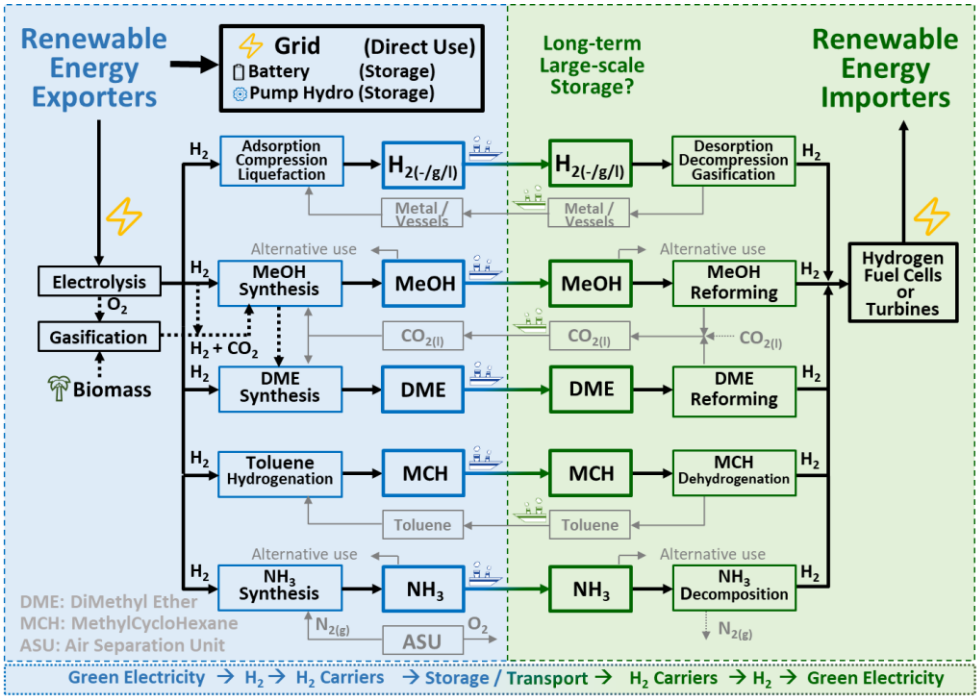

Figure 1 International renewable energy supply chains.

When considering MeOH, DME and MCH as energy carriers, it's crucial to address the by-products of MeOH or DME reforming (CO_2) and MCH dehydrogenation (toluene). These by-products should be efficiently transported back to the exporting country for MeOH or DME synthesis or toluene hydrogenation, creating a closed-loop circulation system that minimizes waste. On the other hand, transporting the by-product of NH_3 decomposition, nitrogen, is not cost-effective. Instead, utilizing an air separation unit (ASU) to produce nitrogen proves to be a more economically viable solution, eliminating the need for nitrogen transportation.

In comparison to gas-phase H_2 (Moradi and Groth, 2019) and NH_3 (Klerke et al., 2008), MeOH stands out due to its ability to be stored in a liquid state at room temperature and atmospheric pressure. This characteristic results in lower storage costs and improved safety. While DME requires liquefaction at -33°C for transportation, it boasts a significantly higher gravimetric and volumetric energy density when compared to MeOH, MCH, and NH_3 (Table 1). Despite the need for careful handling due to its narrow explosive limit in air, the safety perspective suggests that DME is a suitable candidate as an energy carrier. While extensive research focuses on MeOH, MCH, and NH_3 as energy carriers, there is a noticeable scarcity of comprehensive analyses on DME, particularly in the context of an international renewable energy supply chain. Therefore, an in-depth exploration of the DME-based international renewable energy supply chain is a worthwhile avenue for further study.

Table 1. Properties of chemical energy carriers.

Properties	H_2	MeOH	DME	MCH	NH_3
Boiling point (°C)	-253	64.7	-25	101	-33
Gravimetric energy density (MJ/kg)	120	15	28	7.4	21.2
Volumetric energy density (MJ/L)	8.5	11.9	19	5.7	14.4
Explosive limit in air (vol%)	4-75	6.7-36	3.2-18.6	1.2-6.7	15-28

To aligns with the ambitious 2050 net-zero carbon emissions goal, this study presents a feasibility analysis of the international renewable electricity supply chain that utilizes DME as energy carrier which fosters a vital connection between two countries. One rich in renewable energy resources, serving as an energy-exporting country, and the other deficient in these resources, acting as an energy-importing country. In the exporting country, renewable energy is employed for electrolysis, generating H_2 and DME is produced through the synthesis process of H_2 and captured carbon dioxide (CO_2) (Wu and Chien, 2022), then transported to the importing country via shipping.

Upon arrival in the importing country, two practical methods for utilizing DME come to the forefront. As illustrated in Figure 2(a), the first approach involves the conversion of DME back into H_2 through a steam reforming process. This H_2 can then be utilized in fuel cells to generate electricity. The second option, depicted in Figure 2(b), involves using DME as a fuel source in oxy-combustion CO_2 power plants, known as the Allam cycle, for electricity generation. Simultaneously, the resulting CO_2 is captured and transported back to the exporting country for DME synthesis. This research is therefore comparing the feasibility of the supply chain using both power generation approaches, considering engineering, economic and environmental aspects. Furthermore, simulations and analyses of the chemical processes are carried out, along with the economic evaluations of these processes, electrolysis, fuel cells and transportation. Lastly, the costs of DME, H_2 and green electricity in the importing country are evaluated to analyze the feasibility of this supply chain.

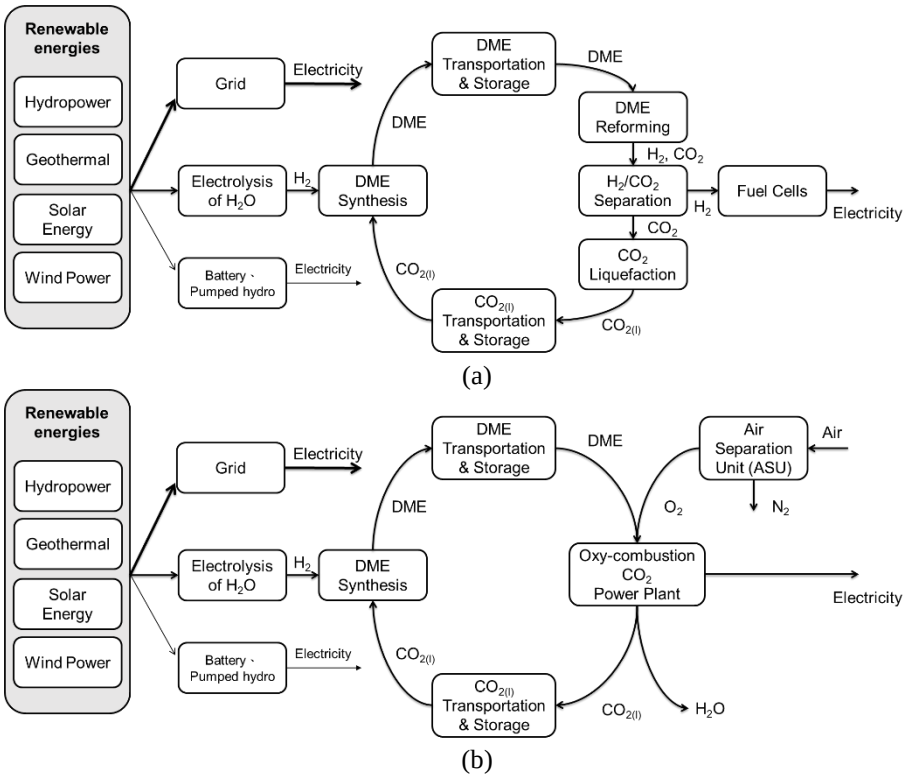

Figure 2 Conceptual design of DME-based international renewable electricity supply chain generating electricity with (a) fuel cells (b) oxy-combustion power plant.

Based on the simulation using Aspen Plus, the capital and operating costs of various chemical processes, including DME synthesis, H_2 production through DME reforming, CO_2 liquefaction and oxy-combustion CO_2 power plant can be calculated. Additionally, economic assessments are also conducted for water electrolysis (Hodges et al., 2022), fuel cells (Jamil et al., 2022), and transportation (Placek, 2023). To account for advancing technology and ensure sustainability, the efficiency of electrolysis in sustainable future is assumed at 98%, based on the higher heating value (HHV) of H_2 (39.39 MWh_e/t). The cost of water electrolysis is estimated at 200 USD/kW. Solid oxide fuel cells (SOFC) are assumed to have an efficiency of 30% for thermal heat (LHV) and 55% for electricity (LHV), with a cost of 1,000 USD/kW.

The cost of green H_2 production is significantly influenced by renewable energy electricity prices. The levelized cost of electricity (LCOE) for utility-scale solar photovoltaics (PV) is assumed to be USD 45/MWh_e, with a projected decrease to USD 15/MWh_e by 2050. Therefore, cost of renewable energy is assumed to be USD 30/MWh_e in this study. Additionally, the carbon emissions associated with this process are estimated at 11 kg/MWh_e from a life cycle perspective (Bruckner et al., 2014). On the other hand, the transportation of DME and CO_2 between exporting and importing countries predominantly relies on shipping. Assume that a ship has a capacity of 312,500 cubic meters and travels at a speed of 12 knots. For the shipping route from Australia to Japan, which spans approximately 10,000 km, the ship is assumed to operate for 350 days each year, with a turnover time of one day. The capital cost associated with the DME/CO_2

shipping vessel is estimated at 150.2 million USD (Al-Breiki and Bicer, 2020). In general, very low sulfur fuel oil (VLSFO) is chosen as the fuel source, and its approximate cost is 550 USD/t. It's worth noting that for every metric tonne of this fuel consumed, it generates 3.15t of CO_2 emissions. The sensitivity analysis of each important variables will be carried for optimization.

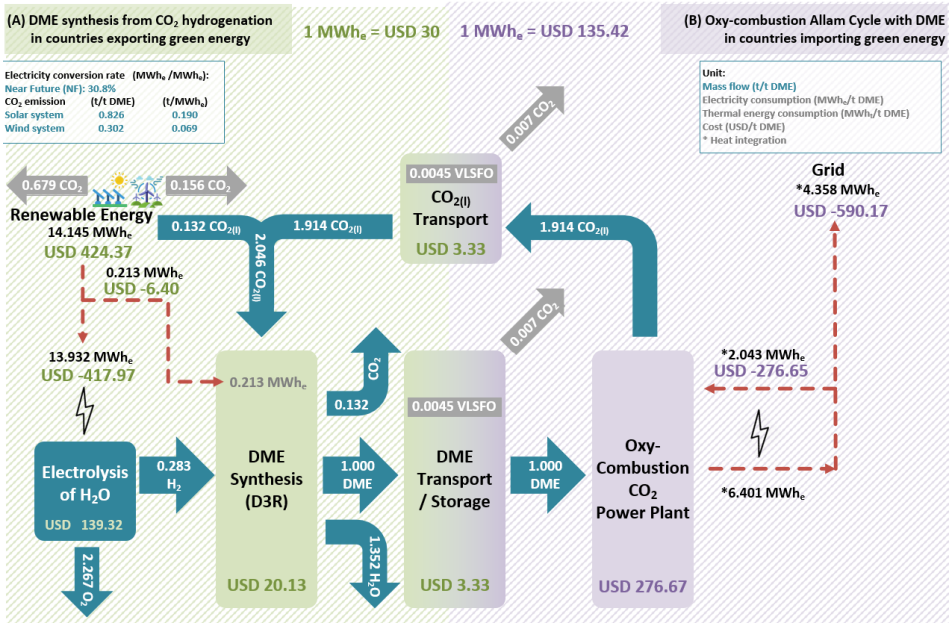

Figure 3 Techno-economic and carbon emission analyses result of DME-based international renewable electricity supply chain generating electricity with oxy-combustion power plant.

The process simulations of the chemical processes using Aspen Plus and techno-economic analysis of both DME-based international renewable electricity supply chains are carried out in this study. The techno-economic and carbon emission analyses result of DME-based international renewable electricity supply chain generating electricity with oxy-combustion power plant are depicted in Figure 3. The cost of imported electricity is USD 135.42/MWh_e with an electricity conversion rate between both regions is 30.8% (=4.358/14.145), and the carbon emission of this supply chain using solar and wind power are 0.190 and 0.069 t/MWh_e respectively. To compare the performance, the electricity conversion rate between the imported electricity and renewable electricity and the cost of imported electricity of the other pathway will be discussed in future.

2. Conclusions

In conclusion, the utilization of dimethyl ether (DME) as an energy carrier in an international renewable electricity supply chain is seen as a promising solution to address the global issues of climate change and the uneven distribution of renewable resources. The supply chain design offers two power generation options: hydrogen (H_2) fuel cells and oxy-combustion power plants. To determine a more economical, environmentally friendly and efficient choice, the chemical processes simulations and techno-economic analysis of both supply chains are carried out.

References

M. Al-Breiki, and Y. Bicer. (2020). "Comparative cost assessment of sustainable energy carriers produced from natural gas accounting for boil-off gas and social cost of carbon." *Energy Reports*, 6, 1897-1909.

G. Brändle, M. Schönfisch, and S. Schulte. (2021). "Estimating long-term global supply costs for low-carbon hydrogen." *Applied Energy*, 302, 117481.

T. Bruckner, L. Fulton, E. Hertwich, A. McKinnon, D. Perczyk, J. Roy, R. Schaeffer, S. Schlömer, R. Sims, and P. Smith. (2014). "Technology-specific cost and performance parameters [annex III]", *Climate Change 2014: Mitigation of Climate Change*. Cambridge University Press, pp. 1329-1356.

E. Catizzone, C. Freda, G. Braccio, F. Frusteri, and G. Bonura. (2021). "Dimethyl ether as circular hydrogen carrier: Catalytic aspects of hydrogenation/dehydrogenation steps." *Journal of Energy Chemistry*, 58, 55-77.

F. Dalena, A. Senatore, A. Marino, A. Gordano, M. Basile, and A. Basile. (2018). "Methanol production and applications: an overview." *Methanol*, 3-28.

M.H. Hasan, T.M.I. Mahlia, M. Mofijur, I. Rizwanul Fattah, F. Handayani, H.C. Ong, and A. Silitonga. (2021). "A comprehensive review on the recent development of ammonia as a renewable energy carrier." *Energies*, 14(13), 3732.

A. Hodges, A.L. Hoang, G. Tsekouras, K. Wagner, C.-Y. Lee, G.F. Swiegers, and G.G. Wallace. (2022). "A high-performance capillary-fed electrolysis cell promises more cost-competitive renewable hydrogen." *Nature communications*, 13(1), 1304.

A. Jamil, S. Rafiq, T. Iqbal, H.A.A. Khan, H.M. Khan, B. Azeem, M.Z. Mustafa, and A.S. Hanbazazah. (2022). "Current status and future perspectives of proton exchange membranes for hydrogen fuel cells." *Chemosphere*, 303, 135204.

A. Klerke, C.H. Christensen, J.K. Nørskov, and T. Vegge. (2008). "Ammonia for hydrogen storage: challenges and opportunities." *Journal of Materials Chemistry*, 18(20), 2304-2310.

K. Matsuoka, K. Miyoshi, and Y. Sato. (2017). "Electrochemical reduction of toluene to methylcyclohexane for use as an energy carrier." *Journal of Power Sources*, 343, 156-160.

R. Moradi, and K.M. Groth. (2019). "Hydrogen storage and delivery: Review of the state of the art technologies and risk and reliability analysis." *International Journal of Hydrogen Energy*, 44(23), 12254-12269.

M. Placek. (2023). " Average monthly price of very low sulfur fuel oil (VLSFO) from November 2019 to May 2023 ". City: statista.

F. Wang, R. Swinbourn, and C.e. Li. (2023). "Shipping Australian sunshine: Liquid renewable green fuel export." *International Journal of Hydrogen Energy*, 48(39), 14763-14784.

A.T. Wijayanta, T. Oda, C.W. Purnomo, T. Kashiwagi, and M. Aziz. (2019). "Liquid hydrogen, methylcyclohexane, and ammonia as potential hydrogen storage: Comparison review." *International Journal of Hydrogen Energy*, 44(29), 15026-15044.

T.-W. Wu, and I.-L. Chien. (2022). "A novel energy-efficient process of converting CO2 to dimethyl ether with techno-economic and environmental evaluation." *Chemical Engineering Research and Design*, 177, 1-12.

ESCAPE-34 PSE-2024
European Symposium on Computer Aided Process Engineering
&
Process Systems Engineering

Flavio Manenti, Gintaras V. Reklaitis (Eds.), Book of Abstract of the 34th European Symposium on Computer Aided Process Engineering / 15th International Symposium on Process Systems Engineering (ESCAPE34/PSE24), June 2-6, 2024, Florence, Italy.

Conceptual Process Design for Hydrogenating Carbon Dioxide to Produce Ethanol

Hao-Chu Chang, Chong Wei Ong, Cheng-Liang Chen*

Department of Chemical Engineering, National Taiwan University, Taipei 10617, Taiwan CCL@ntu.edu.tw

Abstract

Global warming and the energy crisis have become some of the most significant challenges facing the world today. With the finite nature of fossil fuels and ever-increasing carbon emissions, there is an urgent need to transition to renewable energy sources to mitigate the irreversible impact on our planet. This study aims to design a process flowsheet for ethanol synthesis by carbon dioxide hydrogenation using Aspen Plus. Ethanol serves a dual purpose as a renewable energy carrier and a fuel, aligning with Carbon Capture and Utilization (CCU) and contributing to carbon reduction efforts.

Keywords: Global warming, CO_2 hydrogenation, Ethanol synthesis, Process design, Aspen Plus.

1. Introduction

Nowadays we are facing the challenges of global warming and energy shortages. Conventional energy production methods, such as fossil fuels, are major contributors to increased CO2 emissions, a primary greenhouse gas. In response to these issues, this study focuses on hydronation of CO2 to synthesize ethanol, which satisfies the concept of Carbon Capture and Utilization (CCU). Ethanol serves two primary purposes. Firstly, ethanol's liquid state under normal conditions and its limited flammability in the air make it a potential candidate for energy carrier within the renewable energy supply chain. However, a comprehensive evaluation is needed when compared to other energy carriers like methanol and ammonia. Secondly, ethanol can also function as a fuel, combusting with oxygen. Moreover, CO2 hydrogenation to synthesize ethanol doesn't compete with food supplies, a key distinction from conventional starch fermentation. Thus, the investigation into ethanol synthesis through CO2 hydrogenation is a promising studying.

The overall framework is shown in Figure 1,including both export and import sides, and illustrates the entire ethanol supply chain. The process uses two reactants - hydrogen and carbon dioxide. Hydrogen comes from renewable energy sources through water electrolysis and carbon dioxide comes from carbon capture. Once ethanol has been synthesized, the intermittent nature of most renewables means that the storage and transport part is essential. When ethanol as an energy carrier arrives on the import side, it can be used in two ways as described above. This study will focus on the synthesis part of ethanol.

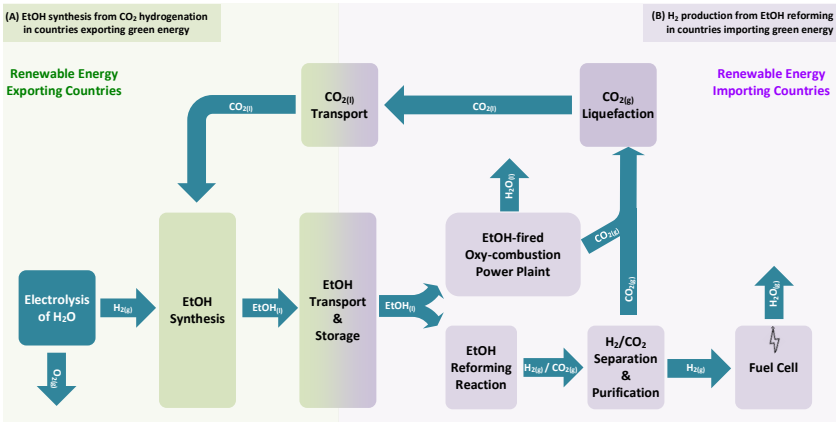

Figure 1. The overall framework of the synthesis and use of ethanol

2. Process Design for Hydrogenating Carbon Dioxide to Produce Ethanol

2.1. Thermodynamic Models & Chemical Reactions

The process of hydrogenating carbon dioxide is simulated by Aspen Plus using two thermodynamic models: the Peng-Robinson equation of state in the reaction section and the UNIQUAC model with Henry's constant in the separation section.

A total of three reactions are considered in this study: the reverse Water Gas Shift reaction (rWGS), the ethanol (EtOH) synthesis, and the Methane Steam Reforming (MSR). All have been verified, and further details are given below. The rWGS reaction is provided in the work of Zhang *et al.*[4] and Vendas and Maria[5].

$$CO_2 + H_2 \rightleftharpoons CO + H_2O \quad (1)$$

The EtOH synthesis reaction includes five reactions provided by Portillo *et al.*[6]. All of them are assumed to be irreversible except the rWGS reaction (6).

$$CO + 2H_2 \rightarrow CH_3OH \quad (2)$$

$$CO + 2H_2 + CH_3OH \rightarrow C_2H_5OH + H_2O \quad (3)$$

$$CO + 2H_2 + C_2H_5OH \rightarrow C_3H_7OH + H_2O \quad (4)$$

$$H_2 + CH_3OH \rightarrow CH_4 + H_2O \quad (5)$$

$$CO + H_2O \rightleftharpoons CO_2 + H_2 \quad (6)$$

The MSR reaction includes two reactions, which utilize the power-law model (Eq. 7 - Eq. 8) provided by Chen *et al.*[7].

$$CH_4 + H_2O \rightarrow CO + 3H_2 \quad (7)$$

$$CH_4 + 2H_2O \rightarrow CO_2 + 4H_2 \quad (8)$$

2.2. Process Statements

This study includes two distinct designs, each detailed in the process block flow diagrams shown in Figure 2 and Figure 3.

In Design 1, shown in Figure 2, CO_2 is hydronated to syngas in the rWGS reactor using a Pt-based catalyst. Subsequently, syngas is converted to ethanol in the EtOH synthesis reactor using an alkali-Co doped MoS_2 catalyst. The low conversion of CO and selectivity of ethanol results in the need to recycle the stream exiting the EtOH synthesis reactor for sending back to the EtOH synthesis reactor. However, the development of Design 1 reveals the presence of significant methane, necessitating a purge process. The purged gas includes methane and reactants (CO_2, CO, H_2), leading to the wastage of valuable reactants and contributing to process inefficiency. Consequently, this finding has promoted the development of Design 2.

In Design 2, shown in Figure 3, in addition to the reactions mentioned in Design 1, we introduce the MSR reaction to solve excessive methane, turning methane into CO_2, CO, and H_2. This reaction occurs in the MSR reactor, positioned after the EtOH synthesis reactor, and the exiting stream of the MSR reactor is recycled to the rWGS reactor. The methane is completely consumed after the MSR reactor, eliminating the need for a purging process. Moreover, the consumption of reactants is decreased, and the amount of ethanol is increased. Thus, we can use fewer reactants to produce more ethanol. Figure 4 depicts the details of Design 2.

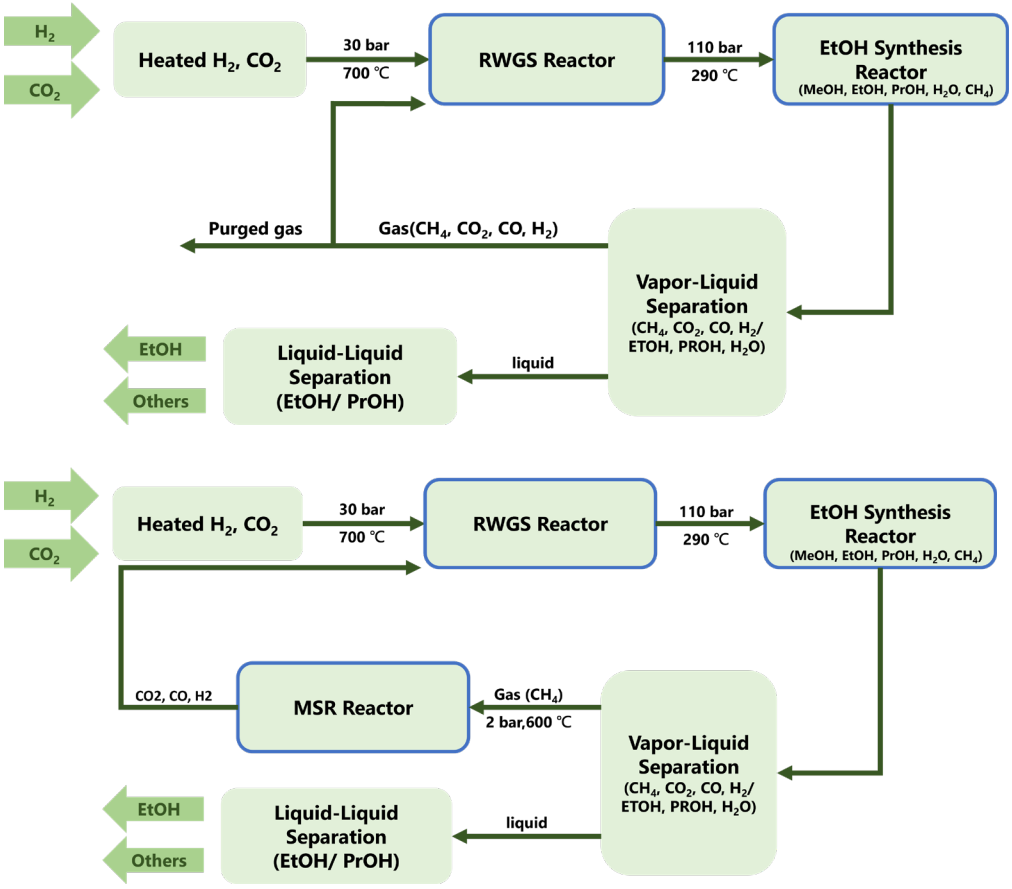

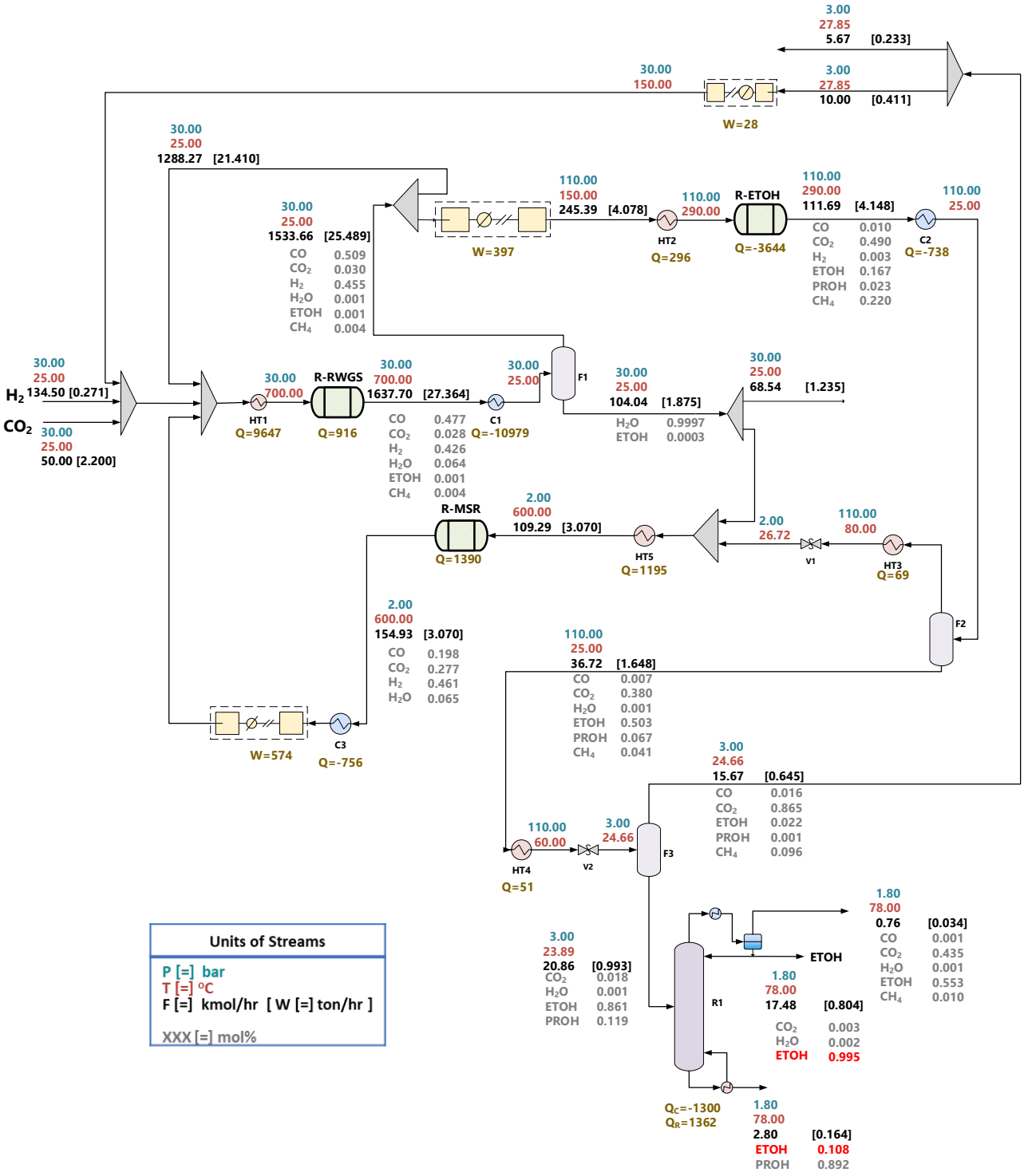

Figure 4. Process flow sheet of Design 2

3. Conclusion

This study simulates the process of CO_2 hydrogenation to ethanol, offering a promising solution to the challenges posed by global warming, carbon emissions, and the need for renewable energy sources. The reactant, CO, undergoes an initial conversion to syngas through the reverse water-gas shift (rWGS) reaction, as CO hydrogenation to ethanol is thermodynamically more favorable. Both the thermodynamic model and kinetic parameters used in the process have been thoroughly verified.

Through exploration of various reaction pathways and designs, the study evolves from an initial process (Design 1) to an enhanced version (Design 2). Design 2, incorporating the Methane Steam Reforming (MSR) reaction, effectively mitigates excessive methane production, reduces the need for a purge stream, and minimizes reactant wastage. This modification results in decreased reactant consumption, increased ethanol production, and improved purity. The simulation results, presented in Table 1, indicate a 21% reduction in H_2 consumption, a 52% reduction in CO_2 consumption, and a 43% increase in ethanol production compared to Design 1, and the final purity of ethanol is 99.5% (mol%) These findings underscore the potential of CO_2 conversion into ethanol as a sustainable and efficient pathway for renewable energy and carbon reduction.

For future work, there is a need for in-depth research on optimizing the CO_2-to-ethanol process. This involves refining and fine-tuning the various stages of the process to enhance efficiency and overall performance. Additionally, efforts should be directed towards seamless integration of CO_2-to-ethanol processes into the renewable energy supply chain. This integration calls for the development of advanced methods for the storage, transportation, and reforming of ethanol. Efficient and sustainable solutions in these areas are crucial for the successful incorporation of ethanol as a renewable fuel within the broader energy infrastructure. Furthermore, exploring the multifaceted role of ethanol as an energy carrier and investigating its diverse applications within the supply chain will be paramount. By placing a strong emphasis on process optimization and integration, future research endeavours can significantly contribute to the creation of a more sustainable, resilient, and environmentally friendly energy ecosystem.

Table 1. simulation results

Process		Design 1	Design 2
mole flow rate (kmol/h)	H_2	170	134.5
	CO_2	105	50
	ETOH	12.25	17.48
purity	ETOH	0.98	0.995

References

[1] Pang, Jifeng, Et Al. “Chapter Two - Synthesis Of Ethanol And Its Catalytic Conversion.” Sciencedirect, Academic Press, 1 Jan. 2019, Www.Sciencedirect.Com/Science/Article/Pii/S036005641930001x.

[2] Kang, Jincan, Et Al. “Single-Pass Transformation Of Syngas Into Ethanol With High Selectivity By Triple Tandem Catalysis.” Nature Communications, Vol. 11, No. 1, 11 Feb. 2020, P. 827, Www.Nature.Com/Articles/S41467-020-14672-8, Https://Doi.Org/10.1038/

[3] Li, Xiaopeng, Et Al. “Research Progress Of Hydrogenation Of Carbon Dioxide To Ethanol.” Chemical Engineering Science, Vol. 282, 5 Dec. 2023, P. 119226, Www.Sciencedirect.Com/Science/Article/Pii/S0009250923007820?Dgcid=Rss_Sd_All, Https://Doi.Org/10.1016/J.Ces.2023.119226. Accessed 6 Nov. 2023.

[4] Zhang, Lei, Et Al. “Entropy Generation Minimization For Reverse Water Gas Shift (Rwgs) Reactors.” Entropy, Vol. 20, No. 6, 29 May 2018, P. 415, Https://Doi.Org/10.3390/E20060415. Accessed 10 Oct. 2019.

[5] Vendas, Maria. Co Production Via Reverse Water-Gas Shift Reaction For Fischer-Tropsch Applications Maria Da Luz Pais Vendas Dissertação De Mestrado Apresentada À Faculdade De Engenharia Da Universidade Do Porto Em Chemical Engineering M 2020.

[6] Portillo, M. A., Et Al. “A Kinetic Model For The Synthesis Of Ethanol From Syngas And Methanol Over An Alkali-Co Doped Molybdenum Sulfide Catalyst: Model Building And Validation At Bench Scale.” Fuel Processing Technology, Vol. 151, 1 Oct. 2016, Pp. 19–30, Https://Doi.Org/10.1016/J.Fuproc.2016.05.027. Accessed 24 Oct. 2023.

[7] Chen, Kun, Et Al. “The Intrinsic Kinetics Of Methane Steam Reforming Over A Nickel-Based Catalyst In A Micro Fluidized Bed Reaction System.” International Journal Of Hydrogen Energy, Dec. 2019, Https://Doi.Org/10.1016/J.Ijhydene.2019.11.080. Accessed 23 Dec. 2019.

ESCAPE-34 PSE-2024
European Symposium on Computer Aided Process Engineering
&
Process Systems Engineering

Flavio Manenti, Gintaras V. Reklaitis (Eds.), Book of Abstract of the 34th European Symposium on Computer Aided Process Engineering / 15th International Symposium on Process Systems Engineering (ESCAPE34/PSE24), June 2-6, 2024, Florence, Italy.

Data-driven Epidemic Inference Through Decomposition of Large-scale Nonlinear Optimization Problems

Laurens R. Lueg[a], Michael L. Bynum[b], Carl D. Laird[a]*, Lorenz T. Biegler[a]

[a]*Chemical Engineering Department, Carnegie Mellon University, Pittsburgh, PA, USA*
[b]*Sandia National Laboratories, Albuquerque, NM, USA*
claird@andrew.cmu.edu

Abstract

The COVID-19 pandemic has demonstrated that a systematic understanding of the dynamics of infectious diseases is crucial to reduce their impact on a population. To this end, the use of epidemiological models has proved effective for both parameter estimation and epidemic control problems. In this work, we formulate a compartmental epidemic model on a US national scale with county-level granularity and fit relevant spatio-temporal parameters to data collected during the early stages of the COVID-19 pandemic. Conventional, serial solvers struggle to solve large-scale, nonlinear optimization problems such as this within reasonable time limits. Instead, we exploit the problem's structure to apply a Schur complement decomposition. This allows for the computationally most expensive operation in an interior point method, the computation of the step direction, to be parallelized. We demonstrate promising scaling properties of this method when applied to large-scale epidemic inference problems on a moderately-sized parallel computer.

Keywords: large-scale nonlinear optimization, parallel computing, decomposition, epidemic modeling

1. Introduction

The outbreak of the COVID-19 pandemic had an unprecedented impact across the world. Significant excess deaths, stress on medical infrastructures and sustained economic fallout were amongst the most acute direct consequences. Toward the goal of guiding public health responses, epidemiological models are an important tool to understand the dynamics of infectious diseases and plan mitigation strategies accordingly. In this work, we present efficient computational approaches to solve large-scale parameter estimation problems arising from epidemic models.

2. Methodology

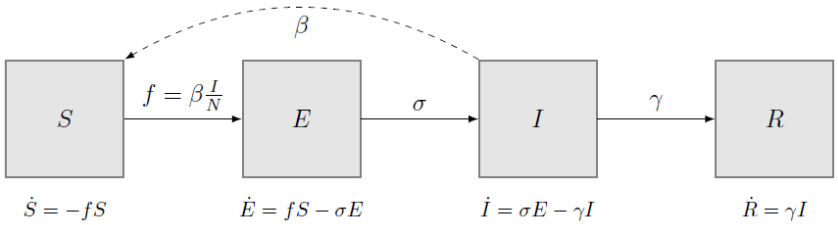

Figure 1: SEIR model for a single population. Rectangles depict the compartments, solid arrows, the movements of individuals between them. The dashed arrow visualizes contact between compartments, leading to transmission of the disease.

Compartmental models have proved effective in describing the spread of various infectious diseases (Rock et al., 2014). The population is divided into compartments, which represent different stages of a disease, i.e., susceptible (*S*), exposed (*E*), infectious (*I*) or recovered (*R*). The dynamics of individuals between compartments over time are determined by the contact, incubation, and recovery rates (β, σ and γ, respectively), which may vary across time and space. For a visualization of this dynamic model for a single population see Fig. 1.

In this work, we applied a large-scale, model-based approach to estimate epidemic model parameters based on policy-related descriptors. To reflect the spatial heterogeneity in the US, separate epidemiological compartments are defined on a county level. Interaction between counties is modeled using information on mobility patterns, in this work we use census data on commuting flows (US Census Bureau, 2020). The contact rate parameters for each county are defined as piecewise-constant functions, depending on the implementation of public health responses, such as mask mandates, over time in each county. Additional terms accounting for demographic or seasonal factors are possible. This defines a large-scale, nonlinear system of ordinary differential equations with ~10^4 differential state variables (epidemiological compartments for ~3000 counties in the US), discretized over a time horizon of several months. The parameters of this model are fitted to case data collected during the beginning of the COVID-19 pandemic.

Optimization problems such as this are usually solved using interior point algorithms. Serial implementations struggle to solve problems of this scale within reasonable time limits. Instead, we exploit the problem's structure to apply a Schur complement decomposition (Kang et al., 2014). This allows for the computationally most expensive operation in an interior point method, the computation of the step direction, to be parallelized. The epidemic model at hand is amenable to this decomposition, as there are only a few shared variables between counties, i.e., the factors associated with the effect of different non-pharmaceutical interventions (NPIs) on the local contact rates. Below, the promising scaling properties of this method are demonstrated.

3. Results

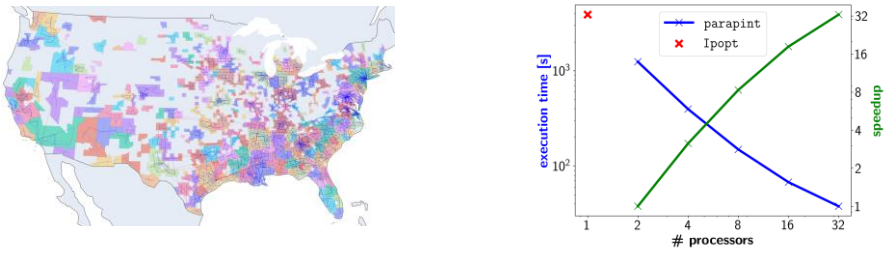

(a) (b)

Figure 2: (a) Map of counties considered for national scale model. Shading is based on the spatial decomposition of counties for parallelization. (b) Strong scaling of parallel Schur complement method. Speedup computed relative to two core execution. Solution time using *Ipopt* solver is shown for serial case.

The parameter estimation problem was solved simultaneously for 1900 counties in the US (see Fig. 2a) over the first 170 days of the pandemic. The full 3142 counties of the US were not considered because those with fewer total cases than 0.1% of the county population during this period were discarded. All parameters other than β were fixed to common values from literature (Yang et al., 2021). Three NPIs were included in the model: mask mandates, school closings and stay-at-home orders, with state-level implementation dates taken from the sources listed in Yang et al. (2021). All tests were performed using an x86 machine with 32 cores, each with a clock rate of 3.3 GHz. The parallel Schur complement method was applied to this problem using the *parapint* package (Rodriguez et al., 2023). The scaling of the solution time with an increasing number of parallel processors was observed, with results shown in Fig. 2b. In our model, each of the NPIs considered in this work reduced the contact rate by 11-15% when implemented in the respective counties. These values are reasonably close to statistical estimates listed in other works (Yang et al., 2021), but come with yet unquantified confidence intervals stemming from both model and measurement uncertainty.

4. Conclusion

We use a dynamic compartmental model for COVID-19 with county-level granularity, which considers inter-county infections through commuters and quantifies the effect of non-pharmaceutical interventions (NPIs) on the contact rate between individuals. The parallel Schur complement method was applied to solve this large-scale nonlinear programming problem on a US national scale, with significant speedup when using 32 cores, compared to the serial state-of-the-art solver *Ipopt* (Wächter and Biegler, 2006). The qualitative results suggest that the implementation of NPIs had an adverse effect on the spread of COVID-19. Uncertainty quantification for these results remains as future work.

Acknowledgements

Sandia National Laboratories is a multi-mission laboratory managed and operated by National Technology & Engineering Solutions of Sandia, LLC (NTESS), a wholly owned subsidiary of Honeywell International Inc., for the U.S. Department of Energy's National Nuclear Security Administration (DOE/NNSA) under contract DE-NA0003525. This written work is authored by an employee of NTESS. The employee, not NTESS, owns the right, title and interest in and to the written work and is responsible for its contents. Any subjective views or opinions that might be expressed in the written work do not necessarily represent the views of the U.S. Government. The publisher acknowledges that the U.S. Government retains a non-exclusive, paid-up, irrevocable, world-wide license to publish or reproduce the published form of this written work or allow others to do so, for U.S. Government purposes. The DOE will provide public access to results of federally sponsored research in accordance with the DOE Public Access Plan.

References

J. Kang, Y. Cao, D. P.Word, and C. D. Laird, 2014. An interior-point method for efficient solution of block-structured nlp problems using an implicit schur-complement decomposition. Computers & Chemical Engineering, 71:563–573.

K. Rock, S. Brand, J. Moir, and M. J. Keeling, 2014. Dynamics of infectious diseases. Reports on Progress in Physics, 77(2):026602.

J. S. Rodriguez, R. B. Parker, C. D. Laird, B. L. Nicholson, J. D. Siirola, and M. L. Bynum, 2023, Scalable parallel nonlinear optimization with pynumero and parapint. INFORMS Journal on Computing, 35(2):509–517.

United States Census Bureau, 2020 Census Results, retrieved in July 2023. URL: https://www.census.gov/data/tables/2020/demo/metro-micro/commuting-flows-2020.html

A. Wächter and L. T. Biegler, 2006, On the implementation of an interior-point filter line-search algorithm for large-scale nonlinear programming, Mathematical programming, 106:25–57.

B. Yang, A. T. Huang, B. Garcia-Carreras, W. E. Hart, A. Staid, M. D. Hitchings, E. C. Lee, C. J. Howe, K. H. Grantz, A. Wesolowksi, et al., 2021, Effect of specific non-pharmaceutical intervention policies on sars-cov-2 transmission in the counties of the united states. Nature communications, 12(1):3560.

ESCAPE-34 PSE-2024
European Symposium on Computer Aided Process Engineering
&
Process Systems Engineering

Flavio Manenti, Gintaras V. Reklaitis (Eds.), Book of Abstract of the 34th European Symposium on Computer Aided Process Engineering / 15th International Symposium on Process Systems Engineering (ESCAPE34/PSE24), June 2-6, 2024, Florence, Italy.

Feasibility Analysis of Dimethyl Ether-based International Renewable Energy Supply Chain

Chong Wei Ong,[a] Sheng-Chi Lien,[a] Tsai-Wei Wu,[b] Cheng-Liang Chen[a]*

[a]*Department of Chemical Engineering, National Taiwan University, No. 1, Sec. 4, Roosevelt Rd., Taipei 106319, Taiwan (R.O.C.)*
[b]*Department of Frontier Science for Advanced Environment, Graduate School of Environmental Studies, Tohoku University, 468-1 Aramaki Aza Aoba, Aoba-ku Sendai, Miyagi, Japan, 980-8572*
**CCL@ntu.edu.tw*

Abstract

To tackle the urgent global challenge of climate change and the unequal distribution of renewable resources, a transition plan toward sustainable, low-carbon energy systems is imperative. This study introduces an international renewable energy supply chain leveraging dimethyl ether (DME) as an energy carrier. In pursuit of the 2050 net-zero carbon emissions target, this supply chain establishes a connection between two nations: one abundant in renewable energy resources as an energy-exporting country and the other lacking such resources as an energy-importing country. In the exporting country, renewable energy is harnessed for electrolysis to produce hydrogen (H_2). Due to the high costs associated with H_2 in terms of transportation and storage, using DME as an energy carrier for H_2 enhance the feasibility of implementing this supply chain. Consequently, DME is synthesized from H_2 and captured CO_2 and transported to the importing country via shipping. Upon reaching the importing country, two viable methods for DME utilization emerge. The first option involves converting DME back into H_2 via steam reforming process, which can then be employed in fuel cells for electricity generation. The second option entails introducing DME as fuel into oxy-combustion CO_2 power plants, generating electricity. Simultaneously, the resultant CO_2 is captured and transported to the exporting country for DME synthesis. This research assesses the feasibility of both application approaches, considering engineering, economic and environmental aspects. Furthermore, simulations and analyses of the chemical processes are carried out, along with the economic evaluations of these processes, electrolysis, fuel cells and transportation. Lastly, the costs of DME, H_2 and green electricity in the importing country are evaluated to analyse the feasibility of this supply chain. The current result show that the cost of imported electricity is USD 135.42/MWh_e with an electricity conversion rate between both regions is 30.8% (=4.358/14.145), and the carbon emission of this supply chain using solar and wind power are 0.190 and 0.069 t/MWh_e respectively.

Keywords: Dimethyl ether, Energy carrier, Hydrogen fuel cells, Oxy-combustion, International renewable energy supply chain

1. Introduction

To address the urgent global challenge posed by climate change and the uneven distribution of renewable resources, it is crucial to implement a transition plan towards sustainable, low-carbon energy systems. Countries such as Australia and Saudi Arabia (Wang et al., 2023), which possess abundant natural resources, have the capacity to generate significant amounts of renewable energy. This surplus energy can be efficiently transformed into green hydrogen (H_2) through electrolysis and stored for future use. However, the transportation of H_2 is costly (Brändle et al., 2021). Therefore, to provide a cost-effective alternative, the international renewable energy supply chain relies on chemical energy carriers, which include H_2, methanol (MeOH) (Dalena et al., 2018), ammonia (NH_3) (Hasan et al., 2021), dimethyl ether (DME) (Catizzone et al., 2021) and methylcyclohexane (MCH) (Matsuoka et al., 2017). These carriers can be transported to energy-importing nations like Japan and Germany (Wijayanta et al., 2019), as depicted in Figure 1. Subsequently, these carriers can be used directly or converted into H_2, facilitating the transfer of renewable energy between countries.

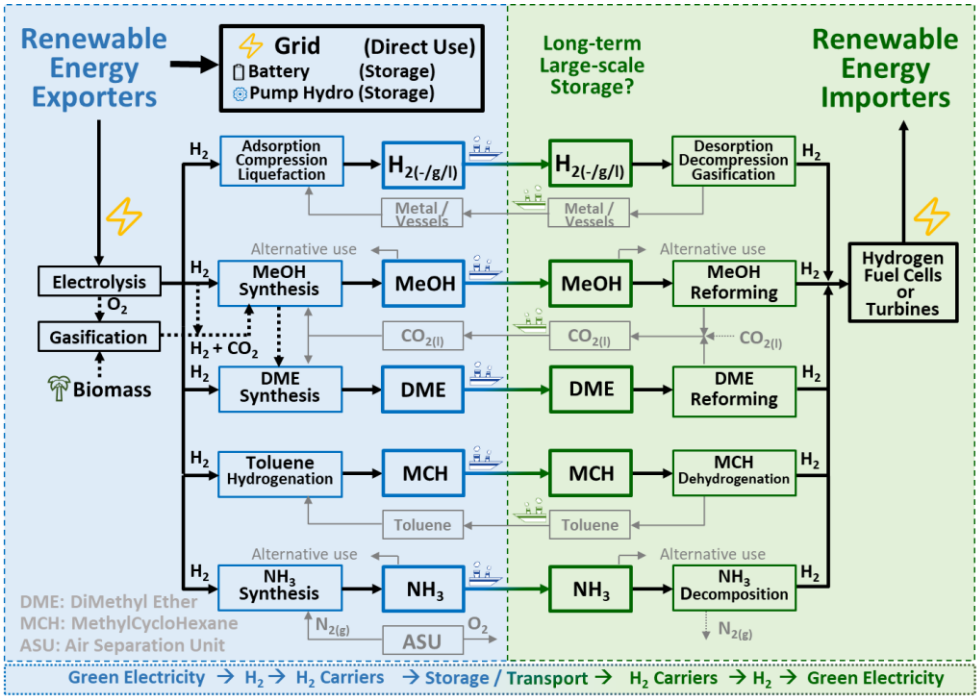

Figure 1 International renewable energy supply chains.

When considering MeOH, DME and MCH as energy carriers, it's crucial to address the by-products of MeOH or DME reforming (CO_2) and MCH dehydrogenation (toluene). These by-products should be efficiently transported back to the exporting country for MeOH or DME synthesis or toluene hydrogenation, creating a closed-loop circulation system that minimizes waste. On the other hand, transporting the by-product of NH_3 decomposition, nitrogen, is not cost-effective. Instead, utilizing an air separation unit (ASU) to produce nitrogen proves to be a more economically viable solution, eliminating the need for nitrogen transportation.

In comparison to gas-phase H_2 (Moradi and Groth, 2019) and NH_3 (Klerke et al., 2008), MeOH stands out due to its ability to be stored in a liquid state at room temperature and atmospheric pressure. This characteristic results in lower storage costs and improved safety. While DME requires liquefaction at -33°C for transportation, it boasts a significantly higher gravimetric and volumetric energy density when compared to MeOH, MCH, and NH_3 (Table 1). Despite the need for careful handling due to its narrow explosive limit in air, the safety perspective suggests that DME is a suitable candidate as an energy carrier. While extensive research focuses on MeOH, MCH, and NH_3 as energy carriers, there is a noticeable scarcity of comprehensive analyses on DME, particularly in the context of an international renewable energy supply chain. Therefore, an in-depth exploration of the DME-based international renewable energy supply chain is a worthwhile avenue for further study.

Table 1. Properties of chemical energy carriers.

Properties	H_2	MeOH	DME	MCH	NH_3
Boiling point (°C)	-253	64.7	-25	101	-33
Gravimetric energy density (MJ/kg)	120	15	28	7.4	21.2
Volumetric energy density (MJ/L)	8.5	11.9	19	5.7	14.4
Explosive limit in air (vol%)	4-75	6.7-36	3.2-18.6	1.2-6.7	15-28

To aligns with the ambitious 2050 net-zero carbon emissions goal, this study presents a feasibility analysis of the international renewable electricity supply chain that utilizes DME as energy carrier which fosters a vital connection between two countries. One rich in renewable energy resources, serving as an energy-exporting country, and the other deficient in these resources, acting as an energy-importing country. In the exporting country, renewable energy is employed for electrolysis, generating H_2 and DME is produced through the synthesis process of H_2 and captured carbon dioxide (CO_2) (Wu and Chien, 2022), then transported to the importing country via shipping.

Upon arrival in the importing country, two practical methods for utilizing DME come to the forefront. As illustrated in Figure 2(a), the first approach involves the conversion of DME back into H_2 through a steam reforming process. This H_2 can then be utilized in fuel cells to generate electricity. The second option, depicted in Figure 2(b), involves using DME as a fuel source in oxy-combustion CO_2 power plants, known as the Allam cycle, for electricity generation. Simultaneously, the resulting CO_2 is captured and transported back to the exporting country for DME synthesis. This research is therefore comparing the feasibility of the supply chain using both power generation approaches, considering engineering, economic and environmental aspects. Furthermore, simulations and analyses of the chemical processes are carried out, along with the economic evaluations of these processes, electrolysis, fuel cells and transportation. Lastly, the costs of DME, H_2 and green electricity in the importing country are evaluated to analyze the feasibility of this supply chain.

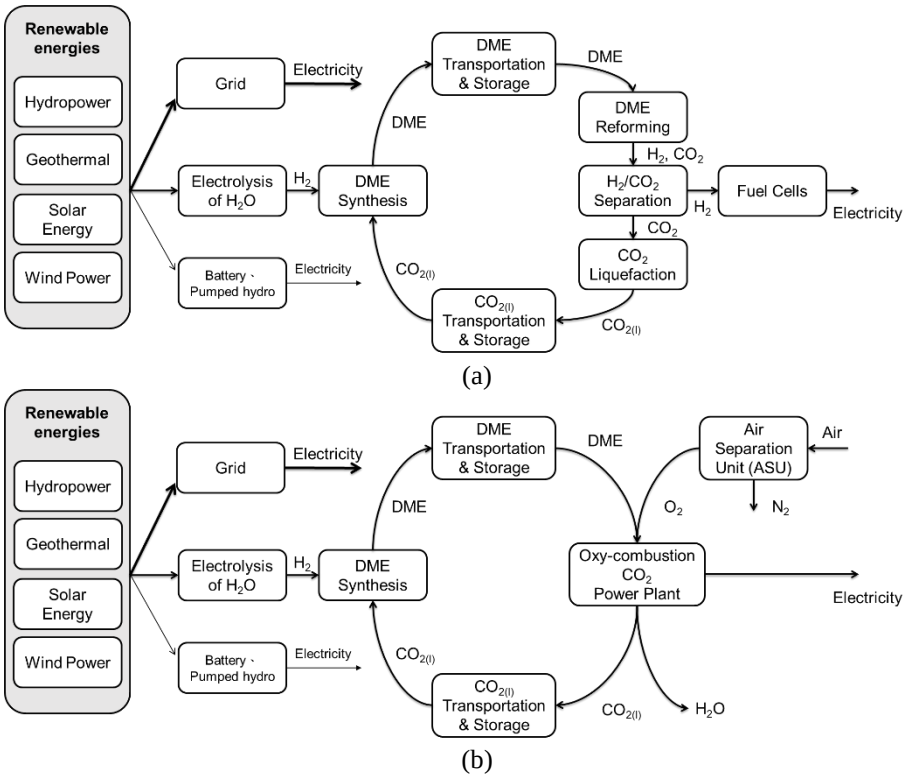

Figure 2 Conceptual design of DME-based international renewable electricity supply chain generating electricity with (a) fuel cells (b) oxy-combustion power plant.

Based on the simulation using Aspen Plus, the capital and operating costs of various chemical processes, including DME synthesis, H_2 production through DME reforming, CO_2 liquefaction and oxy-combustion CO_2 power plant can be calculated. Additionally, economic assessments are also conducted for water electrolysis (Hodges et al., 2022), fuel cells (Jamil et al., 2022), and transportation (Placek, 2023). To account for advancing technology and ensure sustainability, the efficiency of electrolysis in sustainable future is assumed at 98%, based on the higher heating value (HHV) of H_2 (39.39 MWh_e/t). The cost of water electrolysis is estimated at 200 USD/kW. Solid oxide fuel cells (SOFC) are assumed to have an efficiency of 30% for thermal heat (LHV) and 55% for electricity (LHV), with a cost of 1,000 USD/kW.

The cost of green H_2 production is significantly influenced by renewable energy electricity prices. The levelized cost of electricity (LCOE) for utility-scale solar photovoltaics (PV) is assumed to be USD 45/MWh_e, with a projected decrease to USD 15/MWh_e by 2050. Therefore, cost of renewable energy is assumed to be USD 30/MWh_e in this study. Additionally, the carbon emissions associated with this process are estimated at 11 kg/MWh_e from a life cycle perspective (Bruckner et al., 2014). On the other hand, the transportation of DME and CO_2 between exporting and importing countries predominantly relies on shipping. Assume that a ship has a capacity of 312,500 cubic meters and travels at a speed of 12 knots. For the shipping route from Australia to Japan, which spans approximately 10,000 km, the ship is assumed to operate for 350 days each year, with a turnover time of one day. The capital cost associated with the DME/CO_2

shipping vessel is estimated at 150.2 million USD (Al-Breiki and Bicer, 2020). In general, very low sulfur fuel oil (VLSFO) is chosen as the fuel source, and its approximate cost is 550 USD/t. It's worth noting that for every metric tonne of this fuel consumed, it generates 3.15t of CO_2 emissions. The sensitivity analysis of each important variables will be carried for optimization.

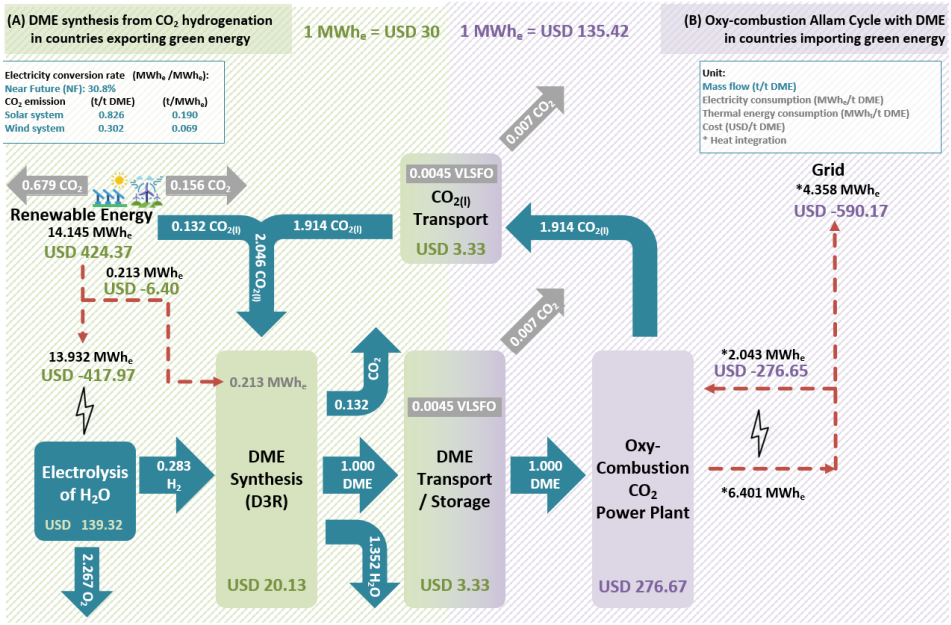

Figure 3 Techno-economic and carbon emission analyses result of DME-based international renewable electricity supply chain generating electricity with oxy-combustion power plant.

The process simulations of the chemical processes using Aspen Plus and techno-economic analysis of both DME-based international renewable electricity supply chains are carried out in this study. The techno-economic and carbon emission analyses result of DME-based international renewable electricity supply chain generating electricity with oxy-combustion power plant are depicted in Figure 3. The cost of imported electricity is USD 135.42/MWh_e with an electricity conversion rate between both regions is 30.8% (=4.358/14.145), and the carbon emission of this supply chain using solar and wind power are 0.190 and 0.069 t/MWh_e respectively. To compare the performance, the electricity conversion rate between the imported electricity and renewable electricity and the cost of imported electricity of the other pathway will be discussed in future.

2. Conclusions

In conclusion, the utilization of dimethyl ether (DME) as an energy carrier in an international renewable electricity supply chain is seen as a promising solution to address the global issues of climate change and the uneven distribution of renewable resources. The supply chain design offers two power generation options: hydrogen (H_2) fuel cells and oxy-combustion power plants. To determine a more economical, environmentally friendly and efficient choice, the chemical processes simulations and techno-economic analysis of both supply chains are carried out.

References

M. Al-Breiki, and Y. Bicer. (2020). "Comparative cost assessment of sustainable energy carriers produced from natural gas accounting for boil-off gas and social cost of carbon." *Energy Reports*, 6, 1897-1909.

G. Brändle, M. Schönfisch, and S. Schulte. (2021). "Estimating long-term global supply costs for low-carbon hydrogen." *Applied Energy*, 302, 117481.

T. Bruckner, L. Fulton, E. Hertwich, A. McKinnon, D. Perczyk, J. Roy, R. Schaeffer, S. Schlömer, R. Sims, and P. Smith. (2014). "Technology-specific cost and performance parameters [annex III]", *Climate Change 2014: Mitigation of Climate Change*. Cambridge University Press, pp. 1329-1356.

E. Catizzone, C. Freda, G. Braccio, F. Frusteri, and G. Bonura. (2021). "Dimethyl ether as circular hydrogen carrier: Catalytic aspects of hydrogenation/dehydrogenation steps." *Journal of Energy Chemistry*, 58, 55-77.

F. Dalena, A. Senatore, A. Marino, A. Gordano, M. Basile, and A. Basile. (2018). "Methanol production and applications: an overview." *Methanol*, 3-28.

M.H. Hasan, T.M.I. Mahlia, M. Mofijur, I. Rizwanul Fattah, F. Handayani, H.C. Ong, and A. Silitonga. (2021). "A comprehensive review on the recent development of ammonia as a renewable energy carrier." *Energies*, 14(13), 3732.

A. Hodges, A.L. Hoang, G. Tsekouras, K. Wagner, C.-Y. Lee, G.F. Swiegers, and G.G. Wallace. (2022). "A high-performance capillary-fed electrolysis cell promises more cost-competitive renewable hydrogen." *Nature communications*, 13(1), 1304.

A. Jamil, S. Rafiq, T. Iqbal, H.A.A. Khan, H.M. Khan, B. Azeem, M.Z. Mustafa, and A.S. Hanbazazah. (2022). "Current status and future perspectives of proton exchange membranes for hydrogen fuel cells." *Chemosphere*, 303, 135204.

A. Klerke, C.H. Christensen, J.K. Nørskov, and T. Vegge. (2008). "Ammonia for hydrogen storage: challenges and opportunities." *Journal of Materials Chemistry*, 18(20), 2304-2310.

K. Matsuoka, K. Miyoshi, and Y. Sato. (2017). "Electrochemical reduction of toluene to methylcyclohexane for use as an energy carrier." *Journal of Power Sources*, 343, 156-160.

R. Moradi, and K.M. Groth. (2019). "Hydrogen storage and delivery: Review of the state of the art technologies and risk and reliability analysis." *International Journal of Hydrogen Energy*, 44(23), 12254-12269.

M. Placek. (2023). " Average monthly price of very low sulfur fuel oil (VLSFO) from November 2019 to May 2023 ". City: statista.

F. Wang, R. Swinbourn, and C.e. Li. (2023). "Shipping Australian sunshine: Liquid renewable green fuel export." *International Journal of Hydrogen Energy*, 48(39), 14763-14784.

A.T. Wijayanta, T. Oda, C.W. Purnomo, T. Kashiwagi, and M. Aziz. (2019). "Liquid hydrogen, methylcyclohexane, and ammonia as potential hydrogen storage: Comparison review." *International Journal of Hydrogen Energy*, 44(29), 15026-15044.

T.-W. Wu, and I.-L. Chien. (2022). "A novel energy-efficient process of converting CO2 to dimethyl ether with techno-economic and environmental evaluation." *Chemical Engineering Research and Design*, 177, 1-12.

ESCAPE-34 PSE-2024
European Symposium on Computer Aided Process Engineering
&
Process Systems Engineering

Flavio Manenti, Gintaras V. Reklaitis (Eds.), Book of Abstract of the 34th European Symposium on Computer Aided Process Engineering / 15th International Symposium on Process Systems Engineering (ESCAPE34/PSE24), June 2-6, 2024, Florence, Italy.

Conceptual Process Design for Hydrogenating Carbon Dioxide to Produce Ethanol

Hao-Chu Chang, Chong Wei Ong, Cheng-Liang Chen*

Department of Chemical Engineering, National Taiwan University, Taipei 10617, Taiwan CCL@ntu.edu.tw

Abstract

Global warming and the energy crisis have become some of the most significant challenges facing the world today. With the finite nature of fossil fuels and ever-increasing carbon emissions, there is an urgent need to transition to renewable energy sources to mitigate the irreversible impact on our planet. This study aims to design a process flowsheet for ethanol synthesis by carbon dioxide hydrogenation using Aspen Plus. Ethanol serves a dual purpose as a renewable energy carrier and a fuel, aligning with Carbon Capture and Utilization (CCU) and contributing to carbon reduction efforts.

Keywords: Global warming, CO_2 hydrogenation, Ethanol synthesis, Process design, Aspen Plus.

1. Introduction

Nowadays we are facing the challenges of global warming and energy shortages. Conventional energy production methods, such as fossil fuels, are major contributors to increased CO2 emissions, a primary greenhouse gas. In response to these issues, this study focuses on hydronation of CO2 to synthesize ethanol, which satisfies the concept of Carbon Capture and Utilization (CCU). Ethanol serves two primary purposes. Firstly, ethanol's liquid state under normal conditions and its limited flammability in the air make it a potential candidate for energy carrier within the renewable energy supply chain. However, a comprehensive evaluation is needed when compared to other energy carriers like methanol and ammonia. Secondly, ethanol can also function as a fuel, combusting with oxygen. Moreover, CO2 hydrogenation to synthesize ethanol doesn't compete with food supplies, a key distinction from conventional starch fermentation. Thus, the investigation into ethanol synthesis through CO2 hydrogenation is a promising studying.

The overall framework is shown in Figure 1,including both export and import sides, and illustrates the entire ethanol supply chain. The process uses two reactants - hydrogen and carbon dioxide. Hydrogen comes from renewable energy sources through water electrolysis and carbon dioxide comes from carbon capture. Once ethanol has been synthesized, the intermittent nature of most renewables means that the storage and transport part is essential. When ethanol as an energy carrier arrives on the import side, it can be used in two ways as described above. This study will focus on the synthesis part of ethanol.

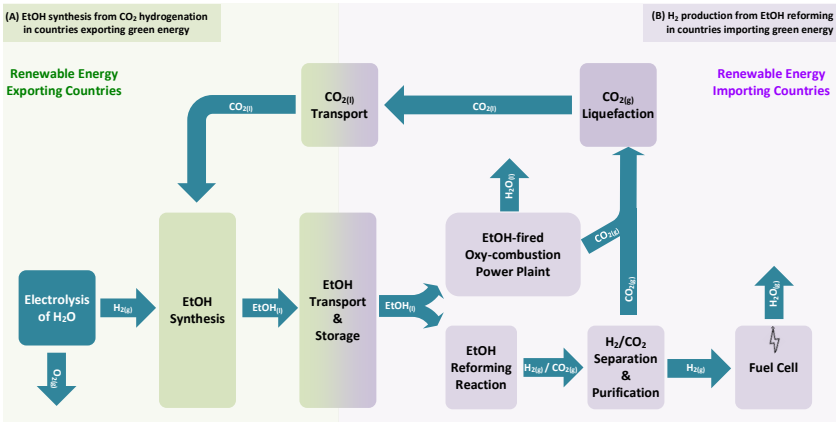

Figure 1. The overall framework of the synthesis and use of ethanol

2. Process Design for Hydrogenating Carbon Dioxide to Produce Ethanol

2.1. Thermodynamic Models & Chemical Reactions

The process of hydrogenating carbon dioxide is simulated by Aspen Plus using two thermodynamic models: the Peng-Robinson equation of state in the reaction section and the UNIQUAC model with Henry's constant in the separation section.

A total of three reactions are considered in this study: the reverse Water Gas Shift reaction (rWGS), the ethanol (EtOH) synthesis, and the Methane Steam Reforming (MSR). All have been verified, and further details are given below. The rWGS reaction is provided in the work of Zhang *et al.*[4] and Vendas and Maria[5].

$$CO_2 + H_2 \rightleftharpoons CO + H_2O \quad (1)$$

The EtOH synthesis reaction includes five reactions provided by Portillo *et al.*[6]. All of them are assumed to be irreversible except the rWGS reaction (6).

$$CO + 2H_2 \rightarrow CH_3OH \quad (2)$$

$$CO + 2H_2 + CH_3OH \rightarrow C_2H_5OH + H_2O \quad (3)$$

$$CO + 2H_2 + C_2H_5OH \rightarrow C_3H_7OH + H_2O \quad (4)$$

$$H_2 + CH_3OH \rightarrow CH_4 + H_2O \quad (5)$$

$$CO + H_2O \rightleftharpoons CO_2 + H_2 \quad (6)$$

The MSR reaction includes two reactions, which utilize the power-law model (Eq. 7 - Eq. 8) provided by Chen *et al.*[7].

$$CH_4 + H_2O \rightarrow CO + 3H_2 \quad (7)$$

$$CH_4 + 2H_2O \rightarrow CO_2 + 4H_2 \quad (8)$$

2.2. Process Statements

This study includes two distinct designs, each detailed in the process block flow diagrams shown in Figure 2 and Figure 3.

In Design 1, shown in Figure 2, CO_2 is hydronated to syngas in the rWGS reactor using a Pt-based catalyst. Subsequently, syngas is converted to ethanol in the EtOH synthesis reactor using an alkali-Co doped MoS_2 catalyst. The low conversion of CO and selectivity of ethanol results in the need to recycle the stream exiting the EtOH synthesis reactor for sending back to the EtOH synthesis reactor. However, the development of Design 1 reveals the presence of significant methane, necessitating a purge process. The purged gas includes methane and reactants (CO_2, CO, H_2), leading to the wastage of valuable reactants and contributing to process inefficiency. Consequently, this finding has promoted the development of Design 2.

In Design 2, shown in Figure 3, in addition to the reactions mentioned in Design 1, we introduce the MSR reaction to solve excessive methane, turning methane into CO_2, CO, and H_2. This reaction occurs in the MSR reactor, positioned after the EtOH synthesis reactor, and the exiting stream of the MSR reactor is recycled to the rWGS reactor. The methane is completely consumed after the MSR reactor, eliminating the need for a purging process. Moreover, the consumption of reactants is decreased, and the amount of ethanol is increased. Thus, we can use fewer reactants to produce more ethanol. Figure 4 depicts the details of Design 2.

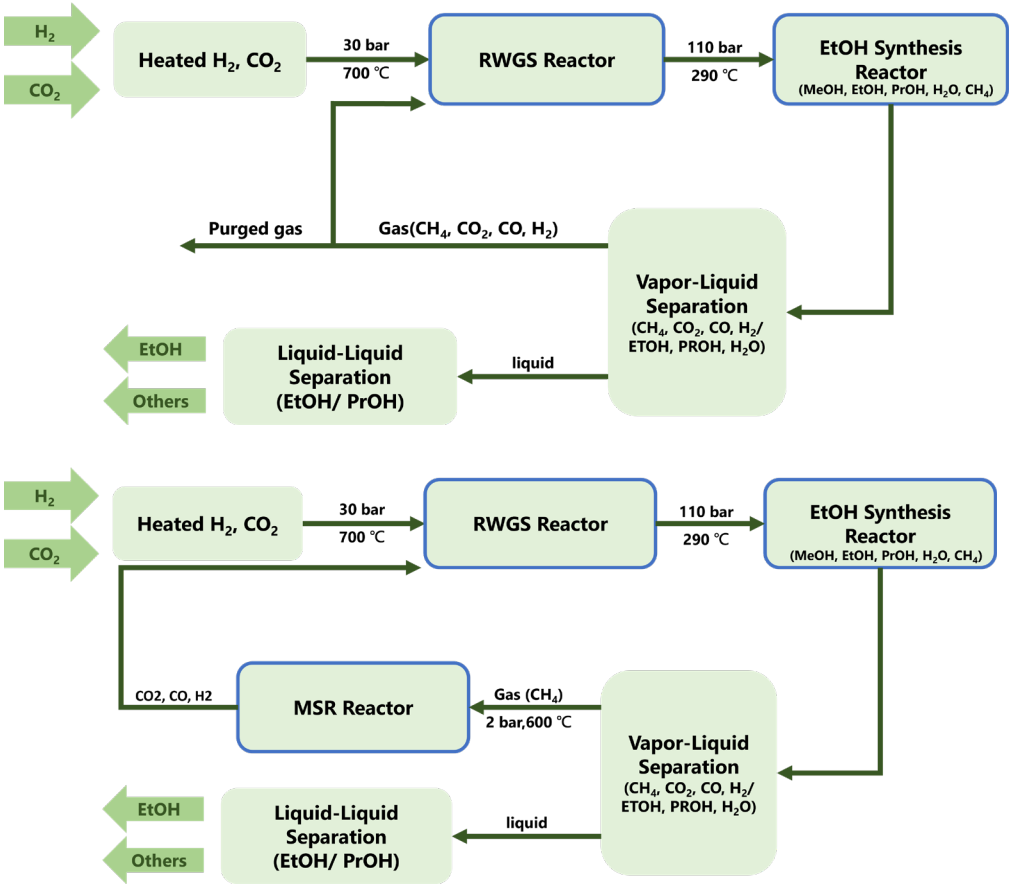

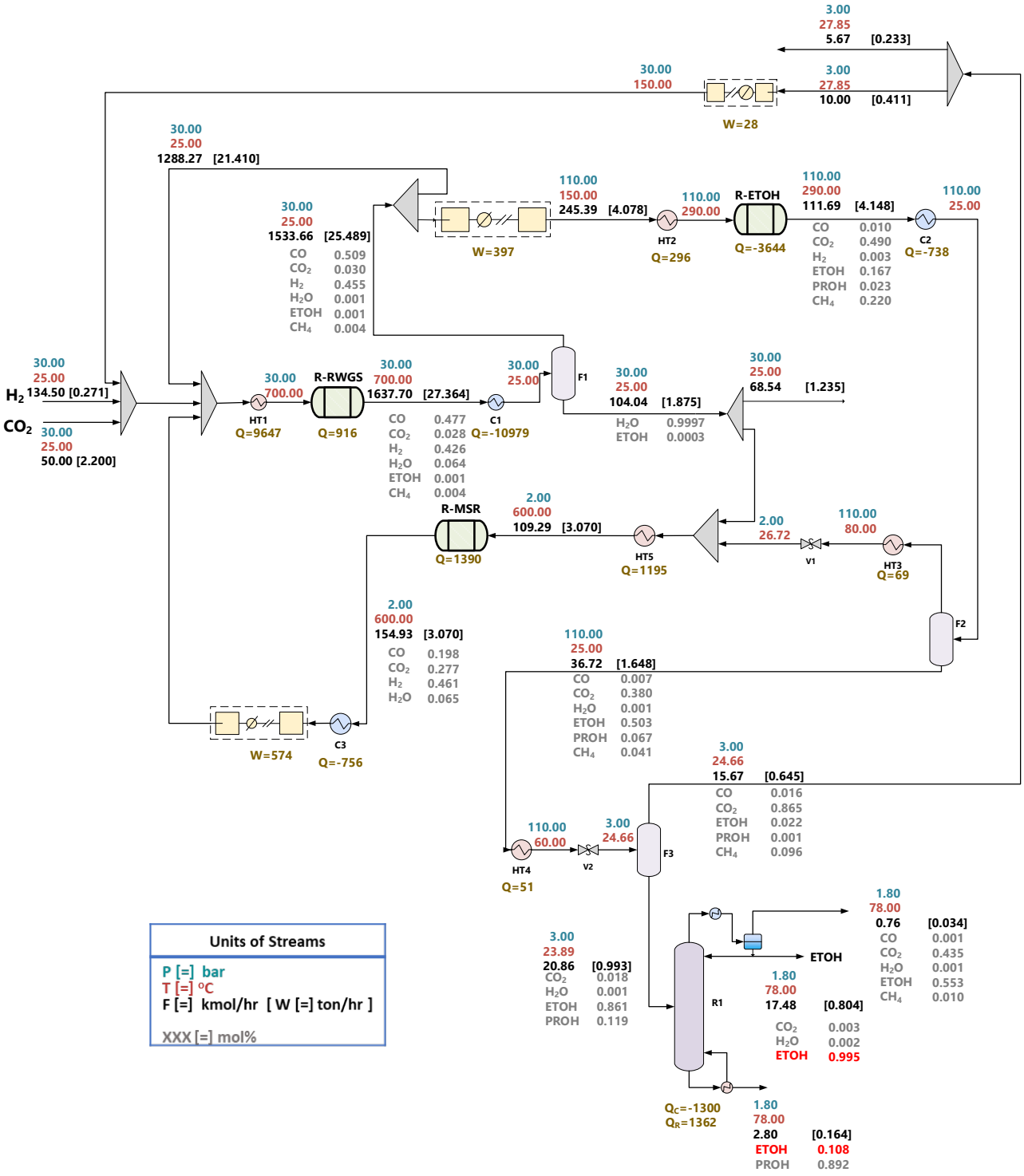

Figure 4. Process flow sheet of Design 2

3. Conclusion

This study simulates the process of CO_2 hydrogenation to ethanol, offering a promising solution to the challenges posed by global warming, carbon emissions, and the need for renewable energy sources. The reactant, CO, undergoes an initial conversion to syngas through the reverse water-gas shift (rWGS) reaction, as CO hydrogenation to ethanol is thermodynamically more favorable. Both the thermodynamic model and kinetic parameters used in the process have been thoroughly verified.

Through exploration of various reaction pathways and designs, the study evolves from an initial process (Design 1) to an enhanced version (Design 2). Design 2, incorporating the Methane Steam Reforming (MSR) reaction, effectively mitigates excessive methane production, reduces the need for a purge stream, and minimizes reactant wastage. This modification results in decreased reactant consumption, increased ethanol production, and improved purity. The simulation results, presented in Table 1, indicate a 21% reduction in H_2 consumption, a 52% reduction in CO_2 consumption, and a 43% increase in ethanol production compared to Design 1, and the final purity of ethanol is 99.5% (mol%) These findings underscore the potential of CO_2 conversion into ethanol as a sustainable and efficient pathway for renewable energy and carbon reduction.

For future work, there is a need for in-depth research on optimizing the CO_2-to-ethanol process. This involves refining and fine-tuning the various stages of the process to enhance efficiency and overall performance. Additionally, efforts should be directed towards seamless integration of CO_2-to-ethanol processes into the renewable energy supply chain. This integration calls for the development of advanced methods for the storage, transportation, and reforming of ethanol. Efficient and sustainable solutions in these areas are crucial for the successful incorporation of ethanol as a renewable fuel within the broader energy infrastructure. Furthermore, exploring the multifaceted role of ethanol as an energy carrier and investigating its diverse applications within the supply chain will be paramount. By placing a strong emphasis on process optimization and integration, future research endeavours can significantly contribute to the creation of a more sustainable, resilient, and environmentally friendly energy ecosystem.

Table 1. simulation results

Process		Design 1	Design 2
mole flow rate (kmol/h)	H_2	170	134.5
	CO_2	105	50
	ETOH	12.25	17.48
purity	ETOH	0.98	0.995

References

[1] Pang, Jifeng, Et Al. “Chapter Two - Synthesis Of Ethanol And Its Catalytic Conversion.” Sciencedirect, Academic Press, 1 Jan. 2019, Www.Sciencedirect.Com/Science/Article/Pii/S036005641930001x.

[2] Kang, Jincan, Et Al. “Single-Pass Transformation Of Syngas Into Ethanol With High Selectivity By Triple Tandem Catalysis.” Nature Communications, Vol. 11, No. 1, 11 Feb. 2020, P. 827, Www.Nature.Com/Articles/S41467-020-14672-8, Https://Doi.Org/10.1038/

[3] Li, Xiaopeng, Et Al. “Research Progress Of Hydrogenation Of Carbon Dioxide To Ethanol.” Chemical Engineering Science, Vol. 282, 5 Dec. 2023, P. 119226, Www.Sciencedirect.Com/Science/Article/Pii/S0009250923007820?Dgcid=Rss_Sd_All, Https://Doi.Org/10.1016/J.Ces.2023.119226. Accessed 6 Nov. 2023.

[4] Zhang, Lei, Et Al. “Entropy Generation Minimization For Reverse Water Gas Shift (Rwgs) Reactors.” Entropy, Vol. 20, No. 6, 29 May 2018, P. 415, Https://Doi.Org/10.3390/E20060415. Accessed 10 Oct. 2019.

[5] Vendas, Maria. Co Production Via Reverse Water-Gas Shift Reaction For Fischer-Tropsch Applications Maria Da Luz Pais Vendas Dissertação De Mestrado Apresentada À Faculdade De Engenharia Da Universidade Do Porto Em Chemical Engineering M 2020.

[6] Portillo, M. A., Et Al. “A Kinetic Model For The Synthesis Of Ethanol From Syngas And Methanol Over An Alkali-Co Doped Molybdenum Sulfide Catalyst: Model Building And Validation At Bench Scale.” Fuel Processing Technology, Vol. 151, 1 Oct. 2016, Pp. 19–30, Https://Doi.Org/10.1016/J.Fuproc.2016.05.027. Accessed 24 Oct. 2023.

[7] Chen, Kun, Et Al. “The Intrinsic Kinetics Of Methane Steam Reforming Over A Nickel-Based Catalyst In A Micro Fluidized Bed Reaction System.” International Journal Of Hydrogen Energy, Dec. 2019, Https://Doi.Org/10.1016/J.Ijhydene.2019.11.080. Accessed 23 Dec. 2019.